CRANFIELD UNIVERSITY

LEIGH MOODY

SENSORS, SENSOR MEASUREMENT FUSION AND MISSILE TRAJECTORY OPTIMISATION

COLLEGE OF DEFENCE TECHNOLOGY

PhD THESIS

CRANFIELD UNIVERSITY

COLLEGE OF DEFENCE TECHNOLOGY

DEPARTMENT OF AEROSPACE, POWER AND SENSORS

PhD THESIS

Academic Year 2002 - 2003

Leigh Moody

Sensors, Measurement Fusion and Missile Trajectory Optimisation

Supervisor: Professor B.A. White

July 2003

ABSTRACT

When considering advances in “smart” weapons it is clear that air-launched systems have adopted an integrated approach to meet rigorous requirements, whereas air-defence systems have not. The demands on sensors, state observation, missile guidance, and simulation for air-defence is the subject of this research. Historical reviews for each topic, justification of favoured techniques and algorithms are provided, using a nomenclature developed to unify these disciplines.

Sensors selected for their enduring impact on future systems are described and simulation models provided. Complex internal systems are reduced to simpler models capable of replicating dominant features, particularly those that adversely effect state observers.

Of the state observer architectures considered, a distributed system comprising ground based target and own-missile tracking, data up-link, and on-board missile measurement and track fusion is the natural choice for air-defence. An IMM is used to process radar measurements, combining the estimates from filters with different target dynamics. The remote missile state observer combines up-linked target tracks and missile plots with IMU and seeker data to provide optimal guidance information.

The performance of traditional PN and CLOS missile guidance is the basis against which on-line trajectory optimisation is judged. Enhanced guidance laws are presented that demand more from the state observers, stressing the importance of time-to-go and transport delays in strap-down systems employing staring array technology. Algorithms for solving the guidance two-point boundary value problems created from the missile state observer output using gradient projection in function space are presented.

A simulation integrating these aspects was developed whose infrastructure, capable of supporting any dynamical model, is described in the air-defence context. MBDA have extended this work creating the Aircraft and Missile Integration Simulation (AMIS) for integrating different launchers and missiles. The maturity of the AMIS makes it a tool for developing pre-launch algorithms for modern air-launched missiles from modern military aircraft.

ACKNOWLEDGEMENTS

Professor B.A. White from the Royal Military College of Science (Shrivenham) kindly supervised this research, leading to PhD thesis submission in July 2003.

Many of the ideas explored in this research were formulated when I was a member of the MBDA Guidance and Control research department at Bristol. During this time the work on missile guidance with Dr. D. Vorley was particularly stimulating; I am indebted to him for the many useful ideas in the field of weave tuning and trajectory optimisation. Although it is difficult to isolate individuals from those researchers referenced and whose work has contributed fundamental to my own, I feel that Kerr, Fitzgerald, Lobia, Li, and Pulford, et. al. deserve a special mention.

Having created a simulation infrastructure for this research it was gratifying that MBDA were prepared to take a radical approach, build upon it, and create a Pan-Project Aircraft and Missile Integration Simulation (AMIS); Akram Ghulam being the most prominent supporter. The synergy between the programs has I believe resulted in two robust, flexible and complimentary simulations; thanks to all those involved in developing the AMIS, for their suggestions and patience during software testing. I would especially like to thank Ian McBride and Rob Zukowski without whom the AMIS would not have flourished; and in particular Paul Heath who alone is responsible for the excellent interactive interface.

Finally, I would like to acknowledge the financial support provided by MBDA and the patience shown over the many years it has taken to produce this work.

LIST OF CONTENTS

LIST OF TABLES

LIST OF FIGURES

Acronyms And Abbreviations

A

A/A	-	Anti-Aliasing Filters
AC	-	Alternating Current
ADC	-	Analogue to Digital Converter
AMIS	-	Aircraft and Missile Integration Simulation
APN	-	Augmented Proportional Navigation
ASRAAM	-	Advanced Short Range Air-to-Air Missile
ATPN	-	Augmented True Proportional Navigation

B

BFGS	-	Broyden-Fletcher-Goldfarb-Shanno VMM
BTT	-	Bank-To-Turn

C

CEP	-	Circular Error Probable
CLOS	-	Command to Line-Of-Sight
CMKF	-	Converted Measurement Kalman Filter
COLOS	-	Command Off Line-Of-Sight
CPU	-	Central Processing Unit
CRT	-	Cathode Ray Tube

D

DAC	-	Digital to Analogue Converter
DC	-	Direct Current
DCL	-	DEC Digital Command Language
DEC	-	Digital Equipment Corporation

DFP	-	Davidon-Fletcher-Powell VMM
DLMS	-	Digital LandMass Survey
DME	-	Direct Measuring Equipment
DoD	-	US Department Of Defense
DoF	-	Degrees Of Freedom
DTED	-	Digital Terrain Elevation Data
DTG	-	Dynamically Tuned Gyroscope

E

ECEF	-	Earth Centred - Earth Fixed frame of reference
ECI	-	Earth Centred Inertial frame of reference
EF 2000	-	Euro-Fighter 2000
EKF	-	Extended Kalman Filter
ENU	-	East-North-Up LGA
EO	-	Electro-Optical tracker
E-W	-	East-West

F

FLIR	-	Forward Looking Infra-Red
FOG	-	Fibre Optical Gyroscope
FOH	-	First Order Hold
FORTRAN	-	FORmat TRANslation
FoR	-	Field-Of-Regard
FoV	-	Field-Of-View
FRD	-	Forward-Right-Down frame of reference

G

GCB	-	Global Common Block
GDOP	-	NAVSTAR GPS Global Dilution Of Precision
GMT	-	General Mean Time
GOT	-	Goal Orientated Tracking
GPB	-	Generalised Pseudo-Bayesian
GPS	-	NAVSTAR Global Positioning System
GTPN	-	Generalised True Proportional Navigation
GUI	-	Graphical User Interface

H

HDOP	-	NAVSTAR GPS Horizontal Dilution Of Precision
HF	-	High Frequency
HMS	-	Helmet Mounted Sight
HUD	-	Head Up Display
HWIL	-	HardWare-In-the-Loop
Hz	-	Hertz

I

ICBM	-	Inter-Continental Ballistic Missile
IEEE	-	The Institute of Electrical and Electronics Engineers
IEKF	-	Iterated Extended Kalman Filter
I/F	-	InterFace
IMM	-	Interacting Multiple Model
IMU	-	Inertial Measurement Unit
INS	-	Inertial Navigation System
I/O	-	Input/Output
IR	-	Infra-Red
ITPN	-	Ideal True Proportional Navigation

J

JSF	-	Joint Strike Fighter

K

KF	-	Kalman Filter

L

LED	-	Light Emitting Diode
LF	-	Low Frequency
LGA	-	Local Geodetic Axes
LORAN	-	LOng RAnge Navigation
LOS	-	Line-Of-Sight
LQR	-	Linear Quadratic Regulator
LRM	-	Long Range Missiles

LSB	-	Least Significant Bit

M

MATLAB	-	MATrix LABoratory
MGEKF	-	Modified Gain Extended Kalman Filter
MIL-STD	-	MILitary-STanDard
MM	-	Multiple Model
MMAE	-	Multiple Model Adaptive Estimator
MRAAM	-	Medium Range Air-to-Air Missile
MSS	-	Multi-Spectral Seeker
MTBF	-	Mean Time Between Failures

N

NASA	-	North American Space Association
NATO	-	North Atlantic Treaty Organisation
NED	-	North-East-Down LGA
N-S	-	North-South

O

OPN	-	Optimum Proportional Navigation

P

PAAMS	-	Principal Air-to-Air Missile System
PDOP	-	NAVSTAR GPS Position Dilution Of Precision
PI	-	Performance Index
PIP	-	Predicted Intercept Point
PN	-	Proportional Navigation
PRF	-	Pulse Repetition Frequency
PSD	-	Power Spectral Density
PPN	-	Pure Proportional Navigation
PPS	-	NAVSTAR GPS Precise Positioning Service
PRBS	-	Pseudo-Random Binary Sequence
PV(A)	-	Position, Velocity and Acceleration
PVT	-	NAVSTAR GPS Position, Velocity and Time
PWM	-	Pulse Width Modulator

R

RCS	-	Radar Cross Section
RF	-	Radio Frequency
RLG	-	Ring Laser Gyroscope
RPY and RP	-	Roll-Pitch-Yaw ordered Euler rotations
RGTPN	-	Realistic Generalised True Proportional Navigation
RTPN	-	Realistic True Proportional Navigation

S

SA	-	NAVSTAR GPS Selective Availability
SDINS	-	StrapDown Inertial Navigation System
SOF	-	Second Order Filter
SI	-	System International units
SITAN	-	Sandia Inertial Terrain Aided Navigation
S/N	-	Signal to Noise
SNR	-	Signal to Noise ratio
SOF	-	Second Order Filter
SRM	-	Short Range Missile
STT	-	Skid-to-Turn

T

TACAN	-	TACtical Air Navigation
TBTPN	-	Target Biased TPN
TDOP	-	NAVSTAR GPS Time Dilution Of Precision
TERCOM	-	TERrain COntour Matching
TERPROM	-	TERrain PROfile Matching
TFA	-	TransFer Alignment
TF	-	Terrain Following
TI	-	Tracking Index
TIALD	-	Thermal Imaging and Laser Designator
TPBVP	-	Two Point Boundary Value Problem
TPN	-	True Proportional Navigation
TRN	-	Terrain Referenced Navigation
TTG	-	Time-To-Go

U

UERE	-	NAVSTAR GPS User Equivalent Range Error
UHF	-	Ultra-High Frequency
UK	-	United Kingdom
US(AF)	-	United States (Air Force)

V

VDOP	-	NAVSTAR GPS Vertical Dilution Of Precision
VHF	-	Very High Frequency
VMM	-	Variable Metric Method
VOR	-	Very high frequency Omni-Range navigation
VS-IMM	-	Variable Structure IMM

W

WGS84	-	World Geodetic System, circa 1984

Y

YP(R)	-	Yaw-Pitch-Roll ordered Euler rotations

Z

ZOH	-	Zero Order Hold

NUMERIC

1D	-	One-Dimension(al)
2D	-	Two-Dimension(al)
3D	-	Three-Dimension(al)

GLOSSARY

A challenge when dealing with several broad disciplines within one application is the nomenclature required to express algorithms in a unified framework. The difficulties faced are compounded when expanding 2-dimensional (2D) algorithms to operate in 3-dimensions (3D), particularly when these relate to a multiple target, launcher and missile environment. As a weapon system gets progressively larger, starting with one-on-one scenarios, and progressing to battlefield models, specific definitions in a central Glossary become unwieldy. Such difficulties are often ignored and disparate nomenclatures accepted as inevitable. During the development of even small weapon systems this can lead to confusion when integrating functionality at the Specification and Simulation level.

This Glossary contains a nomenclature created to unify the disciplines here, and one that provides an association between the algorithms and simulation. The method demands a rigorously enforced approach, particularly when dealing with vectors and matrices. Although the nomenclature presented in this Glossary can be applied generally, for a particular application, it must be related to a set of critical geometric points (Appendix A) and a set of frames (Appendix B). This information provides a unified framework for this application and one that is reflected in the simulation variable naming convention.

Specific issues, conflicts, and historical precedence were resolved in-the-main by resorting to Zwillinger[Z.1] and Garnell[G.1] as standard references. The nomenclature presented has been developed for this research and has since been used for algorithm specification on a number of MBDA Projects providing a wider user base promoting its evolution and robustness.

0.1 Predicate Calculus (Quantifiers)

$:A \ \ldots$	Such that (A) …
$\exists A : (..)$	The existential quantifier - there exists an (A) such that (..)
$\forall A : (..)$	The universal quantifier - for all (A) such that (..)

0.2 Propositional Calculus (Connectives)

$A \vee B$	Disjunction of propositions (A) or (B), equivalent to "or"
$A \wedge B$	Conjunction of propositions (A) and (B), equivalent to "and"
$A \Rightarrow B$	Conditional proposition, if (A) then (B) by implication
$\neg A$	not (A)
$A \Leftrightarrow B$	Bi-conditional proposition, (A) if and only if (B)

The truth table for Propositional Calculus is as follows:

A	B	$A \vee B$	$A \wedge B$	$A \Rightarrow B$	$\neg A$	$A \Leftrightarrow B$	
T	T	T	T	T	F	T	
T	F	T	F	F	F	F	
F	T	T	F	T	T	F	
F	F	F	F	T	T	T	

0.3 Logical Operators

$A > B$	(A) is greater than (B)
$A < B$	(A) is less than (B)
$A \geq B$	(A) is greater than or equal to (B)
$A \leq B$	(A) is less than or equal to (B)
$A = B$	(A) is strictly equal to (B); not an assignment

0.4 Set Nomenclature and Operations

$A := \{..\}$	Finite sets, or ordered n-tuplets (the set A). Sets are identified by uppercase letters. In the absence of an explicit definition a set denoted by an upper case letter has elements that are denoted by the same letter in lower case and sequentially indexed,

$$A \equiv \{ a_i \; ; \; \forall i \in [1(1)N(A)] \}$$

$a \in A$	(a) is an element of the set (A)
$a \notin A$	(a) is not an element of the set (A)
$N(A)$	Number of elements in the set (A)
$N_{MAX}(A)$	Maximum number of elements allowed in the set (A)
max (A)	Maximum value of the elements in the set (A)
min (A)	Minimum value of the elements in the set (A)
$A := \varnothing$	The set (A) is the null, or empty set
$A \subseteq B$	Set (A) is a subset of the set (B)
$A \not\subset B$	Set (A) is not a subset of the set (B), i.e. sets (A) and (B) are disjoint.
$A \cap B$	Intersection of sets - the set containing the elements that are common to both set (A) and set (B) : $\{ x : x \in A \wedge x \in B \}$
$A \cup B$	Union of sets - the set containing the elements in both set (A) and set (B) : $\{ x : x \in A \vee x \in B \}$
$A - B$	Elements in set (A) that are not in set (B) : $\{ x : x \in A \wedge x \notin B \}$
$\bigcup_{i:=n}^{m} (A_i)$	Union of sets A_i , $\forall i \in [n(1)m]$; the set $A_n \cup A_{n+1} \cup \cdots \cup A_m$
$\bigcap_{i:=n}^{m} (A_i)$	Intersection of sets A_i , $\forall i \in [n(1)m]$; the set $A_n \cap A_{n+1} \cap \cdots \cap A_m$

0.5 Number Ranges

[A,B]	Real number range including (A) and (B), i.e. the closed interval $\{ x : A \le x \le B \}$
[A,B[	Real number range including (A) but not (B), i.e. $\{ x : A \le x < B \}$

]A,B]	Real number range including (B) but not (A), i.e. $\{ x : A < x \leq B \}$
]A,B[	Real number range excluding (A) and (B), i.e. the open interval or set $\{ x : A < x < B \}$
[A(1)B]	Set of integers { A , A+1 , A+2 ... B } including (A) and (B)
[A(2)B[	Set of integers { A , A+2 , A+4 ... B-2 } including (A) but not (B)
]A(1)B]	Set of integers { A+1 , A+2 ... B } including (B) but not (A)
]A(3)B[	Set of integers { A+3 , A+6 ... B-3 } excluding (A) and (B)

0.6 Function Definitions

$A \equiv B$	(A) is directly equivalent to (B), and may be replaced by it
$a := a + 1$	The assignment statement, e.g. (a) is replaced by (a) + 1.
$A := B \Big\vert_{]C,D]}$	(A) is equal to (B) subject to exclusive lower limit (C), and inclusive upper limit (D). In this example the value of (A) is limited to the range]C,D].
$A := B \Big\vert_{D[}$	(A) is equal to (B) subject to exclusive upper limit (D). In this example the value of (A) is limited above by (D) with an arbitrary lower bound.
$A := B \Big\vert_{[C}$	(A) is equal to (B) subject to inclusive lower limit (C). In this example the value of (A) is limited above by (C) with an arbitrary upper bound.
sign(A,B)	Magnitude of (A) with the sign of (B)
$\sum_{i:=m}^{n} (a_i)$	Sum of elements of (A), where $a_i \in A$, i.e. $a_m + a_{m+1} + \cdots + a_n$
$\prod_{i:=m}^{n} (a_i)$	Product of elements of (A), where $a_i \in A$, i.e. $a_m \cdot a_{m+1} \cdot \cdots \cdot a_n$
$\sum a_i$	Sum of all the elements in set (A)

$\prod a_i$	Product of all the elements in set (A)

0.7 Scalar Operators

A^{-1}	Scalar inversion ($A^{-1} \equiv 1/A \Leftrightarrow A \neq 0$)
$A + B$	Scalar addition
$A - B$	Scalar subtraction (A) less (B)
$A \cdot B$	Scalar product of (A) and (B)
$A \,/\, B$	Scalar division of (A) by (B)
$\lvert A \rvert$	Magnitude of a scalar (A)

0.8 Vector Operators

$\underline{A}$	Vectors are denoted by underlining
A(n)	The n'th component of a vector
$\underline{A} + \underline{B}$	Addition of vectors ($\underline{A}$) and ($\underline{B}$)
$\underline{A} - \underline{B}$	Subtraction of vectors ($\underline{A}$) and ($\underline{B}$)
$\underline{A} \bullet \underline{B}$	Inner (dot) product of vectors ($\underline{A}$) and ($\underline{B}$)
$\underline{A} \times \underline{B}$	Vector cross product between 3-vectors ($\underline{A}$) and ($\underline{B}$)
$\underline{A} \otimes \underline{B}$	Element by element multiplication of vectors ($\underline{A}$) and ($\underline{B}$)
$\lVert \underline{A} \rVert$	Euclidean length of vector ($\underline{A}$)
$\underline{n}\,(\underline{A})$	Unit vector function operating on vector ($\underline{A}$)
$\underline{n}^{A}_{b,c}$	Unit vector at point (b) through point (c) expressed in frame (A) located at point (a)
max ($\underline{A}$)	Maximum value of the components of vector ($\underline{A}$)
min ($\underline{A}$)	Minimum value of the components of vector ($\underline{A}$)
N ($\underline{A}$)	Number of components in vector ($\underline{A}$)

0.9 Matrix Operators

$[\,M\,]$	Square brackets are used to denote matrices (optional)
$m(\,i\,,\,j\,)$	The component in the i'th row and j'th column of [M]
$[\,A\,]\cdot[\,B\,]$	Matrix product of matrices [A] and [B]
$[\,A\,]\otimes[\,B\,]$	Element by element multiplication of matrices [A] and [B]
$\det[\,M\,]$	Determinant of matrix [M]
$\mathrm{tr}[\,M\,]$	Trace of matrix [M]
$[\,M\,]^{T}$	Transpose of matrix [M]
$[\,M\,]^{-1}$	Inverse of matrix [M], defined $\Leftrightarrow$ $\det[M] \neq 0$.
$\|\,M\,\|_{L2}$	Matrix-2 norm of a matrix [M]
$\|\,M\,\|_{F}$	Frobenius norm of a matrix [M]
$U[\,M\,]$	The upper triangular matrix extracted from matrix [M] including the main diagonal
$L[\,M\,]$	The lower triangular matrix extracted from matrix [M] excluding the main diagonal

0.10 Quaternion Operators

Q_A^B	Quaternion representing the orientation of frame (B) with respect to frame (A)
$Q_B^C \otimes Q_A^B$	Quaternion product
$\left(Q_A^B\right)^*$	Quaternion transposition equivalent to Q_B^A

0.11 Uncertainty and Covariance Operators

$\langle\,A\,\rangle$	Auto-covariance of random variable (A)
$\langle\,A\,,\,B\,\rangle$	Cross-covariance of random variable (A,B)
$E(A)$	Expectation operator acting on variable (A)

0.12 Kinematic Types

A	Reference value of parameter (A)
$\tilde{A}$	Measured value of parameter (A)
$\hat{A}$	Filtered value of parameter (A)
$\breve{A}$	Optimised value of parameter (A)
$\overline{A}$	Mean value of parameter (A)

Kinematic types may be omitted when it is clear that all the data involved is of the same type. Strict typing is only required when the different types interact, as for example, in the computation of system errors.

0.13 Time Rate of Change

$\dot{A}$	First derivative with respect to time (if (A) is position, then velocity)
$\ddot{A}$	Second derivative with respect to time (if (A) is position, then acceleration)
$\dddot{A}$	Third derivative with respect to time (if (A) is position, then jerk)

0.14 General Vector Notation

0.14.1 Vector Components

A general n-dimensional vector behaves as an (n,1) matrix (n-rows,1-column), however, it is denoted by an underline and its components are numbered (1,2,…n),

$$\underline{V} \equiv \begin{pmatrix} V(1) \\ V(2) \\ \vdots \\ V(n) \end{pmatrix}$$

A superscript "T" is used to indicate vector transposition thereby maintaining a clear distinction between row and column vectors. By definition, all general n-vectors denoted by an underlined kernel letter, here ($\underline{V}$), are column vectors. A row vector is denoted explicitly using the superscript "T", for example $\underline{V}^T$, which behaves as an (1,n) matrix.

0.14.2 Special Vectors

Zero and unity vectors are written as follows (in this example, for a 4-vector),

$$\underline{0}_4 \equiv \left(0 \ , \ 0 \ , \ 0 \ , \ 0\right)^T$$

$$\underline{1}_4 \equiv \left(1 \ , \ 1 \ , \ 1 \ , \ 1\right)^T$$

The subscript defining the vector dimension may be omitted if it is obvious from context.

0.14.3 Vector Partitioning

Row vector partitioning uses the following pro-forma,

$$\underline{V} := \left(\left(\underline{V}_X\right) \vdots \left(\underline{V}_Y\right) \vdots \left(\underline{V}_Z\right)\right)$$

Column vector partitioning uses the following pro-forma,

$$\underline{V} := \begin{pmatrix} \underline{V}_X \\ \cdots \\ \underline{V}_Y \\ \cdots \\ \underline{V}_Z \end{pmatrix}$$

Note that the subscripts (X,Y,Z) in these equations do not refer to Cartesian components. Vector partitioning is not required when dealing with the components of a vector.

0.14.4 Vector Jacobians

The column vector representing the partial derivative of a vector ($\underline{Y}$) with (m) elements with respect to a scalar (x) is,

$$\frac{\partial \underline{Y}}{\partial x} := \left(\frac{\partial y_1}{\partial x} \ , \ \cdots \ , \ \frac{\partial y_m}{\partial x}\right)^T$$

The row vector representing the partial derivative of a scalar (y) with respect to a vector ($\underline{X}$) with (n) elements is,

$$\frac{\partial y}{\partial \underline{X}} := \left(\frac{\partial y}{\partial x_1} \ , \ \cdots \ , \ \frac{\partial y}{\partial x_n}\right)$$

0.14.5 General State Vectors

The term vector is used in the context of state observers and controllers to describe an ordered-array of (n,1) elements. The following notation is reserved for state vectors and state observers. For a Position-Velocity-Acceleration (PVA) tracking filter, with the obvious reduction for PV filters,

$$\underline{X} \;:=\; \begin{pmatrix} \underline{X}_P \\ \cdots \\ \underline{X}_V \\ \cdots \\ \underline{X}_A \end{pmatrix}$$

0.15 Three Dimensional Cartesian Vector Notation

0.15.1 Euclidean Space

Euclidean space (E^3) is essentially a set of points each described by an ordered triplet. Cartesian vectors in Euclidean space have all the properties of the general n-dimensional vectors described previously, however, they have additional structure and may represent geometrical objects. Position triplets conform to the axioms of a vector space can be treated as vectors and no distinction is required between the two.

0.15.2 Vector Components

All 3D Cartesian vectors have components in some Frame of Reference, i.e. they are in a "Cartesian Frame". The Cartesian axes can be numbered (1,2,3) or labelled (X,Y,Z). Hence the components of a general 3D Cartesian vector ($\underline{V}$) are written,

$$\underline{V} \;\equiv\; \left(V^X \;,\; V^Y \;,\; V^Z \right)^T \;\equiv\; \begin{pmatrix} V(1) \\ V(2) \\ V(3) \end{pmatrix}$$

As for a general n-vector, a superscript "T" is used to indicate vector transposition thereby maintaining a clear distinction between row and column vectors.

0.15.3 Points and Position Vectors

The position vector of a point (b) relative to point (a) is represented geometrically by a directed line segment (arrow) with its head at (b) and its tail at (a). The notation for this vector, in the "Cartesian Frame" (C) is

$$\underline{P}^{C}_{a,b} \equiv \left(P^{XC}_{a,b} \;,\; P^{YC}_{a,b} \;,\; P^{ZC}_{a,b} \right)^{T} \equiv \begin{pmatrix} P^{C}_{a,b}(1) \\ P^{C}_{a,b}(2) \\ P^{C}_{a,b}(3) \end{pmatrix}$$

Capital "P" is reserved for position vectors. To simplify the nomenclature where a line segment starts at the origin of a Frame it is permissible to write,

$$\underline{P}^{C}_{b} \equiv \underline{P}^{C}_{a,b}$$

In this example the Frame (C) is by definition located at point (a).

0.15.4 Cartesian Frames and Spanning Vectors

Vectors along the axes of an orthogonal right-handed Cartesian Frame are referred to by $(\underline{X}^C,\underline{Y}^C,\underline{Z}^C)$. Unit vectors in these directions are denoted by $[\underline{n}^C \equiv (\underline{i}^C,\underline{j}^C,\underline{k}^C)]$. For Cartesian Frames $(\underline{X}^C,\underline{Y}^C)$ span the basic plane, $(\underline{Y}^C,\underline{Z}^C)$ the transverse plane, and $(\underline{X}^C,\underline{Z}^C)$ the longitudinal plane. The basic plane may be referred to as the "horizontal" plane as per common convention.

The projections of a vector $\underline{V}$ onto the planes spanned by $(\underline{X},\underline{Y})$, $(\underline{Y},\underline{Z})$, $(\underline{X},\underline{Z})$ and are denoted by $\underline{V}^h$, $\underline{V}^r$ and $\underline{V}^v$ respectively, where (h), (r) and (v) refer to the projection of the vector in the "basic", "transverse" and "longitudinal" planes of the Frame . Hence for a position vector $\underline{P}^{C}_{a,b}$, for example, the following notation is used:

$$\underline{P}^{hC}_{a,b} := \left(P^{XC}_{a,b} \;,\; P^{YC}_{a,b} \;,\; 0 \right)^{T} \equiv \text{basic plane vector}$$

$$\underline{P}^{rC}_{a,b} := \left(0 \;,\; P^{YC}_{a,b} \;,\; P^{ZC}_{a,b} \right)^{T} \equiv \text{transverse plane vector}$$

$$\underline{P}^{vC}_{a,b} := \left(P^{XC}_{a,b} \;,\; 0 \;,\; P^{ZC}_{a,b} \right)^{T} \equiv \text{longitudinal plane vector}$$

When dealing with the principal planes of a Frame they may be referred to as C^h, C^r and C^v respectively.

0.15.5 Position Vector Time Derivatives

Consider the time rate of change of a vector in an inertial Frame (I) and rotating Frame (R). In the inertial Frame,

$$\frac{d}{dt}\left(\underline{P}^{I}_{b} \right) \equiv \dot{\underline{P}}^{I}_{b} \equiv \underline{V}^{I}_{b}$$

Inertial velocity is denoted by ($\underline{V}$), acceleration by ($\underline{A}$) and jerk by ($\underline{J}$). The time rate of change operator of a vector in inertial space is (D_I). Similarly, the time rate of change operator of a vector in the rotating frame is (D_R). The angular velocity of frame (r) with respect to frame (I), expressed in the rotating frame,

$$\underline{\omega}^{R}_{I,R} \equiv \left(\omega^{XR}_{I,R} \;,\; \omega^{YR}_{I,R} \;,\; \omega^{ZR}_{I,R} \right)^{T}$$

The relationship between these time rate of change operators on any vector,

$$D_I \left(\underline{*} \right) := \left(D_R + \underline{\omega}^{R}_{I,R} \times \right) \left(\underline{*} \right)$$

0.15.6 Length, Scalar and Cross Products of Vectors and Unit Vectors

For this section ($\underline{V}$) and ($\underline{W}$) denote 3D vectors in a common Cartesian frame (C). The length of ($\underline{V}$) is denoted by $\| \underline{V} \|$, or by omitting the underline; the former being useful when taking the length of vector expressions such as $\| \underline{V} + \underline{W} \|$. For any vector ($\underline{V}$),

$$V := \sqrt{\left(V^X\right)^2 + \left(V^Y\right)^2 + \left(V^Z\right)^2}$$

$$V \equiv \sqrt{\left(V(1)\right)^2 + \left(V(2)\right)^2 + \left(V(3)\right)^2}$$

The length of a position vector ($\underline{P}^{C}_{a,b}$),

$$P^{C}_{a,b} \equiv \left\| \underline{P}^{C}_{a,b} \right\| := \sqrt{\left(P^{XC}_{a,b}\right)^2 + \left(P^{YC}_{a,b}\right)^2 + \left(P^{YC}_{a,b}\right)^2}$$

$\dot{P}^{C}_{a,b}$ denotes the length of the derivative of $\underline{P}^{C}_{a,b}$, *not* the derivative of the length of $\underline{P}^{C}_{a,b}$. The inner or scalar product representing the projection of ($\underline{V}$) onto ($\underline{W}$) is,

$$\underline{V} \bullet \underline{W} := \sum_{i:=\{X,Y,Z\}} \left(V^i \cdot W^i \right) \equiv \sum_{i:=1}^{3} \left(V^i \cdot W^i \right)$$

Equivalently, the scalar product may be written as,

$$\underline{V} \bullet \underline{W} := V \cdot W \cdot \cos \xi \qquad \text{where} \quad \xi \in [0, \pi]$$

If $\underline{V}$ and $\underline{W}$ are directed line segments (ξ) is interpreted as the angle subtended by $\underline{V}$ and $\underline{W}$. In particular, two vectors of non-zero length are said to be orthogonal when their scalar product is zero. The length of a vector expressed in terms of its scalar product is,

$$V \equiv \| \underline{V} \| := \sqrt{\underline{V} \bullet \underline{V}}$$

The unit vector function returns the unit vector associated with a non-zero length vector ($\underline{V}$),

$$\underline{n}(\underline{V}) := \underline{V} / \| \underline{V} \|$$

The cross product between ($\underline{V}$) and ($\underline{W}$) which subtend an angle (ξ) results in a bi-normal vector in the direction of the unit vector ($\underline{n}$) defined by,

$$\underline{V} \times \underline{W} := V \cdot W \cdot \sin \xi \cdot \hat{n}$$

The direction of the unit vector ($\underline{n}$) is determined by the right-hand screw rule as ($\underline{V}_{a,b}$) rotates towards ($\underline{W}$) through angle (ξ). The skew symmetric matrix operator associated with vector ($\underline{V}$) is,

$$[\, \underline{V} \times \,] := \begin{bmatrix} 0 & , & -V^Z & , & V^Y \\ V^Z & , & 0 & , & -V^X \\ -V^Y & , & V^X & , & 0 \end{bmatrix}$$

The relationship between the vector cross product and skew symmetric operator is then,

$$[\, \underline{V} \times \,] \cdot \underline{W} \equiv \underline{V} \times \underline{W}$$

0.15.7 Simulation Naming Convention

Generic vectors ($\underline{V}^C_{a,b}$) are represented by *V_CAB*, with components *VX_CAB* etc., and magnitude *V_AB*. Position vectors are typically *P_CAB*. Inertial velocity, acceleration and jerk vectors are *V_CAB*, *A_CAB*, and *J_CAB*, respectively. Non-inertial velocity, acceleration and jerk vectors are *DP_CAB*, *D2PCAB* and *D3PCAB* respectively. Vector projections onto the transverse, longitudinal and basic (horizontal) planes of a frame are *VR_CAB*, *VV_CAB* and *VH_CAB* respectively. Angular velocity vectors ($\underline{\omega}^C_{A,B}$) are named *W_CAB* with components *WX_CAB* etc.; likewise angular acceleration and jerk vectors are *DW_CAB* and *D2WCAB* respectively.

0.16 Matrix Definitions

0.16.1 General Notation

Matrices are denoted by [M], their transpose by $[M]^T$, and their inverse by $[M]^{-1}$. If it is necessary to associate a matrix with a frame, as with the

transformation of covariance matrices, we have $[M^C]$. Providing that matrices are clear in context the square bracket notation may be omitted.

0.16.2 Diagonalisation

When converting a vector into a diagonal matrix (in this case for a position 3-vector),

$$\operatorname{diag}\left(\underline{P}^{C}_{a,b} \right) \equiv \operatorname{diag}\left(P^{XC}_{a,b} \; , \; P^{YC}_{a,b} \; , \; P^{ZC}_{a,b} \right)$$

$$\operatorname{diag}\left(\underline{P}^{C}_{a,b} \right) \equiv \begin{bmatrix} P^{XC}_{a,b} & , & 0 & , & 0 \\ 0 & , & P^{YC}_{a,b} & , & 0 \\ 0 & , & 0 & , & P^{ZC}_{a,b} \end{bmatrix}$$

The trace of a square matrix of dimension (N) is the sum of its diagonal elements,

$$\operatorname{tr}\left[A \right]_{NxN} := \sum_{i:=1}^{N} a(i,i)$$

0.16.3 Special Matrices

The identity matrix is written as (in this example, for a matrix of dimension N := 3),

$$I_3 \equiv \left[I \right]_3 \equiv \begin{bmatrix} 1 & , & 0 & , & 0 \\ 0 & , & 1 & , & 0 \\ 0 & , & 0 & , & 1 \end{bmatrix}$$

Zero matrices are written (in this case for a (2,3) matrix),

$$0_{2x3} \equiv \left[0 \right]_{2x3} \equiv \begin{bmatrix} 0 & , & 0 & , & 0 \\ 0 & , & 0 & , & 0 \end{bmatrix}$$

The dimensions may be omitted if they are obvious in context

0.16.4 Matrix Partitioning

Components of a matrix [M] will be referred to as m(i,j). Matrix partitioning uses the following pro-forma:

$$[M] \equiv \begin{bmatrix} m_{XX} & \vdots & m_{XY} & \vdots & m_{XZ} \\ \cdots & \vdots & \cdots & \vdots & \cdots \\ m_{YX} & \vdots & m_{YY} & \vdots & m_{YZ} \\ \cdots & \vdots & \cdots & \vdots & \cdots \\ m_{ZX} & \vdots & m_{ZY} & \vdots & m_{ZZ} \end{bmatrix}$$

The combined partition, component and frame notation being $m^{C}_{XY}(i,j)$. The upper triangular matrix [B], including the main diagonal terms, extracted from matrix [A] is,

$$[B] := U[A] \equiv \begin{bmatrix} a(1,1) & , & a(1,2) & , & \cdots & , & a(1,n) \\ 0 & , & a(2,2) & , & \cdots & , & a(2,n) \\ \vdots & , & \vdots & , & \ddots & , & \vdots \\ 0 & , & \cdots & , & 0 & , & a(m,n) \end{bmatrix}$$

The lower triangular matrix [C], excluding the main diagonal terms, extracted from matrix [A] is,

$$[C] := L[A] \equiv \begin{bmatrix} 0 & , & 0 & , & \cdots & , & 0 \\ a(2,1) & , & 0 & , & \cdots & , & 0 \\ \vdots & , & \vdots & , & \ddots & , & \vdots \\ a(m,1) & , & \cdots & , & a(m,n-1) & , & 0 \end{bmatrix}$$

0.16.5 Matrix Norms

The 2-norm of a matrix [M] is defined as,

$$\|M\|_{L2} := \sqrt{\lambda_{MAX}\left([M]^{T} \cdot [M]\right)}$$

Where λ_{MAX} is the largest eigenvalue of $\left([M]^{T} \cdot [M]\right)$. The Frobenius norm of a matrix [M(m,n)] is defined as,

$$\left\| M \right\|_F := \sqrt{\sum_{i:=1}^{m} \sum_{j:=1}^{n} \left| M(i,j) \right|}$$

0.16.6 Matrix Jacobians

Given vectors ($\underline{X}$) and ($\underline{Y}$) with (n) and (m) elements respectively, the following matrix of partial derivatives is defined,

$$\frac{\partial \underline{Y}}{\partial \underline{X}} := \begin{pmatrix} \frac{\partial y_1}{\partial x_1} & \cdots & \frac{\partial y_1}{\partial x_n} \\ \vdots & \ddots & \vdots \\ \frac{\partial y_m}{\partial x_1} & \cdots & \frac{\partial y_m}{\partial x_n} \end{pmatrix}$$

0.17 Quaternion Definitions

0.17.1 General Notation

Quaternions are a 4-parameter method of defining the orientation of a vector in E^3 with respect to a frame. Quaternions are preferred to Euler angles since they exhibit no singularities, and avoid the computation of direction cosine trigonometrical functions required for vector transformations. A quaternion defining the orientation of frame (B) with respect to frame (A) comprises a scalar and a vector part associated with unit vectors coincident with frame (A),

$$Q_A^B \equiv \left(q_A^B \ , \ \underline{q}_A^B \right) \quad \text{where} \quad q_A^B \geq 0$$

The components of the vector part can be written as,

$$\underline{q}_A^B := i \cdot q_1 + j \cdot q_2 + k \cdot q_3$$

Where (i,j,k) are non-commutative, hyper-imaginary numbers related to each other by,

$$i^2 := j^2 := k^2 := -1$$

$$i \cdot j := -j \cdot i := k$$

$$j \cdot k := -k \cdot j := i$$

$$k \cdot i := -i \cdot k := j$$

Only the subset of quaternions of unit magnitude will be used with the form,

$$Q_A^B \;\coloneqq\; \left(\cos\left(\alpha_A^B / 2 \right) \;,\; \sin\left(\alpha_A^B / 2 \right) \cdot \underline{n}_b^A \right)$$

A rotation through angle (α_A^B) about a unit vector along $\underline{X}^B$ through point (b) whose components with respect to frame A located at point (a) are denoted by ($\underline{n}_b^A$) brings frame (A) into alignment with frame (B). In which case,

$$\underline{n}_b^A \;\equiv\; \left(n_{a,b}^{XA} \;,\; n_{a,b}^{XA} \;,\; n_{a,b}^{XA} \right) \;\equiv\; (\; i \;,\; j \;,\; k \;)$$

0.17.2 Quaternion Components

Expanding into elemental components,

$$Q_A^B \;\equiv\; \left(q_A^B(0) \;,\; q_A^B(1) \;,\; q_A^B(2) \;,\; q_A^B(3) \right)$$

When the two axis systems associated with a quaternion are clear in context this nomenclature may be relaxed,

$$Q_A^B \;\equiv\; (\; q_0 \;,\; q_1 \;,\; q_2 \;,\; q_3 \;)$$

0.17.3 Quaternion Conjugate

The conjugate of a quaternion is a quaternion whose vector part is negated and represents the axis transformation from frame (B) to frame (A),

$$\left(Q_A^B \right)^* \;\equiv\; Q_B^A \;\coloneqq\; \left(\; q_A^B \;,\; -\underline{q}_A^B \; \right)$$

$$Q \otimes {}^*Q \;\equiv\; {}^*Q \otimes Q \;\coloneqq\; \left(\; \| Q \|^2 \;\; \underline{0}_3 \; \right)$$

0.17.4 Compound Quaternions

Consider two quaternions that define the orientation of frame (B) relative to frame (A) and frame (C) relative to frame (B). The quaternion product represents the compound transformation from frame (A) to frame (C),

$$Q_A^C \;\coloneqq\; Q_B^C \otimes Q_A^B \;\equiv\; T_A^C \;\coloneqq\; T_B^C \cdot T_A^B$$

0.17.5 Simulation Naming Convention

A quaternion is denoted by *Q_AB* with a scalar component *Q_AB(0),* and vector components *Q_AB(1)* to *Q_AB(3)*. The rate of change of a quaternion is *DQ_AB* with a scalar component *DQ_AB(0),* and vector components *DQ_AB(1)* to *DQ_AB(3)*.

0.18 **Filtering and Covariance Transformation**

The symbol (Δ) is used to denote a generic propagation time interval that is defined locally in the form,

$$\Delta \equiv t_{k+1} - t_k$$

When a specific reference to time is required rather than a cyclic index,

$$\underline{X}_k \equiv \underline{X}\left(t_k \right)$$

$$\Phi_k^{k+1} \equiv \Phi\left(t_k , t_{k+1} \right) \equiv \Phi\left(\Delta \right)$$

Predicted and updated parameters at a common time are denoted by (-) and (+), for example,

$$P_{k+1}^{-} := \Phi_k^{k+1} \cdot P_k^{+} \cdot \left[\Phi_k^{k+1} \right]^T + Q_k$$

It is permissible to drop the inference to time "k" (but not "k+1") in discrete equations since it is clear in context that current values should be used. For example, the previous equation becomes,

$$P_{k+1}^{-} := \Phi \cdot P^{+} \cdot \Phi^T + Q$$

The index notation referring to time may be replaced by (t) or (τ) when dealing with continuous time equivalents. Using matrix partitioning notation (e.g. partition XY), when transforming the uncertainty of a 3-vector state expressed as a (3x3) covariance matrix from Cartesian Frames (A) to (B),

$$P_{XY}^{B} := T_A^B \cdot P_{XY}^{A} \cdot T_B^A \equiv T_A^B \cdot P_{XY}^{A} \cdot \left[T_A^B \right]^T$$

Combining this notation with a change of co-ordinate system in Frame (A) using the Jacobian notation,

$$P_{XY}^{B|C} := \left[T_A^B \cdot C_{A|R}^{A|C} \right] \cdot P_{XY}^{A|R} \cdot \left[T_A^B \cdot C_{A|R}^{A|C} \right]^T$$

Applying the allowable simplifications when dealing with Cartesian axes,

$$P_{XY}^{B} :=$$

$$\left[T_A^B \cdot C_{A|R}^{A} \right] \cdot P_{XY}^{A|R} \cdot \left[T_A^B \cdot C_{A|R}^{A} \right]^T \equiv T_A^B \cdot C_{A|R}^{A} \cdot P_{XY}^{A} \cdot \left[C_{A|R}^{A} \right]^T \cdot T_B^A$$

0.19 Systeme Internationale D'Unites

0.19.1 Base Units

PARAMETER	UNITS	SYMBOL	
Length	metres	m	
Mass	kg	kg	
Time	seconds	s	
Temperature	degrees kelvin	K	

0.19.2 Supplementary Units

PARAMETER	UNITS	SYMBOL	
Plane angle	radians	rad	
Solid angles	Steradians	sr	

0.19.3 Derived Units

PARAMETER	UNITS	SYMBOL	
Force	Newton	N	
Frequency	Hertz	Hz	
Power	Watt	W	
Pressure	Pascal	Pa	

Linear velocity, acceleration and jerk are specified in (m/s), (m/s^2) and (m/s^3).

Angular velocity, acceleration and jerk are specified in (rad/s), (rad/s^2) and (rad/s^3).

0.20 Absolute and Relative Time

Time is denoted by (t) which is usually referenced to a common standard such as NAVSTAR GPS, IRIG-B etc. The time when an object exists at point (p) is (t_p). When geometric points and frames are not explicitly time referenced they exist at the current time (t). For example, the estimated target position at its predicted impact time with the missile, expressed in the current Missile Body frame is,

$$\underline{\hat{P}}^{B(t)}_{o,t(t_i)} \equiv \underline{\hat{P}}^{B}_{o,t(t_i)}$$

The time taken to travel between points (a) and (b) is (t_a^b). When the time difference is small it is permissible to use the delta notation (Δt_a^b) to emphasis this fact. All variables are treated as "current", for example, A(k) represents the current value of (A). When the same variable is required one or more algorithmic cycles ago separate variables are used in the simulation to represent A(k-1), A(k-2) etc.

The following nomenclature associated with time is reserved for:

- t_S The time at which the missile is committed to launch and its sensors are activated.
- t_L The launch time when the firing chain is complete and first motion in the launcher is allowed.

When dealing with time stamped asynchronous sensor measurements from different sources their source is identified, for example, ($_{GR}t$) represents data from the ground radar.

The measurement sources that may be referenced in this way are:

- GR : Ground Radar
- GS : Missile Gyroscope triad
- AC : Missile Accelerometer triad
- BA : Barometric altimeter
- RA : Radar altimeter
- SK : Seeker
- FN : Control surface actuators
- GP : NAVSTAR GPS
- HM : Helmet mounted sight
- AD : Air data system

Chapter 1

INTRODUCTION

1.1 Politics and Markets

The Persian Gulf and Bosnia crises highlighted the importance of high precision stand-off weapon systems for "surgical" strikes against heavily defended, high value targets where collateral damage was politically unacceptable. The result has been mounting pressure from military leaders on research establishments for highly accurate munitions and standoff delivery systems.

Stealthy delivery and high kill probabilities, without endangering the launch platform, will be key factors in future strategic planning. The demand for a single-shot capability has also promoted the importance of high reliability, and the emergence of reversionary mode capabilities.

These pressures are influencing research into new missile systems with more emphasis on reliable designs and minimising collateral damage in limited military engagements. Weapon procurement agencies are now placing contracts that demand unprecedented levels of performance:

- Expansion of operating envelopes with higher kill probability
- All weather capability
- Increased stealth
- Resistance to sophisticated and multiple countermeasures
- Ability to cope with highly manoeuvrable targets in a cluttered, multiple target environment

These requirements are being met by new and emerging technologies combined with an unprecedented increase in computing power leading to the production of the most expensive and sophisticated weapon systems ever built. These are the so called "smart" weapons, integrated onto equally expensive launchers such as the EF2000 and Type 45 destroyer, in some cases at a cost beyond the capacity of any one country to produce.

The proportion of the missile market by theatre of application is reproduced in Table 1-1[P.1]. Over the last decade aerospace companies have merged,

entering into joint ventures, pooling technological expertise, increasing production runs so as to maintain profit whist forcing down unit and development costs.

Table 1-1 : Missile Markets by Theatre of Operation

AIR-TO-AIR	15 %	ANTI-SHIP	10 %	
SURFACE TO AIR	50 %	ANTI-ARMOUR	15 %	
STAND-OFF	5 %	ANTI-RADIATION	5 %	

Europe is no exception but still only attracts 34% of the tactical missile market, most of the remainder going to the United States (US) domestic and world markets. Table 1-2 lists some of the missile systems that have traditionally filled these roles, and replacements under development.

Table 1-2 : Missile Systems and their Theatre of Operation

AIR-TO-AIR	Advanced Short Range Air-to-Air Missile (ASRAAM) , IRIS-T , Aspide , Skyflash , Mica , Magic	
SURFACE-TO-AIR	Sea-Wolf, Rapier, Patriot, Aspide, Aster, Mistral, Starstreak, Roland	
STAND-OFF	Storm Shadow, SCALP, Taurus, Apache, Tomahawk, SLAM, Starburst	
ANTI-SHIP	Sea Eagle , Harpoon , RBS-15 , Exocet , Kormoran , Otoman , Penguin	
ANTI-ARMOUR	Trigat , Brimstone , Milan , HOT	
ANTI-RADIATION	Alarm , Martel	

As missile systems become more sophisticated their interaction with the launcher becomes more complex; communication between the two enhancing the independent targeting of missiles, track association, firing solutions, and launcher steering optimised for kill probability. In the opinion of the Joint Advanced Strike Technology (JAST) programme manager the challenges facing future designers will not be the hardware, or the embedded software, but information management, its use in automated systems and its presentation at the human interface. Weapon systems can no longer be restricted to developing missile algorithms independent of the launcher, and as their capabilities expand, so does the cost of performance proving by trials. Demand for comprehensive and validated simulations will inevitably increase, a central theme of this research.

The world's leading aerospace companies, supported by academia, are undertaking research programmes in the key areas of sensors, tracking and missile guidance design. To maintain dynamic stability and high kill probability when intercepting intelligent targets performing sophisticated avoidance manoeuvres demands a unified approach to data fusion, state observation and guidance optimisation, disciplines that are at the core of this research.

Whereas advanced air-launched missile design has progressed in the UK, driven by the need to arm the Euro-fighter (EF2000), surface-to-air systems have been relatively immune to the multi-sensor data fusion approach. As the new air-launched systems enter service there will be a demand for equally sophisticated ground defence systems that traditionally command the largest market share. Therefore, the application selected to illustrate the techniques considered is naturally drawn from this theatre of operation.

1.2 Research Objectives

1.2.1 Specific Objective

The primary (overall) objective of the research is to select, develop and integrate algorithms for "fifth" generation[1] air-defence missiles using on-line trajectory optimisation, multiple-model target tracking and centralised state observation with distributed sensor track and plot fusion.

The work comprises ground based state observation using multiple-model tracking driven by phased array radar plots. Up-linked target track and own-missile plots fused into a missile observer together with gyroscope, accelerometer and seeker measurements. Conventional Proportional Navigation (PN) and Command-to-Line of Sight (CLOS) guidance laws to be compared with on-line (real-time) guidance solutions.

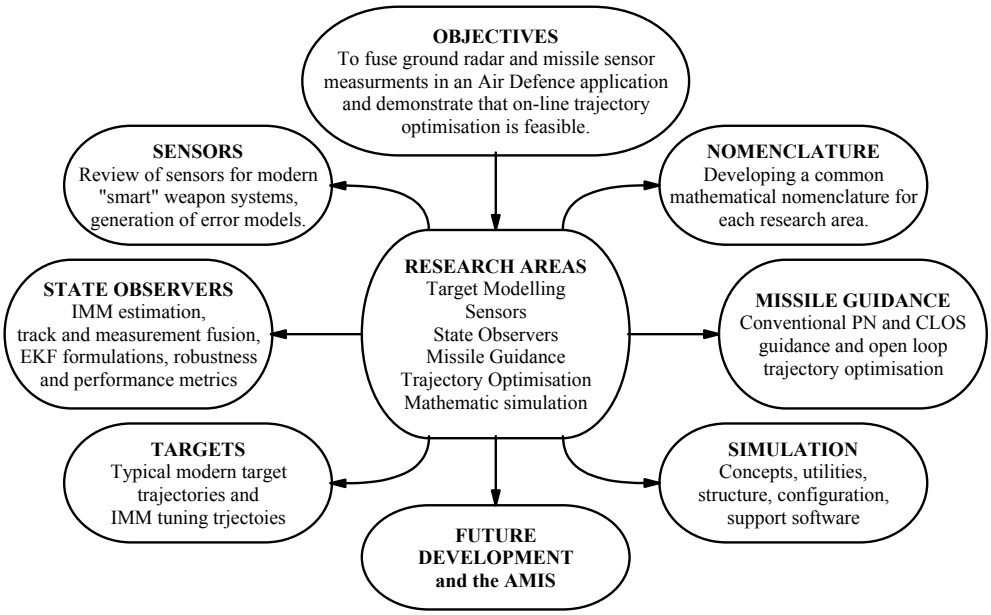

Figure 1-1 : Research Overview

Missile trajectories subject to miss, speed and attitude terminal constraints plus minimisation of control effort commensurate with up-link transmission

[1] "Fifth generation" – refers in this context to centralised state observation by distributed sensor fusion, avoiding localised parameter estimation for isolated functions.

aspect and jamming avoidance. These research areas are captured in Figure 1-1. The research focuses on providing a basis for work on providing stable boundary conditions from the state observers for on-line guidance solutions that are capable of reacting to changing environmental conditions and different target scenarios free of the curse of dimensionality and large databases.

1.2.2 Devolved Objectives

Key components when designing modern missile systems are:

- Target capability, decoy and evasion tactics
- Reliable sensors providing sufficient data for state and parameter estimation depending on the guidance law to be employed with the accuracy needed to meet target kill probability requirements.
- State observation employing all the available sensor data to provide optimal estimates for fire control and in-flight missile guidance.
- Missile airframe and aerodynamic characteristics allowing the autopilot to maintaining a stable configuration whilst meeting the guidance demands.
- Weapon system simulation for design proving and software verification.

Since the mid-1950s these have been, and remain, fruitful areas for research; the cumulative body of information available in the public domain is staggering. Never-the-less, literature on these topics will be assessed, techniques down-selected and, where necessary, developed for this application using a unifying nomenclature created for the purpose. The following secondary objectives will be observed:

- Create a target simulator for providing idealised and complex target trajectories by merging elemental dynamic components, particularly avoidance manoeuvres. Although this work is to concentrate on targets in the air-defence theatre it should briefly consider the provision of trajectories with respect to a moving reference for air-to-air scenarios. Multiple-target provision, terrain following, the application of constraints for the purpose of target selection within a sensors Field-of-View (FoV) are to be explored.
- Select sensors that will shape future development of missile systems and their launchers. Create a simulator supporting system level models of these sensors in which typical errors are superimposed on reference data. The models are to be transportable, capable of cloning for use in both missile and launcher, and duplicated as required for multi-spectral devices.
- Create a target-tracking simulator for studying multiple-model algorithms containing individual filters. The structure should allow for the introduction of additional filters, different formulations of a particular type of filter and the extraction of commonly used performance metrics.

- Create a missile simulator structure supporting separate missile models one of which is a point mass missile for this research. These should access alternative PN, CLOS and trajectory optimised guidance laws and autopilot constraints found in Bank-to-Turn (BTT) and Skid-to-Turn (SST) missiles.
- Create a simulation infrastructure to support any simulator with dynamics states, and in particular the aforementioned simulators. The infrastructure should promote rapid development and use by the provision of interactive controls, on-line data visualisation, self-contained utility software interaction, and communication with external applications (MATLAB).

1.3 Document Structure

The scene is set by considering the political, military and economic factors driving weapon system development; factors that underpin the objectives of this research and the structure of the document. §2 to §7 follow the natural design process shown in Figure 1-2. At each stage alternative algorithms are reviewed, down-selected and implemented in simulators embedded in the simulation infrastructure described in §8, a simulation used to explore performance in §9. Conclusions, future work, references and bibliography form §10 to §13. Basic mathematics and simulation functionality supporting the main text appears in Appendix A to Appendix I (§14 to §22).

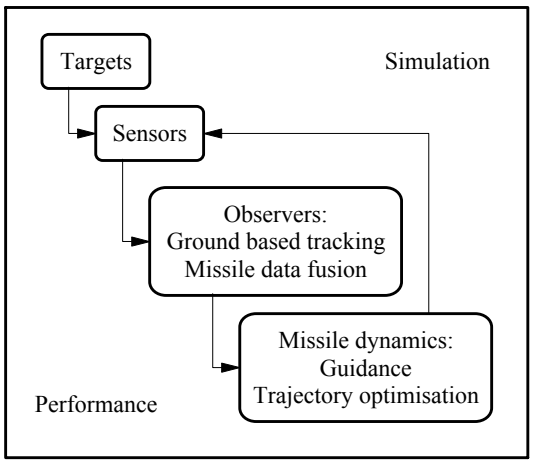

Figure 1-2 : Document Structure

There follows an overview of each chapter introducing some philosophical discussion and placing the work in the overall context of missile system design. This is then re-enforced by an in-situ precise to each chapter expanding on the aims of the work and content. The main chapters conclude by assessing the status of the work therein, conclusions drawn, exploring closely related extensions and noting deficiencies.

1.3.1 Chapter 2 : Targets

Missile design starts with the intended target; the critical element being the ability to accurately predict its position from noisy measurements. The system must be capable of detecting targets at ranges beyond that of the defending missile, and react rapidly to the onset of target manoeuvres. Nowadays targets are less co-operative than they once were being capable of high acceleration avoidance manoeuvres, and radiating jamming signals whilst ejecting all manner of decoys. The primary requirement imposed on

a missile system is usually target kill probability subject to target dynamic capability and countermeasure limitations. High speed targets travelling along ballistic arcs with superimposed coning, targets performing sea-skimming weaves, and those capable of terrain following, present a considerable challenge when predicting impact points and providing rapid reaction times.

§2 deals with the creation of sophisticated, single-target manoeuvres from simple elemental motions in a target simulator. One-on-many situations are beyond the scope of this work, to the detriment of sensor data association studies requiring a multiple-target environment, a deficiency addressed in the associated Aircraft and Missile Integration Simulation (AMIS). Idealised target trajectories are created for tuning each of the filters in the multiple-model target state observer. More complex trajectories are constructed to expose any state observer shortcomings are for performance assessment. These trajectories are embedded in the target simulator to promote direct comparison between tracking comparisons and ease configuration control. The physical characteristics of typical airborne targets are provided, and the dynamic relationship between demanded and actual target acceleration used to generate realistic target responses. The simulator description covers bespoke track creation using the elemental target models, tracks that can be interactively modified.

1.3.2 Chapter 3 : Sensors

Sensors are key to successful missile system providing relative target and missile motion for guidance, their characteristics determining the operational envelope, state observation complexity, guidance capability and hence kill probability. They also impose design constraints: on the missile airframe in respect of shape, size, weight, and aerodynamics; limitations in range, Field-of-Regard (FoR), Field-of-View (FoV), saturation, error characteristics, time-to-first-measurement, availability, and dynamics. In the opinion of the author, the following sensors will dominate weapon development into the 21st century:

- Gyroscopes
- Accelerometers
- Barometric altimeters
- Radar altimeters + digital maps
- Gimballed missile seekers
- RF phased array radar
- Fin position transducers
- NAVSTAR Global Positioning System
- Air data sensors and magnetometers
- Helmet mounted sight (HMS)
- Forward looking Infra-Red (FLIR)
- Thermal Imaging & Laser Designation

Just as missile navigation and guidance depends on data from state observers, so these in turn depend on the type and quality of sensors selected. Sensor selection is a balance between high quality, expensive instruments, whose measurements provide the data required directly requiring no observer, to poorer but cheap sensors requiring estimation of both the system state and their error characteristics. As neither extreme is

generally acceptable a balance is struck between capability and cost; sensor technology, more than most, being prone to requirement creep. Recent advances in digital processing capability means that powerful algorithms can now be employed to improve sensor performance in an attempt to keep their cost under control. Table 1-3 provides an indication as to the sensor used in the various Theatres of Operation.

The work on sensors presented in §3 concentrates on the system integration aspects of sensors, particularly those errors that may impact on data fusion algorithms. For contractual reasons it has become the norm to embed detailed manufacturer sensor development models in performance simulations. These models tend to be overly complicated for assessing overall system performance and often restrict such studies when time and resources are limited. The ethos here is to replace high frequency functions with approximate low frequency models retaining the characteristics that affect the performance of the state observers. Perfect measurements derived directly from the reference-state are corrupted by dominant error sources before delivery to the state observer via a digital interface, or radio link. Two status flags accompany each measurement; one indicates that a particular measurement is available, the other that it is ready for processing, i.e. it is valid and operating within the sensors operational limits. The sensor models are self-contained entities so that they are transportable, and can be cloned dependent on application. Their generic nature means they can be characterised to represent a range of similar sensors, for example, gimballed Infra-Red (IR) seekers representing FLIR and TIALD, similarly, a rotating phased array radar becomes a strapped-down device, or a steered electro-optical tracker.

Table 1-3 : Sensors and Theatres of Operation

SENSORS	Air Launched		Ship Launched		Ground Launched	
	Launch	Missile	Launch	Missile	Launch	Missile
IMU gyroscope triad	✔	✔	✔	✔		✔
IMU accelerometer triad	✔	✔	✔	✔		✔
Barometric altimeter	✔					
Radar altimeter/DLMS	✔	✔		✔		✔
RF/IR seekers	✔	✔		✔		✔
NAVSTAR GPS	✔	✔	✔			
RF radar	✔		✔		✔	
Helmet Mounted Sight	✔					
Air data sensors	✔					
FLIR and TIALD	✔					

§3.1 introduces the sensor simulator, control of the individual sensor models, and their interaction with the simulation infrastructure. There are a number of errors that are commonly found in many of the sensors. These are described generically in §3.2 in the context of the simulator and a Matrix

Laboratory (MATLAB) facility used to aid sensor model development. The mathematical nested functional form is introduced, a shorthand notation promulgated throughout the individual sensor descriptions.

Before dealing with the individual sensors, §3.3 introduces the Navigation equation, the basis of terrestrial mid-course guidance and master-slave Transfer Alignment (TFA). The relative merits of Strap-Down Inertial Navigation Systems (SDINS) combining gyroscope, accelerometer and height stabilisation sensors are compared with older platform systems. Although TFA algorithms are beyond the scope of this research, the focus is on deriving accurate inputs to the inertial navigation sensors in a flexure environment from geodetically referenced waypoints.

The individual sensors are described in §3.4 to §3.13 in the same general format. Each starts with their evolution and relevance to weapon development. The reference input to the sensor is then derived from the reference-state, dominant errors superimposed and dynamic limitations applied, algorithms including typical default values. The measurements are passed to the output interface at a selected cyclic rate where their validity flags are and additional interface errors superimpose.

1.3.3 Chapters 4 and 5 : State Observation

Data fusion is a partial solution to the problem of escalating cost vs. performance of weapon systems; the cost of improving performance by fusing data from several sensors offset by developing missiles with multi-role capability. Where reliable, but less accurate and cheaper weapons will suffice, sensors can be calibrated to meet a system requirement that would otherwise be too costly. Sensor advances, and an integrated approach to state observation and guidance, will eventually lead to global performance optimisation and a commensurate improvement in weapon functions such as:

- Mid-course guidance and navigation
- Height keeping and terrain avoidance
- Missile targeting
- GPS receiver control
- Terminal guidance
- Airframe stabilisation
- Calibration of poor grade sensors
- Fire control solutions
- Seeker inertial stabilisation

State observers are used to amalgamate all the sensor measurements to produce data for missile guidance that is in some cases not directly measurable. The most flexible observer architecture for this application is target track formation on the ground dealt with in §4, an up-link to a central observer in the missile covered in §5.

Comprehensive studies into tracking, each with an extensive bibliography, have been produced by Blackman[B.6], Bar-Shalom[B.5], Pulford[P.5], Sammons[S.21], and Mazor[M.2] and are drawn upon when formulating the

radar target state observer in §4. Bar-Shalom categorises tracking filters considered as:

- Static, non-switching models
- Optimally Multiple-Model (MM) estimators
- Sub-optimal MM estimators with Markov switching

Fixed gain filters tend to be inflexible and ignore cross coupling effects resulting in poor performance against complex targets. Since processor loading is less of an issue that it once was, these are rarely in modern state observers having been replaced by time-varying stochastic alternatives. Of these the sub-optimal Interacting-Multiple-Model (IMM) was chosen for its flexibility, stability through re-initialisation, and its potential for expansion into the variable-structured algorithm suggested by Li[L.5].

The core of the IMM comprises filters with different dynamic models driven by the same radar measurements. Although the IMM can accommodate many types of filter the reasons for using the conventional Extended Kalman Filter (EKF) are discussed. Whilst other options were considered, EKF iterative and adaptive forms, Second Order Filters (SOF), many were discounted due to computational burden, indirect access to covariance data, inability to process range and range-rate data, etc. The suitability of the EKF and its iterated form is discussed in the context of operating in Cartesian or polar state-space, measurement conversion, and initialisation using α–β–γ filters and least squares algorithms. §4 concludes with a description of the tracking simulator, its controls, and interaction with the target and sensor simulators.

§5 extends the state observation started in §4 with a review of centralised and decentralised observer architectures covering the benefits of track and measurement data fusion. The hybrid architecture chosen for this application combines the up-linked IMM target track with the radar's missile measurements, and the missile gyroscope, accelerometer and seeker measurements. The track is fused into the missile observer target state using information filtering techniques favoured by Lobbia[L.8] and Durrant-White[J.2].

The measurements are serial processed in a conventional EKF whose process model is purposely simple so as to promote high frequency propagation. State cross-coupling is introduced using directed process noise and pseudo-measurement updates. Constraining the process model through the measurement update provides a flexible observer since executive control can be exercised over the type and frequency of the pseudo-measurements used. Pseudo-measurements are derived from aerodynamic constraints, circular target models, PN goal orientation, and quaternion normalisation. Protecting the observers from spurious measurements and failing sensors is crucial. Commonly employed integrity algorithms are discussed noting the work of Daum and Fitzgerald[D.3], Kerr[K.6] amongst others in this field. §5

concludes with a description of the tracking simulator, its control and interaction with the target and sensor simulators, and the simulation infrastructure.

1.3.4 Chapter 6 : Conventional Missile Guidance

§2 to §5 provide the target and missile data required for missile guidance. §6 closes the loop on this process through the autopilot, starting with a description of the missile simulator, its interaction with preceding simulators, and the simulation infrastructure. It ends with the conversion of the guidance demands into STT and BTT missile motion first constrained by the launcher, then by speed dependent g-limiting up to Mach 1, before free-flight. The order of presentation is dictated by the simulator, starting with missile mass, thrust and drag characteristics, and their Jacobians for trajectory optimisation. The focus of §6 thereafter is on conventional guidance laws, as distinct from on-line trajectory optimisation dealt with in §7.

Fossier [F.2] reviews the course of sensor development and its links with conventional missile command (3 point), homing (2 point), and inertial guidance since World War 2. Inertial guidance to a geodetic reference point is the province of long range ballistic and cruise missiles, although it can be employed for mid-course guidance of medium-range missiles. Command guidance uses ground-based target tracking data and up-linked CLOS guidance commands. Homing guidance is autonomous using seeker data and PN guidance commands.

By the mid-60s the improvement in radar tracking and ground processing capacity proved irresistible and expensive seekers/PN were replaced by radar/CLOS in many air-defence systems. These systems rely on up-linked steering commands to eliminate the differential angle between the missile and target after "gathering" into the radar beam. Phased array radar technology introduced in the 80s uses separate beams to reduce the initial gathering acceleration demands. These systems have proven remarkably adaptable considering the advances in target manoeuvrability and defensive countermeasures. However, both command and homing guidance systems can be compromised by reliance on a single sensor exhibiting sub-optimal characteristics during some part of the engagement. By the late-80s it was recognised that their performance could not be improved indefinitely and so research began into multi-spectral seekers, data fusion and the combination of PN and CLOS. Systems are emerging in which approach angle controlled PN guidance is generated from inertial information combined with up-linked radar data before switching to homing using the re-established seeker.

A review of PN guidance laws in two and three dimensions (2D and 3D) derived by conventional solution of the underlying differential equations defining the relative motion between the missile and target. The removal of steady-state constraints is charted over 50 years and the emergence of

simpler optimal guidance solutions in the 80s. It is the Linear Quadratic Regulator (LQR) problem, and its solution via the Ricatti equation, that forms the link with the "open-loop" trajectory optimisation. The LQR is a Bolza Two-Point-Boundary-Value-Problem (TPBVP) constrained to linear systems and a quadratic Performance Index (PI), thereby limiting its potential.

Basic and augmented forms of PN are provided, highlighting their sensitivity to parasitic errors and the relationship between the kinematic gain and time-to-go estimates. Similarly, CLOS feed-forward and stability acceleration demands are derived incorporating weave tuning by Vorley[V.3], and compensation for straight flying targets introduced by Lee[L.4]. These conventional guidance laws provide an insight into the closed form optimisation and the cost functions used in their derivation, information that can be exploited in open-loop formulations. They are used for missile model proving since their underlying principles are relatively simple compared with open-loop equivalents, and to create a performance baseline to compared with on-line trajectory optimisation; the province of §9.

1.3.5 Chapter 7 : Trajectory Optimisation

Increasing coverage, rear hemisphere engagements, higher impact speeds and controlled approach angles avoiding jamming regions to improve kill probability against agile targets requires sophisticated trajectory optimisation. Such optimisation irrefutably improves performance dependent on the PI used compared with conventional missile guidance in respect of,

- Increased impact speed for given range
- Increased coverage for a given impact speed
- Increased warhead lethality by approaching the target at an optimal aspect
- Reduce impact time for close-range high speed engagements
- Compensate for model mismatches and abnormal missile performance
- Increased resistance to target electronic counter-measures
- Avoidance of exclusion zones
- Maintenance of up-link communications
- Maintain sensor tracking-lock within pointing and beam-width limitations
- Promote a smooth transition of from mid-coarse to terminal guidance
- Improve state observability

Off-line optimisation often involves approximations over a range of engagement scenarios that are detrimental to those few cases actually encountered. Indeed LQR solutions, if they exist, tend to over-control with emphasis on the terminal conditions, Archer[A.1]. Posing closed loop

guidance problems with explicit solutions becomes ever more difficult as the complexity of the constraints imposed increases, solutions existing only for the most basic cases. As a result problems are often over-simplified: reduced missile dynamics, no measurement noise, etc., hence their solutions are of limited value.

Recently Shooting and Simulated Annealing techniques have emerged to deal TPBVP involving more sophisticated PI however, their implementation is by necessity simple and therefore restrictive. Such guidance laws are often tuned for a limited number of scenarios and require state observer data to select the appropriate parameter maps for the prevailing conditions, maps requiring large storage capacities.

An alternative strategy is proposed in §7, in which gradient projection methods are used to solve the TPBVP on-line. These techniques, discarded for off-line optimisation in favour of more advanced methods, converge surprisingly rapidly from a reasonable initial trajectory to a near optimal solution, and remain robust, Moody[M.12]. An optimal control set is maintained subject to PI change reflecting current conditions and priorities using range dependant weighting functions. For example, weights favouring pre-launch state observability and approach angle that change gradually after launch to miss distance and energy consumption mitigating the dominance of the terminal constraints reported by Speyer[S.9].

Yang[Y.9] observed that guidance laws in literature avoid real-time solutions in a varied threat environment. Moreover, in attempting to optimise time-to-go and impact speed, he stated that on-line solutions were impractical due to numerical instability. The stability of the boundary conditions provided by the state observation is crucial for convergence. Not only must the optimiser be relatively insensitive to noisy boundary conditions it must also be robust for a wide range of target engagements, from constant velocity crossing targets to weaving targets and extreme avoidance manoeuvres.

§7 starts by describing the gradual use of optimised controls in the missile autopilot whilst the remainder are re-optimised commensurate with the processing time available. The missile model dynamic constraints are defined, and the generation of lateral acceleration demands from the controls established. The TPBVP is formulated using incidence controls, dynamic initial conditions, variable impact time, and a PI requiring inequality constraints and penalty functions. Pontryagin theory is used to reduce the problem to a univariate optimisation of the Hamiltonian created by adjoining dynamic constraints to the cost function. Techniques for selecting the best search direction and step-length are reviewed that includes Wolfe's step-length conditions.

The chapter ends with a description of the trajectory optimisation "simulator". This alternative guidance law is embedded inside the missile simulator together with the conventional alternatives provided. The concept of using the simulation host processor clock to limit the amount of re-

optimisation that can be undertaken is introduced for assessing real-time system performance.

1.3.6 Chapter 8 : Simulation

The discussion on the role of simulation for developing and proving modern weapon systems is extended. To recap, the complexity of missile systems has raised the status of the validated simulations required to predict performance over an extended envelope without resort to expensive trials. This is discussed in the context of creating a simulation environment capable of supporting several systems with common launcher interfaces and a shared infrastructure cost. §8 describes such an infrastructure designed to support any dynamical model covering external and interactive control, on-line visualisation, internal data communication, I/O facilities, their interaction with external applications, post processing and Monte-Carlo ensemble analysis supported by:

- Software configuration
- Software utilities that are the basis for rapid model development (Appendix I).
- External interface with MATLAB for graphics, time series and signal analysis.

Within this infrastructure reside the "separate" simulators shown in Figure 1-3 forming a common thread through §2 to §7, each incorporating the functionality of those preceding it, and designed so that they can be executed in isolation:

- Target trajectory generation.
- Sensor modelling – generic error model characterisation.
- Target state observation – multiple-model track formation.
- Missile state observation – central fusion of up-linked and sensor data.
- Missile simulator – flight dynamics, PN and CLOS guidance, and open loop trajectory optimisation.

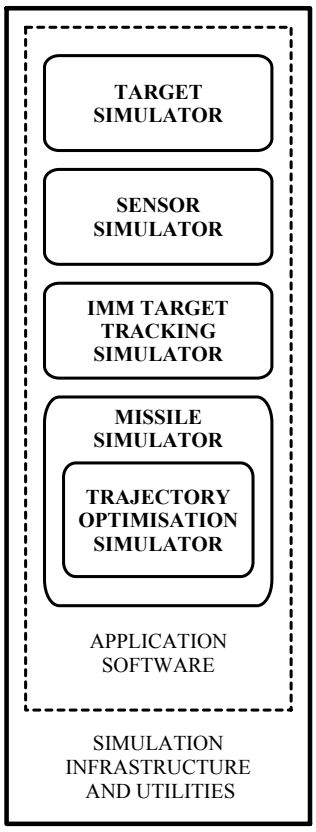

Figure 1-3
Embedded Simulators

The interaction between modern air-launched missiles and their launchers is discussed in the context of a new breed of simulation. In the mid-90s MBDA agreed that this infrastructure and many of the utilities and generic sensor models created should form the basis for the Aircraft and Missile

Integration Simulation (AMIS). This program was designed by the author for MBDA, and together with a team of engineers, developed for missile algorithm development and performance assessment. Common facilities between the two simulations now play an important role in the development of the following MBDA products:

- ASRAAM
- Storm Shadow
- Black Shaheen
- Meteor
- PAAMS
- Long range navigation assessment software suite comprising flight data reconstruction, SDINS GPS and TFA

The AMIS has been used for performance assessment and integration on current fighter aircraft including:

- EF 2000
- Tornado
- Harrier Gr. 7
- F-16 Fighting Falcon
- F-18 Hornet

Although the simulations share models, for Commercial and Security purposes they are treated as separate entities. The results in this study are not representative of the performance and design of any of the above products.

1.3.7 Chapter 9 : Performance

Before dealing with specific performance issues, §9 presents a typical air-defence launch event sequence from target detection, fire control, through the launch sequence, and free-flight to impact. Various constraints and critical events are noted, and performance metrics established, the whole providing a framework supporting performance discussions.

A performance baseline is established using PN and CLOS guidance laws, stimulated using perfect observer data and targets designed for performance assessment. These results will eventually provide a baseline against which on-line trajectory optimisation can be assessed.

§9 closes with individual IMM filter performance and tuning, exploring the order in which the radar measurements are processed, filter stability and conditioning. The conclusions drawn here will provide a useful basis for future work in pursuit of the stated objectives.

1.3.8 Appendices A and B : Geometric Points and Frames of Reference

The Glossary, provides a general framework for describing motion in Euclidean space and transcribing it into simulation variables. Appendices A and B provide the application specific geometric points and frames for target and missile motion with respect to terrestrial and inertial references. Any additional points and frames required for defining sensor errors are defined locally with respect to the frames here.

1.3.9 Appendix C : Transformation Between Frames

Appendix C defines the rotational transformations between the primary frames whose origins are located at critical geometric points. Euler triplets and skew-symmetric forms are introduced to describe the relationships between Euler rotations, direction cosines and quaternions. Nomenclature is introduced to cope with the transformation between Cartesian, Polar and UVR co-ordinates with respect to a common frame.

1.3.10 Appendix D : Point Mass Kinematics

The geometry in the previous appendices forms the basis for defining direction cosine propagation, transformation matrix dynamics, angular rate and its skew-symmetric form, and their relationship with Euler triplets. The linear and angular velocity, acceleration and jerk dynamics of a point moving with respect to an inertial frame are developed.

1.3.11 Appendix E : Earth Geometry

Missile systems often involve terrestrial motion over long distances using navigation aids requiring a mathematical representation of the ground beneath. Expressions for earth radius, meridian and polar earth curvature are derived for a general ellipsoid. The defining characteristics of a number of commonly used ellipsoids are given, and WGS84 selected to explore the variation in these radii with latitude.

1.3.12 Appendix F : Atmospheric Characteristics

Expressions for the atmospheric pressure, temperature, and density variation with geodetic height are given up to 32km together with their relationship with the speed of sound and Mach number. The variation in these parameters with respect to the reference-state is provided for use in trajectory optimisation.

1.3.13 Appendix G : Gravitational Acceleration

Gravity acting at a point above the Earth is defined, and approximations relating to near-earth operation explored. Its variation with geodetic height and latitude is expressed in terms of the reference-state for trajectory optimisation.

1.3.14 Appendix H : Fixed-Gain Filters

This appendix deals with the fixed-gain counterparts of the stochastic filters used in the target state observer. Historical reviews precede the formulation of velocity, acceleration and weave filters that arise from the solution to the associated Ricatti equation. This information complements the presentation of filter utilities in Appendix J-8 and provides a useful insight into the quasi-steady state performance of stochastic filters. Conceptually, state observers

provide all the data required for missile guidance however, fixed-gain filters are still required in local control loops to provide stability.

1.3.15 Appendix I : Software Utilities

This appendix contains a mathematical definition for the software utilities listed in Appendix I underpinning the simulation. The definitions draw on material presented in other appendices packaged for software use however, if none exists additional information is provided where justification is necessary. Some utilities, particularly those dealing with filters and transforms, are provided with a functional form $\varphi(\ldots)$. This is an integral part of the nomenclature for concise presentation of nested processes that can then be directly linked to utility definitions.

Chapter 2

TARGET MODELLING

When dealing with specific applications selection of typical airborne targets is a subjective topic often surrounded by implacable argument. As air-to-air and air-defence missile system complexity increases so does target selection for design and performance proving. When dealing with tracking algorithms realistic target dynamics and flight regimes transition are more important than physical airframe characteristics that are important for sensor development.

The aim was to create a simulator within the program infrastructure capable of functioning in isolation, providing target trajectories for internal use and other off-line applications. Combined with the initialisation, characterisation and wire-frame visualisation software in the program infrastructure this simulator provides a powerful tool for target trajectory synthesis.

§2 deals with the creation of complex target trajectories from relatively simple dynamic models. Elemental acceleration demand models are selected from which it is possible to create a wide range of trajectories in Earth referenced Cartesian space. Demands in Target Velocity axes are filtered using local integrators, before transformation, and centralised state integration.

Idealised trajectories are always needed for design proving. Here trajectories are required with dynamics matched to the IMM filters for initialisation, proving and tuning purposes. These are in stark contrast to trajectories that are capable of exposing target state observer shortcomings that are based on weaves and dog-leg avoidance manoeuvres.

§2 concludes with a general discussion, initially covering the models required for this research. Natural extensions to these models are then explored in the context of AMIS air-to-air scenario generation based on the author's considerable experience in this field.

2.1 Target Simulator

The program infrastructure described in §9 supports a number of application dependent simulators. The most basic of these is the Target simulator shown in Figure 2-1, whose software is stored using the DEC Code Management System (CMS) in group [TARGET].

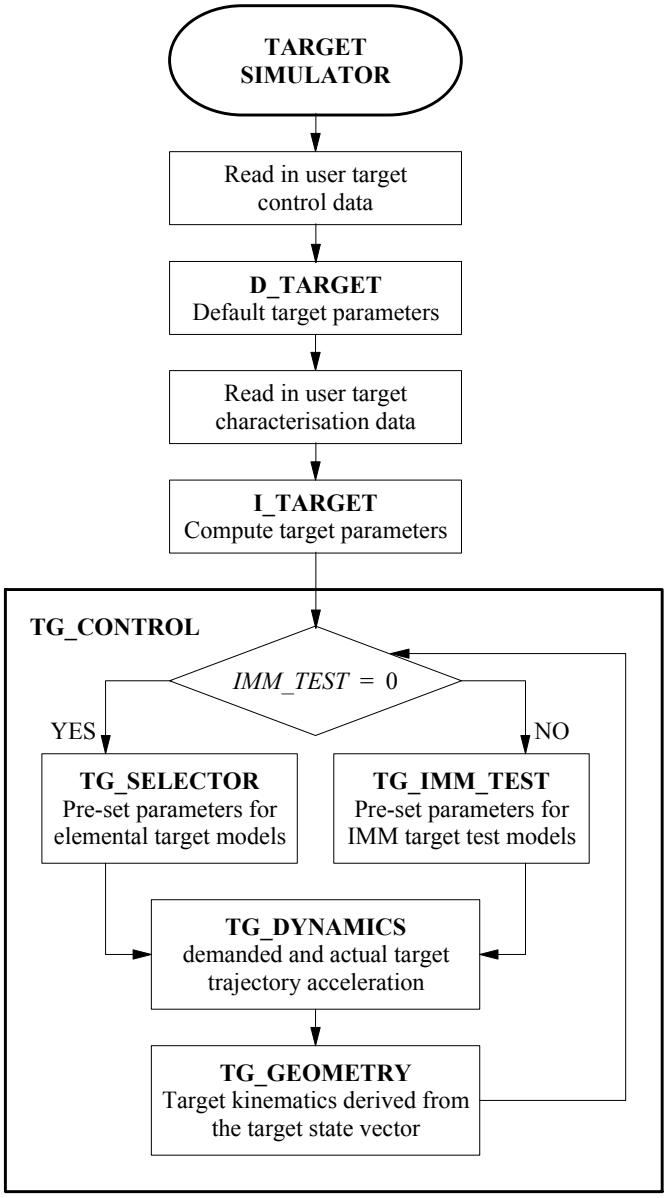

Figure 2-1 : Target Simulator

The target model is isolated by setting the missile launch time to a value greater than the simulation end time, and de-select the target tracking filters:

$$TIMEND < TLAUNCH$$

$$IMM\_TP = 0$$

Target motion is defined in the Alignment frame using a Cartesian state vector ($\underline{X}_T$) comprising 3D position, velocity and acceleration states. Sufficient flexibility has been provided so that the user can construct target trajectories from a number of target models. The target models provided are the basic building blocks that can be characterised by the user, either in isolation, or to create more complex trajectories. This Simulator contains a number of pre-programmed trajectories *IMM_*_TEST*, controlled by *TG_IMM_TEST*, each designed to tune the separate IMM target tracking filters. An important feature is the activation the Target Simulator in conjunction with the target tracking sensors so that their corrupted measurements can be assessed against reference target kinematics. The reference target data listed in §22.2.3 is computed directly from the target state vector in module *TG_GEOMETRY*.

Initially default target data is loaded by module *D_TARGET* for a constant velocity flypast trajectory using Target Trajectory 2 and Target Model 1 that are described in §2.3.2 and §2.2.4 respectively. The program then reads the users target control and characterisation data provided from external files. This data contains *TGT_SEL*, used to select one of the Target Trajectories described later. Target initialisation is then completed in *I_TARGET*. *TG_SELECTOR* provides the generic target type sequence and peak acceleration profiles for each of the pre-set trajectories identified by *TGT_SEL*. The target demanded and actual accelerations are transformed into the Alignment frame by *TG_DYNAMICS* at the simulation reference rate of 4 kHz. If the acceleration demand filter bandwidths are set to zero the aircraft "stick" to acceleration dynamics are by-passed.

2.1.1 Target Default Parameters

The default target type *TG_TYPE* in the range [1(1)6] for the wire frame model is set to 1 representative of a MiG-29 (Fulcrum). The initial target class described in §2.2.1 is a head-on aspect. For glint modelling, an important element in the ground radar and missile seeker measurement error models, the physical dimensions of a typical air superiority fighter along its Target Body axes are loaded,

$$\underline{l}_t^{TB} := \left(19 \;,\; 13 \;,\; 5 \right)^T$$

Equation 2.1-1

The dimensions of modern military aircraft vary greatly depending on their role and design. From published data the following are typical:

- Trainers/light strike Fighters $\underline{l}_t^{TB} := \left(13 \;,\; 10 \;,\; 4 \right)^T$
- Attack Helicopter (incl. main rotor) $\underline{l}_t^{TB} := \left(12 \;,\; 11 \;,\; 3 \right)^T$
- Transport Helicopter (incl. main rotor) $\underline{l}_t^{TB} := \left(18 \;,\; 20 \;,\; 5 \right)^T$

- Tankers and large bombers $\underline{l}_t^{TB} := \left(45 \quad , \quad 50 \quad , \quad 12 \right)^T$

The demanded acceleration, and its relationship with the applied acceleration defined in the generic target models, depend on the target dynamic lag (s), PN gain and weave frequency with default values,

$$\underline{t}_{ta} := \left(0.3 \quad , \quad 0.5 \quad , \quad 0.5 \right)^T$$

Equation 2.1-2

$$\lambda_t := 3 \; ; \; \underline{\omega}_w := \left(0 \quad , \quad \pi / 2 \quad , \quad \pi / 2 \right)^T$$

Equation 2.1-3

The target class *TARGET* is set to 2 for a crossing target. *D_TARGET* ends by setting the default parameters and initial target state associated with the target trajectory acceleration model selected by the user dependent on the acceleration type *TAGACC*. The initial target state vector is obtained from one of the pre-set target trajectories defined in §2.3. These data may be replaced using program characterisation data.

$$\underline{X}_T(0) := \left(\left({}^I\underline{P}_t^A \right)^T \quad , \quad \left({}^I\dot{\underline{P}}_t^A \right)^T \quad , \quad \left({}^I\ddot{\underline{P}}_t^A \right)^T \right)^T$$

Equation 2.1-4

2.2 Generic Target Models

2.2.1 Target Classes

The mutually exclusive target model classes are selected by setting the value of *TARGET*:

- 0 Stationary Target
- 1 Head-on Target
- 2 Crossing Target

Class dependent target initialisation is performed by *I_TARGET*. For stationary targets, the target dynamic states are removed from the processed reference state vector and any user velocity/acceleration input ignored.

$$TARGET = 0 \Rightarrow \underline{X}_T := \left(\left({}^I\underline{P}_t^A \right)^T \quad , \quad \left(\underline{0}_3 \right)^T \quad , \quad \left(\underline{0}_3 \right)^T \right)^T$$

Equation 2.2-1

For head-on targets, the absolute value of the x-component of the user input velocity vector is taken to represent the velocity along the target LOS from

the launcher. The remaining velocity components are ignored. This velocity is converted into components with respect to the Alignment frame such that the target initially flies directly towards the launcher.

$$TARGET = 1 \Rightarrow$$

$$\underline{X}_T(0) := \left(\left({}^{I}\underline{P}_t^A \right)^T , \left(-T_T^A \left({}^{I}\underline{P}_t^A \right) \cdot \left| {}^{I}\dot{P}_t^{XA} \right| \right)^T , \left(\underline{0}_3 \right)^T \right)^T$$

Equation 2.2-2

From §16.15, the Alignment to Target LOS frame transformation is defined by the initial position of the target. For crossing targets, the initial target state is provided with respect to the Alignment frame and is used directly.

$$TARGET = 2 \Rightarrow \underline{X}_T(0) := \left(\left({}^{I}\underline{P}_t^A \right)^T , \left({}^{I}\underline{\dot{P}}_t^A \right)^T , \left({}^{I}\underline{\ddot{P}}_t^A \right)^T \right)^T$$

Equation 2.2-3

2.2.2 Target Acceleration Models

The generic target acceleration demand models are mutually exclusive and are selected by setting the variable *TAGACC*:

- 0 Stationary target
- 1 Constant linear acceleration in the Alignment frame
- 2 Constant linear acceleration in the Target Velocity frame
- 3 Sinusoidal weave in the Target Velocity frame
- 4 Square wave weave in the Target Velocity frame
- 5 PN onto defending radar and launcher
- 6 PN with superimposed sinusoidal weave
- 7 PN with superimposed square wave weave

These models are defined in *TG_DYNAMICS*. The acceleration demand *DEMACC* ($\underline{A}_D$) is set at the leading edge of the simulation reference clock, and is then subject to a ZOH over the integration period (Δt_I). This demand passes through a 1st order lag representing the finite dynamics of the target.

For Target Model 1 the dynamic lags are applied to the demanded acceleration acting along the Alignment axes. For Target Models 2 to 7 the dynamic lags are applied to the demanded acceleration acting along the Target Velocity axes. If the target time constant is set to zero, or a value that cannot be modelled accurately using the simulation integration period, the dynamic lag is ignored,

$$t_{ac}^{i} < 10 \cdot \Delta t_I \Rightarrow \ddot{P}_t^i := A_D^i$$

Equation 2.2-4

If the true acceleration of the target is too small along any individual axis (i) it is set to the demanded acceleration along that axis. Any initial time constants provided by the user are similarly tested in *I_TARGET* to ensure that they are commensurate with the internal digital integration filter rates used. If they are too small, they are set to zero causing the acceleration demand filters to be bypassed. Target acceleration is determined in *TG_DYNAMICS* using bi-linear digital filters operating at the simulation reference rate. The reference position and velocity of the target is obtained by integrating the true acceleration from its initial state using a Runge-Kutta algorithm. The functional form of the 1st order digital lag (φ_{D1L}) used to describe the following target models is described in §22.7.1.

2.2.3 Target Model 0

The target is held stationary at its initial position. Any default, or user provided, accelerations and velocities are set to zero.

$$TAGACC = 0 \Rightarrow \underline{X}_T := \left(\left({}^{I}\underline{P}_t^A \right)^T , \left(\underline{0}_3 \right)^T , \left(\underline{0}_3 \right)^T \right)^T$$

Equation 2.2-5

2.2.4 Target Model 1

The demanded acceleration is used directly in the Alignment frame,

$$TAGACC = 1 \Rightarrow \underline{\ddot{P}}_t^A := \underline{\varphi}_{D1L} \left(\underline{A}_D^A , \underline{t}_{ta}^{XA} \right)$$

Equation 2.2-6

2.2.5 Target Model 2

The demanded acceleration is used in the Target Velocity frame,

$$TAGACC = 2 \Rightarrow \underline{\ddot{P}}_t^A := T_{TV}^A \cdot \underline{\varphi}_{D1L} \left(\underline{A}_D^{TV} , \underline{t}_{ta} \right)$$

Equation 2.2-7

The transformation from the Alignment to Target Velocity frame is a function of target velocity with the Euler roll angle set to (π) to accommodate their respective verticals. The Euler triplet between frames used in Equation 16-5 is therefore,

$$E_A^{TV} := \left(\pi \;,\; -\tan^{-1}\left(\frac{\dot{P}_t^{ZA}}{\dot{P}_t^{hA}} \right) \;,\; \tan^{-1}\left(\frac{\dot{P}_t^{YA}}{\dot{P}_t^{XA}} \right) \right)$$

Equation 2.2-8

2.2.6 Target Model 3

The demanded acceleration represents the amplitude of a sinusoidal weave expressed in the Target Velocity frame,

$$TAGACC = 3 \;\Rightarrow\; \underline{\ddot{P}}_t^A := T_{TV}^A \cdot \underline{\varphi}_{D1L}\left(\underline{A}_D^{TV} \cdot \cos\left(\underline{\omega}_w \cdot t \right), \underline{t}_{ta} \right)$$

Equation 2.2-9

2.2.7 Target Model 4

The demanded acceleration represents the amplitude of a "square" wave weave expressed in the Target Velocity frame.

$$TAGACC = 4 \;\Rightarrow\; \underline{\ddot{P}}_t^A := T_{TV}^A \cdot \underline{\varphi}_{D1L}\left(\text{sign}\left(\underline{A}_D^{TV}, \cos\left(\underline{\omega}_w \cdot t \right) \right), \underline{t}_{ta} \right)$$

Equation 2.2-10

2.2.8 Target Model 5

The demanded acceleration in the Target Velocity frame is derived using a PN guidance law with the missile launcher as the intercept point.

$$TAGACC = 5 \;\Rightarrow\; \underline{\ddot{P}}_t^A := T_{TV}^A \cdot \varphi_{D1L}\left(\begin{pmatrix} A_D^{XTV} \\ \lambda_t \cdot \dot{P}_t^{XT} \cdot \omega_{A,T}^{ZT} \\ \lambda_t \cdot \dot{P}_t^{XT} \cdot \omega_{A,T}^{YT} \end{pmatrix}, \underline{t}_{ta} \right)$$

Equation 2.2-11

The longitudinal acceleration remains the same as for Target Model 2, providing the facility to model accelerating attacks on the launcher.

2.2.9 Target Model 6

The demanded acceleration is a combination of Target Models 4 and 5. The result is an accelerating PN track with a superimposed sinusoidal weave.

$$TAGACC = 6 \Rightarrow$$

$$\underline{\ddot{P}}_t^A := T_{TV}^A \cdot \underline{\varphi}_{D1L} \left(\begin{pmatrix} A_D^{XTV} \\ A_D^{YTV} \cdot \cos\left(\omega_w^{YTV} \cdot t \right) + \lambda_t \cdot \dot{P}_t^{XT} \cdot \omega_{A,T}^{ZT} \\ A_D^{ZTV} \cdot \sin\left(\omega_w^{ZTV} \cdot t \right) + \lambda_t \cdot \dot{P}_t^{XT} \cdot \omega_{A,T}^{YT} \end{pmatrix}, \underline{t}_{ta} \right)$$

Equation 2.2-12

2.2.10 Target Model 7

The demanded acceleration is a combination of Target Models 3 and 5. The result is similar to Target 6, an accelerating PN track with a superimposed square wave weave.

$$TAGACC = 7 \Rightarrow \underline{\ddot{P}}_t^A(t) :=$$

$$T_{TV}^A \cdot \begin{pmatrix} \varphi_{D1L}\left(A_D^{XTV}, t_{ta}^{XA} \right) \\ \varphi_{D1L}\left(\operatorname{sign}\left(A_D^{YTV}, \cos\left(\omega_w^{YTV} \cdot t \right) \right) + \lambda_t \cdot \dot{P}_t^{XT} \cdot \omega_{A,T}^{ZT}, t_{ta}^{YA} \right) \\ \varphi_{LAG}\left(\operatorname{sign}\left(A_D^{ZTV}, \cos\left(\omega_w^{ZTV} \cdot t \right) \right) + \lambda_t \cdot \dot{P}_t^{XT} \cdot \omega_{A,T}^{YT}, t_{ta}^{ZA} \right) \end{pmatrix}$$

Equation 2.2-13

2.3 Programmed Target Trajectories

The simulator contains pre-loaded target trajectories (not to be confused with target models) that are designed to fulfil two requirements:

- Relatively benign targets for comparing tracking, sensor fusion and guidance techniques
- More exacting targets performing evasive manoeuvres designed to expose a filtering technique's shortcomings.

These target trajectories are constructed from the target models defined in §2.2, and are activated by setting the value of *TGT_SEL*:

- 1 User specified trajectory defined using only input data.
- 2 Alternating periods of constant velocity and acceleration along $\underline{X}^A$ applied to a crossing target.
- 3 Same as (2) with an evasive turn 2 s before missile impact.
- 4 Same as (2) with an evasive barrel roll 2 s before missile impact.

- 5 Accelerating PN attack on the missile launch point (o).
- 6 Accelerating PN attack on the missile launch point with an evasive turn 2 s before missile impact.
- 7 Accelerating PN attack on the missile launch point (o) with superimposed weave motion.

When *TGT_SEL* is set in the range [2(1)7] user input is ignored and a programmed sequence of events is activated by *TG_SELECTOR*:

2.3.1 Target Trajectory 1: User Defined

If *TGT_SEL* is invalid the program uses input state data controlled by the class and generic target model selected. The default values for the case *TGT_SEL* := 1 in D_TARGET invoke Target Model 1 with the initial state,

$$\underline{X}_T(0) := \left(17\_000 \;,\; 6\_000 \;,\; 5\_000 \;,\; -400 \;,\; (\underline{0}_5)^T\right)^T$$

Equation 2.3-1

The user can change the acceleration demand, and target model, any time during the flight.

2.3.2 Target Trajectory 2: X-Axis Acceleration Bursts

TGT_SEL := 2 activates crossing Target Model 1 starting from,

$$\underline{X}_T(0) := \left(17\_000 \;,\; 6\_000 \;,\; 5\_000 \;,\; -250 \;,\; (\underline{0}_5)^T\right)^T$$

Equation 2.3-2

After 5 s, there follows alternating 5 s periods of constant demanded acceleration along $\underline{X}^A$ and constant velocity, until 40 s after which the target velocity remains constant.

$$t \in]m, m+5] : m = [0(10)40] \Rightarrow \underline{A}_D^A := \underline{0}_3$$

Equation 2.3-3

$$t \in]m, m+5] : m = [5(10)35] \Rightarrow \underline{A}_D^A := (5 \;,\; 0 \;,\; 0)^T$$

Equation 2.3-4

2.3.3 Target Trajectory 3: Evasive Turn Close to Impact

TGT_SEL := 3 activates Target Model 2 starting from the same initial state as Trajectory 1. If the missile is launched the target remains on a constant velocity crossing trajectory until an accelerating evasive turn is commanded (t_{AM} := 2 s) before impact.

$$t_{GO} \geq t_{AM} \Rightarrow \underline{A}_D^{TV} := \underline{0}_3$$

Equation 2.3-5

$$t_{GO} < t_{AM} \Rightarrow \underline{A}_D^{TV} := \left(30 \ , \ 64 \ , \ 64 \right)^T$$

Equation 2.3-6

The lateral target acceleration is set to the maximum "g" levels sustainable by human physiology, an absolute value of 9 g. Time-to-go (t_{GO}) is determined from closing speed and range between the missile and the target.

$$t_{GO} := -\frac{P_{m,t}}{\underline{P}_{m,t}^A \bullet \underline{P}_{m,t}^A} := \frac{\left\| \underline{P}_t^A - \underline{P}_m^A \right\|}{T_A^S \cdot \left(\underline{\dot{P}}_t^A - \underline{\dot{P}}_m^A \right) \cdot \underline{\hat{i}}^S}$$

Equation 2.3-7

2.3.4 Target Trajectory 4: Crossing Target with Evasive Barrel Roll

TGT_SEL := 4 activates Target Model 2 starting from the same initial state as Trajectory 1. After 5 s Target Model 3 is activated resulting in an evasive coning motion with a peak acceleration demand,

$$t \in [0 \, , 5[\Rightarrow \underline{A}_D^{TV} := \underline{0}_3$$

Equation 2.3-8

$$t \in [5 \, , \infty[\Rightarrow \underline{A}_D^{TV} := \left(0 \ , \ 64 \ , \ 64 \right)^T$$

Equation 2.3-9

2.3.5 Target Trajectory 5: Accelerating PN Attack

TGT_SEL := 5 activates Target Model 2 starting from,

$$\underline{X}_T(0) := \left(16\_000 \ , \ 13\_000 \ , \ 5\_000 \ , \ -300 \ , \ \left(\underline{0}_5 \right)^T \right)^T$$

Equation 2.3-10

After 5 s an attack on the launcher is activated using Target Model 5 resulting in a PN trajectory with a superimposed evasive coning motion,

$$t \in [5 \, , \infty[\Rightarrow \underline{A}_D^{TV} := \left(5 \ , \ A_D^{YTV} \ , \ A_D^{ZTV} \right)^T$$

Equation 2.3-11

2.3.6 Target Trajectory 6: Accelerating PN Attack with Evasive Turn

TGT_SEL := 6 activates Target Model 2 starting from the same initial state as Trajectory 5. The attack on the launcher is initiated after 5 s using Target Model 5. If the missile is launched, this is replaced by Target Model 2 with the following acceleration demand.

$$t_{GO} < t_{AM} \Rightarrow \underline{A}_D^{TV} := (5, -64, 64)^T$$

Equation 2.3-12

If the missile is not launched, Target Model 2 is still activated but under the following conditions,

$$t \in [36, 41[\Rightarrow \underline{A}_D^{TV} := (5, -64, 64)^T$$

Equation 2.3-13

$$t \in [41, 46[\Rightarrow \underline{A}_D^{TV} := (5, 64, -64)^T$$

Equation 2.3-14

After the avoidance manoeuvre, the 0.5 g accelerating PN attack is re-established using Target Model 2 prior to impact.

2.3.7 Target Trajectory 7: Accelerating PN Attack with Evasive Weave

TGT_SEL := 7 activates Target Model 2 starting from the same initial state as Trajectory 5. After 5 s an attack on the launcher and ground radar is initiated using Target Model 6 resulting in an accelerating PN attack with the coning avoidance manoeuvre until impact.

2.4 Target Trajectories for IMM Filter Tuning

The target trajectories defined thus far use input data files, or pre-set data, with *IMM_TE*ST set to zero as shown in Figure 2-1. The individual IMM target tracking filters are tuned using trajectories that are activated by setting the following bits of *IMM_TE*ST:

- Constant velocity (bit 1)
- Constant acceleration in the Alignment frame (bit 2)
- Stepped acceleration through a 1st order lag (bit 3)
- Weave motion (bit 4)

The pre-set dynamics built into *TG_IMM_TEST*, once invoked, replace the programmed target trajectories in *TG_SELECTOR* and cannot be altered by the user. These test trajectories are characterised in the program using demanded accelerations expressed in the Alignment frame before conversion into the Target Velocity frame. The acceleration demands are

then subjected to filtering followed by transformation back to the Alignment frame thereby preserving the Target model interfaces in *TG_DYNAMICS*. These idealised target motions start after 10 s of constant velocity flight, and end after 30 s; Missile launch is suspended when IMM filter tuning.

2.4.1 Constant Velocity

Target Model 1 is activated with the Alignment frame acceleration set to zero. The target trajectory is a flypast at a constant velocity of - 400 m/s parallel to $\underline{X}^A$ starting from the same initial state as Target Trajectory 2.

2.4.2 Constant Acceleration

This trajectory starts the same as that for the constant velocity case. After 10 s the following acceleration profile is invoked:

$$t \in [0,10] \cup]24,30] \Rightarrow \underline{\ddot{P}}_t^A := \underline{0}_3$$

Equation 2.4-1

$$t \in]10,17] \Rightarrow \underline{\ddot{P}}_t^A := \underline{\varphi}_{D1L}\left((10 \;,\; 10 \;,\; -10)^T, \underline{t}_{ta} \right)$$

Equation 2.4-2

$$t \in]17,24] \Rightarrow \underline{\ddot{P}}_t^A := \underline{\varphi}_{D1L}\left((-10 \;,\; -10 \;,\; 10)^T, \underline{t}_{ta} \right)$$

Equation 2.4-3

2.4.3 Lagged Motion

Again the target starts as for the constant velocity case. After 10 s the target performs a 50 g "U" turn retreating at high speed. The demanded accelerations in this case are,

$$t \in [0,10] \cup]24,30] \Rightarrow \underline{\ddot{P}}_t^A := \underline{0}_3$$

Equation 2.4-4

$$t \in]10,17] \Rightarrow \underline{\ddot{P}}_t^A := \underline{\varphi}_{D1L}\left((50 \;,\; 50 \;,\; -50)^T, \underline{t}_{ta} \right)$$

Equation 2.4-5

$$t \in]17,24] \Rightarrow \underline{\ddot{P}}_t^A := \underline{\varphi}_{D1L}\left((50 \;,\; -50 \;,\; 50)^T, \underline{t}_{ta} \right)$$

Equation 2.4-6

2.4.4 Weave Motion

This trajectory is a characterised version of Target Trajectory 7 with motion constrained to the horizontal plane with an initial state,

$$\underline{X}_T := \left(16\_000 \;,\; 0 \;,\; 0 \;,\; -300 \;,\; \left(\underline{0}_5\right)^T\right)^T$$

Equation 2.4-7

After 3 s of constant velocity flight, the acceleration demand is set to,

$$t \in [36, 41[\;\Rightarrow\; \underline{A}_D^{TV} := \left(0 \;,\; 64 \;,\; 64\right)^T$$

Equation 2.4-8

The resulting weave is not monochromatic since low frequency PN is applied to ensure that the target motion is predominantly about $\underline{X}^A$.

2.5 Target Trajectories for Performance Assessment

Target trajectories 3 (fly-past with dog-leg) and 7 (weaving) were selected to assess guidance law and state observer performance.

2.5.1 Target Trajectory 3 - Definition

For guidance studies, a 400 m/s constant velocity, crossing target, with a 9 g avoidance manoeuvre applied normal to its velocity vector equally allocated between yaw and pitch, activated when the missile is 2 s from impact. For tracking studies, the missile is not launched and the manoeuvre is extended, starting after 37 s using the following demanded acceleration profile.

$$t \in [0, 37[\;\Rightarrow\; \underline{A}_D^{TV} := \underline{0}_3$$

Equation 2.5-1

At 37 s the target turns away from the missile launcher, diving from an altitude of 5 km to some 3 km to add to the radar clutter,

$$\dot{P}_t^{XA} \le -100 \;\Rightarrow\; \underline{A}_D^{TV} := \left(0 \;,\; 64 \;,\; 64\right)^T$$

Equation 2.5-2

As the turn develops and the velocity of the target parallel to $\underline{X}^A$ increases the target climbs at 9 g until it is climbing at 60°.

$$\left(\dot{P}_t^{XA} > -100 \right) \Rightarrow$$

$$\left\{ \begin{array}{c} \left(\Theta_A^{TV} \leq \frac{\pi}{3} \right) \Rightarrow \underline{A}_D^{TV} := T_A^{TV} \cdot \left(0, 0, 90 \right)^T \\ \left(\Theta_A^{TV} > \frac{\pi}{3} \right) \Rightarrow \underline{A}_D^{TV} := \underline{0}_3 \end{array} \right\}$$

Equation 2.5-3

2.5.2 Target Trajectory 7 - Definition

A 0.5 g accelerating PN attack against the launcher with a superimposed weave with a frequency of 0.25 Hz.

2.5.3 Target Trajectory Characteristics

The 3D trajectory, and the range, speed, bearing and elevation for these two trajectories are shown in Figure 2-2 to Figure 2-7. The impact points shown on these figures are based on a missile PN trajectory launched at 30 s. The data is contained in files *TGT_003* (blue trace) and *TGT_007* (red trace).

Both targets fly straight and level for the first 37 s at a constant speed of 400 m/s before any acceleration profiles are initiated. Low pass filters are applied to the acceleration demands with longitudinal and lateral time constants of 0.3 s and 0.5 s respectively.

2.6 Discussion

The target simulator is common to the other simulators supported by the program infrastructure. This simulator is not so much isolated, as the others are deactivated leaving only target trajectory generation. The target models, being relatively simple, generate trajectory data from the PVA states at the simulation reference rate so as to appear as "continuous" to the sensor simulator.

Default target characterisation is provided in respect of the physical dimensions and dynamic capabilities of military aircraft for glint modelling. Although military aircraft appear to come in all shapes and sizes they do in fact fall into distinct categories with relatively small variances. Typical dimensions are provided for fighters, trainers, helicopter and bombers.

The target models focus on motion in the Earth fixed Alignment frame provided that is a reflection of the air-launched application. Three target classes are established during program initialisation depending on user input data: stationary, head-on and crossing. The stationary case is often ignored however, it is relevant for land fixed targets, helicopters and vertically launched aircraft.

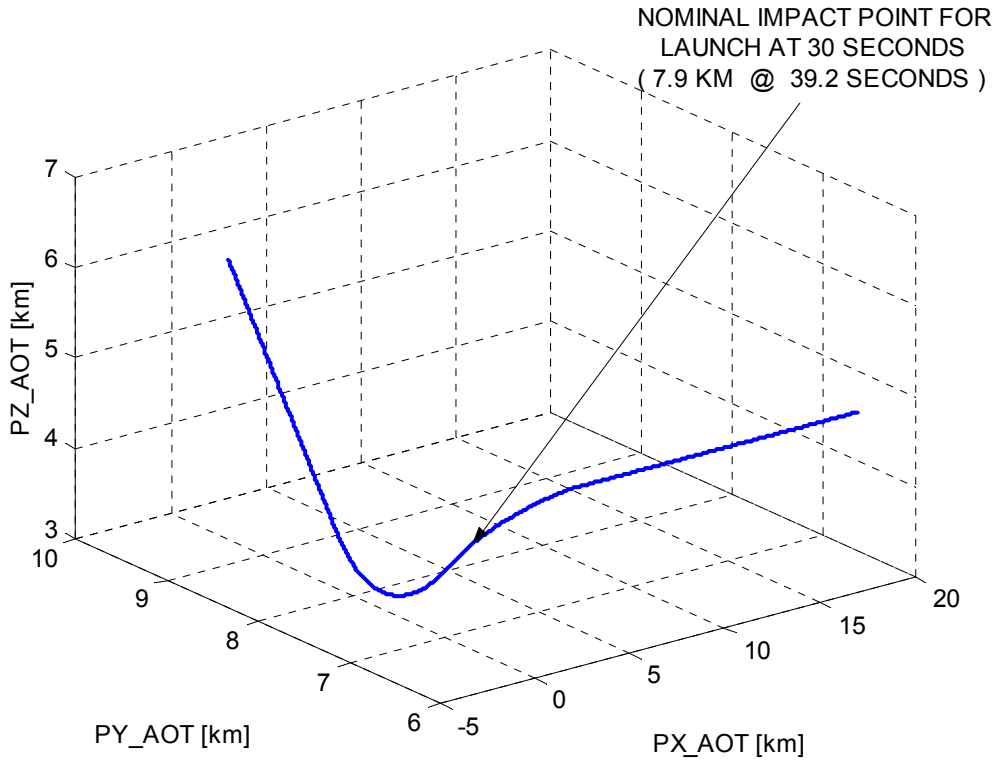

Figure 2-2 : Target Trajectory 3

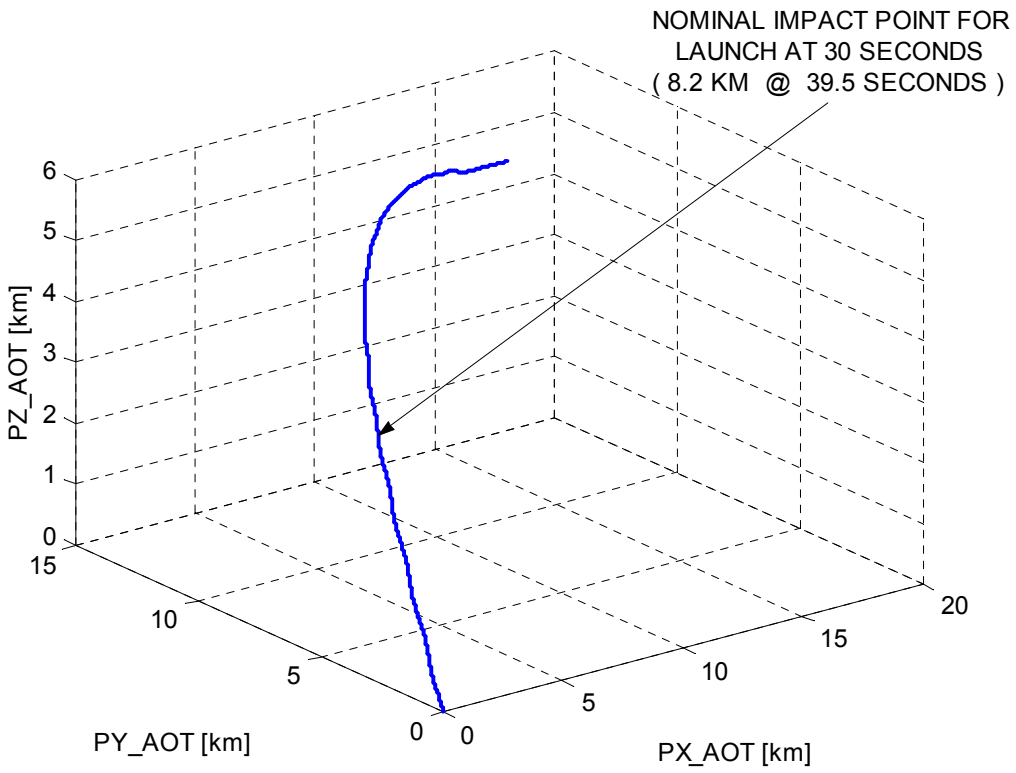

Figure 2-3 : Target Trajectory 7

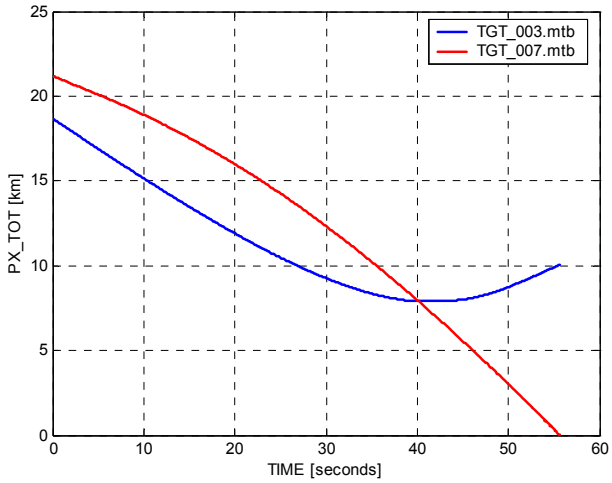

Figure 2-4 : Target LOS Range

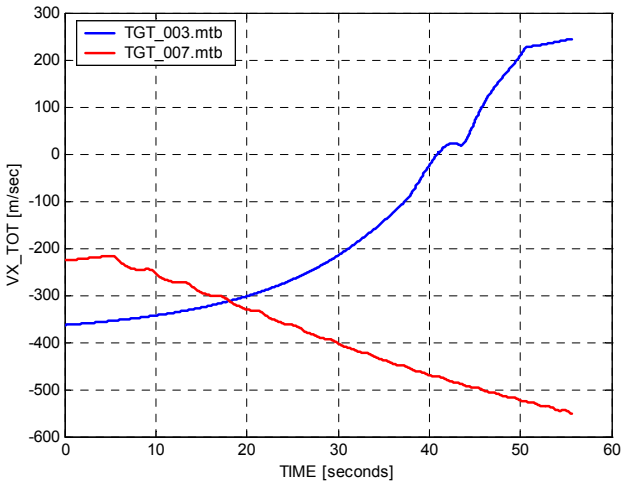

Figure 2-5 : Target Range Rate

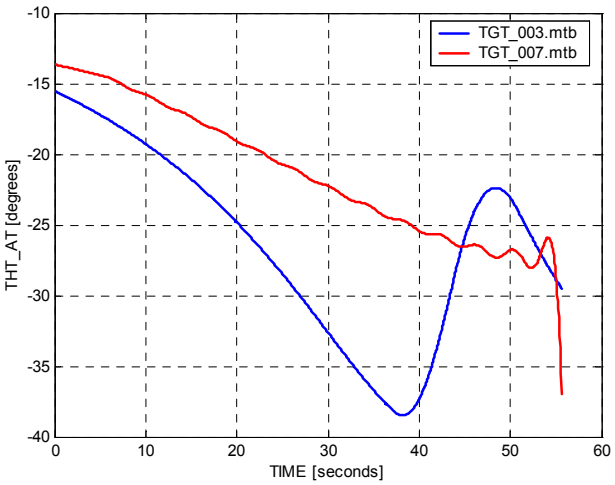

Figure 2-6 : Target Elevation

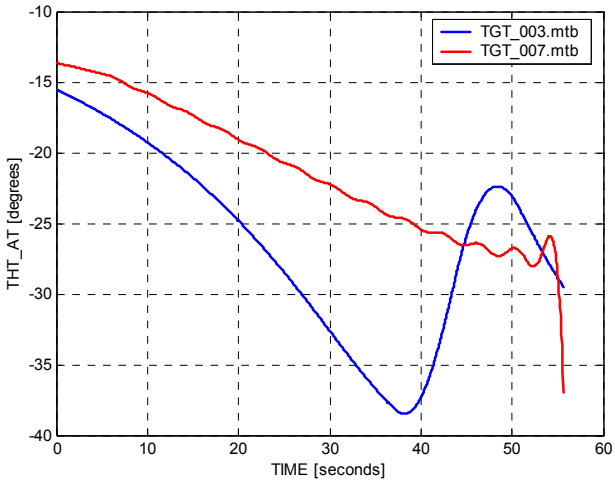

Figure 2-7 : Target Bearing

Accelerations provided by the user are treated as demands to be filtered so as to obtain the reference target-state, thereby preventing unrealistic jumps caused by changes in the elemental model characterisation. Eight elemental motions are provided: stationary, independent accelerations in the Alignment and Target Velocity frames, sinusoidal or "square" weaves, accelerating PN track onto the Alignment axis origin with, or without, superimposed weaves.

Square wave demanded acceleration profiles are important for assessing performance against weaving targets as they represent the infinite spectral case that is more representative of target motion than are sinusoidal weaves. Idealised trajectories are provided for tuning the IMM. Weave and dog-leg manoeuvres are provided for performance assessment as these are notoriously difficult to track using fixed-gain and single filter formulations.

Three enhancements are proposed to the current target simulator:

- The initial phase of the weave models should be randomised as this can significantly effect the miss distance attainable by low bandwidth guidance laws.

- Target goal-orientated trajectories are currently constrained to the position of the missile launcher. The facility would be greatly enhanced by providing the target's tracking point with PVA dynamics, starting from an initial state defined in the Alignment frame.

- The last enhancement concerns intelligent targets. Given adequate information a target could optimise its escape envelope on the basis of a 2-player pursuit-evasion game, Shinar[S.5&8]. Differential game theory provides the direction the target must turn, and the time at which to stop the turn, and fly in a direction maximising the probability of reaching a perceived no-escape boundary. The target manoeuvre causes the missile to turn and in doing so reduce speed as a tail-chase develops. Future targets

may respond in this way to radar illumination and missile launch performing bang-bang manoeuvres at the optimal switching times. The simulator should provide an elemental model based on this theory to facilitate 2-player guidance solutions.

This discussion concludes by exploring some alternative target models, in the main directed at air-launched munitions, some of which are potentially applicable to the current simulator:

- One important field of research is the re-creation of dynamics from a vehicle's position with respect to the earth and its body referenced dynamics. Generally, splines are fitted through way-points in LGA to obtain PVAJ linear dynamics, orientation and angular body rate. Although route generation is normally the province of long-range navigation, terrain following targets are useful for studying low-level target designation in a highly dynamic environment.

- Air-to-air engagements are often easier to simulate when target dynamics are defined with respect to the moving launcher. One of the most flexible approaches to this problem is to provide a target reference frame, located in the launcher, whose position with respect to launcher fixed axes is defined by some angular dynamic. The target is then constrained to move linearly along the x-axis of the target reference frame. This has obvious applications to air-launched scenarios in which the launcher is fixed and idealised polar dynamics are provided.

- The current target simulator provides a single target, and of course such targets can be cloned. However, consider a further extension to the previous model. The position of the single target becomes the location of a bi-normal plane to the target reference x-axis. The motion of multiple targets is then defined in this plane. The target are easily constrained to the FoV of sensors, within association gates, and to specific positions with respect to sensor sight-lines to test target selection algorithms and critical loci.

  These target scenarios have been developed for the AMIS. They are useful for creating idealised scenarios when dealing with relative motion, reducing highly complex motions to simpler cases amenable to analysis.

Chapter 3

SENSORS

Sensors are selected for their importance to future weapon systems in respect of targeting, geodetic referencing, and aided navigation. Although the latter are rarely used for air-defence, they perform critical functions such as height-keeping in cruise and sea-skimming missiles. Boundaries that were once distinct in this respect are now blurred, for example, GPS playing an important role in short-range munitions guided to a terrestrial reference.

This work on sensors is not restricted to the instruments required for air-launch weapon systems, models are provided for all the sensors. The focus is on providing system level models, ignoring high frequency effects well beyond the bandwidths of the state observers which process the measurements provided.

A sensor simulator is introduced, concentrating on controls that allow sensor and measurement subsets to be activated. There are many common elements between sensors and a symbolic framework is created and used to define these generic elements. Before dealing with individual sensors the generation of inertial inputs from LGA referenced data in a flexible structure for Master/Slave transfer alignment and inertial navigation is considered.

Historical reviews are provided for each sensor charting notable improvements leading to advances in missile capability. The design ethos is to encapsulate each sensor so that it is easily transported, cloned and characterised for applications beyond the needs of this research. Each sensor is stimulated by inputs derived locally from reference state data, corrupted by errors selected for their detrimental effect on state observation, and error estimation by the observers.

The chapter concludes with a discussion on the approach taken to modelling generic sensors, MATLAB SIMULINK alternatives, and enhancements to the current models that would widen their applicability.

3.1 Simulation Sensor Initialisation and Control

Consider the simulation initialisation description provided in the program infrastructure of §8.6. During the first stage of initialisation all the sensors are characterised using programmed default data. This process is controlled by *INIT_CONTROL* that activates sub-controller *D_SENSOR* that in turn stimulates the "default" modules listed in Table 3-1. This default sensor characterisation can be overwritten using external data. *INIT_CONTROL* then calls sub-controller *I_SENSOR* to activate the "initial" modules listed in Table 3-1. These complete the initialisation of all the sensor models, computing parameters based on default and user provided data. This process is independent of whether the sensors are activated later by the user.

Table 3-1 : Sensor Defaults, Initialisation and Update Modules

SENSOR	DESCRIPTOR	DEFAULT	INITIAL	
Ground radar	RD	D_TRACKER	I_TRACKER	
Gyroscopes	GS	D_GYRO	I_GYRO	
Accelerometers	AC	D_ACCN	I_ACCN	
Barometer	BA	D_BARO	I_BARO	
Radar altimeter	RA	D_RADALT	I_RADALT	
Missile seeker	SK	D_SEEKER	I_SEEKER	
Fin actuators	FN	D_FINS	I_FINS	
NAVSTAR GPS	GP	D_GPS	I_GPS	
Helmet mounted Sight	HS	D_HMS	I_HMS	
Air data system	AD	D_AIR	I_AIR	

The "descriptor" in Table 3-1 is a unique 2-character identifier for each sensor for use in the mathematical descriptions.

The user selects sensors by setting the bits of *MS_SN_AV* listed in Table 3-2. When initialisation is complete the selected sensor modules are activated at their update rate by *SM_CONTROL,* part of the state integration process controlled by *DX_CONTROL*. The missile actuators that convert guidance demands into fin positions for use with a full aerodynamic model are an exception. These are part of the missile dynamic model and are the only measurement source that is not controlled by *SM_CONTROL*.

Each sensor model is encapsulated in the modules listed in Table 3-2. Once a sensor has been selected it remains active until the program is terminated. Any combination of measurements from these sensors can be activated or de-activated during execution. The high-frequency "update" rates in Table 3-2 are commensurate with the provision of accurate reference input data and dynamic error propagation and cannot be changed by the user. Sensor measurements are updated at one of the clock rates provided in Table 22-1, defaulting to the "output" rate listed here. The output rate may be the same as, but must not exceed, the associated update rate.

Table 3-2 : *MS_SN_AV* Controlled Sensor Output Provision

BIT	SENSOR MODULE	UPDATE f_R (Hz)	OUTPUT f_O (Hz)	SENSOR AVAILABILITY	
1	MS_ACCN	800	400	ACCELEROMETER TRIAD	
2	MS_GYRO	800	400	GYROSCOPE TRIAD	
3	MS_BARO	400	20	BAROMETRIC ALTIMETER	
4	MS_RADALT	400	20	RADAR ALTIMETER	
5	MS_SEEKER	2000	400	MISSILE SEEKER	
6	MS_FINS	2000	400	MISSILE FIN TRANSDUCER	
7	MS_GPS	10	10	NAVSTAR GPS	
8	GB_RADAR	400	10	MISSILE /TARGET TRACKER	
9	GB_HMS	800	50	HELMET MOUNTED SIGHT	
10	MS_AIR	400	20	AIR DATA SENSORS	
11	MS_SDINS	400	100	STRAPDOWN INS	

In the simulation functionally similar switches are often implemented using the bits of a 32 bit integer word to reduce the number of variables. Table 3-3 provides the integer values for bit pattern control setting.

Table 3-3 : Control Integer Bit Pattern Values

2^N	VALUE	2^N	VALUE	2^N	VALUE	
0	1	11	2_048	22	4_194_304	
1	2	12	4_096	23	8_388_608	
2	4	13	8_192	24	16_777_216	
3	8	14	16_384	25	33_554_432	
4	16	15	32_768	26	67_108_864	
5	32	16	65_536	27	134_217_728	
6	64	17	131_072	28	268_435_456	
7	128	18	262_144	29	536_870_912	
8	256	19	524_288	30	1_073_741_824	
9	512	20	1_048_567	31	2_147_483_648	
10	1_024	21	2_097_152			

Sensor measurements are selected by setting the appropriate bits in *MS_MSAV1* and *MS_MSAV2* as listed in Table 3-4 and Table 3-5. When a sensor measurement has been updated the same bits in *MS_MSRY1* and *MS_MSRY2* are set. If a measurement is de-activated it is still computed but it is not flagged as ready at the sensor output interface where its value remains frozen until it is re-activated.

Table 3-4 : *MS_MSAV1* and *MS_MSRY1* Measurement Availability

BIT	MEASUREMENT AVAILABLE	BIT	MEASUREMENT AVAILABLE	
0	**NOT USED**	16		
1	ROLL GYROSCOPE INERTIAL DATA	17	TRACKER/TARGET RANGE	
2	PITCH GYROSCOPE INERTIAL DATA	18	TRACKER/TARGET RANGE RATE	
3	YAW GYROSCOPE INERTIAL DATA	19	TRACKER/TARGET PITCH ANGLE	
4		20	TRACKER/TARGET YAW ANGLE	
5		21	TRACKER/MISSILE RANGE	
6		22	TRACKER/MISSILE RANGE RATE	
7	ROLL ACCELEROMETER DATA	23	TRACKER/MISSILE PITCH ANGLE	
8	PITCH ACCELEROMETER DATA	24	TRACKER/MISSILE YAW ANGLE	
9	YAW ACCELEROMETER DATA	25	SDINS VELOCITY	
10		26	SDINS HORIZONTAL POSITION	
11		27	SDINS HEIGHT	
12		28		
13	BAROMETRIC HAMSL	29	SEEKER PITCH GIMBAL ANGLE	
14		30	SEEKER YAW GIMBAL ANGLE	
15	RADAR ALTIMETER HAGL	31	**NOT USED**	

Table 3-5 : *MS_MSAV2* and *MS_MSRY2* Measurement Availability

BIT	MEASUREMENT AVAILABLE	BIT	MEASUREMENT AVAILABLE
0	**NOT USED**	16	HMS TARGET BEARING
1	MISSILE/TARGET RANGE	17	FLIR TARGET ELEVATION[#]
2	MISSILE/TARGET RANGE RATE	18	FLIR TARGET BEARING[#]
3	MISSILE/TARGET YAW ANGLE	19	AIR-DATA GEODETIC HEIGHT
4	MISSILE/TARGET PITCH ANGLE	20	AIR DATA MACH NUMBER
5		21	AIR DATA TRUE AIRSPEED
6		22	X-Y CONTROLLER ELEVATION[#]
7	MISSILE UPPER FIN POSITION	23	X-Y CONTROLLER BEARING[#]
8	MISSILE RIGHT FIN POSITION	24	GPS LGA POSITION
9	MISSILE DOWN FIN POSITION	25	GPS LGA VELOCITY
10	MISSILE LEFT FIN POSITION	26	
11		27	QUATERNION NORMALISATION
12		28	AERODYNAMIC CONSTRAINTS
13		29	TARGET CIRCULAR MOTION
14		30	GOAL ORIENTATED TRACKING
15	HMS TARGET ELEVATION	31	**NOT USED**

[#] - Measurements allocated bits exclusive to the AMIS

3.2 Generic Sensor Modelling

Figure 3-1 captures the generic approach applied to sensor modelling. When a sensor is active its reference input is derived locally from reference state vector at the sensor update rate.

A feature of this program and the AMIS is the way in which the sensors are isolated from the reference environment. Figure 3-2 shows the sensors receiving data derived from the reference-state vector rather than the reference environment directly. In the AMIS the reference environment is defined by internal models, or by external data sources such as telemetry, HardWare-In-the-Loop (HWIL), and other simulations such as the Route Generation Program.

Although this design approach leads to some inefficiency, it results in a single-thread modular structure. The interface between reference models and state vector can be fixed early in the design and data pre-processors put in place. Sensor models can then be developed in isolation without knowledge of the referenced model beyond the content of the reference state vector.

Returning to Figure 3-1. The sensor dynamics and time dependent errors are modelled at the sensor reference rate, whether they are superimposed on the reference input or not, so as to avoid discontinuities in the output when toggling measurement availability or changing the output rate. The errors induced by Analogue-to-Digital Conversion (ADC) are an exception. These are applied at the output rate so as to respect the Zero-Order-Hold (ZOH) process on which they are based.

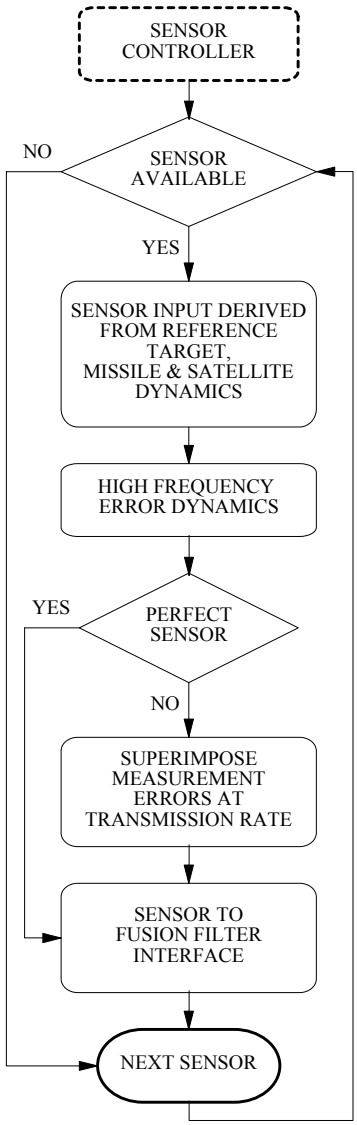

Figure 3-1
Generic Sensor Error Model

The output interface model described in §0 can be characterised to represent system errors induced by various forms of digital interface between the sensors and state observers. The measurement errors are determined in each sensor module by comparing the reference input with the output from the digital interface.

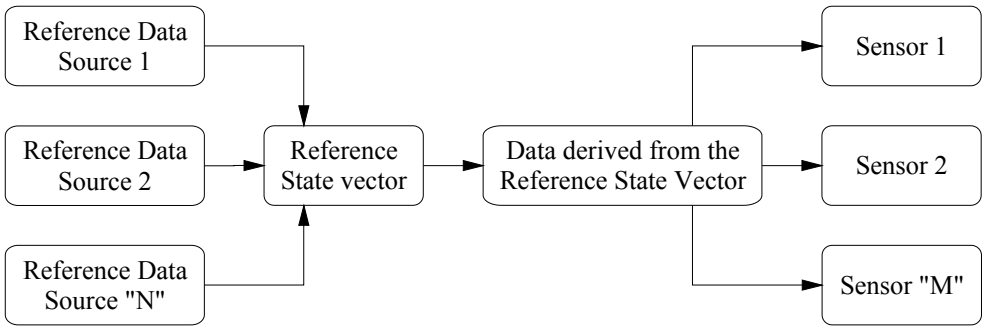

Figure 3-2 : Sensor Interaction with the Reference Environment

§3.2.2 deals with errors that are common to many sensors. These generic errors are permanently allocated the bits listed in Table 3-6 in each sensor's error control word. If a sensor does not use one, or more, of these generic error models their bits are left unused. Error models unique to a sensor are then allocated one of the remaining unused bits. If an error control word is set to zero, its default condition, a sensor provides perfect measurements at the selected output rate.

Table 3-6 : Sensor Error Model Selection

BIT	SENSOR ERROR	BIT	SENSOR ERROR	
0	[illegible]	15	Sensor measurement range limitation	
1	Unspecified	16	Sensor measurement rate limitation	

	elay			
2	Relative initiating	21	ADC Anti-Aliasing filter	
3	High frequency dynamics	22	ADC measurement saturation	
4	Constant bias	23	ADC quantisation	
5	Cau	24	ADC reference noise	

	s s i a n n c i s e			
6	F i r s t c r c e r c c r r e l a t e d n c i s e	27	Output interface quantisation	
7	S e c o n d c r d e r c c r r e	28	Output interface range limiting	

	latedi ncise			
8	Constant scale factor error	29	Output interface 2s compliment wrap	
9	Quadratic scale fac	30	Output interface cyclic delay	

	tcr error			
10	Asynmetric scale factor error	31	**UNUSED**	

Sensor limitations based on range, Field-of-View (FoV), Field-of-Regard (FoR) etc. are treated as error sources. If a limit is activated, and subsequently violated, the appropriated bit in the measurement ready flag is not set. The bits controlling the inclusion of sensor errors and measurement limitations can be interactively toggled and their parameters changed during program execution.

Each sensor is provided with a word whose bits are set according to which limitation has been violated. Failure to provide a measurement at the user request is indicated by setting bit 0 of this word; the remaining bits are specific to a particular sensor's limitations.

3.2.1 SIMULINK Sensor Modelling

SIMULINK sensor models were developed in parallel with the simulation to improve development times and provide an independent source of software

verification. The graphical nature of this tool is ideal for illustrating sensor descriptions, and to provide intermediate results showing the operation of sub-models. The models are stored in the MATLAB script file *SENSORS.M* and their default data in *SENDAT.M*. Once the default data has been loaded from the MATLAB Command Window the sensors are presented as seen in Figure 3-3.

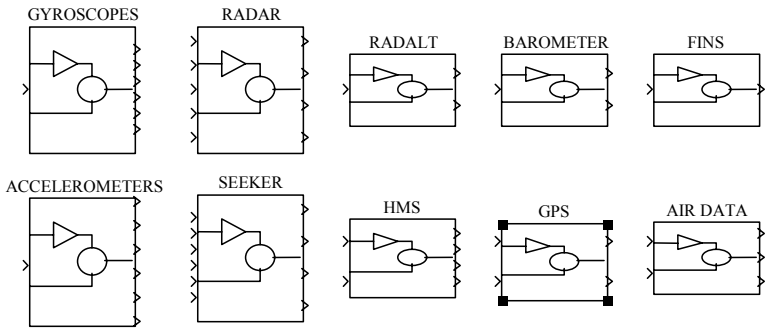

Figure 3-3 : SIMULINK Generic Sensor Model Library

Figure 3-4 shows the generic form of a SIMULINK sensor model that is conceptually the same as that in the simulation and decomposes into the basic sensor and its output interface. The measurement *SM_O* and the sensor error superimposed on the reference input *SN_E* are available for analysis in the MATLAB Command Window.

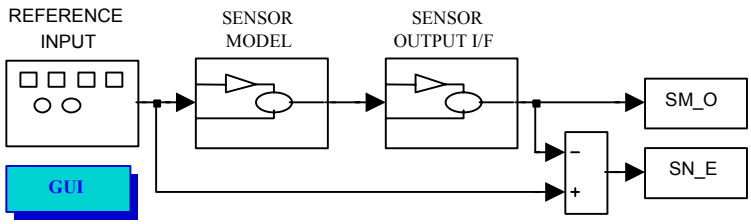

Figure 3-4 : SIMULINK Generic Sensor Model

The error model data may be configured using the Graphical User Interface (GUI). Sensor limitations preventing measurement output are not modelled in SIMULINK.

Double clicking the GUI icon using the left mouse button drops down a menu similar to the one shown in Figure 3-5. Clicking on “select options” activates that part of the sensor error model. To view the parameters associated with an error model click on the “edit parameters” button and a drop down menu similar to the one in Figure 3-6 for ADC quantisation appears, into which new values can inserted. When finished clicking on the “OK” buttons loads the new data and collapses the window.

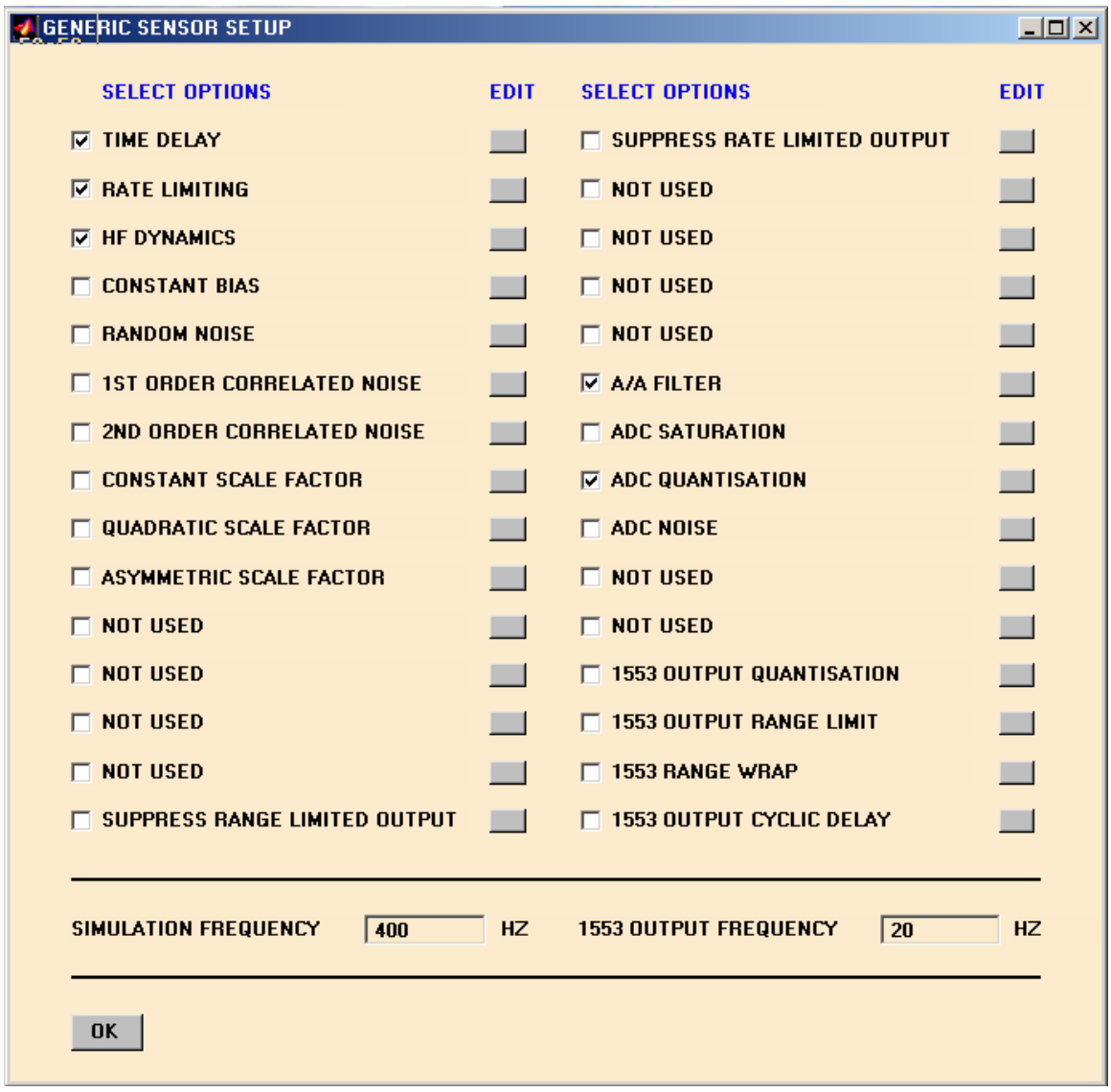

Figure 3-5 : SIMULINK Sensor Model GUI

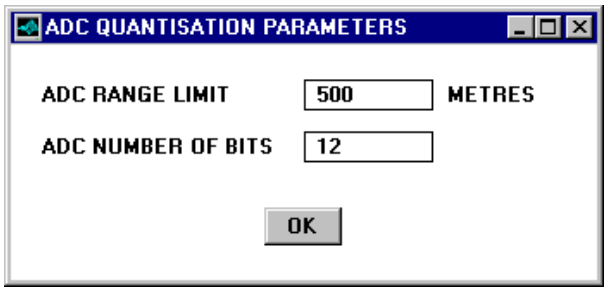

Figure 3-6 : Sensor Parameter Changes

3.2.2 Common Error Models

Although sensors exhibit a wide variety of errors, many are common and can dealt with using relatively few modelling elements. To avoid repetition when describing particular sensors, the common generic error models are grouped as shown in Figure 3-7, defined here, and characterised using default values in-situ.

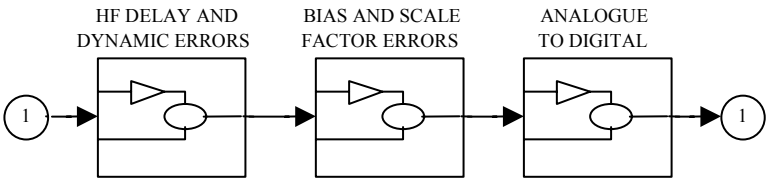

Figure 3-7 : Sensor Model - Generic Error Grouping

The functional notation (φ) provides a concise mathematical framework for sensor error definition. When treating the errors in the time domain the functional notation between input (x) and the output (y) from a model is,

$$y(t) := \varphi(x(t))$$

Equation 3.2-1

In the frequency domain the equivalent notation is,

$$y(s) := \varphi(x(s))$$

Equation 3.2-2

The functions in Table 3-7 provide a cross-reference to their implementation using the utilities defined in §22. For convenience, the function arguments listed are not referred to explicitly, they are implicitly assumed. Default arguments are characterised when describing a particular sensor using subscripted prefix to identify the sensor according to the "descriptor" listed in Table 3-1 - here the generic sensor descriptor "SN" is used.

3.2.2.1 Dynamic Errors

The common dynamic errors comprise the lumped time delay, rate limiting, and 1st and 2nd order lags shown in Figure 3-8.

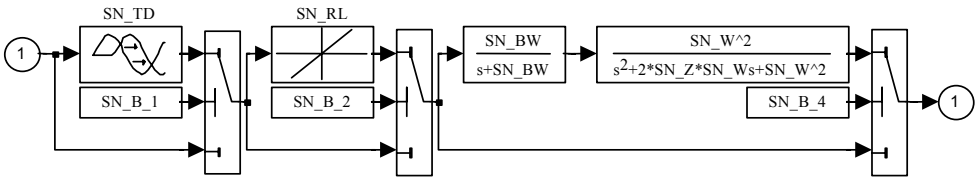

Figure 3-8 : HF Time Delay, Rate Limiting and Dynamic Errors

Table 3-7 : Sensor Functional Notation and Associated Utilities

FUNTION	UTILITY	DESCRIPTION	ARGUMENTS
φ_{TD}	§2.7.17	Time delay function	Time delay ≡ ${}_{SN}t_{TD}$
φ_{RL}	§2.7.21	Rate limiting function	Rate limit ≡ ${}_{SN}\dot{X}_{L}$
φ_{D1L}	§2.7.1	Digital 1st order lag filter	Break frequency ≡ ${}_{SN}\omega_{D1L}$
φ_{D2L}	§2.7.6	Digital 2nd order lag filter	Natural frequency ≡ ${}_{SN}\omega_{D2L}$ Damping ratio ≡ ${}_{SN}\zeta_{D2L}$
φ_{DLL}	§2.7.3	Digital lead-lag filter	Zero break frequency ≡ ${}_{SN}\omega_{N}$ Pole break frequency ≡ ${}_{SN}\omega_{D}$

${}^{AD}\varphi_{AA}$	§3.2.7.24	Anti-Aliasing filter associated with ADC conversion	Filter order ≡ ${}^{AD}_{SN}N_{AA}$ Break frequency ≡ ${}^{AD}_{SN}\omega_{AA}$
${}^{AD}\varphi_{Q}$	§3.2.7.16	Quantisation function associated with ADC conversion	Number of bits ≡ ${}^{AD}_{SN}N_{B}$ Lower range limit ≡ ${}^{AD}_{SN}X_{LL}$ Upper range limit ≡ ${}^{AD}_{SN}X_{UL}$
${}^{AD}\varphi_{QN}$	§3.2.7.10	Quantised noise function associated with ADC conversion	Number of noise bits ≡ ${}^{AD}_{SN}N_{NB}$ Lower range limit ≡ ${}^{AD}_{SN}X_{LL}$ Upper range limit ≡ ${}^{AD}_{SN}X_{UL}$
${}^{AD}\varphi_{LIM}$	§3.2.7.14	Range limiting function associated with ADC conversion	Lower range limit ≡ ${}^{AD}_{SN}X_{LL}$ Upper range limit ≡ ${}^{AD}_{SN}X_{UL}$
${}^{IF}\varphi_{Q}$	§3.2.7.12 §3.2.7.16	Quantisation function associated with the sensor output interface	Number of bits ≡ ${}^{IF}_{SN}N_{B}$ Lower range limit ≡ ${}^{IF}_{SN}X_{LL}$ Upper range limit ≡ ${}^{IF}_{SN}X_{UL}$

${}^{IF}\varphi_{LIM}$	§22.7.12 §22.7.14	Range limiting function associated with the sensor output interface	Lower range limit ≡ ${}^{IF}_{SN}X_{LL}$ Upper range limit ≡ ${}^{IF}_{SN}X_{UL}$
${}^{IF}\varphi_{TD}$	§22.7.12 §22.7.17	Time delay function associated with the sensor output interface	Number of delay cycles ≡ ${}^{IF}_{SN}N_{TD}$

Expressed in the frequency domain used in Figure 3-8 (rate limit omitted) and in functional form,

$$y(s) := \frac{{}_{SN}\omega_{D1L} \cdot {}_{SN}\omega_{D2L}^2 \cdot \exp(-{}_{SN}t_{TD} \cdot s)}{(s + {}_{SN}\omega_{D1L}) \cdot (s^2 + 2 \cdot {}_{SN}\zeta \cdot {}_{SN}\omega_{DL2} + {}_{SN}\omega_{DL2}^2)} \cdot x(s)$$

Equation 3.2-3

In the functional form this becomes,

$$y(x(t)) := \varphi_{D2L}(\varphi_{D1L}(\varphi_{RL}(\varphi_{TD}(x(t)))))$$

Equation 3.2-4

In the simulation the sensor time delays are gathered together, excluding the transport delay due to the output interface, and modelled to an accuracy commensurate with the high frequency update rate (f_R). When undertaking linear systems analysis the exponential function is replaced by 1st or 2nd order Pade approximations with unity gain,

$$y(s) := \left(\frac{2 \cdot {}_{SN}f_O - s}{2 \cdot {}_{SN}f_O + s}\right) \cdot x(s)$$

Equation 3.2-5

$$y(s) := \left(\frac{12 \cdot {}_{SN}f_O^2 - 6 \cdot {}_{SN}f_O \cdot s + s^2}{12 \cdot {}_{SN}f_O^2 + 6 \cdot {}_{SN}f_O \cdot s + s^2}\right) \cdot x(s)$$

Equation 3.2-6

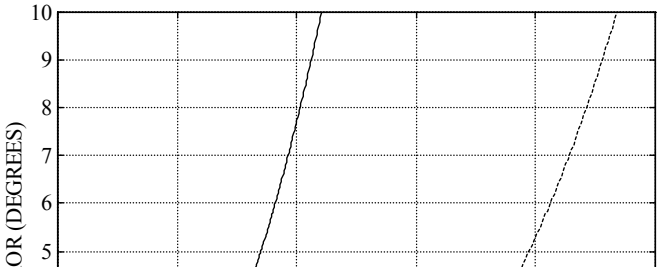

Figure 3-9 : Time Delay Phase Error

(1st order – solid ; 2nd order – dashed)

The phase error introduced by these approximations shown in Figure 3-9 must be closely monitored. The normalised frequency in this figure is a function of the time delay and the input signal frequency (f_I).

$$\bar{f} := \frac{1}{f_I \cdot {}_{SN}t_{TD}}$$

Equation 3.2-7

3.2.2.2 Bias, Noise and Scale Factor Errors

Although it is debatable whether the bias and noise errors should be subject to scale factor errors, the most complex error form for sensor error estimation arises when the errors involved are substantial and compounded as shown in Figure 3-10.

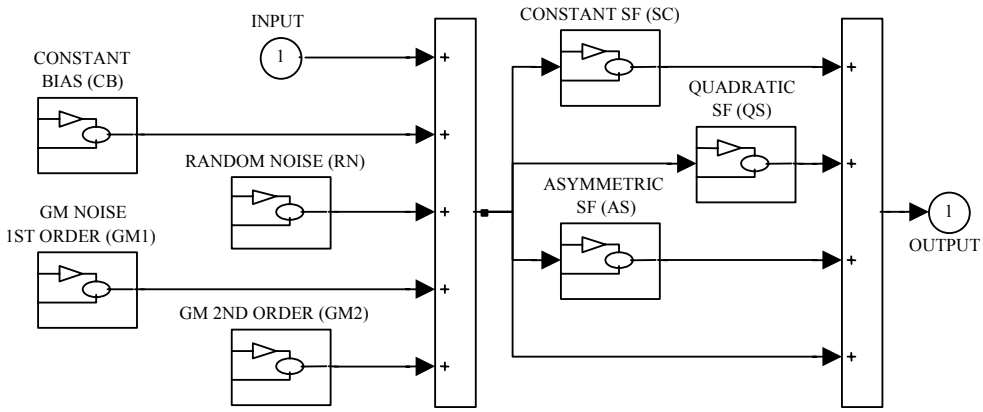

Figure 3-10 : Bias, Noise and Scale Factor Errors

$$y(t) := \varphi_{SF}\left(x(t) + \varphi_B \right)$$

Equation 3.2-8

The bias component comprises separately selectable constant bias, Gaussian noise, random walk and 2nd order Markov motion,

$$\varphi_B(t) := \varphi_{CB} + \varphi_{RN} + \varphi_{GM1} + \varphi_{GM2}$$

Equation 3.2-9

The constant bias is initialised from a Gaussian distribution defined by its standard deviation (σ_{CB}).

$$\varphi_{CB}\left({}_{SN}\sigma_{CB} \right) \equiv N\left(0, {}_{SN}\sigma_{CB} \right)\Big|_{t:=0}$$

Equation 3.2-10

Gaussian noise is characterised by its constant double sided Power Spectral Density (PSD) (Φ_{RN}) up to the Nyquist frequency ($f_R/2$), the standard deviation (σ_{RN}) for noise generator being,

$$\varphi_{RN}\left({}_{SN}\sigma_{RN}\right) \equiv N\left(0, \sqrt{{}_{SN}\Phi_{RN} \cdot {}_{SN}f_R}\right)$$

Equation 3.2-11

Maintaining a constant PSD when modelling noise characterised by its standard deviation (σ_N) at a Nyquist frequency (f_N) beyond ($f_R/2$) requires,

$${}_{SN}\sigma_{RN} := \sqrt{f_R / f_N} \cdot \sigma_N$$

Equation 3.2-12

Consider Gauss-Markov noise generators in which Gaussian noise with a continuous input standard deviation (σ_x) is passed through a linear filter represented by its transfer function G(s),

$$y(s) := G(s) \cdot N(0, \sigma_x)$$

Equation 3.2-13

Band limited noise is dealt with as a random walk where G(s) is a 1st order lag with a bandwidth (ω_{RW}). In the frequency and continuous time domains,

$$y(s) := \left(\frac{{}_{SN}\omega_{GM1}}{s + {}_{SN}\omega_{GM1}}\right) \cdot N(0, \sigma_x)$$

Equation 3.2-14

$$\dot{y}(t) := {}_{SN}\omega_{GM1} \cdot \left(-y(t) + N(0, \sigma_x)\right)$$

Equation 3.2-15

Modelling this using a 1st order digital lag filter at a rate of (${}_{SN}\omega_R := 2\pi/f_R$),

$$y(t) := \varphi_{D1L}\left(N\left(0, {}_{SN}\sigma_{GM1}\right), {}_{SN}\omega_{GM1}\right)$$

Equation 3.2-16

Random walks are characterised by their output standard deviation in the continuous time domain. To obtain the equivalent deviation for a random number generator consider the output propagation using this digital filter,

$$y_{k+1} := y_k \cdot \exp\left(-{}_{SN}\omega_{GM1} / {}_{SN}\omega_R\right) + N\left(0, {}_{SN}\sigma_{GM1}\right)_k$$

Equation 3.2-17

Taking expectations,

$$E\left(y_{k+1}^2\right) := E\left(y_k^2\right) \cdot \exp\left(-2 \cdot {}_{SN}\omega_{GM1} / {}_{SN}\omega_R\right) + {}_{SN}\sigma_{GM1}^2$$

Equation 3.2-18

$$\sigma_y^2 := \sigma_y^2 \cdot \exp\left(-2 \cdot {}_{SN}\omega_{GM1} / {}_{SN}\omega_R\right) + {}_{SN}\sigma_{GM1}^2$$

Equation 3.2-19

The standard deviation used by the random noise generator is therefore,

$${}_{SN}\sigma_{GM1} := \sigma_y \cdot \sqrt{1 - \exp\left(-2 \cdot {}_{SN}\omega_{GM1} / {}_{SN}\omega_R\right)}$$

Equation 3.2-20

Although the continuous frequency domain is useful for descriptive purposes care is required when filtering Gaussian noise in SIMULINK. This must be done in the discrete time domain as shown in Figure 3-11. SN_SF being equivalent to the update frequency f_R.

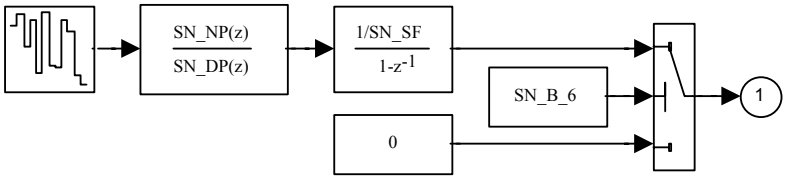

Figure 3-11 : 1st Order Gauss-Markov Motion

Converting from the continuous to discrete domain using the MATLAB command "c2dm" requires,

$$\left[SN\_NP, SN\_DP\right] := c2dm\left({}_{SN}\omega_{GM1}, \left[1, {}_{SN}\omega_{GM1}\right], {}_{SN}\omega_R\right)$$

Equation 3.2-21

For Gauss-Markov errors generated using a 2nd order lag for G(s), with a damping ratio of unity and a bandwidth of (ω_{GM2}), the correlation time is ($2.146 / \omega_{GM2}$) compared with ($1 / \omega_{GM1}$) for the random walk. In the frequency, continuous time and discrete domains,

$$y(s) := \left(\frac{{}_{SN}\omega_{GM2}^2}{s^2 + 2 \cdot {}_{SN}\omega_{GM2} \cdot s + {}_{SN}\omega_{GM2}^2}\right) \cdot N\left(0, {}_{SN}\sigma_{GM2}\right)$$

Equation 3.2-22

$$\ddot{y} + 2 \cdot {}_{SN}\omega_{GM2} \cdot \dot{y} + {}_{SN}\omega_{GM2}^2 \cdot y := N\left(0, \sigma_x\right)$$

Equation 3.2-23

$$y(t) := \varphi_{D2L}\left(N\left(0, {}_{SN}\sigma_{GM2}\right), 1, {}_{SN}\omega_{GM2}\right)$$

Equation 3.2-24

The SIMULINK conversion from the continuous to the discrete domain,

$$[SN\_NP, SN\_DP] :=$$

$$c2dm\left({}_{SN}\omega_{GM2}^2, \left[1, 2\cdot {}_{SN}\omega_{GM1}, {}_{SN}\omega_{GM2}^2\right], {}_{SN}\omega_R\right)$$

Equation 3.2-25

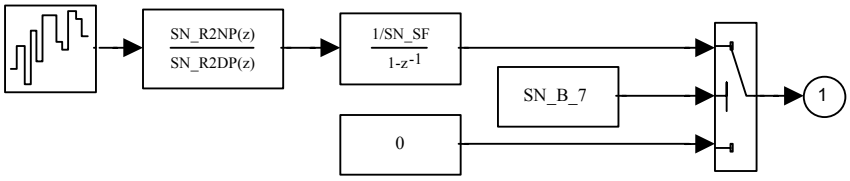

Figure 3-12 : 2nd Order Gauss-Markov Motion

The scale factor error is a combination of separately selectable constant, quadratic and asymmetric terms,

$$\varphi_{SF}(x) := \varphi_{CS}\left(x, {}_{SN}\sigma_{CS}\right) + \varphi_{QS}\left(x, {}_{SN}\sigma_{QS}\right) + \varphi_{AS}\left(x, {}_{SN}\sigma_{AS}\right)$$

Equation 3.2-26

The scale factor coefficients are initialised using Gaussian distributions defined by appropriate standard deviations,

$$\varphi_{SF}(x) :=$$

$$x\cdot N\left(0, {}_{SN}\sigma_{CS}\right)\Big|_{t:=0} + |x|\cdot\left(x\cdot N\left(0, {}_{SN}\sigma_{QS}\right)\Big|_{t:=0} + N\left(0, {}_{SN}\sigma_{AS}\right)\Big|_{t:=0}\right)$$

Equation 3.2-27

3.2.2.3 Analogue to Digital Conversion

The reference input, dynamics and error models are processed at a frequency representative of their analogue equivalent. The error models arising from the conversion of the analogue measurements into digital form are shown in Figure 3-13 and comprise:

- Anti-Aliasing filter (bit 23)
- Range limiting (without word length wrapping) (bit 24)
- Quantisation (bit 25)
- Uniformly distributed “N” bit ADC noise (bit 26)

Expressing the ADC errors and anti-aliasing (A/A) filter in functional form,

$$y(t) :=$$

$$\varphi_{ADC}\left(\varphi_{AA}\left(x(t), {}^{AD}_{SN}N_{AA}, {}^{AD}_{SN}\omega_{AA}\right), {}_{SN}f_O, {}^{AD}_{SN}N_B, {}^{AD}_{SN}N_{NB}, {}^{AD}_{SN}X_{LL}, {}^{AD}_{SN}X_{UL}\right)$$

Equation 3.2-28

$$\varphi_{ADC}\left(x(t)\right) \equiv {}^{AD}\varphi_{LIM}\left({}^{AD}\varphi_Q\left(\varphi_{ZOH}\left(x(t), {}_{SN}f_O\right)\right) + {}^{AD}\varphi_{QN}\right)$$

Equation 3.2-29

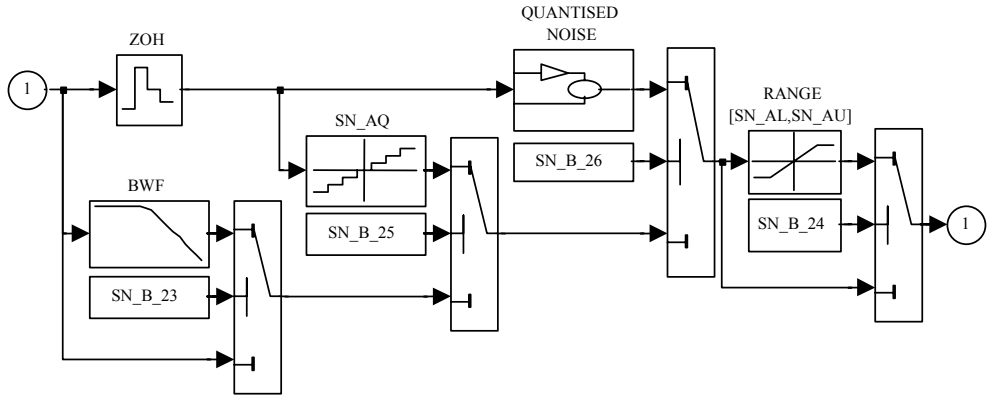

Figure 3-13 : Analogue to Digital Conversion Errors

A Butterworth A/A filter attenuates high frequency noise preventing it from folding back into the sensor bandwidth about the Nyquist frequency. The ADC here operates at the same frequency as the sensor output interface (f_O). To reduce the time delays, or produce a signal for further digital filtering, the ADC can be over-sampled at a frequency greater than that of the output interface - not modelled. In the frequency domain a ZOH is represented by,

$$s \cdot y(s) := \left(1 - \exp\left(-s / {}_{SN}f_O\right)\right) \cdot x(s)$$

Equation 3.2-30

For linear systems analysis the exponential function is replaced here by 1st and 2nd order Pade approximations,

$$y(s) := \left(\frac{2 \cdot {}_{SN}f_O}{2 \cdot {}_{SN}f_O + s}\right) \cdot x(s)$$

Equation 3.2-31

$$y(s) := \left(\frac{12 \cdot {}_{SN}f_O}{12 \cdot {}_{SN}f_O^2 + 6 \cdot {}_{SN}f_O \cdot s + s^2}\right) \cdot x(s)$$

Equation 3.2-32

As with time delays, the gain and phase errors plotted against normalised frequency in Figure 3-14 and Figure 3-15 must be closely monitored. ADC scale factors and biases are usually small and are ignored.

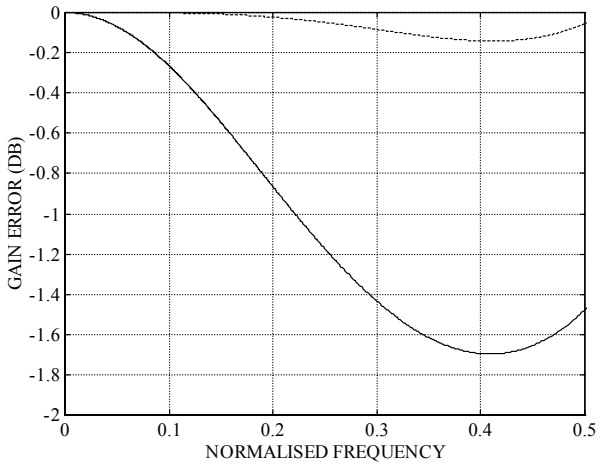

Figure 3-14 : ZOH Gain Error

(1st order – solid ; 2nd order – dashed)

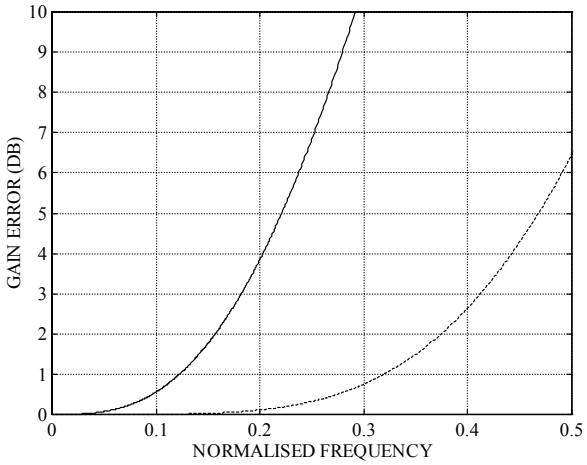

Figure 3-15 : ZOH Phase Error

(1st order – solid ; 2nd order – dashed)

Consider a unit amplitude, 1 Hz signal passing through a 4th order Butterworth A/A filter with a 20 Hz bandwidth. A 40 Hz ZOH "freezes" the input whilst the 12 bit ADC output is raised to within ± 0.5*LSB of the input.

By design, the ADC must be capable of settling within the ZOH time if the internal measure passed to the output buffer is to be the correct value, in which case their internal high frequency dynamics can be ignored.

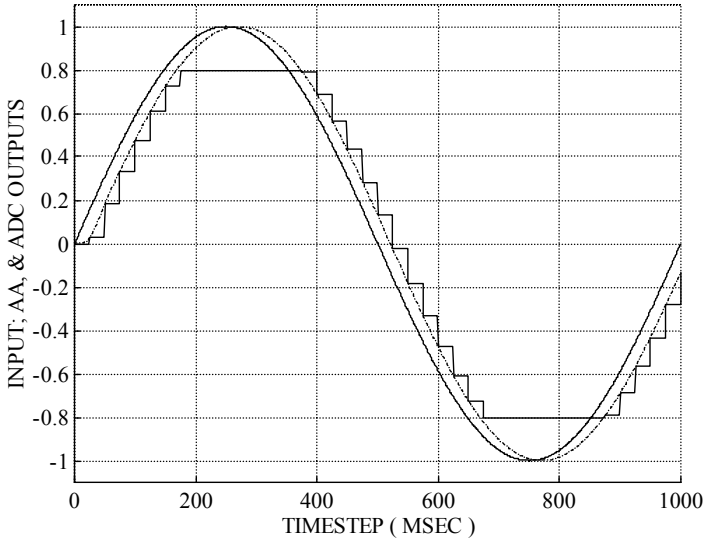

Figure 3-16 : Digitised Analogue Output

The filtered input signal is quantised with a Least Significant Bit (LSB) of 0.00627 representing the ADC reference voltage scaling. This is then clipped to 0.8 of the input signal due to internal word length limitations (a bad design but one chosen to illustrate the effect).

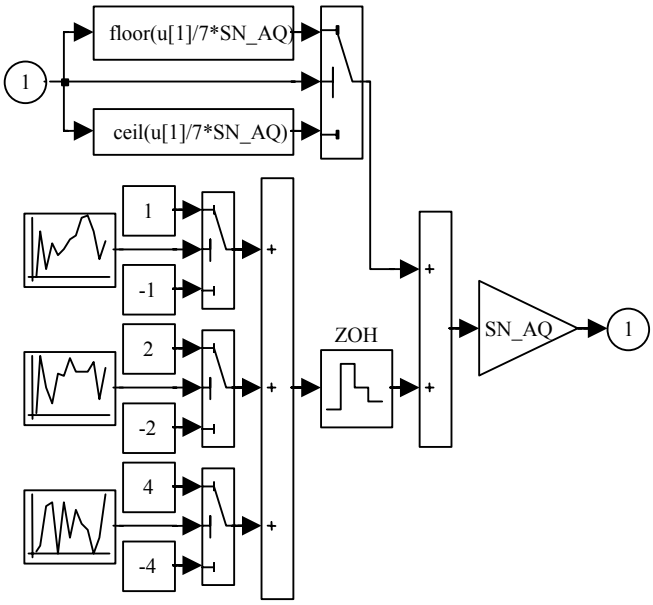

Figure 3-17 : ADC/DAC Noise Model

The ADC quantised noise was disabled. Figure 3-16 clearly shows the expected the combined A/A and ADC time delay of 0.04 s that may be compensated for in a state observer, or in the sensor itself. ADC noise levels of 1 LSB often quoted but these are usually optimistic, even carefully design results in noise affecting the lowest 3 bits, i.e. noise of up to 7*LSB.

A model of this error currently fixed at 3 bits of quantised noise is shown in Figure 3-17 and its output in Figure 3-18.

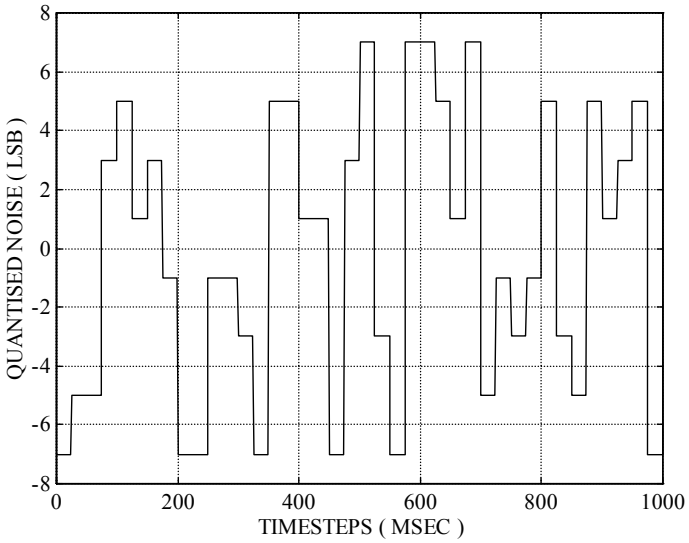

Figure 3-18 : ADC 3 Bit Random Noise

If this error is present on measurements used in a state observer based on Kalman filtering principles it can have a destabilising effect unless compensated for, since it is not Gaussian in nature.

3.2.2.4 Sensor Output Interface

In the simulation each sensor measurement passes through module *IF_1553* described in §22.7.13. This superimposes the following digital interface (I/F) transmission errors:

- I/F range quantisation (bit 27)
- I/F range limiting without 2s compliment wrapping (bit 28)
- I/F range limit with 2s compliment wrapping (bit 29)
- I/F time delay based on complete output intervals (bit 30)

The error control word is applied at sensor level hence the errors invoked are applied to all the measurements from a sensor. The equivalent MATLAB model is shown in Figure 3-19 in which the low frequency update ZOH is evident to the sensor measurement output rate.

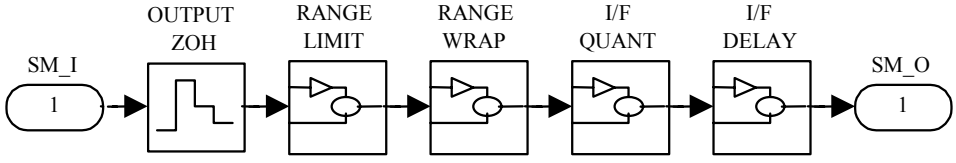

Figure 3-19 : Sensor Output Interface

The functional form of the individual elements in this interface model is,

$$y(t) := {}^{IF}\varphi_{TD}\left({}^{IF}\varphi_{Q}\left({}^{IF}\varphi_{LIM}\left({}^{IF}\varphi_{ZOH}\left(x(t), {}_{SN}f_{O}\right)\right)\right)\right)$$

Equation 3.2-33

Range limiting is mutually exclusive with 2's compliment wrapping shown in Figure 3-20. In the event that both are selected only the latter is applied. The number of time delay cycles is commensurate with the output rate (f_O).

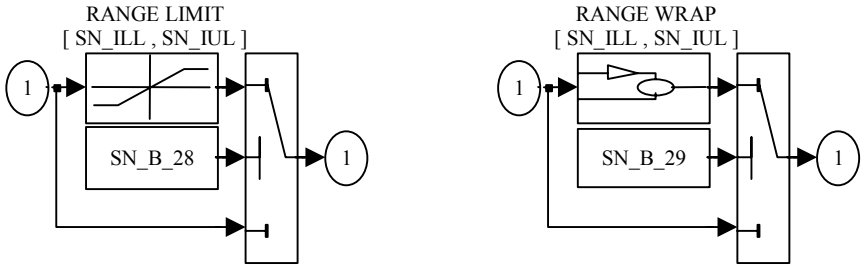

Figure 3-20 : Output Interface - Alternative Range Limiting Models

The "range wrap" function referred to here for SIMULINK is defined in Figure 3-21.

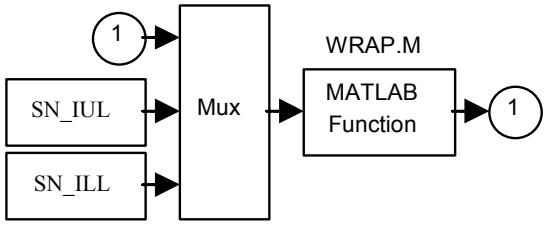


```
function [IF_O] = WRAP(IF_I)

if IF_I(1) >= IF_I(2)
   IF_O = IF_I(1)-IF_I(2)+IF_I(3);
elseif IF_I(1) < IF_I(3)
   IF_O = IF_I(2)-IF_I(1)-IF_I(3);
else
   IF_O = IF_I(1) ;
end

return
```

Figure 3-21 : MATLAB Function - WRAP.M

3.3 Inertial Navigation and Airframe Stabilisation

Before dealing with individual Inertial Navigation System (INS) sensors it is useful to consider how they combine to provide navigation data for aircraft and long-range missiles. Typical accuracy requirements for ship, aircraft and cruise missile navigation are 0.1, 1 and 10 nm/hr respectively. An INS comprises an Inertial Measurement Unit (IMU), containing gyroscopes, accelerometers and temperature measuring devices for thermal calibration, and an autonomous height reference such as a barometer. GPS can be used instead but the importance of height stabilisation is such that only an autonomous instrument can satisfy safety critical applications. IMU data is also required for stabilising the highly manoeuvrable airframes used in modern weapon systems, as well as for terrestrial referenced positioning.

Conceptually, gyroscopes provide a space stable reference frame in which the accelerometer outputs can be integrated. For navigation the temperature inside the IMU case is continuously monitored and used to correct the sensor output using manufacturer's calibration data. Coriolis corrections are then applied so that the multiplexed, non-coincident output from each sensor is referred to a single instant in time and a common reference point. For airframe stabilisation and inertial seeker pointing, where accuracy requirements may be relaxed, the IMU output is often used without these corrections. The primary IMU outputs are increment angle and velocity, i.e. the angle the IMU has turned through since the last output. Thus the orientation of the IMU case is maintained with respect to the space stable frame, and the change in velocity along the IMU reference axes. In an INS these data are combined to produce the following vertically stabilised, geodetic data:

- Longitude, latitude and geodetic height above the World Geodetic System (WGS) 84 ellipsoid
- Geodetic velocity
- Orientation of the IMU case (vehicle body axes) with respect to Local Geodetic Axes (LGA)

In addition to these data incremental sensor output is often processed to obtain:

- Angular rate of the IMU axes (vehicle body axes) with respect to LGA
- Specific acceleration along the IMU axes (vehicle body axes)

For navigation the incremental data is used directly, whereas data derived from it is often adequate and simpler to use for less accurate applications. Under no circumstances should both sets of data be used to update a state observer as the derived data contains no new information. Low bandwidth barometer data is mixed with the high bandwidth accelerometer output to prevent vertical acceleration biases from integrating into a rapidly increasing height error.

SDINS using single-axis sensors are simpler to manufacture and maintain and have generally replaced gimballed INS and dual-axis instruments. Although autopilot and guidance functions require a low dynamic range, typically 10^3 comparable with platform systems, for navigation and mid-course guidance a dynamic range of 10^9 is required, i.e. from 0.01 deg/hr to 400 °/s.

The replacement of mechanical gimbals with SDINS software became possible once gyroscopes could be mass produced with scale factors small enough to cope with this wide dynamic range. Low scale factors are inherent in optical instruments such as Ring Laser Gyroscopes (RLG), Fibre Optical Gyroscopes (FOG) and resonating gyroscopes whose development started in the early 60's. Optical sensors also exhibit excellent linearity, high bandwidths, insensitivity to high accelerations, and in the case of the FOG they are relatively low cost and compact. These are dominant factors in their development and rapid introduction into the aerospace environment, not the mythical Mean Time Between Failures (MTBF) which is in fact lower than for equivalent mechanical sensors due to their higher electronic content which is comparably less reliable.

SDINS are particularly susceptible to rectified noise though its supports up to 80-100 Hz. This effects short-term performance, an is an error source often overlooked, and probably least understood, as it involves the local flexure environment. The reference gyroscope and accelerometer inputs are considered next in the context of master-slave TFA within a flexible structure. TFA is the calibration of a low-grade missile INS using the more accurate launcher INS velocity and attitude output to levels commensurate the structural flexure. In the absence of flexure i.e. during ground alignment, the slave INS can be levelled to an accuracy equivalent to the accelerometer biases.

3.3.1 Reference Inertial Angular Rate

Figure 3-22 shows the frame of references used when determining the reference input data to two IMUs. The master IMU-1 in the launcher is referenced to point (u), and the slave IMU_2 in the missile to point (m). In the description of the master-slave IMU sensor inputs some of the definitions given in §16 have been locally re-defined. The geodetic position of IMU-1 is denoted by point (d) on the Earth's surface, shown on the same equatorial parallel plane as the Alignment frame origin at point (o) for convenience. The IMU-1 and IMU-2 are aligned with the Launcher Body frame (B) and the Missile Body frame (M) located at points (u) and (m) respectively. For aircraft, the Wing and Pylon frames (W) and (P) originate from point (n) located on the front face of the forward missile support. In the absence of low frequency wing bending and flexure (W) are coincident with (B). Pylon axes are defined relative to the wing and account for the missile dispersion angle excluding harmonisation errors (small errors due to pylon and rail manufacturing and fitting errors) and high frequency flexure.

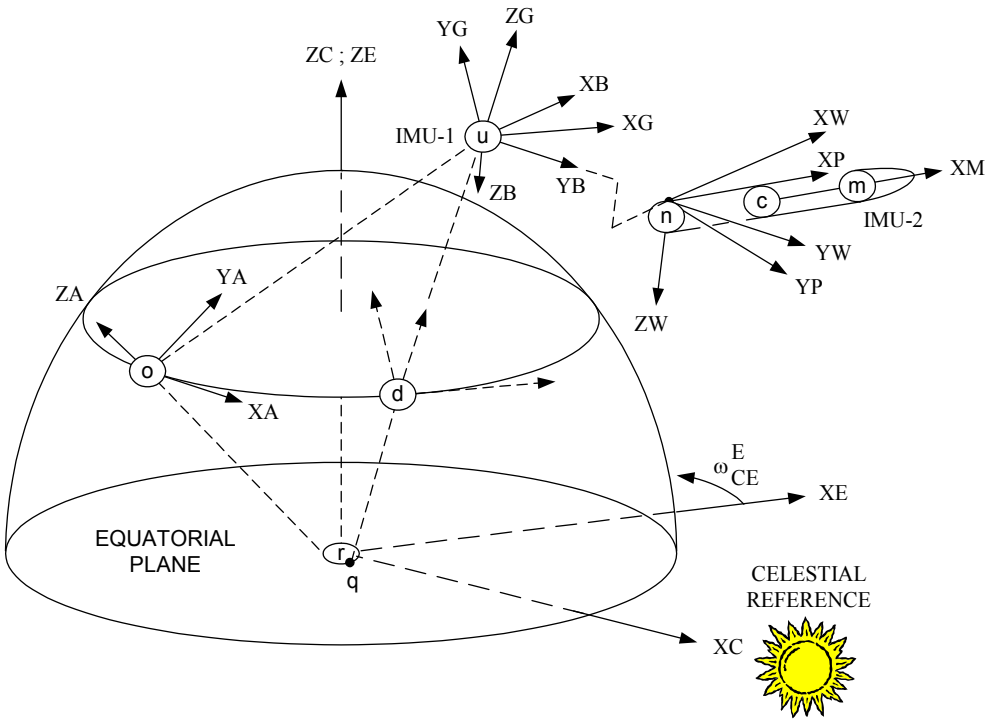

Figure 3-22 : Transfer Alignment Frames of Reference

3.3.1.1 IMU-1 Input Derived From External LGA Data

Suppose that the position of point (u) is defined by 3D geodetically referenced way-points. Its geodetic velocity, acceleration and piecewise constant jerk can then be obtained at the IMU reference frequency (f_R) of 800 Hz (a sub-frame interval Δ_R of 1.25 ms) from cubic splines passing through the way-points. The inertial angular rate expressed in the Body frame comprises the Earth's Siderial rate, tilt rate and the rate of rotation of the missile with respect to East-North-Up (ENU) LGA,

$$\underline{\omega}^{B}_{C,B} \coloneqq T^{B}_{G} \cdot \underline{\omega}^{G}_{C,G} + \underline{\omega}^{B}_{G,B} \coloneqq T^{B}_{G} \cdot \left(T^{G}_{E} \cdot \underline{\omega}^{E}_{C,E} + \underline{\omega}^{G}_{E,G} \right) + \underline{\omega}^{B}_{G,B}$$

Equation 3.3-1

The Earth rate and the tilt rate of (G) over the Earth are respectively,

$$\underline{\omega}^{G}_{C,G} \coloneqq T^{G}_{E} \cdot \underline{\omega}^{E}_{C,E} + \left(-\dot{\lambda}_d \quad , \quad \dot{\mu}_d \cdot \cos\lambda_d \quad , \quad \dot{\mu}_d \cdot \sin\lambda_d \right)^{T}$$

Equation 3.3-2

$$\underline{\omega}_{C,G}^{G} := \begin{pmatrix} 0 \\ \omega_{C,E}^{ZE} \cdot \cos\lambda_d \\ \omega_{C,E}^{ZE} \cdot \sin\lambda_d \end{pmatrix} + \begin{pmatrix} -\dot{P}_u^{YG} \,/\, R_{\lambda d} \\ \dot{P}_u^{XG} \,/\, R_{\mu d} \\ \dot{P}_u^{XG} \cdot \tan\lambda_d \,/\, R_{\mu d} \end{pmatrix}$$

Equation 3.3-3

The Earth radii at point (d), adjusted for the geodetic height of point (u), used in the conversion of metres into radians are defined in §18.4 and §18.5. The LGA (G) to the Body frame (B) transform is obtained using spline-data in the functions defined in §22.4.1 and §22.4.7.

$$T_G^B := \varphi_E^{DC}\left(\varphi_{LD}^{E}\left(\underline{\ddot{P}}_u^G, \underline{\dot{P}}_u^G, g_u^{ZG}\right)\right)$$

Equation 3.3-4

From §19.5, the local gravitational acceleration at point (u) is,

$$\underline{g}_u^G = -\underline{g}_d^G + 3\cdot\left(\omega_{C,E}^{ZE}\right)^2 \cdot P_u^{ZG} \cdot \cos\lambda_d \cdot \left(0 \;,\; -\sin\lambda_d \;,\; \cos\lambda_d\right)^T$$

Equation 3.3-5

The average angular body rate with respect to LGA over the 800 Hz sub-frame interval is obtained using the function defined in §22.5.3,

$$\underline{\omega}_{G,B}^{B} \equiv \underline{\overline{\omega}}_{G,B}^{B} := \overline{\varphi}_{AR}\left(T_G^B\left(t-\Delta_R\right), T_G^B, \Delta_R\right)$$

Equation 3.3-6

From the Navigation Equation the accelerometers sense specific acceleration comprising mass attraction and Earth centripetal acceleration components at point (u),

$$\underline{f}_{r,u} := \underline{A}_{r,u} - \underline{G}_u := \underline{A}_{r,u} - \underline{g}_u - \underline{\omega}_{C,E} \times \underline{\omega}_{C,E} \times \underline{P}_{r,u}$$

Equation 3.3-7

The acceleration of point (u) with respect to the Earth's centre is obtained by applying the time rate of change operator twice with respect to LGA axes, expanding and combining with Equation 3.3-7,

$$D_I^2\left(\underline{P}_{r,u}\right) := \left(D_G + \underline{\omega}_{C,G} \times\right)^2\left(\underline{P}_{r,u}\right)$$

Equation 3.3-8

$$\underline{A}_{r,u} \;:=$$

$$\ddot{\underline{P}}_{r,u} + \left(2 \cdot \underline{\omega}_{C,E} + \underline{\omega}_{E,G} \right) \times \dot{\underline{P}}_{r,u} + \dot{\underline{\omega}}_{C,G} \times \underline{P}_{r,u} + \underline{\omega}_{C,E} \times \underline{\omega}_{C,E} \times \underline{P}_{r,u}$$

Equation 3.3-9

$$\underline{f}_{r,u} \;:=\; \ddot{\underline{P}}_{r,u} + \left(2 \cdot \underline{\omega}_{C,E} + \underline{\omega}_{E,G} \right) \times \dot{\underline{P}}_{r,u} + \dot{\underline{\omega}}_{C,G} \times \underline{P}_{r,u} - \underline{g}_{u}$$

Equation 3.3-10

Mechanisation of this equation can be performed in the Inertial, Wander Azimuth, LGA or Body frames. When defining sensor inputs the accelerations are required in the Body frame. The linear velocity and acceleration of point (d) is zero with respect to the Earth's centre, and the angular acceleration of frame (G) with respect to frame (C) can be ignored. Making these approximations and expressing Equation 3.3-10 in terms of cubic spine data,

$$\underline{f}^{B}_{r,u} \;:=\; T^{B}_{G} \cdot \left(\ddot{\underline{P}}^{G}_{u} + \left(2 \cdot \underline{\omega}^{G}_{C,E} + \underline{\omega}^{G}_{E,G} \right) \times \dot{\underline{P}}^{G}_{u} - \underline{g}^{G}_{u} \right)$$

Equation 3.3-11

Expanding the coriolis acceleration components,

$$\left(2 \cdot \omega^{G}_{C,E} + \omega^{G}_{E,G} \right) \cdot \dot{\underline{P}}^{G}_{u} \;:=$$

$$\begin{pmatrix} 2 \cdot \omega^{ZE}_{C,E} \cdot \left(\dot{P}^{YG}_{u} \cdot \sin\lambda_{d} - \dot{P}^{ZG}_{u} \cdot \cos\lambda_{d} \right) + \dot{P}^{XG}_{u} \cdot \left(\dot{P}^{YG}_{u} \cdot \tan\lambda_{d} - \dot{P}^{ZG}_{u} \right) / R_{\mu d} \\ - 2 \cdot \omega^{ZE}_{C,E} \cdot \dot{P}^{XG}_{u} \cdot \sin\lambda_{d} - \left(\dot{P}^{XG}_{u} \right)^{2} \cdot \tan\lambda_{d} \,/\, R_{\mu d} \;-\; \dot{P}^{YG}_{u} \cdot \dot{P}^{ZG}_{u} \,/\, R_{\lambda d} \\ 2 \cdot \omega^{ZE}_{C,E} \cdot \dot{P}^{XG}_{u} \cdot \cos\lambda_{d} + \left(\dot{P}^{XG}_{u} \right)^{2} / R_{\mu d} + \left(\dot{P}^{YG}_{u} \right)^{2} / R_{\lambda d} \end{pmatrix}$$

Equation 3.3-12

The angular acceleration of Body axes with respect to LGA is obtained by backward differencing over the sub-frame interval,

$$\dot{\underline{\omega}}^{B}_{G,B} \;\equiv\; \dot{\underline{\omega}}^{B}_{G,B} \;:=\; \Delta_{R} \cdot \left(\underline{\omega}^{B}_{G,B} - \underline{\omega}^{B}_{G,B} \left(t - \Delta_{R} \right) \right)$$

Equation 3.3-13

Although this derivation of the IMU inputs from the spline data provides a useful insight into INS processing, in the simulation the sensors inputs are derived from the reference state vector. The orientation of frame (B) with respect to the Alignment frame (A) is derived using the function defined in §22.10.8 for converting direction cosines to quaternions.

$$Q_A^B \;:=\; \varphi_{DC}^Q\left(T_A^B\right) \;\equiv\; \varphi_{DC}^Q\left(T_G^B \cdot T_E^G \cdot T_A^E\right)$$

Equation 3.3-14

Both frames (E) and (A) are Earth fixed, hence the angular rate and acceleration of frame (B) with respect to frame (A) is,

$$\underline{\omega}_{A,B}^B \;:=\; T_G^B \cdot \underline{\omega}_{E,G}^G + \underline{\omega}_{G,B}^B$$

Equation 3.3-15

$$\dot{\underline{\omega}}_{A,B}^B \;\mapsto\; \underline{\dot{\omega}}_{A,B}^B \;:=\; \Delta_R \cdot \left(\underline{\omega}_{A,B}^B - \underline{\omega}_{A,B}^B\left(t-\Delta_R\right)\right)$$

Equation 3.3-16

The position of point (u) with respect to the Alignment frame is,

$$\underline{P}_u^A \;:=\; T_E^A \cdot \left(\underline{P}_d^E + T_G^E \cdot \underline{P}_u^G - \underline{P}_o^E\right) \;;\; \underline{P}_u^G \;\equiv\; \left(0 \;,\; 0 \;,\; P_u^{ZG}\right)^T$$

Equation 3.3-17

Equating the inertial velocity expressed in the Geodetic and Alignment frames,

$$\underline{\dot{P}}_u^A \;:=\; T_E^A \cdot T_G^E \cdot \left(\underline{\dot{P}}_u^G + \underline{\omega}_{C,G}^G \cdot \left(T_E^G \cdot \underline{P}_d^E + \underline{P}_u^G\right)\right) + \underline{\omega}_{C,E}^A \cdot \left(T_E^A \cdot \underline{P}_o^E + \underline{P}_u^A\right)$$

Equation 3.3-18

And similarly for the inertial acceleration of point (u),

$$\underline{\ddot{P}}_u^A \;:=\; T_E^A \cdot T_G^E \cdot \underline{A}_u^G - 2 \cdot \omega_{C,E}^A \times \underline{\dot{P}}_u^A - \omega_{C,E}^A \times \omega_{C,E}^A \times \left(T_E^A \cdot \underline{P}_o^E + \underline{P}_u^A\right)$$

Equation 3.3-19

$$\underline{A}_u^G \;=\; \underline{\ddot{P}}_u^G + 2 \cdot \underline{\omega}_{C,G}^G \times \underline{\dot{P}}_u^G + \underline{\omega}_{C,G}^G \times \underline{\omega}_{C,G}^G \times \left(T_E^G \cdot \underline{P}_d^E + \underline{P}_u^G\right)$$

Equation 3.3-20

3.3.1.2 IMU Reference Data Derived from the State Vector

The average inertial angular rate over the 800 Hz sub-frame, expressed in terms of the state vector components,

$${}_{800}\overline{\underline{\omega}}_{C,B}^B \;:=\; \overline{T}_A^B \cdot T_E^A \cdot \underline{\omega}_{C,E}^E + \overline{\varphi}_{AR}\left(T_A^B\left(t-\Delta_R\right), T_A^B, \Delta_R\right)$$

Equation 3.3-21

$$\overline{T}_A^B := \varphi_E^{DC}\left(0.5\cdot\left(\varphi_Q^E\left(Q_A^B\left(t-\Delta_R\right)\right)+\varphi_Q^E\left(Q_A^B\right)\right)\right)$$

Equation 3.3-22

The functions converting Quaternions to Euler angles to direction cosines are defined in §22.10 and §22.4.7 respectively. The Earth and tilt rate errors induced by taking current rather than average values are small in comparison with the average angular rate of frame (B) with respect to frame (A) over a sub-frame hence,

$${}_{800}\overline{\underline{\omega}}_{A,B}^B := \overline{\varphi}_{AR}\left(T_A^B\left(t-\Delta_R\right), T_A^B, \Delta_R\right)$$

Equation 3.3-23

The specific acceleration along the Alignment axes is,

$$\underline{f}_{r,u} := \underline{A}_{r,o} + \underline{A}_{o,u} - \underline{g}_u - \underline{\omega}_{C,E}\times\underline{\omega}_{C,E}\times\underline{P}_{r,u}$$

Equation 3.3-24

Since point (o) is fixed on the Earth, and there is no angular acceleration of frame (A) with respect to frame (C),

$$\underline{A}_{r,o} := \underline{\omega}_{C,E}\times\underline{\omega}_{C,E}\times\underline{P}_{r,o}$$

Equation 3.3-25

$$\underline{A}_{o,u} := \ddot{\underline{P}}_{o,u} + 2\cdot\underline{\omega}_{C,E}\cdot\dot{\underline{P}}_{o,u} + \underline{\omega}_{C,E}\times\underline{\omega}_{C,E}\times\underline{P}_{o,u}$$

Equation 3.3-26

Combining terms,

$$\underline{f}_{r,u}^B := T_A^B\cdot\left(\ddot{\underline{P}}_u^A + 2\cdot\left(T_E^A\cdot\underline{\omega}_{C,E}^E\right)\times\dot{\underline{P}}_u^A - T_G^E\cdot\underline{g}_u^G\right)$$

Equation 3.3-27

$${}_{800}\overline{\underline{f}}_{r,u}^B := 0.5\cdot\left(\overline{\underline{f}}_{r,u}^B\left(t-\Delta_R\right) + \overline{\underline{f}}_{r,u}^B\right)$$

Equation 3.3-28

The reference incremental angle turned through over a sub-frame is then,

$${}_{800}\Delta E_C^B := \Delta_R\cdot{}_{800}\overline{\underline{f}}_{r,u}^B$$

Equation 3.3-29

3.3.1.3 IMU-2 Kinematics

Extending the dynamic analysis of the Master IMU to the angular rate of the Missile Body frame (M) in a flexible missile attached to a pylon on the wing of an aircraft,

$$\underline{\omega}^{M}_{C,M} := T^{M}_{P} \cdot \left(\underline{\omega}^{P}_{W,P} + T^{P}_{W} \cdot \left(\underline{\omega}^{W}_{B,W} + T^{W}_{B} \cdot \underline{\omega}^{B}_{C,B} \right) \right) + \underline{\omega}^{M}_{P,M}$$

Equation 3.3-30

Wing motion with respect to the fuselage comprises wing bending and low frequency wing flexure in the frequency range < 1 Hz and 5-15 Hz; these are complex functions of fuel and armament load, aircraft speed, turn rate, buffet and vortex shedding. Pylon motion with respect to the wing has a spectral content of typically 30-50 Hz. Missile vibration is constrained by its supports, stiffness, and the mode of vibration, a function of the number of supports and the distance between them. The effect of these static and dynamic components is twofold. Low frequency motion effects target designation performance and the ability of the weapon system to keep the target in the seeker field-of-view. High frequency motion causes the energy falling on the seeker detector to be smeared when using IR staring arrays reducing the acquisition range and accuracy. When studying the effect of this motion on the seeker smear it must be modelled, not at the highest modal frequency within the seeker bandwidth (70-100 Hz), but at a frequency commensurate with the internal gimbal dynamics and the detector stare time, typically > 2 kHz.

These models are derived from instrumented wing, pylon and missile data and it is extremely difficult to isolate the individual noise components comprising the overall spectra and the cross coupling between axes. Data reduction invariably results in separate, none co-ordinated roll-pitch-yaw spectra that are a function of the operating conditions. Flexure models are thus partitioned into a static elements associated with the wing, pylon attachment, missile supports and missile body misalignment. Thus the orientation of the Missile Body frame with respect to the Launcher Body frame comprises a nominal orientation, onto which is superimposed small angle transforms representing the quasi-static and flexure components denoted by “N”, “S” and “F” respectively,

$$T^{M}_{B} := {}_{D}T^{M}_{B} \cdot {}_{S}T^{M}_{B} \cdot \left({}_{N}T^{M}_{P} \cdot {}_{N}T^{P}_{W} \cdot {}_{N}T^{W}_{B} \right)$$

Equation 3.3-31

The various static misalignments, such as the residual harmonisation angle of the pylon and missile, are modelled as initial zero mean, Gaussian errors. Wing bending is treated as a quasi-static misalignment that is a function of say speed and turn rate. When designating targets it is this component of structural motion that some aircraft attempt to compensate for, not the higher frequency pylon noise that invariably requires a small scan pattern.

Wing, pylon and missile noise at the seeker are often defined by none co-ordinated angular acceleration power spectra. These are converted into state-space models driven by band limited white noise derived using spectral matching techniques such as Yule-Walker. For roll,

$$U(t) := N(0, \gamma)$$

Equation 3.3-32

$$\underline{X} := [A] \cdot \underline{X}\left(t - \frac{1}{SK\, f_R} \right) + [B] \cdot U$$

Equation 3.3-33

$$\Delta\Phi_B^M :=$$

$$\varphi_{D1L}\left(\varphi_{D1L}\left([C] \cdot \underline{X}\left(t - \frac{1}{SK\, f_R} \right) + [D] \cdot U \, , \frac{1}{f_{WF1}} \right) , \frac{1}{f_{WF2}} \right)$$

Equation 3.3-34

Matching even simple spectra is a balance between accuracy, dimensionality (< 10-12) and model execution time. The angle and angular velocity output is tuned to measured levels using the integration bandwidths that also attenuate the aforementioned quasi-static bias. Tuning and sensitivity studies require a scaling factor (γ) that adjusts the overall output level across all frequencies. Flexure models must have a short-term, zero mean, angular output since a non-zero mean implies that the structure is permanently deforming. Any residual bias not removed by the integration process must be removed using low frequency angle and angular rate feedback in a way that does not significantly alter the low frequency spectra.

The production of verifiable flexure models is a large topic and one that is beyond the scope of the work here. Hopefully, this introduction to the sensor modelling for distributed weapon systems attached to flexible structures is useful, however, for the current work the dynamics established for the master IMU are sufficient to define the reference input to the IMU sensors of an in-flight missile.

3.4 Gyroscopes

3.4.1 Review

Mechanical sensors such as the twin-axis Dynamically Tuned Gyroscope (DTG), and single-axis suspended instruments with their spinning rotors, were dominant from the mid-40s until the late 80s. Conceptually, mechanical floated gyroscopes contain a rotor turning at high speed about its spin axis. Rotation about an orthogonal input axis results in a processional rotation of the float containing the spinning rotor about the third orthogonal output axis so as to keep the total angular momentum constant. The torque causing the rotor cage to precess is balanced by passing a measured current through a torquer that is directly proportional to the angular rate about the input axis.

RLG and FOG based on the Sagnac effect were developed in the early 60s and early 80s respectively. These are rate-integrating devices - they do not provide instantaneous angular rate. In the RLG, coherent light passes both ways round a resonant cavity filled with an inert gas, whereas in a FOG it passes through an optical fibre. The light resonates and an inertially stable standing wave is created comprising a constant number of wavelengths around the light pathway. Rotation of the optical path means the distance between the two light paths is different creating a frequency shift. Interferometry techniques are used to mix the two light beams, creating fringes that pass beneath a detector, to measure this frequency shift. The number of fringes detected in a fixed period is proportional to incremental angle of rotation. Sensitivity is reduced since the waves are locked together until the frequency shift is large enough to be detectable.

Solid state resonant vibrating shell gyroscopes discovery by Bryan in 1890 are an alternative to optical devices. These rely on changes in the modal shape of the shell caused by coriolis acceleration, and were mechanised in the mid-80s. Solid state and optical sensors are rapidly replacing mechanical devices. They are rugged, high bandwidth, low scale factor with large dynamic range making them ideal for strap-down applications, few moving parts, insensitive to magnetic fields and high accelerations, rapid reaction times and require little power. There are problems of course: the RLG accuracy is proportional to cavity size, high voltages, contaminated gas, gas leakage and electro-optical links resulting in loss of sensitivity. Never-the-less optical gyroscopes are now widely used in weapon systems, the more accurate RLGs in launch platforms, cruise and Inter-Continental Ballistic Missile (ICBM). Less accurate FOGs are used in medium and short-range missiles where space and weight are at a premium. The electronically dithered RLG is now mature technology, whilst FOGs and solid state devices are emerging technologies that promote compact packaging and resistance to high “g” levels. Future development is expected not so much in the fundamental operation of the gyroscope, but on reliable electronics and miniaturisation whilst maintaining accuracy (i.e. a gyroscope on a chip).

As mentioned earlier the RLG suffers from low angular rate "lock-in" caused by imperfect lasing path mirror reflectivity. Back scattered light returns from whence it came causing the two beams to synchronise and the standing wave to become locked to the moving cavity, instead of the inertial reference, causing a dead-band. The mechanical solution is to superimpose a zero mean oscillation (dither) onto the input angular rate some 2-3 orders higher than the lock-in threshold. Less time is then spent in the lock-in region although there remains a residual random drift in the output after the dither is removed. This is the dominant RLG error noise characteristic and careful design is required to prevent rectified noise from appearing within their operational bandwidth.

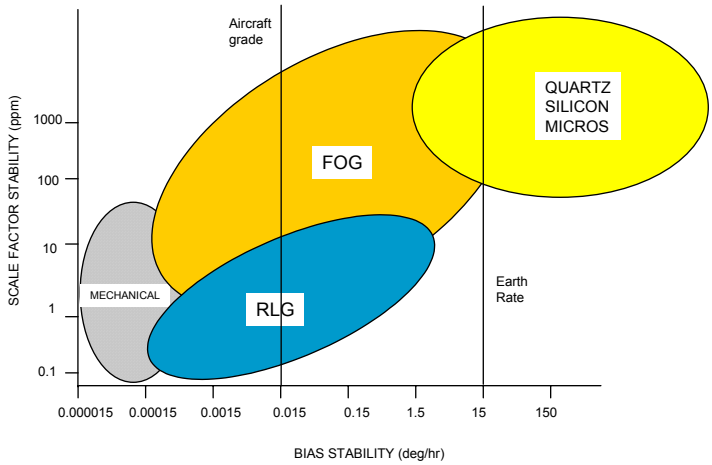

Figure 3-23 : Gyroscope Relative Performance

Figure 3-23 compares the accuracy of the different types of gyroscope - data supplied by Dr. P. Jones from original material published by QinetiQ.

3.4.2 Description

The triad of rate-integrating, single-axis gyroscopes shown in Figure 3-24 provides inertial angular increments (*M_W_INC*), and average inertial angular rates (*M_W_BCB*), with respect to the IMU reference frame (U). The model is flexible enough to accommodate the following types of gyroscopes:

- Mechanical, torque re-balanced floated rotor gyroscope
- Ring laser gyroscope
- Fibre optical gyroscope
- Resonant gyroscopes

There is a wealth of literature on gyroscopes. The work of Lawrence[L.10] and The Institute of Electrical and Electronics Engineers (IEEE) standard[I.1] are useful references.

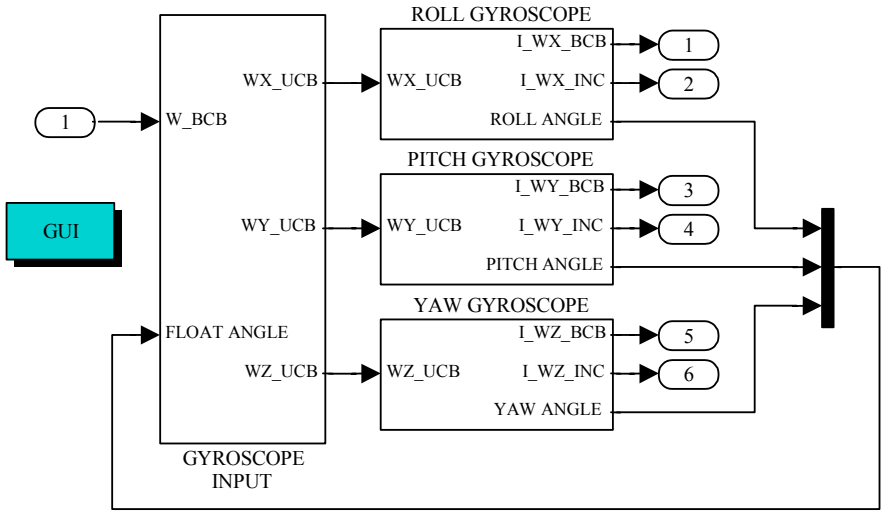

Figure 3-24 : Gyroscope Triad Model

The generic gyroscope model here is adequate for both IMU-1 and IMU-2 in §3.3.1. The reference data will be described in terms of IMU-1 although IMU-2 reference inputs can be treated likewise.

3.4.3 Reference Angular Rate

The average inertial angular rate is processed at the reference rate ($_{GS}f_R$) of 800 Hz. The angular rate about each input axis depends on the alignment and orthogonality of the case with respect to the missile body, and each sensor relative to the case as shown Figure 3-25.

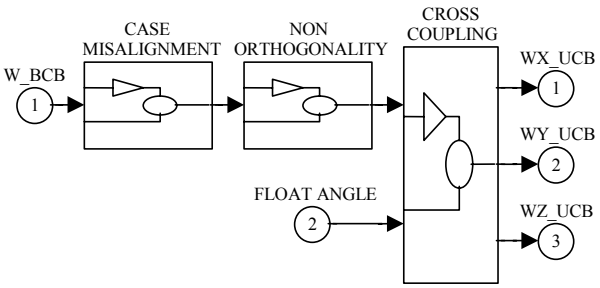

Figure 3-25 : Gyroscope Input Models

Mechanical instruments are also subject to cross-coupling errors that depend on the float angle. These additional error sources are invoked by setting *MS_GS_ER* bits 11-13 listed in Table 3-8. To deal with these errors additional Cartesian axes associated with the IMU case, and each sensor therein, are required. Frame "D" is fixed in the IMU and originates at a common reference point (u), and describes the orientation of the case with respect to the Missile Body frame. An orthogonal "sensor" frame is attached to each gyroscope referred to as "R", "P" and "Y" respectively, their individual reference points coinciding with (u). The manufacturing

process ensures that the internal components in a sensor are accurately aligned compared with the sensor location in the case.

Table 3-8 : Gyroscope Reference Errors

MS_GS_ER	Sensor Error Source	
11	IMU case misalignment	
12	Non-orthogonality wrt case	
13	Cross coupling error	

Errors arising from the multiplexing process (poling the sensor output at different times), and Coriolis corrections associated with distributed sensors in the case, are not modelled explicitly.

3.4.3.1 IMU Case Misalignment Error

Manufacturing tolerances mean that the case containing the gyroscopes is rotated with respect to the Missile Body frame, an alignment error that preserves sensor triad orthogonality. For small angles, assuming that the expected error is the same about each axis,

$$\Delta E_B^D \in N\left(0, {}_{IMU}\sigma_{MA}\right) \Rightarrow \underline{\omega}_{C,B}^D := \left[I_3 + \Delta E_B^D \times \right] \cdot \underline{\omega}_{C,B}^B$$

Equation 3.4-1

The IMU case misalignment error is initialised from a zero-mean Gaussian distribution with a deviation of $({}_{IMU}\sigma_{MA})$. This error is common to both gyroscope and accelerometer triads and is computed in both sensor modules so that they can be activated in isolation.

3.4.3.2 Sensor Triad Non-Orthogonality Error

The orientation of each sensor with respect to the case results in a non-orthogonality error between sensors that is initialised from a zero-mean Gaussian distribution with a deviation of $({}_{GS}\sigma_{NO})$. If the expected error is the same for each axis,

$$\forall i \in \{ R, P, Y \} \Rightarrow \underline{\omega}_{C,B}^i := \left[I_3 + \Delta E_D^i \times \right] \cdot \left(M_B^i \cdot \underline{\omega}_{C,B}^D \right)$$

Equation 3.4-2

When selected values from symmetrical statistical distributions the sign of the rotations in the transform are irrelevant. Although the input axes are nominally aligned with Missile Body axis, in mechanical systems, the Output and Spin axes can be selected to minimise acceleration sensitive drifts. The dominant g (mass unbalance) and g^2-sensitive (anisoelastic) drifts are stimulated by accelerations along the spin and output axes.

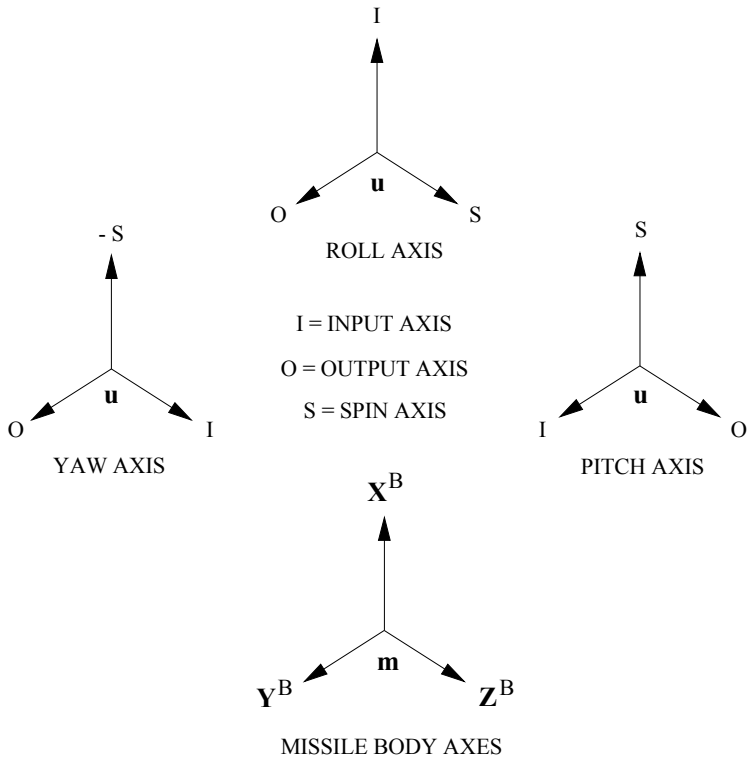

Figure 3-26 : Gyroscope Triad Orientation (Lateral Rate Tolerant)

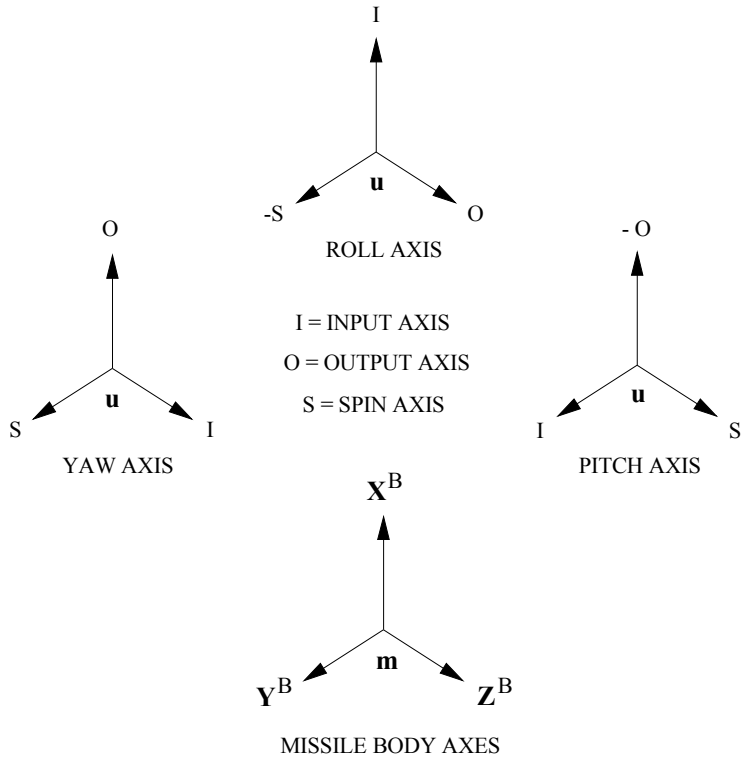

Figure 3-27 : Gyroscope Triad Orientation (Roll Rate Tolerant)

The configurations shown in Figure 3-26 and Figure 3-27 contain 6 of the possible 12 sensor orientations (6 more are obtained by rotating each input axis through 180°). The negative signs in these figures indicate that the positive sensor axis is in the opposite direction to that shown.

For each sensor, let the (X,Y,Z) Missile Body axes be aligned with the Input-Output-Spin (I,O,S) sensor axes such that a clockwise spinning rotor about the Spin axis implies positive output and input angular rates. The configurations in Figure 3-26 and Figure 3-27 minimise torque due to missile lateral and longitudinal acceleration respectively. For long-range missiles the spin axis of the roll gyroscope should be aligned with $\underline{Z}^B$ since roll motion is often restricted and pitch manoeuvres are rare, except when terrain following. For the orientation shown in Figure 3-26 the mapping of the case inputs to the (I,O,S) axes for mechanical RPY gyroscopes is,

$$M_D^R := \begin{bmatrix} 1 & 0 & 0 \\ 0 & 1 & 0 \\ 0 & 0 & 1 \end{bmatrix} \; ; \; M_D^P := \begin{bmatrix} 0 & 1 & 0 \\ 0 & 0 & 1 \\ 1 & 0 & 0 \end{bmatrix} \; ; \; M_D^Y := \begin{bmatrix} 0 & 0 & 1 \\ 0 & 1 & 0 \\ -1 & 0 & 0 \end{bmatrix}$$

Equation 3.4-3

For optical instruments the mappings are simply the identity matrix since these sensors are insensitive to acceleration induced errors.

3.4.3.3 Mechanical Sensor Cross-Coupling Error

Unlike optical gyroscopes mechanical instruments are also affected by cross-coupling errors. Imperfect and finite bandwidth re-balancing of the float assembly supporting the rotor causes misalignment of the Spin and Input axes. The angular displacement of the float about the Output axis (γ) is usually < 0.5°. The angular rate experienced by each gyroscope is thus,

$$\forall i \in \{ R, P, Y \} \Rightarrow \underline{\omega}_{C,B}^{i} := \begin{bmatrix} 1 & 0 & -\gamma_i \\ 0 & 1 & 0 \\ \gamma_i & 0 & 1 \end{bmatrix} \cdot \begin{pmatrix} \omega_{C,B}^{Ii} \\ \omega_{C,B}^{Oi} \\ \omega_{C,B}^{Si} \end{pmatrix} + \begin{pmatrix} 0 \\ \dot{\gamma}_i \\ 0 \end{pmatrix}$$

Equation 3.4-4

The error induced by the angular rate of the float assembly is small compared with some of the other error sources. The float angle is obtained from the typical torquer model shown in Figure 3-28 using the parameters:

Float inertia	J	2.5×10^{-6}	kg m^2
Float angular momentum	H	0.005	kg m^2/s
Viscous torque coefficient	C	0.004	Nm/(rad/s)
Pulse-Width-Modulator (PWM) gain	$_{GS}G_{PM}$	500	(rad/s)/rad
Torquer bandwidth		4000	rad/s

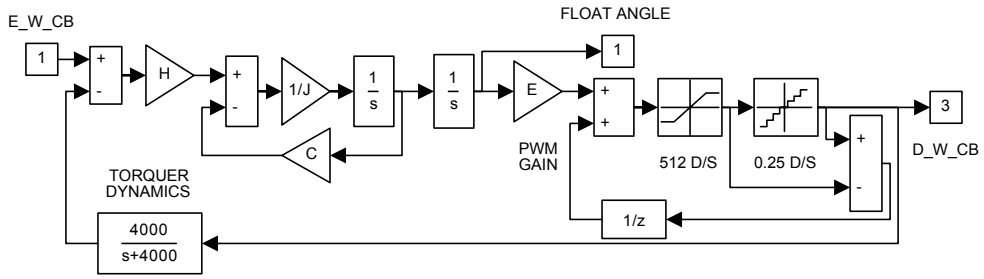

Figure 3-28 : Torquer Model

The PWM and torquer can be reduced to a 2nd order lag with a damping of 0.67 and natural frequency of 160 Hz range followed by limiting and quantisation. The linear model response to a 1° step is compared to this 2nd order closed loop response in Figure 3-29.

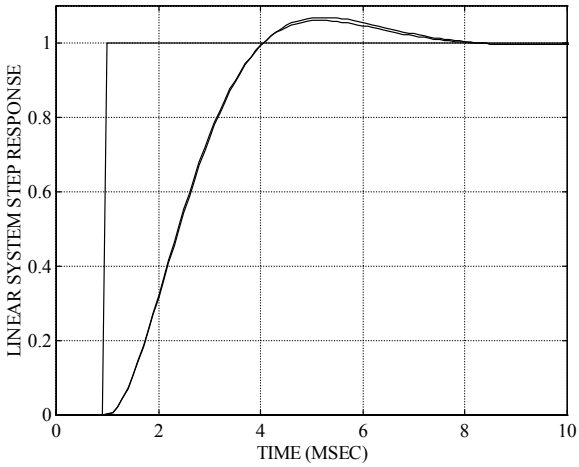

Figure 3-29 : Closed Loop Step Response

The maximum float angle depends on the PWM gain and the maximum expected angular rate,

$$G_{PWM} \cdot \gamma_{MAX} := {}_{MAX}\omega_{C,B}$$

Equation 3.4-5

The PWM gain is 500 (°/s)/° for a saturation limit of 250°/s and a maximum float angle of 0.5°. The quantisation for this saturation limit, given 2^{11} pulses per output cycle, is 0.244°/s. The cross-coupling misalignment angle (γ) is determined from the 2nd order PWM dynamics when bit 3 of *MS_GS_ER* is set. The input to the mechanical gyroscope triad is therefore,

$$\underline{\omega}^{U}_{C,B} := \begin{pmatrix} \omega^{IR}_{C,B} \\ \omega^{IP}_{C,B} \\ \omega^{IY}_{C,B} \end{pmatrix} - \begin{pmatrix} \gamma_R \\ \gamma_P \\ \gamma_Y \end{pmatrix} \otimes \begin{pmatrix} \omega^{SR}_{C,B} \\ \omega^{SP}_{C,B} \\ \omega^{SY}_{C,B} \end{pmatrix}$$

Equation 3.4-6

$$ {}_{GS}\underline{\gamma} \;:=\; \left(\gamma_R \;,\; \gamma_P \;,\; \gamma_Y \right)^T $$

Equation 3.4-7

Applying a masking matrix [GXM] to deal with the different Spin axis orientations, and relating the Spin axis to individual sensor (R,P,Y) axes,

$$ \underline{\omega}^{U}_{C,B} \;:=\; \begin{pmatrix} \omega^{XR}_{C,B} \\ \omega^{XP}_{C,B} \\ \omega^{XY}_{C,B} \end{pmatrix} - {}_{GS}\underline{\gamma} \otimes \left(\left[\mathrm{GXM} \right] \cdot \begin{bmatrix} \omega^{YR}_{C,B} & \omega^{XP}_{C,B} & \omega^{XY}_{C,B} \\ \omega^{ZR}_{C,B} & \omega^{ZP}_{C,B} & \omega^{YY}_{C,B} \end{bmatrix} \right) $$

Equation 3.4-8

For the configuration selected,

$$ \left[\mathrm{GXM} \right] \;:=\; \begin{bmatrix} 0 & 1 \\ 1 & 0 \\ -1 & 0 \end{bmatrix} $$

Equation 3.4-9

3.4.4 Measured Angular Rate and Angular Increments

Non-gyroscopic torques, and imperfect electronics, that cause application dependent measurement errors are subject to physical constraints, financial and technical trade-offs. Ignoring rotor speed variation drift, float angular velocity and acceleration, Savage's model of a single axis mechanical gyroscope expressed in (I,O,S) axes reduces to,

$$ \tilde{\omega}^{I}_{C,B} \;:=\; \varphi_{SF} \cdot \left(\omega^{I}_{C,B} + {}_{GS}B^{I} + \left(\frac{J_S - J_I}{H_W} \right) \cdot \omega^{I}_{C,B} \cdot \omega^{S}_{C,B} - \frac{J_O \cdot \dot{\omega}^{O}_{C,B}}{H_W} \right) $$

Equation 3.4-10

The float inertia about the axes is denoted by (J_I, J_O, J_S), and (H_W) is the angular momentum of the rotor about the spin axis. Float dynamics, aniso-elastic drift, and output rate induced errors are minimising by careful design. This leaves constant bias (${}_{GS}B$) and scale factor errors common to both optical and mechanical sensors. These errors are controlled by the bit pattern of *MS_GS_ER* listed in Table 3-9. Bits 22-23 reserved in Table 3-6 for ADC errors, are replaced by PWM errors in mechanical sensors, and fringe counting in optical systems. The anti-aliasing filter and quantised noise associated with the ADC, controlled by bits 21 and 24, are not applicable.

The inertial angular rate is corrupted at the reference rate by a time delay and 2nd order dynamics,

$$ {}^{D}\underline{\omega}^{B}_{C,B} \coloneqq \underline{\varphi}_{TD}\left(\underline{\varphi}_{D2L}\left(\underline{\omega}^{U}_{C,B}, {}_{GS}\zeta_{D2L}, {}_{GS}\omega_{D2L} \right), {}_{GS}t_{TD} \right) $$

Equation 3.4-11

The output of the 2nd order dynamics determines the cross coupling error,

$$ {}_{GS}G_{PM} \cdot {}_{GS}\underline{\gamma} \coloneqq \underline{\omega}^{U}_{C,B} - \underline{\varphi}_{D2L}\left(\underline{\omega}^{U}_{C,B} \right) $$

Equation 3.4-12

Table 3-9 : Gyroscope Triad Errors

MS_GS_ER	Sensor Error Source
17	G-dependent drift
18	G^2-dependent drift
19	Digital compensation filter
22	Pulse count range limit
23	Pulse quantisation

Although a time delay is not included in the Savage and IEEE models delays exist in the torquer and internal digital processor. The dynamic output is subject to a constant bias, random noise and scale factor errors effecting both mechanical and optical sensors, and a bias affecting only mechanical sensors ($_{GS}B_G$).

$$ {}^{A}\underline{\tilde{\omega}}^{B}_{C,B} \coloneqq \underline{\varphi}_{SF}\left({}^{D}\underline{\omega}^{B}_{C,B} + \underline{\varphi}_{CB}\left({}_{GS}\sigma_{CB} \right) + \underline{\varphi}_{RN}\left({}_{GS}\sigma_{RN} \right) + {}_{GS}\underline{B}_{G} \right) $$

Equation 3.4-13

In mechanical gyroscopes bias is caused by:

- residual torques due to thermal gradient induced fluid motion
- magnetic reaction torques induced by spin motor generated eddy currents in the float cylinder
- residual flex-lead torques
- pivot stiction
- torque loop/pulse electronics

In optical sensors bias results from thermal gradients in the RLG lasing path, and micro-kinks in the FOG winding. Noise in optical sensors is some 3-4 times larger than in equivalent mechanical systems, and is caused by:

- Photon (quantum) shot noise; light quantised in photons at the detector
- Fringe count over the output sampling period inducing quantisation noise
- Residual dither from the process used to minimise lock-in bias

In high grade RLGs used for navigation quantum and quantisation noise is similar, and both are larger than residual dither. Noise is often specified in (deg/√hr) referenced to the sensor output rate. From §3.2.2.2,

$$ {}_{GS}\sigma_{RN} = \frac{\pi \cdot \sqrt{{}_{GS}\Phi_{RN} \cdot {}_{GS}f_R}}{180 \cdot 60 \cdot {}_{GS}f_O} $$

Equation 3.4-14

The quantisation model in Figure 3-30 adds the residual from the current pulse count to the next counting period to prevent non-existent drifts. The maximum number of pulses during the output period and the pulse weight (rad/s/pulse) determine the internal range. The analogue measurements pass through this quantising function (φ_Q) and a pulse count saturation limit commensurate with the output interface angular rate range.

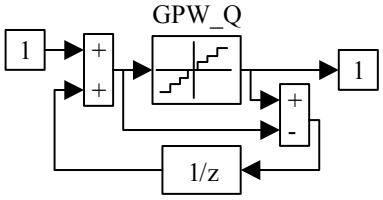

Figure 3-30 : Quantisation Noise Model

Scale factor errors in the torquer electronics are made as small as possible by designing a "stiff" system in which float rotation is minimised. They are caused by variation in the magnetic field strength due to thermal sensitivity. Scale factor errors in optical sensor fringe counting are small whereas those in mechanical system torquers are inherently larger. The IEEE cubic scale factor error has been omitted since it is rarely known.

The acceleration dependent drifts effecting mechanical gyroscopes are driven by accelerations along the Input and Spin axes. For a single sensor,

$$ {}_{GS}B_G^I := B_S^I \cdot f_{r,u}^S + B_I^I \cdot f_{r,u}^I + B_{SI}^I \cdot f_{r,u}^S \cdot f_{r,u}^I $$

Equation 3.4-15

G-dependent drift is caused by mass unbalance of the float about the spin and input axes. G^2-dependent drift is caused by unequal compliance of the float assembly between axes, and in particularly the spin and input axes. In the simulation all the combinations of error terms are available with user specified masks [G1M] and [G2M] provided to obtain the required "g" and g^2 -sensitive errors respectively. These errors should be a function of the specific accelerations acting along the sensor RPY axes. Since the misalignment angles are small, to improve modularity and allow the gyroscope and accelerometer triads to be used in isolation the acceleration along the Missile Body axes is used instead.

$$ {}_{GS}\underline{B}_{G} \coloneqq $$

$$ \left(\left[\mathrm{GDM} \right] \otimes \left[{}_{GD}\mathrm{G} \right] \right) \cdot \underline{f}^{B}_{r,u} + \left(\left[\mathrm{GGM} \right] \otimes \left[{}_{GG}\mathrm{G} \right] \right) \cdot \underline{f}^{B}_{r,u} \cdot \left(\underline{f}^{B}_{r,u} \right)^{T} $$

Equation 3.4-16

For the configuration selected,

$$ \left[\mathrm{GDM} \right] \coloneqq \begin{pmatrix} 1 & 0 & 1 \\ 1 & 1 & 0 \\ -1 & 0 & 1 \end{pmatrix} \; ; \; \left[{}_{GD}\mathrm{B} \right] \coloneqq \begin{pmatrix} {}_{GD}B^{R}_{X} & {}_{GD}B^{R}_{Y} & {}_{GD}B^{R}_{Z} \\ {}_{GD}B^{P}_{X} & {}_{GD}B^{P}_{Y} & {}_{GD}B^{P}_{Z} \\ {}_{GD}B^{Y}_{X} & {}_{GD}B^{Y}_{Y} & {}_{GD}B^{Y}_{Z} \end{pmatrix} $$

Equation 3.4-17

$$ \left[\mathrm{GGM} \right] \coloneqq \begin{pmatrix} 0 & 0 & 1 \\ 1 & 0 & 0 \\ -1 & 0 & 0 \end{pmatrix} \; ; \; \left[{}_{GG}\mathrm{B} \right] \coloneqq \begin{pmatrix} 0 & {}_{GG}B^{R}_{XY} & {}_{GG}B^{R}_{XZ} \\ {}_{GG}B^{P}_{YX} & 0 & {}_{GG}B^{P}_{YZ} \\ {}_{GG}B^{Y}_{ZX} & {}_{GG}B^{Y}_{ZY} & 0 \end{pmatrix} $$

Equation 3.4-18

The effect of the masks on the available error sources is to extract,

$$ {}_{GS}\underline{B}_{G} \coloneqq \begin{pmatrix} {}_{GD}B^{R}_{Z} \cdot f^{ZB}_{r,u} + {}_{GD}B^{R}_{X} \cdot f^{XB}_{r,u} + {}_{GG}B^{R}_{XZ} \cdot f^{XB}_{r,u} \cdot f^{ZB}_{r,u} \\ {}_{GD}B^{P}_{X} \cdot f^{XB}_{r,u} + {}_{GD}B^{P}_{Y} \cdot f^{YB}_{r,u} + {}_{GG}B^{P}_{XY} \cdot f^{XB}_{r,u} \cdot f^{YB}_{r,u} \\ {}_{GD}B^{Y}_{Z} \cdot f^{ZB}_{r,u} - {}_{GD}B^{Y}_{X} \cdot f^{XB}_{r,u} - {}_{GG}B^{Y}_{XZ} \cdot f^{XB}_{r,u} \cdot f^{ZB}_{r,u} \end{pmatrix} $$

Equation 3.4-19

When errors are selected from zero mean, symmetric distributions the negative terms in these equations are superfluous. Time delays associated with stabilisation of seeker IR detectors are detrimental to performance. The measurements are therefore passed through filters compensating for the deterministic time delays in the system and the sensor's dynamics,

$$ {}_{800}\underset{\sim}{\omega}^{B}_{C,B} \coloneqq $$

$$ \underline{\varphi}_{DLL} \left({}^{PWM}\underline{\varphi}_{Q} \left({}^{PWM}\underline{\varphi}_{LIM} \left({}^{A}\underset{\sim}{\omega}^{B}_{C,B} \right), {}^{PWM}_{GS}\mathrm{Q} \right), {}_{GS}\omega_{NC}, {}_{GS}\omega_{DC} \right) $$

Equation 3.4-20

In the simulation the output range limit and the maximum number of pulses ($_{GS}N_{MP}$) determine the quantisation level, e.g. for ± 400°/s and 2^{12} pulses the

quantisation is $400/2^{11} \approx 0.2°/s$. Default values are set to compensation for the time delay and 2nd order dynamics.

$$\left({}_{GS}\omega_{NC} \quad , \quad {}_{GS}\omega_{DC} \right) := \left(\frac{{}_{GS}\omega_{2DL}}{2 \cdot {}_{GS}\zeta_{2DL} + {}_{GS}\omega_{2DL} \cdot {}_{GS}t_{TD}} \quad , \quad \frac{1}{{}_{GS}t_{TD}} \right)$$

Equation 3.4-21

Typical values for the gyroscope error sources used in aircraft (AC), cruise missile (LRM), and a short-range missile (SRM) are given in Table 3-10. For mechanical instruments the scale factor, constant and g-sensitive bias characteristics are initialised from Gaussian distributions. Mechanical instrument errors tend to be bi-modally distributed having passed through a manufacturing grading process. This is reflected in the provision of bi-modal distributions defined by $N(0.75\sigma,0.25\sigma)$ as described in §22.1.4.3.

Table 3-10 : Gyroscope Error Characteristics

Error Characteristic	Alias	AC	LRM	SRM	Units
Case misalignment	${}_{GS}\sigma_{MA}$	0.1	0.3	5	mrad
Non-orthogonality	${}_{GS}\sigma_{NO}$	0.1	0.3	5	mrad
Constant bias	${}_{GS}\sigma_{CB}$	0.01	1.0	50	deg/hr
In-run bias stability		0.002	0.2	10	deg/hr
Gaussian noise (Optical)	${}_{GS}\Phi_{RN}$	0.02	1.0	10	deg/√hr
Gaussian noise (Mechanical)	${}_{GS}\Phi_{RN}$	0.005	0.02	3	deg/√hr
Constant scale factor error	${}_{GS}\sigma_{CS}$	20	80	300	ppm
Scale factor linearity	${}_{GS}\sigma_{AS}$	10	30	100	ppm
Maximum pulse/output	${}_{GS}N_{MP}$	2^{24}	2^{20}	2^{16}	-
Bandwidth	${}_{GS}\omega_{D2L}$	100			Hz
Natural Frequency	${}_{GS}\zeta_{D2L}$	0.7			-
Mechanical g-dependent drift	${}_{GS}\sigma_{GD}$	0.2	0.2	-	deg/hr/g
Mechanical g^2-dependent drift	${}_{GS}\sigma_{GG}$	0.003	0.003	-	deg/hr/g^2

The position (ΔP) and velocity (ΔV) errors induced by the constant drift, Gaussian noise and constant scale factor errors over a time period (Δt) are,

$$E\left(\Delta V_{CB} \quad , \quad \Delta P_{CB} \right) := \frac{\pi \cdot {}_{GS}\sigma_{CB}}{180 \cdot 3600} \cdot g_u \cdot \left(\Delta t^2 / 2 \quad , \quad \Delta t^3 / 6 \right)$$

Equation 3.4-22

$$E\left(\Delta V_{RN} \quad , \quad \Delta P_{RN}\right) := \frac{\pi \cdot {}_{GS}\Phi_{RN}}{60 \cdot 180} \cdot g_u \cdot \left(\sqrt{\Delta t^3 / 3} \quad , \quad \sqrt{\Delta t^5 / 20}\right)$$

Equation 3.4-23

$$E\left(\Delta V_{SC} \quad , \quad \Delta P_{SC}\right) := {}_{GS}\sigma_{SC} \cdot 10^{-6} \cdot g_u \cdot \omega_{C,B} \cdot \left(\Delta t^2 / 2 \quad , \quad \Delta t^3 / 6\right)$$

Equation 3.4-24

For systems tolerant to time delays the 400 Hz output is the average of the previous two sub-frames. For this application time delays are critical and the average rate is that over the last sub-frame,

$${}_{400}\underline{\widetilde{\omega}}^{B}_{C,B} := {}_{800}\underline{\widetilde{\omega}}^{B}_{C,B}$$

Equation 3.4-25

The incremental angle over the integration (output) period,

$${}_{400}\Delta\widetilde{E}^{B}_{C} := \frac{1}{{}_{GS}f_O} \cdot \left({}_{800}\underline{\widetilde{\omega}}^{B}_{C,B} + {}_{800}\underline{\widetilde{\omega}}^{B}_{C,B}\left(t - \frac{1}{{}_{GS}f_O}\right)\right)$$

Equation 3.4-26

For convenience the accelerometer outputs are collected together,

$$\underline{\widetilde{Z}} \equiv \begin{pmatrix} \underline{\widetilde{Z}}_{GR} \\ \cdots \\ \underline{\widetilde{Z}}_{GI} \end{pmatrix} \equiv \begin{pmatrix} {}_{400}\underline{\widetilde{\omega}}^{B}_{C,B} \\ \cdots \\ {}_{400}\Delta\widetilde{E}^{B}_{C} \end{pmatrix}$$

Equation 3.4-27

3.4.5 Sensor Limitations

Provision of measurements at the output interface depends on:

- User measurement selection (*MS_MSAV1* bit 1-3 cleared)
- PWM angular rate limiting (*MS_GS_ER* bit 22 is set)

When active, if any of these limitations are violated, bits 1-3 (RPY) in the measurement ready flag *MS_MSRY1* are cleared. Failure to provide measurement at the user's request is indicated by setting bits 1-3 of *MS_GS_VF*. If the angular rate limit is exceeded bits 4-6 of *MS_GS_VF* are set depending on which of the gyroscopes is affected.

3.4.6 Output Interface

The inertial angular rate and angular increments pass through a signed 16 bit digital interface at a frequency ($_{GS}f_O$) of 400 Hz (clock 9). These

measurements are subject to interface range limits of ± 1° and ± 400°/s respectively, and a one-cycle transmission delay.

$$ {}_{GS}\underline{\tilde{Z}} := {}^{IF}\underline{\varphi}_{TD}\left({}^{IF}\underline{\varphi}_{Q}\left({}^{IF}\underline{\varphi}_{LIM}\left({}^{IF}\underline{\varphi}_{ZOH}\left(\underline{\tilde{Z}} \right) \right) \right) \right) $$

Equation 3.4-28

3.5 Accelerometers

3.5.1 Review

Accelerometers are inertial sensors that conceptually measure the relative displacement between an elastically or electrically restrained proof mass moving with respect to its rigid support. Pickoffs sense any displacement of the proof mass whose position is restored, the restoring current being directly proportional to specific acceleration. Pendulous re-balanced accelerometers are still preferred for launcher applications below 1nm/hr with their small misalignment error and resistance to vibro-pendulous rectification. For missiles requiring accuracies no better than 10nm/hr the constrained pendula accelerometers employing piezoelectric driven vibrating beams are making an impact due to their inherently digital operation and relatively low cost. Vibrating string beam and tuning fork accelerometers rely on measuring changes in resonant frequency caused by acceleration. Conceptually, a proof mass on the end of a string vibrating at a frequency dependent on the acceleration sensed along it, the change in frequency being proportional to the applied acceleration. The resonant frequency of quartz crystals is similarly effected by the compression and tension caused by acceleration. Only recently have these devices, proposed in the late 20s, been ruggedised and miniaturised and will probably dominate the future missile market.

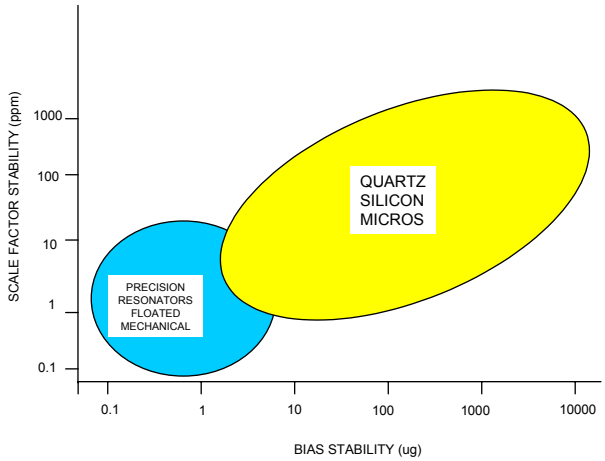

Figure 3-31 : Accelerometer Relative Performance

Figure 3-31 compares the accuracy of the different types of accelerometers - data supplied by Dr. P. Jones from original material published by QinetiQ.

3.5.2 Description

The triad of single-axis accelerometers shown in Figure 3-32 provides velocity increments (*M_V_INC*) at the IMU reference point (u) over the output period, and derived average specific acceleration (*M_F_BRU*). The

model is implemented so that errors are superimposed on the specific accelerations from which velocity increments are derived.

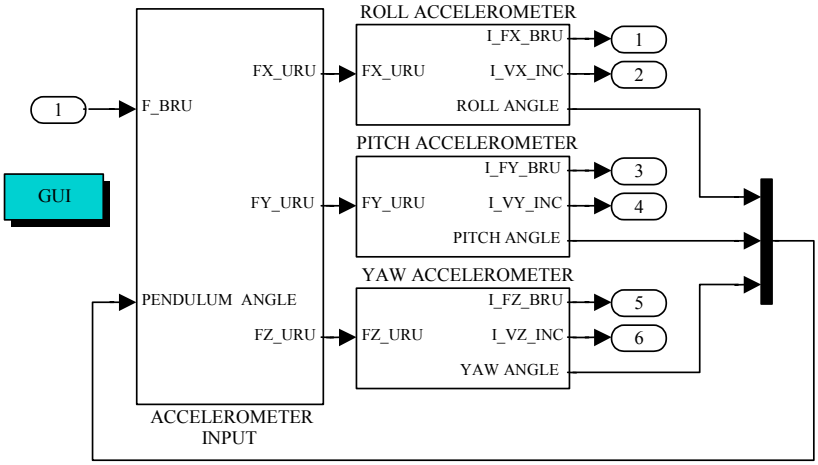

Figure 3-32 : Accelerometer Triad Model

3.5.3 Reference Specific Acceleration

The average specific acceleration along Missile Body axes is processed at the reference rate ($_{AC}f_R$) of 800 Hz. The acceleration acting along each input axis depends on the alignment and orthogonality of the case with respect to the missile body, and each sensor relative to the case as shown in Figure 3-33.

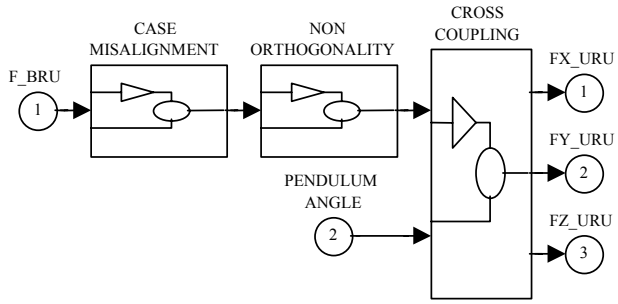

Figure 3-33 : Accelerometer Input Model

Mechanical instruments are also subject to cross-coupling errors that depend on the pendulum angle that require similar RPY sensor axes defined for gyroscopes in §3.4.3. These additional error sources are invoked by setting the *MS_GS_ER* bits 11-13 listed in Table 3-11.

Table 3-11 : Accelerometer Reference Errors

MS_AC_ER	Sensor Error Source	
11	IMU case misalignment	
12	Non-orthogonality wrt case	
13	Cross coupling error	

3.5.3.1 IMU Case Misalignment Error

Manufacturing tolerances mean that the case containing the accelerometers is rotated with respect to the Missile Body frame, an alignment error that preserves sensor triad orthogonality. For small angles, assuming that the expected error is the same about each axis,

$$\Delta E_B^D \in N\left(0 , {}_{IMU}\sigma_{MA} \right) \Rightarrow \underline{f}_{r,u}^D := \left[I_3 + \Delta E_B^D \right] \cdot \underline{f}_{r,u}^B$$

Equation 3.5-1

The IMU case misalignment error is initialised from a zero-mean Gaussian distribution with a deviation of $({}_{IMU}\sigma_{MA})$. This error is common to both gyroscope and accelerometer triads and is computed in both sensor modules so that they can be activated in isolation.

3.5.3.2 Sensor Triad Non-Orthogonality Error

The orientation of each sensor axis with respect to the case results in a non-orthogonality error between sensors that is initialised from a zero-mean Gaussian distribution with a deviation of $({}_{AC}\sigma_{NO})$. If the expected error is the same for each axis,

$$\forall i \in \{ R , P , Y \} \Rightarrow \underline{f}_{r,u}^i := \left[I_3 + \Delta E_D^i \right] \cdot \left(M_B^i \cdot \underline{f}_{r,u}^D \right)$$

Equation 3.5-2

When selected values from symmetrical statistical distributions the sign of the rotations in the transform are irrelevant. Although the input axes are nominally aligned with Missile Body axes, the Hinge (output) and Pendulum axes can be selected to minimise acceleration sensitive drifts. The dominant g-sensitive biases are stimulated by accelerations along the Input and Pendulum axes.

The configurations shown in Figure 3-34 and Figure 3-35 contain 6 of the possible 12 sensor orientations (6 more are obtained by rotating each input axis through 180°). The negative signs in these figures indicate that the positive axis is in the opposite direction to that shown.

For each sensor, let the (X,Y,Z) Missile Body axes be aligned with the Input-Hinge-Pendulum (I,H,P) sensor axes such that a clockwise pendulum motion about the Hinge axis implies positive output and input accelerations. The configurations in Figure 3-34 and Figure 3-35 minimise torque due to missile lateral and longitudinal acceleration respectively. For the orientation shown in Figure 3-34 the mapping of the case inputs to the (I,H,P) axes for mechanical RPY accelerometers is the same as that for the gyroscopes in §3.4.3.2. For solid state devices that are insensitive to acceleration induced errors the mappings are simply the identity matrix.

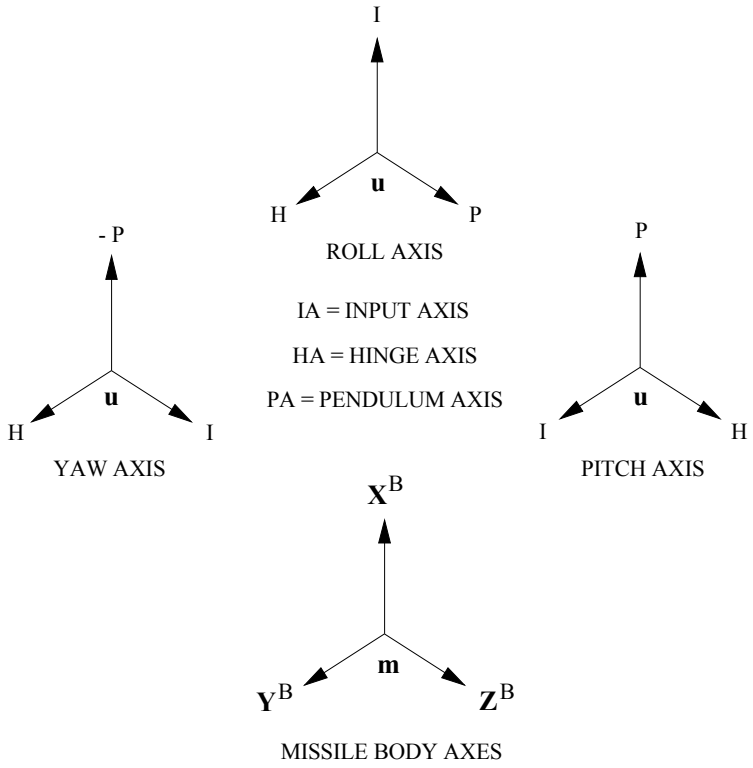

Figure 3-34 : Accelerometer Triad Orientation (Latax Tolerant)

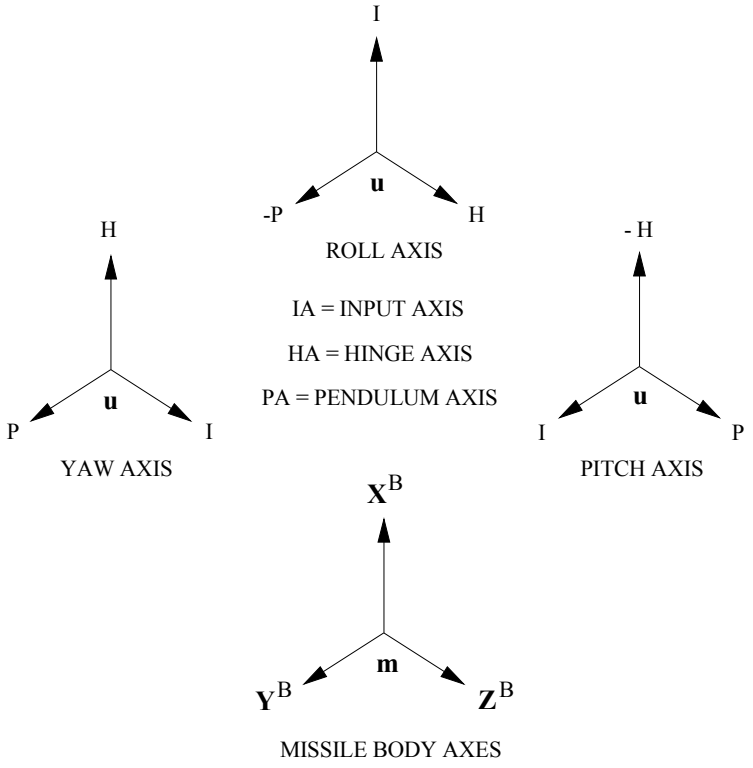

Figure 3-35 : Accelerometer Triad Orientation (Longax Tolerant)

3.5.3.3 Sensor Cross Coupling Error

Imperfect and finite bandwidth re-balancing of the pendulum causes misalignment of the Pendulum and Input axes. The angular displacement of the pendulum about the Hinge axis (γ) is kept as small as possible commensurate with pick-off scale factor. The specific acceleration experienced by each accelerometer is thus,

$$\forall\, i \in \{R, P, Y\} \;\Rightarrow\; \underline{f}^{i}_{r,u} := \begin{bmatrix} 1 & 0 & -\gamma_i \\ 0 & 1 & 0 \\ \gamma_i & 0 & 1 \end{bmatrix} \cdot \begin{pmatrix} f^{Ii}_{r,u} \\ f^{Hi}_{r,u} \\ f^{Pi}_{r,u} \end{pmatrix} + \begin{pmatrix} 0 \\ \dot{\gamma}_i \\ 0 \end{pmatrix}$$

Equation 3.5-3

The pendulum forcer is similar in principle to the gyroscope torquer, with typical PWM re-balancing loop bandwidths of 80-150 Hz and a damping of 0.6-0.8. The forcer can be reduced to the 2nd order lag with range limiting and quantisation described later. Applying a masking matrix [AXM] to deal with the different Hinge axis orientations, and relating the Hinge axis to individual sensor RPY axes,

$$\underline{f}^{U}_{r,u} := \begin{pmatrix} f^{XR}_{r,u} \\ f^{XP}_{r,u} \\ f^{XY}_{r,u} \end{pmatrix} - {}_{AC}\underline{\gamma} \otimes \left([\,AXM\,] \cdot \begin{bmatrix} f^{YR}_{r,u} & f^{XP}_{r,u} & f^{XY}_{r,u} \\ f^{ZR}_{r,u} & f^{ZP}_{r,u} & f^{YY}_{r,u} \end{bmatrix} \right)$$

Equation 3.5-4

$${}_{AC}\underline{\gamma} := \left({}_{AC}\gamma_R \;,\; {}_{AC}\gamma_P \;,\; {}_{AC}\gamma_Y \right)^T$$

Equation 3.5-5

For the configuration selected,

$$[\,AXM\,] := \begin{bmatrix} 0 & 1 \\ 1 & 0 \\ -1 & 0 \end{bmatrix}$$

Equation 3.5-6

The cross-coupling misalignment angle (γ) is determined from the 2nd order PWM dynamics activated by setting bit 3 of *MS_AC_ER*.

3.5.4 Measured Specific Acceleration and Velocity Increments

Ignoring biases caused by pendulum angular velocity and acceleration, Savage's model of a single axis mechanical accelerometer expressed in (I,H,P) axes reduces to,

$$\tilde{f}^{I}_{r,u} \coloneqq \varphi_{SF}\left(f^{I}_{r,u} + {}_{AC}B^{I} + \left(\frac{J_X - J_Y - J_Z}{m \cdot L_{CG}} \right) \cdot \omega^{I}_{C,B} \cdot \omega^{P}_{C,B} \right)$$

Equation 3.5-7

The product of the pendulum mass (m), and the moment arm from the hinge line to the mass centre (L_{CG}), is known as its pendulocity ($_{AC}P$). Relating the inertia of the pendulum assembly about the (I,H,P) axes when perfectly re-balanced to the inertia about a set of (X,Y,Z) axes attached to the pendulum itself,

$$\gamma = 0 \Rightarrow \begin{pmatrix} J_I & J_H & J_P \end{pmatrix} \coloneqq \begin{pmatrix} J_X & J_Y + m \cdot L^2_{CG} & J_Z \end{pmatrix}$$

Equation 3.5-8

The inertia about the Hinge axis (J_Y) applies to torques caused by angular acceleration about this axis. Angular acceleration induced errors can be minimising by careful design leaving only bias ($_{AC}B_{CB}$), aniso-inertial and scale factor errors. These errors are controlled by the bit pattern of *MS_AC_ER* listed in Table 3-12. Bits 22-23, reserved in Table 3-6 for ADC errors, are replaced by PWM errors. The anti-aliasing filter and quantised noise associated with the ADC that are controlled by bits 21 and 24, are not applicable.

Table 3-12 : Accelerometer Triad Errors

MS_AC_ER	Sensor Error Source	
17	Aniso-inertial bias	
18	G^2-dependent bias	
19	Digital compensation filter	
22	Pulse count range limit	
23	Pulse quantisation	

The specific acceleration is corrupted at the reference rate by a time delay and 2nd order dynamics,

$${}^{D}\underline{f}^{B}_{r,u} \coloneqq \underline{\varphi}_{TD}\left(\underline{\varphi}_{D2L}\left(\underline{f}^{U}_{r,u}, {}_{AC}\zeta_{D2L}, {}_{AC}\omega_{D2L} \right), {}_{AC}t_{TD} \right)$$

Equation 3.5-9

The output of the 2nd order dynamics determines the cross coupling error,

$${}_{AC}G_{PM} \cdot {}_{AC}\underline{\gamma} \coloneqq \underline{f}^{U}_{r,u} - \underline{\varphi}_{D2L}\left(\underline{f}^{U}_{r,u} \right)$$

Equation 3.5-10

Although a time delay is not included in the Savage and IEEE models delays exist in the forcer and internal digital processor. The dynamic output

is subject to a constant bias, random noise, acceleration sensitive biases ($_{AC}B_G$), and scale factor errors,

$$\underset{\sim}{f}^{A\,B}_{r,u} :=$$

$$\underline{\varphi}_{SF}\left({}^{D}\underline{f}^{B}_{r,u} + \underline{\varphi}_{CB}\left({}_{AC}\sigma_{CB} \right) + \underline{\varphi}_{RN}\left({}_{AC}\sigma_{RN} \right) + {}_{AC}\underline{B}_{\omega\omega} + {}_{AC}\underline{B}_{G} \right)$$

Equation 3.5-11

In pendulous accelerometers the constant bias is caused by pick-off offset and residual spring torque in the pivots about the hinge line. Noise is caused by rapidly fluctuating instabilities in the assembly and under-damped rectified inputs. Scale factor errors are restricted to the forcer electronics and variations in magnetic field strength due to thermal sensitivity. These are made as small as possible by designing a "stiff" system in which the pendulum rotation is minimised. Noise is often specified in (μg/√Hz) referenced to the sensor output rate. From §3.2.2.2,

$${}_{AC}\sigma_{RN} := \frac{10 \cdot \sqrt{{}_{AC}\Phi_{RN} \cdot {}_{AC}f_R}}{10^6 \cdot {}_{AC}f_O}$$

Equation 3.5-12

The following aniso-inertial bias model is provided,

$${}_{AC}\underline{B}_{\omega\omega} := \left(\left[AWM \right] \otimes \left[{}_{AW}B \right] \right) \cdot \underline{\omega}^{B}_{C,B} \cdot \left(\underline{\omega}^{B}_{C,B} \right)^{T}$$

Equation 3.5-13

As in the gyroscope model, modularity is improved by using the inertial angular rate and accelerations referenced to the Missile Body axes instead of sensor specific axes. The mask for the configuration selected is,

$$\left[AWM \right] := \begin{pmatrix} 0 & 0 & 1 \\ 1 & 0 & 0 \\ -1 & 0 & 0 \end{pmatrix}$$

Equation 3.5-14

$$\left[{}_{AW}B \right] := \begin{pmatrix} 0 & {}_{AW}B^{R}_{XY} & {}_{AW}B^{R}_{XZ} \\ {}_{AW}B^{P}_{YX} & 0 & {}_{AW}B^{P}_{YZ} \\ {}_{AW}B^{Y}_{ZX} & {}_{AW}B^{Y}_{ZY} & 0 \end{pmatrix}$$

Equation 3.5-15

The g^2-dependent biases are stimulated by accelerations acting along the (I,H,P) axes according to,

$$ {}_{AC}B^{I}_{G} \;:=\; B^{I}_{IP}\cdot f^{I}_{r,u}\cdot f^{P}_{r,u} + B^{I}_{IH}\cdot f^{I}_{r,u}\cdot f^{H}_{r,u} $$

Equation 3.5-16

G^2-dependent drift (aniso-elasticity) is caused by unequal compliance relative to the pivots of the pendulum float assembly, particularly loading along input and pendulum axes. All combinations of error terms are simulated with user specified mask [AAM] provided to obtain the required g^2-dependent biases. For the configuration selected,

$$ {}_{AC}\underline{B}_{G} \;:=\; \left(\left[\, AAM \,\right] \otimes \left[\, {}_{AA}B \,\right] \right) \cdot \underline{f}^{B}_{r,u} \cdot \left(\underline{f}^{B}_{r,u} \right)^{T} $$

Equation 3.5-17

$$ \left[\, AAM \,\right] \;:=\; \begin{pmatrix} 0 & 1 & 1 \\ 1 & 0 & 1 \\ -1 & 0 & 1 \end{pmatrix} $$

Equation 3.5-18

$$ \left[\, {}_{AA}B \,\right] \;:=\; \begin{pmatrix} 0 & {}_{AA}B^{R}_{XY} & {}_{AA}B^{R}_{XZ} \\ {}_{AA}B^{P}_{YX} & 0 & {}_{AA}B^{P}_{YZ} \\ {}_{AA}B^{Y}_{ZX} & {}_{AA}B^{Y}_{ZY} & 0 \end{pmatrix} $$

Equation 3.5-19

$$ {}_{AC}\underline{B}_{G} \;:=\; \begin{pmatrix} {}_{AW}B^{R}_{XZ}\cdot\omega^{XB}_{C,B}\cdot\omega^{ZB}_{C,B} + {}_{AA}B^{R}_{XY}\cdot f^{XB}_{r,u}\cdot f^{YB}_{r,u} + {}_{AA}B^{R}_{XZ}\cdot f^{XB}_{r,u}\cdot f^{ZB}_{r,u} \\ {}_{AW}B^{P}_{YX}\cdot\omega^{YB}_{C,B}\cdot\omega^{XB}_{C,B} + {}_{AA}B^{P}_{YX}\cdot f^{YB}_{r,u}\cdot f^{XB}_{r,u} + {}_{AA}B^{P}_{XZ}\cdot f^{YB}_{r,u}\cdot f^{ZB}_{r,u} \\ -{}_{AW}B^{Y}_{ZX}\cdot\omega^{ZB}_{C,B}\cdot\omega^{XB}_{C,B} - {}_{AA}B^{Y}_{ZX}\cdot f^{ZB}_{r,u}\cdot f^{XB}_{r,u} + {}_{AA}B^{Y}_{ZY}\cdot f^{ZB}_{r,u}\cdot f^{YB}_{r,u} \end{pmatrix} $$

Equation 3.5-20

If the errors are selected from zero-mean, symmetric distributions the negative terms in these equations are irrelevant. The measurements are then passed through compensating filters,

$$ {}_{800}\underline{\tilde{f}}^{B}_{r,u} \;:= $$

$$ \underline{\varphi}_{DLL}\left({}^{PWM}\underline{\varphi}_{Q}\left({}^{PWM}\underline{\varphi}_{LIM}\left({}^{A}\underline{\tilde{f}}^{B}_{r,u} \right), {}^{PWM}_{AC}Q \right), {}_{AC}\omega_{NC}, {}_{AC}\omega_{DC} \right) $$

Equation 3.5-21

The output range limit and the maximum number of pulses (${}_{AC}N_{MP}$) determine the quantisation level, e.g. for ± 400 (m/s^2)/s and 2^{12} pulses the quantisation is $400/2^{11} \approx 0.2$ m/s^2. Default values are set to compensation for the time delay and 2nd order dynamics,

$$\left({}_{AC}\omega_{NC} \quad , \quad {}_{AC}\omega_{DC} \right) := \left(\frac{{}_{AC}\omega_{2DL}}{2 \cdot {}_{AC}\zeta_{2DL} + {}_{AC}\omega_{2DL} \cdot {}_{AC}t_{TD}} \quad , \quad \frac{1}{{}_{AC}t_{TD}} \right)$$

Equation 3.5-22

Typical accelerometer errors used in aircraft (AC), long and short-range missiles (LRM) and (SRM) are given in Table 3-13. The selection of constant, scale factor and g-sensitive bias characteristics from Gaussian and bi-modal distributions introduced in §3.4.4 applies equally to accelerometers based on mechanical technology.

Table 3-13 : Accelerometer Error Characteristics

Error Characteristic	Alias	AC	LRM	SRM	Units
Case misalignment	${}_{AC}\sigma_{MA}$	0.1	0.3	3	mrad
Non-orthogonality	${}_{AC}\sigma_{NO}$	0.1	0.3	3	mrad
Constant bias	${}_{GS}\sigma_{CB}$	100	300	1000	μg
Gaussian noise	${}_{AC}\Phi_{RN}$	80	200	500	μg/√Hz
Constant scale factor error	${}_{AC}\sigma_{SC}$	100	200	500	ppm
Scale factor linearity	${}_{AC}\sigma_{SA}$	20	50	200	ppm
G^2-dependent drift	${}_{AC}\sigma_{GG}$	10	40	100	μg/g^2
Maximum pulse/output	${}_{AC}N_{MP}$	2^{24}	2^{20}	2^{16}	-
Forcer loop natural frequency	${}_{AC}\omega_{D2L}$	100			Hz
Forcer loop damping	${}_{AC}\zeta_{D2L}$	0.7			

The position (ΔP) and velocity (ΔV) errors induced by the constant bias and random noise are respectively,

$$E\left(\Delta V_{CB} \quad , \quad \Delta P_{CB} \right) := {}_{AC}\sigma_{CB} \cdot 10^{-5} \cdot \left(\Delta t \quad , \quad \Delta t^2 / 2 \right)$$

Equation 3.5-23

$$E\left(\Delta V_{RN} \quad , \quad \Delta P_{RN} \right) := {}_{AC}\Phi_{RN} \cdot 10^{-5} \cdot \left(\sqrt{\Delta t} \quad , \quad \sqrt{\Delta t^3 / 3} \right)$$

Equation 3.5-24

The specific acceleration at the output rate (f_O) of 400 Hz is the average value over the previous two sub-frames, as delays in accelerometer data tend to be less critical than gyroscope angular velocity.

$$ {}_{400}\underline{\tilde{f}}^{B}_{r,u} \coloneqq \frac{1}{2} \cdot \left({}_{800}\underline{\tilde{f}}^{B}_{r,u} + {}_{800}\underline{\tilde{f}}^{B}_{r,u}\left(t - \frac{1}{{}_{AC}f_R} \right) \right) $$

Equation 3.5-25

$$ {}_{400}\underline{\Delta\tilde{V}}^{B}_{r,u} \coloneqq {}_{400}\underline{\tilde{f}}^{B}_{r,u} \Big/ {}_{AC}f_O $$

Equation 3.5-26

For convenience the accelerometer outputs are collected together,

$$ \underline{\tilde{Z}} \equiv \begin{pmatrix} \underline{\tilde{Z}}_{AA} \\ \cdots \\ \underline{\tilde{Z}}_{AI} \end{pmatrix} \equiv \begin{pmatrix} {}_{400}\underline{\tilde{f}}^{B}_{r,u} \\ \cdots \\ {}_{400}\underline{\Delta\tilde{V}}^{B}_{r,u} \end{pmatrix} $$

Equation 3.5-27

3.5.5 Sensor Limitations

Provision of accelerometer measurements at the sensor output interface depends on:

- User measurement selection (*MS_MSAV1* bit 7-9 cleared)
- Forcer acceleration limiting (*MS_AC_ER* bit 22 is set)

When active, if any of these limitations are violated, bits 7-9 (RPY) in the measurement ready flag *MS_MSRY1* are cleared. Failure to provide measurements at the user's request is indicated by setting bits 1-3 of *MS_AC_VF*. If the acceleration limit is exceeded bits 4-6 of *MS_AC_VF* are set depending on which of the accelerometers is affected.

3.5.6 Output Interface

The acceleration and velocity increments pass through a signed 16 bit digital interface at a frequency ($_{AC}f_O$) of 400 Hz (clock 9). These measurements are subject to interface range limits of ± 1 m/s and ± 400 m/s^2 respectively, and a one-cycle transmission delay.

$$ {}_{AC}\underline{\tilde{Z}} \coloneqq {}^{IF}\underline{\varphi}_{TD}\left({}^{IF}\underline{\varphi}_{Q}\left({}^{IF}\underline{\varphi}_{LIM}\left({}^{IF}\underline{\varphi}_{ZOH}\left(\underline{\tilde{Z}} \right) \right) \right) \right) $$

Equation 3.5-28

3.6 Barometric Altimeter

Interest in barometers in the civil aviation community has been re-kindled as a result of the reduction the clearance height between aircraft in air corridors with a consequential impact on the military. The result has been a 10-fold improvement in sensor accuracy with high stability for use in these safety critical systems. Barometers are designed with a dynamic lag to damp out short term pressure fluctuations making them ideal for long term stabilisation of integrated accelerometer outputs in inertial navigation systems. Barometers are rarely used in long-range missiles due to location problems not experienced with radar altimeters and GPS receivers, whereas on aircraft location is less of a problem.

3.6.1 Description

Barometric altimeters and equivalent pressure transducers measure the static pressure above sea-level which is converted into geodetic height above the earth using standard atmospheric data.

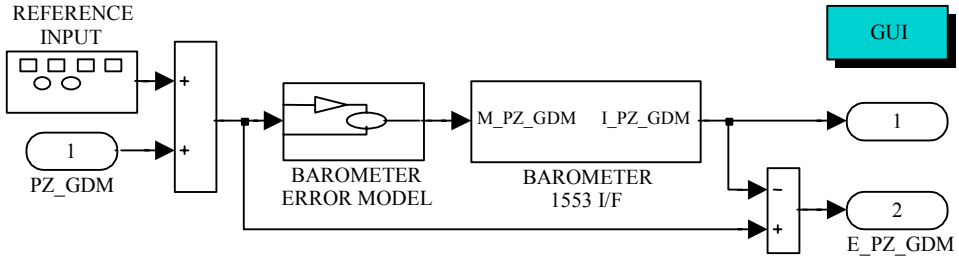

Figure 3-36 : Barometric Altimeter Model

In military aircraft any constant bias present in the barometer is usually calibrated out during their INS warm-up on the ground using a known reference height leaving only a residual error that is applied in the model shown in Figure 3-36.

3.6.2 Reference Barometric Altitude

The reference height of the missile above the earth's surface,

$$P_{d,m}^{ZG} := T_E^G \cdot \left(\underline{P}_m^E - \underline{P}_d^E \right) \bullet \hat{\underline{k}}^G$$

Equation 3.6-1

This data is provided at a reference frequency (${}_{BA}f_R$) of 400 Hz. The transform from the Earth frame to LGA, and the Earth radius at point (d) beneath the missile, are defined in §17.10 and §18.3 respectively.

3.6.3 Measured Barometric Altitude

The injection of independently selectable errors is controlled by the bit pattern of *MS_BA_ER*. The reference height is corrupted at the reference rate by a time delay, height rate limit and 1st order dynamics.

$$ {}^{D}\widetilde{P}^{ZG}_{d,m} \;:=\; \varphi_{D1L}\left(\varphi_{RL}\left(\varphi_{TD}\left(P^{ZG}_{d,m}\right)\right)\right) $$

Equation 3.6-2

A time delay is 0.01 s is followed by a height rate limit of 600 m/s and a 1st order lag with a bandwidth of 5 Hz. Constant bias, random noise and a random walk are then superimposed representing fluctuations in the local atmospheric pressure and distributed pressure fronts whose temporal correlation are a function of the missile's along-track speed.

$$ {}^{A}P^{ZG}_{d,m} \;:=\; \varphi_{SF}\left({}^{D}P^{ZG}_{d,m} + \varphi_{CB} + \varphi_{RN} + \varphi_{D1L}\left(N\left(0,5\right), \frac{2\cdot\pi\cdot \dot{P}^{hG}_{d,m}}{10^{4}} \right) \right) $$

Equation 3.6-3

The residual constant bias is initialised using a Gaussian distribution with a deviation of 3 m. The Gaussian noise has a PSD of 0.9 m^2/Hz at the reference frequency, equivalent to 3 m at 10 Hz. The random walk output deviation is 5 m with a distance between pressure fronts of 10 km. The constant, quadratic and asymmetric scale factor deviations are 0.03, 0.01 and 0.01 respectively.

$$ \widetilde{P}^{ZG}_{d,m} \;:=\; {}^{AD}\varphi_{LIM}\left({}^{AD}\varphi_{Q}\left({}^{AD}\varphi_{ZOH}\left(\varphi_{AA}\left({}^{A}\widetilde{P}^{ZG}_{d,m} \right) \right), {}_{BA}f_{O} \right) + {}^{AD}\varphi_{QN} \right) $$

Equation 3.6-4

These values are typical for nap-of-the-earth navigation. For aircraft subject to the latest civil separation distances, the scale factor errors are 100 times less in sensors manufactured by the likes of Honeywell. The analogue measurement is converted into digital form using a 10 Hz, 4th order Butterworth filter, and a 12 bit ADC subject to 3 bits of noise with a sampling rate and range matched to the output interface.

3.6.4 Sensor Limitations

The provision of barometer measurements at the output interface depends on:

- User measurement selection (*MS_MSAV1* bit 13 cleared)
- Height limiting (*MS_BA_ER* bit 15 is set)
- Height rate limiting (*MS_BA_ER* bit 16 is set)

When active, if any of these limitations are violated, measurement transmission is suspended and bit 13 in the measurement ready flag *MS_MSRY1* is cleared. Failure to provide a measurement at the user's request is indicated by setting bit 0 of *MS_BA_VF*. If the height, or height rate, limits of 500 m and 600 m/s are exceeded bits 1-2 of *MS_BA_VF* are set respectively.

3.6.5 Output Interface

The measured barometric (pressure) height passes through an unsigned 16 bit digital interface at a frequency ($_{BA}f_O$) of 20 Hz (clock 17). The measurement is subject to an interface range limit of 500 m and a one-cycle transmission delay.

$$ {}_{BA}\widetilde{P}^{ZG}_{d,m} := {}^{IF}\varphi_{TD}\left({}^{IF}\varphi_{Q}\left({}^{IF}\varphi_{LIM}\left({}^{IF}\varphi_{ZOH}\left(\widetilde{P}^{ZG}_{d,m} \right) \right) \right) \right) $$

Equation 3.6-5

3.7 Radar Altimeter

Radar altimeters measuring the height above the ground have become increasingly important in aircraft, cruise, and sea-skimming missiles operating at low level to evade defensive systems. Early continuous wave altimeter designs suffered from large scale factors and were limited to applications below 1 km. Pulsed altimeters could not processing very short pulses restricting their use to heights above 1 km. As electronics and signal processing techniques improved so these limitations were removed. Today both types of altimeter are available for applications ranging from nap-of-the-earth navigation to height keeping at the ceiling of military aircraft.

Their high measurement rate means the sea-state can be estimated thereby reducing the wave clearance height in sea-skimming missiles. For military aircraft their simplest function is as an all weather terrain avoidance system when low-level dog fighting. Since the mid-80s their greatest impact has been on integrated navigation systems:

- US Sandia Inertial Navigation System (SITAN)
- US Terrain Contour Matching (TERCOM)
- UK Terrain Profile Matching (TERPROM)

In these systems radar altimeter measurements are combined with digital map data to provide covert Terrain Reference Navigation (TRN) and Terrain Following (TF). When used on roll stabilised vehicles operating close to the earth the first return power usually comes from the geodetic vertical and can be used with the digital map height. The footprint is small and stealthy, particularly when reducing emissions using power scheduling. When manoeuvring, or over defended terrain, these sensors can be muted with little affect on the short-term navigation accuracy and as a result they have virtually replaced Doppler radar. The laser altimeter is the ultimate high frequency covert device but it requires more accurate geodetic levelling to constrain its narrow beam to the vicinity of the geodetic vertical. Using lasers the TRN algorithms must extract map heights, not at the current position, but at their estimated impact point on the ground, a more complex problem altogether.

Altimeters are still being developed and packaged into ever smaller volumes with antennas shaped to the curvature of missile body to improve airframe stealth characteristics. Low frequency (3-6 GHz) devices are preferred for TRN since they measure the mean distance to the ground. Higher frequency (16-20 GHz) devices are favoured for ground avoidance as they measure to the top of objects and were used to classify terrain type, i.e. urban, forest, etc. in a largely unsuccessful attempt to improve TRN performance.

3.7.1 Description

The altimeter model shown in Figure 3-37 provides measurements when the geodetic vertical lies within its RF beam half power points, and its height is

within prescribed limits. A "wide" beam sensor is modelled that can be characterised as either a continuous wave or a pulsed device whose first return represents the geodetic ground height. Digital LandMass Survey (DLMS) map data is used to obtain an estimate of the ground height. The true ground height is obtained by removing statistical map triangulation and interpolation height errors from the Digital Terrain Elevation Data (DTED). The reference height is the difference between the geodetic height above the earth's surface and the corrected map height.

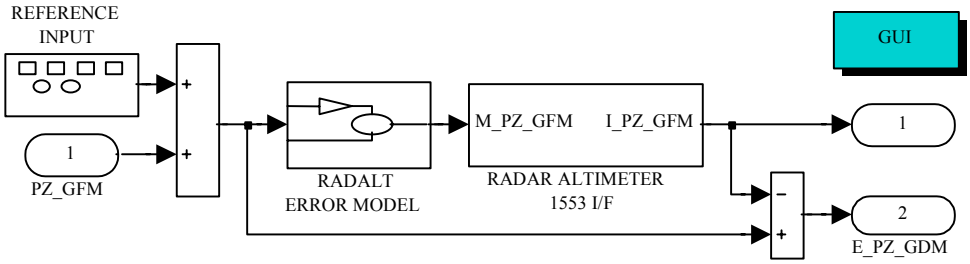

Figure 3-37 : Radar Altimeter Model

The radar altimeter model does not support narrow beam devices that require DLMS data at the point of ground impact. When the DTED is de-activated the geodetic height is referred to the WGS 84 ellipsoid and is thus comparable with barometric altimeter data.

3.7.2 Reference Height Above the Ground

Since the DTED contains map errors the reference ground height is,

$$P_{f,m}^{ZG} := T_E^G \cdot \left(\underline{P}_m^E - \underline{P}_d^E \right) \bullet \underline{\hat{k}}^G - \tilde{P}_{d,f}^{ZG} + \Delta P_{d,f}^{ZG}$$

Equation 3.7-1

This data is provided at a reference frequency ($_{RA}f_R$) of 400 Hz. The transform from the Earth to LGA frame, and the Earth radius at point (d) directly beneath the missile, are defined in §17.10 and §18.3 respectively. Assuming that the first energy returns represent the geodetic vertical,

$$P_{f,m}^{ZG} := P_{d,m}^{ZG} - \tilde{P}_{d,f}^{ZG} + \Delta P_{d,f}^{ZG}$$

Equation 3.7-2

The measured height of the ground below the missile along the geodetic vertical is obtained by 3rd order bi-cubic interpolation between a 4x4 ordinate height patch centred at the missile position, a process described in §22.6. Whilst transitions between map squares is free from discontinuities, the mapping and interpolation processes used in generating paper maps and their digitisation, result in four major errors:

- A zero mean Gaussian height error (ΔM_1) in metres

- A correlated height error (ΔM_2) in metres arising from individual hill shifts
- A correlated height error (ΔM_3) in m/rad due to East-West (E-W) map shifts arising from triangulation errors - terrain slope dependent
- A correlated height error (ΔM_4) in m/rad due to North-South (N-S) map shifts arising from triangulation errors - terrain slope dependent

Combining these errors and converting the gradients from m/rad to m/m,

$$\Delta P_{d,f}^{ZG} := \Delta M_1 + \Delta M_2 + \frac{\Delta M_3}{R_{p,d} \cdot \cos\lambda_d} \cdot \frac{\partial P_{d,f}^{ZG}}{\partial \mu_d} + \frac{\Delta M_4}{R_{md}} \cdot \frac{\partial P_{d,f}^{ZG}}{\partial \lambda_d}$$

Equation 3.7-3

The E-W and N-S earth curvatures (R_{pd} and R_{md} respectively) are defined in §18.3. The Gaussian noise due to digitisation and interpolation,

$$\Delta M_1 := N(0, 2)$$

Equation 3.7-4

The vertically correlated noise due to local hill shifting is modelled as a 20 m random walk whose temporal correlation is a function of the missile's along-track speed over 400 m.

$$\Delta M_2 := \varphi_{DL1}\left(N(0, 2), \frac{2 \cdot \pi \cdot \dot{P}_{d,m}^{hG}}{400} \right)$$

Equation 3.7-5

The E-W and N-S horizontal map shifts due to inaccuracies in locating the triangulation points used to align the paper maps are also modelled as random walks. The horizontal map shift is 20 m correlated over 10 km.

$$(\Delta M_3, \Delta M_4) := \underline{\varphi}_{DL1}\left(N(0, 20), \frac{2 \cdot \pi \cdot \dot{P}_{d,m}^{hG}}{10^4} \right)$$

Equation 3.7-6

The author has taken flight data over UK and German terrain, and using Kalman Filter parameter estimation techniques, extracted typical 1:5000 scale map errors. The process involved taking the difference between the INS/barometer mix and the radar altimeter output plus map heights along the aircraft track, Moody[M.11]. The results showed that the constants used in this simple map error model are functions of the rms ground slope ($\bar{g}_{RMS}$).

Taking ground slopes every 100 m over an along-track distance of,

$$\Delta P_{\bar{g}}^{hG} := 3000 \cdot \left(1 - 2 \cdot \bar{g}_{RMS} \right)$$

Equation 3.7-7

The random deviation (σ_{M1}) over flat ground was found to be 2 m to 3 m increasing with rms ground slope,

$$\sigma_{M1} := 3 + 23.5 \cdot \bar{g}_{RMS}$$

Equation 3.7-8

The vertically correlated noise (σ_{M2}) variation with rms ground slope,

$$\bar{g}_{RMS} < 0.02 \Rightarrow \sigma_{MV} := \left(273.8 - 6465 \cdot \bar{g}_{RMS} \right) \cdot \bar{g}_{RMS}$$

Equation 3.7-9

$$\bar{g}_{RMS} > 0.02 \Rightarrow \sigma_{MV} := 2.6 - 15.2 \cdot \bar{g}_{RMS}$$

Equation 3.7-10

The rms horizontal map shifts (σ_{M3}) were 13.7 m to 25.7 m. The results also showed that the nature of map-errors change from a 1st to a 2nd order Gauss-Markov process for ground slopes in excess of 10%.

3.7.3 Measured Height Above the Ground

The injection of errors is controlled by the bit pattern of *MS_RA_ER*. The reference height is corrupted at the reference rate by a time delay, height rate limit and 1st order dynamics,

$${}^{D}\tilde{P}_{f,m}^{ZG} := \varphi_{D1L}\left(\varphi_{RL}\left(\varphi_{TD}\left(P_{f,m}^{ZG} \right) \right) \right)$$

Equation 3.7-11

A time delay of 0.01 s is followed by a height rate limit of 300 m/s and a 1st order lag with a bandwidth of 50 Hz. For sea-skimming missiles the low pass filter bandwidth should be greater than twice the sea-wave encounter frequency for sea-state estimation for missile height keeping. Constant bias, random noise and a random walk are then superimposed.

$${}^{A}P_{f,m}^{ZG} := \varphi_{SF}\left({}^{D}P_{f,m}^{ZG} + \varphi_{CB} + \varphi_{RN} + \varphi_{MB1} \right)$$

Equation 3.7-12

The constant bias is small in solid state devices and is initialised using a Gaussian distribution with a deviation of 2 m. The Gaussian noise has a PSD of 0.45 m^2/Hz at the reference frequency, equivalent to 3 m at 20 Hz. The random walk deviation is 5 m with a correlation time of 500 s without

justification. The constant, quadratic and asymmetric scale factor deviations are 0.03, 0.01 and 0.01 respectively.

$$\widetilde{P}^{ZG}_{f,m} := {}^{AD}\underline{\varphi}_{LIM}\left({}^{AD}\underline{\varphi}_{Q}\left({}^{AD}\underline{\varphi}_{ZOH}\left(\underline{\varphi}_{AA}\left({}^{A}\widetilde{P}^{ZG}_{f,m} \right) \right), {}_{RA}f_{O} \right) + {}^{AD}\varphi_{QN} \right)$$

Equation 3.7-13

The analogue measurement is converted to digital form using a 40 Hz, 4th order Butterworth filter, and a 12 bit ADC subject to 3 bits of noise with a sampling rate and range matched to the output interface.

3.7.4 Sensor Limitations

The provision of altimeter measurements at the output interface depends on:

- User measurement selection (*MS_MSAV1* bit 15 cleared)
- Height limiting (*MS_RA_ER* bit 15 is set)
- Height rate limiting (*MS_RA_ER* bit 16 is set)
- Pitch and roll limiting (*MS_RA_ER* bit 17 is set)

When active, if any of these limitations are violated, bit 15 in the measurement ready flag *MS_MSRY1 is* cleared. Failure to provide a measurement at the user's request is indicated by setting bit 0 of *MS_RA_VF*. If the height, or height rate, limits of 200 m and 600 m/s are exceeded bits 1-2 of *MS_BA_VF* are set respectively. If either the missile roll or pitch angle deviate from the geodetic vertical by more than 20° bits 3-4 of *MS_BA_VF* are set respectively.

3.7.5 Output Interface

The measured height above the ground height passes through an unsigned 16 bit digital interface at a frequency (${}_{RA}f_{O}$) of 20 Hz (clock 17). The measurement is subject to an interface range limit of 200 m and a one-cycle transmission delay.

$${}_{RA}\widetilde{P}^{ZG}_{f,m} := {}^{IF}\varphi_{TD}\left({}^{IF}\varphi_{Q}\left({}^{IF}\varphi_{LIM}\left({}^{IF}\varphi_{ZOH}\left(\widetilde{P}^{ZG}_{f,m} \right) \right) \right) \right)$$

Equation 3.7-14

3.8 Radar

3.8.1 Description

The radar model in Figure 3-38 comprises an electro-mechanical gimbal arrangement pointing an electro-optical detector; a decomposition shown in Figure 3-39. For simplicity, the radar tracks the missile and a single target "simultaneously" forming separate beams along the predicted LOS to each object, whereas in reality the beams would be multiplexed.

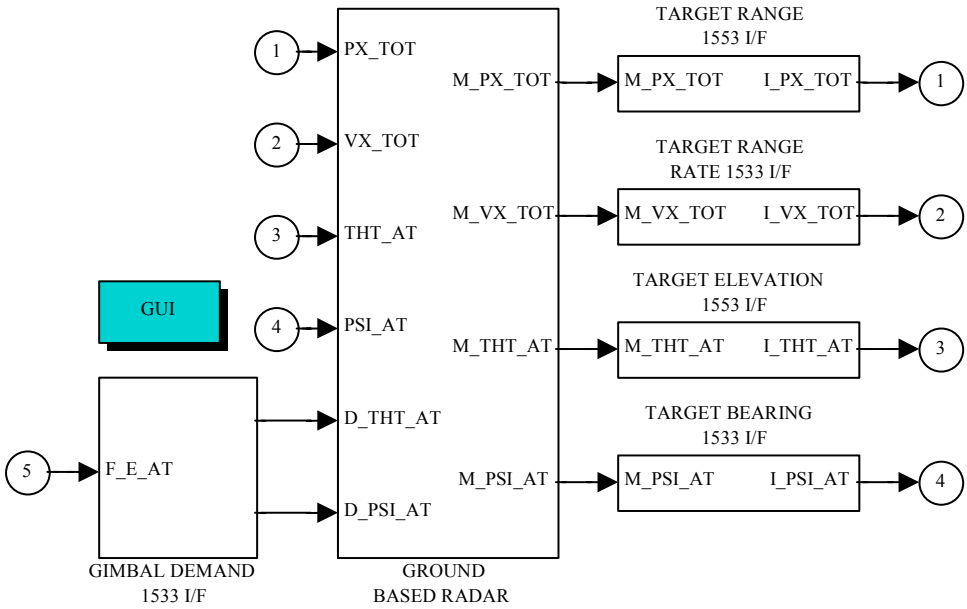

Figure 3-38 : Radar Model

The model has been characterised as a static phased array radar operating in the North Atlantic Treaty Organisation (NATO) F band. Surveillance prior to dedicated target tracking is ignored, however, the expected beam pointing error when switching modes is approximately 1/12 of the beam-width. For convenience, the detector reference point is located at point (o) the origin of the Alignment frame. It is with respect to this frame that the radar provides target and missile range, range rate, bearing and elevation measurements.

3.8.2 Gimbal Demands

The detector boresight initially points north and is elevated to 45° the missile and target beams formed with locked gimbals remaining within the maximum squint angle for the trajectories described in §2. If the gimbals are free, the radar uses low frequency (LF) gimbal demands at its output interface rate ($_{RD}f_O$) of 10 Hz (clock 18), from one of the following sources depending on the value of *GB_TR_DS*:

1 Reference angles

2 Radar detector outputs

3 Target state observer output

Steering commands are not down-linked from the missile state observer described in §5. With the gimbals locked the gimbal demands are treated as beam pointing commands with respect to the detector. When the gimbals are free to rotate the beams are formed along the detector boresight.

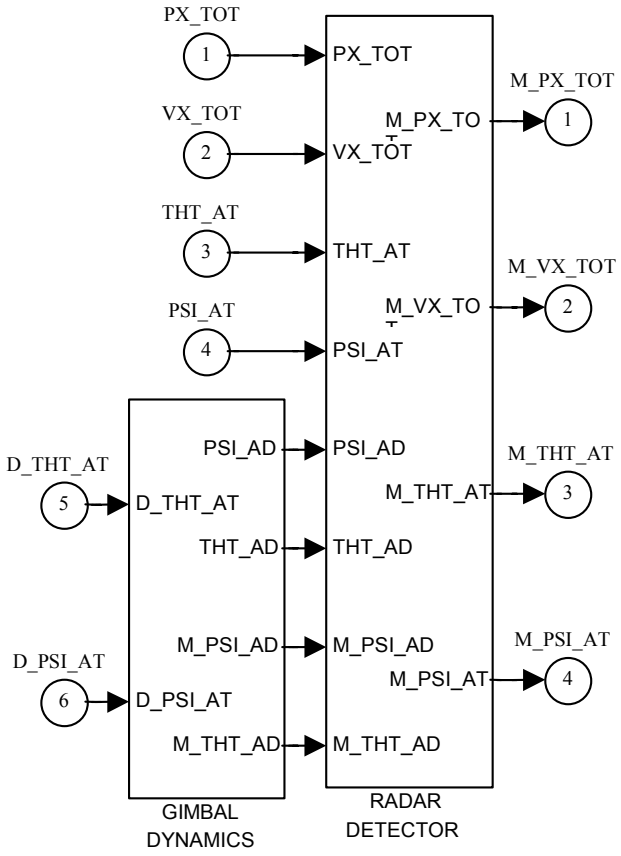

Figure 3-39 : Radar Model Decomposition

For convenience, the gimbal angles are collected together,

$$ {}_{RD}\underline{Z}_G \equiv \left(\Psi_A^{TD} , \Theta_A^{TD} \right)^T $$

Equation 3.8-1

Except when using the detector outputs, the YP gimbal demands pass through a signed 16 bit digital interface where they are subject to range limits of ± 180° and ± 90° respectively, and a one-cycle transmission delay,

$$ {}_{10}^{D}\underline{Z}_G := {}^{IF}\underline{\varphi}_{TD}\left({}^{IF}\underline{\varphi}_{Q}\left({}^{IF}\underline{\varphi}_{LIM}\left({}^{IF}\underline{\varphi}_{ZOH}\left({}_{RD}^{D}\underline{Z}_G , {}_{RD}f_O \right) \right) \right) \right) $$

Equation 3.8-2

Gimbal demand interface errors are activated using the same bits as the radar output interface - bits 27-30 of *GB_RD_ER* listed in Table 3-6. These

LF demands are processed using weave-tuned αβγ filters providing a smooth input to the gimbal dynamics at 100 Hz. A weave tuned αβγ filter is used with a bandwidth (ω_{DB}) of 2 Hz and the weave frequency (ω_{DW}) set to zero, reducing it to a normal αβγ filter. Its output provides target angular velocity and acceleration estimates that can be used for CLOS guidance. The high frequency (HF) demands pass through a phase compensation filter prior to digital to analogue conversion,

$$ {}^{D}_{100}\underline{Z}_{G} := $$

$$ \underline{\varphi}_{DAC}\left(\underline{\varphi}_{DDL}\left({}^{WT}\underline{\varphi}_{\alpha\beta\delta}\left({}^{D}_{10}\underline{Z}_{G} + \underline{N}\left(0, {}_{RD}\sigma_{GA}\right), {}_{RD}\omega_{DB}, {}_{RD}\omega_{DW}\right), {}_{RD}\omega_{NC}, {}_{RD}\omega_{DC}\right)\right) $$

Equation 3.8-3

($_{RD}\sigma_{GA}$) is the physical misalignment of the radar with respect to the Alignment frame. This misalignment is constant and initialised using a zero-mean Gaussian error with a deviation of 3mrad. The compensation filter characteristics are matched to the phase loss due to the time delay and 2nd order actuator dynamics that follow,

$$ \left({}_{RD}\omega_{NC}, {}_{RD}\omega_{DC}\right) := \left(\frac{1}{2\cdot {}_{RD}\zeta_{C}\cdot {}_{RD}\omega_{C} + {}_{RD}t_{C}}, \frac{1}{{}_{RD}t_{C}}\right) $$

Equation 3.8-4

$$ \left({}_{RD}\zeta_{C}, {}_{RD}\omega_{C}, {}_{RD}t_{C}\right) := \left({}_{RD}\zeta_{D2L}, {}_{RD}\omega_{D2L}, {}_{RD}t_{TD}\right) $$

Equation 3.8-5

Table 3-14 : Gimbal Demand Processing Errors

GB_RD_ER	Gimbal Errors	
11	Gimbal demand weave filtering	
12	Gimbal demand slew rate limiting	
13	Gimbal demand control filtering	
14	Weave frequency estimate	

The HF demands are converted to analogue using a 12 bit ADC subject to 3 bits of noise with a sampling rate and range matched to the input interface. The injection of gimbal errors is controlled by the bit pattern of *GB_RD_ER* according to Table 3-6. ADC errors are controlled by bits 21-24 the same as the DAC, the bit controlling the A/A filter being redundant. The additional gimbal demand processing errors are activated using the spare bits in *GB_RD_ER* listed in Table 3-14.

3.8.3 Gimbal Pick-Off Measurements

The large inertia of the radar compared to missile seekers means that the gimbal controllers, motors and pick-off dynamics can be simplified. The resulting open loop model operates at a reference frequency ($_{RD}f_R$) of 400 Hz. The gimbal angles are corrupted at this rate by a time delay of 10 msec, a motor rate limit of 40°/s, and 2nd order dynamics with a damping ratio (ζ_G) of 0.7 and a natural frequency (ω_G) of 6 Hz,

$$ {}^{A}\tilde{\underline{Z}}_G := \underline{\varphi}_{SF}\left(\underline{\varphi}_{D2L}\left(\underline{\varphi}_{RL}\left(\underline{\varphi}_{TD}\left({}^{D}_{100}\tilde{\underline{Z}}_G , {}_{RD}t_D \right) \right) , {}_{RD}\zeta_{D2L} , {}_{RD}\omega_{D2L} \right) + {}_{RD}\underline{\varphi}_{RN} \right) $$

Equation 3.8-6

This output is corrupted by Gaussian noise with a PSD of 2.25×10^{-6} rad^2/s at the reference frequency, equivalent to 3 mrad at 100 Hz, and constant, quadratic and asymmetric scale factors of 0.003, 0.001 and 0.001 respectively.

$$ {}^{D}\tilde{\underline{Z}}_G := {}^{AD}\underline{\varphi}_{LIM}\left({}^{AD}\underline{\varphi}_{Q}\left({}^{AD}\underline{\varphi}_{ZOH}\left(\underline{\varphi}_{AA}\left({}^{A}\tilde{\underline{Z}}_G \right) \right) , {}_{FN}f_{DP} \right) + {}^{AD}\varphi_{QN} \right) $$

Equation 3.8-7

The analogue measurements are converted into digital form using a 20 Hz, 4th order Butterworth filter, and a 12 bit ADC subject to 3 bits of noise with a sampling rate and range matched to the 100 Hz DAC processing. When the gimbals are locked the time delay and pickoff errors represent electronic beam steering inaccuracies; the rest of the gimbal errors must be disabled.

3.8.4 Reference Radar Detector Inputs

The reference range, range rate, bearing and elevation of the target and missile with respect to the true position of the antennae boresight are updated at the output rate ($_{RD}f_O$) of 10 Hz,

$$ \left(P_{o,t} , P_{o,m} \right) := \left(\sqrt{\underline{P}_t^A \bullet \underline{P}_t^A} , \sqrt{\underline{P}_m^A \bullet \underline{P}_m^A} \right) $$

Equation 3.8-8

$$\left(\dot{P}_t^{XT} \quad , \quad \dot{P}_m^{XT} \right) := \left(\frac{\underline{P}_t^A \bullet \underline{\dot{P}}_t^A}{P_{o,t}} \quad , \quad \frac{\underline{P}_m^A \bullet \underline{\dot{P}}_m^A}{P_{o,m}} \right)$$

Equation 3.8-9

$$\begin{pmatrix} \Psi_{TD}^T \\ \cdots \\ \Psi_{TD}^M \end{pmatrix} := \begin{pmatrix} \tan^{-1}\left(P_t^{YA} / P_t^{XA} \right) \\ \cdots \\ \tan^{-1}\left(P_m^{YA} / P_m^{XA} \right) \end{pmatrix} - \Psi_A^{TD}$$

Equation 3.8-10

$$\begin{pmatrix} \Theta_{TD}^T \\ \cdots \\ \Theta_{TD}^M \end{pmatrix} := \begin{pmatrix} -\tan^{-1}\left(P_t^{ZA} / P_t^{hA} \right) \\ \cdots \\ -\tan^{-1}\left(P_t^{ZA} / P_t^{hA} \right) \end{pmatrix} - \Theta_A^{TD}$$

Equation 3.8-11

3.8.5 Radar Measurements

The target and missile detector measurements are combined with gimbal pick-off outputs to produce the radar measurements,

$$\underline{Z} \equiv \begin{pmatrix} \underline{Z}_T \\ \cdots \\ \underline{Z}_M \end{pmatrix} \equiv \begin{pmatrix} \left(P_{o,t} \quad , \quad \dot{P}_{o,t}^{XT} \quad , \quad \Psi_A^T \quad , \quad \Theta_A^T \right)^T \\ \cdots \\ \left(P_{o,m} \quad , \quad \dot{P}_{o,m}^{XT} \quad , \quad \Psi_A^M \quad , \quad \Theta_A^M \right)^T \end{pmatrix}$$

Equation 3.8-12

The detector measurements are subject to the errors listed in Table 3-15 whose inclusion depends on the bit pattern of *GB_TR_ER*.

Table 3-15 : Radar Detector Error Model Switching

GB_TR_ER	Detector Measurement Errors	
1	Borden and Mumford glint error	
2	SNR dependent Gaussian noise	
3	Uncorrelated Gaussian noise	
4	Correlated Gaussian noise	

3.8.5.1 Range

Range is corrupted by random errors taken from a zero-mean Gaussian distribution assuming that Gabor's theorem applies for matched filter reception (the product of the receiver bandwidth and pulse-width is 1).

$$\tilde{P}_{o,t} := P_{o,t} + N\left(0, \frac{c \cdot {}_{RD}t_{CP}}{\sqrt{8 \cdot {}_{RD}SN_T}}\right)$$

Equation 3.8-13

$$\tilde{P}_{o,m} := P_{o,m} + N\left(0, \frac{c \cdot {}_{RD}t_{CP}}{\sqrt{8 \cdot {}_{RD}SN_M}}\right)$$

Equation 3.8-14

The compressed pulse width (${}_{RD}t_{CP}$) is a range dependent function modelled as a linear function in which the slope is determined by the maximum range (${}_{RD}R_{MAX}$) commensurate with the detector output interface,

$${}_{RD}t_{CP} := \left(10 + 30 \cdot \left(\frac{P_{o,t}}{{}_{RG}R_{MAX}}\right)\right) \cdot 10^{-6}$$

Equation 3.8-15

3.8.5.2 Range Rate

Range-rate measurements are corrupted by zero-mean Gaussian noise that is a function of the transmission frequency (λ_T) and the Signal-to-Noise Ratio (SNR) (${}_{RD}SN$).

$$\tilde{\dot{P}}_t^{XT} := \dot{P}_t^{XT} + N\left(0, \frac{{}_{RD}\lambda_T}{{}_{RD}t_O \cdot \sqrt{8 \cdot {}_{RD}SN_T}}\right)$$

Equation 3.8-16

$$\tilde{\dot{P}}_m^{XM} := \dot{P}_m^{XM} + N\left(0, \frac{{}_{RD}\lambda_T}{{}_{RD}t_O \cdot \sqrt{8 \cdot {}_{RD}SN_M}}\right)$$

Equation 3.8-17

The radar illuminates a target long enough to coherently process a number of pulse returns which reduces eclipsing losses and measurement noise associated with a single pulse. This is the observation, or dwell time (${}_{RD}t_O$), which is a function of the measured target range and squint angle,

$${}_{RD}t_O := 0.002 + 2\,x10^{-6} \cdot \hat{P}_{o,t} + \left(0.002 + 5\,x10^{-6} \cdot \hat{P}_{o,t}\right) \cdot \frac{\hat{\xi}_{TD}^{T}}{\pi}$$

Equation 3.8-18

3.8.5.3 Bearing and Elevation

The target and missile angles with respect to the Alignment frame are the sum of the detector orientation and the position of the target with respect to the detector boresight,

$$\left(\widetilde{\Psi}_A^T \;,\; \widetilde{\Theta}_A^T \;,\; \widetilde{\Psi}_A^M \;,\; \widetilde{\Theta}_A^M \right) :=$$

$$\left(\widetilde{\Psi}_A^{TD} + \widetilde{\Psi}_{TD}^T \;,\; \widetilde{\Theta}_A^{TD} + \widetilde{\Theta}_{TD}^T \;,\; \widetilde{\Psi}_A^{TD} + \widetilde{\Psi}_{TD}^M \;,\; \widetilde{\Theta}_A^{TD} + \widetilde{\Theta}_{TD}^M \right)$$

Equation 3.8-19

The beam shape is circular and defined by its half power points ($_{RD}\xi_{BW}$) at ±2° about the beam centre.

$$\begin{pmatrix} \widetilde{\Psi}_{TD}^T \\ \cdots \\ \widetilde{\Psi}_{TD}^M \end{pmatrix} := \begin{pmatrix} \widetilde{\Psi}_{TD}^T + N\left(0 , \frac{{}_{RD}\xi_{BW}}{\sqrt{2 \cdot {}_{RD}SN_T}} \right) + {}_{RD}\Psi_{CN} + {}_{RD}\Psi_{RNT} + {}_{RD}\Psi_G \\ \cdots \\ \widetilde{\Psi}_{TD}^M + N\left(0 , \frac{{}_{RD}\xi_{BW}}{\sqrt{2 \cdot {}_{RD}SN_M}} \right) + {}_{RD}\Psi_{CN} + {}_{RD}\Psi_{RNM} \end{pmatrix}$$

Equation 3.8-20

$$\begin{pmatrix} \widetilde{\Theta}_{TD}^T \\ \cdots \\ \widetilde{\Theta}_{TD}^M \end{pmatrix} := \begin{pmatrix} \widetilde{\Theta}_{TD}^T + N\left(0 , \frac{{}_{RD}\xi_{BW}}{\sqrt{2 \cdot {}_{RD}SN_T}} \right) + {}_{RD}\Theta_{CN} + {}_{RD}\Theta_{RNT} + {}_{RD}\Theta_G \\ \cdots \\ \widetilde{\Theta}_{TD}^M + N\left(0 , \frac{{}_{RD}\xi_{BW}}{\sqrt{2 \cdot {}_{RD}SN_M}} \right) + {}_{RD}\Theta_{CN} + {}_{RD}\Theta_{RNM} \end{pmatrix}$$

Equation 3.8-21

The angular errors comprise:

- Zero-mean Gaussian noise dependent on beam-width ($_{RD}\xi_{BW}$) and the SNRs ($_{RD}SN_T$,$_{RD}SN_M$) for the target and the missile.
- Correlated, zero-mean Gaussian noise (Ψ_{CN},Θ_{CN}) with a deviation of 3 mrad, representing planar array vibration common to both target and missile measurements.
- Un-correlated, zero-mean Gaussian noise (Ψ_{RNT},Θ_{RNM}) with a deviation of 3 mrad that is different for the target and missile measurements representing processing and electronic effects.
- Glint errors ($_{RD}\Psi_G$,$_{RD}\Theta_G$) defined in §3.8.7 that effect only the target measurements as it is assumed that the missile is fitted with a transponder.

3.8.6 Radar Equation and Signal-to-Noise Ratios

The SNR is derived from the Radar Equation that appears in many radar texts, Barton[B.10]. The prefix identifying the parameters as those from the radar "RD" is ignored in the derivation of the SNR with respect to the target. The signal strength for an isotropic reflector and a perfect receiving antenna (S) is the product of the reflected power density at the receiver (I_R) and its effective receiver aperture (A_E).

$$S := I_R \cdot A_E$$

Equation 3.8-22

The receiver aperture depends on the receiver gain (G_R), the average gain over the angle illuminated by the target's motion during the observation time, and (λ_t) the transmission wavelength. Assuming reciprocity,

$$A_E := \frac{G_R \cdot \lambda_T^2}{4 \cdot \pi}$$

Equation 3.8-23

If (P_T) represents the maximum power in a single pulse from the transmitting antenna, (G_T) its average gain, the power density at the target,

$$I_S := \frac{P_T \cdot G_T}{4 \cdot \pi \cdot P_{o,t}^2}$$

Equation 3.8-24

The effective radiating area of the target is often referred to as its Radar Cross Section (RCS) (σ_{RCS}). Typical values of RCS are subjective depending not only on physical size, but shape and materials for stealth - the following list is merely a guide:

- Missile 10^{-2} to 10^{1}
- Fighter aircraft 10^{-1} to 10^{2}
- Bombers and transports 10^{0} to 10^{3}
- Armoured vehicles 10^{1} to 10^{2}
- Small ships 10^{2} to 10^{4}
- Large ships 10^{2} to 10^{6}

A default RCS of 1 has been selected. Combining terms, the signal power collected by the receiving antenna from an isotropic reflector using the same antenna for transmission and reception with a common gain (G),

$$S := \frac{I_S \cdot \sigma_{RCS}}{4 \cdot \pi \cdot P_{o,t}^2} := \frac{P_T \cdot G^2 \cdot \lambda_T^2 \cdot \sigma_{RCS}}{(4 \cdot \pi)^3 \cdot P_{o,t}^4}$$

Equation 3.8-25

For a circular Gaussian radiation pattern the directive gain is a function of the antenna beam width and the antenna efficiency (λ_E),

$$G := \lambda_E \cdot \pi^2 \,/\, \xi_{BW}^2$$

Equation 3.8-26

The noise power (N) available for a single pulse at the perfect receiving antenna measured in (W/Hz),

$$N := k_B \cdot T_S \,/\, t_P$$

Equation 3.8-27

(k_B) is Boltzmann's constant, and (t_P) the uncompressed transmitted pulse length which is a piecewise constant function of target range, a typical approximation being,

$$t_P := 0.0027 \cdot P_{o,t}^{XT} \left| \begin{matrix} 1 \times 10^{-4} \\ 1 \times 10^{-6} \end{matrix} \right.$$

Equation 3.8-28

The system noise temperature (T_S) is the sum of,

$$T_S = T_A + T_R + L_R \cdot T_E$$

Equation 3.8-29

(T_A) is the antenna noise comprising atmospheric and ground components,

$$T_A := \frac{9 \cdot T_{TS} + T_O}{10 \cdot L_O} + \frac{T_O}{1 + L_O}$$

Equation 3.8-30

(L_O) is the antenna ohmic loss factor, and (T_O) the ground temperature. The sky noise temperature (T_{TS}) is a function of beam elevation with respect to the Alignment frame.

$$\left| \Theta_A^{TB} \right| < \frac{30 \cdot \pi}{180} \Rightarrow T_{TS} := 9.3433 + 0.03715 \cdot \left| \Theta_A^{TB} \right|$$

Equation 3.8-31

$$\left| \Theta_A^{TB} \right| \geq \frac{30 \cdot \pi}{180} \Rightarrow$$

$$T_{TS} := 2.54687 - 0.45388 \cdot T_1 + 0.16024 \cdot T_2 - 0.09488 \cdot T_3 - 0.03043 \cdot T_4$$

Equation 3.8-32

Above 30° the a 4th order Chebyshev polynomial of the 1st kind is used whose coefficients (T_*) are a function of the normalised elevation angle,

$$\overline{\Theta}_A^{TB} := \frac{1}{15} \cdot \left| \Theta_A^{TB} \right| - 1$$

Equation 3.8-33

These equations are used for the missile with the appropriate beam elevation angle. The transmission line noise (T_R) from the antenna to the receiver,

$$T_R := T_O \cdot \left(L_R - 1 \right)$$

Equation 3.8-34

The receiver electronic noise is a function of the receiver noise factor (L_{RN}),

$$T_E := T_O \cdot \left(L_{RN} - 1 \right)$$

Equation 3.8-35

Combining and inserting typical numerical values, the noise temperature is,

$$T_S := 746 + 0.85 \cdot T_{TS}$$

Equation 3.8-36

The target SNR at the receiver of a perfect antenna for a single pulse is,

$$SN_P := \frac{P_T \cdot G^2 \cdot t_P \cdot \lambda_T^2 \cdot \sigma_{RCS}}{\left(4 \cdot \pi \right)^3 \cdot k_B \cdot T_S \cdot P_{o,t}^4}$$

Equation 3.8-37

The radar transmits (n_P) pulses during the observation time, the number depending mainly on target range and squint angle. For relatively short ranges, below 20-30 km, the number of pulses is independent of range,

$$n_P := \text{int}\left(20 + 0.7 \cdot \xi_{TD}^{TB} \right)$$

Equation 3.8-38

For coherently integrated pulses by a perfect receiver,

$$SN_T := \frac{P_T \cdot n_P \cdot t_P \cdot \lambda_T^2 \cdot \sigma_{RCS} \cdot \lambda_A \cdot \pi}{64 \cdot k_B \cdot T_S \cdot P_{o,t}^4 \cdot \xi_{BW}^4}$$

Equation 3.8-39

A number of loss factors must be taken into account that reduce the SNR and hence radar measurement accuracy. Lumping these losses together into a total loss factor (L_F),

$$SN_T := \frac{P_T \cdot n_P \cdot t_P \cdot \lambda_T^2 \cdot \sigma_{RCS} \cdot \lambda_A \cdot \pi}{64 \cdot k_B \cdot T_S \cdot L_F \cdot P_{o,t}^4 \cdot \xi_{BW}^4}$$

Equation 3.8-40

When the missile carries a transponder transmission losses are one-way and the SNR must be modified to account for the transponder power, gain and pulse length,

$$SN_M := \frac{P_{TR} \cdot G_{TR} \cdot n_P \cdot t_{TP} \cdot \lambda_T^2}{16 \cdot k_B \cdot T_S \cdot L_F \cdot P_{o,m}^2 \cdot \xi_{BW}^2}$$

Equation 3.8-41

A comprehensive description of the effect of the SNR for Over-the-Horizon radar studies is provided by Weiner[W.6]. A phased array radar switches the beam direction faster and it is easier to control dwell time thereby increasing the SNR, target detection probability and measurement accuracy, compared with say a mechanically rotated track-whilst-scan radar. The total loss factor is typically 10-12 dB and comprises,

$$L_F := L_A^2 \cdot L_S^2 \cdot L_B \cdot L_M$$

Equation 3.8-42

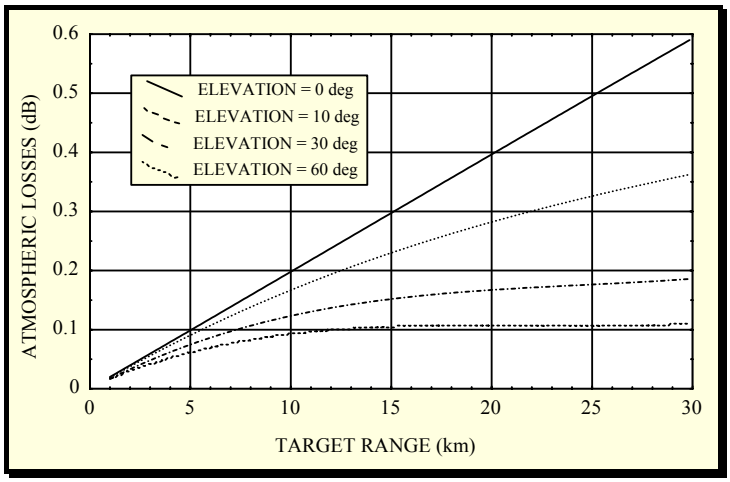

Figure 3-40 : Atmospheric Loss vs Range

This comprises from left to right, atmospheric, squint, beam broadening, and miscellaneous losses. For the missile, taking into account those losses which are applicable only in the receiving direction,

$$L_F := L_A \cdot L_S \cdot L_B \cdot L_M$$

Equation 3.8-43

The receiver, noise factor and ohmic losses have already been accounted for in the receiver noise temperature. The one-way clear air atmospheric transmission loss in dB for ranges of up to 30 km, and elevation angles [0°,60°] is shown in Figure 3-40. If the range or elevation exceed these limits the bounds are applied. The atmospheric losses are modelled using a B-spline surface fit the spline coefficients (C_{ij}) for which are listed in Table 3-16.

$$L_a := C_{ij} \cdot M_i\left(P_{o,t}\right) \cdot N_j\left(\Theta_A^{TB}\right)$$

Equation 3.8-44

Table 3-16 : Spline Coefficients and Knots for Atmospheric Loss (L_a)

$\lambda_i := \left((1\_000)_{1x4} \quad 12\_000 \quad (60\_000)_{1x4}\right)$			$\mu_j := \left((0)_{1x4} \quad 20 \quad (60)_{1x4}\right)$		
C(1,1)	0.020137	C(2,4)	0.081786	C(4,2)	0.461584
C(1,2)	0.019144	C(2,5)	0.080725	C(4,3)	0.103283
C(1,3)	0.015621	C(3,1)	0.484391	C(4,4)	0.124817
C(1,4)	0.017414	C(3,2)	0.419847	C(4,5)	0.098113
C(1,5)	0.016732	C(3,3)	0.201075	C(5,1)	1.150142
C(2,1)	0.091582	C(3,4)	0.162224	C(5,2)	0.461883
C(2,2)	0.091696	C(3,5)	0.131589	C(5,3)	0.137247
C(2,3)	0.094576	C(4,1)	0.870763	C(5,4)	0.133738
				C(5,5)	0.112892

The beam widens as the target moves off the detector boresight resulting in a squint loss that depends on the cosine of the off-boresight angle,

$$L_S := \sec \xi_{TD}^{TB}$$

Equation 3.8-45

Beam broadening losses depend on the angle from the beam to target LOS,

$$L_B := 6 \cdot \left(\left(\frac{\Theta_{TB}^T}{\xi_{BW} \cdot \sec \Theta_{TB}^T} \right)^2 + \left(\frac{\Psi_{TB}^T}{\xi_{BW} \cdot \sec \Psi_{TB}^T} \right)^2 \right)$$

Equation 3.8-46

3.8.7 Glint Errors

To the radar a target, far from being a point in space, appears as a set of multiple reflectors which regularly change their intensity and orientation. When these reflections are combined at the receiver the result is highly complex and can result in measurements at a point beyond the target's physical shape. Frequency agility is often employed in modern radar designs to eliminate the effects of glint. Glint errors are de-correlated by changing the transmission frequency between measurements by at least ($0.5c/l_T$) Hz, where ($\underline{l}_t$) is the physical size of the target and (c) is the speed of light. The glint error spectrum is thus broadened to the extent that the angular glint errors may be obtained from a Gaussian distribution,

$$\left(\Psi_G \quad , \quad \Theta_G \right) :=$$

$$\left(N\left(0 , \frac{\underline{l}_t^T \bullet \hat{\underline{j}}}{4 \cdot P_{o,t} \cdot \sqrt{3 \cdot N_F}} \right) \quad , \quad N\left(0 , \frac{\underline{l}_t^T \bullet \hat{\underline{k}}}{4 \cdot P_{o,t} \cdot \sqrt{3 \cdot N_F}} \right) \right)$$

Equation 3.8-47

The error is a function of target range, and the number of frequencies used by the radar during the dwell time (N_F). The target dimensions when viewed in a plane normal to the target LOS are,

$$\underline{l}_t^T := T_A^T \cdot T_{TV}^A \cdot \left(l_t^{XTV} \quad 0 \quad 0 \right)^T$$

Equation 3.8-48

Glint errors are often modelled as a 1st order Gauss-Markov process with a LF bandwidth representing bright spot wander. Nesline[N.7] uses this glint model with a 3 m output, and a 2 Hz bandwidth. The errors produced by this simple model are a poor representation of true glint effects and usually lead to optimistic results, particularly if the state observer includes error states with these dynamics. Borden[B.11] developed a statistical model that is a better representation of glint, the errors taken from a more realistic long-tailed, Student-t distribution. In Figure 3-42 the Borden glint model is compared with a normal distribution. Deviation from the straight line indicates non-Gaussian statistical outliers. The model represents an infinite number of reflectors in a line that is adequate for targets turning slowly through small angles between observations. One of the criticisms of this model is that it leads to pessimistic results since target tend to have a limited number of highly reflective points. It provide range and doppler glint which are ignored. The normalised glint and RCS errors (ξ_G,σ_{RCS}) are related to the transmission frequency ($_{RD}f_T$) of 4 GHz through the wave number,

$$_{RD}k_{WN} := 2 \cdot \pi \cdot {}_{RD}f_T / c$$

Equation 3.8-49

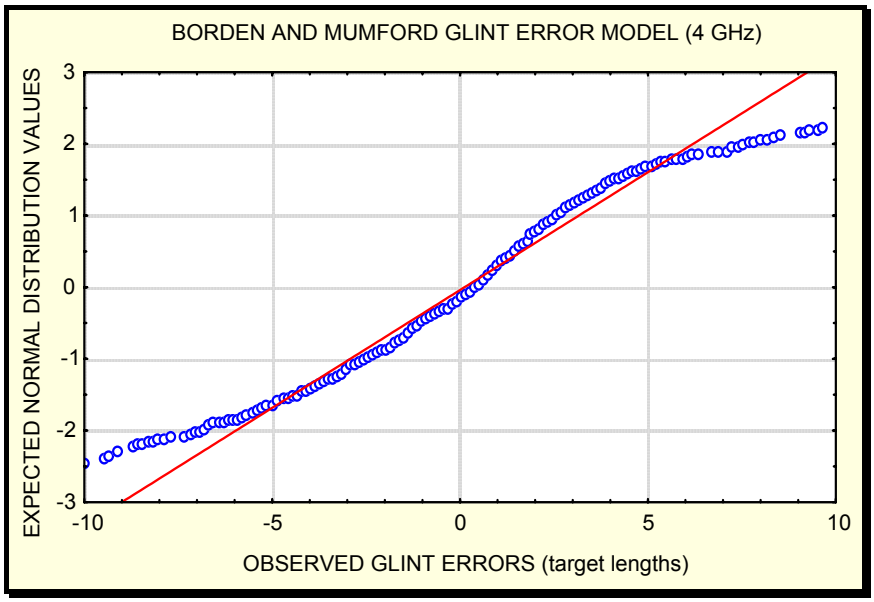

Figure 3-41 : Glint Error Distribution

The glint bandwidth computed at the detector and output interface rate,

$$ {}_{RD}\omega_G := 2 \cdot l_t^{rT} \cdot \omega_{T,TV}^{rT} \cdot {}_{RD}k_{WN} $$

Equation 3.8-50

$$ \underline{\omega}_{T,TV}^{T} := T_{TV}^{T} \cdot \left(\frac{\dot{\underline{P}}_{o,t}^{TV} \times \ddot{\underline{P}}_{o,t}^{TV}}{\dot{P}_{o,t}^{2}} \right) - \underline{\omega}_{A,T}^{T} $$

Equation 3.8-51

$$ {}_{RD}k_{RCS} := 1.128 \cdot \sqrt{\frac{{}_{RD}f_R}{{}_{RD}\omega_G}} $$

Equation 3.8-52

The normalised RCS of the target when viewed along the target LOS,

$$ \left({}_{RD}S_X \;,\; {}_{RD}S_Y \right)^T := {}_{RD}k_{RCS} \cdot \underline{\varphi}_{DIL}\left(N(0,1), 0.5 \cdot {}_{RD}\omega_G \right) $$

Equation 3.8-53

$$ {}_{RD}\overline{\sigma}_{RCS} := {}_{RD}S_X^2 + {}_{RD}S_Y^2 $$

Equation 3.8-54

The glint error measured in target size in a plane normal to the radar beam,

$$\left({}_{RD}S_W \quad , \quad {}_{RD}S_Z \right) \coloneqq$$

$$2 \cdot {}_{RD}k_W \cdot l_t^{rT} \cdot {}_{RD}k_{RCS} \cdot \left(\frac{s}{{}_{RD}\omega_G} \right) \cdot \left(\underline{\varphi}_{D1L} \left(N(0,1), \frac{{}_{RD}\omega_G}{2} \right), \frac{{}_{RD}\omega_G}{2} \right)$$

Equation 3.8-55

$${}_{RD}\xi_G \coloneqq \frac{{}_{RD}S_X \cdot {}_{RD}S_W + {}_{RD}S_Y \cdot {}_{RD}S_Z}{{}_{RD}\overline{\sigma}_{RCS}}$$

Equation 3.8-56

The angular glint errors are,

$$\left({}_{RD}\Psi_G \quad , \quad {}_{RD}\Theta_G \right) \coloneqq \left(\tan^{-1}\left(\frac{{}_{RD}\xi_G \cdot l_t^{YT}}{P_{o,t}^{XT}} \right) \quad , \quad \tan^{-1}\left(\frac{{}_{RD}\xi_G \cdot l_t^{ZT}}{P_{o,t}^{XT}} \right) \right)$$

Equation 3.8-57

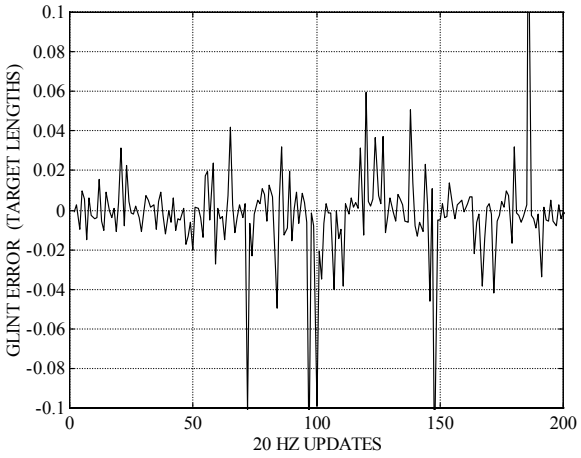

Figure 3-42 : Radar Glint Position Error

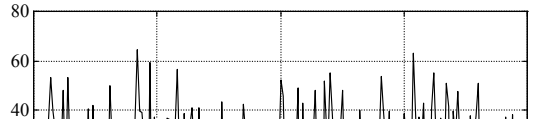

Figure 3-43 : Radar Glint RCS Variation

Figure 3-42 and Figure 3-43 show the non-dimensional glint error and the normalised RCS for a target rotating at 1 Hz with respect to the target sight-line with the radar operated at 20 Hz.

3.8.8 Sensor Limitations

Provision of radar range, range-rate, bearing and elevation measurements of the target and missile at the sensor interface depends on:

- User target measurement selection (*MS_MSAV1* bits 17 to 20 cleared)
- User missile measurement selection (*MS_MSAV1* bits 21 to 24 cleared)
- Range limiting (*GB_TR_ER* bit 20 is set)
- Squint threshold limiting (*GB_TR_ER* bit 21 is set)
- Out-of-beam limitations (*GB_TR_ER* bit 22 is set)
- Fade (*GB_TR_ER* bit 23 is set)

When active, if any of these limitations are violated, bits 1-4 in the measurement ready flag *MS_MSRY1* are cleared. Failure to provide measurements at the user request is indicated by setting bits 1-4 of *GB_TR_VF* depending those measurements affected.

Measurements are provided if the target (or missile) range is within $[R_{MIN},R_{MAX}]$, defaulting to [1,60] km. Failure to provide target measurements due to minimum or maximum range limiting is indicated by setting bits 5-6 of *GB_TR_VF* respectively, and bits 7-8 of *GB_TR_VF* for the missile measurements.

The beam angle with respect to the detector boresight is usually restricted to prevent excessive squint losses. Trunk[T.2] determined that the optimum number of phased array faces was 3, a maximum squint angle (ξ_{SQ}) of 60°. Target and missile measurements are only provided when the off-boresight beam angle is less than the maximum squint angle,

$$\left(T_{TD}^{T} \quad , \quad T_{TD}^{M} \right) := \left(T_{A}^{T} \cdot T_{TD}^{A} \quad , \quad T_{A}^{M} \cdot T_{TD}^{A} \right)$$

Equation 3.8-58

$$\begin{pmatrix} \xi_{TD}^{T} \\ \cdots \\ \xi_{TD}^{M} \end{pmatrix} := \begin{pmatrix} \cos^{-1}\left(\cos\Theta_{TD}^{T} \cdot \cos\Psi_{TD}^{T} \right) \\ \cdots \\ \cos^{-1}\left(\cos\Theta_{TD}^{M} \cdot \cos\Psi_{TD}^{M} \right) \end{pmatrix} \leq {}_{RD}\xi_{SQ}$$

Equation 3.8-59

Failure to provide measurements due to excessive squint is indicated by the setting of bits 9-10 in *GB_TR_VF* for the target and missile respectively. Measurements are also suspended if the target (or missile) lies outside a beam angle ($_{RD}\xi_{BW}$) of ± 2°,

$$\left(T_{TB}^{T} \quad , \quad T_{MB}^{M} \right) := \left(T_{A}^{T} \cdot T_{TB}^{A} \quad , \quad T_{A}^{M} \cdot T_{MB}^{A} \right)$$

Equation 3.8-60

$$\begin{pmatrix} \xi_{TB}^{T} \\ \cdots \\ \xi_{MB}^{M} \end{pmatrix} := \begin{pmatrix} \cos^{-1}\left(\cos\Theta_{TB}^{T} \cdot \cos\Psi_{TB}^{T} \right) \\ \cdots \\ \cos^{-1}\left(\cos\Theta_{MB}^{M} \cdot \cos\Psi_{MB}^{M} \right) \end{pmatrix} \leq {}_{RD}\xi_{BW}$$

Equation 3.8-61

Failure to provide measurements because the target, or missile, is not in the main beam is indicated by the setting of bits 11-12 in *GB_TR_VF* respectively.

Detection probability is usually based on Swerling's five idealised target models. Swirling-0 is simply a constant velocity sphere. When illuminating a fast jet comprising one dominant reflector, and a number of minor reflectors, which change little over the observation period using a single frequency the Swerling-3 model is most appropriate. The Swerling-1 model is for slower targets with no dominant reflector. Swerling-2 (no dominant reflector) and Swerling-4 (one dominant reflector) are for pulse-to-pulse fluctuations associated with frequency agility.

The Swerling-3 model is based on an approximation to the Rician distribution however, if sea and land clutter is considered this is often replaced by Log-Normal, or Weibull distributions. The reflected echoes from the target or missile are correlated with the transmitted waveform creating a detection peak against background noise. The radar applies its detection criteria to determine when an object is present in a particular cell. When the SNR is low the threshold between reliable target detection and a false alarms is marginal. Under these circumstances there is a finite probability that a target will be falsely identified, or the threshold set such that a target it will go undetected. These effects have been replaced by the fade from the Borden glint model. Failure to provide target pitch and yaw measurements due to the normalised RCS dropping below –30 dB is indicated by setting bits 13-14 in *GB_TR_VF* respectively.

3.8.9 Output Interface

Measured range, range-rate, bearing and elevation pass through a 16 bit interface (signed except for range) at a frequency (${}_{RD}f_O$) of 10 Hz (clock 18). All measurements are subject to a one-cycle transmission delay and target limits of [0,60_000] m, ± 1000 m/s, ± 180° and ± 90° respectively; the range and range rate limits [0,15_000] m and ± 1_500 m/s for the missile.

$${}_{RD}\underline{\underline{\tilde{Z}}} := {}^{IF}\underline{\varphi}_{TD}\left({}^{IF}\underline{\varphi}_{Q}\left({}^{IF}\underline{\varphi}_{LIM}\left({}^{IF}\underline{\varphi}_{ZOH}\left(\underline{\underline{\tilde{Z}}}, {}_{RD}f_O \right) \right) \right) \right)$$

Equation 3.8-62

3.9 Missile Seeker

3.9.1 Review

The development of RF and IR seekers, from the continuous wave devices of the 60s to the phased and staring arrays of today is an immense subject. The 60s single element detectors were capable of lock-before-launch against short-range targets with a tail-on aspect. During the 70s multiple element devices provided improved counter-measure performance. Dual frequency sensors were introduced in the 80s improving range with an all aspect attack. The single frequency imaging seekers of the 90s provide aim-point refinement with increasing FoR to 50°-60° off-boresight with clutter and counter-measure rejection. The next decade will bring all-weather Multi-Spectral Seekers (MSS) combining RF/IR and Laser/IR for stealth, 3D imaging to obtain range data, increased acquisition ranges, and improvement in clutter and countermeasure rejection.

The phased array radar, once restricted to large facilities such as Pave-Paws for ICBM launch detection and Aegis class missile frigates, is now used in aircraft, and even missiles. Future RF improvements are expected in the Pulse Repetition Frequencies (PRF) used, and in frequency agility to improve jamming resistance, reducing glint errors, and avoiding range and range-rate ambiguities.

Passive IR seekers with staring arrays are an important alternative to active RF devices with a number of modern short-range missiles using IR staring arrays. These impose exacting demands on the gimbal controllers to provide inertial stabilisation thereby preventing image smearing that reduces acquisition range. This requires smaller integration times commensurate with the high frame rates needed for agile missiles. The cost of ensuring that array elements remain in their response range with uniform random noise, spectral response and photon conversion is inevitably increasing. The presence of dead-elements and fixed pattern noise requires calibration, element acceptance criteria, and complex signal processing.

The MSS warrants special attention since it will be a catalyst for air-defence sensor data fusion. Conceptually the MSS contains two sensors operating on different wavelengths providing resistance to countermeasures, clutter, false alarms etc. The IR staring array provides accurate bearing and elevation measurements whilst the RF phased array adds range, range rate, and a second source of less accurate angular data. If radome transmittance at high off-boresight angles permits, the two sensors may use a common gimbal arrangement, and hence a single aperture. Alternatively, and more likely, two sets of gimbals and separate apertures will be required, each system being developed separately. Although ideal for modular design, the state observers and more complex autopilot will be required to point each sensor at the target, the acquiring sensor steering the other onto the target.

When multiple targets appear in the FoV of a single sensor, or a single target in the FoV of a number of sensors, there is the problem of track association. This is more complicated with the MSS since each sensor will generate tracks relating to common targets requiring correlated, a problem studied by Singer and Kanyuck (1971). Track fusion in Figure 3-44 deals with the problem of correlated estimation errors as process noise enters from each sensor.

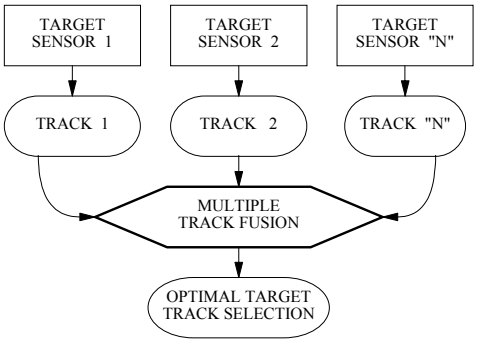

Figure 3-44 : Track Fusion Principle

Measurement fusion in Figure 3-45 maintains optimal tracks using information from a number of sensors assuming that gating isolates the targets under observation in a multiple target environment.

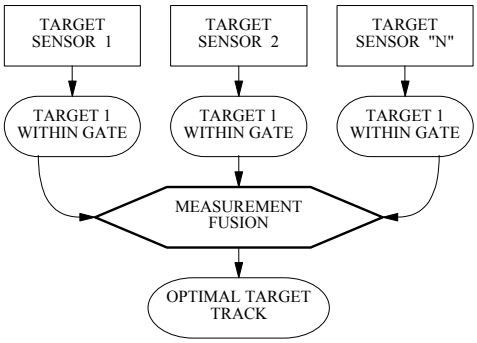

Figure 3-45 : Measurement Fusion Principle

Measurement fusion gives more accurate target state estimates, sensor calibration, and a faster response to target manoeuvres, whereas track fusion is better in cluttered environments and against countermeasures. This comparison of track and measurement fusion is continued in §5.1.

3.9.2 Description

The seeker model in Figure 3-46 comprises a single gimbal set (outer yaw, inner pitch gimbals) that can be locked to the missile boresight in strap-down applications supporting the detector shown in Figure 3-47. It has been assumed that the mass imbalance between the gimbals is minimised by careful design, and the pitch and yaw gimbal models do not interact.

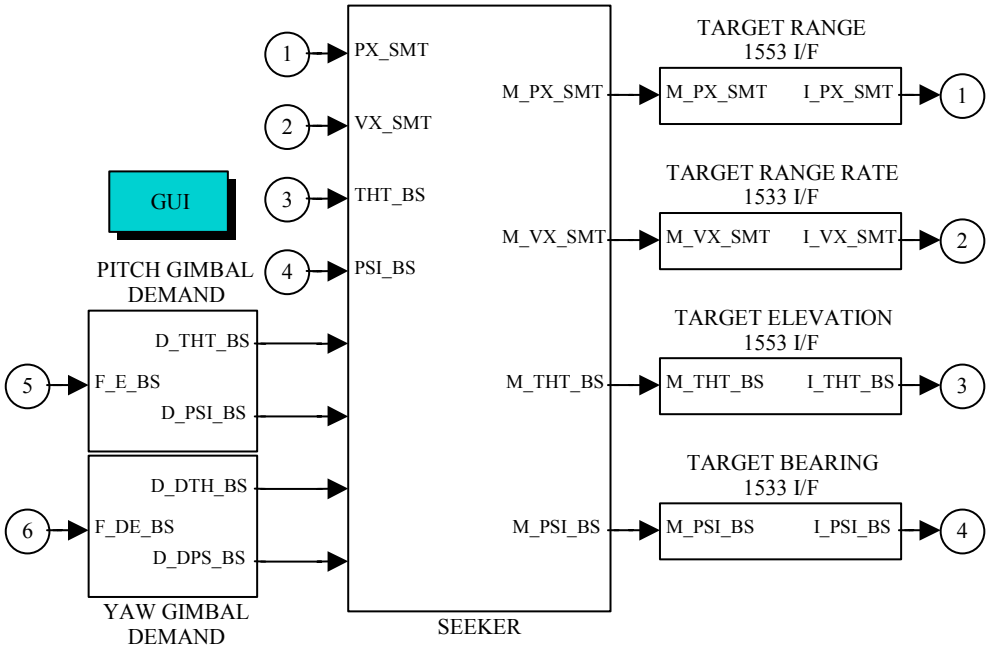

Figure 3-46 : Seeker Model

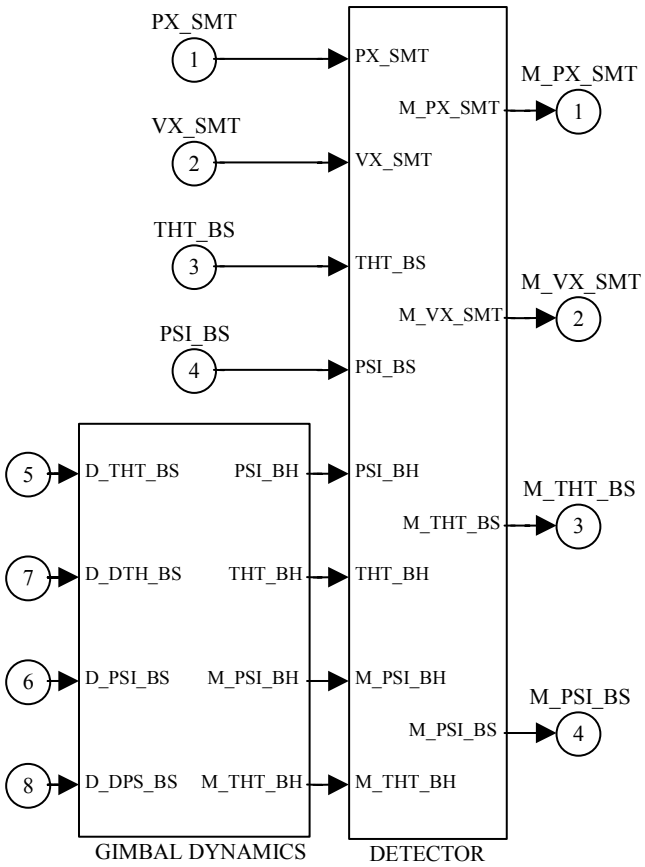

Figure 3-47 : Seeker Model Decomposition

The gimbals support a detector that provides range, range rate, and angular measurements depending on model characterisation for a single target using a single transmission frequency. The target position with respect to the detector is combined with the measured gimbal positions to give the target data with respect to the Missile Body frame.

The seeker is inertially de-coupled from missile body motion using state observer demands to the gimbal torquers rather than dedicated gyroscopic devices. This is a critical function since it limits the homing accuracy of the missile, Nesline[N.7]. Imperfect de-coupling due to seeker errors correlated with IMU outputs excites parasitic loops through the LF state observer demands, a subject dealt with in more detail in §6.6.3. When stabilisation is provided locally parasitic errors are a function of the gyroscope angular body rates, whereas in systems employing data fusion they dependent on all the sensors, in particular the accelerometers.

The closed loop flow of parasitic disturbances in the LF and HF models used for the seeker and ground radar is shown in Figure 3-48 and Figure 3-49 respectively. In the LF model the errors are imposed on the demands serially, the HF feedback having been reduced to a simple transfer function with input limiting.

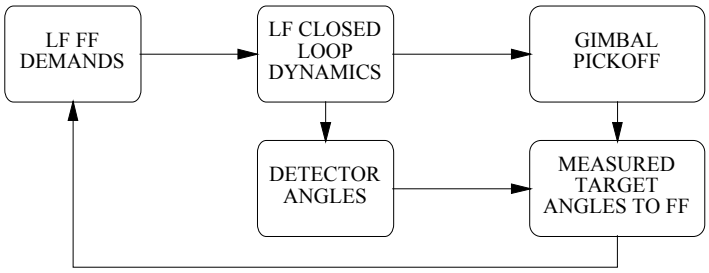

Figure 3-48 : LF Detector Pointing Loop

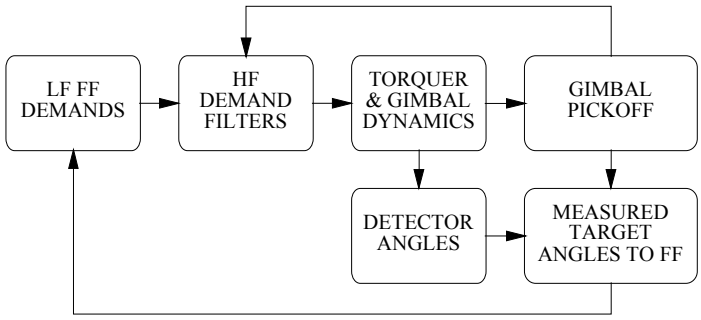

Figure 3-49 : HF Detector Pointing Loop

In the HF model the internally closed loop error model includes gimbal control, torquer, and gimbal pick-offs. Both models are provided, the HF model for studying the effect of parasitic errors, and the LF model for system studies assuming that parasitic errors can be ignored.

3.9.3 State Observer Gimbal Demand Processing

The detector is initially locked with its boresight along the longitudinal axis of the missile. After launch the seeker is provided with LF gimbal demands at the seeker output interface rate ($_{SK}f_O$) of 400 Hz (clock 9), from one of the following sources depending on the value of *SK_SK_DS*:

- 1 Zero with respect to the missile boresight for strap-down applications
- 2 Reference target position with respect to the Missile Body frame
- 3 Seeker measurements
- 4 Missile state observer

If the gimbal demands are set to zero they are treated as RF phased array beam pointing commands with respect to the locked-down detector. When the gimbals are free the RF beam is formed along the detector boresight. For convenience, the Euler angles and angular rates associated with the gimbals are collected together,

$$ {}_{SK}\underline{Z}_G \equiv \left(\Psi_B^H \;,\; \Theta_B^H \right)^T \;;\; {}_{SK}\underline{\dot{Z}}_G \equiv \left(\dot{\Psi}_B^H \;,\; \dot{\Theta}_B^H \right)^T $$

Equation 3.9-1

If LF gimbal demands are used directly in high bandwidth sensors the seeker head jitter for IR staring arrays is unacceptable. This causes the returning energy to be smeared across the detector pixels during a stare time lasting several milliseconds reducing the acquisition range. To prevent this, LF demands are processed at 400 Hz using First-Order-Hold (FOH) filters,

$$ {}^{D}_{400}\underline{Z}_G := \left(\tan^{-1}\left(\frac{T_B^S(4)}{T_B^S(1)} \right) \;,\; -\sin^{-1}\left(T_B^S(7) \right) \right)^T + \underline{N}\left(0 \,,\, {}_{SK}\sigma_{GA} \right) $$

Equation 3.9-2

$$ T_B^S := T_A^S \cdot \left[T_A^B \right]^T $$

Equation 3.9-3

(σ_{GA}) represents the physical misalignment of the seeker with respect to the Missile Body frame. This error is constant and is selected from a zero-mean Gaussian error with a deviation of 1 mrad. The Euler rate demands are obtained from the missile body referenced target LOS rate,

$$ {}^{D}_{400}\underline{\dot{Z}}_G := \left(\omega_{B,S}^{YS} \;,\; \omega_{B,S}^{ZS} \cdot \sec\Theta_B^S \right) $$

Equation 3.9-4

$$\underline{\omega}^{S}_{B,S} \coloneqq T^{S}_{A} \cdot \left[T^{T}_{A} \right]^{T} \cdot \underline{\omega}^{T}_{A,T} - T^{S}_{B} \cdot \underline{\omega}^{B}_{A,B}$$

Equation 3.9-5

The LF Euler angle and angular rate demands pass through a signed 16 bit digital interface where they are subject to range limiting of ± 60° and ± 600°/s respectively, and a one-cycle transmission delay,

$${}^{D}_{400}\underline{Z}_{G} \coloneqq {}^{IF}\underline{\varphi}_{TD}\left({}^{IF}\underline{\varphi}_{Q}\left({}^{IF}\underline{\varphi}_{LIM}\left({}^{IF}\underline{\varphi}_{ZOH}\left({}^{D}_{400}\underline{Z}_{G} , {}_{SK}f_{O} \right) \right) \right) \right)$$

Equation 3.9-6

The gimbal demand interface errors are invoked by setting bits 27-30 of *MS_SK_ER* from Table 3-6. The additional functions listed in Table 3-17 are controlled by spare bits in *MS_SK_ER*.

Table 3-17 : Seeker Gimbal Errors

MS_SK_ER	GIMBALS ERRORS	
11	H/F gimbal demand processing	
12	Complex gimbal dynamics	
13	Gimbal friction model	
14	Gimbal torque model	

Gimbal travel is designed for front hemisphere coverage, however, radome quality, squint losses and other mechanical constraints limit the practical off-boresight angle. YP demands require the application of an off-boresight limit of 85° as a consequence of Equation 3.9-4,

$${}^{D}_{400}\underline{Z}_{G} \coloneqq \varphi^{YP}_{RP}\left(\underline{\varphi}_{LIM}\left(\varphi^{RP}_{YP}\left({}^{D}_{400}\underline{Z}_{G} \right), \begin{pmatrix} [-\pi , \pi] \\ \cdots \\ [-\pi / 3 , \pi / 3] \end{pmatrix} \right) \right)$$

Equation 3.9-7

The angular rate limit matching the controller gain and the motor current limit used later is ± 1440°/s assuming a perfect motor and gimbals. Fortunately, it is rare that the full angular rate of the seeker is required, and a lesser value is often substituted commensurate with the turning capability of the missile and target. As the gimbal demand interface provides angle and angular rate limits, separate limits inside the seeker are not necessary.

3.9.4 Seeker Gimbal Demand Processing

If bit 11 of *MS_SK_ER* is set, HF gimbal demands are obtained at the seeker gimbal frequency (${}_{SK}f_{GR}$) of 2 kHz (clock 4) using an FOH,

$$\forall n \in [0(1),4] \Rightarrow {}^{D}_{2000}\underline{Z}_G(n) := {}^{D}_{400}\underline{Z}_G + \frac{n \cdot {}^{D}_{400}\dot{\underline{Z}}_G}{{}_{SK}f_{GR}}$$

Equation 3.9-8

If bit 11 is not set the 400 Hz angle demands are passed without change, and the angular rates are ignored.

3.9.5 Simple Gimbal Dynamics

The full gimbal model presented later imposes a processing load that is unwarranted for general studies. If bit 12 in *MS_SK_ER* is not set (default), the gimbal demands pass through a time delay (${}_{SK}t_D$) followed by a 2nd order transfer function operating at the HF gimbal demand frequency.

$${}_{2000}\tilde{\underline{Z}}_G :=$$

$$\varphi_{SF}\left(\varphi_{D2L}\left(\varphi_{TD}\left({}^{D}_{2000}\underline{Z}_G, {}_{SK}t_{GD}\right), {}_{SK}\zeta_{SG}, {}_{SK}\omega_{SG}\right) + N(0, {}_{SK}\sigma_{GRN})\right)$$

Equation 3.9-9

The gimbal dynamics have a damping ratio (${}_{SK}\zeta_{SG}$) of 0.7, and a natural frequency (${}_{SK}\omega_{SG}$) of 50 Hz, that are matched to the response of the closed loop model to follow. DAC and ADC quantisation and noise tend to be negligible using the 14-16 bit devices required by seekers, and the resolver dynamics are too higher frequency to be of concern, all have been ignored. Zero-mean, Gaussian noise with a variance (${}_{SK}\sigma_{GRN}$) of 0.3 mrad is superimposed, and the result is subject to resolver constant, quadratic and asymmetric scale factor errors of 0.0003, 0.0001 and 0.0001 respectively.

3.9.6 Complex Gimbal Dynamics

The complex gimbal model shown in Figure 3-50 is required when the friction effects, and disturbance torques, are studied in conjunction with parasitic errors.

DAC GAIN AND
GIMBAL MOTOR

Figure 3-50 : Gimbal Torquer Error Model

This model is activated by setting bit 12, and either bit 13 or bit 14 of *MS_SK_ER*, invoking the torque and friction models respectively. Consider the yaw gimbal dynamic model shown in Figure 3-51 (the pitch gimbal model has exactly the same form). The model comprises in order, from left to right: a lead-lag gimbal controller, DAC gain, motor current limit, motor dynamics and gimbal inertia.

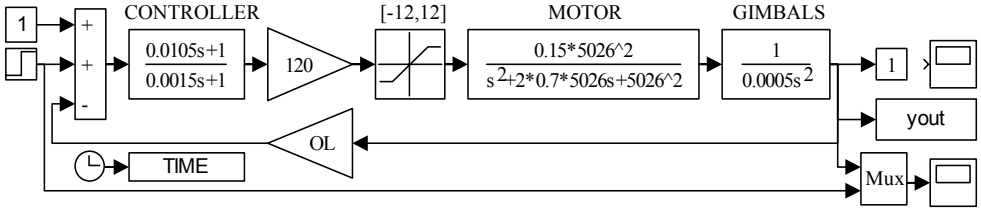

Figure 3-51 : Complex Yaw Gimbal Dynamic Model

This open loop model is modelled at the seeker reference rate (${}_{SK}f_R$) of 4 kHz. The yaw gimbal demand is subject to a time delay before the gimbal error is passed through a controller and DAC gain providing the motor current (${}_{SK}I_G$) which is limited to protect the electronics and motor coils,

$$ {}_{SK}I_{G\Psi} \coloneqq $$

$$ \varphi_{LIM}\left(K_{A\Psi} \cdot \varphi_{DLL}\left(\varphi_{TD}\left({}^{D}_{2000}\Psi_{G_k} \right) - {}^{D}_{2000}\Psi_{G_{k-1}}, \frac{2\cdot\pi}{{}_{SK}K_{CZ}}, \frac{2\cdot\pi}{{}_{SK}K_{CP}} \right) - I_{M\Psi}, I_{M\Psi} \right) $$

Equation 3.9-10

The torque generated by the gimbal motor depends on the input current,

$$ {}_{SK}\tau_{M\Psi} \coloneqq {}_{SK}K_{M\Psi} \cdot \underline{\varphi}_{D2L}\left({}_{SK}I_{G\Psi} + {}_{SK}\tau_{F\Psi}, {}_{SK}\zeta_{G\Psi}, {}_{SK}\omega_{G\Psi} \right) $$

Equation 3.9-11

The gimbal angles and angular rate obtained by separating the integrators to accommodate the torque and friction models,

$$ {}^{A}_{5000}\Psi \coloneqq $$

$$ \varphi_{DI}\left(\varphi_{DI}\left(\frac{{}_{SK}\tau_{M\Psi} + {}_{SK}\tau_{E\Psi}\left(I_{G\Psi}, \Psi_{G_{k-1}} \right)}{{}_{SK}J_{G\Psi}} \right) + {}_{SK}\tau_{F\Psi}\left({}_{SK}\tau_{M\Psi}, {}_{SK}\tau_{E\Psi}, \dot{\Psi}_{G_{k-1}} \right) \right) $$

Equation 3.9-12

The gimbal characteristics listed in Table 3-18 were selected so that the closed loop response of both gimbals was a 3 dB overshoot, and stability margins of 18 dB and 45° as shown in Figure 3-52 and Figure 3-53. The step response without motor current limiting is shown in Figure 3-54. Introducing motor current limiting trades response time for a reduction in

the overshoot as shown in Figure 3-55. In practice the motor voltage and winding resistance limit the current and an artificially low limit is usually imposed below this value.

Table 3-18 : Complex Gimbal Dynamic Characteristics

MATH	DESCRIPTION	PITCH	YAW	UNITS	
$_{SK}K_{CZ}$	Controller zero time constant	9.1	1.3	msec	
$_{SK}K_{CP}$	Controller pole time constant	10.5	1.5	msec	
$_{SK}K_{A}$	Controller/DAC gain	40	120	Amp/rad	
$_{SK}I_{M}$	Motor current limit	6	12	Amps	
$_{SK}K_{M}$	Motor gain	0.05	0.15	N-m/Amp	
$_{SK}\zeta_{G}$	Motor damping ratio	0.7	0.7		
$_{SK}\omega_{G}$	Motor natural frequency	800	800	Hz	
$_{SK}J_{G}$	Gimbal inertia	0.05	0.5	g m^2	

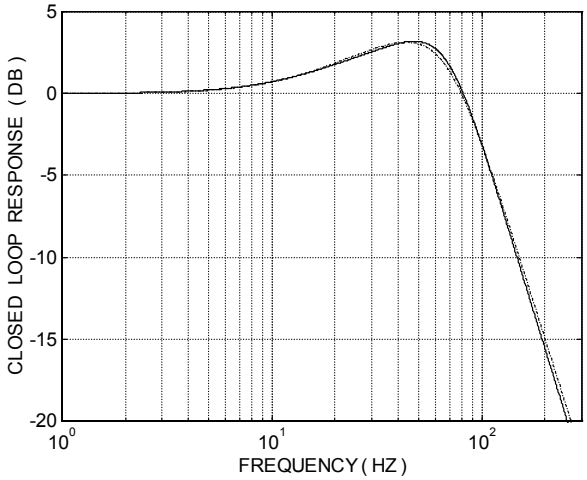

Figure 3-52 : Closed Loop Frequency Response

The torque disturbances ($_{SK}\tau_{E}$) comprise spring, cogging and ripple torques.

$$
{}_{SK}\tau_{E\Psi} :=
$$

$$
{}_{SK}K_{G1\Psi} \cdot \Psi_B^H + {}_{SK}K_{G2\Psi} \cdot \cos\left({}_{SK}K_{G3\Psi} \cdot \Psi_B^H + {}_{SK}K_{G4\Psi} \right)
$$

$$
+
$$

$$
{}_{SK}K_{G5\Psi} \cdot {}_{SK}I_{G\Psi} \cdot \cos\left({}_{SK}K_{G6\Psi} \cdot \Psi_B^H + {}_{SK}K_{G7\Psi} \right)
$$

Equation 3.9-13

The effect of gimbal mass imbalance leading to a cross coupling of the motor torque has been ignored. The outer (yaw) gimbal is usually connected by slip rings, the leads bringing power to the inner gimbals increasingly resist gimbal motion as the off-boresight angle increases.

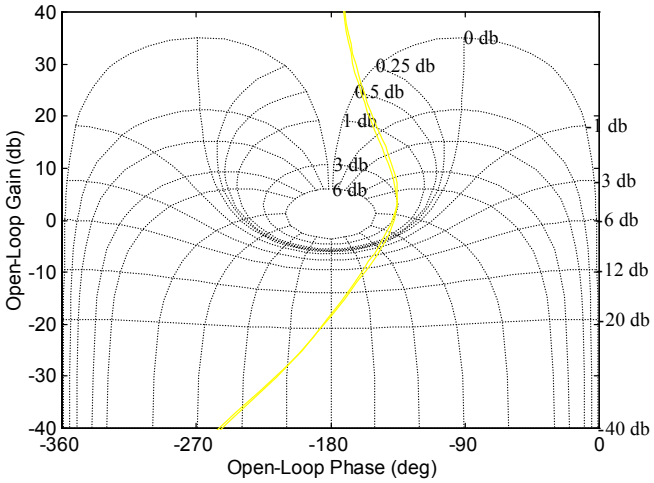

Figure 3-53 : Stability Margins

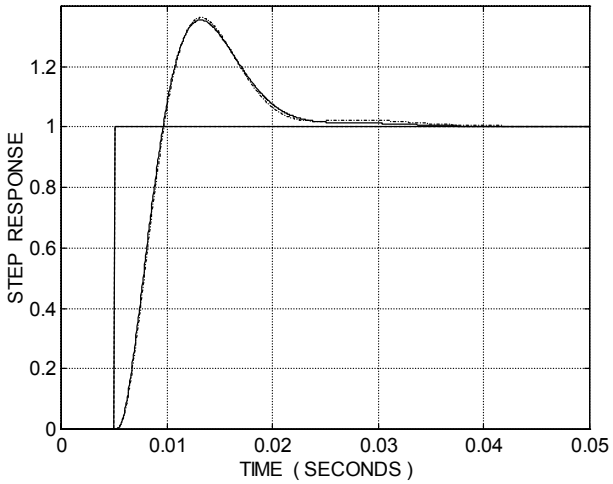

Figure 3-54 : Step Response - No Current Limiting

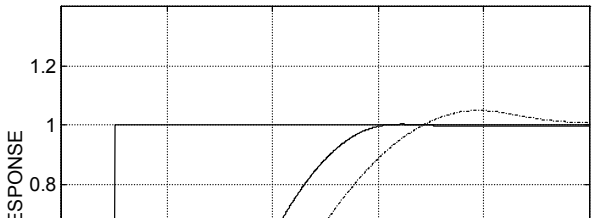

Figure 3-55 : Step Response - With Current Limiting

Key : Solid Line - Pitch Gimbal ; Dashed Line - Yaw Gimbal

The segmented design of the motor's commutator results in a fixed frequency sinusoidal torque disturbance and an induced magnetic component modelled so that they can operate out-of-phase. The torque disturbance characteristics are listed in Table 3-19.

Table 3-19 : Complex Gimbal Torque Characteristics

MATH	DESCRIPTION	PITCH	YAW	UNITS	
K_{G1}	Flexi-lead torque	0.005	0.025	Nm	
K_{G2}	Motor torque amplitude	0.002	0.02	Nm	
K_{G3}	Motor torque frequency	30	15	rad/rad	
K_{G4}	Motor torque phase offset	[$-\pi$, π]	[$-\pi$, π]	rad	
K_{G5}	Magnetic torque amplitude	0.005	0.01	Nm/Amp	
K_{G6}	Magnetic torque frequency	25	50	Hz	
K_{G7}	Magnetic torque phase offset	[$-\pi$, π]	[$-\pi$, π]	rad	

The friction torque disturbances (${}_{SK}\tau_F$) comprise stiction, viscous and coulomb damping. Stiction is the torque needed to induce motion in a stationary gimbal. Viscous friction arises from resistance to motion due to eddy currents, induced magnetic fields and lubrication. Coulomb friction is due to abnormal loads on gimbal bearings when subject to vibration. These torque disturbances, characterised using data listed in Table 3-20, oppose the motion of the gimbals. When the applied torque is greater than Stiction,

$$\left| \dot{\Psi}_B^H \right| \geq {}_{SK}K_{G9\Psi} \quad \Rightarrow$$

$$\tau_F \quad := \quad \left(\text{sign} \left({}_{SK}K_{G10\Psi} , \dot{\Psi}_B^H \right) + {}_{SK}K_{G11\Psi} \right) \cdot \dot{\Psi}_B^H$$

Equation 3.9-14

When the applied torque is less than stiction,

$$\left| \dot{\Psi}_B^H \right| < {}_{SK}K_{G9\Psi} \quad \wedge$$

$$\left\{ \begin{array}{c} {}_{SK}\tau_{M\Psi} + {}_{SK}\tau_{E\Psi} \leq - {}_{SK}K_{G8\Psi} \quad \Rightarrow \quad {}_{SK}\tau_{F\Psi} \quad := \quad - {}_{SK}K_{G8\Psi} \\ \left| {}_{SK}\tau_{M\Psi} + {}_{SK}\tau_{E\Psi} \right| < {}_{SK}K_{G8\Psi} \quad \Rightarrow \quad {}_{SK}\tau_{F\Psi} \quad := \quad {}_{SK}\tau_{M\Psi} + {}_{SK}\tau_{E\Psi} \\ {}_{SK}\tau_{M\Psi} + {}_{SK}\tau_{E\Psi} \geq {}_{SK}K_{G8\Psi} \quad \Rightarrow \quad {}_{SK}\tau_{F\Psi} \quad := \quad {}_{SK}K_{G8\Psi} \end{array} \right\}$$

Equation 3.9-15

Table 3-20 : Complex Gimbal Friction Characteristics

MATH	DESCRIPTION	PITCH	YAW	UNITS	
${}_{SK}K_{G8}$	Coulomb friction	0.005	0.05	Nm	
${}_{SK}K_{G9}$	Stiction threshold	15	15	mrad/s	
${}_{SK}K_{G10}$	Stiction level	0.005	0.05	Nm	
${}_{SK}K_{G11}$	Viscous friction	2×10^{-5}	4×10^{-5}	Nm/rad/s	

The time delay, gimbal noise, ZOH and scale factor errors are identical to those used in the simple gimbal model,

$$ {}_{2000}\underline{Z}_{G_k} := \underline{\varphi}_{SF}\left(\underline{\varphi}_{ZOH}\left({}_{8000}\underline{Z}_{OTF}\ ,\ {}_{SK}f_{GR} \right) + \underline{N}\left(0\ ,\ {}_{SK}\sigma_{GRN} \right) \right) $$

Equation 3.9-16

When the gimbals demands are set to zero the time delay and the pickoff errors represent electronic beam steering inaccuracies - the other gimbal demand shaping and dynamic errors should be disabled.

3.9.7 Reference Detector Input

The reference range, range rate, bearing and elevation of the target with respect to the true position of the antennae boresight are updated at the output interface rate (${}_{SK}f_O$),

$$ P_{m,t} = \left\| \underline{P}^{A}_{o,t} - \underline{P}^{A}_{o,m} \right\| $$

Equation 3.9-17

$$ \dot{P}^{XS}_{m,t} := \underline{P}^{A}_{m,t} \bullet \underline{\dot{P}}^{A}_{m,t} \Big/ P_{m,t} $$

Equation 3.9-18

$$ \Psi^{S}_{H} := -\sin^{-1}\left(T^{S}_{B}(7) \right) - \Theta^{H}_{B} $$

Equation 3.9-19

$$ \Theta^{S}_{H} := \tan^{-1}\left(T^{S}_{B}(4) \Big/ T^{S}_{B}(1) \right) - \Psi^{H}_{B} $$

Equation 3.9-20

3.9.8 Seeker Measurements

For convenience, the target parameters provided by the detector, when combined with gimbal pick-off output, are collectively referred to by,

$$\underline{\tilde{Z}} \equiv \left(\tilde{P}_{o,t} \;,\; \tilde{\dot{P}}^{XT}_{o,t} \;,\; \tilde{\Psi}^{T}_{A} \;,\; \tilde{\Theta}^{T}_{A} \right)^{T}$$

Equation 3.9-21

The detector measurements are constructed in the same way as those for the radar dealt with in §3.4.5. In this case they are subject to the errors listed in Table 3-21 whose inclusion depends on the bit pattern of *MS_SD_ER*.

Table 3-21 : Seeker Detector Errors

SK_SD_ER	DETECTOR ERRORS	
1	SNR dependent Gaussian noise	
2	Gaussian Noise	
3	Glint error	
4	Radome abberation	
5	Range limitation	
6	Out of beam limitation	
7	Fading limitation	

A constant bias occurs when dealing with IR detector fixed frame artefacts caused by stray light paths, or non-uniform dome heating, and is mistaken for targets. In response to this fixed target offset the gimbal controller generates a constant seeker sight line rate that can cause the missile to turn continuously towards the artefact. No errors of this type have been included in the model because they must be designed out of the system hardware.

3.9.8.1 Range

Target range is corrupted by zero-mean Gaussian noise. This is a function of pulse width ($_{SK}t_P$), signal-to-noise ratio ($_{SK}SN$), and the speed of light,

$$\tilde{P}_{m,t} := P_{m,t} + N\left(0 \;,\; \frac{c \cdot {}_{SK}t_P}{\sqrt{8 \cdot {}_{SK}SN}} \right)$$

Equation 3.9-22

3.9.8.2 Range Rate

Target range-rate is corrupted by zero-mean Gaussian noise. This is a function of transmission wavelength ($_{SK}\lambda_T$), pulse width, and the SNR ratio,

$$\tilde{\dot{P}}_{m,t} := \dot{P}_{m,t} + N\left(0 \;,\; \frac{{}_{SK}\lambda_T \cdot {}_{SK}t_P}{\sqrt{8 \cdot {}_{SK}SN}} \right)$$

Equation 3.9-23

3.9.8.3 Bearing and Elevation

The target angles with respect to the Missile Body frame are the sum of the measured gimbal angles and the measured position of the target with respect to the detector boresight,

$$\left(\tilde{\Psi}_B^S \quad , \quad \tilde{\Theta}_B^S \right) := \left(\tilde{\Psi}_B^H + \tilde{\Psi}_H^S \quad , \quad \tilde{\Theta}_B^H + \tilde{\Theta}_H^S \right)$$

Equation 3.9-24

The target angles with respect to the detector are corrupted by signal-to-noise dependent random noise, zero-mean Gaussian noise with a deviation of 2 mrad, residual radome aberration, and glint.

$$\tilde{\Theta}_H^S := \Theta_H^S + N\left(0 , \frac{{}_{SK}\xi_{BW}}{\sqrt{2 \cdot {}_{SK}SN}} \right) + N\left(0 , {}_{SK}\sigma_{\Theta RN} \right) + N\left(0 , {}_{SK}\sigma_{\Theta RA} \right) + {}_{SK}\Theta_G$$

Equation 3.9-25

$$\tilde{\Psi}_H^S := \Psi_H^S + N\left(0 , \frac{{}_{SK}\xi_{BW}}{\sqrt{2 \cdot {}_{SK}SN}} \right) + N\left(0 , {}_{SK}\sigma_{\Psi RN} \right) + N\left(0 , {}_{SK}\sigma_{\Psi RA} \right) + {}_{SK}\Psi_G$$

Equation 3.9-26

Missile radomes are calibrated to reduce optical aberration effects leaving residual errors whose generic form is given by Garnel[G.1]. From Burks[B.12],

$$\left| \Theta_B^H \right| < \frac{\pi}{6} \Rightarrow {}_{SK}\sigma_{\Theta RA} := 0.005 \cdot \sin\left(6 \cdot \left| \Theta_B^H \right| \right)$$

Equation 3.9-27

$$\left| \Psi_B^H \right| < \frac{\pi}{6} \Rightarrow {}_{SK}\sigma_{\Psi RA} := 0.0025 \cdot \sin\left(12 \cdot \left| \Psi_B^H \right| \right)$$

Equation 3.9-28

3.9.8.4 Signal to Noise Ratio

From the Radar Equation in §3.8.6 the SNR for mono-pulse extraction,

$${}_{SK}SN := \frac{{}_{SK}P \cdot {}_{SK}G^2 \cdot {}_{SK}t_P \cdot {}_{SK}\lambda_T^2 \cdot {}_{SK}\sigma_{RCS}}{(4 \cdot \pi)^3 \cdot k_B \cdot {}_{SK}T \cdot {}_{SK}L \cdot P_{m,t}^4}$$

Equation 3.9-29

The beam width for a cosine radiation pattern depends on a radiating frequency ($_{SK}\lambda_T$) of 17 GHz, and the antenna diameter, 70% of the missile diameter (d_m) defined in §6.3,

$$_{SK}\xi_{BW} := \frac{1.3 \cdot {}_{SK}\lambda_T}{0.7 \cdot d_m}$$

Equation 3.9-30

Including the antenna efficiency in with the general loss term leaves the directive gain as a function of the antenna beam-width ($_{SK}\xi_{BW}$) of 2°,

$$_{SK}G := 4 \cdot \pi \,/\, {}_{SK}\xi_{BW}^2$$

Equation 3.9-31

The SNR is therefore,

$$_{SK}SN := \frac{{}_{SK}P \cdot (0.7 \cdot d_m)^4 \cdot {}_{SK}t_P \cdot {}_{SK}\sigma_{RCS}}{(4 \cdot \pi)^3 \cdot k_B \cdot {}_{SK}T_S \cdot {}_{SK}\lambda_T^2 \cdot {}_{SK}L_S \cdot P_{m,t}^4}$$

Equation 3.9-32

The RCS area ($_{SK}\sigma_{CSA}$) is set to 1.0. Assuming a sky noise temperature of 290 K, and negligible antennae to receiver input loss, the system noise temperature ($_{SK}T_S$) is dominated by the electronic noise factor ($_{SK}L_{RN}$),

$$_{SK}T_S := 290 \cdot {}_{SK}L_{RN}$$

Equation 3.9-33

Additional loss factors due to clear air atmospheric attenuation (L_A) and constant signal processing loss ($_{SK}L_S$) are taken into consideration but not rain attenuation, clutter or multipath errors. The total loss factor,

$$_{SK}L_S := 10^{0.1}$$

Equation 3.9-34

3.9.8.5 Glint Error

The glint model described in §3.8.7 is repeated for the RF seeker, the wave number and bandwidth computed at the detector and output interface rate,

$$\left({}_{SK}k_{WN}\ ,\ {}_{SK}\omega_G\right) := \left(2 \cdot \pi \cdot {}_{SK}f_T / c\ ,\ 2 \cdot l_t^{rS} \cdot \omega_{S,TV}^{rS} \cdot {}_{SK}k_{WN}\right)$$

Equation 3.9-35

The target dimensions normal to the seeker LOS and the angular velocity of the rotating line of reflectors along the target longitudinal axis are,

$$\underline{l}_t^S := T_A^S \cdot T_{TV}^A \cdot \left(l_t^{XTV} \quad 0 \quad 0 \right)^T$$

Equation 3.9-36

$$\underline{\omega}_{S,TV}^S := T_{TV}^S \cdot \left(\frac{\dot{\underline{P}}_t^T \times \ddot{\underline{P}}_t^T}{\dot{P}_{o,t}^2} \right) - \omega_{A,S}^S$$

Equation 3.9-37

$${}_{SK}k_{RCS} := 1.128 \cdot \sqrt{\frac{{}_{SK}f_R}{{}_{SK}\omega_G}}$$

Equation 3.9-38

The normalised RCS of the target when viewed along the target LOS is,

$$\left({}_{SK}S_X \quad , \quad {}_{SK}S_Y \right)^T := {}_{SK}k_{RCS} \cdot \underline{\varphi}_{DIL}\left(N(0,1), 0.5 \cdot {}_{SK}\omega_G \right)$$

Equation 3.9-39

$${}_{SK}\overline{\sigma}_{RCS} := {}_{SK}S_X^2 + {}_{SK}S_Y^2$$

Equation 3.9-40

The glint error measured in target size in the plane normal to the target line of sight substituting for the seeker beam centre,

$$\left({}_{SK}S_W \quad , \quad {}_{SK}S_Z \right) :=$$

$$2 \cdot {}_{SK}k_W \cdot l_t^{rS} \cdot {}_{SK}k_{RCS} \cdot \left(\frac{s}{{}_{SK}\omega_G} \right) \cdot \left(\underline{\varphi}_{DIL}\left(N(0,1), \frac{{}_{SK}\omega_G}{2} \right), \frac{{}_{SK}\omega_G}{2} \right)$$

Equation 3.9-41

$${}_{SK}\xi_G := \frac{{}_{SK}S_X \cdot {}_{SK}S_W + {}_{SK}S_Y \cdot {}_{SK}S_Z}{{}_{SK}\overline{\sigma}_{RCS}}$$

Equation 3.9-42

The angular glint errors,

$$\left({}_{SK}\Psi_G \quad , \quad {}_{SK}\Theta_G \right) := \left(\tan^{-1}\left(\frac{{}_{SK}\xi_G \cdot l_t^{YS}}{P_{m,t}^{XS}} \right) \quad , \quad \tan^{-1}\left(\frac{{}_{SK}\xi_G \cdot l_t^{ZS}}{P_{m,t}^{XS}} \right) \right)$$

Equation 3.9-43

3.9.9 Sensor Limitiations

Provision of seeker range, range-rate, bearing and elevation measurements at the output interface depends on:

- User target measurement selection (*MS_MSAV2* bits 1 to 4 cleared)
- Range limiting (*SK_SD_ER* bit 20 is set)
- Out-of-beam limitations (*SK_SD_ER* bit 21 is set)
- Fade (*SK_SD_ER* bit 22 is set)

When active, if any of these limitations are violated, bits 1-4 in the measurement ready flag *MS_MSRY2* are cleared. Failure to provide measurements at the user request is indicated by setting bits 1-4 of *MS_SK_VF* depending on the measurements affected. Measurements are provided if the target range is within $[R_{MIN},R_{MAX}]$, defaulting to [0.1,5] km. Failure to provide measurements due to minimum or maximum limiting is indicated by setting bits 5-6 of *MS_SK_VF* respectively. Measurements are also suspended if the target lies outside the ± 2° beam angle ($_{SK}\xi_{BW}$),

$$T_S^{SB} := T_H^{SB} \cdot T_B^H \cdot T_A^B \cdot \left(T_A^S \right)^T$$

Equation 3.9-44

$$\xi_S^{SB} := \cos^{-1}\left(\cos\Psi_S^{SB} \cdot \cos\Theta_S^{SB} \right) < {}_{SK}\xi_{BW}$$

Equation 3.9-45

Failure to provide measurements when the target is not in the beam is indicated by the setting of bit 7 in *MS_SK_VF*.

If the detector is being used in strap-down mode the missile boresight to seeker head angles are zero. If the gimbals are free to rotate the angle between the detector and beam is zero. For a brief review of Swirling target models refer to §3.8.8. Failure to provide detector measurements due fade is indicated by setting bit 8 of *MS_SK_VF*.

3.9.10 Output Interface

The unsigned range, signed range-rate and target angles are pass through a 16 bit digital interface at a frequency ($_{SK}f_O$) of 400 Hz (clock 9). They are subject to interface range limits of [0,5000] m, ± 5000 m/s and ± 90°, and a one-cycle transmission delay.

$${}_{SK}\underline{\tilde{Z}} := {}^{IF}\underline{\varphi}_{TD}\left({}^{IF}\underline{\varphi}_{Q}\left({}^{IF}\underline{\varphi}_{LIM}\left({}^{IF}\underline{\varphi}_{ZOH}\left(\underline{\tilde{Z}}, {}_{SK}f_O \right) \right) \right) \right)$$

Equation 3.9-46

3.10 Missile Fin Position Transducers

3.10.1 Review

Fin positions and IMU measurements provide the missile autopilot with data it needs to generate the guidance demands and compensate for gravity. The autopilot rolls the missile into the manoeuvring plane, desensitising it to pitch-yaw cross coupling, body flexure, body incidence, mass property and aerodynamic load variations with speed and height. For GPS and radar altimeters it is important that the missile roll is controlled to ensure that their FoV restrictions are not violated. For missile state observers, fin positions are part of the force and moment balance used in the filter dynamic model in conjunction with quasi-static aerodynamic data.

3.10.2 Description

Guidance demands are converted into individual fin demands (${}_{A/P}\underline{\delta}_D$) subject to flight dependent limitations as described in §6.8.

$$ {}_{AP}\underline{\delta}_D \equiv \left(\xi_D \ , \ \zeta_D \ , \ \eta_D \right)^T $$

Equation 3.10-1

The convention adopted for fin displacement is that positive demands cause positive angular rotations about the FRD Missile Body axes according the right hand screw rule, as shown in Figure 3-56.

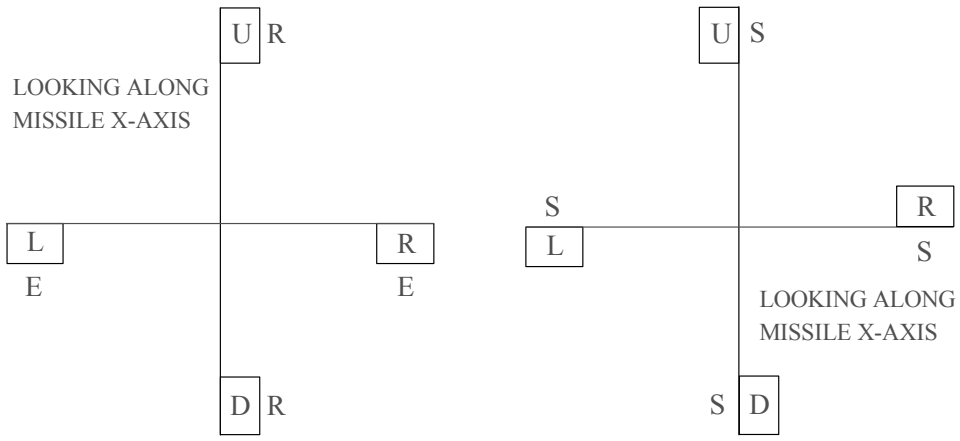

Figure 3-56 : Aileron, Rudder and Elevator Deflections

A positive fin deflection is a clockwise rotation about its hinge line when looking outwards from the missile. The individual fin demands are,

$$ {}_{FN}\underline{\delta}_D \equiv \left({}_{FN}\delta_{DU} , {}_{FN}\delta_{DR} , {}_{FN}\delta_{DD} , {}_{FN}\delta_{DL} \right)^T := $$

$$ \left(\zeta_D - \xi_D , \eta_D - \xi_D , -\zeta_D - \xi_D , -\eta_D - \xi_D \right)^T $$

Equation 3.10-2

The actuators at the core of the fin model are treated as a closed loop analogue system avoiding the internal detail associated with high frequency controller and torque motor effects. Each fin actuator model shown in Figure 3-57 is identical with randomly varying error characteristics.

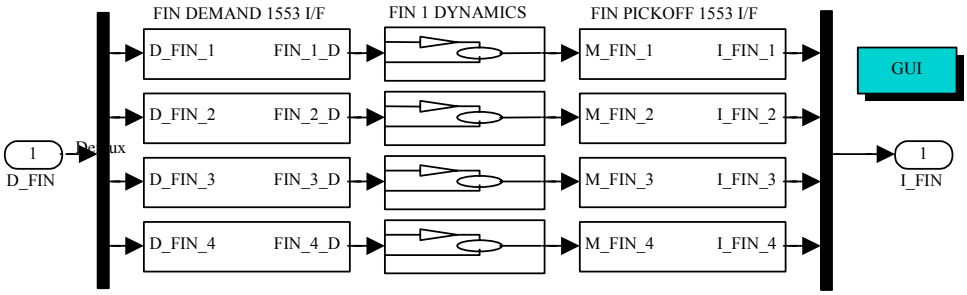

Figure 3-57 : Fin Actuator Model

The fins are locked until the missile has reached a safe aerodynamic speed to prevent missile over-rotation. Once released, the fin demand limit expands linearly with speed until Mach 1 - treated as a physical limit in the model. The measured fin deflections are re-combined for closed loop guidance and state observer purposes,

$$ {}_{AP}\underline{\tilde{\delta}} := $$

$$ \left(\frac{-{}_{FN}\tilde{\delta}_U - {}_{FN}\tilde{\delta}_D - {}_{FN}\tilde{\delta}_R - {}_{FN}\tilde{\delta}_L}{4} , \frac{{}_{FN}\tilde{\delta}_R - {}_{FN}\tilde{\delta}_L}{2} , \frac{{}_{FN}\tilde{\delta}_U - {}_{FN}\tilde{\delta}_D}{2} \right)^T $$

Equation 3.10-3

3.10.3 Fin Position Demands

The fin demands pass through a signed 16 bit digital interface at a frequency ($_{FN}f_O$) of 400 Hz (clock 9). The measurements are subject to an interface range limit of 24° and a one-cycle transmission delay, exactly the same as the output interface described in §3.10.6.

$$ \underline{\delta}_D := {}^{IF}\underline{\varphi}_{TD}\left({}^{IF}\underline{\varphi}_{Q}\left({}^{IF}\underline{\varphi}_{LIM}\left({}^{IF}\underline{\varphi}_{ZOH}\left({}_{FN}\underline{\delta}_D , {}_{FN}f_O \right) \right) \right) \right) $$

Equation 3.10-4

Application of the input interface errors is controlled by the same bits as the output interface; bits 27-30 of *MS_FN_ER*. The digital fin demands pass

through a phase compensation filter, followed by a 2nd order, 50 Hz Butterworth filter prior to D-to-A conversion.

$$ {}^{D}\underline{\delta}_{D} \coloneqq \varphi_{AI}\left(\varphi_{DDL}\left(\underline{\delta}_{D}, 2 \cdot {}_{FN}\zeta_{C} \cdot {}_{FN}\omega_{C} + {}_{FN}t_{C}, {}_{FN}t_{C} \right) \right) $$

Equation 3.10-5

The compensation filter characteristics are matched to the phase loss due to the time delay and 2nd order actuator dynamics that follow,

$$ \left({}_{FN}\zeta_{C}, {}_{FN}\omega_{C}, {}_{FN}t_{C} \right) \coloneqq \left({}_{FN}\zeta_{D2L}, {}_{FN}\omega_{D2L}, {}_{FN}t_{TD} \right) $$

Equation 3.10-6

3.10.4 Fin Position Measurements

Digital fin demands are converted to analogue using a 12 bit ADC subject to 3 bits of noise with a sampling rate and range matched to the input interface. Fin ADC errors are controlled by the same bits as the DAC, i.e. bits 21-24, an anti-imaging filter replacing the A/A filter,

$$ {}^{A}\underline{\delta}_{D} \coloneqq {}^{DA}\underline{\varphi}_{LIM}\left({}^{DA}\underline{\varphi}_{Q}\left({}^{D}\underline{\delta}_{D} \right) + {}^{DA}\underline{\varphi}_{QN} \right) $$

Equation 3.10-7

The analogue demands are subject to a time delay, rate limit, 2nd order dynamics representing the output from analogue loop closure, scale factor errors and a physical limit to fin travel matched to the output interface. The analogue models are updated at the fin reference rate ($_{FN}f_R$) of 2 kHz.

$$ {}^{A}\underline{\tilde{\delta}} \coloneqq $$

$$ \underline{\varphi}_{LIM}\left(\underline{\varphi}_{SF}\left(\underline{\varphi}_{D2L}\left(\underline{\varphi}_{RL}\left(\underline{\varphi}_{TD}\left({}^{A}\underline{\delta}_{D} \right) \right), {}_{FN}\zeta_{D2L}, {}_{FN}\omega_{D2L} \right) + {}_{FN}\underline{\delta}_{B} + {}_{FN}\underline{\delta}_{RN} \right) \right) $$

Equation 3.10-8

A time delay of 0.005 s is followed by an angular rate limit of 600°/s. The closed analogue loop, damping ratio ($_{FN}\zeta_{D2L}$) is 0.6, with a natural frequency dependent on the aerodynamic loading,

$$ {}_{FN}\omega_{D2L} \coloneqq \omega_{NL} + \left(\omega_{NH} - \omega_{FL} \right) \cdot \frac{\left| \delta \right|}{\delta_{L}} \cdot \left(\frac{\dot{P}_{o,m}}{V_{MAX}} \right)^{2} $$

Equation 3.10-9

The bandwidth of the actuator under no load ($_{FN}\omega_{D2L}$) and full aerodynamic loading (ω_{FH}) is 250 rad/s and 100 rad/s respectively. The maximum speed expected (V_{MAX}) and maximum fin deflection (δ_L) are typically 1200 m/s

and 24° respectively. The constant bias ($_{FN}\delta_B$) is initialised from a Gaussian distribution with a deviation of 0.2°. The Gaussian noise has a PSD of $25x10^{-6}$ deg^2/Hz at the reference frequency, equivalent to 0.1° at 400 Hz. The constant, quadratic and asymmetric scale factor deviations are set to 0.003, 0.001 and 0.001 respectively. An additional hard travel limit equal to the output interface range is controlled by bit 11 of *MS_FN_ER*.

$$\underset{\sim}{\tilde{\delta}} \coloneqq {}^{AD}\underline{\varphi}_{LIM}\left({}^{AD}\underline{\varphi}_{Q}\left({}^{AD}\underline{\varphi}_{ZOH}\left(\underline{\varphi}_{AA}\left({}^{A}\underset{\sim}{\tilde{\delta}} \right) \right), {}_{FN}f_O \right) + {}^{AD}\varphi_{QN} \right)$$

Equation 3.10-10

The analogue measurement is converted into digital form using a 100 Hz, 4th order Butterworth filter, and a 12 bit ADC subject to 3 bits of noise with a sampling rate and range matched to the output interface.

3.10.5 Sensor Limitiations

Provision of fin deflection measurements at the output interface depends on:

- User measurement selection (*MS_MSAV2* bits 7-10 cleared)
- Physical travel limiting (*MS_FN_ER* bit 15 is set)
- Angular rate limiting (*MS_FN_ER* bit 16 is set)

When active, if any of these limitations are violated, bits 7-10 in the measurement ready flag *MS_MSRY2* are cleared. Failure to provide a measurement at the user's request is indicated by setting bits 0-3 of *MS_FN_VF*, one per fin. If the rate limits of 24° and 600°/s are exceeded bits 4-7 and bits 8-11 of *MS_FN_VF* are set respectively.

3.10.6 Output Interface

The measured fin positions pass through a signed 16 bit digital interface at a frequency ($_{FN}f_O$) of 400 Hz (clock 9). The measurements are subject to an interface range limit of 24° and a one-cycle transmission delay.

$${}_{FN}\underset{\sim}{\tilde{\delta}} \coloneqq {}^{IF}\underline{\varphi}_{TD}\left({}^{IF}\underline{\varphi}_{Q}\left({}^{IF}\underline{\varphi}_{LIM}\left({}^{IF}\underline{\varphi}_{ZOH}\left(\underset{\sim}{\tilde{\delta}} \right) \right) \right) \right)$$

Equation 3.10-11

3.11 NAVSTAR Global Positioning Service

3.11.1 Review

Hyperbolic radio navigation systems such DECCA were introduced in the UK in the early 40s. Others followed that are still used today:

- Very High Frequency (VHF) Omni-Range/Ultra High Frequency (UHF) Direction Measuring Equipment (VOR/DME),
- Tactical Air Navigation (TACAN),
- OMEGA, Long Range Navigation (LORAN)

These systems provide position fixes over 70 km to 150 km that are accurate to 50 m to 8 km, using transmission frequencies between 0.1-1 GHz. In the mid-70s the USA DoD proposed a satellite navigation system capable of measuring position and height over the earth's surface with a spherical accuracy of 100 m (rms), down to 15 m for military use. NAVSTAR GPS is now a mature world-wide, all-weather, day or night, satellite based radio navigation system providing accurate range and range-rate measurements between the a missile receiver and a number of "visible" satellites. These data are filtered to obtain geodetic Position-Velocity-Time (PVT) solutions. GPS comprises 3 segments: a 24-satellite constellation, a receiver, and a control comprising a centre at Colorado Springs (USA), 5 monitoring stations, and 4 upload stations that providing updated Ephemeris and atomic clock data every 8 hours. The system became fully operational in 1994 with block IIR satellite launches commencing in 1995 enhancing the current system by introducing communication between the satellites. The inter-satellite communication improves autonomy by reducing accuracy degradation if up-linked Ephemeris data corrections are suspended.

The satellites travel at a radius of 20,183 km, orbiting the Earth twice per sidereal day (23hrs 56min 4.01s), i.e. they pass over the same point on the Earth approximately 4 minutes earlier each day. The satellites are equally apportioned to 6 orbital planes inclined at 55° to the equatorial plane. The position of the 4 satellites in an orbital plane depends on prevailing geo-political considerations. For research purposes a symmetric constellation is provided in which the satellites are 90° apart, with the satellites in the orbit to the east 40° ahead.

Each satellite transmits a precise P-code and an acquisition C-code Pseudo-Random Binary Sequence (PRBS). These are superimposed at 10.23 MHz and 1.023 MHz onto two carrier waves L1 and L2 (P-code only) operating at 1575.42 MHz and 1227.60 MHz. The Precise Positioning Service (PPS) PRBS repeats every 7 days and is reset Saturday midnight GMT, whereas the Civil Positioning Service (CPS) PRBS repeats every millisecond. The CPS, although less accurate, is easier to acquire compared with the accurate PPS which is encrypted and requires USA DoD authorisation to acquire the encryption key.

GPS receivers track four or more satellites, demodulating their carrier waves to extract the PRBS that are correlated with stored PRBS sequences. Autocorrelation techniques extract the time delay between the two PRBS representing the distance of the receiver from each satellite. The time delays contain a common receiver clock bias hence the term pseudo-range. The receiver also tracks the Doppler shift in the carrier waves from each satellite from which pseudo-range rate is extracted using tracking bandwidths of the order of 5-6 kHz.

Each satellite transmits its navigation message on the carrier wave at 50 Hz, the total transmission time being 12.5 minutes. Amongst other things, the message contains Ephemeris data defining the satellite's position with respect to the earth, correction factors for the atomic clock data, and details of the ionosphere's composition.

Modern receivers track all "visible" satellites, usually providing between 6-11 pseudo-measurements using an Earth screening angle of 7.5°. These data are processed in an over-specified least-squares solution that improves the systems tolerance to high receiver dynamics and lower SNRs. Those that do not, resort to optimum satellite selection procedures attempt to minimise the Global Dilution Of Precision (GDOP), Kihara[K.8], Stein[S.19]. Whichever method of triangulation is used to fix the receiver's position a minimum of 4 satellites is required to estimate the clock bias common to each pseudo-range measurement. Receivers capable of tracking both carrier waves correct the pseudo-measurements for atmospheric transmission delays, whereas civil equipment tends to track only a single frequency computing the required correction from Ephemeris data. The receiver's position with respect to the Earth is converted to the WGS 84 ellipsoid using the Molodenskii transform using pre-programmed incremental translation and ellipsoidal parameters for the local area.

The PPS rms errors are typically 10-15 m and 0.1-0.2 m/s and those for CPS are purposely degraded to give 50-100 m and 0.3-0.5 m/s when Selective Availability (SA) is disabled. SA is the term used when the satellite clock frequencies are jittered which reduces the accuracy of the CPS whilst still meeting its stated design accuracy.

In "loosely coupled" INS/GPS systems both "sensors" work independently. In "closely coupled" systems INS PVA data is used to speed up signal acquisition and to reduce the carrier and code tracking loop bandwidths making GPS less susceptible to jamming. Cold starts can take several minutes whereas aided starts provide the first fix within about 30 s.

As the number of satellites increased to the full compliment of 24 in the early 90s, GPS black box geodetic PVT measurements were combined with INS and terrain data leading to the integrated TRN now used in modern fighter aircraft and cruise missiles. No other sensor has had such an impact on navigation and mid-course guidance, however, several factors have prevented GPS from replacing TRN entirely:

- US ownership has lead to doubts over satellite availability
- SA is applied unpredictably, and at levels that cause the system to degrade beyond the stated design accuracy, although the US have agreed to permanently disable this facility.
- Worries about the ease with which the low power carrier waves can be jammed
- The vulnerability of the satellites to attack

Despite these concerns, GPS remains the navigation reference system for the foreseeable future. Commercial considerations concerning INS/GPS integration have forced a "black box" solution on weapon system designers that delivers a PVT solution rather than direct access to the raw pseudo-measurements. The latter are preferred for state observation since the pre-filtered PVT solution contains non-Gaussian measurement errors. For agile airframes the availability of sufficient satellites for triangulation is uncertain due to tracking difficulties, Earth or self-screening. In these circumstances a limited number of pseudo-measurements could still be used to constrain the position and velocity error along the satellite LOS.

3.11.2 Description

The GPS model shown in Figure 3-58 outputs geodetic position and velocity providing that at least 4 satellites are available after applying self screening, dynamic limitations, and a 7.5° atmospheric horizon.

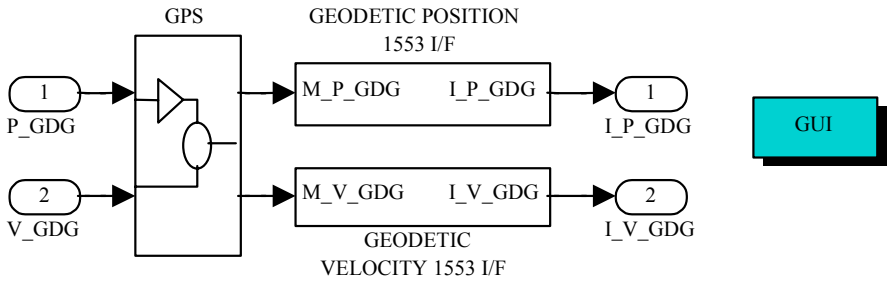

Figure 3-58 : NAVSTAR GPS Model

Three triangulation options are provided. 4 satellites can be selected using Gram-Smidt orthogonalisation minimising the enclosed tetrahedron volume between the satellites and the receiver, and hence the Global Dilution Of Precision (GDOP), Higgins[H.13]. Alternatively, the GDOP is computed for all combinations of 4 satellites from the "visible" satellite set and the combination with the lowest GDOP selected. Finally, all the "visible" satellites are used in an over-specified least-squares solution.

Closely coupled GPS receiver aiding and terrain obscuration for nap-of-the-earth navigation purposes are not included in this model. The model is flexible enough to cope with both PPS and CPS operation at either 1 Hz or

10 Hz. The model is based on information from STANAG 4294[N.8] and papers on Navigation (GPS) published by the Institute Of Navigation[N.9].

3.11.3 Satellite Ephemeris Data

Five monitoring stations have been set up in various parts of the world to continuously track the orbit of each satellite. The orbital data collected is passed to a master control station where precise values of each satellite's orbital "constants" for the next two weeks are predicted using Kalman Filtering techniques. The 4 ground transmission stations up-link a fresh set of predicted orbital constants, atomic clock corrections and atmospheric composition to each satellite as they pass overhead. These can be used with confidence for approximately 1.5 hrs, Dierendonck(D.17). The Ephemerides contains corrections to these constants to account for solar radiation pressure, polar wander, earth wobble, gravitational distortion due to the Sun and Moon, etc.

The model is based on a 24 satellite symmetrical constellation that is never found in practice but gives an even coverage over the earth surface without the need to determine satellite position from their Ephemerides. In Appendix G, whilst discussing Newton's universal law of gravitation, it was muted that position in space requires 6 constants of integration. In practice each satellite's position is defined in terms of 5 of the 6 classical Keplerian orbital parameters transmitted in the Navigation message together with the time of applicability (t_{REF}) accurate to 1 s:

Semi-Major Axis ($\sqrt{P_{r,s}} := \sqrt{20183000\ m^{1/2}}$)

The semi-major axis is the orbital radius of the satellite at the reference time measured from the earth's geometric centre. This is transmitted in terms of its square root to preserve accuracy. The navigation message also contains correction coefficients and therefore the semi-major axis,

$$P_{r,s} := \left(\sqrt{P_{r,s}} \right)^2 + C_{rs} \cdot \sin\left(2 \cdot \varphi_S \right) + C_{rc} \cdot \cos\left(2 \cdot \varphi_S \right)$$

Equation 3.11-1

Where (φ) is the argument of latitude defined later.

Eccentricity (e_S)

The eccentricity of the satellite orbit. Although the orbits are supposed to be circular ($e_S := 0$), orbital perturbations lead to values of some 0.005.

Orbital Inclination (ι_O)

The orbital inclination of the orbital plane relative to the equatorial plane at the reference time is nominally 55°. The navigation message contains the inclination angular rate and correction coefficients,

$$\iota_S := \iota_O + i_S \cdot \left(t - t_{REF} \right) + C_{is} \cdot \sin\left(2 \cdot \varphi_S \right) + C_{ic} \cdot \cos\left(2 \cdot \varphi_S \right)$$

Equation 3.11-2

Argument of Perigee (ω_S)

The perigee of a satellite's orbit is the point at which the satellite is closest to the centre of the Earth with respect to the ascending node.

Right Ascension (Longitude) of the Ascending Node (Ω_O)

The right ascension of the ascending node is the angle from $\underline{X}^C$ to the satellite's ascending node in the equatorial plane. This is the point at which the satellite crosses the equatorial plane when travelling from south to north measured positive eastwards at the reference time. The navigation message contains the rate of right ascension and correction coefficients accounting for earth wobble and polar wander.

$$\Omega_S\left(t \right) := \Omega_O + \left(\dot{\Omega}_O - \omega_{C,E}^E \right) \cdot \left(t - t_{REF} \right) - \omega_{C,E}^E \cdot t_{REF}$$

Equation 3.11-3

Mean Anomoly (M_O)

The 6th classical Keplerian parameter is the Time-of-Perigee Passage, the time when the satellite last passed through the perigee. This is replaced in GPS by the Mean Anomaly at the reference time to improve the stability of the algorithms for near circular orbits. The Mean Anomaly is the phase of a satellite in its circular orbit measured from the ascending node at the reference time when it is travelling at a uniform angular velocity.

3.11.3.1 Satellite Position Derived from Ephemeris Data

The GPS model superimposes errors on the LOS range caused by the extraction of satellite position from Ephemeris data. It is therefore useful to understand how satellite position is derived. One of the simplest methods amongst those available is successive substitution in Kepler's transendental equation, Carvalho[C.4]. This relates the True Anomaly to the relative orbital position known as the Eccentric Anomaly (E_S),

$$M_S := E_S - e_S \cdot \sin\left(E_S \right)$$

Equation 3.11-4

Since the orbital eccentricity is small, Duris[D.5] and Dailey [D.6] solve this equation by iteration,

$$\left(E_S \right)_{k+1} := E_S + e_S \cdot \sin\left(E_S \right)_k \quad \text{where} \quad \left(E_S \right)_0 := M_O$$

Equation 3.11-5

Dierendonck[D.17] reports on 7 iterative schemes, including this one, assessing their performance in terms of accuracy, clarity, duty cycle, and memory requirements. This algorithm takes the least memory, and is average for computational speed taking 41 ms/iteration; the other algorithms considered lie in the range [13,55] ms. The navigation message contains correction coefficients for the argument of latitude,

$$\varphi_S \coloneqq \omega_S + 2 \cdot \tan^{-1}\left(\sqrt{\frac{1+e_S}{1-e_S}} \cdot \tan\left(\frac{E_S}{2} \right) \right) + C_{us} \cdot \sin\left(2 \cdot \varphi_S \right) + C_{uc} \cdot \cos\left(2 \cdot \varphi_S \right)$$

Equation 3.11-6

From STANAG 4294, the satellite position in the Orbital and Earth frames,

$$\underline{P}_s^O \coloneqq P_{r,s} \cdot \left(1 - e_S \cdot \cos\left(E_S \right) \right) \cdot \begin{pmatrix} \cos\left(\varphi_S + \Omega_S \right) \\ \sin\left(\varphi_S + \Omega_S \right) \\ 0 \end{pmatrix}$$

Equation 3.11-7

$$\underline{P}_s^E \coloneqq \begin{bmatrix} \cos\Omega_S & -\sin\Omega_S \cdot \cos\iota_S & 0 \\ \sin\Omega_S & \cos\Omega_S \cdot \cos\iota_S & 0 \\ 0 & \sin\iota_S & 0 \end{bmatrix} \cdot \underline{P}_s^O$$

Equation 3.11-8

The time taken for signals to travel between the receiver and each satellite is obtained in the receiver by auto-correlating identical satellite and receiver PRBS. The correlation time is the corrected for satellite clock bias and relativistic effects, the remainder forms the pseudorange since the correlation time includes the receiver clock bias. The navigation message provides the coefficients (a,b,c) used to correct the satellite clock bias, and the receive itself applies the relativistic correction,

$$\delta_{CK} \coloneqq a + b \cdot \left(t - t_{REF} \right) + c \cdot \left(t - t_{REF} \right)^2 + 2 \cdot \underline{P}_{g,s} \cdot \dot{\underline{P}}_{g,s} \,/\, c^2$$

Equation 3.11-9

$$\frac{2 \cdot \underline{P}_{g,s} \cdot \dot{\underline{P}}_{g,s}}{c^2} \equiv -\frac{2 \cdot e_S \cdot \sqrt{\mu_G \cdot P_{r,s}}}{c^2} \cdot \sin\left(E_S \right)$$

Equation 3.11-10

The universal navigation constant (G), and the Earth mass (M) define the WGS 84 gravitational constant (μ_G),

$$\mu_G \coloneqq G \cdot M \coloneqq 3.986005 \times 10^{14}$$

Equation 3.11-11

Transmission quantisation errors and the use of 2nd order satellite clock corrections, introduces a pseudorange error of < 0.1 m in the first 1.5 hrs after a navigation message up-link. Thereafter, the degradation reaches 90 m after 3.5 hrs, Dierendonck[D.17].

3.11.4 Reference Pseudo-Data

From Kepler's laws, the satellite period (T_S) is related to its orbital rate (ω_S),

$$T_S \coloneqq \frac{2 \cdot \pi}{\omega_S} \coloneqq 2 \cdot \pi \sqrt{\frac{P_{r,s}^3}{\mu_G}}$$

Equation 3.11-12

The satellite period is revised using the correction for the computed orbital rate ($\Delta\omega_S$) in the Ephemeris data. For simplicity, 24 satellites are modelled travelling in circular orbits about the Earth centre at a radius ($P_{r,s}$) of 20_183 km with an orbital speed (ω_S) of 0.00833333 rad/s. The position of the j'th satellite in the i'th orbital plane is defined by the Mean Anomaly with respect to the rising node (κ_{ij}),

$$\forall (i, j) : i = [1(1)6] ; j = [1(1)4] \Rightarrow$$

$$\kappa_{ij} \coloneqq \omega_S \cdot t_m + \frac{\pi}{6} \cdot (2 \cdot i + 3 \cdot j - 5)$$

Equation 3.11-13

(t_m) is the time after midnight General Mean Time (GMT). The position of a particular satellite in the Orbital frame,

$$\underline{P}_{r,s}^O \coloneqq P_{r,s} \cdot (\cos\kappa \quad , \quad \sin\kappa \quad , \quad 0)^T$$

Equation 3.11-14

A satellite's position with respect to the Celestial frame is therefore,

$$\underline{P}_s^C \coloneqq T_O^C \cdot \underline{P}_s^O$$

Equation 3.11-15

The position of the receiver with respect to the Celestial frame is,

$$\underline{P}_g^C := T_E^C \cdot \left(\underline{P}_o^E + T_A^E \cdot \left(\underline{P}_m^A + T_B^A \cdot \underline{P}_g^B \right) \right)$$

Equation 3.11-16

The reference LOS range to each satellite is therefore,

$$P_{g,s}^C := \left\| T_O^C \cdot \underline{P}_s^O - T_E^C \cdot \left(\underline{P}_o^E + T_A^E \cdot \left(\underline{P}_m^A + T_B^A \cdot \underline{P}_g^B \right) \right) \right\|$$

Equation 3.11-17

The velocity of each satellite with respect to the missile GPS receiver is,

$$\underline{V}_{g,s}^C := \underline{V}_s^C - \underline{V}_g^C$$

Equation 3.11-18

Expressed with respect to the "natural" co-ordinate systems,

$$\underline{V}_{g,s}^C := T_O^C \cdot \underline{V}_s^O - T_E^C \cdot \left(\underline{V}_o^E + T_A^E \cdot \left(\underline{V}_m^A + T_B^A \cdot \underline{V}_g^B \right) \right)$$

Equation 3.11-19

The inertial velocity of each satellite expressed in the Orbital frame is,

$$\underline{V}_s^O := P_{r,s} \cdot \omega_{OS} \cdot \begin{pmatrix} -\sin\kappa & \cos\kappa & 0 \end{pmatrix}^T$$

Equation 3.11-20

The inertial velocity components of the receiver are,

$$\left(\underline{V}_o^E \quad , \quad \underline{V}_m^A \quad , \quad \underline{V}_g^B \right) :=$$

$$\left(\underline{\omega}_{C,E}^E \times \underline{P}_o^E \quad , \quad \dot{\underline{P}}_m^A + \underline{\omega}_{C,E}^A \times \underline{P}_m^A \quad , \quad \underline{\omega}_{A,B}^B \times \underline{P}_g^B \right)$$

Equation 3.11-21

Combining these velocity terms,

$$\underline{V}_{g,s}^C := P_{r,s} \cdot \omega_{OS} \cdot \begin{pmatrix} -\sin\kappa & , & \cos\kappa & , & 0 \end{pmatrix}^T - \cdots$$

$$\cdots - T_E^C \cdot \left(\underline{\omega}_{C,E}^E \times \underline{P}_o^E + T_A^E \cdot \left(\dot{\underline{P}}_m^A + \underline{\omega}_{C,E}^A \times \underline{P}_m^A + T_B^A \cdot \left(\underline{\omega}_{A,B}^B \times \underline{P}_g^B \right) \right) \right)$$

Equation 3.11-22

From §17.6 the reference LOS rates are,

$$V_s^{XL} \;:=\; \left(T_C^L \cdot \underline{V}_{g,s}^C \right) \bullet \hat{\underline{i}} \;\equiv\; \underline{V}_{g,s}^C \bullet \underline{P}_{g,s}^C \;/\; P_{g,s}$$

Equation 3.11-23

3.11.5 Satellite Obscuration

Earth screening in Figure 3-59 shows the geometry involved in atmosphere obscuration of the satellite LOS. The figure portrays nap-of-the-earth navigation where $P_{d,g} << P_{r,d}$. Points (d) and (g) are assumed to be coincident for geometrical analysis.

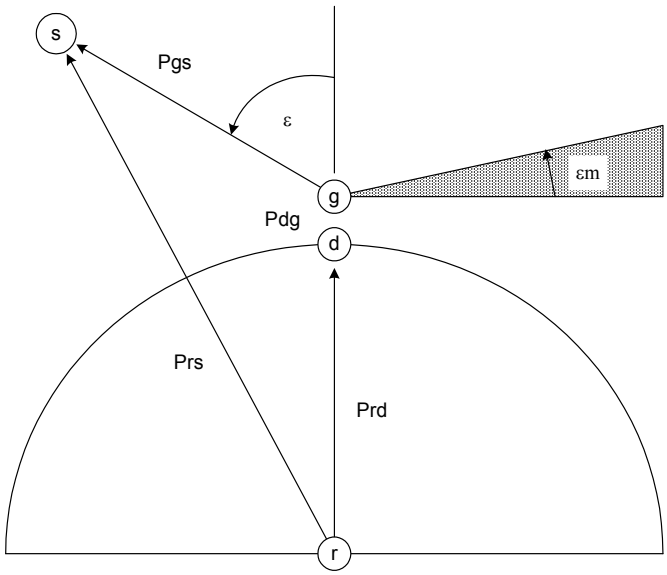

Figure 3-59 : GPS Satellite Obscuration Model

For a spherical Earth, the angle between the zenith ($\underline{P}_{r,g}$) and each satellite LOS ($\underline{P}_{g,s}$),

$$\varepsilon \;:=\; \cos^{-1}\left(\frac{\underline{P}_{g,s}^C \bullet \underline{P}_g^C}{P_{g,s} \cdot P_{r,g}} \right)$$

Equation 3.11-24

When satellites are close to the visible horizon defined by screening angle (ε_m) of 7.5°, the error induced by the additional delay in transmission is avoided by removing the offending satellites from the navigation solution. A satellite is only "visible" if,

$$\varepsilon \;<\; \pi - \sin^{-1}\left(\frac{P_{r,d}}{P_{r,d} + P_{d,g}^{ZG}} \right) - \varepsilon_m$$

Equation 3.11-25

$$\varepsilon \quad < \quad \pi - \sin^{-1}\left(\frac{P_{r,d}}{P_{r,o} + P_m^{ZA} + T_B^A \cdot \left(P_g^B \quad 0 \quad 0 \right)^T \bullet \hat{\underline{k}}} \right) - \varepsilon_m$$

Equation 3.11-26

For self-screening, with the receiver on the upper surface of the missile in the plane spanned by $\underline{X}^B$ and $\underline{Z}^B$ the position of a satellite expressed in the Missile Body frame,

$$\underline{P}_{g,s}^B \quad := \quad T_A^B \cdot T_E^A \cdot T_C^E \cdot \underline{P}_{g,s}^C$$

Equation 3.11-27

A satellite's transmission can only be tracked if it is in the hemisphere bounded by the plane spanned by $\underline{X}^B$ and $\underline{Y}^B$ and excluding $\underline{Z}^B$, i.e. if the z-component of this vector is less than zero.

3.11.6 LOS Pseudo-Measurements

GPS is so different compared with the other sensors that its error control word *MS_GP_ER* does not conform to the standard defined in Table 3-6, apart from the errors superimposed by the output interface.

3.11.6.1 Pseudorange

The receiver's crystal clock provides a crude measure of time compared with the satellite's atomic clock. As there is no synchronisation between the two, an unknown time bias is introduced into each LOS range. The LOS range is corrupted by a range equivalent clock error (ΔR_{CK}), and by satellite position and atomic clock errors, atmospheric effects (ΔR_{TX}), and receiver errors (ΔR_{RX}). This partitioning means that multiple receivers can be modelled in pre-launch aircraft and missile applications. When combined they are referred to as the User Equivalent Range Error (UERE) ($\Delta P_{g,s}$),

$$\tilde{P}_{g,s} \quad := \quad P_{g,s} + \Delta P_{g,s} \quad := \quad P_{g,s} + \Delta R_{TX}(i, j) + \Delta R_{RX} + \Delta R_{CK}$$

Equation 3.11-28

The receiver clock effective range error (ΔR_{CK}) is common to each pseudo-measurement and contains a constant bias and a random walk, Wong[W.7].

$$\Delta R_{CK} \quad := \quad c \cdot \left(\Delta t_{RX0} + \varphi_{DIL}\left(N(0, \sigma_{PCC}), 1 / \tau_{PC} \right) \right)$$

Equation 3.11-29

The constant bias (Δt_{RX0}) is a function of the satellite pulse modulation frequency and is initialised from a uniform distribution in the range $\pm$ 0.1 μsec. The clock drift is modelled as a random walk with a correlation

time (τ_{PC}) of 500 s, and an output of (σ_{PCC}) of 10^{-12} s. The effective range error due to the receiver,

$$\Delta R_{RX} \coloneqq B_{PR} + N\left(0, \sigma_{PRR}\right) + \varphi_{RX}$$

Equation 3.11-30

$$\varphi_{RX} \coloneqq$$

$$\varphi_{D1L}\left(N\left(0, \sigma_{PRFC}\right), 1 / \tau_{PRFC}\right) + \varphi_{D2L}\left(N\left(0, \sigma_{PRSW}\right), \zeta_{PRSW}, \omega_{PRSW}\right)$$

Equation 3.11-31

For each satellite,

$$\Delta R_{TX} \coloneqq B_{PS} + N\left(0, \sigma_{PSR}\right) + \varphi_{TX} + \xi_{SA}$$

Equation 3.11-32

$$\varphi_{TX} \coloneqq$$

$$\varphi_{D1L}\left(N\left(0, \sigma_{PFC}\right), 1 / \tau_{PFC}\right) + \varphi_{D2L}\left(N\left(0, \sigma_{PWB}\right), \zeta_{PWB}, \omega_{PWB}\right)$$

Equation 3.11-33

Although this model covers the most of the errors found in GPS, identifying individual error contributions is difficult. Some appreciation of the complexity of GPS error modelling is provided in the work of Feess[F.4]. The Gauss-Markov processes here all have a common correlation time of 7200 s associated with the mean time between navigation data up-links. By comparison most missile flight times are relatively short and these correlated errors may be treated as constant biases, Parkinson[P.7] and Kao[K.9]. The random and time independent bias contributions to the effective range error are listed in Table 3-22.

Table 3-22 : GPS Random Errors and Biases

Random Errors	rms (m)	Time Independent Biases	rms (m)	
Satellite clock stability	2.7	Satellite orbital perturbations	1.0	
Tropospheric delay residuals	2.0	Satellite Ephemeris prediction	2.5	
Receiver multipath errors	1.2	Ionospheric delay compens'n	2.3	
Receiver noise and resolution	1.5	Receiver process noise	1.0	
Receiver miscellaneous errors	0.9			

Combining these errors gives a satellite and receiver bias, (B_{PS}) and (B_{PR}) of 3.5 m and 1.0 m respectively (the receiver bias is embodied in its clock error). The satellite and receiver noise levels (σ_{PSR}) and (σ_{PRR}) are 3.4 m

and 2.1 m. The overall UERE is the rss combination of these biases and noise errors, hence the (σ_{UERE}) is 5.4 m excluding clock and SA errors.

3.11.6.2 Atmospheric Transmission Induced Position Errors

In military receivers the two carrier frequencies are used to remove most of the transmission errors in the pseudo-range measurements caused when the signals transmitted collide with free-electrons in the ionosphere,

$$\widetilde{P}_{g,s} := \frac{\widetilde{P}_{g,s}(f_1) - (f_2/f_1)^2 \cdot \widetilde{P}_{g,s}(f_2)}{1 - (f_2/f_1)^2}$$

Equation 3.11-34

The residual error after dual frequency correction is given in Table 3-22. This effect depends on the Sun's intensity and modelling it is difficult. For single frequency receivers a standard model is provided whose parameters are updated in the navigation message. Transmission errors through the troposphere are caused by signals travelling at less than the speed-of-light (c). Greenspan[G.17] proposes a simple receiver correction model leaving only a small residual error that depends only on the elevation of the satellite from the local horizontal (ε), and the missile's geodetic height,

$$B_{TROP} := c \cdot \left(\frac{2.4224}{0.026 + \cos\varepsilon} \right) \cdot \exp\left(-0.13345 \cdot P_{d,m}^{ZG} \right)$$

Equation 3.11-35

Numerous correction models have been developed of great complexity, many using the Ephemerides, Feess[F.5] and Klobuchar[K.10]. If a more complex correction model is needed, consider Carvahlo's[C.4] simplification of the Goad[G.16] model which estimates the tropospheric range error to be 5-90 m, with a residual error of [0.25,0.45] m.

3.11.6.3 Pseudorange Rates

The pseudorange rate from the missile to each satellite is given by,

$$\widetilde{V}_{g,s}(i,j) := V_{g,s}(i,j) + \Delta RR_{TX}(i,j) + \Delta RR_{RX}(i,j) + \Delta RR_{CK}$$

Equation 3.11-36

The receiver clock effective range rate error (ΔRR_{CK}) is common to each pseudo-measurement and contains a constant bias and Gaussian noise,

$$\Delta RR_{CK} := c \cdot \left(\Delta\dot{t}_{PC0} + N(0, \sigma_{VCR}) \right)$$

Equation 3.11-37

A constant drift rate of 10^{-9} s/s is typical of a quartz clock, Carvalho[C.4]. The effective range rate error due to the receiver,

$$\Delta RR_{RX} \coloneqq B_{VR} + N\left(0, \sigma_{VRR}\right) + \dot{\varphi}_{RX}$$

Equation 3.11-38

$$\dot{\varphi}_{RX} \coloneqq$$

$$\varphi_{D1L}\left(N\left(0, \sigma_{VRFC}\right), 1/\tau_{VRFC}\right) + \varphi_{D2L}\left(N\left(0, \sigma_{VRSW}\right), \zeta_{VRSW}, \omega_{VRSW}\right)$$

Equation 3.11-39

For each satellite,

$$\Delta RR_{TX} \coloneqq B_{VS} + N\left(0, \sigma_{VSR}\right) + \dot{\varphi}_{TX} + \dot{\xi}_{SA}$$

Equation 3.11-40

$$\dot{\varphi}_{TX} \coloneqq$$

$$\varphi_{D1L}\left(N\left(0, \sigma_{VSFC}\right), 1/\tau_{VSFC}\right) + \varphi_{D2L}\left(N\left(0, \sigma_{VSSW}\right), \zeta_{VSSW}, \omega_{VSSW}\right)$$

Equation 3.11-41

Although this model covers all the typical errors affecting pseudo-range rates, only a Gaussian clock error with an rms value of 0.1 m/s at 1 Hz is implemented.

3.11.6.4 Selective Availability

SA affects only the CPS and is the dominant error source - when using the PPS in the simulation SA must be de-activated. The following 2nd order Gauss-Markov model of SA is from RTCA[R.15] for measurements at 1 Hz,

$$\begin{pmatrix} \xi_{SA} \\ \dot{\xi}_{SA} \end{pmatrix}_{k+1} \coloneqq [A] \cdot \begin{pmatrix} \xi_{SA} \\ \dot{\xi}_{SA} \end{pmatrix}_{k} + [B] \cdot \begin{pmatrix} N_R(0,1) \\ N_{RR}(0,1) \end{pmatrix}_{k}$$

Equation 3.11-42

$$[A] \coloneqq \begin{bmatrix} 0.9999284 & 0.9915387 \\ -0.0001428 & 0.9831014 \end{bmatrix}_{1Hz} \equiv \begin{bmatrix} 0.9999993 & 0.0999152 \\ -0.0000144 & 0.9983037 \end{bmatrix}_{10Hz}$$

Equation 3.11-43

$$[B] := \begin{bmatrix} 0.0146771 & 0.0252060 \\ 0 & 0.0504133 \end{bmatrix}_{1Hz} \equiv \begin{bmatrix} 0.0014677 & 0.0002469 \\ 0 & 0.0050800 \end{bmatrix}_{10Hz}$$

Equation 3.11-44

The equivalent model for 10 Hz operation was obtained from MATLAB using a ZOH conversion of the 1 Hz case. Typical 1 Hz PV errors are shown in Figure 3-60.

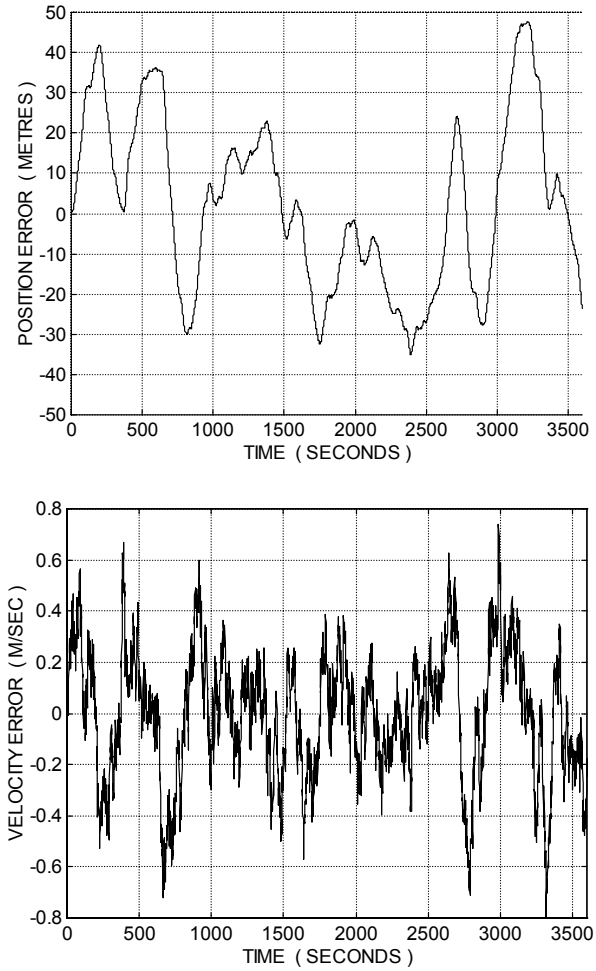

Figure 3-60 ; Selective Availability PV Errors (1 Hz Update)

This model was used by Rao[R.14] to show that the performance of a Kalman filter observer is degraded by non-Gaussian measurement errors. He then when on to demonstrate that estimating bias and bias rate correction states with appropriate dynamics improves the PV estimates considerably.

3.11.7 Receiver Tracking Limitations

Under extreme dynamic conditions the receiver tracking loops can lose the satellite carrier signal. The LOS velocity to each satellite is given in §3.11.4 and the LOS acceleration of each satellite with respect to the receiver by,

$$\underline{A}_{g,s}^{C} := \underline{A}_{s}^{C} - \underline{A}_{g}^{C}$$

Equation 3.11-45

Expanding the acceleration in terms of the "natural" co-ordinate systems,

$$\underline{A}_{g,s}^{C} := T_{O}^{C} \cdot \underline{A}_{s}^{O} - T_{E}^{C} \cdot \left(\underline{A}_{o}^{E} + T_{A}^{E} \cdot \left(\underline{A}_{m}^{A} + T_{B}^{A} \cdot \underline{A}_{g}^{B} \right) \right)$$

Equation 3.11-46

The orbital acceleration of a satellite acts towards the earth's centre,

$$\underline{A}_{s}^{O} := -P_{r,s} \cdot \omega_{OS}^{2} \cdot \left(\cos\kappa \quad , \quad \sin\kappa \quad , \quad 0 \right)^{T}$$

Equation 3.11-47

The inertial acceleration of the GPS reference point (g) comprises,

$$\underline{A}_{o}^{E} := \underline{\omega}_{C,E}^{E} \times \underline{\omega}_{C,E}^{E} \times \underline{P}_{o}^{E}$$

Equation 3.11-48

$$\underline{A}_{m}^{A} := \ddot{\underline{P}}_{m}^{A} + 2 \cdot \underline{\omega}_{C,E}^{A} \times \dot{\underline{P}}_{m}^{A} + \underline{\omega}_{C,E}^{A} \times \underline{\omega}_{C,E}^{A} \times \underline{P}_{m}^{A}$$

Equation 3.11-49

$$\underline{A}_{g}^{B} := \underline{\omega}_{C,B}^{B} \times \underline{\omega}_{C,B}^{B} \times \underline{P}_{g}^{B} + \dot{\underline{\omega}}_{C,B}^{B} \times \underline{P}_{g}^{B}$$

Equation 3.11-50

The terms involving Earth rate are small in the context of GPS receiver thresholds and can be ignored. Substituting the remaining terms into the satellite acceleration with respect to the receiver, the LOS acceleration is determined from,

$$\underline{A}_{g,s}^{C}(i,j) :=$$

$$-T_{C}^{L}(i,j) \cdot T_{E}^{C} \cdot T_{A}^{E} \cdot \left(\ddot{\underline{P}}_{m}^{A} + T_{B}^{A} \cdot \left(\underline{\omega}_{A,B}^{B} \times \underline{\omega}_{A,B}^{B} \times \underline{P}_{g}^{B} + \dot{\underline{\omega}}_{A,B}^{B} \times \underline{P}_{g}^{B} \right) \right)$$

Equation 3.11-51

Typically, a receiver loses lock if the angular rate and acceleration in the Missile Body frame exceed ± [6,1,1] rad/s and ± [18,6,3] rad/s^2 respectively. Similarly, when the linear velocity and acceleration thresholds along the satellite LOS are 1200 m/s and 90 m/s^2. These limitations are only applied in the simulation if bit 26 of *MS_GP_ER* from Table 3-23 is set.

3.11.7.1 Triangulation Using All Visible Satellites

Vectorising the GPS measurements for convenience,

$$\underline{M}_P := \left(\mu_d \quad , \quad \lambda_d \quad , \quad P^{GZ}_{d,m} \quad , \quad \underline{\dot{P}}^{G}_{d,m} \right)^T$$

Equation 3.11-52

The error in the i'th satellite pseudo-range is the associated UERE ($\Delta P_{r,s}$) and the receiver clock bias (ΔR_{CK}),

$$P_{r,s} := \left\| \underline{P}^{E}_{s} - \underline{P}^{E}_{g} \right\| + \Delta R_{CK}$$

Equation 3.11-53

Expressing the reference parameters in terms of measurements and errors,

$$\widetilde{P}_{r,s} - \Delta P_{r,s} - \Delta R_{CK} := \left\| \underline{P}^{E}_{s} - \underline{\widetilde{P}}^{E}_{g} + \underline{\Delta P}^{E}_{g} \right\|$$

Equation 3.11-54

$$\left(\widetilde{P}_{r,s} - \Delta P_{r,s} - \Delta R_{CK} \right)^2 :=$$

$$\left(P^{XE}_{s} - P^{XE}_{g} - \Delta P^{XE}_{g} \right)^2 + \left(P^{YE}_{s} - P^{YE}_{g} - \Delta P^{YE}_{g} \right)^2 + \left(P^{ZE}_{s} - P^{ZE}_{g} - \Delta P^{ZE}_{g} \right)^2$$

Equation 3.11-55

Linearising with respect to 4 unknowns and expanding [G] for (n) satellites,

$$\underline{\Delta P}^{L}_{s} := [\,G\,] \cdot \begin{pmatrix} \underline{\Delta P}^{E}_{g} \\ \cdots \\ \Delta R_{CK} \end{pmatrix}$$

Equation 3.11-56

$$[\,G\,] := \begin{bmatrix} \dfrac{P^{XE}_{g,s_1} - P^{XE}_{g}}{P_{g,s_1} - \Delta R_{CK}} & \dfrac{P^{YE}_{g,s_1} - P^{YE}_{g}}{P_{g,s_1} - \Delta R_{CK}} & \dfrac{P^{ZE}_{g,s_1} - P^{ZE}_{g}}{P_{g,s_1} - \Delta R_{CK}} & -1 \\ \vdots & \vdots & \vdots & \vdots \\ \dfrac{P^{XE}_{g,s_n} - P^{XE}_{g}}{P_{g,s_n} - \Delta R_{CK}} & \dfrac{P^{YE}_{g,s_n} - P^{YE}_{g}}{P_{g,s_n} - \Delta R_{CK}} & \dfrac{P^{ZE}_{g,s_n} - P^{ZE}_{g}}{P_{g,s_n} - \Delta R_{CK}} & -1 \end{bmatrix}$$

Equation 3.11-57

The least squares solution to this problem is,

$$\begin{pmatrix} \underline{\Delta P}_g^E \\ \cdots \\ \Delta R_{CK} \end{pmatrix} := \left(\frac{[G]^T}{[G]^T \cdot [G]} \right) \cdot \underline{\Delta P}_s^L$$

Equation 3.11-58

The measured geodetic position is given by the conversion in §22.5.4,

$$\left(\tilde{\mu}_g \quad \tilde{\lambda}_g \quad \tilde{P}_{d,g}^G \right)^T := \varphi_E^G \left(\underline{P}_g^E + \underline{\Delta P}_g^E \right)$$

Equation 3.11-59

The expected pseudo-range measurement errors,

$$E \begin{pmatrix} \underline{\Delta P}_g^E \otimes \underline{\Delta P}_g^E \\ \cdots \\ \Delta R_{CK}^2 \end{pmatrix} := E \left(\frac{[G]^T \cdot \underline{\Delta P}_{g,s}^L}{[G]^T \cdot [G]} \right) := \frac{\sigma_{UERE}^2}{[G]^T \cdot [G]}$$

Equation 3.11-60

The GDOP is the geometric scaling factor UERE,

$$GDOP^2 := \text{trace} \left([G]^T \cdot [G] \right)^{-1}$$

Equation 3.11-61

$$\sigma_{UERE}^2 \cdot GDOP^2 := E\left(\Delta P_g^{XE} \right)^2 + E\left(\Delta P_g^{YE} \right)^2 + E\left(\Delta P_g^{ZE} \right)^2 + E\left(\Delta R_{CK} \right)^2$$

Equation 3.11-62

The Position Dilution of Precision (PDOP),

$$\sigma_{UERE}^2 \cdot PDOP^2 := E\left(\Delta P_g^{XE} \right)^2 + E\left(\Delta P_g^{YE} \right)^2 + E\left(\Delta P_g^{ZE} \right)^2$$

Equation 3.11-63

The Horizontal Dilution of Precision (HDOP),

$$\sigma_{UERE}^2 \cdot HDOP^2 := E\left(\Delta P_g^{XE} \right)^2 + E\left(\Delta P_g^{YE} \right)^2$$

Equation 3.11-64

The Vertical Dilution of Precision (VDOP),

$$\sigma_{UERE} \cdot VDOP \;\coloneqq\; E\left(\Delta P_g^{ZE} \right)$$

Equation 3.11-65

The Time Dilution of Precision (TDOP),

$$\sigma_{UERE} \cdot TDOP \;\coloneqq\; E\left(\Delta R_{CK} \right)$$

Equation 3.11-66

3.11.7.2 Satellite Selection using Geometrical Methods

Whilst receivers now track all visible satellites, earlier systems with limited CPU capacity selected 4 satellites using geometrical techniques. The GDOP is simply the rss value of the diagonal elements of $[G]^{-1}$. The 4 satellites can be chosen simply on the basis of which combination has the smallest GDOP. Alternatively, the combination is chosen that minimises the tetrahedron formed with the receiver using the Gram-Schmidt orthogonalisation proposed by Kihara[K.8] and Higgins[H.13]. This volume is equivalent to the smallest GDOP with a theoretical lower bound of 1.581. The 1st satellite selected is the one closest to the zenith through the receiver. The first row in [G], the vector ($\underline{G}_1$), is then calculated and normalised,

$$\underline{U}_1 \;\coloneqq\; \underline{G}_1 \,/\, \sqrt{2}$$

Equation 3.11-67

The 2nd satellite is the one closest to 90° from the first. This is determined by taking the satellite with the smallest dot product between vector ($\underline{G}_1$) and ($\underline{G}_i$) for the remaining visible satellites. The Gram-Schmidt procedure is then used to produce a normalised vector orthogonal to ($\underline{U}_1$),

$$\underline{U}_2 \;\coloneqq\; \frac{\underline{G}_1 - \left(\underline{U}_1 \bullet \underline{G}_2 \right) \cdot \underline{U}_1}{\left\| \underline{G}_1 - \left(\underline{U}_1 \bullet \underline{G}_2 \right) \cdot \underline{U}_1 \right\|}$$

Equation 3.11-68

The 3rd satellite is chosen such that its ($\underline{G}_i$) minimises the following parameter for the remaining visible satellites,

$$\varphi_1 \;\coloneqq\; \left\| \left(\underline{U}_1 \bullet \underline{G}_i \right) \cdot \underline{U}_1 - \left(\underline{U}_2 \bullet \underline{G}_i \right) \cdot \underline{U}_2 \right\|$$

Equation 3.11-69

The Gram-Schmidt procedure gives a normalised vector orthogonal to ($\underline{U}_1$),

$$\underline{U}_3 \;=\; \frac{\underline{G}_3 - \left(\underline{U}_1 \bullet \underline{G}_3 \right) \cdot \underline{U}_1 - \left(\underline{U}_2 \bullet \underline{G}_3 \right) \cdot \underline{U}_2}{\left\| \underline{G}_3 - \left(\underline{U}_1 \bullet \underline{G}_3 \right) \cdot \underline{U}_1 - \left(\underline{U}_2 \bullet \underline{G}_3 \right) \cdot \underline{U}_2 \right\|}$$

Equation 3.11-70

The 4th satellite is chosen such that its ($\underline{G}_i$) minimises the following parameter from the remaining visible satellites,

$$\varphi_2 \coloneqq \left\| \left(\underline{U}_1 \bullet \underline{G}_i \right) \cdot \underline{U}_1 + \left(\underline{U}_2 \bullet \underline{G}_i \right) \cdot \underline{U}_2 + \left(\underline{U}_3 \bullet \underline{G}_i \right) \cdot \underline{U}_3 \right\|$$

Equation 3.11-71

3.11.8 Sensor Limitations

Provision of GPS measurements at the sensor output interface depends on:

- User measurement selection (*MS_MSAV2* bit 22/25 cleared)
- Receiver tracking limitations (*MS_GP_ER* bit 24 is set)

When active, if any of these limitations are violated, bits 24-25 in the measurement ready flag *MS_MSRY2* are cleared. Failure to provide measurements at the user's request is indicated by setting bit 0 of *MS_BA_VF*. The effect of receiver tracking failures is dealt with in §3.11.7. If any of these thresholds are exceeded for any satellite bit 2 of *MS_BA_VF* is set and the effected satellites are treated as "invisible".

The following limitations are not user selectable. If there are insufficient satellites for triangulation bit 3 of *MS_BA_VF* is set. When the satellites are near to coplanar with a GDOP > 1000 triangulation is not performed and bit 4 is set.

3.11.9 Output Interface

The GPS measurement vector passes through a signed digital interface at a frequency ($_{GP}f_O$) of 1 Hz (clock 23).

$${}_{GP}\underline{\tilde{Z}} \coloneqq \underline{\varphi}_{TD}\left(\underline{\varphi}_{Q}\left(\underline{\varphi}_{LIM}\left(\underline{\varphi}_{ZOH}\left(\underline{\tilde{Z}} \right) \right) \right) \right)$$

Equation 3.11-72

The longitude and latitude pass through a 32 bit interface with range limits of ± 180° and ± 90° respectively, subject to a 1/50 cycle transmission delay. The geodetic height and velocity are limited to ± 300 m and ± 350 m/s by a 16 bit interface with the same cyclic delay.

Table 3-23 : Satellite and Receiver Error Selection

MS_GP_ER	Satellite and Transmission Errors
0	UNUSED
1	Selective availability
2	Range biases
3	Range rate biases
4	Range Gaussian noise
5	Range rate Gaussian noise
6	Range 1st order Markov drift
7	Range rate 1st order Markov drift
8	Range 2nd order Markov drift
9	Range rate 2nd order Markov drift
MS_GP_ER	**Receiver Clock Errors**
11	Clock effective range bias
12	Clock effective range rate bias
13	Clock effective range Gaussian noise
14	Clock range rate Gaussian noise
15	Clock 1st order Markov range drift
16	Clock 1st order Markov range rate drift
MS_GP_ER	**Receiver Tracking Errors**
17	Range bias
18	Range rate bias
19	Range Gaussian noise
20	Range rate Gaussian noise
21	Range 1st order Markov drift
22	Range rate 1st order Markov drift
23	Range 2nd order Markov drift
24	Range rate 2nd order Markov drift
26	Receiver tracking dynamic limitations
27	Maximum GDOP threshold

Bits 27-28 are reserved for the output interface in the normal way.

The selective availability model was derived from de-biased empirical data that includes Gaussian and time correlated noise (excluding the receiver clock Gaussian noise). When this error source is activated (*MS_GP_ER* bit 1 set) all the remaining satellite noise sources are automatically de-activated.

3.12 Helmet Mounted Sight

3.12.1 Review

The HMS is a recent innovation for fighter aircraft used for designating short-range air-to-air missiles with a high off-boresight capability. It is also used to steer other targeting sensors such as radar or FLIR however, its use for air-defence has yet to be exploited. It is a misconception that the HMS is a 360° rear hemisphere target sensor. Constraints arising from human physiology, an inability to rotate the head directly in line with the target (squinting will not do), buffeting, the G-suit and ejector seat assembly conspire to reduce the field-of-regard to ≈135°. None-the-less, the HMS is revolutionising short-range air warfare tactics with a rear-hemisphere capability limited only by the aforementioned constraints. The consequential expansion of missile operating envelopes demands greater agility from missiles, possibly obtained by thrust vectoring, speed optimised turns, sophisticated seeker scanning and improved radome characteristics.

3.12.2 Description

The head moves so that the right eye (in a monocular system) places an aiming symbol projected onto the helmet visor using a Cathode Ray Tube (CRT) over the target. An optical or magnetic helmet tracker attached to the canopy measures the linear and rotational helmet position with respect to Aircraft body axes. These data are used to correct the target elevation and bearing measurements for optical and magnetic distortions with respect to a local reference axis. This process is only performed when the pilot's head is within a pre-determined "box" for which the canopy distortion correction is valid. The system is re-aligned at regular intervals by placing the aiming symbol over a fixed point in the cockpit.

Optical helmet tracking systems are attractive because they are not affected by metal structures, nor do they require cockpit mapping or regular alignment after initial installation. Multiple helmet mounted Light Emitting Diodes (LEDs) are attached to the canopy, avoiding obscuration of the helmet light source, each energised in turn and the position of the helmet determined by triangulation. Electro-magnetic systems are susceptible to stray electromagnetic fields, particularly those employing Alternating-Current (AC) devices compared with Direct-Current (DC). AC systems are sensitive to both conductive metals and ferromagnetic materials whereas DC systems are only sensitive to the latter, and to a lesser degree. Eddy currents are induced in nearby metals by AC systems resulting in magnetic field distortion that is 3-10 times greater compared with DC systems. DC generated pulses induce transient eddy currents that rapidly die away and measurements can be taken once a steady state condition is reached.

Video retina tracking is being developed that may replacing the existing magnetic/optical helmet orientation sensing systems. If successful this would avoid the need for magnetic mapping of cockpits and remove

pointing errors due to the relative motion between head and helmet. A speculative alternative (not mentioned in pilot earshot) is the surgical implant of sensors in the muscles responsible for controlling the position of the eyeball.

Time is needed for this technology to mature on deployed systems and to assess its impact on combat tactics and the presentation of data on the visor. The HMS model shown in Figure 3-61 is placed in the context of a surface-to-air targeting rather than the usual aircraft role and hence the angular measurements are defined with respect to the Alignment frame which is also the origin of the target tracking radar.

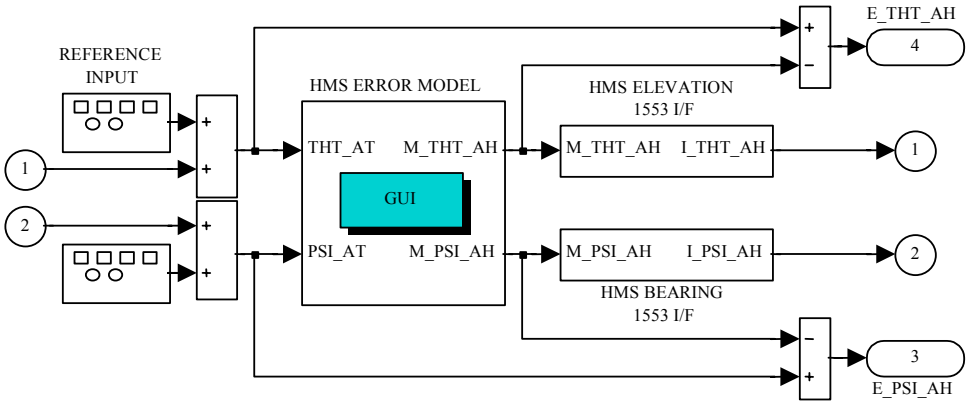

Figure 3-61 : HMS Sensor Model

Head box restrictions have been ignored and measurements are provided subject only to residual canopy distortion independent of head position. The error model provided is flexible enough to deal with both IR and magnetic trackers, night and day, monocular and binocular systems.

3.12.3 Reference Target Angles

For air launched applications the reference target angles are measured with respect to the Aircraft body axes. For ground based, surface-to-air, applications they are measured with respect to the Alignment frame,

$$\underline{Z} \equiv \left(\Psi_A^T \;,\; \Theta_A^T \right) := \left(\tan^{-1}\left(\frac{P_t^{YA}}{P_t^{XA}} \right) \;,\; -\tan^{-1}\left(\frac{P_t^{ZA}}{P_t^{hA}} \right) \right)$$

Equation 3.12-1

This data is provided at a reference frequency ($_{HS}f_R$) of 400 Hz.

3.12.4 Measured Target Angles

The data for the HMS error model has been taken from the public domain, most of it supplied by H. Waruszewski (Lockheed Martin F-22 HMS system

manager). The following assumptions were made when setting the default error parameters:

- A monocular daytime sight is used.
- The head remains in the head box so that measurements are always valid.
- The eye, head and helmet act as a single unit without slippage. This is true only when the visor reticule is close to the target. Although helmet slippage is expected whilst the head is in motion, and when subject to heavy vibration, the helmet returns to its original position once the dynamic conditions moderate.
- Residual canopy distortion is independent of helmet position in the head box and target position.
- The system has just been calibrated.

The injection of independently selectable errors is controlled by the bit pattern of *GB_HS_ER*. The reference angles are corrupted at the reference rate by a time delay, an angular rate limit, and 2nd order dynamics associated with the human physiology and helmet slippage.

$$\underline{\tilde{Z}} := \underline{\varphi}_{SF}\left(\underline{\varphi}_{D2L}\left(\underline{\varphi}_{RL}\left(\underline{\varphi}_{TD}\left(\underline{Z}\right)\right)\right) + \underline{\varphi}_{CB} + \underline{\varphi}_{RN} + \underline{\varphi}_{MBI}\right)$$

Equation 3.12-2

A time delay of 0.08 s is followed by an angular rate limit of 200°/s, and a 2nd order lag with a damping ratio of 0.7 and a natural frequency of 4 Hz, default values that apply to both axes. Constant bias, random noise and a random walk are superimposed on the filtered measurements representing the effect of stray magnetic fields on the helmet tracker and changes in canopy distortion. The constant bias is initialised from a Gaussian distribution with a deviation of 0.008 rad comprising:

• Helmet tracking : Electro-Optical static accuracy	(2 – 10)	mrad
• Helmet tracking : Resolution	(1 – 2)	mrad
• Residual optical distortion from canopy	(5 – 8)	mrad
• Boresight misalignment	(2 – 6)	mrad
• Residual magnetic distortion	(2 – 6)	mrad
• Reticule symbol line width and dimensional stability	(1 – 2)	mrad

The Gaussian noise has a PSD of 0.005 $mrad^2$/Hz at the reference frequency, equivalent to 0.5 mrad @ 50 Hz. The random walk output deviation is 9 mrad with a correlation time of 200 s (chosen arbitrarily for test purposes) although it could be much larger in magnetic tracking systems where the build up of stray magnetic fields is the dominant effect. The constant, quadratic and asymmetric scale factor deviations are 0.03, 0.01 and 0.01 respectively for both measurements.

$$ {}^{D}\underline{\tilde{Z}} := {}^{AD}\underline{\varphi}_{LIM}\left({}^{AD}\underline{\varphi}_{Q}\left(\underline{\varphi}_{ZOH}\left(\underline{\varphi}_{AA}\left(\underline{\tilde{Z}} \right) \right), {}_{HS}f_{O} \right) + {}^{AD}\varphi_{QN} \right) $$

Equation 3.12-3

The analogue measurements are converted into digital form using a 100 Hz, 4th order Butterworth filter, and a 12 bit ADC subject to 3 bits of noise and a sampling rate and range matched to the output interface.

3.12.5 Sensor Limitations

The provision of HMS measurements at the output interface depends on:

- User measurement selection (*MS_MSAV2* bit 15/16 cleared)
- Maximum range limiting (*GB_HS_ER* bit 15 is set)
- Angular rate limiting (*GB_HS_ER* bit 16 is set)
- Maximum angular rotation limiting (*GB_HS_ER* bit 17 is set)

When active, if any of these limitations are violated, bits 15 - 16 in the measurement ready flag *MS_MSRY2* are cleared. Failure to provide a measurement at the user request is indicated by setting bit 0 of *GB_HS_VF*. If the target range exceeds 12 km, the segmentation capability of the human eye in blue-sky conditions, bit 1 of *GB_HS_VF* is set. When target LOS angular rate limiting is active measurement transmission is suspended and bits 2 - 3 of *GB_HS_VF* are set (rate limiting in elevation and bearing respectively). If the elevation or bearing angles exceeds (± 60°, ± 120°) bits 4 - 5 of *GB_HS_VF* are set respectively.

3.12.6 Output Interface

The measured target angles pass through a signed 16 bit digital interface at a frequency ($_{HS}f_{O}$) of 50 Hz (clock 14). They are subject to bearing and elevation interface range limits of ± 180° and ± 90° respectively, and a one-cycle transmission delay.

$$ {}_{HS}\underline{\tilde{Z}} := {}^{IF}\underline{\varphi}_{TD}\left({}^{IF}\underline{\varphi}_{Q}\left({}^{IF}\underline{\varphi}_{LIM}\left({}^{IF}\underline{\varphi}_{ZOH}\left({}^{D}\underline{\tilde{Z}}, {}_{HS}f_{O} \right) \right) \right) \right) $$

Equation 3.12-4

3.13 Air Data System

3.13.1 Review

Sensors measuring the local atmospheric conditions, post-processed to obtain pressure height, air speed and Mach number are a constant feature on aircraft. They are particularly important for generating an estimate of body incidence required to stabilising fly-by-wire airframes. This function apart, the plethora of alternative sensors has relegated air data to a reversion role for dead-reckoning navigation and height keeping in the event of a major systems failure. This work ignores magnetometers often found in air data suites included to provide direction relative to the Earth. Air data also provides an alternative height reference to barometers and NAVSTAR GPS for stabilising a SDINS. One of its drawbacks in small vehicles is that the sensors must be positioned in the free air stream and its recovery ratio in bringing the free stream to rest calibrated. No fundamental change is expected in these sensors, or their electronics and post processing.

3.13.2 Description

Collinson[C.8] provides a comprehensive description of air data sensors and associated systems. The sensors measure three atmospheric properties, the total and static pressures using a Pitot static tube, and the static air temperature. These reference data are derived in the model shown in Figure 3-62 from the true geodetic height and the Mach Number (a Dryden wind model is not included).

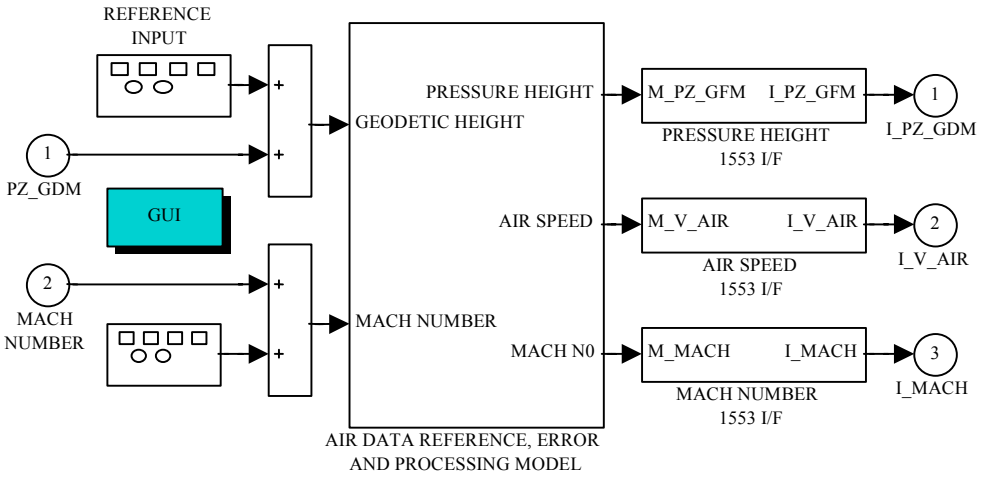

Figure 3-62 : Air Data Model

A transducer measures the total pressure exerted on the Pitot tube. This comprises free stream static pressure and the pressure required to bring it to rest. A temperature probe measures the total air temperature: the sum of the free stream air temperature and the temperature rise in bringing it to rest. These measurements are processed to obtain geodetic (pressure) height, true airspeed and Mach number as shown in the decomposition in Figure 3-63.

3.13.3 Reference Air Data

The static pressure (P_S) and the static air temperature (T_S) are obtained from §19. These together with the missile Mach number and Pitot static tube recovery ratio, are used to determine the total pressure and temperature.

$$M_m < 1 \Rightarrow \left\{ \begin{array}{rcl} P_T & := & P_S \cdot \left(1 + 0.2 \cdot M_m^2 \right)^{3.5} \\ T_M & := & \left(1 + 0.2 \cdot R_F \cdot M_m^2 \right) \cdot T_S \end{array} \right\}$$

Equation 3.13-1

$$M_m \geq 1 \Rightarrow \left\{ \begin{array}{rcl} P_T & := & 166.92 \cdot M_m^7 \cdot P_S \cdot \left(7 \cdot M_m^2 - 1 \right)^{-2.5} \\ T_M & := & \left(\frac{1 + 0.2 \cdot R_F \cdot M_m^2}{1 + 0.2 \cdot M_m^2} \right) \cdot T_T \end{array} \right\}$$

Equation 3.13-2

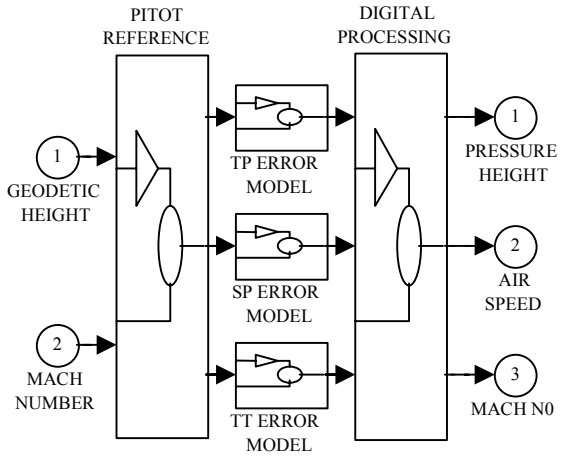

Figure 3-63 : Air Data Model Decomposition

The true recovery factor (R_F) is set to 0.2. When the temperature sensor is placed at a stagnation point the measured and total air temperatures are identical. The recovery ratio is a measure of the efficiency of the probe in bringing the air to rest and can vary significantly when flying through rain and cloud. This data is provided at a reference frequency ($_{AD}f_R$) of 400 Hz,

$$\underline{M} := \left(P_T \;,\; P_S \;,\; T_T \right)^T$$

Equation 3.13-3

3.13.4 Measured Air Data

The total and static pressure, and the total temperature are subject to the same functional error model, characterised appropriately. The injection of independently errors is controlled by the bit pattern of *MS_AD_ER*. The reference angles are corrupted at the reference rate by a time delay of 0.05 s followed by constant bias and random noise.

$$\underline{\tilde{M}} \;:=\; \underline{\varphi}_{SF}\left(\underline{\varphi}_{TD}\left(\underline{M}\right) + \underline{\varphi}_{CB} + \underline{\varphi}_{RN}\right)$$

Equation 3.13-4

The constant biases are initialised from a Gaussian distribution with pressure and temperature deviations of 50 N/m^2 and 20 deg K respectively. The respective Gaussian noises have a PSD of 25 $N^2/m^4/Hz$ and 20 $(deg\ K)^2/Hz$ at the reference frequency. The constant, quadratic and asymmetric scale factor deviations are set to 0.005, 0.02 and 0.02 respectively and applied to all measurements.

$${}^{D}\underline{\tilde{M}} \;:=\; {}^{AD}\underline{\varphi}_{LIM}\left({}^{AD}\underline{\varphi}_{Q}\left({}^{AD}\underline{\varphi}_{ZOH}\left(\underline{\varphi}_{AA}\left(\underline{\tilde{M}}\right)\right), {}_{HS}f_{O}\right) + {}^{AD}\varphi_{QN}\right)$$

Equation 3.13-5

The analogue measurements are converted into digital form using a 40 Hz, 4^{th} order Butterworth filter, and a 12 bit ADC subject to 3 bits of noise with a sampling rate and range matched to the output interface.

3.13.5 Derived Air Data

Air data measurements are pre-processing to determine the pressure altitude, Mach number and true airspeed.

$$\underline{M}_{P} \;:=\; \left(P_{d,m}^{GZ} \;,\; M_{m} \;,\; V_{TAS}\right)^{T}$$

Equation 3.13-6

The process used is simple compared with civil air data systems based on Bernouilli's Equation and air data provided by NASA. The variation in geodetic height with static pressure shown in Figure 3-64 is determined by,

$$P_{d,m}^{GZ} < 11\_000 \;\Rightarrow\; \tilde{P}_{d,m}^{GZ} \;:=\; 44331\cdot\left(1-\left(\tilde{P}_{S}\,/\,101325\right)^{-5.255879}\right)$$

Equation 3.13-7

$$11\_000 \geq P_{d,m}^{GZ} < 23\_000 \;\Rightarrow\; \tilde{P}_{d,m}^{GZ} \;:=\; 11000 - 6342\cdot\ln\left(\frac{\tilde{P}_{S}}{22632}\right)$$

Equation 3.13-8

If insufficient processing power is available, a look-up table with linear interpolation may be used to obtain the height. The relationship between the maximum height error using linear table interpolation as a function of the height interval chosen is shown in Figure 3-65.

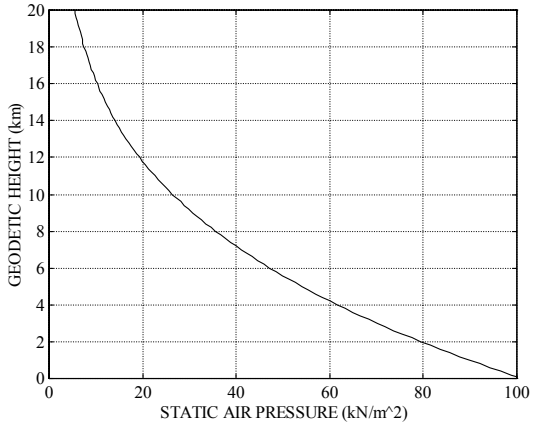

Figure 3-64 : Static Pressure vs Geodetic height

For heights up to 5 km an 800 m interval introduces errors < 9 m, reducing to 2.5 m at 400 m. A look-up table based on the total to static pressure ratio is used to determine the Mach Number that varies as shown in Figure 3-66.

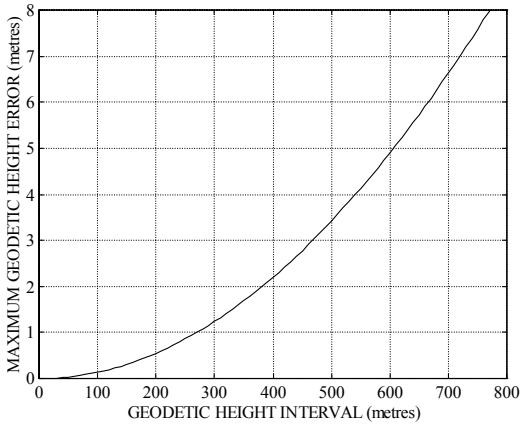

Figure 3-65 : Geodetic Height Interval

$$M_m < 1 \Rightarrow \tilde{P}_T / \tilde{P}_S := \left(1 + 0.2 \cdot \tilde{M}_m^2\right)^{3.5}$$

Equation 3.13-9

$$M_m < 1 \Rightarrow \tilde{P}_T / \tilde{P}_S := 166.92158 \cdot \tilde{M}_M^7 \cdot \left(7 \cdot \tilde{M}_M^2 - 1\right)^{-2.5}$$

Equation 3.13-10

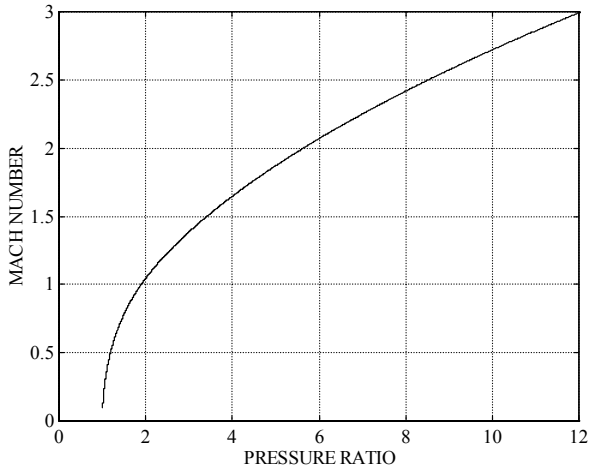

Figure 3-66 : Pressure Ratio vs MACH Number

To minimise low speed errors in the Mach number range [0,1.5] the total Mach number range considered is scaled using,

$$[\,0\,,3\,] \xrightarrow{\text{Ln}} [\,-2.3026\,(\,0.17\,)\,1.0986\,]$$

Equation 3.13-11

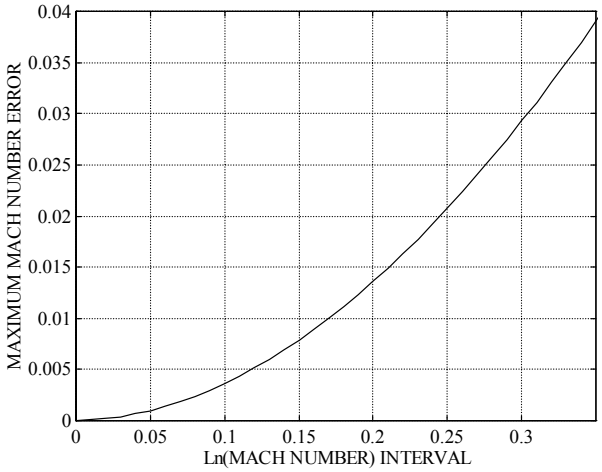

Figure 3-67 : Mapped MACH Number Interval

The result of this scaling is shown in Figure 3-67. Constant interpolation intervals in the range [0,0.34] introduce Mach number errors up to 0.04. Selecting an interval of 0.17 reduces the error to 0.01, see Figure 3-68. The true airspeed is the speed of the missile relative to the undisturbed air and is the magnitude of the vector sum of the true airspeed vector and the wind velocity vector. The true airspeed is derived from the Mach number and measured air temperature taking into account an estimate of the sensor recovery ratio (R_K) whose default value is set to the reference value of 0.2.

$$\widetilde{V}_{TAS} := 20.0468 \cdot \widetilde{M}_M \cdot \sqrt{\frac{\widetilde{T}_M}{1 + 0.2 \cdot \widetilde{R}_K \cdot \widetilde{M}_M^2}}$$

Equation 3.13-12

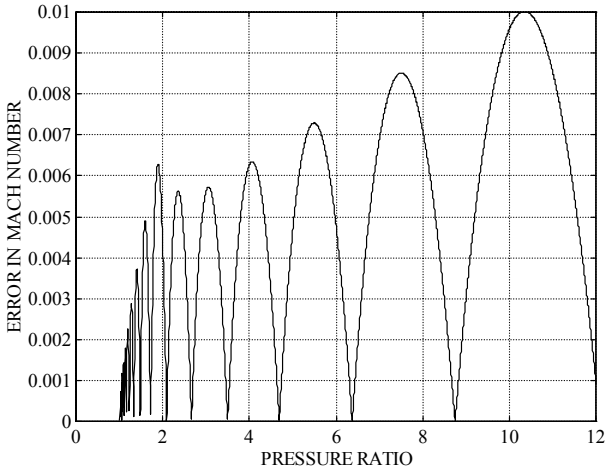

Figure 3-68 : MACH No. Interpolation Error

The look-up tables are invoked instead of the inverse mathematical expressions if bit 17 (Height) and bit 18 (Mach Number) are set.

3.13.6 Sensor Limitations

Provision of air data at the sensor output interface depends on:

- User measurement selection (*MS_MSAV2* bits 19-21 cleared)
- Rate limiting (*MS_AD_ER* bit 16 is set)

When active, if any limitations are violated bits 19-21 in the measurement ready flag *MS_MSRY2* are cleared. Failure to provide all the primary measurements at the user request is indicated by setting bits 0 - 2 of *MS_AD_VF*. If primary measurement rate limiting is active, measurement transmission is suspended and bits 3 - 5 of *MS_AD_VF* are set.

3.13.7 Output Interface

The air data passes through an unsigned 16 bit digital interface at a frequency ($_{AD}f_O$) of 20 Hz (clock 17). They are subject to height, speed and Mach number interface range limits of [0,500] m, [0,1200] m/s, and [0,3] respectively, and a one-cycle transmission delay.

$$_{AD}\underline{\widetilde{M}}_P := {}^{IF}\underline{\varphi}_{TD}\left({}^{IF}\underline{\varphi}_{Q}\left({}^{IF}\underline{\varphi}_{LIM}\left(\underline{\varphi}_{ZOH}\left(\left(\underline{\widetilde{M}}_P\right), {}_{AD}f_O\right)\right)\right)\right)$$

Equation 3.13-13

3.14 Discussion

It is only through a fundamental understanding of sensors and their limitations that a sound selection of observer architectures and algorithms can be made for any data fusion process. Data fusion solutions presented in literature all too often ignore detrimental sensor features. In practice this leads to inappropriate algorithm selection and eventual requirement creep as software solutions are sought to overcome hardware deficiencies. In industry, to be sure of capturing these features manufacturer's sensor development models are often used however, these tend to be highly complex and require too much processing, making them unsuitable for rapid system level performance assessment. There exists a need for a set of technologically current sensor models pitched at the systems analysis level - the key driver for this part of the research.

Following a review of modern missile systems Figure 3-69 shows the sensors and their measurements that the author believes will have an enduring impact on future weapon systems in respect of targeting, geodetic referencing, and aided navigation. Although the latter are rarely used for air-defence, they perform critical functions such as height keeping in cruise and sea-skimming missiles. Boundaries that were once distinct are now blurred, for example, GPS is likely to play an important role in short-range munitions guided to a terrestrial reference point.

SDINS are the bedrock of most sensor suites, here considered in a Master-Slave relationship required for transfer alignment, i.e. the calibration of low-grade inertial sensors. Although SDINS themselves are not strictly sensors, they integrate the output from inertial sensors and height stabilisation instruments to provide long-term navigation data.

FLIR and TIALD can be treated as specific characterisations of the generic seeker model. Fin transducers are part of the autopilot loop closure generating the acceleration demanded by the missile guidance law. They are also required for the pseudo-measurement proposed in §5 for constraining the missile dynamics in the missile observer.

§3 starts by describing how to select a sensor measurement suite in the simulation, the activation of each sensor in turn, and how their output at a digital interface is passed to the state observers. The models are designed so that they can be added or removed from the sensor suite at the controller level without interacting with those that remain. The creation of a parallel set of MATLAB sensor models for verification, and to speed up sensor development is briefly introduced before dealing with common error sources. Errors such bias, scale factor and digital interface limitations found in many sensors are treated generically using a functional notation with default values provided in-situ. The characteristics associated with digital input filtering, random noise, 1^{st} and 2^{nd} order Gauss-Markov noise, the ZOH and uniform noise resulting from fixed word-length digital processing are explored.

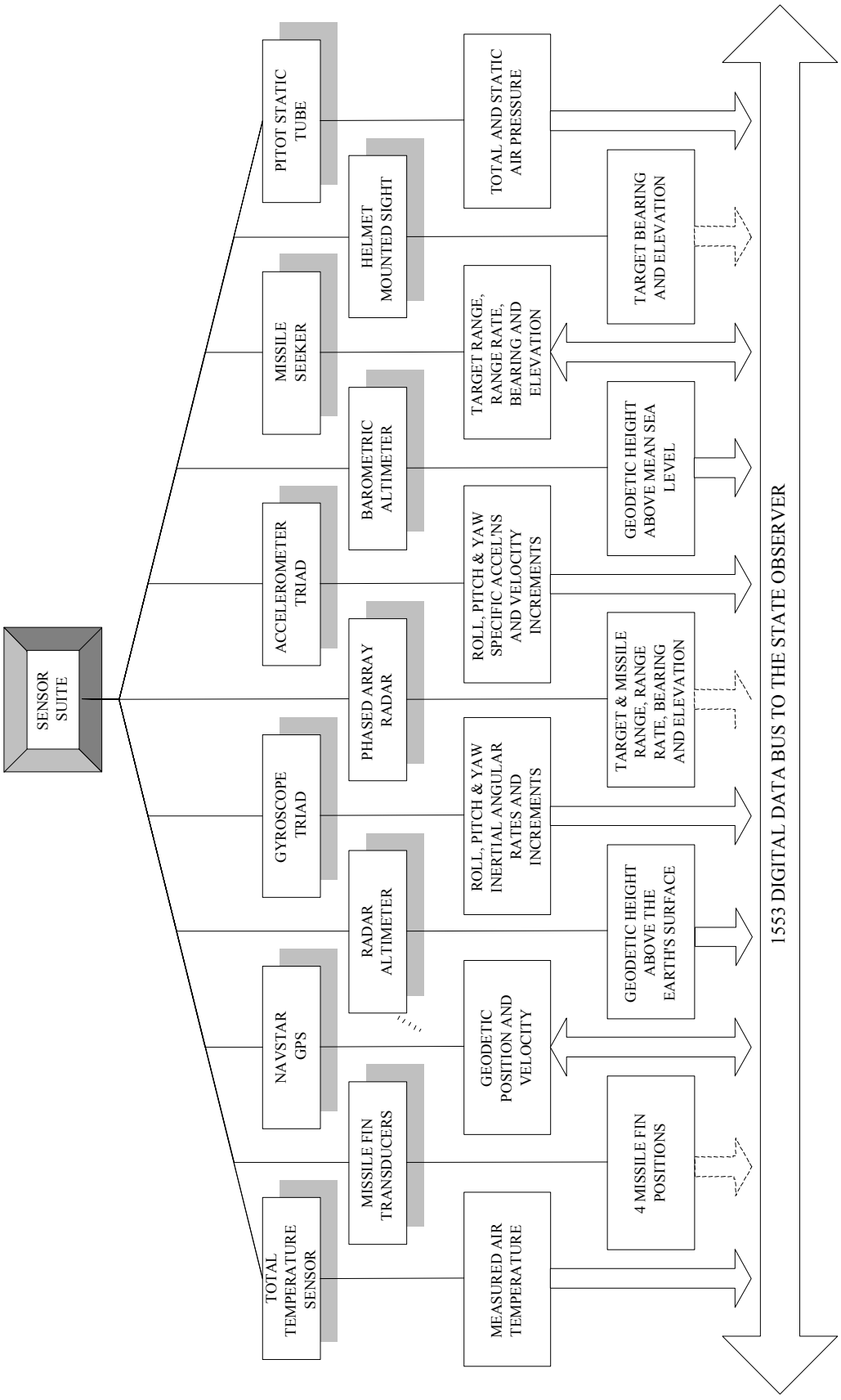

Figure 3-69 : Sensor Measurement Suite

Inertial sensors and height stabilising devices are discussed in the context of SDINS, explaining why this mechanisation and optical sensors have replaced platform and mechanical alternatives. The Navigation Equation is derived as part of a wider discussion concerning the derivation of inertial inputs into master/slave IMU sensor packs. The effect of structural flexure on the IMU input is considered, although specific models are application specific, notoriously complex, and beyond the scope of this research. The remainder of this chapter deals with each sensor in turn.

Historical reviews are provided for each sensor charting notable improvements and technological leaps that have lead to advances in missile capability. The reference input to each sensor is derived from the reference-state vector that is defined with respect to an earth fixed frame of reference. This was a crucial design decision enabling sensor models to be developed in isolation from the simulated "real" world itself stimulated from various sources - an approach that provides self-contained models ideal for cloning.

These reference inputs are corrupted, on command, by the dominant errors and limitations provided, all with typical default values. Complex sensor errors and high frequency internal dynamics are reduced to simple models for studying observer performance at the systems level. This approach promotes modularisation and is ideal for superposition of individual, non-interacting error sources. The errors imposed tend to fall into 3 categories: Gaussian for stochastic filtering, systematic for error state observation, and non-Gaussian. The later are of particular interest since they can degrade the performance of stochastic filters based on Kalman Filtering techniques.

3.14.1 Inertial Sensors (Gyroscopes and Accelerometer triads)

Recent weapon systems have seen the introduction of optical and solid state devices replacing mechanical equivalents. The gradual intrusion of this new technology is charted, and the benefits and pitfalls associated with each noted. In the authors opinion FOG gyroscopes and silicon accelerometers will dominate the scene by the turn of the century. Although the error models provided are capable of dealing with both optical and mechanical devices, digital variants of the former are relatively insensitive to acceleration and scale factor induced errors than can often be ignored. Conversely, the wider bandwidth of these strap-down devices makes them susceptible to noise, particularly vibration rectification. Typical errors are given for aircraft, long and short range missile IMUs.

Vibration rectification is hard to quantify being application specific, and for air-launch scenarios subject to high levels of structural flexure. This error source cannot be treated simply using band-limited noise as structural vibrations usually exhibit significant power levels at specific frequencies. For instruments attached to an aircraft, noise arising from manoeuvre dependent wing bending, pylon and missile flexure all lie within the bandwidth of the sensors and must be considered. Producing coherent zero-

mean angular rate and acceleration noise models is difficult and a low-frequency adaptive correction is often necessary.

3.14.2 Barometers

These are the most mature of the sensors considered. However, recent changes in civil air-traffic height separation requirements will inevitably spill over to military aircraft and result in significantly reduced scale factor errors. For aircraft their role is secure as a stealthy, reliable secondary sensor, although in long-range missiles they have been replaced by solid state CW and pulsed altimeter devices.

3.14.3 Radar Altimeters

The model provides geodetic height associated with the first returns from the terrain directly below and it is the "terrain" definition that is the most interesting aspect. Work by the author on terrain characteristics is presented concerning map digitisation and triangulation errors as a function of the average local gradients.

Considering operational scenarios where covert height keeping is required there is little call for slant-range to the terrain aside the geodetic vertical. This is fortunate since as the sensor height increases it becomes more difficult to determine the first return slant-range for narrow beam and laser devices. There is an enhancement to the current model that would be beneficial and that is the replacement of the land profile by a sea-surface. This involves the missile along-track encounter frequency with fully developed, and shoaling, sea-wave profiles using wide beam devices for studying sea-state estimation, height-keeping, and terrain following land-sea transitions.

Beyond the scope of this work, but of interest, is the cloning of independent altimeters that are in close proximity, as is required for the AMIS. The sensors can no longer be treated in isolation and it must be possible for both to access the common elements of the map error models.

3.14.4 Radar and Seekers

These sensors are key to targeting in general and deserve more attention than most of the other sensors. As with most sensors the concepts are simple at a systems level, the devil is in the detail, in this case capturing the essence of glint, multipath, clutter, the effect of frequency agility using simple models.

The radar and the seeker models comprise yaw/pitch gimbals with a single detector. There is interest in strap-down detectors, devices that can be accommodated in the models provided by locking the gimbals. When free to rotate the detector is pointed using reference, sensor measurement, observer, or trajectory optimised impact point data. Gimbal position measurements are combined with the detector output to provide range,

range-rate and Euler angle measurements with respect to an earth-fixed frame (ground radar), and body referenced frame (seeker).

For this research it is important that a radar phased array detector is used so that separate beams can be formed on the target and missile, reflecting modern tracking systems. The gimbals are locked, their error sources ignored, and separate beams formed instantaneously, i.e. measurements produced at a common reference time, in keeping with the system level ethos of keeping things simple.

Using generic models to deal with sensors of similar type, for example, FLIR and TIALD, requires an extensive array of characterised error models. The work presented concentrates on typical SNR dependent noise and glint errors associated with RF devices. The following enhancements to the existing error models are recommended for the future:

- Capture the essence of multiple frequency effects that reduce glint levels, and introduce the Swirling models described dependent on target type.
- Characterise and model the gross effect of multipath and clutter for RF devices, and similarly IR detector errors caused by dome heating, smear, fixed pattern noise, speckle etc.

The current seeker model comprises a single detector in a dedicated set of gimbals. One of the most recent and exciting developments in the field of missile state observation is the fusion of measurements from several detectors. To accommodate research in this field the simulator must be capable of providing two-colour seeker output, from errors models characterised as laser, RF or IR devices.

3.14.5 NAVSTAR GPS

A simple geometrical model of a symmetric 24-satellite constellation is presented. Earth-referenced (LGA) position and velocity measurements are derived from pseudo-range and pseudo range-rate measurements at 1 Hz or 10 Hz. No pseudo-measurement data passes through the output interface in keeping with manufacturer's reluctance to provide such information. Essentially, the errors imposed fall into 3 categories: selective availability, pseudo-measurement and geometric errors. Selective availability dominates the others although this may not be required if the practice of jittering the satellite atomic clocks ceases as promised. The geometric errors arise from the relative position of the satellites with respect to the receiver. Three schemes are provided for selecting satellites for triangulation: selection of 4 with the optimal GDOP, the same using a Gram-Schmidt process, and finally an over specified least squares solution involving all "visible" satellites. During this research the latter has become the norm due to improvements in receiver design over the last 10 years.

The availability of "visible" satellites is an area of particular interest when studying the navigation performance of low-flying, agile vehicles, and one

in which the current model might be enhanced. The model already deals with earth and self-screening, but does ignore satellites blocked by the local terrain. This effect can be crudely studied using the current model by increasing the earth-screening angle. This enhancement to the GPS model should not be undertaken lightly as it is complex and will need considerable computational effort.

Currently the satellite position required for the pseudo-range data is computed from the symmetric constellation geometry. This is quick and simple, but prevents the study of performance using actual satellite constellations. Equations are provided that process published Ephemeris data to determine the actual position of each satellite at any particular time; equations that have yet to be implemented.

3.14.6 Helmet Mounted Sights

Helmet Mounted Sights are an evolving technology compared with the other sensors. Conceptually they are simple although they involve human factors that are always likely to complicate any error model. The author, having first hand experience of the system, has (he believes) introduced sufficient elements into the model to deal with vibration, helmet slippage, hysteresis, and head dynamics.

3.14.7 Air-Data Sensors

The processing of temperature and Pitot measurements to obtain height, air-speed and Mach number is presented. As was the case with GPS data, the outputs from the air-data computer are not strictly measurements in the sense that it is processed data. Fortunately, measurement errors are transformed rather than filtered which would have created difficulties for measurement fusion.

The current model does not provide attitude that is usually available from air-data systems. This requires the introduction of a generic sensor to deal with instruments such as the magnetometer. For completeness, this enhancement to the current model is recommended.

Chapter 4

TARGET TRACKING

For air-defence a ground-based phased-array tracker provides position and doppler measurements of the target and missile. The target-track formulated here in §4 is fused in the missile with measurements from gyroscopes, accelerometers and a seeker, to obtain optimal state estimates from which the guidance parameters are obtained. A review of centralised and de-centralised architectures for track and measurement fusion in the missile is deferred until §5.

For this application, if the up-link bandwidth and on-board processing are limited, as is always the case, sophisticated ground target-track formation is inevitable. Whether a missile-track, or the radar measurements are up-link for centralised fusion is less obvious - the latter is used.

Single-axis, steady-state filters are inadequate against agile targets and multiple-model alternatives are considered: optimal Bayesian, pseudo-Bayesian, Gaussian Sum and the IMM with a fixed mode set.

Stochastic filter formulations are reviewed for the individual IMM filters, and the conventional EKF selected with different target dynamics: constant velocity, constant acceleration, dog-leg (Singer) and weaving. An earth-referenced Cartesian state space is chosen, and filter initialisation explored.

The IMM is modified to accommodate serial measurement processing to improve linearisation. Using filters that accurately propagate covariance statistics in high-dynamic engagements is avoided at this stage. Transition probabilities are selected so that system noise is always injected between target flight regime changes. Measurement processing at 10 Hz means multi-rate IMM operation, re-initialisation taking place at a lower rate. Sufficient information from the IMM is up-linked to extract the information added between measurement updates that is required for track fusion.

The target simulator is described concentrating on its isolation, stimulation using either reference data or corrupt sensor measurements, and the use of each tracking filter separately, or combined using an IMM algorithm.

4.1 Multiple-Model Architectures

Magill[M.3] was the first to used a set of filters in 1965, each filter with a different dynamic model to improve robustness, updated using a set of (m) measurements. The non-interacting adaptive multiple-model filter in Figure 4-1 appeared in 1987 in which the dynamic model resulting in the highest conditional probability was selected, Maybeck[M.4] and Stepaniak[S.11].

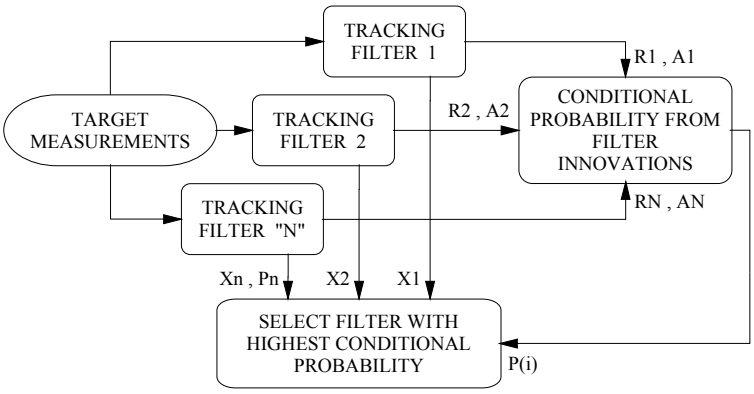

Figure 4-1 : Multiple-Model Estimator

The conditional probability is obtained for each filter using the Probability Density Function (PDF),

$$p := \frac{\exp\left(-0.5 \cdot \underline{\Delta Z}^{T} \cdot A^{-1} \cdot \underline{\Delta Z}\right)}{\sqrt{\left(2 \cdot \pi\right)^{m} \cdot \det\left(A\right)}}$$

Equation 4.1-1

The PFD (p) depends on m-measurement innovations ($\underline{\Delta Z}$) and covariance matrix [A], terms defined in §4.4.1. The next major development was to combine the state and covariance output from each filter weighted by their normalised conditional probabilities without filter re-initialisation. This is the Multiple-Model Adaptive Estimator (MMAE) shown in Figure 4-2.

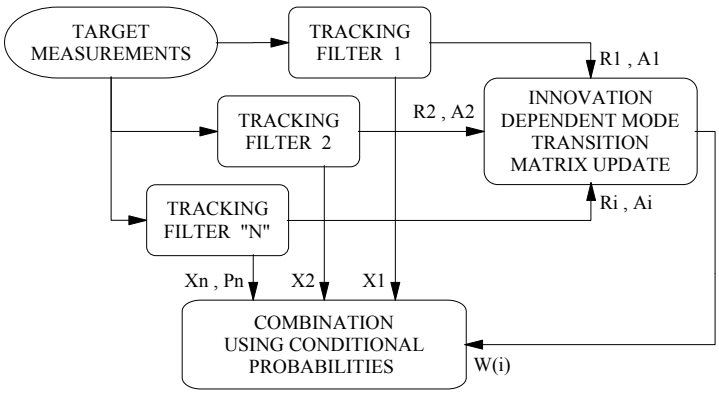

Figure 4-2 : Multiple-Model Adaptive Estimator

Further improvements were introduced by Li[L.5] and Bar-Shalom resulting in the Interacting Multiple-Model (IMM) shown in Figure 4-3. The IMM is attractive proposition being simple to implement and acts as host to many types of stochastic filter. Pulford[P.5], reviews different tracking algorithms supported by the IMM structure: static filters, conventional and Extended Kalman Filters (EKF) and adaptive, iterative and 2nd order variants, renewal processes and input estimators. The characteristic separating the IMM from other MMAE filters is the periodic re-initialisation of the filter with the normalised weighted sum of the states and covariances. The filter whose dynamics best match those of the target will dominate this process and prevent long-term problems with inappropriate filter dynamics. However, if a filter probability drops to zero it is permanently excluded from the ensemble. Li[L.5] extended the work of Zhang[Z.2] to producing a robust algorithm that prevents filter lock-out without using artificial lower bounds on the filter probabilities. Initial results presented when compared with the conventional IMM formulation were inconclusive and as yet do not warrant the considerable computational load increase involved. The speed of the transition between models as the target changes its flight regime depends on the relative change in the numerator and denominator of the PDF. Wheaton[W.2] showed that response can be improved by de-sensitising the effect of the denominator in Equation 4.1-1.

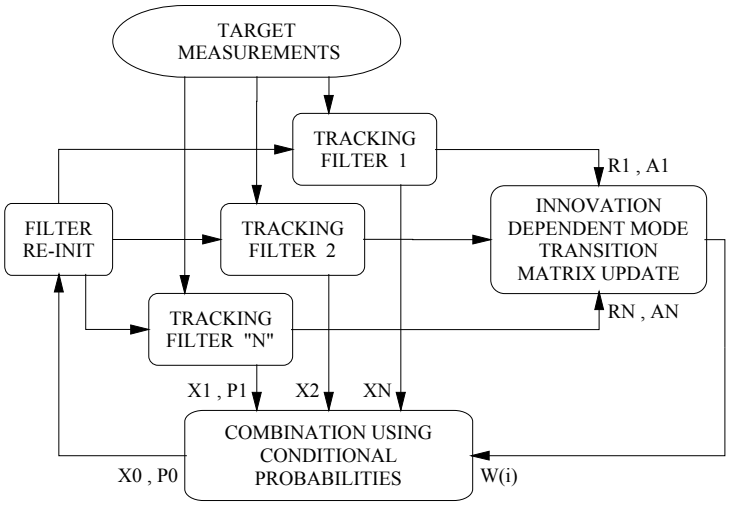

Figure 4-3 : Interacting Multiple Model

Eventually, increasing the number of filters degrades the accuracy of the combined output. Filters with inappropriate dynamics are kept active to prevent lock-out and contribute to the weighted sum. The problem of large filter banks to cope with complex target dynamics can be avoided by using a Variable-Structure IMM (VS-IMM), Kirubarajan[K.2]. An additional layer of logic is needed to select those dynamic models closest to the estimated dynamics of the target, removing filters from the active set, and initialising new filters. Research by Li, Zhang and Zhi into the VS-IMM may prove to be the basis of future tracking systems, providing that sufficient processing power is available. To minimise processor load Hanlon[H.6] established that

updating EKFs, each with different dynamics, can be performed using perturbations. He showed that this technique is equivalent to updating separate filters however, by taking advantage of the resulting sparseness the processing load is reduced. The relative merits of the fixed and variable structure multiple-model trackers is given in a comprehensive review of target tracking up to 1998 by Mazor[M.2]. The IMM is more robust than the MMAE since any divergence of a model with unsuitable dynamics is constrained within the re-initialisation period. Willsky[W.3] and Zhang[Z.2] reported that the IMM approach with EKFs was robust even when updated using measurements corrupted by non-Gaussian noise. The flexibility of the IMM is demonstrated when dealing with glint, typically a non-Gaussian measurement error. Two filters are provided, one tuned for Gaussian measurement errors, the another to deal with statistical outliers conforming to a Laplacian distribution, Daeipeur[D.4]. The IMM is shown to be more accurate than the Scoring Function technique pioneered by Masraliez[M.5], and renewal filters, even when the nature of the glint was ill-defined.

4.2 Tracking Filter States

Selecting the best tracking co-ordinates is highly subjective as it depends on the likely target dynamics ranging from non- manoeuvring flight to polar arcs. Although little definitive evidence exists, opinion tends to favour Cartesian rather than Polar states when dealing with non-specific target dynamics, Song[S.12], Bar_Shalom[B.5] and Mahapatra[M.6]. Notable experts such as Daum, Fitzgerald and Kerr favour polar co-ordinates as these are suited to the radar measurements provided and independent filters can be used in the measurement space. For long-range targets the stability of these filters is superior, avoiding the biases that arise due to inaccurate measurement conversion. The accurate radar range and range-rate measurements are not corrupted by less accurate angle measurements. When tracking short-range agile targets the cross-correlation between axes is lost and at high target LOS rates expected the performance of these filters can be poor, Ohmuro[O.2]. Sammons[S.21] found that tracking of manoeuvring targets using EKF formulations in polar space led to divergence, and although steps can be taken to mitigate the effect, they perform no better than Cartesian alternatives.

For the IMM it would be inconvenient to combine filter outputs expressed in different co-ordinate systems. Earth referenced Cartesian states have therefore been selected for the state observers, an ideal common reference for sensor alignment,

$$ {}_{IMM}\underline{X}_{TL} \equiv \left(\left(\underline{P}_t^A \right)^T , \left(\dot{\underline{P}}_t^A \right)^T , \left(\ddot{\underline{P}}_t^A \right)^T \right)^T $$

Equation 4.2-1

The use of "hat" identifying filtered data has been dropped for convenience, only measurements retain their kinematic type described in the Glossary.

When dealing with non-linear systems that require high accuracy from a conventional covariance EKF error states are often used. It is often the case that although the states change rapidly, the error in the states does not. The required parameters are obtained by combining the estimated errors and the measurements. The filter equations tend to be more complicated and require a larger processing capacity. Unless the system is expected to be so non-linear that EKF linearisation is likely to fail, the additional complication of error states is not justified for relatively short-range applications.

4.3 Tracking Filter Initialisation

Ideally, targets are tracked at long-range using surveillance radar and their track established long before they become a threat. This process provides smooth track data with which to initialise the IMM filters. In environments where targets can "pop-up" in the threat zone, radar plots are all that is available for rapid initialisation. Two methods are considered, least squares and $\alpha-\beta-\gamma$ filtering in each Cartesian axis,

$$ {}_{RD}\underline{\tilde{Z}}_T := \left(\tilde{P}_t^{XT} \quad , \quad \dot{\tilde{P}}_t^{XT} \quad , \quad \tilde{\Theta}_A^T \quad , \quad \tilde{\Psi}_A^T \right)^T $$

Equation 4.3-1

Transforming the range and angle measurements into Cartesian space,

$$ \underline{\tilde{P}}_t^A := \tilde{P}_t^{XT} \cdot \left(\cos\tilde{\Psi}_A^T \cdot \cos\tilde{\Theta}_A^T \quad , \quad \sin\tilde{\Psi}_A^T \cdot \cos\tilde{\Theta}_A^T \quad , \quad \sin\tilde{\Theta}_A^T \right)^T $$

Equation 4.3-2

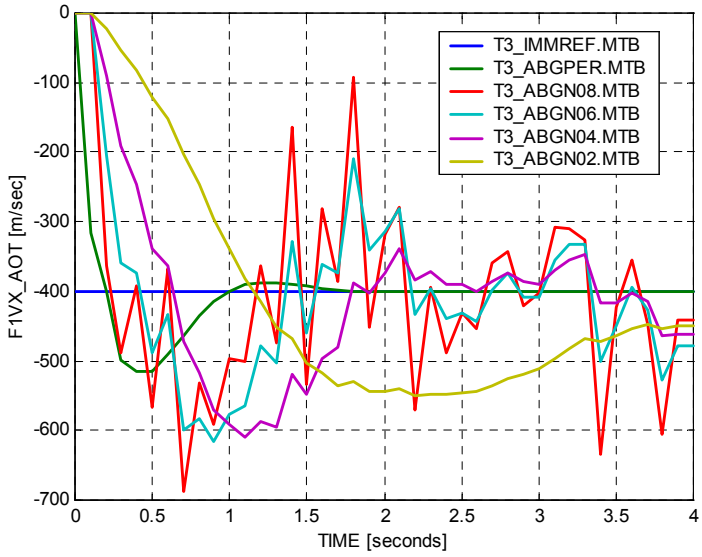

Figure 4-4 : $\alpha-\beta-\gamma$ Filtered Velocity (X-component)

Target 3 travelling at 400 m/s along $\underline{X}^A$ was used for the comparison (*IMMREF*). The range and angle measurements used to update the filters at

10 Hz was corrupted by 10m and 3 mrad (1σ) Gaussian noise. Position was initialised using the first measurement, and the remaining states were set to zero. Figure 4-4 shows the estimated velocity along $\underline{X}^A$ using α–β–γ filter bandwidths [0.2(0.2)0.8] Hz compared with the noise free case (ABGPER).

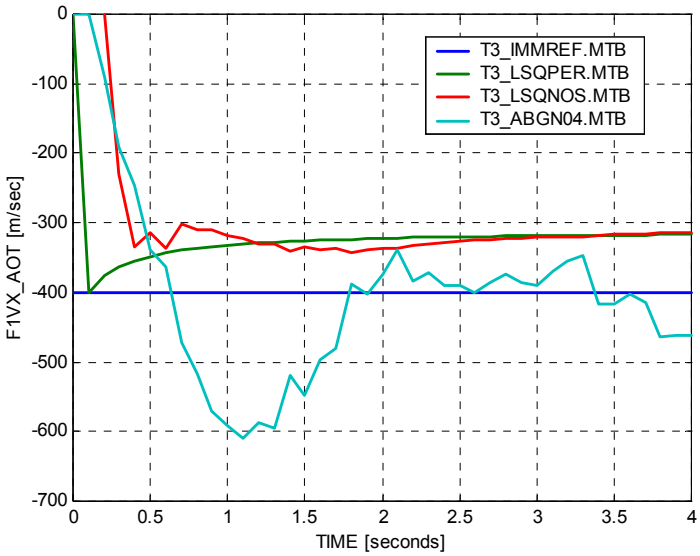

Figure 4-5 – Least Squares Velocity (X-component)

In Figure 4-5 an α–β–γ filter with a 0.4 Hz bandwidth is compared with a least-squares solution using (N) measurements proposed by Mahapatra[M.6],

$$\left(\hat{P}_t^{XA} \quad , \quad \hat{\dot{P}}_t^{XA} \quad , \quad \frac{\hat{\ddot{P}}_t^{XA}}{2} \right)^T := \begin{bmatrix} N & , & \sum_{i:=1}^{N} \Delta t & , & \sum_{i:=1}^{N} \Delta t^2 \\ \sum_{i:=1}^{N} \Delta t & , & \sum_{i:=1}^{N} \Delta t^2 & , & \sum_{i:=1}^{N} \Delta t^3 \\ \sum_{i:=1}^{N} \Delta t^2 & , & \sum_{i:=1}^{N} \Delta t^3 & , & \sum_{i:=1}^{N} \Delta t^4 \end{bmatrix}^{-1} \cdot [A]$$

Equation 4.3-3

$$[A] := \begin{bmatrix} \sum_{i:=1}^{N} \tilde{P}_t^{XA}(i) & , & \sum_{i:=1}^{N} \tilde{P}_t^{YA}(i) & , & \sum_{i:=1}^{N} \tilde{P}_t^{ZA}(i) \\ \sum_{i:=1}^{N} \tilde{P}_t^{XA}(i) \cdot \Delta t & , & \sum_{i:=1}^{N} \tilde{P}_t^{YA}(i) \cdot \Delta t & , & \sum_{i:=1}^{N} \tilde{P}_t^{ZA}(i) \cdot \Delta t \\ \sum_{i:=1}^{N} \tilde{P}_t^{XA}(i) \cdot \Delta t^2 & , & \sum_{i:=1}^{N} \tilde{P}_t^{YA}(i) \cdot \Delta t^2 & , & \sum_{i:=1}^{N} \tilde{P}_t^{ZA}(i) \cdot \Delta t^2 \end{bmatrix}$$

Equation 4.3-4

Although the least-squares method provides smooth estimates they are biased in this dynamic environment. An α–β–γ filter was used to initialise the IMM filters with a bandwidth of 0.4 Hz and a 3 s settling time. The IMM filter position covariances are determined from the Polar to Cartesian transformation,

$$E\left(\underline{\Delta P}_t^A\right)^2 := \left(\frac{\partial \underline{P}_t^A}{\partial \underline{\tilde{Z}}}\right) \cdot \operatorname{diag}\left(4\cdot\sigma_R^2 \quad , \quad 4\cdot\sigma_\Theta^2 \quad , \quad 4\cdot\sigma_\Psi^2\right) \cdot \left(\frac{\partial \underline{P}_t^A}{\partial \underline{\tilde{Z}}}\right)^T$$

Equation 4.3-5

The measurement uncertainty is doubled to accommodate any initialisation transients.

$$\left(\sigma_R^2 \quad , \quad \sigma_\Theta^2 \quad , \quad \sigma_\Psi^2\right) := \left(10^2 \quad , \quad 0.003^2 \quad , \quad 0.003^3\right)$$

Equation 4.3-6

$$E\left(\underline{\Delta \dot{P}}_t^A\right)^2 := 4\cdot 50^2 \cdot I_3$$

Equation 4.3-7

Normally the acceleration uncertainty reflects the sustained acceleration capability of the target, particularly if the radar can discriminate between target types. However, as a result of the initialisation pre-filtering used in this example,

$$E\left(\underline{\Delta \ddot{P}}_t^A\right)^2 := 4\cdot 50^2 \cdot I_3$$

Equation 4.3-8

A better approach to filter initialisation might be to isolate the IMM acceleration filter by setting its mode probability to 1 and transitional probabilities to 0. This method utilises the range-rate measurement thereby accelerating convergence and improving accuracy. The initial velocity and acceleration would be zero, and their uncertainties set commensurate with target capabilities; 300 m/s and 7 g for aircraft, increasing to 20 g for missiles.

4.4 Stochastic Filtering

Kalman[K.3] (1964) developed the most widely used minimum variance solution to a set of linear differential equations assuming Gaussian initialisation, process and measurement noise. When used for non-linear tracking the process and measurement models are linearised in a form known as an EKF, a form often reported to be sub-optimal when updated using measurements corrupted by non-Gaussian errors. Much research has been undertaken to mitigate the effect of non-linear measurements on

Kalman Filters. Notable are the scoring functions by Masreliez[M.7], their practical implementation resulting in near optimal performance by Wu[W.4-5], particle filtering by Carvelho[C.4], pre-whitening of glint distributions by Hewer[H.7]. In practice the EKF has proven remarkably robust, providing good estimates providing that its basic tenants are only weakly violated, Bowles[B.7]. In most practical situations all filters tend to be non-linear and therefore sub-optimal, Chang[C.5]. The EKF has significant advantages compared with more complex algorithms that tend to outweigh their detrimental features:

- Simple to implement
- Amenable to matrix partitioning
- Processor load reduction when dealing with sparse systems
- Accessible covariances for firing solutions and missile guidance
- Simple prediction to compensate for deterministic time delays
- Parallel, serial and asynchronous measurements accommodated in a wide variety of forms, with rate variations and loss of data
- Automatically accounts for the correlations between states
- Process and measurement noise adaptation based on innovation statistics

Inevitably, more advanced filters will be compared with performance of the humble EKF of which the Iterated EKF (IEKF) and the Second Order Filters (SOF) are the most prominent. These formulations improve the EKF's state and measurement linearisation, hence the evolution of the probability density function associated with the covariance matrix. Adaptive noise formulations must not be used for the IMM as the dynamical models used must be distinct for filter transition. The IMM combines the state and covariance from each active filter making the conventional covariance formulation ideal. Persistent use of system noise, and the longer word-lengths used in modern processors, has seen the demise of the more robust EKF square root and UDU^T formulations attributed to Carlson[C.6] and Bierman[B.7], possibly because the state covariance is not a direct available. In IMM filters the system noise must be kept to a minimum (sufficient to accommodate filter digitisation) to enhance filter selection.

4.4.1 Extended Kalman Filter

The continuous dynamics of a system are defined in the filter process model using a set of stochastic differential equations,

$$\dot{\underline{X}}(t) := \underline{f}\left(\underline{X}(t), \underline{U}(t), t\right) + G(t) \cdot \underline{w}_c(t)$$

The vector function ($\underline{f}$) depends on the reference state ($\underline{X}$), deterministic input ($\underline{U}$), and Gaussian noise. For this application the "deterministic" input is an unknown piecewise constant acceleration that is usually dealt with using process noise. In the context of IMM filters several acceleration

levels might be used as inputs rather change a single filter's input - the term was ignored. [G] is the continuous noise distribution matrix, and ($\underline{w}_c$) is a zero mean Gaussian noise vector of power spectral density ($\underline{q}$) where,

$$E\left(\underline{w}_c\right) = \underline{0} \quad \Rightarrow \quad \underline{w}_c(t) \coloneqq N\left(0, \underline{q}(t)\right)$$

Equation 4.4-1

When the dynamics of a system are non-linear the states are usually propagated directly from an initial estimate of the state,

$$\dot{\hat{\underline{X}}}(t) \coloneqq \underline{f}\left(\hat{\underline{X}}(t), t\right)$$

Equation 4.4-2

The discrete form of Equation 4.4-2 is,

$$\underline{X}_{k+1} \coloneqq \Phi_k^{k+1} \cdot \underline{X}_k + \Gamma_k \cdot \underline{w}_k$$

Equation 4.4-3

With noise characteristics,

$$\left(E\left(\underline{w}_k\right), E\left(\underline{w}_k \cdot \underline{w}_k^T\right)\right) \coloneqq \left(\underline{0}, \sigma_w^2\right)$$

Equation 4.4-4

The state transition matrix [Φ] over the propagation interval (Δt) from time (t_k) to (t_{k+1}), assuming that ($\underline{f}$) is slowly varying,

$$\Phi_k^{k+1} \coloneqq \exp\left(\Delta t \cdot \frac{\partial f}{\partial \underline{X}}\right) \approx \left[I_n\right] + \Delta t \cdot \frac{\partial f}{\partial \underline{X}}$$

Equation 4.4-5

In an EKF the exponential is expanded about the estimated state ($\hat{\underline{X}}$) state at time (t_k) and truncating to 1st order. The error in the state estimate,

$$\underline{\Delta X} \coloneqq \hat{\underline{X}} - \underline{X}$$

Equation 4.4-6

The expected error in the estimated state is embodied in the symmetric, positive definite state covariance matrix,

$$C \coloneqq E\left(\Gamma \cdot \underline{\omega}_k, \left(\Gamma \cdot \underline{\omega}_k\right)^T\right) \equiv E\left(\underline{\Delta X} \cdot \underline{\Delta X}^T\right)$$

Equation 4.4-7

Propagating the state covariance matrix over the time interval (Δt),

$$C_{k+1}^{-} \coloneqq \Phi_k^{k+1} \cdot C_k^{-} \cdot \left[\Phi_k^{k+1} \right]^T + \Gamma_k \cdot Q_k \cdot \Gamma_k^T$$

Equation 4.4-8

The symmetric, semi-definite, covariance matrix (Q) is computed between measurement updates from,

$$\Gamma_k \cdot Q_k \cdot \Gamma_k^T \coloneqq$$

$$\int_{t_k}^{t_{k+1}} \left(\Phi_\tau^{k+1} \cdot G(\tau) \cdot \mathrm{diag}\left(\underline{q}(\tau) \right) \cdot \left[G(\tau) \right]^T \cdot \left[\Phi_\tau^{k+1} \right]^T \right) d\tau$$

Equation 4.4-9

If Δt is small, the transition matrix collapses to the identity matrix and,

$$Q_k \coloneqq G_k \cdot \mathrm{diag}\left(\underline{q}(k) \right) \cdot G_k^T \cdot \Delta t$$

Equation 4.4-10

Assuming that the sensor measurements ($\underline{\tilde{Z}}$) are non-linear functions of the reference state vector at time (t_{k+1}) plus zero mean Gaussian noise,

$$\underline{\tilde{Z}} \coloneqq \underline{h}\left(\underline{X} \right) + \underline{\upsilon}$$

Equation 4.4-11

$$E\left(\underline{\upsilon} \right) \coloneqq 0 \Rightarrow E\left(\underline{\upsilon} \cdot \underline{\upsilon}^T \right) \coloneqq R$$

Equation 4.4-12

[R] is the symmetric, positive definite measurement covariance matrix. The expected measurement is computed using the state approximation propagated to the measurement reference time (t_{k+1}),

$$\underline{\hat{Z}} \coloneqq \underline{h}\left(\underline{\hat{X}}_{k+1}^{-} \right)$$

Equation 4.4-13

Expanding the measurement functions in a series about the estimated state,

$$\underline{h}\left(\underline{X}_{k+1} \right) \coloneqq \underline{h}\left(\underline{\hat{X}}_{k+1}^{-} \right) + H \cdot \underline{\Delta X} + 2^{-1} \cdot \underline{\Delta X} \cdot G \cdot \underline{\Delta X}^T + \cdots$$

Equation 4.4-14

The innovation ($\underline{\Delta Z}$) is the difference between the actual and predicted measurements,

$$\underline{\Delta Z} \;:=\; \underline{\tilde{Z}} - \underline{\hat{Z}} \;:=\; \left(\frac{\partial \underline{h}}{\partial \underline{X}} \cdot \underline{\Delta X} + 2^{-1} \cdot \underline{\Delta X}^{T} \cdot \frac{\partial^2 \underline{h}}{\partial \underline{X}^2} \cdot \underline{\Delta X} + \cdots \right) + \underline{\upsilon}$$

Equation 4.4-15

The measurement Jacobian (H), and Hessian [G], are computed using the state at time (t_{k+1}) - in the EKF the Hessian is ignored. The measurement innovation is then apportioned between the states by the Kalman gains so as to minimise the trace of the covariance matrix, Gelb[G.12] (p186),

$$\underline{\hat{X}}_{k+1}^{+} \;:=\; \underline{\hat{X}}_{k+1}^{-} + K_{k+1} \cdot \underline{\Delta Z}_{k+1}$$

Equation 4.4-16

$$K_{k+1} \;:=\; \frac{C_{k+1}^{-} \cdot H_{k+1}^{T}}{H_{k+1} \cdot C_{k+1}^{-} \cdot H_{k+1}^{T} + R_{k+1}} \;\equiv\; \frac{C_{k+1}^{-} \cdot H_{k+1}^{T}}{A_{k+1}}$$

Equation 4.4-17

The covariance matrix is update using the simple expression,

$$C_{k+1}^{+} \;=\; \left(I_3 - K_{k+1} \cdot H_{k+1} \right) \cdot C_{k+1}^{-}$$

Equation 4.4-18

Nishimara[N.3] showed that Joseph's form of this equation yields the correct covariance whether the Kalman gains are optimal or not. This form should always be used in the IEKF, Kerr[K.4],

$$C_{k+1}^{+} \;:=\; \left(I - K_{k+1} \cdot H_{k+1} \right) \cdot C_{k+1}^{-} \cdot \left(I - K_{k+1} \cdot H_{k+1} \right)^{T} + K_{k+1} \cdot R_{k+1} \cdot K_{k+1}^{T}$$

Equation 4.4-19

Measurements should be processed serially to avoid matrix inversion, and to accommodate reduced order and asynchronous measurement sets. The effect of process model and linearisation errors on [A], [H], [Φ] and ($\underline{\Delta Z}$) is quantified by Hanlon[H.8].

4.4.2 Iterated EKF

EKF measurement linearisation can be performed about any trajectory. If the filter is to be well conditioned the trajectory about which linearisation is performed should ideally be close to the reference trajectory. If the state estimates become too inaccurate, as might be the case after a long period of prediction, transformed measurements are often substituted. The IEKF iterates process and measurement linearisation, a process that if taken to

convergence is equivalent to a maximum likelihood estimator. When the system model is linear the iterative process can be restricted to the measurement update.

$$\underline{\eta}_0 \coloneqq \hat{\underline{X}}^{-}_{k+1}$$

Equation 4.4-20

$$H\left(\underline{\eta}_i\right) \coloneqq \partial \underline{h}\left(\underline{\eta}_i\right) / \partial \underline{X}$$

Equation 4.4-21

$$K_{k+1}\left(\underline{\eta}_i\right) \coloneqq \frac{C^{-}_{k+1}\left(\underline{\eta}_0\right) \cdot H^{T}_{k+1}\left(\underline{\eta}_i\right)}{H_{k+1}\left(\underline{\eta}_i\right) \cdot C^{-}_{k+1}\left(\underline{\eta}_0\right) \cdot H^{T}_{k+1}\left(\underline{\eta}_i\right) + R_{k+1}\left(\underline{\eta}_i\right)}$$

Equation 4.4-22

$$\underline{\eta}_{i+1} \coloneqq$$

$$\hat{\underline{X}}^{-}_{k+1} + K_{k+1}\left(\underline{\eta}_i\right) \cdot \left(\tilde{\underline{Z}}_{k+1} - \hat{\underline{Z}}_{k+1}\left(\underline{\eta}_i\right) - H_{k+1}\left(\underline{\eta}_i\right) \cdot \left(\hat{\underline{X}}^{-}_{k+1} - \underline{\eta}_i \right) \right)$$

Equation 4.4-23

After (N) iterations,

$$\hat{\underline{X}}^{+}_{k+1} \coloneqq \underline{\eta}_N$$

Equation 4.4-24

This formulation differs from that usually presented, Gelb[G.12]. Here the covariance matrix is updated after the state estimate has converged to reduce processor load, Kerr[K.4]. When serially processing measurements their innovations, [H], and [C] must be computed using (η_i) and not the intermediate state vector resulting from a partial measurement set update. In practice iteration is usually restricted to processes updated an infrequent intervals rather than the relatively high frequency used in this application.

4.4.3 Second Order Filter

When measurements are non-linear in the state space neglecting higher order terms during linearisation introduces biases. The SOF retains the Hessian in Equation 4.4-15 and although the SOF is a natural extension of the EKF it is strictly a separate class of filter, Kerr[K.4]. The following modifications are required to the EKF as a result,

$$\hat{\underline{X}}^{+} \;:=\; \hat{\underline{X}}^{-} + [K] \cdot \left(\underline{\Delta Z} - \frac{1}{2} \cdot \sum_{i,j} \left(C(i,j) \cdot \frac{\partial^2 \underline{h}}{\partial \underline{X}_i \cdot \partial \underline{X}_j} \right) \right)$$

Equation 4.4-25

$$K \;:=\; \frac{P^{-} \cdot H^{T}}{H \cdot P^{-} \cdot H^{T} + R + 2^{-1} \cdot S}$$

Equation 4.4-26

$$S(i,j) \;:=\; \sum_{i,m,n,j} \left(\frac{\partial^2 \underline{h}}{\partial \underline{X}_i \cdot \partial \underline{X}_m} \cdot C(m,n) \cdot C(i,j) \cdot \frac{\partial^2 \underline{h}}{\partial \underline{X}_n \cdot \partial \underline{X}_j} \right)$$

Equation 4.4-27

The EKF projects the covariance surface linearly along the gradient to the estimated state trajectory. Although the SOF replaces this with parabolic projection, in highly non-linear systems even this can result in deviation from the true covariance. A crude approach is to increase the system noise thereby expanding the uncertainties to ensure that they encompass the true errors at the expense of observability. A promising technique presented by Julier[J.2] propagates defining points on the covariance surface using (f) and re-computes the correct mean and covariance statistics after projection,. Although the method is only accurate to 2nd order it is shown to improve the 3rd and 4th moments that by definition are zero in the SOR.

4.4.4 Converted Measurement Kalman Filter

In the Converted Measurement KF (CMKF) the measurements and their uncertainties are converted into the state space before performing the measurement update. Park[P.6] showed that the CMKF is more accurate than the conventional EKF formulation if the bearing error is < 1.5º. Bar-Shalom[B.5] also obtained better results from the CMKF for measurement errors > 0.5º albeit using a de-biasing transformation algorithm. Near-optimal results for bearing errors up to 10° are possible providing the angular uncertainty is know accurately, Longbin[L.6] and Lerro[L7]. In this application the measurement errors are relatively small, certainly less than 6 mrad, and the technique was not considered.

4.4.5 Modified Gain EKF

Universal linearisation implies that (h) can be expressed as, Speyer[S.13],

$$h(\underline{X}) - h\left(\hat{\underline{X}}^{-}\right) \;:=\; g\left(Z, \hat{\underline{X}}^{-}\right) \cdot \underline{\Delta X}$$

Equation 4.4-28

$$C := (I - K \cdot g) \cdot C \cdot (I - K \cdot g)^T + K \cdot R \cdot K^T$$

Equation 4.4-29

The stability of the Modified Gain EKF (MGEKF) and the provision of bias free estimates using bearings only measurements with non-Gaussian characteristics was studied by Song[S.14]. Since the range and range-rate measurements are not in the class of modifiable functions this technique is not suitable for this application.

4.5 IMM Mode Conditioned Filters

The dynamics of each filter in an IMM must be distinct, avoiding large injections of system noise making it difficult to distinguish between them, Stepaniak[S.11]. If filters of the same generic type are used their noise levels should differ by a factor of ≈10 so that they operate in distinct frequency bands, particularly when switching between manoeuvring and non-manoeuvring models, Wheaton[W.2]. Filters with noise adaptation are unsuitable for the IMM application. The following target models were selected (identifying their parameters using the letter in parenthesis):

- Constant velocity filter (V)
- Constant acceleration filter (A)
- 1st order Gauss-Markov (Singer) filter (S)
- Weaving tuned target filter (W)

At long-range it is assumed that targets travel at constant speed interrupted by short bursts of acceleration. As the range reduces high acceleration avoidance manoeuvres can be expected. Apart from the 1st order Gauss-Markov (Singer) filter the others use small amounts of system noise. The Singer filter is used to inject omni-directional noise system noise into the IMM to cope with changing target modes when its flight regime is uncertain, rather than target velocity directed noise. The Singer filters expressed in an Earth fixed frame are a poor representation of target dynamics compared with body directed acceleration models and its mode probability should fall once a new flight regime has been established.

4.5.1 Constant Velocity Filter

A non co-ordinated velocity model driven by noise in each Cartesian axis,

$$_V\ddot{P}_t^{iA} := {}_Vw^{iA}$$

Equation 4.5-1

The state transition and system noise matrices for each axis,

$$\left({}_{V}\Phi \quad , \quad {}_{V}Q^{A} \right) := \left(\begin{bmatrix} 1 & , & \Delta t \\ 0 & , & 1 \end{bmatrix} \quad , \quad {}_{V}q_{t} \cdot \begin{bmatrix} \Delta t^{3}/3 & , & \Delta t^{2}/2 \\ \Delta t^{2}/2 & , & \Delta t \end{bmatrix} \right)$$

Equation 4.5-2

$({}_{V}q_{t})$ represents the noise power spectral density in $(m^2/s^4/Hz)$,

4.5.2 Constant Acceleration Filter

Target longitudinal acceleration is generally small compared with lateral manoeuvring accelerations and target motion is best described by a constant "g" turn - the circular dynamic model, Nabaa[N.4]. The acceleration is directed along Target Velocity axes rather than Alignment axes, the state transition and noise covariance matrices being,

$${}_{A}\Phi := \begin{bmatrix} I_3 & \vdots & \Delta t \cdot I_3 & \vdots & 2^{-1} \cdot \Delta t \cdot I_3 \cdot T_{TV}^{A} \\ \cdots & \vdots & \cdots & \vdots & \cdots \\ 0_{3x3} & \vdots & I_3 & \vdots & \Delta t \cdot I_3 \cdot T_{TV}^{A} \\ \cdots & \vdots & \cdots & \vdots & \cdots \\ 0_{3x3} & \vdots & 0_{3x3} & \vdots & I_3 \end{bmatrix}$$

Equation 4.5-3

$${}_{A}Q^{A} :=$$

$$\begin{bmatrix} \frac{\Delta t^5}{20} \cdot T_{TV}^{A} \cdot {}_{A}q^{TV} \cdot T_{A}^{TV} & \vdots & \frac{\Delta t^4}{8} \cdot T_{TV}^{A} \cdot {}_{A}q^{TV} \cdot T_{A}^{TV} & \vdots & \frac{\Delta t^3}{6} \cdot T_{TV}^{A} \cdot {}_{A}q^{TV} \\ \cdots & \vdots & \cdots & \vdots & \cdots \\ \frac{\Delta t^4}{8} \cdot T_{TV}^{A} \cdot {}_{A}q^{TV} \cdot T_{A}^{TV} & \vdots & \frac{\Delta t^3}{3} \cdot T_{TV}^{A} \cdot {}_{A}q^{TV} \cdot T_{A}^{TV} & \vdots & \frac{\Delta t^2}{2} \cdot T_{TV}^{A} \cdot {}_{A}q^{TV} \\ \cdots & \vdots & \cdots & \vdots & \cdots \\ \frac{\Delta t^3}{6} \cdot T_{TV}^{A} \cdot {}_{A}q^{TV} & \vdots & \frac{\Delta t^2}{2} \cdot T_{TV}^{A} \cdot {}_{A}q^{TV} & \vdots & \Delta t \cdot T_{TV}^{A} \cdot {}_{A}q^{TV} \end{bmatrix}$$

Equation 4.5-4

This noise matrix is diagonal and the elements of the PSD vector are selected dependent upon the expected manoeuvring capability of the target,

$$\left[{}_{A}q^{TV} \right] := \operatorname{diag}\left({}_{A}\underline{q}^{TV} \right)$$

Equation 4.5-5

Not only are the propagation equations more complex using directional acceleration states they must be transformed into the Alignment frame before IMM assimilation. As the IMM measurement updates are frequent

(10 Hz), and the system noise used is to be small and omni-directional, this computationally intensive model is replaced by a non co-ordinated mean jerk acceleration model in each Cartesian axis,

$$ {}_A\dddot{P}_t^{iA} \coloneqq {}_A w^{iA} $$

Equation 4.5-6

$$ \left({}_A\Phi \ , \ {}_A Q^A \right) \coloneqq $$

$$ \left(\begin{bmatrix} 1 & \Delta t & \Delta t^2/2 \\ 0 & 1 & \Delta t \\ 0 & 0 & 1 \end{bmatrix} , {}_A q_t \cdot \begin{bmatrix} \Delta t^5/20 & \Delta t^4/8 & \Delta t^3/6 \\ \Delta t^4/8 & \Delta t^3/3 & \Delta t^2/2 \\ \Delta t^3/6 & \Delta t^2/2 & \Delta t \end{bmatrix} \right) $$

Equation 4.5-7

$({}_A q_t)$ represents the noise power spectral density in $(m^2/s^6/Hz)$. The quantity $\sqrt{{}_A q_t \, \Delta t}$ representing the change in acceleration over the sampling period.

4.5.3 <u>1st Order Gauss-Markov Filter</u>

A non co-ordinated 1st order Gauss-Markov model was proposed by Singer[S.15] with a manoeuvre dependent correlation time representing a target turn duration (τ_C) driven by white noise. For each Cartesian axis,

$$ {}_S\underline{\dddot{P}}_t^A \coloneqq - {}_S\tau_C^{-1} \cdot {}_S\underline{\ddot{P}}_t^A + {}_S\underline{w}^A $$

Equation 4.5-8

According to Nabaa[N.4] the correlation time (turn duration) of a typical fighter aircraft is [1,5] s. The state transition matrix,

$$ \Phi \coloneqq \begin{bmatrix} 1 & \Delta t & {}_S\tau_C^2 \cdot \left(\varphi - 1 + \tau_C^{-1} \cdot \Delta t \right) \\ 0 & 1 & {}_S\tau_C \cdot \left(1 - \varphi \right) \\ 0 & 0 & \varphi \end{bmatrix} $$

Equation 4.5-9

$$ \left(\varphi \ , \ \beta \right) \coloneqq \left(\exp\left(-\beta \right) \ , \ \Delta t \ / \ {}_S\tau_C \right) $$

Equation 4.5-10

The elements of the fully expanded system noise covariance matrix where (σ_t) is the rms target acceleration uncertainty,

$$q_{11} := {}_S\sigma_t^2 \cdot {}_S\tau_C^4 \cdot \left(1 - \varphi^2 + 2 \cdot \beta - 2 \cdot \beta^2 + \frac{2}{3} \cdot \beta^3 - 4 \cdot \varphi \cdot \beta \right)$$

Equation 4.5-11

$$q_{12} := {}_S\sigma_t^2 \cdot {}_S\tau_C^3 \cdot \left(1 + \varphi^2 - 2 \cdot \varphi + 2 \cdot \varphi \cdot \beta - 2 \cdot \beta + \beta^2 \right)$$

Equation 4.5-12

$$q_{13} := {}_S\sigma_t^2 \cdot {}_S\tau_C^2 \cdot \left(1 - 2 \cdot \varphi \cdot \beta - \varphi^2 \right)$$

Equation 4.5-13

$$q_{22} := {}_S\sigma_t^2 \cdot {}_S\tau_C^2 \cdot \left(-3 + 4 \cdot \varphi + 2 \cdot \beta - \varphi^2 \right)$$

Equation 4.5-14

$$q_{23} := {}_S\sigma_t^2 \cdot {}_S\tau_C \cdot \left(1 - 2 \cdot \varphi + \varphi^2 \right)$$

Equation 4.5-15

$$q_{33} := {}_S\sigma_t^2 \cdot {}_S\tau_C \cdot \left(1 - 2 \cdot \varphi^2 \right)$$

Equation 4.5-16

When (β) is small these equations tend to the asymptotic form,

$${}_SQ^A := \left(2 \cdot {}_S\sigma_t^2 \,/\, {}_S\tau_C \right) \cdot {}_AQ^A$$

Equation 4.5-17

The acceleration probability in the Singer model is uniformly distributed between the maximum acceleration limit ($\pm A_{MAX}$) with a probability of ($\pm P_{MAX}$); the no manoeuvre probability being (P_0),

$${}_S\sigma_t^2 := A_{MAX}^2 \cdot \left(1 + 4 \cdot P_{MAX} - P_0 \right) / 3$$

Equation 4.5-18

If the maximum acceleration of a manned jet aircraft is 9 g for short periods during evasion manoeuvres,

$${}_S\sigma_t := \sqrt{5 / 3} \cdot A_{MAX} \approx 80\,\mathrm{m/s^2}$$

Equation 4.5-19

A drawback of this model is the apriori selection of maximum acceleration and manoeuvre duration. In the context of the IMM this model is only

required during transients lasting some 5 s. Whilst the non co-ordinated models here are specified in Cartesian axes, fixed wing target motion is best expressed in a body referenced curvature, torsion and bi-normal (Frenet) axes, Chen[C.7]. Much effort has been expended in this field which is reviewed by Nabaa[N.4]. Singer's original model was improved by Gholson[G.13] (1977), Moose[M.8&9] (1975-79), Ricker[R.13] (1978) by including randomly switched mean acceleration input with a Gaussian noise residual.

$$\underline{X}_{k+1} \;:=\; A_k \cdot \underline{X}_k + \Gamma_k \cdot \left(\underline{U}_k + \underline{w}_k \right)$$

Equation 4.5-20

Berg[B.8] (1983) added an adaptive mean jerk term to accommodate co-ordinated target dynamics with constant thrust, drag, lift and zero roll rate,

$$\dddot{\underline{P}}_t^A \;:=\; -\tau_C^{-1} \cdot \left(\ddot{\underline{P}}_t^A - \underline{w}^A \right) + \overline{\dddot{\underline{P}}}_t^A$$

Equation 4.5-21

Song[S.12] (1988) included target dynamics free of Berg's restrictions, mean jerk being a function of target velocity directed lateral acceleration estimated from its mass, velocity and lift coefficient. Mahapatra[M.6] introduced jerk states, significantly improving velocity and acceleration estimates for an idealised circular trajectory, even when jerk was absent. However, Vergez[V.1] showed that increasing the filter order in general degrades tracking performance compared with the Singer and acceleration models.

4.5.4 Weave Filter

Assuming that the target speed and turn rate are constant over the propagation interval,

$${}_W\dddot{\underline{P}}_t^{iA} \;:=\; -\left(\underline{\omega}_{A,TV}^A \right)^2 \times {}_W\dot{\underline{P}}_t^{iA} + {}_W\underline{w}^{iA}$$

Equation 4.5-22

$${}_W\Phi^i \;:=\; \exp\left(\begin{pmatrix} 0 & , & 1 & , & 0 \\ 0 & , & 0 & , & 1 \\ 0 & , & \left(\omega_{A,TV}^{iA} \right)^2 & , & 0 \end{pmatrix} \cdot \Delta t \right)$$

Equation 4.5-23

Expanding and expressing in terms of cosine and sine series,

$$ {}_{W}\Phi^{i} \;:= $$

$$ \begin{pmatrix} 1 & , & \sin\left(\omega^{iA}_{A,TV}\cdot\Delta t\right)/\omega^{iA}_{A,TV} & , & \left(1-\sin\left(\omega^{iA}_{A,TV}\cdot\Delta t\right)\right)/\left(\omega^{iA}_{A,TV}\right)^{2} \\ 0 & , & \cos\left(\omega^{iA}_{A,TV}\cdot\Delta t\right) & , & \sin\left(\omega^{iA}_{A,TV}\cdot\Delta t\right) \\ 0 & , & -\omega^{iA}_{A,TV}\cdot\sin\left(\omega^{iA}_{A,TV}\cdot\Delta t\right) & , & \cos\left(\omega^{iA}_{A,TV}\cdot\Delta t\right) \end{pmatrix} $$

Equation 4.5-24

These dynamics were used by Vorley[V.3] to derive the weave tuned filters presented in §21.5, and by Nabbaa[N.4] when comparing constant and variable speed co-ordinated turning models. The state observer provides an estimation of the weave frequency,

$$ \underline{\omega}^{A}_{A,TV} \;:= \left.\underline{\dot{P}}^{A}_{t}\times\underline{\ddot{P}}^{A}_{t}\;/\;\dot{P}^{2}_{o,t}\right|_{0.16} $$

Equation 4.5-25

For the IMM a lower limit of 0.025 Hz is placed on the weave frequency estimate, first to avoid numerical problems, and also to prevent asymptotic reduction to an acceleration filter. The weave frequency accuracy requirements for CLOS guidance are explored in §6.

4.6 IMM Filter Measurement Updates

Target range, range rate and angle measurements from a phased array radar stimulate each filter in the IMM,

$$ {}_{RD}\underline{\tilde{Z}}_{T} \;:= \left(\tilde{P}^{XT}_{t} \;,\; \tilde{\dot{P}}^{XT}_{t} \;,\; \tilde{\Psi}^{T}_{A} \;,\; \tilde{\Theta}^{T}_{A}\right)^{T} $$

Equation 4.6-1

The estimated target measurements are (kinematic type is clear in context),

$$ {}_{RD}\underline{Z}_{T} \;:= $$

$$ \left(\sqrt{\underline{P}^{A}_{t}\bullet\underline{P}^{A}_{t}} \;,\; \frac{\underline{P}^{A}_{t}\bullet\underline{\dot{P}}^{A}_{t}}{P_{o,t}} \;,\; \tan^{-1}\left(\frac{P^{YA}_{t}}{P^{XA}_{t}}\right) \;,\; -\tan^{-1}\left(\frac{P^{ZA}_{t}}{P^{hA}_{t}}\right)\right)^{T} $$

Equation 4.6-2

The linearised measurement matrix with respect to the IMM states at the measurement reference time,

$$ {}_{RD}H_{TL} \equiv \frac{\partial\, {}_{RD}\underline{Z}_T}{\partial\, {}_{IMM}\underline{X}_{TL}} := \left(\frac{\partial P_t^{XT}}{\partial \underline{X}_{TL}} , \frac{\partial \dot{P}_t^{XT}}{\partial \underline{X}_{TL}} , \frac{\partial \Psi_A^T}{\partial \underline{X}_{TL}} , \frac{\partial \Theta_A^T}{\partial \underline{X}_{TL}} \right)^T $$

Equation 4.6-3

The range measurement Jacobian,

$$ \partial P_t^{XT} / \partial \underline{X}_{TL} := \left(\left(\underline{P}_t^A \right)^T / P_{o,t} , \underline{0}_6^T \right) $$

Equation 4.6-4

The target bearing measurement Jacobian,

$$ \partial \Psi_A^T / \partial \underline{X}_{TL} := \left(P_t^{hA} \right)^{-2} \cdot \left(-P_t^{YA} , P_t^{XA} , \underline{0}_7^T \right) $$

Equation 4.6-5

The target elevation measurement Jacobian,

$$ \partial \Theta_A^T / \partial \underline{X}_{TL} := \left(\frac{P_t^{XA} \cdot P_t^{ZA}}{P_t^{hA} \cdot P_{o,t}^2} , \frac{P_t^{YA} \cdot P_t^{ZA}}{P_t^{hA} \cdot P_{o,t}^2} , -\frac{P_t^{hA}}{P_{o,t}^2} , \underline{0}_6^T \right) $$

Equation 4.6-6

The range-rate measurement Jacobian,

$$ \partial \dot{P}_t^{XT} / \partial \underline{X}_{TL} := \left(\frac{\left(\underline{\dot{P}}_t^A \right)^T}{P_{o,t}} - \frac{\dot{P}_t^{XT} \cdot \left(\underline{P}_t^A \right)^T}{P_{o,t}^2} , \left(\underline{P}_t^A \right)^T / P_{o,t} , \underline{0}_3^T \right) $$

Equation 4.6-7

The measurement covariance,

$$ {}_{RD}R_T := \mathrm{diag} \left(10^2 , 4^2 , 0.003^2 , 0.003^2 \right) $$

Equation 4.6-8

Frequency agility reduces any time dependent error correlation so each measurement can be considered as independent. Phased array radar generally maintain a near-constant SNR which means the measurement errors are independent of range and can be treated as constants rather than functions of the radar SNR.

4.7 IMM Initialisation

Assuming that target-tracking starts at long-range and is quiescent, the individual filter weights are biased towards the constant velocity filter,

$$\mu^{+} := \begin{pmatrix} 0.70 & 0.05 & 0.20 & 0.05 \end{pmatrix}$$

Equation 4.7-1

Switching between filters evolves according to a time-invariant, semi-Markov chain defined by a constant switching probability matrix. This process is characterised by the time between changes in the flight regime, often referred to as the sojourn time. If the switching matrix is diagonally dominant, and each element is close to 1, with small but equal off-diagonal transitional probabilities, the sojourn time is random. This is unrealistic as it implies that a target regime changes rapidly. The transition probabilities chosen are biased towards the existing flight regime (the Singer filter is a transitional mode).

$$\Xi := \begin{bmatrix} 0.70 & 0 & 0.3 & 0 \\ 0 & 0.7 & 0.3 & 0 \\ 0.25 & 0.25 & 0.25 & 0.25 \\ 0 & 0 & 0.3 & 0.7 \end{bmatrix}$$

Equation 4.7-2

The transitions between the filters are shown in Figure 4-6. Direct transitions are prevented so that the Singer filter can expand the filter uncertainties before another flight regime is established. The probability that covariance expansion continues, or another flight regime is established, being equally likely. The injection of system noise is expected to improve the overall filter just after a manoeuvre has started since transition between specific flight regimes is prohibited.

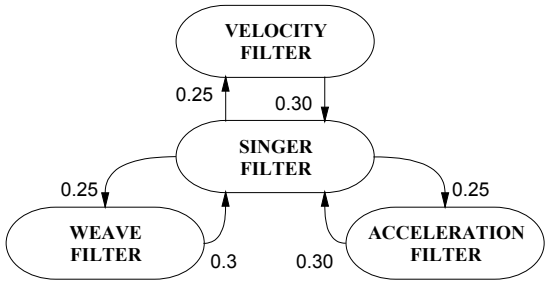

Figure 4-6

Mode Transition Probabilities

In formulations such as renewal filters the sojourn time depends on how long a flight regime has been dominant. The sojourn time increases exponentially implying that the longer a flight regime has existed the more likely it is that a mode transition will occur. The transition probabilities are thus determined by a sojourn time that depends on a Poisson or Gamma distribution rather than a Normal distribution.

4.8 IMM Filter Mixing

Filters require time to evolve so that the measurement innovations from those with inappropriate dynamic models rise above the general noise level for discrimination purposes. This is particularly important for weave filters as even under ideal conditions a quarter of a weave cycle is needed to differentiate between them and other types of manoeuvre. Here radar measurements are used to update the filters at 10 Hz, far in excess of target manoeuvring bandwidths. The states, covariances and weights of the individual filters must be re-initialised at a lower frequency - 1 Hz is often quoted in literature, although little evidence exists yet as to the ideal period. When mixing is invoked the individual filter weights are updated,

$$\forall\, j \in [\, 1(\,1\,)\,N\,] : \quad \hat{\mu}_j \;:=\; \left(\sum_{i:=1}^{N} \mu_i^{+} \cdot \Xi_{i,j} \right) \Bigg|_{0.02}^{0.98}$$

Equation 4.8-1

The individual filter weights are normalised so that they sum to 1. Filter lock-out is prevented by applying limits to the individual weights preventing them falling to zero, Kyger[K.5], Stepaniak[S.11]. The lower limit determines the balance between revival speed and an increase in tracking errors as inappropriate filters contributing to the combined output. Alternatively, zeros in the transitional probability matrix can be replaced by small values although direct control over revival speed is lost. Li[L.5] recasts the IMM algorithm to avoid bounding however, although robust, it is also computationally intensive. The state and covariance mixing weightings,

$$\forall\,(\,i\,,j\,) \in [\,1(\,1\,)\,N\,] : \quad W_{i,j} \;:=\; \mu_i^{+} \cdot \Xi_{i,j} \,/\, \hat{\mu}_j$$

Equation 4.8-2

The state and covariances are mixed prior to the next propagation step,

$$\forall\, j \in [\, 1(\,1\,)\,N\,] :$$

$$\left\{ \begin{array}{c} \hat{\underline{X}}_j \;:=\; \displaystyle\sum_{i:=1}^{N} \left(W_{i,j} \cdot \underline{X}_i^{+} \right) \\ \\ \hat{C}_j \;:=\; \displaystyle\sum_{i:=1}^{N} W_{i,j} \cdot \left(C_i^{+} + \left(\underline{X}_i^{+} - \hat{\underline{X}}_j \right) \cdot \left(\underline{X}_i^{+} - \hat{\underline{X}}_j \right)^{T} \right) \end{array} \right\}$$

Equation 4.8-3

The filter weights, states and covariances are re-initialised at the lower frequency using the mixed values prior to the next propagation step,

$$\left(\mu_i^+ \quad , \quad \underline{X}_i^+ \quad , \quad C_i^+ \right) := \left(\hat{\mu}_i \quad , \quad \hat{\underline{X}}_i \quad , \quad \hat{C}_i \right)$$

Equation 4.8-4

4.9 IMM Filter Propagation and Update

Each filter is propagated to the next measurement reference time. When processing (m) measurements in parallel the filter weights evolve according to an m-dimensional Gaussian distribution. The i'th filter weight being,

$$\mu_i^+ :=$$

$$\mu_i^+ \cdot \frac{\exp\left(-0.5 \cdot \left(\underline{Z} - \underline{Z}\left({}^{i}\underline{X} \right) \right)^T \cdot \left(H \cdot {}^{i}C \cdot H^T + R \right)^{-1} \cdot \left(\underline{Z} - \underline{Z}\left({}^{i}\underline{X} \right) \right) \right)}{\sqrt{(2 \cdot \pi)^m \cdot \det\left(H \cdot {}^{i}C \cdot H^T + R \right)}}$$

Equation 4.9-1

EKF linearisation is usually improved by serially processing each measurement. The maximum likelihood function is then constructed from the individual measurement probability densities,

$$\mu_i^+ := \left(\mu_i^+ \cdot \prod_{k:=1}^{m} \left(\frac{1}{\sigma} \cdot \exp\left(-\frac{\left(\underline{Z} - \underline{Z}\left({}^{i}\underline{X} \right) \right)^2}{2 \cdot \sigma^2} \right) \right) \right) \Bigg|_{0.02}^{0.98}$$

Equation 4.9-2

The measurement uncertainty is represented by (σ). The $\sqrt{(2 \cdot \pi)^{-m}}$ scaling is omitted as the normalisation process ensures that the weights sum to 1.

4.10 IMM Filter Combination

The weighted sum of the IMM states and covariances before and after measurement updates is required to determine the new information for the missile state observer,

$${}_{IMM}\underline{X}^- := \sum_{i:=1}^{N} \left(\mu_i^- \cdot \underline{X}_i^- \right)$$

Equation 4.10-1

$${}_{IMM}C^- := \sum_{i:=1}^{N} \mu_i^- \cdot \left(C_i^- + \left(\underline{X}_i^- - {}_{IMM}\underline{X}^- \right) \cdot \left(\underline{X}_i^- - {}_{IMM}\underline{X}^- \right)^T \right)$$

Equation 4.10-2

The filter weights used are those prior to update by the measurement likelihood function. The 2nd term accounts for the each filters deviation from the weighted mean. The weighted sum of the filter states and covariances after the measurement updates,

$$_{IMM}\underline{X}^{+} := \sum_{i:=1}^{N} \left(\mu_i^{+} \cdot \underline{X}_i^{+} \right)$$

Equation 4.10-3

$$_{IMM}C^{+} := \sum_{i:=1}^{N} \mu_i^{+} \cdot \left(C_i^{+} + \left(\underline{X}_i^{+} - {}_{IMM}\underline{X}^{+} \right) \cdot \left(\underline{X}_i^{+} - {}_{IMM}\underline{X}^{+} \right)^{T} \right)$$

Equation 4.10-4

As well as up-linking missile measurements, the IMM target state and covariance (upper triangular partition) data, measurement reference time and filter probabilities are transmitted to the missile, the later providing a target manoeuvre indicator.

4.11 Target Tracking Simulator

The target-tracking simulator shown in Figure 4-7 contains the embedded target and sensor simulators. Initialisation and characterisation of the tracking function is performed in the normal fashion, although there is no dedicated default data for the tracking simulator. The target simulator is automatically activated inside the integration loop, providing the radar (sensor) with reference data.

The tracking simulator is isolated by setting the program termination time to be less than the missile launch time (*TIMEND* < *TLAUNCH*). Either the radar or HMS sensors must be activated to obtain reference or corrupted measurement data. The selection of a single tracking filter, or the IMM, propagation and measurement update is controlled by *IMM_CONTROL* according to the bit pattern of *IMM_TP*:

- Velocity filter *VEL_FILTER* (bit 1)
- Acceleration filter *ACC_FILTER* (bit 2)
- 1st order Markov filter *MK1_FILTER* (bit 3)
- Weave filter *MK2_FILTER* (bit 4)

If a single tracking filter is selected IMM fusion is by-passed. When a combination of tracking filters are activated the IMM processes are automatically applied. The target observer states and covariances from a single filter or the IMM are processed to determine the parameters and expectations listed in §22.3 and §22.13 respectively.

4.12 Discussion

Multiple-model (MM) filters are generally accepted as being more robust delivering substantially better performance than do single fixed or variable gain filters against manoeuvring targets. The early algorithms selected the best individual filter from a bank of filters. Later, more advanced algorithms combined the output from a bank of active filters according to the likelihood that they represent the true target dynamics. The IMM which is notable for its re-initialisation of filters in the filter bank, does not require a manoeuvre detector, and was selected for its simplicity and a performance that is equivalent to Bayesian filters with 2 hypothesis levels, Blom[B.9].

The tracking simulator hosts a conventional IMM whose filters are stimulated by reference or corrupted radar measurements and can be used either in isolation, or in combination. The IMM track is up-linked with missile plots, data time stamps and the updated IMM modal probabilities to the missile central processor. Here the tracks and plots are fused with IMU and seeker measurements to provide optimal data for missile guidance and stabilisation.

Filters are provided for the most commonly encountered target motions, i.e. constant velocity, constant acceleration, high "g" turning (dog-leg) and weaves. As targets tend to manoeuvre for limited periods time, typically up to 5 s, earth referenced Cartesian position, velocity and acceleration states were selected rather than polar, or radar sight-line alternatives. For short-range tracking of agile targets it is better to retain the cross correlation that exists between the separated axes.

A conventional EKF formulation was selected, even though for IMM application the tight control of system noise is paramount for discrimination purposes. A 10 Hz filter update rate was used for CLOS guidance, which is still high considering modern multi-purpose radar workloads. At this rate measurement

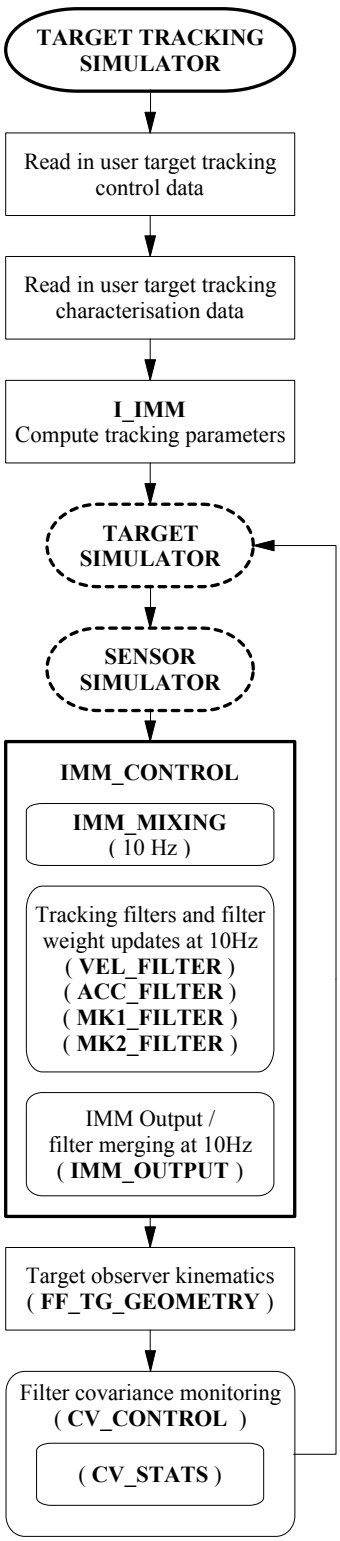

Figure 4-7 : Target Tracking Simulator

linearisation is rarely a problem. Filters that accurately propagate the state error probability density in high dynamic environments using Monte-Carlo methods such as Bootstrapping are considered too expensive at this stage. These type of filters will probably supplant the simpler algorithms used in this study as computer power increases.

Filter initialisation using least-squares and $\alpha-\beta-\gamma$ filtering favoured the latter which did not introduce biases in a dynamic situation. The settling time for a 0.4 Hz bandwidth filter was typically 2-3 s. Probably the best approach for IMM initialisation is to set the acceleration filter probability to 1, and prevent transition to any other filter. Once settled the transitional probabilities can be restored.

Transition between filters as the target changes its flight regime requires a filter with manoeuvre dynamics that inflates the state uncertainty. Direct jumps between the filters, without introducing Singer filter, are prohibited so as to inflate the covariance levels during transients. It is noted from literature that IMM performance is superior after a flight regime change compared with other filters.

The IMM serially processes the radar measurements to improve EKF conditioning. This formulation also accommodates reduced measurement sets, as range-rate data is not always available. Range-rate is often unavailable due to ambiguities linked to geometrical restrictions. The formulation here provides the weighted state and covariance at the measurement reference time prior to any update. This is so that track fusion can be performed using the new information introduced to the IMM avoiding the destabilising effect of correlation at high data rates. The tuning and performance of the individual tracking filters using radar measurements corrupted by Gaussian noise is covered in §9.

Consider now some extensions to the current work:

- At high update rates the benefit of more robust EKF algorithms, and measurements processing order are irrelevant. In multiple target and missile engagements high update rates are often unsustainable. These are precisely the conditions in which poor linearisation of the EKF, and its underlying Gaussian tenants are violated, causing it to diverge. The stability of IMM tracking filters should be assessed for stability at 0.5 Hz and 1 Hz, repeating the filter tuning study presented in §9.
- If linearisation causes filter divergence the iterated EKF should be tried with the emphasis on the number of iterations required. Second order filters are probably too expensive as an alternative.
- Implement Li's robust IMM formulation that avoids bounding the filter transition probabilities and assess its performance. Results published so far are inconclusive and do not warrant the processing load increase.
- Investigate IMM filter re-initialisation rates for typical target manoeuvres.

- The provision of a single generic filter type may prove to be inadequate, particularly the weave filter that depends on weave frequency estimation. Active set maintenance is proposed linked to generic types, reducing the computational load by using EKF incremental updates proposed by Hanlon.
- Optimal filters maintain an exponentially increasing number of filters. Practical, but sub-optimal alternatives maintain a fixed number of filters and are characterised by the way they combine their individual probability density functions (pdf). The IMM provides a normally distributed pdf, whereas Bootstrap and Particle filters preserve higher order moments of the distribution. Although such techniques are more expensive they are reported to be significantly better when tracking agile target. Their performance should be assessed.
- Establish filter probability thresholds to identify the start and end of target manoeuvres, and if possible discriminate between them; a critical function highlighted by the performance of conventional guidance laws in §9.

Chapter 5

MISSILE STATE OBSERVER

Centralised, distributed and hybrid architectures, and the advantages and disadvantages of track and measurement fusion, are discussed. For air-defence a hybrid system is the natural choice since by necessity the ground radar is a distributed node of the full state observer. §4 and §5 together provide the full state observation algorithm. §4 deals with ground tracking, and §5 continues with the up-link to the centralised state observation in the missile. Here the up-linked IMM target track and missile plots are fused with missile sensor measurements.

The sensor measurement characteristics taken from §3, and the up-link interface are described. The missile filter is a conventional EKF whose state space, state partitioning, and launcher initialisation, are defined. The process model is made as simple as possible so that it can be updated using high frequency IMU measurements for seeker steering and airframe stabilisation.

The fusion of correlated target tracks uses only the added information between IMM up-links. Innovations and linearised measurement matrices are defined for serially processing the remaining sensor data. Latency and sensor moment arms are not considered at this stage. Moment arms are essentially deterministic if one ignores error cross-coupling. Similarly, known time delays can be handled using time stamped data and backward state propagation when forming measurement innovations.

Pseudo-measurements are used to constrain the process model. This approach provides flexibility linked to manoeuvre detection using IMM mode probabilities and multi-rate scheduling that is important in practical implementations. Quaternion normalisation, missile dynamics (assuming a full set of normalised aerodynamic derivatives), circular and goal-orientated PN target trajectories are introduced in this fashion.

Conventional EKFs, although flexible and simple to implement compared with many other filters, can become ill-conditioned if the measurements are non-Gaussian. Integrity features commonly used to de-sensitise an EKF whose tenants have been violated are explored and performance metrics introduced for use in §9.

5.1 Data Fusion Architectures

In the past missile guidance has been limited by insufficient processing power that has resulted in the implementation of reduced state observers. The capacity of modern processors should result in the evolution of more sophisticated data fusion and guidance algorithms. There is growing interest in combining the measurements from a number of sensors to expand the operational envelope of air-defence missiles and increase their lethality. Three observer architectures are commonly found in texts for fusing sensor data: centralised measurement fusion, decentralised track fusion and a hybrid fusion. These are now discussed in the context of air-defence drawing on the comments by Noonan[N.1]. Although the discussion is applicable to many systems, the reader is referred to Blackman[B.6] for a more comprehensive treatment of sensor fusion architectures.

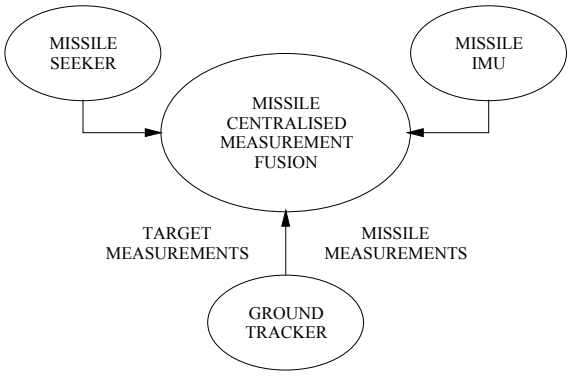

Figure 5-1 : Centralised Fusion Architecture

The centralised architecture shown in Figure 5-1 is the simplest approach when dealing with co-located sensors, although distributed measurements can be transmitted to the fusion centre as shown here.

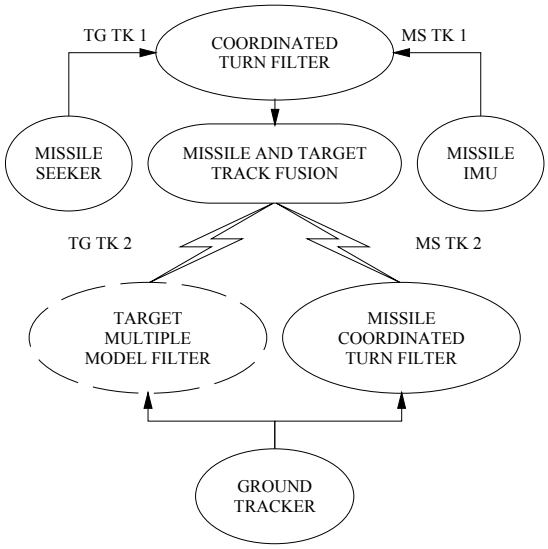

Figure 5-2 : De-centralised Fusion Architecture

The sensors provide raw measurements (plots) that are integrated, usually asynchronously, by a central state observer. Although this places a large, and often unacceptable, computational load on the central processor, it is the only architecture that can achieve fully optimal results. In de-centralised systems, initially studied by Singer[S.22], the output from each sensor is processed to form an optimal track. The local tracks are passed to a central processor that selects the appropriate data using a voting algorithm, or performs track fusion as shown in Figure 5-2. Although track fusion is more robust for multiple target engagements, it being less sensitive to measurement cross correlation errors than measurement fusion, the results obtained are sub-optimal.

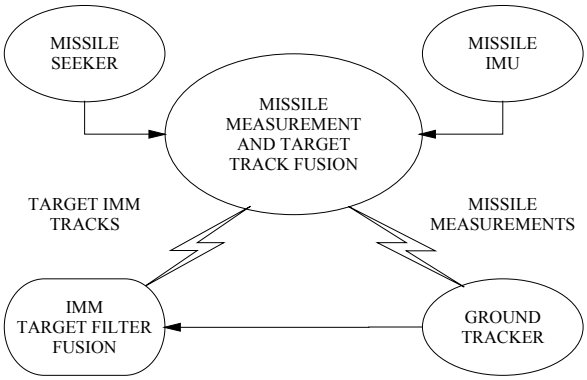

Figure 5-3 : Hybrid Fusion Architecture

The hybrid architecture in Figure 5-3 fuses the external tracks received by the central processor into an observer that is also updated by local sensor measurements. This is the architecture of choice for air-defence in which ground based radar target plots are processed and the resulting track up-linked to the missile. The ground tracker invariably possesses more computing capacity than the missile and can accommodate relatively complex tracking algorithms thereby reducing the load on the central processor. The down-side is the increased up-link bandwidth required to deliver the track data compared with simple target plots.

The missile state observer provides optimal data for guidance. This data is obtained from the observer state that combines gyroscope, accelerometer and seeker data, with up-linked radar target tracks from the IMM, and missile position and range rate measurements as shown in Figure 5-4. The observer is partitioned into target linear, missile linear and missile angular states. The IMU drives both missile partitions, whilst the seeker data is used by all of them, thereby providing the sensor measurement redundancy needed for sensor error estimation. The gyroscope triad plays a pivotal role and is the one critical sensor for missile stabilisation and seeker acquisition. The up-linked missile data is used in the missile linear state partition. The up-linked target track states cannot be treated simply as measurements since the IMM states are correlated and may destabilise the fusion filter.

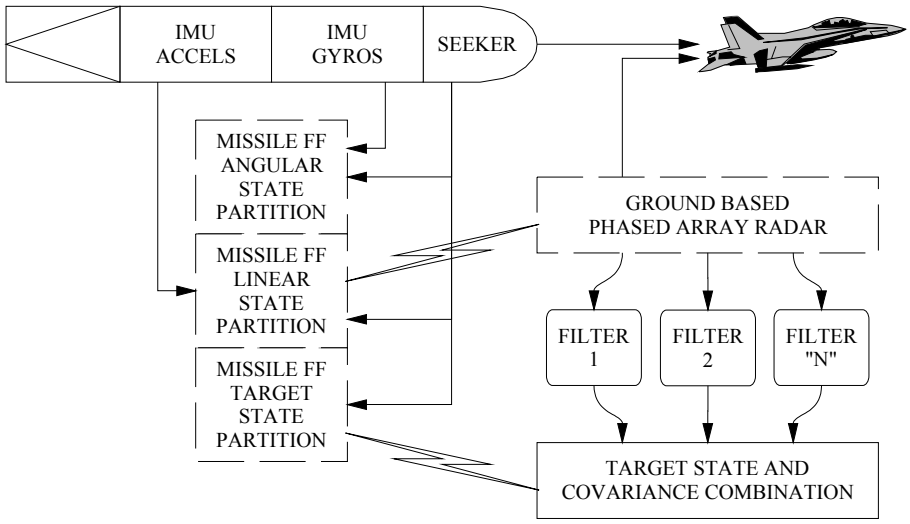

Figure 5-4 : Hybrid Fusion Architecture for Air-Defence

The IMM state and covariance data is up-linked and fused into the target state partition using information fusion techniques. Figure 5-5 encapsulates the measurement and track fusion processes for the air-defence system. The observer states and variances are then used to derive the seeker pointing, guidance and autopilot stabilisation parameters. The hybrid architecture selected for this application is shown in Figure 5-6 combining both track and measurement fusion.

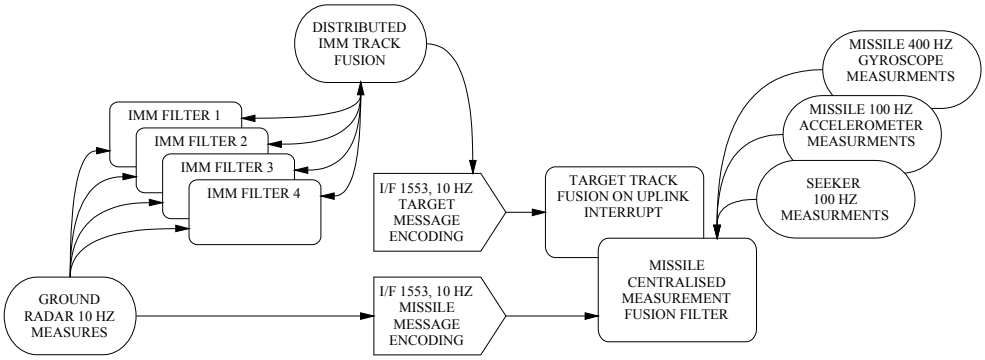

Figure 5-5 : Data flow Within the Air-Defence Architecture

Producing tracks using one or more remote sensors means each sensor can be allocated a dedicated filtering centre with parallel processing. Whilst each tracker is designed and tuned to its sensor the tracks are devoid of sensor characteristics. So, if a sensor is lost system survivability is high with a graceful degradation in overall observer accuracy. It has already been stated that centralised measurement fusion is the only architecture that can provide optimal state estimates, and that this would require up-linking the radar plots directly. Improved observer accuracy leads to better target association as smaller acceptance gates can be employed.

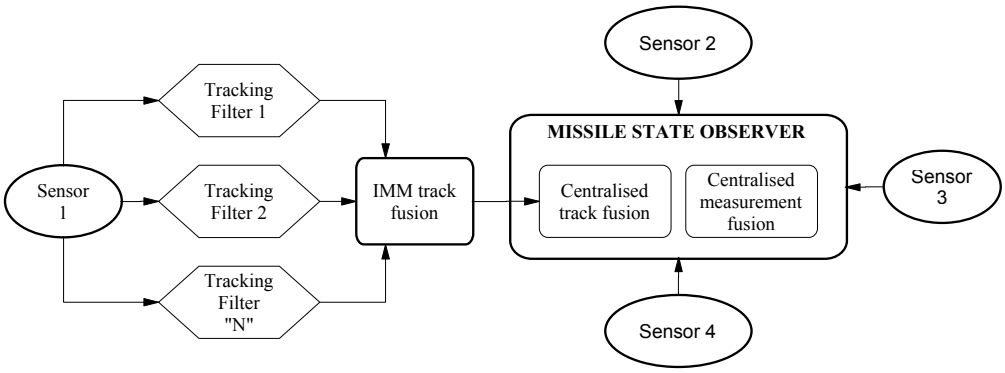

Figure 5-6 : Hybrid Track and Measurement Fusion for Air-Defence

Tracks are correlated and fused at track level leading to a non-optimal result. Measurements are rarely correlated and require no such processing however, they are prone to individual sensor characteristics. Filter integrity is important when dealing with measurements from slowly failing sensors lest they corrupt the observer, particularly those with low measurement uncertainty, whereas tracks are less susceptible.

5.2 Up-Link Interface

The target states and covariance from the IMM are transmitted to the missile with the radar missile measurements. The up-link requires that the angle between the LOS from the transmitter to the missile receiver, and the missile body axis $\underline{X}^B$ is constrained during trajectory optimisation so that the transmissions can be received. The up-link interface is modelled in exactly the same way as the radar output interface in §3.4.9, its functional form for the missile measurements being,

$$ {}_{UL}\underline{\tilde{Z}}_M := {}^{IF}\underline{\varphi}_{TD}\left({}^{IF}\underline{\varphi}_{Q}\left({}^{IF}\underline{\varphi}_{LIM}\left({}^{IF}\underline{\varphi}_{ZOH}\left({}_{RD}\underline{\tilde{Z}}_M \right) \right) \right) \right) $$

Equation 5.2-1

The missile range, range-rate, bearing and elevation measurements with respect to the Alignment frame pass through a 16 bit digital interface (signed except for range) at a frequency ($_{UL}f_O$) of 10 Hz. By default measurements are subject to a one-cycle transmission delay and limits of [0,60_000] m, ± 1000 m/s, ± 180° and ± 90° respectively. The IMM track data is subject to the same interface characteristics with signed limits of ± 60 km, ± 1000 m/s and ± 100 m/s^2 respectively.

$$ {}_{UL}\underline{X}^{+} := {}^{IF}\underline{\varphi}_{TD}\left({}^{IF}\underline{\varphi}_{Q}\left({}^{IF}\underline{\varphi}_{LIM}\left({}^{IF}\underline{\varphi}_{ZOH}\left({}_{IMM}\underline{X}^{+} \right) \right) \right) \right) $$

Equation 5.2-2

$$ {}_{UL}\underline{X}^{-} := {}^{IF}\underline{\varphi}_{TD}\left({}^{IF}\underline{\varphi}_{Q}\left({}^{IF}\underline{\varphi}_{LIM}\left({}^{IF}\underline{\varphi}_{ZOH}\left({}_{IMM}\underline{X}^{-} \right) \right) \right) \right) $$

Equation 5.2-3

The upper triangular partition of the state covariance matrix is transmitted with unsigned PVA covariance limits of 1 km, 200 m/s and 100 m/s^2 respectively and commensurate cross correlation ranges for 10 Hz operation.

$$ {}_{UL}C^{+} \;:=\; {}^{IF}\underline{\varphi}_{TD}\left({}^{IF}\underline{\varphi}_{Q}\left({}^{IF}\underline{\varphi}_{LIM}\left({}^{IF}\underline{\varphi}_{ZOH}\left({}_{IMM}C^{+} \right) \right) \right) \right) $$

Equation 5.2-4

$$ {}_{UL}C^{-} \;:=\; {}^{IF}\underline{\varphi}_{TD}\left({}^{IF}\underline{\varphi}_{Q}\left({}^{IF}\underline{\varphi}_{LIM}\left({}^{IF}\underline{\varphi}_{ZOH}\left({}_{IMM}C^{-} \right) \right) \right) \right) $$

Equation 5.2-5

When fusing IMM track data in the observer weighted apriori and posteriori state and covariance data are required. The up-link also contains the message reference time ($_{UL}t$) for the correct formulation of measurement innovations, and the IMM mode probabilities for manoeuvre detection,

$$ {}_{UL}\mu_{i} \;:=\; {}^{IF}\underline{\varphi}_{TD}\left({}^{IF}\underline{\varphi}_{Q}\left(\mu_{i}^{+} \right) \right) $$

Equation 5.2-6

5.3 Sensor Measurements

The sensor measurements and their limitations selected are dealt with below. Their bandwidths, internal conversion, limitations, and interfaces are commensurate with system capability. For proof-of-principle missile measurements are referred to a its reference point (m) avoiding moment arm terms in the filter gains, sensor error induced cross-correlations being secondary in nature. Data alignment is assured by synchronising all sub-systems to GPS time, initialising the missile before launch, and time stamping tracks and measurements. Deterministic time delays are not introduced as they can be compensated for by state memory, or backward propagation.

5.3.1 Ground Based Tracker

Phased array radar provides target and missile range, range rate, and angle measurements at 10 Hz with respect to the Alignment frame. The radar and launcher are coincident at the origin of this frame. The antenna is fixed, pointing north at a 30° elevation so that the target and missile remain within the 60° squint angle for the trajectories considered. Measurements are provided at ranges above 1 km using a ±2° circular beam.

5.3.2 Missile Gyroscopes and Accelerometers

The IMU strap-down sensors are aligned with the Missile Body frame. The gyroscope and accelerometer triads provide angular rate and specific acceleration measurements at 400 Hz. Accelerometer data is accumulated at 100 Hz. The IMU sensors are activated 5 s prior to launch to allow time for

bias error characterisation. Simple characterisation should reduce constant or long-term correlated biases to a minimum prior to launch commensurate with the local flexure and noise conditions.

5.3.3 Missile Seeker

The RF seeker provides range, range rate, and target angle measurements at 100 Hz with respect to the Missile Body frame. Gimbals with a bandwidth of 80 Hz are pointed using 400 Hz command data. The measurements are provided when the range-to-go is 5 km with a 100 m blind range providing that the target LOS remains in a ± 2° circular beam subject to a ± 30° FoR.

5.4 States and Partitioning

The state vector ($_{SO}\underline{X}$) comprises target and missile states partitioned as shown in Table 5-1. Being clear in context, the use of the identifier (SO), and the observer kinematic type have been dropped. At this stage sensor error states are not included in the filter – this being an alternative to calibrating the IMU whilst the missile is in the launcher. On-line bias, misalignment and scale factor is made possible due to measurement duality and shaped trajectories. The ideal is a combination of both, characterising the IMU biases before launch which are then fixed, and estimating the IMU scale factors and other sensor errors in-flight.

Table 5-1 : Missile State Observer States

SYMBOL			STATE DESCRIPTION	
		$\underline{P}_t^A$	Target position in Alignment axes	
$_{SO}\underline{X}_{TL}$		$\dot{\underline{P}}_t^A$	Target linear velocity in Alignment axes	
		$\ddot{\underline{P}}_t^A$	Target linear acceleration in Alignment axes	
		$\underline{P}_m^A$	Missile position in Alignment axes	
$_{SO}\underline{X}_M$	$_{SO}\underline{X}_{ML}$	$\dot{\underline{P}}_m^A$	Missile linear velocity in Alignment axes	
		$\ddot{\underline{P}}_m^A$	Missile linear acceleration in Alignment axes	
		Q_A^B	Orientation of Missile Body to Alignment axes	
$_{SO}\underline{X}_M$	$_{SO}\underline{X}_{MA}$	$\underline{\omega}_{A,B}^B$	Missile Body frame angular velocity	
		$\dot{\omega}_{A,B}^B$	Missile Body frame angular acceleration	

Partitioning the state vector, and by implication observer state transition, system noise and covariance matrices, identifies sparseness of the process model. When dealing with matrix partitions the following nomenclature is useful (the symmetric state covariance matrix is used as an example),

$$ {}_{SO}C \;:=\; \begin{bmatrix} {}_{SO}C_{TLL} & \vdots & {}_{SO}C_{TML} & \vdots & 0 \\ \cdots & \vdots & \cdots & \vdots & \cdots \\ {}_{SO}C_{MTL} & \vdots & {}_{SO}C_{MLL} & \vdots & {}_{SO}C_{MLA} \\ \cdots & \vdots & \cdots & \vdots & \cdots \\ 0 & \vdots & {}_{SO}C_{MAL} & \vdots & {}_{SO}C_{MAA} \end{bmatrix} $$

Equation 5.4-1

Partitioning to 3 and 4-vector level in the case of the target linear partition (and likewise for the missile linear and rotational partitions),

$$ {}_{SO}C_{TLL} \;:=\; \begin{bmatrix} {}_{TLL}C_{PP} & \vdots & {}_{TLL}C_{PV} & \vdots & {}_{TLL}C_{PA} \\ \cdots & \vdots & \cdots & \vdots & \cdots \\ {}_{TLL}C_{VP} & \vdots & {}_{TLL}C_{VV} & \vdots & {}_{TLL}C_{VA} \\ \cdots & \vdots & \cdots & \vdots & \cdots \\ {}_{TLL}C_{AA} & \vdots & {}_{TLL}C_{AV} & \vdots & {}_{TLL}C_{AA} \end{bmatrix} $$

Equation 5.4-2

5.5 Initialisation

$$ {}_{SO}\underline{X} \;:=\; \left(\left({}_{UL}\underline{X}^{+} \right)^{T} \;,\; \underline{0}_{9}^{T} \;,\; \left({}_{SO}\underline{X}_{MA} \right)^{T} \right)^{T} $$

Equation 5.5-1

$$ {}_{SO}\underline{X}_{MA} \;:= $$

$$ \left(\varphi_{DC}^{Q}\left(\varphi_{X}^{DC}\left({}_{UL}\underline{P}_{t}^{A} \right) \right) \;\vdots\; \left(\varphi_{DE}^{W}\left(\varphi_{X}^{DC}\left({}_{UL}\underline{P}_{t}^{A}, {}_{UL}\dot{\underline{P}}_{t}^{A} \right), \varphi_{X}^{E}\left({}_{UL}\underline{P}_{t}^{A} \right) \right) \right)^{T} \;\vdots\; \underline{0}_{3}^{T} \right)^{T} $$

Equation 5.5-2

The orientation and angular rate of the missile with respect to the Alignment frame is determined using utility functions and up-linked IMM target data. The launcher rotates slowly whilst tracking long-range targets hence the missile velocity, and its linear and angular accelerations are set to zero. The initial missile covariances must never be underestimated, and if necessary inflated to cope with all possible eventualities. If, as here, IMM data is used to initialise the missile state, the uncertainty in that state must include the pointing error of the launcher and the initial position error of the IMM initialisation source. After re-scaling and expanding the up-linked target state expectations the symmetric state covariance matrix,

$$ {}_{SO}C_{TLL} \;:=\; {}_{UL}C^{+} $$

Equation 5.5-3

The missile position uncertainty is commensurate with GPS data. Small values are used for the velocity and acceleration of the launcher with respect to the Earth. This is important if IMU bias states are added to the filter so the filter innovations are directed into the appropriate error states,

$$_{SO}C_{MLL} := \text{diag}\left(30^2 \cdot \underline{1}_3 \quad , \quad \underline{1}_3^2 \quad , \quad \underline{1}_3^2 \right)$$

Equation 5.5-4

The orientation error in this simple case of pointing the launcher at the target is determined by apriori radar bearing and elevation errors. From the relationship between quaternions and half Euler angles in §22.9.2,

$$_{SO}C_{MAA} :=$$

$$\text{diag}\left(\begin{array}{cccc:ccc:c} 0 & 0 & \frac{_{RD}\sigma_\Theta^2}{4} & \frac{_{RD}\sigma_\Psi^2}{4} & \left(\frac{5\cdot\pi}{180}\right)^2 & \left(\frac{5\cdot\pi}{180}\right)^2 & \left(\frac{5\cdot\pi}{180}\right)^2 & \underline{0}_3 \end{array} \right)$$

Equation 5.5-5

5.6 Process Model

The state vector and covariances are propagated at 400 Hz for autopilot and seeker stabilisation using the simple dynamic model,

$$\underline{X}_{k+1} := \Phi_k^{k+1} \cdot \underline{X}_k$$

Equation 5.6-1

$$C_{k+1} := \Phi_k^{k+1} \cdot C_k \cdot \left(\Phi_k^{k+1} \right)^T + Q_k$$

Equation 5.6-2

The target and missile linear state partition transition matrices,

$$\Phi_{TLL} := \Phi_{MLL} := \begin{bmatrix} I_3 & , & \Delta \cdot I_3 & 0.5 \cdot \Delta^2 \cdot I_3 \\ 0_{3x3} & , & I_3 & \Delta \cdot I_3 \\ 0_{3x3} & , & 0_{3x3} & I_3 \end{bmatrix}$$

Equation 5.6-3

Similarly, the missile angular state partition transition components,

$$q_A^B(t+\Delta t) := 0.5 \cdot \Delta t \cdot q_A^B \otimes \left(0 \quad , \quad \underline{\omega}_{A,B}^B \right)$$

Equation 5.6-4

$$\Phi_{MAA} := \begin{bmatrix} {}_{MAA}\Phi_{QQ} & , & {}_{MAA}\Phi_{QW} & , & 0_{3x3} \\ 0_{3x4} & , & I_3 & , & \Delta \cdot I_3 \\ 0_{3x4} & , & 0_{3x3} & , & I_3 \end{bmatrix}$$

Equation 5.6-5

$${}_{MAA}\Phi_{QQ} := \frac{1}{2} \cdot \begin{bmatrix} 1 & \vdots & -\left(\underline{\omega}^B_{A,B} \right)^T \\ \cdots & \vdots & \cdots \\ \underline{\omega}^B_{A,B} & \vdots & I_3 - \left[\underline{\omega}^B_{A,B} \times \right] \end{bmatrix}$$

Equation 5.6-6

$${}_{MAA}\Phi_{QW} := \frac{1}{2} \cdot \begin{bmatrix} -\left(\underline{q}^B_A \right)^T \\ \cdots \quad \cdots \quad \cdots \quad \cdots \\ q^B_A(0) \cdot I_3 - \left[\underline{q}^B_A \times \right] \end{bmatrix}$$

Equation 5.6-7

This non co-ordinated model ignores missile velocity vector rotation coupling the missile linear and rotational states. Process noise is therefore needed to cope with the un-modelled dynamics with state error growth constrained using high frequency IMU data.

$$\Gamma = \left(0.5 \cdot \Delta^2 \quad \Delta \quad 1 \right)^T$$

Equation 5.6-8

$$\left(Q_{TLL} \quad , \quad Q_{MLL} \right) :=$$

$$\left(\Gamma \cdot \mathrm{diag}\left(50^2 \cdot \underline{1}_3 \right) \cdot \Gamma^T \quad , \quad \Gamma \cdot \mathrm{diag}\left(200^2 \cdot \underline{1}_3 \right) \cdot \Gamma^T \right)$$

Equation 5.6-9

$$Q_{MAA} := \begin{pmatrix} {}_{MAA}Q_{QQ} & \vdots & {}_{MAA}Q_{QW} & \vdots & 0_{3x3} \\ \cdots & \vdots & \cdots & \vdots & \cdots \\ - & \vdots & {}_{GS}\sigma^2_{RN} \cdot I_3 & \vdots & 0_{3x3} \\ \cdots & \vdots & \cdots & \vdots & \cdots \\ - & \vdots & - & \vdots & 0_{3x3} \end{pmatrix}$$

Equation 5.6-10

$$\left({}_{MAA}Q_{QQ} \quad , \quad {}_{MAA}Q_{QW} \right) := \left(\frac{\Delta^2}{4} \quad , \quad \frac{1}{4} \right) \cdot \begin{pmatrix} -\underline{q}_A^B \\ q_A^B(0) + \left[\underline{q}_A^B \times \right] \end{pmatrix}$$

Equation 5.6-11

5.7 Up-Linked Target Track Update

The observer propagates at high frequency with asynchronous updates thereby avoiding large differences between the current and data reference times. Had the time difference been significant, the states must be propagated to the measurement time reference, or stored, so as to form innovations at the correct time. Covariance data should not vary significantly over the period and its computationally expensive propagation can be avoided. When available, the up-linked target track is dealt with first. If the interval between track up-links is long compared with the target manoeuvring time the track data can be treated as measurements using the conventional covariance EKF formulation,

$$K := \frac{C_{TLL}^-(t_k)}{C_{TLL}^-(t_k) + {}_{UL}C^+({}_{UL}t)}$$

Equation 5.7-1

$$\underline{X}_{TTL}^+ := \underline{X}_{TTL}^- + K \cdot \left({}_{UL}\underline{X}^+ - \underline{X}_{TTL}^- \right)$$

Equation 5.7-2

$$C_{TTL}^+ := \left[I_9 - K \right] \cdot C_{TTL}^-$$

Equation 5.7-3

Here the IMM provides weighted target state and covariance data at 10 Hz which cannot be treated simply as a plot since the data is correlated and must be fused at track level, Lobbia[L.8]. When dealing with correlated tracks only new information between track updates must be fused into the observer,

$$\underline{X}_{TTL}^+ := \underline{X}_{TTL}^- + \frac{C_{TTL}^+}{{}_{UL}C^+} \cdot \left({}_{UL}\underline{X}^+ - \underline{X}_{TTL}^- \right) - \frac{C_{TTL}^+}{{}_{UL}C^-} \cdot \left({}_{UL}\underline{X}^- - \underline{X}_{TTL}^- \right)$$

Equation 5.7-4

$$\left[C_{TTL}^+ \right]^{-1} := \left[C_{TTL}^- \right]^{-1} + \left[{}_{UL}C^+ \right]^{-1} - \left[{}_{UL}C^- \right]^{-1}$$

Equation 5.7-5

The first two terms in each of these equations represent the standard KF measurement update. The final term removes previous track data already

used to update the observer. Alternative formulations for decentralised systems based on information filtering are provided by Farooq[F.3], Julier[J.2], and Grimes[G.18]. Information filtering, which is directly equivalent to the algorithms presented here, rigorously partitions "new" and "old" information between updates at the transmitting node. The "new" information can then be passed to the neighbouring nodes, in this case the missile observer, for assimilation. Since the nodes here are formulated using conventional covariance filters information filtering has not been pursued further, although it remains a credible alternative.

5.8 Missile Measurement Updates

5.8.1 Missile Gyroscope Measurement Update

The IMU inertial angular rate measurements limit growth in the missile orientation uncertainty with respect to the earth. For agile missiles this must be performed at high rate commensurate with airframe stabilisation,

$$ {}_{GS}\underline{\tilde{Z}} \;\coloneqq\; {}_{400}\underline{\tilde{\omega}}^{B}_{C,B} $$

Equation 5.8-1

The estimated gyroscope measurements and linearised measurement matrix,

$$ {}_{GS}\underline{Z} \;\coloneqq\; \underline{\omega}^{B}_{C,E} + \underline{\omega}^{B}_{A,B} \;\coloneqq\; T^{B}_{A} \cdot T^{A}_{E} \cdot \left(0 \;,\; 0 \;,\; \omega^{ZE}_{C,E} \right)^{T} + \underline{\omega}^{B}_{A,B} $$

Equation 5.8-2

$$ {}_{GS}H \;\equiv\; \partial\, {}_{GS}\underline{Z} \,/\, \partial \underline{X} \;\coloneqq\; \left[0_{3x9} \;\vdots\; 0_{3x9} \;\vdots\; {}_{GS}H_{MA} \right] $$

Equation 5.8-3

Acceleration innovations are apportioned to the missile angular dynamics,

$$ {}_{GS}H_{MA} \;\coloneqq\; \left[\underline{\omega}^{A}_{C,E} \cdot \partial T^{B}_{A} \,/\, \partial Q^{B}_{A} \;\vdots\; I_3 \;\vdots\; 0_{3x3} \right] $$

Equation 5.8-4

The direction cosine Jacobian is given in §22.10.11. For short-range applications earth rate can be ignored and this partition is zero. For gyroscope noise of 10°/√hr the measurement covariance,

$$ {}_{GS}R \;\coloneqq\; \mathrm{diag}\left(1.2^{2} \;,\; 1.2^{2} \;,\; 1.2^{2} \right) $$

Equation 5.8-5

5.8.2 Missile Accelerometer Measurement Update

Airframe stabilisation is less dependent on high frequency accelerometer output compared with gyroscope data. Accelerometer data is therefore accumulated and used at 100 Hz.

$$ {}_{AC}\underline{\tilde{Z}} \;\coloneqq\; {}_{100}\underline{\tilde{f}}^{B}_{r,u} \;\coloneqq\; \sum_{i:=0}^{3} {}_{400}\underline{\tilde{f}}^{B}_{r,u}\left(t_{k-i} \right) $$

Equation 5.8-6

If the IMU and missile reference points are not coincident the estimated accelerometer measurements are determined as in §3.3.1.1,

$$ {}_{AC}\underline{Z} \;\coloneqq\; $$

$$ T^{B}_{A} \cdot \left(\underline{\ddot{P}}^{A}_{m} + 2 \cdot T^{A}_{E} \cdot \underline{\omega}^{E}_{C,E} \times \underline{\dot{P}}^{A}_{m} - T^{A}_{G} \cdot \underline{g}^{G}_{d} \right) + \underline{\dot{\omega}}^{B}_{A,B} \times \underline{P}^{B}_{m,u} + \underline{\omega}^{B}_{A,B} \times \underline{\omega}^{B}_{A,B} \times \underline{P}^{B}_{m,u} $$

Equation 5.8-7

Ignoring coriolis acceleration due to earth rate, assuming the tilt between LGA and Alignment frames is negligible, and the IMU reference point lies on the missile longitudinal axis,

$$ {}_{AC}\underline{Z} \;\cong\; T^{B}_{A} \cdot \left(\underline{\ddot{P}}^{A}_{m} - \left(0 \;,\; 0 \;,\; \underline{g}^{ZG}_{d} \right)^{T} \right) + \varphi^{B}_{ARM} $$

Equation 5.8-8

$$ \underline{\varphi}^{B}_{ARM} \;\coloneqq\; $$

$$ P^{XB}_{m,u} \cdot \left(-\left(\underline{\omega}^{rB}_{A,B} \right)^{2} \;,\; \underline{\omega}^{XB}_{A,B} \cdot \underline{\omega}^{YB}_{A,B} + \underline{\dot{\omega}}^{ZB}_{A,B} \;,\; \underline{\omega}^{XB}_{A,B} \cdot \underline{\omega}^{ZB}_{A,B} - \underline{\dot{\omega}}^{YB}_{A,B} \right)^{T} $$

Equation 5.8-9

The accumulation delay is accounted for using a cyclic stack not backward state propagation. The linearised measurement matrix comprises,

$$ {}_{AC}H \;\equiv\; \partial\, {}_{AC}\underline{Z} \,/\, \partial \underline{X} \;\coloneqq\; \left[0_{3x9} \;\vdots\; {}_{AC}H_{ML} \;\vdots\; {}_{AC}H_{MA} \right] $$

Equation 5.8-10

Apportioning the acceleration innovations to the missile linear dynamics,

$$ {}_{AC}H_{ML} \coloneqq $$

$$ \left[\; 0_{3x2} \quad , \quad \frac{\partial g_d^{ZG}}{\partial P_m^{ZA}} \cdot \left(T_A^B(3) \quad , \quad T_A^B(6) \quad , \quad T_A^B(9) \right)^T \; \vdots \; 0_{3x3} \; \vdots \; T_A^B \right] $$

Equation 5.8-11

Apportioning the acceleration innovations to the missile angular dynamics,

$$ {}_{AC}H_{MA} \coloneqq $$

$$ \left[\frac{\partial T_A^B}{\partial Q_A^B} \cdot \left(\; \underline{\ddot{P}}_m^A - \left(0 \quad , \quad 0 \quad , \quad \underline{g}_d^{ZG} \right)^T \right) \; \vdots \; \frac{\partial \underline{\varphi}_{ARM}^B}{\partial \underline{\omega}_{A,B}^B} \; \vdots \; \frac{\partial \underline{\varphi}_{ARM}^B}{\partial \underline{\dot{\omega}}_{A,B}^B} \right] $$

Equation 5.8-12

The gravitational acceleration and its variation with height are given in §20.2 and §20.3 respectively. When accumulating data the measurement noise can be reduced by √n, where n is the number of measurements averaged. For noise of 500 μg/√Hz the measurement covariance is,

$$ {}_{AC}R \coloneqq \operatorname{diag}\left(\sqrt{4} \cdot 2 \cdot \underline{1}_3 \right) $$

Equation 5.8-13

5.8.3 Ground Radar Missile Measurement Update

The missile range, range rate and angle measurements stimulate the missile linear dynamic partition. The estimated seeker measurements being,

$$ {}_{UL}\underline{\tilde{Z}}_M \coloneqq \left(\tilde{P}_m^{XM} \quad , \quad \tilde{\dot{P}}_m^{XM} \quad , \quad \tilde{\Psi}_A^M \quad , \quad \tilde{\Theta}_A^M \right)^T $$

Equation 5.8-14

$$ {}_{UL}\underline{Z}_M \coloneqq $$

$$ \left(\sqrt{\underline{P}_m^A \bullet \underline{P}_m^A} \quad , \quad \frac{\underline{P}_m^A \bullet \underline{\dot{P}}_m^A}{P_{o,m}} \quad , \quad \tan^{-1}\left(\frac{P_m^{YA}}{P_m^{XA}} \right) \quad , \quad -\tan^{-1}\left(\frac{P_m^{ZA}}{P_m^{hA}} \right) \right)^T $$

Equation 5.8-15

The linearised measurement matrix,

$$ {}_{UL}H_{ML} \equiv \frac{\partial\, {}_{UL}\underline{Z}_M}{\partial \underline{X}_{ML}} := \left(\frac{\partial P_m^{XM}}{\partial \underline{X}_{ML}} , \frac{\partial \dot{P}_m^{XM}}{\partial \underline{X}_{ML}} , \frac{\partial \Psi_A^M}{\partial \underline{X}_{ML}} , \frac{\partial \Theta_A^M}{\partial \underline{X}_{ML}} \right)^T $$

Equation 5.8-16

Absolute range:

$$ \partial P_m^{XM} \Big/ \partial \underline{X}_{ML} := \left(\left(\underline{P}_m^A \right)^T \Big/ P_{o,m} , \underline{0}_6^T \right) $$

Equation 5.8-17

Absolute range-rate:

$$ \partial \dot{P}_m^{XM} \Big/ \partial \underline{X}_{ML} := \left(\frac{\left(\underline{\dot{P}}_m^A \right)^T}{P_{o,m}} - \frac{\dot{P}_m^{XM} \cdot \left(\underline{P}_m^A \right)^T}{P_{o,m}^2} , \left(\underline{P}_m^A \right)^T \Big/ P_{o,m} , \underline{0}_3^T \right) $$

Equation 5.8-18

Absolute bearing:

$$ \left(P_m^{hA} \right)^{-2} \cdot \partial \Psi_A^M \Big/ \partial \underline{X}_{ML} := \left(-P_m^{YA} , P_m^{XA} , \underline{0}_7^T \right) $$

Equation 5.8-19

Absolute elevation:

$$ \partial \Theta_A^M \Big/ \partial \underline{X}_{ML} := \left(\frac{P_m^{XA} \cdot P_m^{ZA}}{P_m^{hA} \cdot P_{o,m}^2} , \frac{P_m^{YA} \cdot P_m^{ZA}}{P_m^{hA} \cdot P_{o,m}^2} , -\frac{P_m^{hA}}{P_{o,m}^2} , \underline{0}_6^T \right) $$

Equation 5.8-20

The measurement variances,

$$ {}_{UL}R_M := \text{diag} \left(10^2 , 4^2 , 0.003^2 , 0.003^2 \right) $$

Equation 5.8-21

In practice the measurement uncertainties would have to be expanded to account for quantisation and timing uncertainty associated with the up-link.

5.8.4 Missile Seeker Measurement Update

The seeker target range, range rate and angle measurements with respect to the Missile Body frame stimulate all the state observer partitions,

$$ {}_{SK}\underline{\tilde{Z}} \;:=\; \left(\tilde{P}^{XS}_{o,m} \;,\; \tilde{\dot{P}}^{XS}_{o,m} \;,\; \tilde{\Psi}^{S}_{B} \;,\; \tilde{\Theta}^{S}_{B} \right)^{T} $$

Equation 5.8-22

The estimated seeker measurements,

$$ {}_{SK}\underline{Z} \;:= $$

$$ \left(\sqrt{\underline{P}^{A}_{m,t} \bullet \underline{P}^{A}_{m,t}} \;,\; \frac{\underline{P}^{A}_{m,t} \bullet \underline{\dot{P}}^{A}_{m,t}}{P_{m,t}} \;,\; \tan^{-1}\left(\frac{T^{S}_{B}(1)}{T^{S}_{B}(4)} \right) \;,\; \sin^{-1}\left(-T^{S}_{B}(7) \right) \right)^{T} $$

Equation 5.8-23

The linearised measurement matrix decomposes as follows,

$$ {}_{SK}H \;\equiv\; \frac{\partial\, {}_{SK}\underline{Z}}{\partial \underline{X}} \;:=\; \left(\frac{\partial\, {}_{SK}\underline{Z}}{\partial \underline{X}_{TL}} \;,\; \frac{\partial\, {}_{SK}\underline{Z}}{\partial \underline{X}_{ML}} \;,\; \frac{\partial\, {}_{SK}\underline{Z}}{\partial \underline{X}_{MA}} \right)^{T} $$

Equation 5.8-24

The range, range-rate, bearing and elevation innovations are apportioned to the target states by,

$$ {}_{SK}H_{TL} \;\equiv\; \frac{\partial\, {}_{SK}\underline{Z}}{\partial \underline{X}_{TL}} \;:=\; \left(\frac{\partial P^{XS}_{m,t}}{\partial \underline{X}_{TL}} \;,\; \frac{\partial \dot{P}^{XS}_{m,t}}{\partial \underline{X}_{TL}} \;,\; \frac{\partial \Psi^{S}_{B}}{\partial \underline{X}_{TL}} \;,\; \frac{\partial \Theta^{S}_{B}}{\partial \underline{X}_{TL}} \right)^{T} $$

Equation 5.8-25

Relative range:

$$ \partial P^{XS}_{m,t} \,/\, \partial \underline{X}_{TL} \;:=\; \left(\left(\underline{P}^{A}_{m,t} \right)^{T} \,/\, P_{m,t} \;,\; \underline{0}^{T}_{6} \right) $$

Equation 5.8-26

Relative range-rate:

$$ \partial \dot{P}^{XS}_{o,m} \,/\, \partial \underline{X}_{TL} \;:=\; \left(\frac{\left(\underline{\dot{P}}^{A}_{m,t} \right)^{T}}{P_{m,t}} - \frac{\dot{P}^{XS}_{m,t} \cdot \left(\underline{P}^{A}_{t} \right)^{T}}{P^{2}_{m,t}} \;,\; \left(\underline{P}^{A}_{t} \right)^{T} \,/\, P_{m,t} \;,\; \underline{0}^{T}_{3} \right) $$

Equation 5.8-27

Relative bearing:

$$\partial \Psi_B^S \,/\, \partial \underline{X}_{TL} \;\coloneqq\; \left(\partial \Psi_B^S \,/\, \partial \underline{P}_t^A \;\;,\;\; \underline{0}_6^T \right)$$

Equation 5.8-28

$$\frac{\partial \Psi_B^S}{\partial \underline{P}_t^A} \;\coloneqq\; \frac{\varphi_1 \cdot \sec^2 \Theta_B^S}{P_{o,t}} \cdot \left(\sin^2 \Psi_B^S \cdot \begin{pmatrix} T_A^B(1) \\ T_A^B(4) \\ T_A^B(7) \end{pmatrix} - \cos^2 \Psi_B^S \cdot \begin{pmatrix} T_A^B(2) \\ T_A^B(5) \\ T_A^B(8) \end{pmatrix} \right)$$

Equation 5.8-29

$$\varphi_1 \coloneqq \begin{pmatrix} 1 - T_A^S(1) \cdot T_A^S(1) & , & T_A^S(1) \cdot T_A^S(2) & , & T_A^S(1) \cdot T_A^S(3) \\ T_A^S(1) \cdot T_A^S(2) & , & 1 - T_A^S(2) \cdot T_A^S(2) & , & T_A^S(2) \cdot T_A^S(3) \\ T_A^S(1) \cdot T_A^S(3) & , & T_A^S(2) \cdot T_A^S(3) & , & 1 - T_A^S(3) \cdot T_A^S(3) \end{pmatrix}$$

Equation 5.8-30

Relative elevation:

$$\partial \Psi_B^S \,/\, \partial \underline{X}_{TL} \;\coloneqq\; \left(\partial \Psi_B^S \,/\, \partial \underline{P}_t^A \;\;,\;\; \underline{0}_6^T \right)$$

Equation 5.8-31

$$P_{m,t} \cdot \cos \Theta_B^S \cdot \partial \Psi_B^S \,/\, \partial \underline{P}_t^A \;\coloneqq\; \varphi_1 \cdot \left(T_A^B(3) \;\;,\;\; T_A^B(6) \;\;,\;\; T_A^B(9) \right)^T$$

Equation 5.8-32

Apportioning the range, range-rate, bearing and elevation innovations to the missile linear states,

$$H_{ML} \;\equiv\; \partial_{\,SK} \underline{Z} \,/\, \partial \underline{X}_{ML} \;\coloneqq\; -\partial_{\,SK} \underline{Z} \,/\, \partial \underline{X}_{TL}$$

Equation 5.8-33

Apportioning the target range, range-rate, bearing and elevation innovations to the missile angular states,

$$H_{MA} \;\equiv\; \partial_{\,SK} \underline{Z} \,/\, \partial \underline{X}_{MA} \;\coloneqq\; \left(0_{10x2} \;\;,\;\; \partial \Psi_B^S \,/\, \partial \underline{X}_{ML} \;\;,\;\; \partial \Theta_B^S \,/\, \partial \underline{X}_{ML} \right)^T$$

Equation 5.8-34

Relative bearing:

$$\partial \Psi_B^S / \partial \underline{X}_{MA} \coloneqq \left(\partial \Psi_B^S / \partial Q_A^B \quad , \quad \underline{0}_6^T \right)$$

Equation 5.8-35

$$\partial \Psi_B^S / \partial Q_A^B \coloneqq$$

$$2 \cdot \left(\varphi_2 \cdot \sin^2 \Psi_B^S - \varphi_3 \cdot \cos^2 \Psi_B^S \right) \cdot \left(T_A^S(1) \quad , \quad T_A^S(4) \quad , \quad T_A^S(7) \right)^T$$

Equation 5.8-36

$$\left(\varphi_2 \quad , \quad \varphi_3 \right) \coloneqq$$

$$\left(\begin{pmatrix} q_A^B(0) & q_A^B(3) & -q_A^B(2) \\ q_A^B(1) & q_A^B(2) & q_A^B(3) \\ -q_A^B(2) & q_A^B(1) & -q_A^B(0) \\ -q_A^B(3) & q_A^B(0) & q_A^B(1) \end{pmatrix} , \begin{pmatrix} -q_A^B(3) & q_A^B(0) & q_A^B(1) \\ q_A^B(2) & -q_A^B(1) & q_A^B(0) \\ q_A^B(1) & q_A^B(2) & q_A^B(3) \\ -q_A^B(0) & -q_A^B(3) & q_A^B(2) \end{pmatrix} \right)$$

Equation 5.8-37

Relative elevation:

$$\partial \Theta_B^S / \partial \underline{X}_{MA} \coloneqq \left(\partial \Theta_B^S / \partial Q_A^B \quad , \quad \underline{0}_6^T \right)$$

Equation 5.8-38

$$\partial \Theta_B^S / \partial Q_A^B \coloneqq$$

$$\frac{2}{\cos \Theta_B^S} \cdot \left(\begin{pmatrix} -q_A^B(2) & , & q_A^B(1) & , & -q_A^B(0) \\ -q_A^B(3) & , & q_A^B(0) & , & -q_A^B(1) \\ -q_A^B(0) & , & -q_A^B(3) & , & q_A^B(2) \\ -q_A^B(1) & , & -q_A^B(2) & , & -q_A^B(3) \end{pmatrix} \cdot \begin{pmatrix} T_A^S(1) \\ T_A^S(4) \\ T_A^S(7) \end{pmatrix} \right)^T$$

Equation 5.8-39

The measurement variances,

$$_{SK}R \coloneqq \text{diag}\left(20^2 \quad , \quad 10^2 \quad , \quad 0.01^2 \quad , \quad 0.01^2 \right)$$

Equation 5.8-40

5.8.5 Quaternion Normalisation

The EFK does not preserve normalised quaternions when processing sensor data, or pseudo-measurements. After each measurement has been processed these states are re-normalised as defined in §22.10.4. The state quaternion covariances must be expanded to accommodate the uncertainty in this process, Choukroun[C.9].

$$_{MAA}C^{+}_{QQ} \coloneqq {}_{MAA}C^{+}_{QQ} + \left(1 - \left\| Q^B_A \right\| \right)^2 \cdot Q^B_A \cdot \left(Q^B_A \right)^T$$

Equation 5.8-41

5.9 Pseudo-Measurements

An elegant approach to constraining the simple filter dynamics is the use of pseudo-measurements appropriate to the current flight regime, Tahk[T.1] and Speyer[S.13]. The extent to which these external dynamic constraints effect the filter states is controlled by the measurement uncertainty applied.

5.9.1 Circular Target Dynamics

The circular target model for co-ordinated turns assumes that velocity and acceleration vectors are orthogonal, Speyer[S.13]. The pseudo-measurement is therefore,

$$_{TPM}\tilde{Z} \coloneqq \underline{\dot{P}}^A_t \bullet \underline{\ddot{P}}^A_t + N\left(0 , {}_{TPM}\sigma \right)$$

Equation 5.9-1

The linearised measurement Jacobians applied to the target states,

$$\partial\, {}_{TPM}Z \,/\, \partial \underline{X}_{TL} \coloneqq \left(0_{1x3} \;\vdots\; \left(\underline{\ddot{P}}^A_t \right)^T \;\vdots\; \left(\underline{\dot{P}}^A_t \right)^T \right)$$

Equation 5.9-2

The orthogonality assumption ignores incidence and the measurement uncertainty (σ_{TPM}) must reflect this, Andrisani[A.3].

5.9.2 Goal Orientated Target Dynamics

This dynamic constraint is an extension of the circular vehicle dynamics in the previous section. Consider a scenario in which the goal of the target is the missile system protecting a facility warranting a higher kill probability at the expense of surrounding targets. The pseudo-measurement,

$$ {}_{GOT}\underline{\tilde{Z}} := \underline{\ddot{P}}_t^A + N\left(0, {}_{GOT}\underline{\sigma}\right) $$

Equation 5.9-3

When the target is guided to its goal using a PN law its heading changes as a function of the navigation gain (λ_t) and the missile-target sight-line rate.

$$ \omega_{A,TV} := \lambda_t \cdot \omega_{A,T} $$

Equation 5.9-4

$$ \dot{P}_{o,t}^{-2} \cdot \left(\underline{\dot{P}}_t^A \times \underline{\ddot{P}}_t^A \right) := \lambda_t \cdot P_{o,t}^{-2} \cdot \left(\underline{P}_t^A \times \underline{\dot{P}}_t^A \right) $$

Equation 5.9-5

$$ \underline{\dot{P}}_t^A \bullet \underline{\ddot{P}}_t^A = 0 \Rightarrow \underline{\ddot{P}}_t^A := \lambda_t \cdot P_{o,t}^{-2} \cdot \left(\underline{\dot{P}}_t^A \times \underline{\dot{P}}_t^A \times \underline{P}_t^A \right) $$

Equation 5.9-6

$$ \underline{\ddot{P}}_t^A := \frac{\lambda_t}{P_{o,t}^2} \cdot \begin{pmatrix} \left(P_t^{YA} \cdot \dot{P}_t^{YA} + P_t^{ZA} \cdot \dot{P}_t^{ZA} \right) \cdot \dot{P}_t^{XA} - \dot{P}_t^{rA} \cdot P_t^{XA} \\ \left(P_t^{XA} \cdot \dot{P}_t^{XA} + P_t^{ZA} \cdot \dot{P}_t^{ZA} \right) \cdot \dot{P}_t^{YA} - \dot{P}_t^{vA} \cdot P_t^{YA} \\ \left(P_t^{XA} \cdot \dot{P}_t^{XA} + P_t^{YA} \cdot \dot{P}_t^{YA} \right) \cdot \dot{P}_t^{ZA} - \dot{P}_t^{hA} \cdot P_t^{ZA} \end{pmatrix} $$

Equation 5.9-7

The measurement Jacobians,

$$ {}_{GOT}H := \partial\, {}_{GOT}\underline{Z} \,/\, \partial \underline{X}_{TL} := \begin{pmatrix} \frac{\partial\, {}_{GOT}\underline{Z}}{\partial \underline{P}_t^A} & \vdots & \frac{\partial\, {}_{GOT}\underline{Z}}{\partial \underline{\dot{P}}_t^A} & \vdots & 0_{3x3} \end{pmatrix} $$

Equation 5.9-8

$$ \partial \underline{\ddot{P}}_t^A \,/\, \partial \underline{\dot{P}}_t^A := \lambda_t \cdot P_{o,t}^{-2} \quad \cdots $$

$$ \begin{pmatrix} P_t^{YA} \cdot \dot{P}_t^{YA} + P_t^{ZA} \cdot \dot{P}_t^{ZA} & \vdots & P_t^{YA} \cdot \dot{P}_t^{XA} - 2 \cdot P_t^{XA} \cdot \dot{P}_t^{YA} & \vdots & P_t^{ZA} \cdot \dot{P}_t^{XA} - 2 \cdot P_t^{XA} \cdot \dot{P}_t^{ZA} \\ \cdots & \vdots & \cdots & \vdots & \cdots \\ P_t^{XA} \cdot \dot{P}_t^{YA} - 2 \cdot P_t^{YA} \cdot \dot{P}_t^{XA} & \vdots & P_t^{XA} \cdot \dot{P}_t^{XA} + P_t^{ZA} \cdot \dot{P}_t^{ZA} & \vdots & P_t^{ZA} \cdot \dot{P}_t^{YA} - 2 \cdot P_t^{YA} \cdot \dot{P}_t^{ZA} \\ \cdots & \vdots & \cdots & \vdots & \cdots \\ P_t^{XA} \cdot \dot{P}_t^{ZA} - 2 \cdot P_t^{XA} \cdot \dot{P}_t^{ZA} & \vdots & P_t^{YA} \cdot \dot{P}_t^{ZA} - 2 \cdot P_t^{YA} \cdot \dot{P}_t^{ZA} & \vdots & P_t^{XA} \cdot \dot{P}_t^{XA} + P_t^{YA} \cdot \dot{P}_t^{YA} \end{pmatrix} $$

Equation 5.9-9

$$\begin{pmatrix} \varphi_X \\ \varphi_Y \\ \varphi_Z \end{pmatrix} := \begin{pmatrix} \left(P_t^{YA} \cdot \dot{P}_t^{YA} + P_t^{ZA} \cdot \dot{P}_t^{ZA} \right) \cdot \dot{P}_t^{XA} - P_t^{XA} \cdot \left(\dot{P}_t^{rA} \right)^2 \\ \left(P_t^{XA} \cdot \dot{P}_t^{XA} + P_t^{ZA} \cdot \dot{P}_t^{ZA} \right) \cdot \dot{P}_t^{YA} - P_t^{YA} \cdot \left(\dot{P}_t^{vA} \right)^2 \\ \left(P_t^{XA} \cdot \dot{P}_t^{XA} + P_t^{YA} \cdot \dot{P}_t^{YA} \right) \cdot \dot{P}_t^{ZA} - P_t^{ZA} \cdot \left(\dot{P}_t^{hA} \right)^2 \end{pmatrix}$$

Equation 5.9-10

$$\partial \underline{\ddot{P}}_t^A \Big/ \partial \underline{P}_t^A := \lambda_t \cdot P_{o,t}^{-4} \quad \cdots$$

$$\begin{pmatrix} -P_{o,t}^2 \cdot \left(\dot{P}_t^{rA} \right)^2 - 2 \cdot P_t^{XA} \cdot \varphi_X & \vdots & P_{o,t}^2 \cdot \dot{P}_t^{XA} \cdot \dot{P}_t^{YA} - 2 \cdot P_t^{YA} \cdot \varphi_X & \vdots & P_{o,t}^2 \cdot \dot{P}_t^{XA} \cdot \dot{P}_t^{ZA} - 2 \cdot \dot{P}_t^{ZA} \cdot \varphi_X \\ \cdots & \vdots & \cdots & \vdots & \cdots \\ P_{o,t}^2 \cdot \dot{P}_t^{XA} \cdot \dot{P}_t^{YA} - 2 \cdot P_t^{XA} \cdot \varphi_Y & \vdots & -P_{o,t}^2 \cdot \left(\dot{P}_t^{vA} \right)^2 - 2 \cdot P_t^{YA} \cdot \varphi_Y & \vdots & P_{o,t}^2 \cdot \dot{P}_t^{YA} \cdot \dot{P}_t^{ZA} - 2 \cdot \dot{P}_t^{ZA} \cdot \varphi_Y \\ \cdots & \vdots & \cdots & \vdots & \cdots \\ P_{o,t}^2 \cdot \underline{\dot{P}}_t^{XA} \cdot \dot{P}_t^{ZA} - 2 \cdot P_t^{XA} \cdot \varphi_Z & \vdots & P_{o,t}^2 \cdot \dot{P}_t^{YA} \cdot \dot{P}_t^{ZA} - 2 \cdot P_t^{YA} \cdot \varphi_Z & \vdots & -P_{o,t}^2 \cdot \left(\dot{P}_t^{hA} \right)^2 - 2 \cdot \dot{P}_t^{ZA} \cdot \varphi_Z \end{pmatrix}$$

Equation 5.9-11

A target kinematic gain of 3 is used thereby avoiding the complication of estimated this parameter in the observer, contrary to the ethos of pseudo-measurements. The variability in this parameter should be accounted for in the measurement uncertainty weighting.

5.9.3 Missile Dynamic Pseudo-Measurements

A simplified set of missile dynamics is often used for the observer process model, with the system noise accounting for thrust, drag airframe and aerodynamic uncertainties. Alternatively these dynamics can be introduced as pseudo-measurements driven by fin measurements, constraining a simple process model. This method provides greater control over the order and rate that measurements are processed to smooth out the computational load. The force and moment balances defined in §6 together with the aerodynamic derivatives, are simplified by assuming that:

- Roll inertia is small compared with the lateral inertia
- Cross inertia terms are small
- The missile is symmetric with equal pitch and yaw inertia
- Aerodynamic damping force is small,
- Earth rate and tilt over its surface are ignored
- Gravitational variations with height are small and are ignored
- The missile reference point lies on the missile centreline
- The forces and moments are related to the missile reference point (m) that is displaced from the centre of gravity

First some nomenclature. The column and row vectors that comprise the transform from frame (A) to frame (B) are referred to using the element numbering system described in §16.1,

$$T_A^B \equiv \left({}^{123}\underline{\varphi}_A^B \;\vdots\; {}^{456}\underline{\varphi}_A^B \;\vdots\; {}^{789}\underline{\varphi}_A^B \right)$$

Equation 5.9-12

$$T_A^B \equiv \left({}^{147}\underline{\varphi}_A^B \;\vdots\; {}^{258}\underline{\varphi}_A^B \;\vdots\; {}^{369}\underline{\varphi}_A^B \right)^T$$

Equation 5.9-13

The nomenclature associated with airframe and aerodynamic characteristics is dealt with in §6. The fin elevator and rudder angles (η,ξ) are to be found in §3.10.

5.9.3.1 Linear Motion Pseudo-Measurements

Applying the simplifying assumptions to the linear equations of motion,

$$\underline{\ddot{P}}_{o,m}^B := m_m^{-1} \cdot \underline{F}_m^B - \underline{\omega}_{A,B}^B \times \left(T_A^B \cdot \underline{\dot{P}}_m^A \right) + g_m^{ZA} \cdot {}^{789}\underline{\varphi}_A^B$$

Equation 5.9-14

$$\underline{F}_m^B := \left(m_m^{-1} \cdot \left(F_T^{XB} + F_D^{XB} \right) \;,\; y_v \cdot \dot{P}_{o,m}^{YB} + y_\xi \cdot \xi \;,\; z_w \cdot \dot{P}_{o,m}^{ZB} + z_\eta \cdot \eta \right)^T$$

Equation 5.9-15

The linear acceleration pseudo-measurement,

$$\underline{\ddot{P}}_{o,m}^A := \left(T_A^B \right)^T \cdot \underline{\ddot{P}}_{o,m}^B$$

Equation 5.9-16

Apportioning the innovations to the missile linear and angular states,

$$\frac{\partial \underline{\ddot{P}}_m^A}{\partial \underline{X}_M} := \left(T_B^A \cdot \frac{\partial \underline{\ddot{P}}_{o,m}^B}{\partial \underline{X}_{ML}} \;\vdots\; \frac{\partial T_B^A}{\partial \underline{X}_{MA}} \cdot \underline{\ddot{P}}_{o,m}^B + T_B^A \cdot \frac{\partial \underline{\ddot{P}}_{o,m}^B}{\partial \underline{X}_{MA}} \right)$$

Equation 5.9-17

The variation in the direction cosines defining the orientation of the missile with respect to the quaternion state is defined in §22.10.11,

$$\partial T_B^A \,/\, \partial \underline{X}_{MA} := \left(\partial T_B^A \,/\, \partial Q_A^B \;\vdots\; 0_{3x6} \right)$$

Equation 5.9-18

The variation in the body acceleration with respect to the linear states,

$$\frac{\partial \underline{\ddot{P}}^{B}_{o,m}}{\partial \underline{X}_{ML}} := \left(0_{3x2} \quad , \quad m_m^{-1} \cdot \partial \underline{F}^{B}_{m} \Big/ \partial P^{ZA}_{m} \quad \vdots \quad \partial \underline{\ddot{P}}^{B}_{o,m} \Big/ \partial \underline{\dot{P}}^{A}_{m} \quad \vdots \quad 0_{3x3} \right)$$

Equation 5.9-19

$$\partial \underline{\ddot{P}}^{B}_{o,m} \Big/ \partial \underline{\dot{P}}^{A}_{m} :=$$

$$m_m^{-1} \cdot \frac{\partial \underline{F}^{B}_{m}}{\partial \underline{\dot{P}}^{A}_{m}} - \left(\underline{\omega}^{B}_{A,B} \times {}^{123}\underline{\varphi}^{B}_{A} \quad , \quad \underline{\omega}^{B}_{A,B} \times {}^{456}\underline{\varphi}^{B}_{A} \quad , \quad \underline{\omega}^{B}_{A,B} \times {}^{789}\underline{\varphi}^{B}_{A} \right)$$

Equation 5.9-20

The linear acceleration innovations are apportioned to the angular states,

$$\frac{\partial \underline{\ddot{P}}^{B}_{o,m}}{\partial \underline{X}_{MA}} := \left(\left(\frac{\partial \ddot{P}^{XA}_{m}}{\partial Q^{B}_{A}} \quad , \quad \frac{\partial \ddot{P}^{YA}_{m}}{\partial Q^{B}_{A}} \quad , \quad \frac{\partial \ddot{P}^{ZA}_{m}}{\partial Q^{B}_{A}} \right)^{T} \quad \vdots \quad \left[\underline{\dot{P}}^{B}_{o,m} \times \right] \quad \vdots \quad 0_{3x3} \right)$$

Equation 5.9-21

$$\partial \underline{\ddot{P}}^{XB}_{o,m} \Big/ \partial Q^{B}_{A} := -2 \cdot g^{ZA}_{m} \cdot \left(-q_2 \quad , \quad q_3 \quad , \quad -q_0 \quad , \quad q_1 \right)^{T}$$

Equation 5.9-22

$$\frac{\partial \underline{\ddot{P}}^{YB}_{o,m}}{\partial Q^{B}_{A}} := 2 \cdot \left(\left(\omega^{ZB}_{A,B} + y_v \right) \cdot \begin{pmatrix} -q_0 & q_3 & -q_2 \\ -q_1 & q_2 & q_3 \\ q_2 & q_1 & -q_0 \\ q_3 & q_0 & q_1 \end{pmatrix} \cdot \underline{\dot{P}}^{A}_{o,m} - g^{ZA}_{m} \cdot \begin{pmatrix} q_1 \\ q_0 \\ q_3 \\ q_2 \end{pmatrix} \right)^{T}$$

Equation 5.9-23

$$\frac{\partial \underline{\ddot{P}}^{ZB}_{o,m}}{\partial Q^{B}_{A}} := 2 \cdot \left(\left(z_w - \omega^{YB}_{A,B} \right) \cdot \begin{pmatrix} q_0 & q_3 & -q_2 \\ q_1 & q_2 & q_3 \\ -q_2 & q_1 & -q_0 \\ -q_3 & q_0 & q_1 \end{pmatrix} \cdot \underline{\dot{P}}^{A}_{o,m} - g^{ZA}_{m} \cdot \begin{pmatrix} q_0 \\ q_1 \\ -q_2 \\ q_3 \end{pmatrix} \right)^{T}$$

Equation 5.9-24

The variation in thrust, drag, and normalised aerodynamic lateral force derivatives with respect to the linear missile states,

$$\frac{\partial \underline{F}_m^B}{\partial \underline{X}_{ML}} := \begin{pmatrix} m_m^{-1} \cdot \left(\frac{\partial F_T^{XB}}{\partial \underline{X}_{ML}} + \frac{\partial F_D^{XB}}{\partial \underline{X}_{ML}} \right) \\ \frac{\partial y_v}{\partial \underline{X}_{ML}} \cdot \dot{P}_{o,m}^{YB} + \frac{\partial y_\xi}{\partial \underline{X}_{ML}} \cdot \xi \\ \frac{\partial z_w}{\partial \underline{X}_{ML}} \cdot \dot{P}_{o,m}^{ZB} + \frac{\partial z_\eta}{\partial \underline{X}_{ML}} \cdot \eta \end{pmatrix} + \begin{pmatrix} 0 \\ y_v \cdot \left({}^{456}\underline{\varphi}_A^B \right)^T \\ z_w \cdot \left({}^{789}\underline{\varphi}_A^B \right)^T \end{pmatrix}$$

Equation 5.9-25

The variation in thrust and drag with respect to the linear missile states is defined in §6.3&4. The normalised lateral force derivatives are themselves functions of Mach Number, geodetic height and incidence. For example, the variation in the lateral lift derivative with respect to the these parameters expressed in the state space,

$$\partial y_v / \partial \underline{X}_{ML} :=$$

$$\left(0_2 \quad , \quad \frac{\partial y_v}{\partial M_m} \cdot \frac{\partial M_m}{\partial P_m^{ZA}} \quad \vdots \quad \frac{\partial y_v}{\partial M_m} \cdot \frac{\partial M_m}{\partial \dot{\underline{P}}_m^A} + \frac{\partial y_v}{\partial \xi_B^{MV}} \cdot \frac{\partial \xi_B^{MV}}{\partial \dot{\underline{P}}_m^A} \quad \vdots \quad 0_3 \right)$$

Equation 5.9-26

Likewise for the other normalised aerodynamic derivatives. For the generic missile, these equations are simplified using the incidence lag and its variation with missile height, velocity and incidence that are defined in §6,

$$\frac{\partial \underline{F}_m^B}{\partial \underline{X}_{ML}} := \begin{pmatrix} m_m^{-1} \cdot \left(\frac{\partial F_T^{XB}}{\partial \underline{X}_{ML}} + \frac{\partial F_D^{XB}}{\partial \underline{X}_{ML}} \right) \\ -\frac{\partial \left(1 / T_I^{YB} \right)}{\partial \underline{X}_{ML}} \cdot \dot{P}_{o,m}^{YB} \\ -\frac{\partial \left(1 / T_I^{ZB} \right)}{\partial \underline{X}_{ML}} \cdot \dot{P}_{o,m}^{ZB} \end{pmatrix} - \begin{pmatrix} 0 \\ \left(1 / T_I^{YB} \right) \cdot \left({}^{456}\underline{\varphi}_A^B \right)^T \\ \left(1 / T_I^{ZB} \right) \cdot \left({}^{789}\underline{\varphi}_A^B \right)^T \end{pmatrix}$$

Equation 5.9-27

5.9.3.2 Angular Motion Pseudo-Measurements

Applying the simplifying assumptions to the angular equations of motion the angular acceleration pseudo-measurement,

$$\underline{\dot{\omega}}_{A,B}^{B} \coloneqq I_m^{-1} \cdot \underline{M}_m^{B} + m_m \cdot P_{m,u}^{XB} \cdot T_A^B \cdot \underline{g}_m^A$$

Equation 5.9-28

$$\left(\dot{\omega}_{A,B}^{YB} \quad , \quad \dot{\omega}_{A,B}^{ZB} \right)^T \coloneqq$$

$$\begin{pmatrix} I_{YY}^{-1} \\ \\ I_{ZZ}^{-1} \end{pmatrix} \otimes \begin{pmatrix} m_w \cdot \dot{P}_{o,m}^{ZB} + m_q \cdot \omega_{A,B}^{YB} + m_\eta \cdot \eta \\ \\ n_v \cdot \dot{P}_{o,m}^{YB} + n_r \cdot \omega_{A,B}^{ZB} + n_\xi \cdot \xi \end{pmatrix} + m_m \cdot P_{m,u}^{XB} \cdot g_m^{ZA} \cdot \begin{pmatrix} T_A^B(9) \\ \\ T_A^B(6) \end{pmatrix}$$

Equation 5.9-29

Apportioning the innovations to the missile linear states,

$$\partial \dot{\omega}_{A,B}^{YA} \,/\, \partial \underline{X}_{ML} \coloneqq \left(0_3 \;\vdots\; m_w \cdot I_{YY}^{-1} \cdot {}^{369}\underline{\varphi}_A^B \;\vdots\; 0_3 \right) + \partial M_m^{YB} \,/\, \partial \underline{X}_{ML}$$

Equation 5.9-30

$$\partial \dot{\omega}_{A,B}^{ZA} \,/\, \partial \underline{X}_{ML} \coloneqq \left(0_3 \;\vdots\; n_v \cdot I_{ZZ}^{-1} \cdot {}^{258}\underline{\varphi}_A^B \;\vdots\; 0_3 \right) + \partial M_m^{ZB} \,/\, \partial \underline{X}_{ML}$$

Equation 5.9-31

$$\begin{pmatrix} \dfrac{\partial M_m^{YB}}{\partial \underline{X}_{ML}} \\ \\ \dfrac{\partial M_m^{ZB}}{\partial \underline{X}_{ML}} \end{pmatrix} \coloneqq \begin{pmatrix} I_{YY}^{-1} \\ \\ I_{ZZ}^{-1} \end{pmatrix} \otimes \begin{pmatrix} \dfrac{\partial m_w}{\partial \underline{X}_{ML}} \cdot \dot{P}_{o,m}^{ZB} + \dfrac{\partial m_q}{\partial \underline{X}_{ML}} \cdot \omega_{A,B}^{YB} + \dfrac{\partial m_\eta}{\partial \underline{X}_{ML}} \cdot \eta \\ \\ \dfrac{\partial n_v}{\partial \underline{X}_{ML}} \cdot \dot{P}_{o,m}^{YB} + \dfrac{\partial n_r}{\partial \underline{X}_{ML}} \cdot \omega_{A,B}^{ZB} + \dfrac{\partial n_\xi}{\partial \underline{X}_{ML}} \cdot \xi \end{pmatrix}$$

Equation 5.9-32

The normalised aerodynamic moment derivative Jacobians are treated the same as the linear equivalents as shown in Equation 5.9-26.

5.10 Filter integrity

For non-linear systems care must be exercised to avoid filter ill-conditioned, and prevent the state expectations from decaying to very small values, when using an EKF when the measurements are not in the state space. The measurements must pass a series of integrity tests to prevent the occasional spurious data from disturbing it, this is particularly serious if the measurements from one sensor are being used to estimate errors in other sensors.

Whilst filter implementation and integrity checking are relatively simple, it is in the selection of thresholds, the interaction between integrity tests, and filter adaptation were the art, and ultimately the robust nature of state observer is assured. Some commonly employed methods to protect filters

from ill-conditioning, and ultimately divergence are now reviewed. An excellent paper on this topic by Daum[D.3] covers many of these techniques in practical filters, although de-coupling of the covariance matrix is not considered for reasons already discussed. The following techniques have already been mentioned,

- Covariance matrix main diagonal lower bounding
- Increased process noise
- Iterative improvement
- Second order measurement function expansion
- Joseph covariance update
- Scalar measurement processing in preferred order (most accurate first)

Using 32 bit processing the order in which equations are computed, and word-length considerations, are less important than was once the case. For air-defence applications the inclusion of position, velocity and angular parameters in the missile state observer results in manipulation of values with a dynamic range of the order of 10^7. Although the results presented in this research are derived using 64 bit calculations, when implementing the missile observer on 32 bit processors the states may have to be scaled to reduce the dynamic range to say 10^2 using units of km, mrad etc.

5.10.1 Measurement Sampling

Sampling sensors at high rates may result in correlated measurements that can destabilise a KF, Guu[G.14]. The simplest approach is to pre-whiten the measurements using a sampling rate less than the correlation bandwidth. A more rigorous approach is to add the correlation dynamics to the filter as proposed by Guu, and used so effectively by Rao[R.14] for GPS measurement fusion in the presence of selective availablitity.

5.10.2 Measurement Averaging

Processor loading is reduced by performing state updates, or more likely covariance updates, at a lower rate. High frequency measurements can be accumulated, reducing noise and short-term correlations, thereby adhering more closely to the EKF tenants concerning Gaussian noise, albeit with increased, but deterministic, measurement latency. Latency is accounted for in the innovation, the states being stored and interpolated given sufficient memory, or by backwards state propagated if sufficient processing power is available. Rarely is the covariance matrix needed at the measurement reference time, nor is it necessary to propagate the filter to the current time after a measurement update.

5.10.3 Serial Measurement Processing and Linearity

Independent measurements in non-linear systems are best processed serially with scalar inversion. This avoids a computationally intensive matrix inversion that is prone to numerical inaccuracies. Serial processing is equivalent to parallel processing for independent measurements however, the intermediate state update provides an opportunity to improve the filter linearisation between measurements that can be a source of filter instability. Miller[M.10] showed that processing angular measurements before range data, with interim re-linearisation, improved tracking performance, virtually eliminating measurement linearisation errors. This improves the EKF tendency to overestimate its ability to derive cross-range data from range measurements that can lead to serious performance degradation, Park[P.6].

5.10.4 Measurement Delays

The time between taking a measurement and its application due to communication and processing delays must be accounted for in high bandwidth systems. Using time stamped measurements these delays are accurately known and easily compensated for, as described in §5.10.2.

5.10.5 Measurement Range Traps

Thresholds can be applied to measurements according to known physical and dynamic characteristics of the missile or sensor. Missile lateral acceleration and angular rate measurements exceeding their capability are ignored and the filter is propagating until a valid measurement is available.

5.10.6 Measurement Consistency Traps

If the difference between successive measurements is inconsistent with their trend, accepted noise levels, and sensor capabilities, they must be discarded. Consistency traps are apply to parameters with low rates of change. For example, checks on target LOS rate derived from ground radar target angles to ensure that it is consistent with the expected capability of the target.

5.10.7 Divergence Traps and Innovation Thresholds

If the expected state error is consistently less than the true rms state error, and growing smaller, the filter is divergent. If the expectations are simply constant and do not match the true rms error the filter is ill-conditioned, a less serious problem. The simplest test is to compare the measurement innovations with their expected √variance. This is the Mahalanobis distance (PI_M) of §22.13.16 a chi-squared metric that measures how well the covariance is tuned to the measurements,

$$PI_M^2 \;:=\; \underline{\Delta Z}^T \cdot \left(H \cdot C \cdot H^T + R \right)^{-1} \cdot \underline{\Delta Z}$$

Equation 5.10-1

If $(PI_M)^2$ is > 2 to 3 the measurements are discarded. If average value of $(PI_M)^2$ exceeds 1 the state and/or measurement noise can be adapted on-line.

5.10.8 Covariance Matrix Conditioning

There are a number of approaches to ensure that the covariance matrix [C] remains symmetric and supposedly positive definite. On-line testing is often restricted to ensure that the main diagonal elements are positive and,

$$C(i,j)^2 < C(i,i) \cdot C(j,j)$$

Equation 5.10-2

These simple tests provide a warning of ill-conditioning in [C] and the possibility of filter divergence; they are not a definitive indicator of positive definiteness. Sylvester's Criteria is often used for the later where the determinant of [C], and all its sub-minors, must be positive. This is computationally intensive test and one rarely employed in practical systems where symmetry is assured by computing only a triangular partition of [C],

$$i \neq j \Rightarrow C(j,i) := C(i,j)$$

Equation 5.10-3

To prevent state lockout indicated by a zero on the main diagonal of [C], and numerical instability if any of these values are negative, an artificially lower bound can be applied, Griffin[G.15]. Such lower thresholds must reflect any state scaling - see the thorough discourse on [C] matrix ill-conditioning by Kerr[K.6].

$$C(i,i) := |C(i,i)|$$

Equation 5.10-4

The off-diagonal terms are then modified,

$$(i \neq j) \wedge (j > i) \Rightarrow C^*(i,j) := \frac{C^2(i,j)}{C^*(i,i) \cdot C^*(j,j)}$$

Equation 5.10-5

Kerr warns that these ad-hoc approaches to protect [C] can significantly alter the matrix beyond reason, and may not prevent filter divergence.

5.10.9 Filter Performance and Observability

Stochastic filters that meet the tenants of the KF are well tuned when the 63% of the actual state errors after a measurement update are matched to the expected covariance [C]. A performance metric based on this principle is the normalised distance (PI_X) provided by the utility defined in §22.13.15,

$$PI_X^2 \;:=\; \underline{\Delta X}^T \cdot C^{-1} \cdot \underline{\Delta X}$$

Equation 5.10-6

As the number of filter states increases it becomes difficult to gain an insight into system observability. It is even more difficult when filtering in Cartesian space when any intuitive link with polar measurements is lost. An alternative observability metric is the filter conditioning number (η) based on the ratio between maximum and minimum eigenvalues of [C],

$$\eta(C) \;:=\; \lambda_{MAX}(C) / \lambda_{MIN}(C)$$

Equation 5.10-7

In general the smaller the eigenvalue the more observable is the associated state. The eigenvectors then represent the direction of "best" observability providing [C] is normalised, Ham[H.11]. Normalising using the initial covariance matrix [C_0],

$$\Omega\left(C^+\right) \;:=\; \begin{bmatrix} \frac{C^+(1,1)}{C_0^-(1,1)} & \cdots & \frac{C^+(1,n)}{\sqrt{C_0^-(1,1)\cdot C_0^-(n,n)}} \\ \cdots & \cdots & \cdots \\ \vdots & \ddots & \vdots \\ \cdots & \cdots & \cdots \\ \frac{C^+(1,n)}{\sqrt{C_0^-(1,1)\cdot C_0^-(n,n)}} & \cdots & \frac{C^+(n,n)}{C_0^-(n,n)} \end{bmatrix}$$

Equation 5.10-8

$$\varphi \;:=\; n \cdot \left(\Omega\left(C^+\right) / \operatorname{trace}\Omega\left(C^+\right)\right) \;\Rightarrow\; PI_E \;:=\; \lambda_{MAX}(\varphi) / \lambda_{MIN}(\varphi)$$

Equation 5.10-9

The eigenvectors also indicate which combinations of states are observable, which may not be obvious from the main diagonal of [C] alone. Daum[D.2] shows that (PI_E) is closely related to the fractional change of the information update components expressed as,

$$A \cdot \underline{X} \;:=\; \underline{b}$$

Equation 5.10-10

$$\left(C^- + H^T \cdot R^{-1} \cdot H\right) \cdot \underline{X}^+ \;:=\; C^- \cdot \underline{X}^- + H \cdot R^{-1} \cdot \underline{\tilde{Z}}$$

Equation 5.10-11

In well-conditioned filters the fractional state change is small and is dominated by (PI_E). This metric quantifies filter improvements, a lower condition number indicates that the fractional error in the state is lower.

However, care is needed when quoting absolute (PI_E) values as a filter can be well conditioned even if the condition number is large. For tracking λ_{MAX} tends to be dominated by the position error normal to the LOS, and λ_{MIN} by range-rate errors. Daum shows that the conditioning number is a sensitive indicator that increases markedly before [C] diagonal thresholds and process noise can take effect.

Two avenues of research linked to observability are of interest. Ohtsuka[O.3] shows that general observability is improved by maximising the information in each measurement update,

$$PI_{OBS} := \det\left(\Phi^T \cdot H^T \cdot H \cdot \Phi \right)$$

Equation 5.10-12

PN is probably the most enduring of the missile guidance laws however, it actively minimises observability by establishing an early constant velocity collision course. Song[S.6] shows that adding terms to the guidance law that cause the LOS to oscillate improves state observation and hence performance. Although their conclusions are self-evident, mechanisation of algorithms to enhance observability is interesting, particularly when states are added to the observer to actively estimate sensor errors.

5.11 Missile State Observer Simulator

The target and missile state observers are placed in context within the overall simulation structure in Figure 6-1, where they are referred to as the "embedded simulators". The numbers associated with particular functions shown in this figure represent the order in which they are performed. *IMM_CONTROL* and *FF_CONTROL* control the target and missile observer functions respectively, as shown in Figure 5-7. These controllers are activated by *DX_CONTROL* at 10 Hz and 400 Hz when the state integrator loop controller *INDEXI* is 1 - see Figure 8-7. The target state observer is initialised by module *I_MM* as described in §4.4, with the missile observer inhibited. Once initialisation is complete the target track and covariance information is up-linked to the missile where module *I_FF* initialises the missile state observer and loads IMM target information.

Individual IMM filters are selected by setting individual bits of control *IMM_TP* as shown in Figure 5-7. When a single filter is selected, IMM combination and re-initialisation is suspended and the filter output is delivered to the missile observer via the up-link module. Each filter propagates its own states and covariances using either a conventional EKF, Iterated EKF, or second order filter formulation.

U_GB_RADAR_T is activated if new radar measurements are ready for processing, and each measurement is processed serially with intermediate re-linearisation. The IMM pre- and post-measurement combined states and

covariances are passed to the up-link module, together with the IMM modal weights and the radar missile measurements.

The missile observer propagates the simple process model at 400 Hz. Any missile sensor measurements ready for processing are used to update the filter at the rates indicated in Figure 5-7. The accelerometer data is accumulated at 400 Hz and applied at 100 Hz. The observer is updated using up-linked missile data at 10 Hz using measurement fusion and target track fusion.

As each measurement is processed its "ready" flag, set originally in the sensor module where it originated, is cleared by *FF_CONTROL*. After the measurements have been processed any combination of the pseudo-measurements provided can be imposed at clock rates up to 400 Hz. These are used to constrain the simple process model dynamics, and introduce state cross-coupling information.

5.12 Discussion

Although centralised measurement fusion and track fusion combining the output from a number of de-centralised (federated) filters for each sensor is explored, architecture selection is often determined by application. This is certainly the case for air-defence in which information is up-linked only, and the missile processing capacity is a fraction of that available on the ground. A hybrid architecture is selected comprising decentralised tracking with centralisation in the missile where this information is fused at track level with the remaining sensor data using measurement fusion.

The central state observer in the missile is a conventional EKF with earth referenced position, velocity and acceleration states, complimenting those in the IMM. These states are augmented by missile orientation, angular rate and angular acceleration with respect to the same frame. The simplest possible dynamic model is used so that it can be propagated at high rate for seeker beam steering, inertial stabilisation of the seeker head and airframe stabilisation without undue latency.

Growth in the expected orientation and angular state errors is controlled using 400 Hz gyroscope measurements. The slower linear dynamics are, in the first instance, driven by accumulated accelerometer data. As up-links are received the target-track is introduced into the observer using track fusion since at 10 Hz the data will certainly be correlated. The up-linked missile measurements provide a further constraint on the missile linear state errors. Seeker data links the target and missile linear states, and it is this duality (radar - IMU) and (IMU - seeker) that provides the opportunity for sensor failure detection and error estimation. Note that both PN and CLOS guidance laws can be generated from the observer output, the gyroscope triad being the one critical set of instruments.

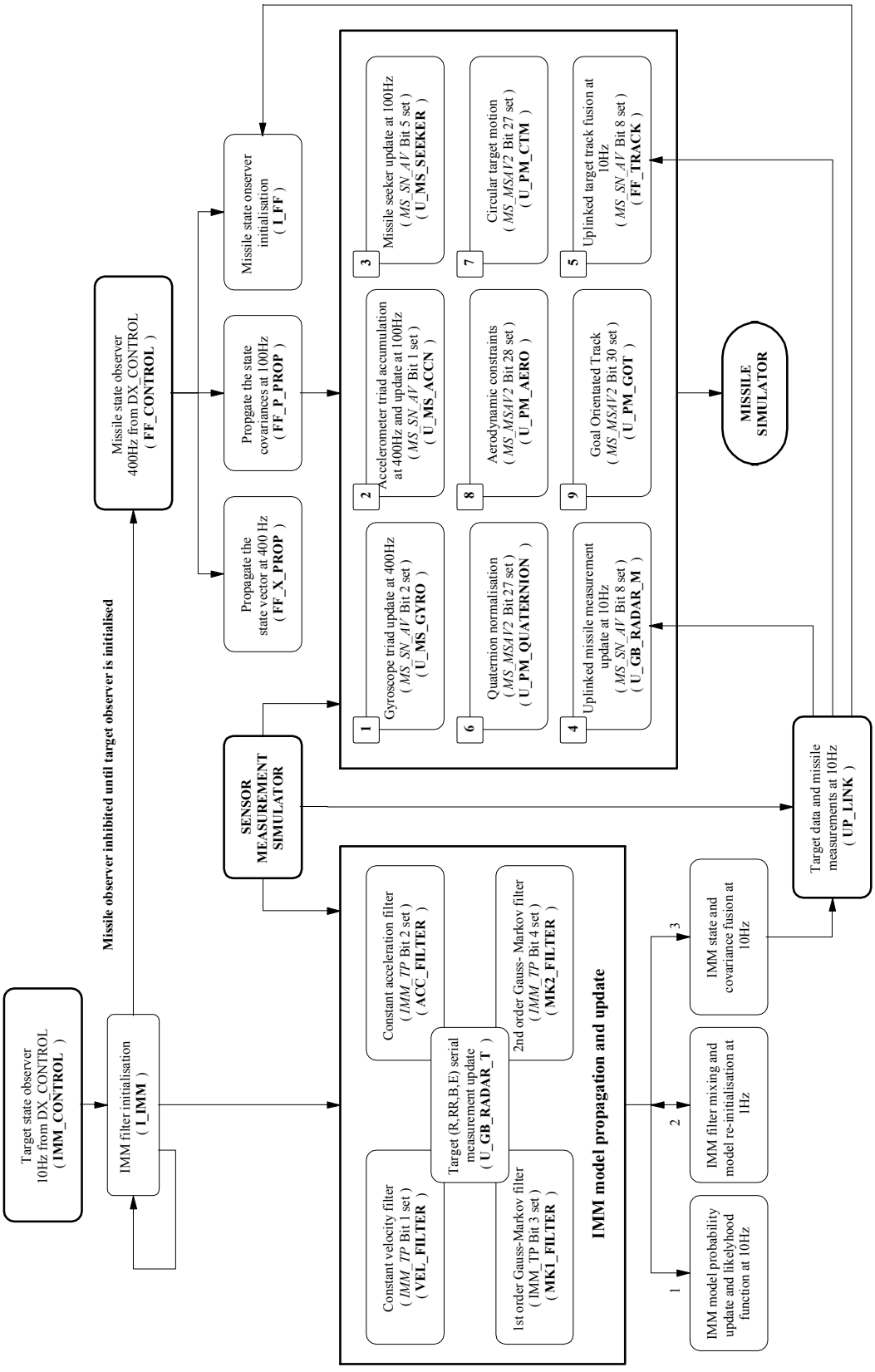

Figure 5-7 : Missile State Observer Simulation

The intention is to further constrain the missile and target dynamics using pseudo-measurements. Since these are not part of the filter propagation they can be processed according to the dictates of loading and system requirements. The "measurement" covariance reflects not only the inherent uncertainty in each, but in the case of target dynamics it flight regime. This is where the IMM filter uncertainties can be used to provide executive control over the introduction of circular motion and GOT dynamics as pseudo-measurements.

It is recognised that the EKF is operating in an environment for which it is ill-suited. Highly non-linear dynamic and sensor measurements with correlated errors violate the basic tenant of EKF design, namely Gaussian statistics. It is a constant source of amazement that this type of filter works as well as it does in such an environment. A list of measures that can be taken to mitigate some of the more serious problems is provided from which ensuring covariance symmetry is probably the most important in practical applications.

Consider now some extensions to the work presented:

- The EKF does not respect quaternion normalisation that is performed after each measurement update affecting the quaternion states. This process is non-optimal and the covariances can be expanded to account for the error in the process. An assessment of the error induced ignoring this correction is needed, as covariance expansion is computationally intense if performed at high frequency.
- A study into the up-link data rate that would avoid correlated target track data so that this data can be treated as a measurement, simplifying both the observer and reducing the up-link bandwidth.
- Whilst the equations relating to pseudo-measurement characterising the observer state dynamics are provided, their systematic application has not yet been considered. Rates, processing order, and links with the IMM filter probabilities acting as manoeuvre detectors, all need to be explored and benefits quantified.
- For air-launched applications, if the missile IMU sensors are of poor quality the opportunity exists to estimate bias errors before launch, subject to launcher rotation and vibration. The biases can be removed from the IMU output leaving only residual and dynamically induced errors.

Chapter 6

MISSILE GUIDANCE

Although the focus of this research is on real-time trajectory optimisation, optimal guidance is rooted in the historical development of conventional PN and CLOS laws. There are good reasons for considering these, not the least being:

- Missile dynamic model verification is easier using a conventional guidance law as the resulting missile trajectory characteristics are well established.
- Guidance laws derived analytically using simple PI provide a baseline against which real-time optimisation algorithms can be verified. If viable on-line optimisation must provide a basic performance that is better than these simple, but robust, alternatives.
- Target tracking limitations, and performance improvement based on manoeuvre detection linked to IMM mode probability are more easily demonstrated and understood using simpler guidance laws.

The missile simulator with embedded trajectory optimiser is introduced. The dynamics of a short-range, agile missile and launcher are developed, dynamics generated by 2^{nd} order STT and BTT autopilots with speed dependent acceleration limits for low speed stability.

A historical review is provided of PN laws and the introduction of optimally derived laws including essential practical constraints for target capture. Missile and target acceleration augmented PN laws are derived and the critical part time-to-go plays in optimal guidance, and observer constraints imposed by inertial stabilisation seekers emphasised.

The basics of CLOS guidance are established and extended to include biasing associated with phased array beam forming. The accuracy required for IMM weave frequency estimation is quantified using linear analysis and steady-state weave tuned filters.

The importance of manoeuvre detection in conventional guidance laws is discussed and its links to the IMM modal probability associated with the constant velocity target-tracking filter introduced in §4.

6.1 Missile Guidance Simulator

Figure 6-1 shows how the previous simulators combine to support the Missile Guidance software that contains a generic missile model, conventional guidance laws, and a trajectory optimiser. This is the final simulator embedded in the software infrastructure described in §8. For security and commercial reasons the MBDA missile models are strictly segregated and only the generic missile is described in this document, The generic missile is activated if (*MS_TYPE* := 0).

Modules *D_MISSILE* and *I_MISSILE* perform initialisation and model characterisation. The Target simulator is activated first within the integration loop controlled by *DX_CONTROL*. The remaining reference data listed in §22.2 are provided at 4 kHz, implemented so as to be robust prior to launch, and whilst the missile is slowly rotating in the launcher. After launch *STOP_MONITOR* and *C_APPROACH* monitor the program termination and impact conditions described in §22.2.1. If *SCREEN* is set to 1, a progress report is written to the screen at 10 Hz containing:

- Simulation time
- Target range
- Missile time-to-go (post launch only)
- Missile to target LOS range (post launch only)
- Missile speed (post launch only)

The missile functions are stimulated by the reference or estimated data listed in §22.2 depending on the active sensors, target tracking and missile state observer controls. This data is provided at a rate commensurate with the fastest element in the missile control system, in this case 400 Hz. When the observers are active the state errors and covariances are analysed by *CV_CONTROL* and *CV_STATS*, as described in §22.12. At launch *MS_CONTROL* is activated comprising the launcher and missile models and their linear and angular dynamics. The missile models are computed on the initial integrator pass when *INDEXI* is 1 at the clock rates shown.

6.2 Missile Airframe

MS_AIRFRAME selects the airframe model, in this case *MS_AF_0* which is is active from launch at time (t_L) to the end of the boost phase lasting (t_B := 4s), after which the airframe parameters remain constant. The generic missile diameter (d_m) used to determining the drag force is 0.18 m. During boost the propellant mass reduces linearly with time,

$$t \in \left[t_L , t_L + t_B \right] \Rightarrow \quad m_m \quad := \quad 80 - 35 \cdot \left(t / t_B \right)$$

Equation 6.2-1

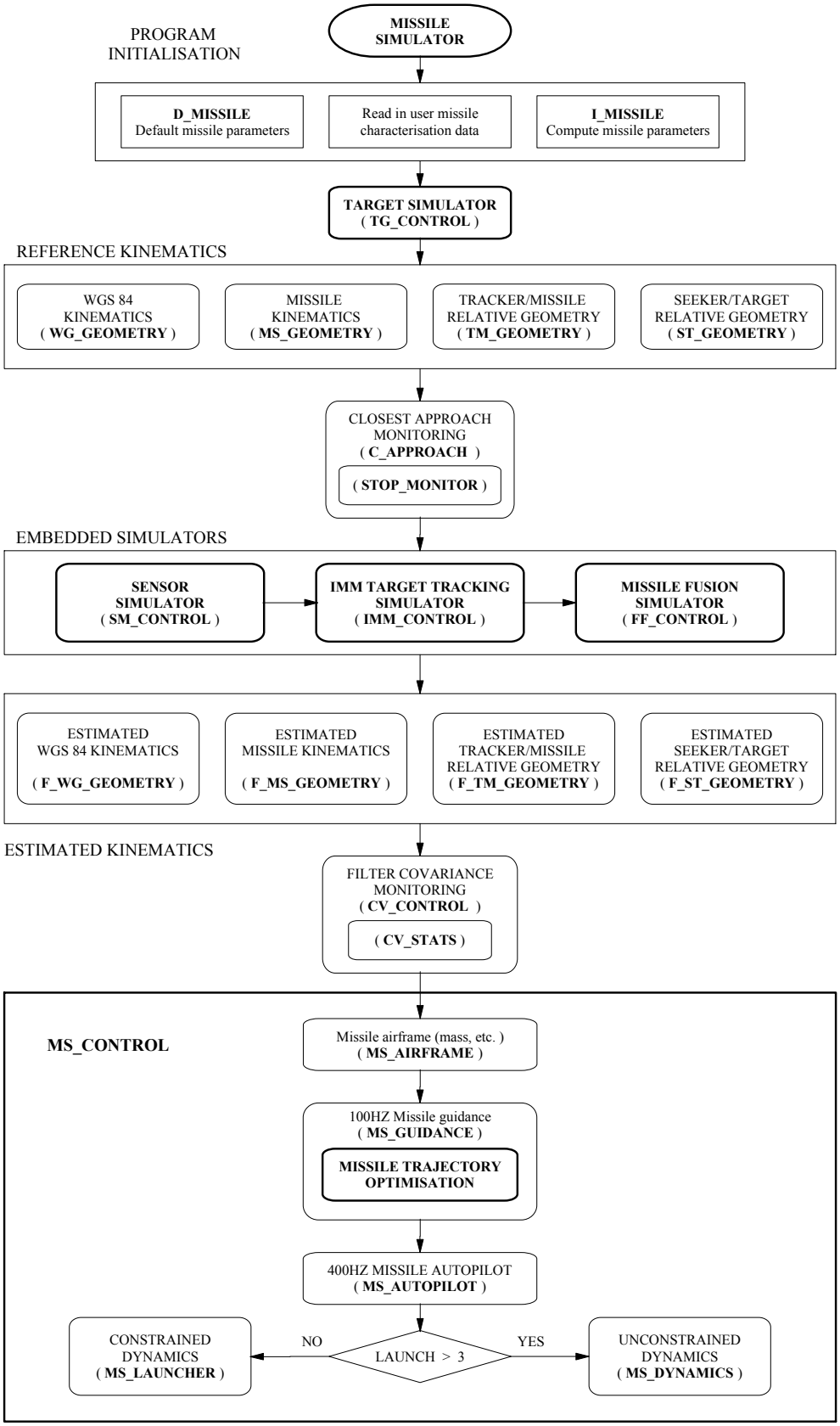

Figure 6-1 : Missile Simulator

As fuel is consumed the centre-of-gravity moves forwards along the missile centreline according to,

$$t \in [\, t_L \,,\, t_L + t_B \,] \;\Rightarrow\; \underline{P}^{B}_{m,c} \;:=\; -1.3 + 0.2 \cdot \left(t \,/\, t_B \right)$$

Equation 6.2-2

As fuel is consumed, ignoring small cross-inertia terms,

$$t \in [\, t_L \,,\, t_L + t_B \,] \;\Rightarrow$$

$$\operatorname{diag}\left(I^{B}_{m} \right) \;:=\; \left(0.35 \quad 30 \quad 30 \right) - \left(0.15 \quad 5 \quad 5 \right) \cdot \left(t \,/\, t_B \right)$$

Equation 6.2-3

6.3 Missile Thrust

THRUST_F invokes one of the thrust models *THRUST_** dependent on the setting of *MS_TYPE*. The generic missile thrust profile defined below is contained in *THRUST_0*. During boost the mass flow through the rocket nozzle remains constant. For a propellant specific heat ratio (γ) of 1.2, combustion temperature (T_C) of 3000 K, specific gas constant (R) of 250 J/deg K/kg, and specific impulse at sea-level (SI) of 2100 Ns/kg the combustion pressure for complete adiabatic expansion of the efflux, and thrust,

$$P_C \;:=\; P_S \cdot \left(1 - SI^2 \cdot \frac{\gamma - 1}{2 \cdot \gamma \cdot R \cdot T_C} \right)^{-\gamma/(\gamma-1)}$$

Equation 6.3-1

$$F^{XB}_{T} \;:=\; \dot{m}_m \cdot \sqrt{\frac{2 \cdot \gamma}{\gamma - 1} \cdot R \cdot T_C \cdot \left(1 - \frac{P_S}{P_C} \right)^{(\gamma-1)/\gamma}}$$

Equation 6.3-2

If the combustion chamber pressure (P_C) remains constant with height the thrust generated by the rocket motor,

$$t \in [\, t_L \,,\, t_L + t_B \,] \;\Rightarrow\; F^{XB}_{T} \;:=\; 10^3 \cdot \sqrt{1089 - 81.3 \cdot P_S^{0.167}}$$

Equation 6.3-3

The thrust variation with geodetic height, using the change in static air pressure (P_S) with height defined in §19.1,

$$\frac{\partial F_T^{XB}}{\partial P_{d,m}^{ZG}} := -\left(\frac{6.7881 \times 10^6}{P_S^{0.833} \cdot F_T^{XB}} \right) \cdot \frac{\partial P_S}{\partial P_{d,m}^{ZG}}$$

Equation 6.3-4

Short-boosting missiles remain in the Troposphere in which case the variation in static pressure is given by Equation 19.1-4.

6.4 Missile Drag

The boost and coast phase drag depends on Mach number (M_m) and air density (ρ_A) defined in §19.3, also missile speed and body incidence (ξ_B^{MV}) defined in §16.6,

$$F_D^{XB} := -8^{-1} \cdot \pi \cdot \rho_A \cdot {d_m}^2 \cdot \dot{P}_{d,m}^2 \cdot C_D$$

Equation 6.4-1

$$C_D := CD_{ij} \cdot M_i\left(M_m\right) \cdot N_j\left(24 \cdot \xi_B^{MV} \,/\, {}_{MAX}\xi_B^{MV}\right)$$

Equation 6.4-2

The drag coefficient (C_D) is determined using the B-splines coefficients (CD_{ij}) listed in Table 6-1 for Mach numbers [1,4], and body incidence [0,24°]. The boost phase variation in (C_D) for Mach numbers and incidence up to 3.5 and 15° respectively is shown in Figure 15-1.

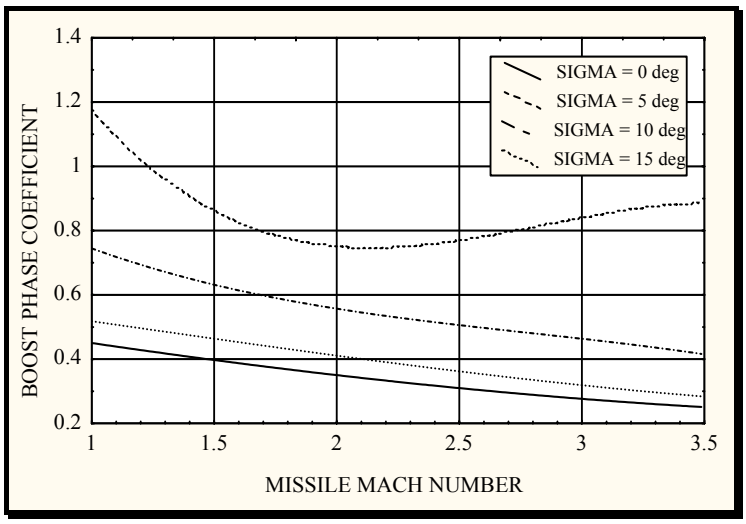

Figure 6-2 : Boost Phase Drag Coefficient

The equivalent coast phase drag (not shown) is larger as the effective missile surface area increases without the motor plume. To accommodate variations in maximum incidence (σ_{MAX}), defaulting to 40°, the output from the B-splines are scaled by 40/24. The drag function state dependencies are,

$$F_D^{XB} :=$$

$$-\varphi_{CSA} \cdot \rho_A\left(P_{d,m}^{ZG}\right) \cdot \dot{P}_{d,m}^2 \cdot C_D\left(M_m\left(P_{d,m}^{ZG}, \dot{P}_{d,m}^{ZG}\right), \xi_B^{MV}\left(P_{d,m}^{ZG}, T_G^B\left(Q_G^B\right) \cdot \dot{P}_{d,m}^G\right)\right)$$

Equation 6.4-3

The drag force variation with geodetic height,

$$\frac{\partial F_D^{XB}}{\partial P_{d,m}^{ZG}} := \frac{F_D^{XB}}{\rho_A} \cdot \frac{\partial \rho_A}{\partial P_{d,m}^{ZG}} + \frac{F_D^{XB}}{C_D} \cdot \frac{\partial C_D}{\partial M_m} \cdot \frac{\partial M_m}{\partial P_{d,m}^{ZG}}$$

Equation 6.4-4

The drag coefficient variation with Mach number and incidence is determined using central differences with ($\Delta M_m := 0.05$; $\Delta\sigma_m := 0.5°$). The drag variation with speed,

$$\frac{\partial F_D^{XB}}{\partial \underline{\dot{P}}_{d,m}^G} := \frac{2 \cdot F_D^{XB} \cdot \underline{\dot{P}}_{d,m}^G}{\left(\dot{P}_{d,m}\right)^2} + \frac{F_D^{XB}}{C_D} \cdot \left(\frac{\partial C_D}{\partial \xi_B^{MV}} \cdot \frac{\partial \xi_B^{MV}}{\partial \underline{\dot{P}}_{d,m}^G} + \frac{\partial C_D}{\partial M_m} \cdot \frac{\partial M_m}{\partial \underline{\dot{P}}_{d,m}^G} \right)$$

Equation 6.4-5

The drag variation with missile body orientation with respect to LGA,

$$\frac{\partial F_D^{XB}}{\partial Q_G^B} := \frac{F_D^{XB}}{C_D} \cdot \frac{\partial C_D}{\partial \xi_B^{MV}} \cdot \frac{\partial \xi_B^{MV}}{\partial Q_G^B}$$

Equation 6.4-6

The missile body incidence variation with velocity and orientation are defined in §16,16. The remaining gradients are defined in §19.3.

6.5 Missile Guidance - Proportional Navigation

6.5.1 Historical Perspective

The first published assessments of Pure Proportional Navigation (PPN) and True Proportional Navigation (TPN) apply linear analysis to the relative missile and target motion in the plane containing their constant velocity vectors. The solution of the highly non-linear PN equations has been a fruitful area of research and one that has taken time even for the simplest cases involving non-manoeuvring targets. The constant speed limitation of these initial analyses has gradually been eroded. Generalised of TPN and PPN laws have to a great extent seen a unification in the analysis however, the purely analytical approach has largely been superseded by optimal LQR techniques as more flexibility has been added. This review charts the evolution of PN guidance laws.

Table 6-1 : B-Spline Coefficients and Knots for the Missile Drag Coefficient

$$\lambda_i = \left\{ (0.0)_{1x4}, (0.5)_{1x3}, (0.7)_{1x3}, (1.0)_{1x3}, (4.0)_{1x4} \right\} \text{ : missile speed}$$

$$\mu_j = \left\{ (0.0)_{1x4}, (8.0°)_{1x2}, (16.0°)_{1x2}, (24.0°)_{1x4} \right\} \text{ : missile total incidence}$$

CD_{ij}	COAST	BOOST	CD_{ij}	COAST	BOOST
C(1,1)	0.3493319	0.2993031	C(4,5)	0.8409478	0.8049040
C(1,2)	0.3803946	0.3148281	C(4,6)	1.2111871	1.1439404
C(1,3)	0.3452788	0.3138402	C(4,7)	1.3898173	1.3352739
C(1,4)	0.6622032	0.5781340	C(4,8)	1.5801607	1.5049016
C(1,5)	0.8109929	0.7893868	C(5,1)	0.3505760	0.3017886
C(1,6)	1.1680494	1.1117658	C(5,2)	0.3419176	0.3148543
C(1,7)	1.3330413	1.2874194	C(5,3)	0.4104381	0.3112649
C(1,8)	1.5102555	1.4548981	C(5,4)	0.6495311	0.5846278
C(2,1)	0.3515963	0.2990082	C(5,5)	0.8445568	0.8141522
C(2,2)	0.3144293	0.3169243	C(5,6)	1.2237409	1.1605085
C(2,3)	0.4583260	0.3109562	C(5,7)	1.3993285	1.3571013
C(2,4)	0.5930083	0.5824756	C(5,8)	1.5952919	1.5217631
C(2,5)	0.8719022	0.7891385	C(6,1)	0.3505762	0.3017887
C(2,6)	1.1960613	1.1130887	C(6,2)	0.3419177	0.3148545
C(2,7)	1.3293432	1.2877475	C(6,3)	0.4104383	0.3112650
C(2,8)	1.5322301	1.4624298	C(6,4)	0.6495315	0.5846281
C(3,1)	0.3499098	0.2994020	C(6,5)	0.8445572	0.8141526
C(3,2)	0.3545203	0.3139365	C(6,6)	1.2237415	1.1605090
C(3,3)	0.3921494	0.3150202	C(6,7)	1.3993292	1.3571019
C(3,4)	0.6509853	0.5757280	C(6,8)	1.5952927	1.5217638
C(3,5)	0.8287587	0.7776473	C(7,1)	0.3501669	0.3067943
C(3,6|)	1.1894513	1.1279875	C(7,2)	0.3429002	0.3282534
C(3,7)	1.3818884	1.3024914	C(7,3)	0.4083936	0.3113138
C(3,8)	1.5521059	1.4769744	C(7,4)	0.6535436	0.6007590
C(4,1)	0.3503882	0.2992947	C(7,5)	0.8500621	0.8303082

CD_{ij}	COAST	BOOST	CD_{ij}	COAST	BOOST
C(4,2)	0.3450481	0.3141154	C(7,6)	1.2307945	1.1908471
C(4,3)	0.4057690	0.3148246	C(7,7)	1.4112756	1.3702513
C(4,4)	0.6486367	0.5766013	C(7,8)	1.6092790	1.5548982
C(8,1)	0.3665307	0.3432541	C(11,1)	0.4361215	0.3388517
C(8,2)	0.3876912	0.3663601	C(11,2)	0.4235852	0.3546896
C(8,3)	0.4030535	0.3915456	C(11,3)	0.4801090	0.4118567
C(8,4)	0.7263453	0.6159778	C(11,4)	0.6271094	0.5434391
C(8,5)	0.8562316	0.9121163	C(11,5)	0.5765324	0.2478791
C(8,6)	1.2992203	1.2784501	C(11,6)	0.2961194	0.3363746
C(8,7)	1.4605259	1.4624824	C(11,7)	0.2474240	-0.092658
C(8,8)	1.7114659	1.6659403	C(11,8)	0.1102814	0.3153458
C(9,1)	0.3572556	0.2788731	C(12,1)	0.2458852	0.5297111
C(9,2)	0.3221679	0.3013441	C(12,2)	0.5254034	0.2717340
C(9,3)	0.4048265	0.2319838	C(12,3)	0.2673452	0.2778131
C(9,4)	0.5978424	0.6469096	C(12,4)	0.4478306	0.4602618
C(9,5)	0.8818750	0.7377599	C(12,5)	0.7491863	1.0491641
C(9,6)	1.1720692	1.2110945	C(12,6)	1.3552679	1.2566758
C(9,7)	1.4342550	1.2114361	C(12,7)	1.6186871	1.9265216
C(9,8)	1.5434015	0.6466226	C(12,8)	1.8760698	1.8343645
C(10,1)	0.5502187	0.4502025	C(13,1)	0.2624769	0.2331812
C(10,2)	0.5900929	0.4871346	C(13,2)	0.2713403	0.2096069
C(10,3)	0.5880890	0.4876289	C(13,3)	0.2693834	0.2711502
C(10,4)	0.8594553	0.7547665	C(13,4)	0.3802224	0.3154113
C(10,5)	1.1151054	1.0271546	C(13,5)	0.7931723	0.5202080
C(10,6|)	1.5696261	1.5059226	C(13,6)	1.3573832	1.4715539
C(10,7)	1.7945591	1.7340382	C(13,7)	1.6710414	1.5371520
C(10,8)	2.0264321	1.8836958	C(13,8)	1.9612307	1.7283003

Whilst reviewing the literature it was surprising how readily the practical application of PN is sacrificed to allow mathematical tractability. Several authors were moved to note that reported improvement in capture regions depends on underlying assumptions that often conflict with the requirements of the weapon system. Unrealistic target assumptions are frequently assumed, PPN targets with constant turn rates and TPN targets accelerating normal to the target LOS. As noted in §2 intelligent targets manoeuvre to counteract the oncoming missile leading to the application of 2-player game theory, Ghose[G.2].

Literature tends to deal only with idealised guidance laws. State observer performance is often ignored as realistic sensor errors often leading to noisy boundary conditions, indifferent target tracking performance during manoeuvres, and manoeuvre detection, Looze[L.2]. The real value of this work is to increase capture regions in limited regions using constrained optimal solutions for specific applications. The most significance enhancements are those supported by the provision of observer data, particularly for target LOS to missile body scaling to ensure that the missile delivers the required lateral acceleration.

6.5.1.1 2D True PN

The first closed form 2D analytical solution of the PN equation was attributed to Guelman[G.3] (1976). The equation was linearised with acceleration normal to the target LOS for constant velocity engagements. Shukla[S.2] (1988) expanded the range of the engagement geometries for practical applications by relaxing the linearisation conditions applied by Guelman. Yang[Y.1] (1987) and Ghose[G.2&4] (1994) showed that the capture region of Generalised TPN (GTPN) reduced when applying acceleration at constant bias angles with respect to the target LOS, angles between the missile acceleration vector and the target LOS for constant closing speeds.

In a review of TPN, GTPN and PPN, Shukla[S.1] (1990) cast doubt on the larger capture regions being quoted for GTPN as they were obtained at the expense of high LOS rates, control effort and unacceptable trajectories. In the early 90's Cochran[C.1&2], Yuan[Y.2-4] and Dhar[D.1] varied the closing speed whilst applying acceleration normal to the target LOS in Realistic TPN (RTPN) laws against non-manoeuvring targets. In most cases the capture region expanded and intercept times were reduced. The acceleration direction constraint was removed by Rao[R.5] (1993) with similar results. Chakravarthy[C.3] (1996) provided a generalised solution of the PN equations without linearisation in which closing speed and applied acceleration angle were varied in what is referred to as Realistic GTPN (RGTPN).

6.5.1.2 3D True PN

3D PN development mirrors that of 2D GTPN laws. Constrained planar solutions to 3D PN motion appeared as early as 1956, Adler[A.2]. Guelman, Cochran (1990) and Yang[Y.5] (1996) provide systematic solutions to

generalised RTPN without resorting to linearisation, initial conditions for capturing manoeuvring targets, PN performance metrics and 2-player game theory are all introduced. TPN generalisation in which all PN parameters are adaptable has reached the stage that the capture region using finite accelerations is comparable with that of PPN, Duflos[D.2] (1999). This unification forms the basis many of the optimal LQR techniques used today, linking the capture region with practical constraints.

6.5.1.3 2D Pure PN

Closed form PPN solutions have proven more elusive. Guelman[G.5] (1971) provided a solution for a limited range of kinematic gain (λ_m) against constant turning targets. This work provides the capture requirements for firing solutions: $V_m > \sqrt{2} \, . \, V_t$ and $\lambda_m \, . \, V_m > V_m + V_t$, where ($V_m$) is the missile speed, and (V_t) the target speed - all targets being reachable if the missile is closing. These conditions can be relaxed to $V_m > V_t$ for constant speed targets. The target LOS angular rate decreases with time-to-go (TTG) providing that $(\lambda_m/2 - 1) \, . \, V_m > V_t$, with ($\lambda_m \geq 4$).

These results were generalised by Becker[B.1] (1990) for constant velocity targets and gains > 2. Further extensions were provided by Guelman[G.6] for manoeuvring targets, and by Shukla[S.1] and Ha[H.2] in (1990) who introduced the Lyapunov function approach to deal with random target motion. Mahapatra[M.1] (1989) dealt with linearised PPN for a constant target acceleration and initial heading errors, and Ha[H.2] for randomly moving targets.

The 90s was a period during which the sufficiency conditions for PPN target capture were expanded for targets with time varying accelerations, notable contributors being Ha[H.2], Song[S.3] and Ghawghawe[G.7] (1990-96).

6.5.1.4 3D Pure PN

When a state observer provides sufficient data 3D PPN is the most efficient and practical of the PN guidance laws. No longitudinal speed control is required and the significant speed advantage required for TPN can be relaxed for PPN.

Adler[A.2] was first to linearised the 3D equations of PPN assuming a constant velocity collision course. Later Guelman[G.8-9] (1972-4) showed that for ($\lambda_M > 2$) PPN requires only a $\sqrt{2}$ speed advantage over the target, with all but the rear LOS reachable.

Ha[H.2] (1990) and Song[S.7] (1994) extended the 2D Lyapunov approach with non-linear system dynamics to show that targets with time varying acceleration normal to their velocity vector can always be intercepted under Guelman's conditions. The increased capture region of PPN compared with TPN against targets with varying acceleration was explained by Oh[O.1] (1999). The Lyapunov function approach was criticised by Ghawghawe[G.7]

(1996) for being too restrictive in the allowable initial conditions to ensure capture, giving this as the reason for reduced capture regions rather than target dynamics.

6.5.1.5 Optimal PN

The development of guidance laws using classical methods has gradually been replaced by optimal techniques with Performance Indices (PI) able to cope with non-linear stochastic systems, Vergez[V.1]. Originally, such laws were derived for linear systems subject to Gaussian disturbances and quadratic PI. The resulting Linear Quadratic Regulator (LQR) problem is one of finding a control vector ($\underline{U}$) that minimises the PI denoted by $J(\underline{U})$:

$$\dot{\underline{X}}(t) := [A]\cdot\underline{X}(t) + [B]\cdot\underline{U}(t)$$

Equation 6.5-1

$$J(U) :=$$

$$\underline{X}^T(t_F)\cdot[G]\cdot\underline{X}(t_F) + \int_t^{t_F}\left(\underline{X}^T\cdot[W]\cdot\underline{X} + \underline{U}^T(t)\cdot[R]\cdot\underline{U}^T(t)\right)dt$$

Equation 6.5-2

The PI comprises terms defined by the system state ($\underline{X}$) and controls ($\underline{U}$) during flight, and at the impact time (t_F). The weighting between them determined by [G], [W] and [R]. The steady-state solution is obtained from the Riccati equation:

$$\dot{P} + P^T\cdot[A] + [A]^T\cdot P - P\cdot[B]\cdot R^{-1}\cdot[B]^T\cdot P^T + [W] := 0$$

Equation 6.5-3

Resulting in the optimal control sequence,

$$\breve{\underline{U}}(t) := -[R]^{-1}\cdot[B]^T\cdot P(t)\cdot\underline{X}^T$$

Equation 6.5-4

Thus the constrained Bolza problem from variational calculus can be solved explicitly to obtain closed loop optimal guidance laws, Rusnack[R.1-4]. The solution involves the state at the integration limits and as such is referred to as a Two Point Boundary Value Problem (TPBVP). The Bolza form is a combination of the Mayer problem, dealing with the terminal cost, and the Lagrangian problem dealing with the cumulative effect of the state and controls. Mayer problems generate control sequences that bring the state of the plant to a desired condition at impact, the optimal control sequence reducing the PI to zero. Whilst ideal for miss distance, impact speed and aspect, and minimal flight times, they disregard the "cost" associated with

excessive control effort, missile incidence and hence drag, range and impact velocity.

Optimal PN solutions started to appear in the late 60s, early 70s, notable early contributors being Axelbrand, Cottrell, Kreider and Asher, and recently Yang[Y.8] (1988) and Guelman[G.10] (1995). Yang[Y.6&7] showed that minimising energy tends to TPN whilst minimising TTG tends to PPN, unification being simply a balance of PI weighting. These optimal approaches treat each type of PN as special case of applied acceleration direction with respect to the target LOS. Vathasal[V.2] (1995) demonstrating that RGTPN and Biased TPN (BTPN) solutions can be derived using optimal theory. Optimising the target acceleration bias angle whilst minimising control effort and LOS deflection have a strong influence on the kinematic gain, Shukla[S.4] (1989) and Yuan [Y.4] (1997).

A review of classical produced and optimised guidance was undertaken by Pastrick[P.2] (1980). Practical implementation of optimal guidance laws was provided by Nesline[N.2] (1981) compared with laws derived using classical techniques. Optimal minimisation of miss distance and control effort results in a kinematic gain of 3, Pfleghaar[P.3]. Increased gains from $\lambda_m := 1.5 + \frac{1}{2}\sqrt{(4\gamma + 9)}$ are obtained when minimising control effort and constant sight-line rate to intercept, where (γ) is the normalised control effort weight, Hutt[H.1]. Kim[K.1] (1985) using the Lyapunov approach to minimise miss-distance, impact angle and control effort, resulting in a near collision course with a gain of 4, the lowest gain for capturing a manoeuvring target, Green[G.11].

An interesting class of optimal guidance laws is based on predicted intercept point, establishing a collision course by minimising time-to-go and energy consumption, Kim[K.1]. Bang-bang controls are generated by minimising TTG alone, followed by no control action once the course is set.

Price[P.4] shows improved performance when the autopilot is taken into account and that the optimum kinematic gain for a manoeuvring target is again 4. Rusnack[R.7] and Nesline[N.2] show that PN guidance is sensitive to errors in the TTG estimate however, many of the algorithms presented in literature assume that this is known, or can be accurately estimated. Ben-Asher[B.2] desensitised PN guidance laws by treating them as an optimal rendezvous problem. Iterative TTG estimates are provided by Lee[L.3] (1985) and Hull[H.5] (1991), algorithms requiring a good initial estimate such as that provided by Riggs[R.8].

The sophistication of modern targets is recognised in the development of guidance laws based on game theory. A comparison of optimal and pursuit-evasion differential games is provided by Shinar[S.5]. Realistic differential games applied to missile guidance usually result in complex optimisation problems solved by numerical means. Solutions are invariably obtained off-line techniques such as Differential Dynamic Programming, Jarmark[J.1].

6.5.1.6 Stability and Observability

The analytical stability of PN is considered by Rew[R.6]. Song[S.6-7] modified the PN law by oscillating the target LOS to make the system more observable and effective for mid-course guidance. Hull[H.4] optimised both control effort and information content, convergence of the shooting technique solution requiring a gradual transfer of weight from control effort to observability.

6.5.2 Conventional PN Guidance Laws

For constant closing speed engagements in which the missile has a speed and lateral acceleration advantage over the target, PN laws have proven to be remarkably robust. Enhancement of the basic PN concept is introduced, reducing the target LOS rate to zero whilst compensating for,

- Short range engagements dominated by the missile boost phase
- Accelerating targets using sophisticated avoidance manoeuvres
- High altitude engagements with increasing missile incident lag

Essentially the PN guidance demands decompose into four terms:

- The basic demand required to reduce the target LOS rate to zero
- Compensate for the uncontrolled missile longitudinal acceleration
- Augmentation to account for quasi-constant target acceleration
- Compensation for gravitational acceleration

Combining these terms, and expressed them in the Missile Body frame so that the autopilot can be closed around the body referenced accelerometer output,

$$ {}_{PN}\underline{\alpha}_{D}^{B} \equiv \left({}_{PN}\alpha_{D}^{YB} \;,\; {}_{PN}\alpha_{D}^{ZB} \right)^{T} := {}_{PN}\underline{\alpha}_{SL}^{B} + {}_{PN}\underline{\alpha}_{MA}^{B} + {}_{PN}\underline{\alpha}_{TA}^{B} + \underline{\alpha}_{GA}^{B} $$

Equation 6.5-5

Acceleration normal to the LOS is determined in different reference frames depending on the form of PN. To generate the equivalent acceleration in the Missile Body frame requires the inverse scaling,

$$ \underline{\ddot{P}}_{o,m}^{B} \equiv \left(\ddot{P}_{o,m}^{YB} \;,\; \ddot{P}_{o,m}^{ZB} \right)^{T} := \left(T_{B}^{F} \right)^{T} \cdot \underline{\ddot{P}}_{o,m}^{F} $$

Equation 6.5-6

$$\underline{\ddot{P}}^{B}_{o,m} := \begin{pmatrix} T^{F}_{B}(5) & , & T^{F}_{B}(8) \\ T^{F}_{B}(6) & , & T^{F}_{B}(9) \end{pmatrix}^{-1} \cdot \begin{pmatrix} \ddot{P}^{YF}_{o,m} \\ \ddot{P}^{ZF}_{o,m} \end{pmatrix}$$

Equation 6.5-7

From the orthogonal properties of transformation matrices,

$$\forall i \in [1(1)3] : T^{S}_{B}(1,i) := T^{S}_{B}(2,i) \times T^{S}_{B}(3,i)$$

Equation 6.5-8

$$T^{S}_{B}(1) := T^{S}_{B}(5) \cdot T^{S}_{B}(9) - T^{S}_{B}(6) \cdot T^{S}_{B}(8)$$

Equation 6.5-9

$$T^{S}_{B}(4) := T^{S}_{B}(8) \cdot T^{S}_{B}(3) - T^{S}_{B}(9) \cdot T^{S}_{B}(2)$$

Equation 6.5-10

$$T^{S}_{B}(7) := T^{S}_{B}(2) \cdot T^{S}_{B}(6) - T^{S}_{B}(3) \cdot T^{S}_{B}(5)$$

Equation 6.5-11

Hence,

$$\begin{pmatrix} \ddot{P}^{YB}_{o,m} \\ \ddot{P}^{ZB}_{o,m} \end{pmatrix} := \frac{1}{T^{F}_{B}(1)} \cdot \begin{pmatrix} T^{F}_{B}(9) & , & -T^{F}_{B}(8) \\ -T^{F}_{B}(6) & , & T^{F}_{B}(5) \end{pmatrix} \cdot \begin{pmatrix} \ddot{P}^{YF}_{o,m} \\ \ddot{P}^{ZF}_{o,m} \end{pmatrix}$$

Equation 6.5-12

6.5.2.1 Basic PN Sight-Line Rate Demand

The basic sight-line PN lateral acceleration demands, normalised by velocity (V_N), reduce the inertial angular rotation of the target LOS to zero,

$${}_{PN}\underline{\alpha}_{SL} := \lambda_m \cdot V_N \cdot \begin{pmatrix} \omega^{ZS}_{A,S} & , & -\omega^{YS}_{A,S} \end{pmatrix}^{T}$$

Equation 6.5-13

For,

- Constant target and missile closing speed
- Non-manoeuvring target
- Missile incidence and lag free guidance
- Perfect missile autopilot

the basic PN demand is optimal and no further control effort is required once a collision course is established. The difference between normalised and traditional PN is in the velocity scaling. Normalised PN is scaled using the closing speed whilst traditional PN is scaled by missile speed. The acceleration demand is applied normal to the missile-target LOS for True PN, and normal to the missile velocity vector for PPN. The four variants in the basic PN demand are therefore,

Normalised - True PN

$$ {}_{PN}\underline{\alpha}^{S}_{SL} \;\coloneqq\; \lambda_m \cdot \dot{P}^{XS}_{m,t} \cdot \left(\; \omega^{ZS}_{A,S} \quad , \quad -\omega^{YS}_{A,S} \; \right)^T $$

Equation 6.5-14

Traditional - True PN

$$ {}_{PN}\underline{\alpha}^{S}_{SL} \;\coloneqq\; \lambda_m \cdot \dot{P}^{XMV}_{o,m} \cdot \left(\; -\omega^{ZS}_{A,S} \quad , \quad \omega^{YS}_{A,S} \; \right)^T $$

Equation 6.5-15

Normalised - Pure PN

$$ {}_{PN}\underline{\alpha}^{MV}_{SL} \;\coloneqq\; \lambda_m \cdot \dot{P}^{XS}_{m,t} \cdot \left(\; \omega^{ZS}_{A,S} \quad , \quad -\omega^{YS}_{A,S} \; \right)^T $$

Equation 6.5-16

Traditional - Pure PN

$$ {}_{PN}\underline{\alpha}^{MV}_{SL} \;\coloneqq\; \lambda_m \cdot \dot{P}^{XMV}_{o,m} \cdot \left(\; -\omega^{ZS}_{A,S} \quad , \quad \omega^{YS}_{A,S} \; \right)^T $$

Equation 6.5-17

Although the speed advantage required for Traditional PN can be relaxed for Normalised PN, the later is prone to acceleration limiting and incidence drag induced speed loss. Although Shukla[S.1] showed that PPN is superior to TPN, PPN is rarely used as it requires missile incidence as well as seeker data. In its basic form TPN requires only seeker data, and ideally a measurement of closing speed. The closing speed and LOS rate are obtained directly from the missile observer states,

$$ P_{m,t} \cdot \dot{P}^{XS}_{t} \;\coloneqq\; -\underline{P}^{A}_{m,t} \bullet \underline{\dot{P}}^{A}_{m,t} $$

Equation 6.5-18

$$ P^2_{m,t} \cdot T^B_S \cdot \underline{\omega}^{S}_{A,S} \;\coloneqq\; \left(\; T^B_A \cdot \underline{P}^{A}_{m,t} \; \right) \times \left(\; T^B_A \cdot \underline{\dot{P}}^{A}_{m,t} \; \right) $$

Equation 6.5-19

Expanding the Normalised TPN demand in terms of polar dynamics,

$$ {}_{PN}\underline{\alpha}^{B}_{SL} := \frac{\lambda_m \cdot \dot{P}^{XS}_{o,m}}{T^S_B(1)} \cdot \begin{pmatrix} T^S_B(9) & , & -T^S_B(8) \\ -T^S_B(6) & , & T^S_B(5) \end{pmatrix} \cdot \begin{pmatrix} \dot{\Psi}^S_A \cdot \cos\Theta^S_A \\ -\dot{\Theta}^S_A \end{pmatrix} $$

Equation 6.5-20

For a seeker with an inner pitch, and an outer yaw gimbal, the elemental Euler rotational matrices defined in §16.1 combine to give,

$$ T^S_B := \left[\Theta^S_B\right] \cdot \left[\Psi^S_B\right] $$

Equation 6.5-21

In terms of the direction cosines from Missile Body to Seeker LOS axes,

$$ {}_{PN}\underline{\alpha}^{B}_{SL} := \lambda_m \cdot \dot{P}^{XS}_t \cdot \begin{pmatrix} \dot{\Psi}^S_A \cdot \cos\Theta^S_A \cdot \sec\Psi^S_B \\ -\dot{\Psi}^S_A \cdot \cos\Theta^S_A \cdot \tan\Theta^S_B \cdot \tan\Psi^S_B - \dot{\Theta}^S_A \cdot \sec\Theta^S_B \end{pmatrix} $$

Equation 6.5-22

6.5.2.2 Missile Acceleration Augmented PN Guidance

Modifying TPN to account for the missile longitudinal acceleration results in Ideal TPN (ITPN) and is important during the boost phase of larger missiles engaging short-range targets. Inserting the relevant direction cosines for a seeker with an inner pitch and outer yaw gimbal into this component of the PN guidance command,

$$ {}_{PN}\underline{\alpha}^{B}_{MA} := -\frac{\ddot{P}^{XB}_{o,m}}{T^S_B(1)} \cdot \begin{pmatrix} T^S_B(9) & , & -T^S_B(8) \\ -T^S_B(6) & , & T^S_B(5) \end{pmatrix} \cdot \begin{pmatrix} T^S_B(2) \\ T^S_B(3) \end{pmatrix} $$

Equation 6.5-23

Expanding, and using the results of §6.5.2,

$$ {}_{PN}\underline{\alpha}^{B}_{MA} := -\frac{\ddot{P}^{XB}_{o,m}}{T^S_B(1)} \cdot \left(T^S_B(4) \quad , \quad T^S_B(7) \right)^T $$

Equation 6.5-24

$$ {}_{PN}\underline{\alpha}^{B}_{MA} := \ddot{P}^{XB}_{o,m} \cdot \left(-\tan\Psi^S_B \quad , \quad \tan\Theta^S_B \cdot \sec\Psi^S_B \right)^T $$

Equation 6.5-25

6.5.2.3 Target Acceleration Augmented PN Guidance

Compensating for constant target acceleration normal to the LOS results in Augmented TPN (ATPN) with the PN guidance command component,

$$ {}^{PN}\underline{\alpha}_{TA}^{B} := \frac{1}{2 \cdot T_B^S(1)} \cdot \begin{pmatrix} T_B^S(9) & , & -T_B^S(8) \\ -T_B^S(6) & , & T_B^S(5) \end{pmatrix} \cdot \begin{pmatrix} \ddot{P}_{o,t}^{YB} \\ \ddot{P}_{o,t}^{ZB} \end{pmatrix} $$

Equation 6.5-26

If target acceleration estimates are unavailable ATPN can be replaced by Target Biased TPN using apriori estimates of maximum target acceleration during avoidance manoeuvres. A target manoeuvre estimator is required to determine target direction with respect to the missile-target LOS. When the target is manoeuvring a bias is applied in the direction of target motion with a gain from optimal analysis of 1.5.

$$ {}_{PN}\underline{\alpha}_{TA}^{B} := \frac{3}{2} \cdot \frac{MAX\,\ddot{P}_{o,t}}{\sqrt{2} \cdot T_B^S(1)} \cdot \begin{pmatrix} T_B^S(9) & , & -T_B^S(8) \\ -T_B^S(6) & & T_B^S(5) \end{pmatrix} \cdot \begin{pmatrix} sign\left(1, \dot{P}_{o,t}^{YS}\right) \\ sign\left(1, \dot{P}_{o,t}^{ZS}\right) \end{pmatrix} $$

Equation 6.5-27

A zero dead-band is needed to deal with target direction uncertainty.

6.5.2.4 Gravitational Acceleration Compensation

Gravitational acceleration compensation is important when using PN against low-level, long-range targets as the sight-line rate is small and height loss occurs close to the ground. The compensation is usually generated automatically by closing the autopilot around the accelerometer output (in straight and level flight the z-accelerometer outputs +1g) however, in the simulation it is added directly to the guidance demand,

$$ \underline{\alpha}_{GA}^{B} := -g_d \cdot \left(\frac{P_{r,d}}{P_{r,d} + P_m^{ZG}} \right)^2 \cdot \left(T_G^B(8) \quad , \quad T_G^B(9) \right)^T $$

Equation 6.5-28

6.5.3 Seeker Inertial Stabilisation

For staring array seekers it is important to divorce the detector from missile body motion in inertial space. Detector motion during the stare time smears IR energy returns over adjacent cells making it more difficult to isolate an object from the background intensity level. This reduces the acquisition

range, and increases the LOS angular error. Conceptually there are two gimbal arrangements: roll-pitch or yaw-pitch.

Roll-pitch configurations take less volume and are preferred for high off-boresight scenarios because the small roll inertia means their response time is shorter. Unfortunately for targets on boresight a singularity exists with sight-line rate errors increase to infinity which requires specialised gimbal steering algorithms in this region. In contrast yaw-pitch gimbals are larger, have higher inertia and hence a slower response time however, they do not magnify the sight-line rate error close to boresight. For both mechanisations hardware obscuration and imperfect radomes at high off-boresight angles placing further restrictions on optimal guidance solutions.

Consider the LOS rate error and its parasitic effect on the PN guidance law. Treating the Alignment frame as an inertial reference for convenience, the inertial LOS rates for a YP seeker,

$$\underline{\omega}^{S}_{A,S} \coloneqq$$

$$T^{S}_{B} \cdot \underline{\omega}^{B}_{A,B} + \underline{\omega}^{S}_{B,S} \coloneqq T^{S}_{B}\left(\Theta^{S}_{B}, \Psi^{S}_{B}\right) \cdot \underline{\omega}^{B}_{A,B} + \left[\Theta^{S}_{B}\right] \cdot \begin{pmatrix} 0 \\ 0 \\ \dot{\Psi}^{S}_{B} \end{pmatrix} + \begin{pmatrix} 0 \\ \dot{\Theta}^{S}_{B} \\ 0 \end{pmatrix}$$

Equation 6.5-29

Expanding, and collecting terms,

$$\dot{\Theta}^{S}_{A} \coloneqq \omega^{YS}_{A,S} + \omega^{XB}_{A,B} \cdot \sin \Psi^{S}_{B} - \omega^{YB}_{A,B} \cdot \cos \Psi^{S}_{B}$$

Equation 6.5-30

$$\dot{\Psi}^{S}_{A} \cdot \cos \Theta^{S}_{B} \coloneqq$$

$$\omega^{ZS}_{A,S} - \omega^{XB}_{A,B} \cdot \sin \Theta^{S}_{B} \cdot \cos \Psi^{S}_{B} - \omega^{YB}_{A,B} \cdot \sin \Theta^{S}_{B} \cdot \sin \Psi^{S}_{B} - \omega^{ZB}_{A,B} \cdot \cos \Theta^{S}_{B}$$

Equation 6.5-31

These equations show that detector stabilisation depends on the gyroscope errors leaking into the gimbal control loop. Combining these results with Equation 6.5-22 confirms that parasitic errors are not magnified in the YP gimbal configuration. Typically gimbal steering loops have bandwidths of 70-90 Hz and care must be taken to minimise parasitic coupling between the airframe and target sight-line dynamics, Nesline[N5-6]. In the past inertial isolation is performed using a dedicated rate sensors in the seeker. This complication, and expense, is removed using a centralised missile observer to fuse gimbal pick-off and gyroscope measurement data. Reduction in acquisition range due to parasitic errors often limits the missile observer bandwidth, a balance between measurement noise suppression and latency.

6.6 Missile Guidance - Command to Line-of-Sight

Although CLOS has received relatively little attention in public literature compared with PN, Roddy[R.10-12] et. al. (1985) published several papers on the control of Bank-to-Turn (BTT) missiles that provide a useful insight to CLOS guidance. Their work treats YP control as separate LQR problems using quadratic PI to minimise differential angle, aileron effort and roll rate induced cross-coupling. Conceptually, CLOS guidance commands consist of feed forward, feedback, Command Of LOS (COLOS) and gravitational acceleration components,

$$ {}_{CLOS}\underline{\alpha}_D \;:=\; \underline{\alpha}_{FB} + \underline{\varphi}_{FF} \otimes \underline{\alpha}_{FF} + \underline{\alpha}_{COLOS} + \underline{\alpha}_{GA} $$

Equation 6.6-1

The elemental parts to this expression perform the following functions:

- $\underline{\alpha}_{FB}$ minimises the angle between the missile LOS and the target LOS
- $\underline{\alpha}_{FF}$ compensates for target sight line dynamics
- $\underline{\alpha}_{COLOS}$ places the missile off the target LOS to aid optical tracking
- $\underline{\alpha}_{GA}$ compensates for gravity as described in §6.5.2.4

A feed-forward weighting ($\underline{\varphi}_{FF}$) was introduced by Lee[L.4] to compensate for the errors introduced using polar dynamics for non-manoeuvring targets. Combining these elemental parts, excluding the gravitational component common to both CLOS and PN,

$$ {}_{CLOS}\underline{\alpha}_D \;:=\; {}_{CLOS}\underline{\alpha}_S + \underline{\alpha}_G $$

Equation 6.6-2

To generate the required acceleration normal to the missile body the guidance demands are again scaled to take account of the body-to-beam angle. Applying the results of §6.5.2 when transforming from Target LOS to the Missile Body axes,

$$ {}_{CLOS}\underline{\alpha}_S^B \;:=\; \frac{1}{T_T^B(1)} \cdot \begin{bmatrix} T_T^B(5) & , & T_T^B(6) \\ T_T^B(8) & , & T_T^B(9) \end{bmatrix} \cdot {}_{CLOS}\underline{\alpha}_S^T $$

Equation 6.6-3

6.6.1 Guidance Loop Definition

In the idealised 2D CLOS guidance scheme shown in Figure 6-3 the target and missile dynamics are assumed to be identical at impact. The missile angular acceleration is doubly integrated and passed through a weave tuned $\alpha-\beta-\gamma$ filter $F_1(s)$ described in §21.4 providing smoothed target angular

offset with respect to an arbitrary frame. The feed forward acceleration comprises weave tuned $\alpha-\beta-\gamma$ filter derivatives $F_2(s)$ and $F_3(s)$.

6.6.2 Guidance Loop Stability

In Figure 6-4 the stability filter F(s), and its companion noise filter N(s), compensate for the destabilising effect of the double integrator I(s). The autopilot A(s), with a damping ratio of 0.5 and a bandwidth (ω_A) of 6 Hz, is assumed to be insensitive to dynamic pressure, speed and incidence variations. For steady-state analysis the delay D(s) was modelled using a 2nd order Tustin approximation equivalent to an update rate of 100 Hz. The missile dynamics M(s) are defined by the incidence lag (T_I).

The design criteria for the stability filter was a bandwidth (ω_G) of 2 Hz. The filter was designed using pole placement ignoring the missile dynamics, using pure double integration, and a 1st order Padé delay approximation,

$$s^2 \cdot G(s) := F(s) \cdot N(s) \cdot A(s) \cdot D(s)$$

Equation 6.6-4

The 5th order stability filter was reduced to 3rd order by gain and phase approximation and split into a phase advance element F(s), and a 1st order lag N(s) applied to both the feed back and feed forward demands.

$$F(s) \cdot N(s) := 13.6 \cdot \left(\frac{13.6 + 5.2605 \cdot s + 0.08770 \cdot s^2}{1 + 0.0427 \cdot s + 0.00144 \cdot s^2} \right) \cdot \left(\frac{63.4}{63.4 + s} \right)$$

Equation 6.6-5

The stability loop used for pole placement provides static margins of 8 dB and 45° shown in Figure 6-5, margins similar to those using the full stability loop at the steady-state condition:

- missile velocity (V_OM) := 550 m/s
- missile acceleration (A_OM) := -115 m/s^2
- impact range (P_OM) := 7800 m
- missile incidence lag (TI) := 0.25 s

Compare the pole placement results with the double phase advance filter proposed by Fox[F.1],

$$F(s) := 23 \cdot \left(\frac{\omega_A + 5.9276 \cdot s}{\omega_A + 1.8745 \cdot s} \right)^2$$

Equation 6.6-6

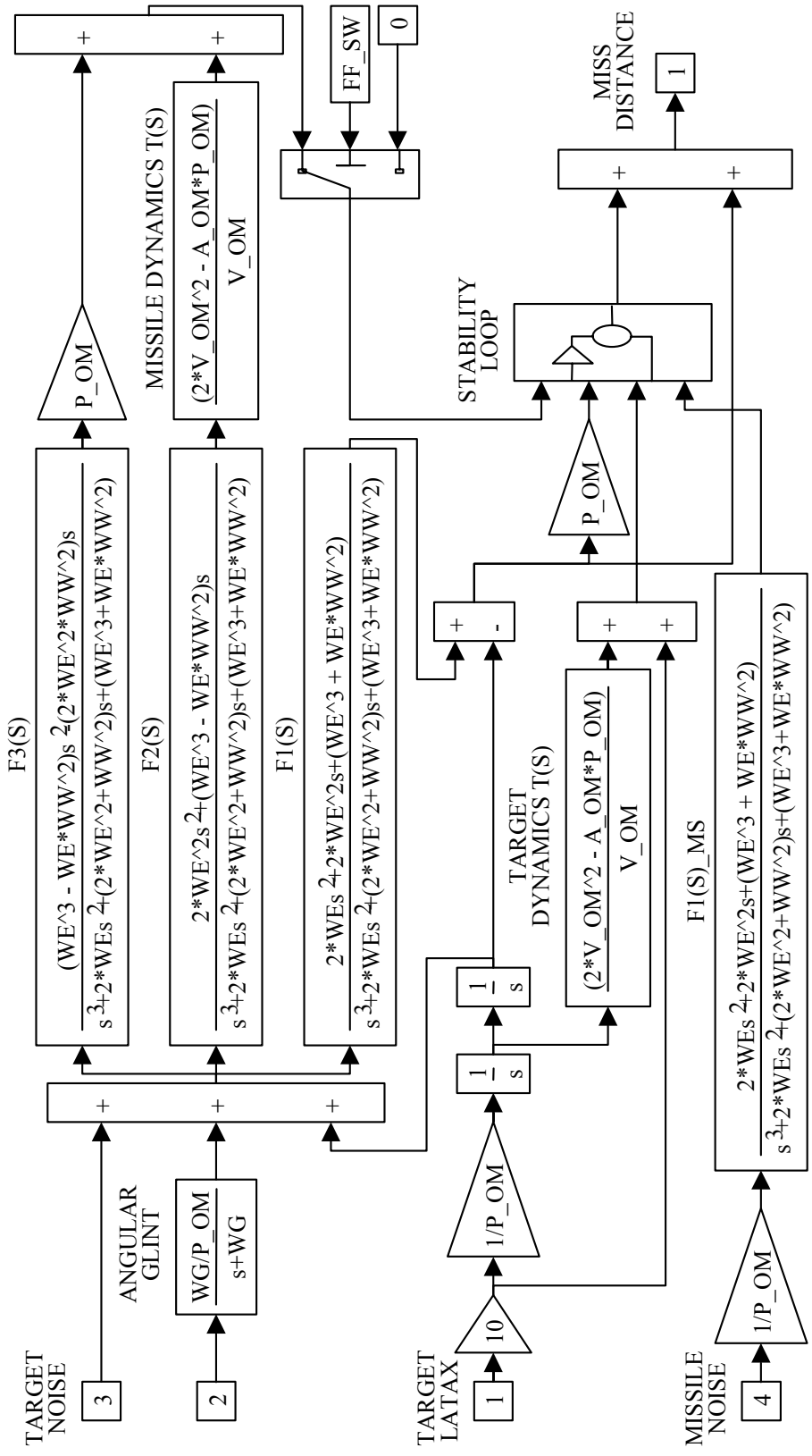

Figure 6-3 : Idealised 2D CLOS Simulation

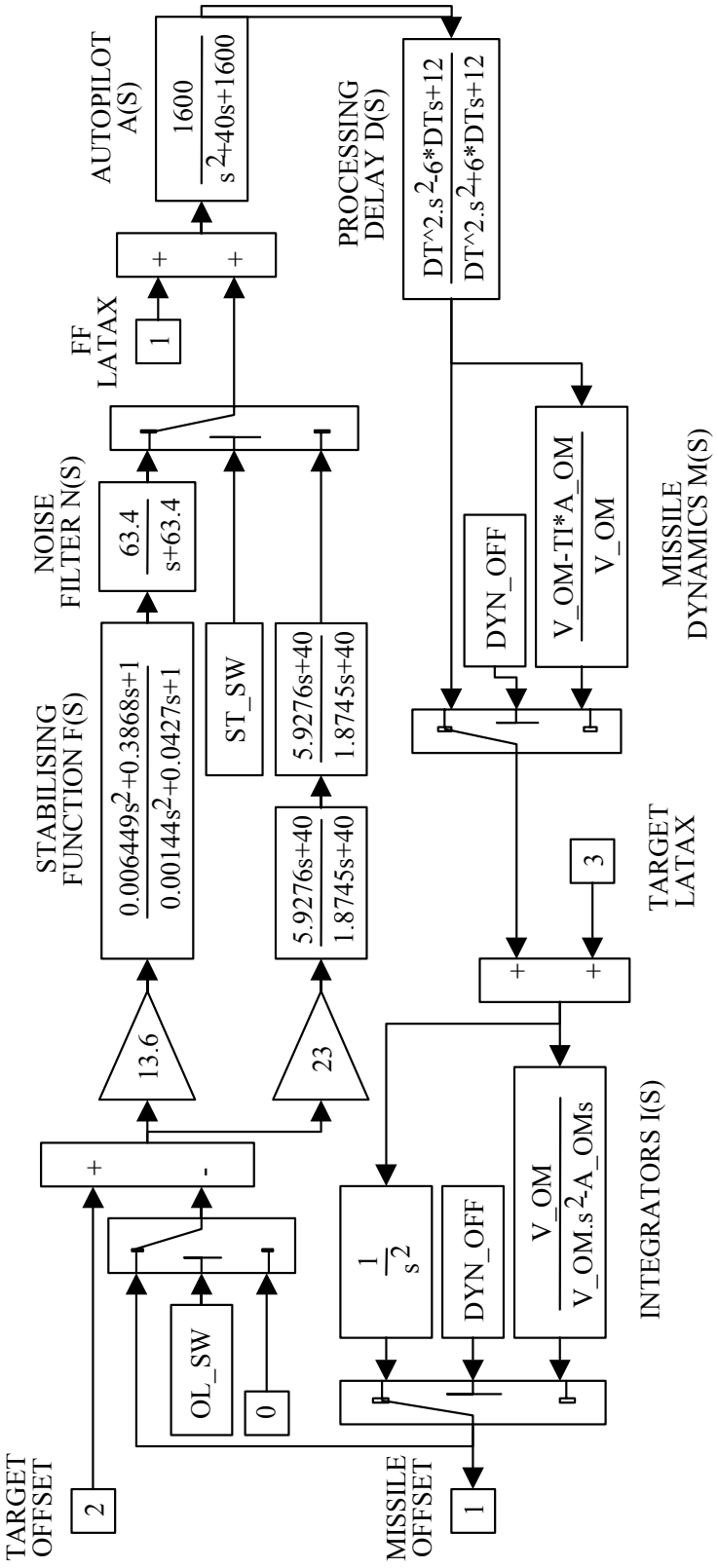

Figure 6-4 : Idealised CLOS Stability Loop

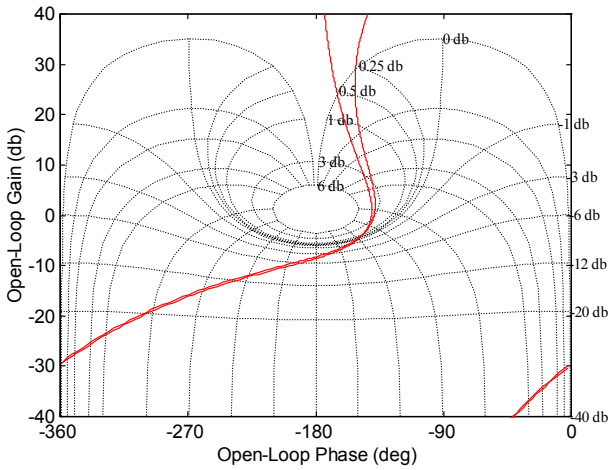

Figure 6-5 : Pole Placement Nichols Chart

Solid – Simplified loop ; Dashed – Full loop

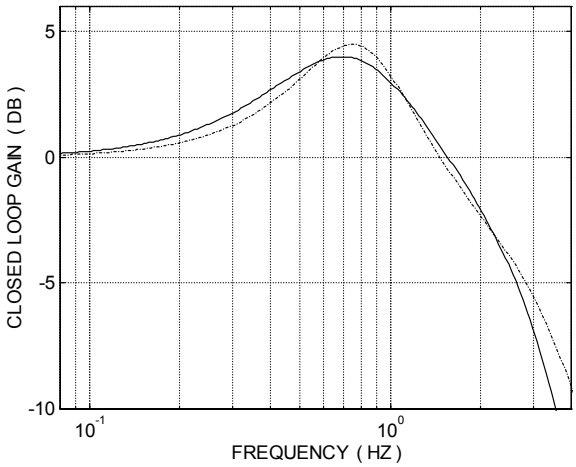

Figure 6-6 : Closed Loop Frequency Response

Solid – Pole Placement ; Dashed – Double Phase Advance

The double phase advance requires a beam stiffness (gain) of 23 $(m/s^2)/m$ compared with 13.6 $(m/s^2)/m$ to meet the 2 Hz closed loop bandwidth shown in Figure 6-6. Although it is a little more responsive at low frequencies it has a lower phase margin of 35°.

Fox also states that for good CLOS performance the tracking and autopilot bandwidths ($\omega_E := 3\omega_G$) and ($\omega_A := 8\omega_G$). In this example this equates to 1.8 Hz and 4.7 Hz, the guidance bandwidth (ω_G) being $\sqrt{13.6}$. When dealing with weaving targets (ω_G) must be considerably larger than weave frequency. However, as fin noise is sensitive to high (ω_G) and tracking accuracy is sacrificed which is why CLOS performance is often poor against weaving targets.

6.6.3 CLOS Feedback Demands for Stability

The noise suppressed feedback demands required for stability,

$$\underline{\alpha}_{FB}^{T} := \left({}_{FB}A_m^{YT} \quad , \quad -{}_{FB}A_m^{ZT} \right)^T$$

Equation 6.6-7

$${}_{FB}\underline{A}_m^T := P_m^{XT} \cdot \left(\frac{13.6 + 5.2605 \cdot s + 0.08770 \cdot s^2}{1 + 0.0427 \cdot s + 0.00144 \cdot s^2} \right) \cdot \begin{pmatrix} \Psi_T^M - \frac{{}_{COLOS}P_m^{YT}}{P_t^{XM}} \\ \Theta_T^M + \frac{{}_{COLOS}P_m^{ZT}}{P_t^{XM}} \end{pmatrix}$$

Equation 6.6-8

The differential angles are adjusted for the COLOS position offset. The notch filters are implemented as defined in §22.7.6.

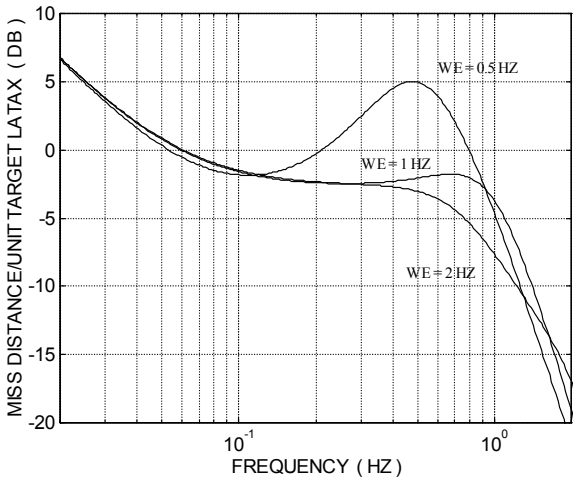

Figure 6-7 : CLOS with Feedback Demand Only

Consider the relationship between miss distance and target lateral acceleration using only feedback demands. Figure 6-7 shows the miss distance in (metres per target lateral acceleration "g" level). For a matching tracking bandwidth and target weave frequency of 0.5 Hz the miss distance is 0.18x the target acceleration in (m/s^2). The low frequency miss distance against slowly turning targets rises at an unacceptable 15 dB/decade.

6.6.4 CLOS Feed Forward Demands

The feed forward CLOS demand keeps the missile on the moving target LOS and removes the low frequency errors. The acceleration of a missile lying on the rotating target LOS,

$$\underline{A}_m^T := \underline{\ddot{P}}_m^T + \underline{\omega}_{A,T}^T \times \underline{\dot{P}}_m^T + \underline{\dot{\omega}}_{A,T}^T \times \underline{P}_m^T + \underline{\omega}_{A,T}^T \times \underline{\omega}_{A,T}^T \times \underline{P}_m^T$$

Equation 6.6-9

If the missile is constrained to fly along the target LOS, the roll angle of the Missile Velocity frame with respect to Alignment axes is set to zero,

$$\underline{\alpha}_{FF}^T := \left(- {}_{FF}A_m^{YT} \quad , \quad - {}_{FF}A_m^{ZT} \right)^T$$

Equation 6.6-10

$${}_{FF}A_m^{YT} := \left(2 \cdot \dot{\Psi}_A^T \cdot \dot{P}_m^{XT} + P_m^{XT} \cdot \ddot{\Psi}_A^T \right) \cdot \cos\Theta_A^T - 2 \cdot P_m^{XT} \cdot \dot{\Theta}_A^T \cdot \dot{\Psi}_A^T \cdot \sin\Theta_A^T$$

Equation 6.6-11

$${}_{FF}A_m^{ZT} := -2 \cdot \dot{P}_m^{XT} \cdot \dot{\Theta}_A^T - P_m^{XT} \cdot \left(\dot{\Psi}_A^T \right)^2 \cdot \sin\Theta_A^T \cdot \cos\Theta_A^T - P_m^{XT} \cdot \ddot{\Theta}_A^T$$

Equation 6.6-12

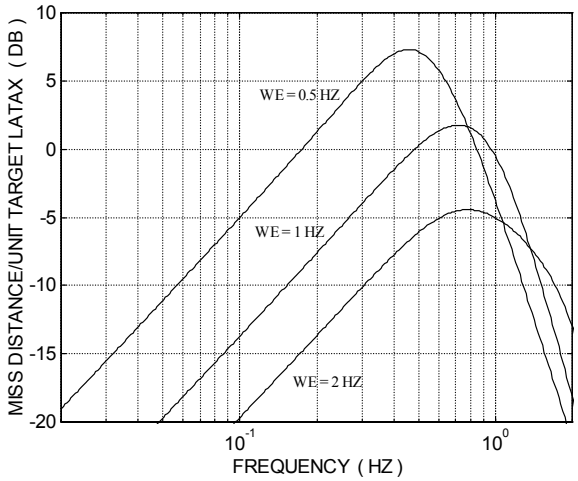

Figure 6-8 : CLOS with Feed-Forward Demand

Consider the performance when the feed-forward terms are added. Figure 6-8 shows that the miss distance against slowly turning targets is small at the expense of the miss distance at typical target weave frequencies. The miss distance for a tracking bandwidth of 0.5 Hz has increased from 0.18 m/(m/s^2) to 0.24 m/(m/s^2). This encapsulates the problem of dealing with non-manoeuvring and weaving targets using a simple tracking filter. Raising the tracking bandwidth to 2 Hz to accommodate weaving targets inevitably increases the fin flutter and fin rate noise, particularly using a phased array device as the angular measurement noise tends to be higher.

6.6.5 CLOS Feed Forward Demands with Weave Tuning

Consider the weave frequency estimation accuracy required from the IMM weave filter. Vorley[V.3] weave tuned the tracking filter to achieve acceptable miss distances without inducing unacceptable fin noise. Using a

tracking bandwidth of 0.5 Hz. Figure 6-9 shows that the miss distance drops from 0.24 m/(m/s^2) to 0.01 m/(m/s^2). The improvement obtained increases with decreasing weave frequency. Increasing the tracking bandwidth to 2 Hz reduces the miss distance by a further 10 dB.

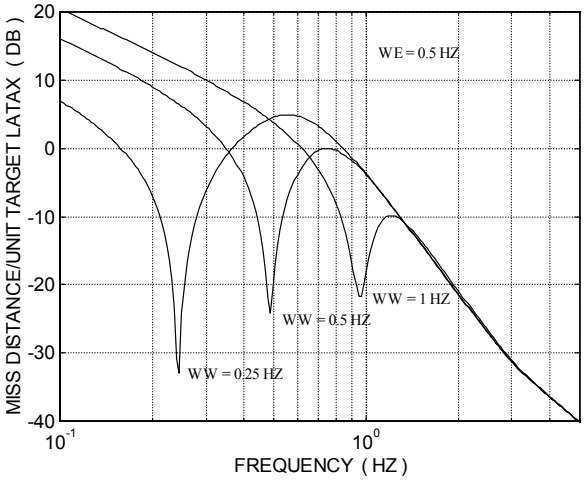

Tracking Bandwidth := 0.5 Hz

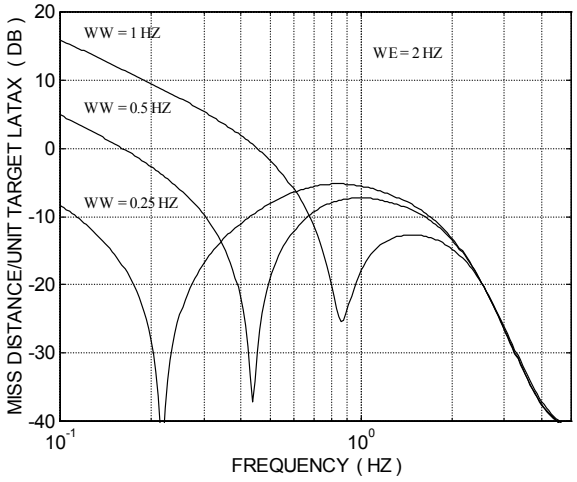

Tracking Bandwidth := 2 Hz

Figure 6-9 : CLOS Miss Distance with Weave Tuning

This performance requires accurate weave frequency estimates. A simple expression for the accuracy required to achieve a particular miss distance provided by Vorley[V.3] is,

$$\frac{\Delta\omega_W}{\omega_W} := \frac{\omega_W^2 \cdot \Delta P_t^{rT}}{\pi \cdot \ddot{P}_t^{rT}}$$

Equation 6.6-13

Typically, for a weave frequency of 0.25 Hz, target acceleration of 10 g, and a miss of 4 m the fractional error is 0.02. This analysis is only a guide to the

accuracy required since weave motion usually contains a spectrum of frequencies in the target observer space.

6.6.6 CLOS Demand Correction for Constant Velocity Targets

The feed-forward demands are based on polar dynamics that are ideal for slowly turning targets, but not for straight flying targets. An interesting piece of research by Lee[L.4] shows that improvement in CLOS performance is possible if the differential angles are corrected when the target is flying at a constant velocity. A 3D extension to Lee's 2D algorithm follows,

$$\underline{\varphi}_{FF}^{T} := \eta_{FF} \cdot \left(\varphi_{FF}^{YT} \quad , \quad \varphi_{FF}^{ZT} \right)^{T}$$

Equation 6.6-14

$$\varphi_{FF}^{ZT} := \frac{\sin\left(\Psi_A^{TV} - \varphi_\Psi \right)}{\sin\left(\Psi_A^{TV} - \Psi_A^{T} \right) \cdot \cos\left(\varphi_\Psi - \Psi_A^{T} \right)}$$

Equation 6.6-15

$$\left| \Psi_A^{TV} \right| \le \frac{\pi}{2} \Rightarrow \varphi_{FF}^{YT} := \frac{\sin\left(\Theta_A^{TV} + \varphi_\Theta \right)}{\sin\left(\Theta_A^{TV} + \Theta_A^{T} \right) \cdot \cos\left(\varphi_\Psi + \Theta_A^{T} \right)}$$

Equation 6.6-16

$$\left| \Psi_A^{TV} \right| > \frac{\pi}{2} \Rightarrow \varphi_{FF}^{YT} := \frac{\sin\left(-\Theta_A^{TV} + \varphi_\Theta \right)}{\sin\left(-\Theta_A^{TV} + \Theta_A^{T} \right) \cdot \cos\left(\varphi_\Psi + \Theta_A^{T} \right)}$$

Equation 6.6-17

$$\varphi_\Psi := \tan^{-1}\left(\frac{2 \cdot P_t^{XT} \cdot \sin \Psi_A^{T} - P_t^{XT}\left(t - \Delta t \right) \cdot \sin \Psi_A^{T}\left(t - \Delta t \right)}{2 \cdot P_t^{XT} \cdot \cos \Psi_A^{T} - P_t^{XT}\left(t - \Delta t \right) \cdot \cos \Psi_A^{T}\left(t - \Delta t \right)} \right)$$

Equation 6.6-18

$$\varphi_\Theta := -\tan^{-1}\left(\frac{2 \cdot P_t^{XT} \cdot \sin \Theta_A^{T} - P_t^{XT}\left(t - \Delta t \right) \cdot \sin \Theta_A^{T}\left(t - \Delta t \right)}{2 \cdot P_t^{XT} \cdot \cos \Theta_A^{T} - P_t^{XT}\left(t - \Delta t \right) \cdot \cos \Theta_A^{T}\left(t - \Delta t \right)} \right)$$

Equation 6.6-19

Implementation requires manoeuvre detection so that the algorithm can be phased-out for manoeuvring targets. This can be formulated directly from missile state observer data, or from the up-linked IMM filter probabilities. To avoid transients in the missile acceleration this algorithm is weighted by the probability associated with the IMM constant velocity filter,

$$\eta_{FF} := 2 \cdot \eta_{FF} \cdot {}_{UL}\mu_1 \Big|_0^1$$

Equation 6.6-20

Inherent in this expression is the assumption that a probability of 0.5 means a particular tracking mode is dominant, an assumption that needs exploration even though it is often encountered in literature.

6.6.7 Command Off LOS Feed Forward Demands

When using electro-optical target tracking sensors it is better if the missile plume does not obscure the target. To force the missile to fly a constant distance off the target LOS the guidance demands are augmented by,

$${}_{COLOS}\underline{\alpha}^T := \left(- {}_{COLOS}A_m^{YT} \quad , \quad - {}_{COLOS}A_m^{ZT} \right)^T$$

Equation 6.6-21

$${}_{COLOS}A_m^{YT} :=$$

$$- {}_{COLOS}P_m^{YT} \cdot \left(\dot{\Psi}_I^T \right)^2 + {}_{COLOS}P_m^{ZT} \cdot \left(\ddot{\Psi}_A^T + 2 \cdot \dot{\Psi}_A^T \cdot \dot{\Theta}_A^T \cdot \cos\Theta_A^T \right)$$

Equation 6.6-22

$${}_{COLOS}A_m^{ZT} :=$$

$$- {}_{COLOS}P_m^{YT} \cdot \ddot{\Psi}_A^T \cdot \sin\Theta_A^T - {}_{COLOS}P_m^{ZT} \cdot \left(\dot{\Theta}_A^T \right)^2 - \left(\dot{\Psi}_A^T \right)^2 \cdot \sin^2\Theta_A^T$$

Equation 6.6-23

If the missile seeker acquires the target in-flight the hand-over from mid-course CLOS guidance to terminal guidance needs to be smooth. This might be implemented by computing a PN demand from missile referenced CLOS parameters derived from ground radar and IMU measurements. Alternatively the COLOS off-boresight distance can be computed so that the CLOS and PN demands are the same, a topic that is outside the scope of this research.

6.6.8 Missile Longitudinal Acceleration Compensation Demand

CLOS demands assume that the uncontrolled longitudinal acceleration of the missile lies along the target LOS. This is rarely the case, and the following CLOS demand compensation is required,

$$\underline{\alpha}_{AXB}^T \equiv \left({}_{AXB}A_m^{YT} \quad , \quad {}_{AXB}A_m^{ZT} \right)^T$$

Equation 6.6-24

$$\underline{\alpha}_{AXB}^{T} := \ddot{P}_{o,m}^{XB} \cdot \left(\sin \Psi_T^B \quad , \quad -\sin \Theta_T^B \right)^T$$

Equation 6.6-25

6.7 Missile Autopilots

A Skid-to-turn (STT) or bank-to-turn (BTT) autopilot is selected by setting *BTT_SW* to 0 or 1 respectively. One of the main benefits of BBT is the reduction in hardware since the guidance requirements can be satisfied using one set of fins, and utilise the inner and therefore faster seeker inner gimbal.

6.7.1 STT Lateral Autopilot

Lateral autopilot demands are formed at launch, but are applied when the missile reaches a stable speed. The conventional pitch and yaw guidance demands are first delayed, lateral acceleration limited, and noise filtered,

$${}^{D}\underline{A}^{rB} := \underline{\varphi}_{DIL}\left(\underline{\varphi}_{TD}\left({}^{D}\underline{A}^{rB} \cdot \min\left(1, \varphi_L\right), \Delta t_A, \tau_{AD} \right), \frac{1}{\omega_N} \right)$$

Equation 6.7-1

By default a transport delay (τ_{AD}) of 2.5 msec is applied at the autopilot update rate (Δt_A) of 1/400 Hz. The noise filter is a 1st order lag implemented as defined in §22.7.1 with a bandwidth (ω_N) of 64 rad/s used in §6.6.2. Low speed acceleration demand limiting is applied up to Mach 1 to prevent excessive incidence, and thereafter an absolute limit (G_{MAX}) of 400 m/s^2.

$$\varphi_L := \frac{\alpha_L}{\sqrt{\left({}^{D}A^{YB}\right)^2 + \left({}^{D}A^{ZB}\right)^2}}$$

Equation 6.7-2

$$M_m < 1 \Rightarrow \alpha_L := G_{MAX} \cdot M_m$$

Equation 6.7-3

$$M_m \geq 1 \Rightarrow \alpha_L := G_{MAX}$$

Equation 6.7-4

6.7.2 BTT Lateral Autopilots

STT acceleration demands are combined to give the single BTT pitch plane demand about $\underline{Y}^R$,

$${}^{D}A^{ZR} := {}^{D}A^{rB} \cdot \operatorname{sign}\left(1, -{}^{D}A^{ZB}\right)$$

Equation 6.7-5

6.7.3 Roll Autopilot

For STT missiles the roll angle changes slowly and the effect of the low frequency roll autopilot can be ignored. Maintaining a zero roll demand results in a slowly changing Euler roll angle as the missile changes heading.

For BTT roll dictates the direction in which the lateral acceleration is applied so YP cross-coupling must be minimised using a fast roll autopilot. Figure 6-10 shows the main elements of a typical roll angle autopilot.

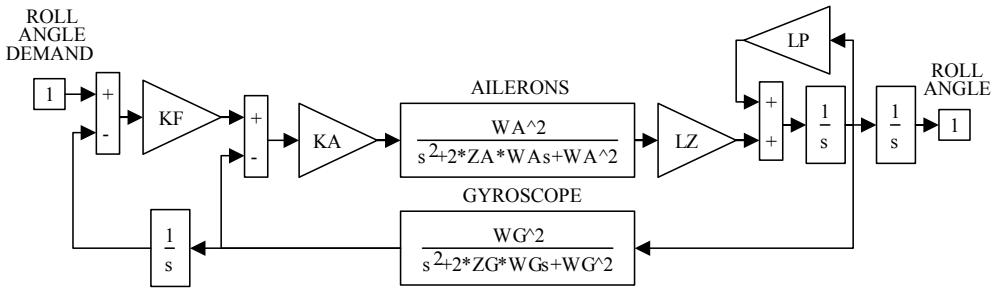

Figure 6-10 : Roll Angle Control and Dynamics

Although roll is prevented until the missile is clear of the tube the roll demand filtering is activated at launch so they can settle. As the missile clears the launcher, the fins are unlocked for roll control, and the missile $\underline{Z}^B$ axis is rotated into the fly-plane,

$$t \le t_L \quad \Rightarrow \quad {}^{D}\Phi_B^R := 0$$

Equation 6.7-6

$$t > t_L \quad \Rightarrow \quad {}^{D}\Phi_B^R := \varphi_{RL}\left(\tan^{-1}\left(-\frac{{}^{D}A^{YB}}{{}^{D}A^{ZB}} \right), \Phi_L \right)$$

Equation 6.7-7

A roll rate limit (Φ_L) of 600 deg/s is applied to prevent roll gyroscope saturation. Fast gyroscope and fin dynamics can be ignored in which case the relationship between the demanded and achieved roll angles reduces to,

$$\frac{\Phi}{{}^{D}\Phi_B^R} \equiv \frac{\omega_\Phi^2}{s^2 + 2\cdot\zeta_\Phi\cdot\omega_\Phi\cdot s + \omega_\Phi^2}$$

Equation 6.7-8

$$\frac{\Phi}{{}^{D}\Phi_B^R} := \frac{K_F\cdot K_A\cdot L_\xi}{s^2 + \left(K_A\cdot L_\xi - L_P \right)\cdot s + K_F\cdot K_A\cdot L_\xi}$$

Equation 6.7-9

The aileron and roll rate derivatives normalised by roll inertia (I_{XX}) satisfy ($K_A.L_\xi >> L_P$), hence the gains expressed in terms of the damping ratio and natural frequency are,

$$\left(K_F \quad , \quad K_A \right) := \left(\frac{\omega_\Phi^2}{2 \cdot \zeta_\Phi \cdot \omega_\Phi + L_P} \quad , \quad \frac{2 \cdot \zeta_\Phi \cdot \omega_\Phi + L_P}{L_\xi} \right)$$

Equation 6.7-10

In modern autopilots these gains are tuned to compensate for variations in the aerodynamic time constant ($-1/L_P$), since L_ξ (Nm) and L_P (Nm/s) are by definition negative. For agile missiles a damping ratio (ζ_Φ) of 0.6, and a bandwidth of 10 Hz ($\omega_\Phi := 8.7$ Hz) are typical over the flight envelope. In which case the actual roll angle of the missile,

$$\Phi_B^R := \varphi_{D2L}\left({}^D\Phi_B^R , \zeta_\Phi , \omega_\Phi \right)$$

Equation 6.7-11

Optimal values of these parameters were obtained by Roddy[R.9-12] whilst attempting to minimising aileron effort and roll rate however, a topic outside the scope of this research.

6.8 Simulation Guidance and Autopilot Implementation

MS_GUIDANCE provides 100 Hz lateral acceleration guidance demands depending on the bit pattern of *GU_DM_TP*. When *GU_DM_TP* is set to 0, trajectory optimisation is invoked. Setting either bit 1 or bit 2 activates one of the two basic forms of PN,

- Traditional PN (precedence) bit 1
- Normalised PN Bit 2
- CLOS without feed forward compensation Bit 3
- CLOS with feed forward compensation Bit 4
- COLOS Bit 5

Bit 3 must be set for all forms of CLOS, and in addition bits 4-5 as required. Augmented PN laws are constructed by setting the bits in *GU_DM_CP*,

- Gravitational compensation Bit 0
- Target acceleration compensation Bit 1
- Missile longitudinal acceleration compensation Bit 2
- Small sight line rate limiting Bit 3
- Realistic PN scaled to missile body axes Bit 8

Augmented CLOS laws are obtained by setting *GU_DM_CP* as follows,

- Gravitational compensation Bit 0
- Linear target trajectory compensation Bit 10
- Missile longitudinal acceleration compensation Bit 11
- Missile body to target beam compensation Bit 12

MS_AUTOPILOT controls the activation of different missile autopilots contained in modules *AP_0*, *AP_1* etc. mapped to *MS_TYPE*. Setting bits in *GU_AP_ER* activates the following errors and processes that act on the guidance demand independently, or combined in the order listed:

- Guidance/Autopilot/Fin - lumped time delay Bit 1
- Low speed lateral acceleration demand limiting Bit 2
- General lateral acceleration demand limiting Bit 3
- Lateral acceleration demand noise filtering Bit 4
- Lateral acceleration aerodynamic filtering Bit 5

It is essential for CLOS stability that bit 4 is set so that the lateral acceleration demands pass through the noise filter described in §. For all guidance laws the low speed demand limiting bit 2 and bit 3 must be set. It is also advisable when using the generic missile model that bit 5 is set to smooth the accelerations used to determine the flight-path and body rates.

6.9 Launcher Dynamics

Only for ground launched missile systems is the concept of a trainable launcher still relevant, as modern ships have universally adopted the vertical launch concept. Prior to launch *MS_LAUNCHER* shown in Figure 6-11 constrains missile rotation to that of the launcher driven by demands from one of the following sources:

- Reference target position $^{D}E_{A}^{B} := \left(\pi \quad \Theta_{A}^{T} \quad \Psi_{A}^{T} \right)$
- Ground radar measurement $^{D}E_{A}^{B} := \left(\pi \quad \tilde{\Theta}_{A}^{T} \quad \tilde{\Psi}_{A}^{T} \right)$
- Ground HMS measurement $^{D}E_{A}^{B} := \left(\pi \quad \tilde{\Theta}_{A}^{H} \quad \tilde{\Psi}_{A}^{H} \right)$
- Target observer (IMM tracking) $^{D}E_{A}^{B} := \left(\pi \quad {}_{IMM}\hat{\Theta}_{A}^{T} \quad {}_{IMM}\hat{\Psi}_{A}^{T} \right)$

The target reference position is used by default if the radar, HMS and target observer have been de-activated. If the target state observer is active it has priority, followed by the radar in order of precedence. The launcher dynamics are modelled using a 2nd order lag with a damping ratio (ζ_L) of 0.7, and a natural frequency (ω_L) of 3 Hz. Using reference data,

$$E_A^B := \left(\pi \quad , \quad \varphi_{D2L}\left({}^{D}\Theta_A^T , \zeta_L , \omega_L \right) \quad , \quad \varphi_{D2L}\left({}^{D}\Psi_A^T , \zeta_L , \omega_L \right) \right)$$

Equation 6.9-1

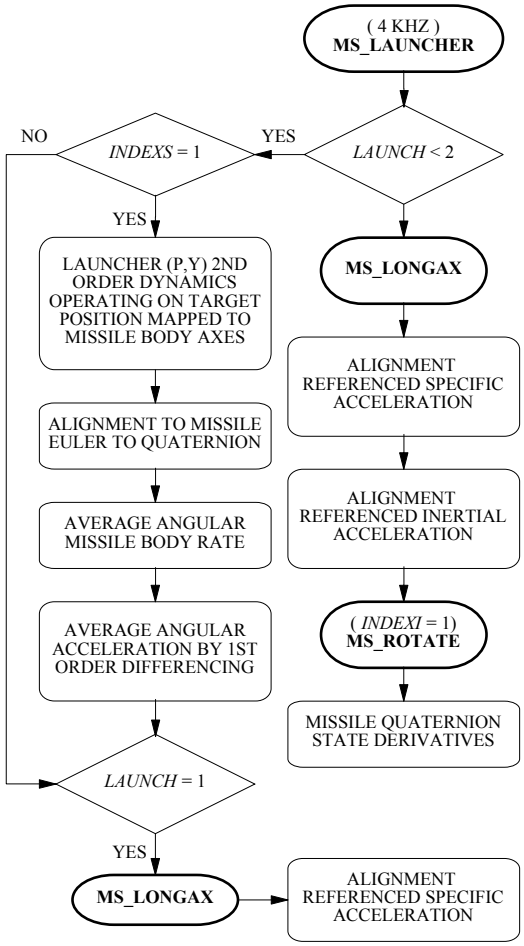

Figure 6-11 : Launcher Simulation

If the launcher bandwidth is set to zero its dynamics are by-passed and the missile is pointed at the selected tracking point,

$$E_A^M := E_A^B + \left(\pi \quad , \quad 0 \quad , \quad 0 \right)$$

Equation 6.9-2

In the launcher (*LAUNCH* < 2) the Missile Velocity and Seeker Head frames are aligned with the Missile Body frame. The missile angular rate and acceleration are determined from its current and previous orientation, and by numerical differences at 4 kHz. Once the missile is clear of the launcher the system state is propagated according to the equations presented in §6.10.2.

6.10 Missile Dynamics

6.10.1 Linear Motion

The reaction of a body to external forces is embodied in Newton's 2nd law of motion for rigid bodies in inertial space. The resultant force at point (m) equals the rate of change of linear momentum with respect to an instantaneous Local Inertial frame located at this point,

$$\underline{F}_m^I := \dot{m}_m \cdot \dot{\underline{P}}_m^I + m_m \cdot d\left(\underline{\dot{P}}_m^I \right) / dt$$

Equation 6.10-1

Mass (m_m) is treated as a quasi-static parameter, and the thrust ($\underline{F}_T$) and drag ($\underline{F}_D$) forces act along the longitudinal axis. The Euler force balance is then,

$$m_m \cdot d\left(T_A^B \cdot T_I^E \cdot \underline{\dot{P}}_m^I \right) / dt := T_B^A \cdot \left(\underline{F}_T^B + \underline{F}_D^B + \underline{F}_A^B \right) + m_m \cdot T_G^A \cdot \underline{G}_m^G$$

Equation 6.10-2

The aerodynamic force ($\underline{F}_A$) acting on the missile is the sum of forces due to incidence and fin deflection (damping forces are small and can be ignored),

$$\underline{F}_A := \underline{F}_v + \underline{F}_\delta := \left(0 \quad , \quad y_v \cdot \dot{P}_{o,m}^{YB} + y_\zeta \cdot \zeta \quad , \quad z_w \cdot \dot{P}_{o,m}^{ZB} + z_\eta \cdot \eta \right)^T$$

Equation 6.10-3

The nomenclature and relationships between the normalised aerodynamic derivatives are given by Garnell[G.1]. Inserting the gravitational acceleration from §20, and using the results in §17.2,

$$m_m \cdot T_B^I \cdot \left(\ddot{\underline{P}}_m^B - \left(\underline{\omega}_{I,E}^B + \underline{\omega}_{A,B}^B \right) \times \dot{\underline{P}}_m^B \right) :=$$

$$T_B^I \cdot \left(\underline{F}_T^B + \underline{F}_D^B + \underline{F}_A^B \right) + m_m \cdot T_G^I \cdot \left(\underline{g}_m^G + \underline{\omega}_{C,E}^G \times \underline{\omega}_{C,E}^G \times \underline{P}_{r,m}^G \right)$$

Equation 6.10-4

Ignoring earth rate and curvature for short-range missile applications,

$$\ddot{\underline{P}}_{o,m}^A := \underline{g}_m^A + T_B^A \cdot \left(m_m^{-1} \cdot \left(\underline{F}_T^B + \underline{F}_D^B + \underline{F}_A^B \right) + \underline{\omega}_{A,B}^B \times \dot{\underline{P}}_{o,m}^B \right)$$

Equation 6.10-5

Initially the missile and ground radar reference points are coincident at the origin of the Alignment frame until launch at time (t_L),

$$t < t_L \Rightarrow \underline{X}_{ML}^{A} := \underline{0}_9$$

Equation 6.10-6

Thereafter, the state is obtained by integrating acceleration expressed in the Alignment frame at 4 kHz. Lateral motion is prevented until the missile has travelled the length of the launcher ($L_T := 3m$). The motion is therefore dictated by the thrust and drag functions are applicable in the launcher,

$$\left(t \geq t_L \right) \wedge \left(P_{o,m} \leq L_T \right) \Rightarrow \underline{\ddot{P}}_m^A := T_B^A \cdot \left(\frac{F_T^{XB} + F_D^{XB}}{m_m} \quad , \quad 0 \quad , \quad 0 \right)^T$$

Equation 6.10-7

The gravitational force acts when the missile is clear of the tube. Gravity, thrust and drag are the only forces modelled until the missile reaches a stable speed ($V_S := 80$ m/s). Without height droop compensation and nose-up attitude develops and the stable speed was set to prevent incidence exceeding 5° if the missile is launched horizontally,

$$\left(P_{o,m} > L_T \right) \wedge \left(\dot{P}_{o,m} < V_S \right) \Rightarrow$$

$$\underline{\ddot{P}}_m^A := T_B^A \cdot \left(\frac{F_T^{XB} + F_D^{XB}}{m_m} \quad , \quad 0 \quad , \quad 0 \right)^T + \underline{g}_m^A$$

Equation 6.10-8

The fins unlock and roll control is established as the missile clears the tube. Lateral control is not invoked until the missile reaches its stable speed. At this point simulator control passes from *MS_LAUNCHER* in Figure 6-11 to *MS_DYNAMICS* in Figure 6-12 when the linear dynamics are,

$$\dot{P}_{o,m} \geq V_S \Rightarrow$$

$$\underline{\ddot{P}}_m^A := T_B^A \cdot \left(\frac{F_T^{XB} + F_D^{XB}}{m} \quad , \quad \ddot{P}_{o,m}^{YB} \quad , \quad \ddot{P}_{o,m}^{ZB} \right) + T_G^A \cdot \underline{g}_m^G$$

Equation 6.10-9

The lateral acceleration achieved in response to the STT autopilot demands,

$$\left(\ddot{P}_{o,m}^{YB} \quad , \quad \ddot{P}_{o,m}^{ZB} \right) :=$$

$$\left(\varphi_{D2L} \left({}^{D}A^{YB} , \zeta_{LA} , {}^{Z}\omega_{LA} \right) \quad , \quad \varphi_{D2L} \left({}^{D}A^{ZB} , \zeta_{LA} , {}^{Y}\omega_{LA} \right) \right)$$

Equation 6.10-10

For BTT, the missile manoeuvres in the pitch plane only,

$$\left(\ddot{P}_{o,m}^{YB} \quad , \quad \ddot{P}_{o,m}^{ZB} \right) := \left(0 \quad , \quad \varphi_{D2L}\left({}^{D}A^{ZR} \cdot \cos\Phi_B^R , \zeta_{LA} , {}^{Y}\omega_{LA} \right) \right)$$

Equation 6.10-11

When *AUTOP_SW* is set to 1 constant values of 0.7 and 6 Hz are used for the damping ratio and natural frequency, otherwise they are incidence and Mach number dependent,

$$M_m < 1 \Rightarrow \left\{ \begin{array}{c} \zeta_{LA} := 0.6 \\ {}^{Y}\omega_{LA} := {}^{Z}\omega_{LA} := 4 \cdot \pi \end{array} \right\}$$

Equation 6.10-12

$$M_m \geq 1 \Rightarrow \zeta_{LA} := 0.6 + 0.1 \cdot \left(M_M - 1 \right)$$

Equation 6.10-13

$$M_m \geq 1 \Rightarrow$$

$$\begin{pmatrix} {}^{Y}\omega_{LA} \\ \cdots \\ {}^{Z}\omega_{LA} \end{pmatrix} := 2 \cdot \pi \cdot \left(2 + \left(M_m - 1 \right) \cdot \left(1.5 + \frac{1}{{}_{MAX}\xi_B^{MV}} \cdot \begin{pmatrix} \left| \Theta_B^{MV} \right| \\ \cdots \\ \left| \Psi_B^{MV} \right| \end{pmatrix} \right) \right)$$

Equation 6.10-14

The natural frequency is subject to an incidence limit (${}_{MAX}\xi_B^{MV}$) of 40°.

6.10.2 Angular Motion

The external moment (M) acting on the missile at the mass centre equals the rate of change of angular momentum (H) in inertial space. When measured in the rotating Missile Body frame,

$$\underline{M}_m := D_I\left(\underline{H}_m \right) := D_B\left(\underline{H}_m \right) + \underline{\omega}_{C,B} \times \underline{H}_m$$

Equation 6.10-15

The local inertial axes are referred to the missile reference point (m). When the mass is evenly distributed the inertial tensor [I_m] is diagonal comprising only moments of inertia. As the Missile Body frame is fixed in the missile,

$$\underline{H}_m^B := \left(I_{XX}^B \quad , \quad I_{YY}^B \quad , \quad I_{ZZ}^B \right)^T \otimes \underline{\omega}_{C,B}^B$$

Equation 6.10-16

Substituting for angular momentum in the moment balance, and treating the moments of inertia as quasi-static parameters results in the Euler equations,

$$I_{XX}^{B} \cdot \dot{\omega}_{C,B}^{XB} \coloneqq \underline{M}_{m}^{XB} + \left(I_{YY}^{B} - I_{ZZ}^{B} \right) \cdot \omega_{C,B}^{YB} \cdot \omega_{C,B}^{ZB}$$

Equation 6.10-17

$$I_{YY}^{B} \cdot \dot{\omega}_{C,B}^{YB} \coloneqq \underline{M}_{m}^{YB} + \left(I_{ZZ}^{B} - I_{XX}^{B} \right) \cdot \omega_{C,B}^{XB} \cdot \omega_{C,B}^{ZB}$$

Equation 6.10-18

$$I_{ZZ}^{B} \cdot \dot{\omega}_{C,B}^{ZB} \coloneqq \underline{M}_{m}^{ZB} + \left(I_{XX}^{B} - I_{YY}^{B} \right) \cdot \omega_{C,B}^{XB} \cdot \omega_{C,B}^{YB}$$

Equation 6.10-19

Earth rotational acceleration has been ignored. The external moments arise from the gravitational force acting at the centre of mass in a uniform field, and the aerodynamic moment ($\underline{M}_A$) referenced to point (m),

$$\underline{M}_{m}^{B} \coloneqq \underline{M}_{A}^{B} + m_{m} \cdot \underline{P}_{m,c}^{B} \times \left(T_{G}^{B} \cdot \underline{G}_{m}^{G} \right)$$

Equation 6.10-20

Substituting for gravity and expressing the result in the Missile Body frame,

$$\underline{M}_{m}^{B} \coloneqq \underline{M}_{A}^{B} + m_{m} \cdot \underline{P}_{m,c}^{B} \times \left(T_{G}^{B} \cdot \underline{g}_{m}^{G} + \underline{\omega}_{C,E}^{B} \times \underline{\omega}_{C,E}^{B} \times \underline{P}_{r,m}^{B} \right)$$

Equation 6.10-21

Expanding and ignoring earth rate and tilt dependent terms,

$$I_{XX}^{B} \cdot \dot{\omega}_{A,B}^{XB} \coloneqq \underline{M}_{A}^{XB} + \left(I_{YY}^{B} - I_{ZZ}^{B} \right) \cdot \omega_{A,B}^{YB} \cdot \omega_{A,B}^{ZB}$$

Equation 6.10-22

$$I_{YY}^{B} \cdot \dot{\omega}_{A,B}^{YB} \coloneqq \underline{M}_{m}^{YB} + \left(I_{ZZ}^{B} - I_{XX}^{B} \right) \cdot \omega_{A,B}^{XB} \cdot \omega_{A,B}^{ZB} + m_{m} \cdot P_{m,c}^{XB} \cdot T_{G}^{B}(9) \cdot g_{m}^{ZA}$$

Equation 6.10-23

$$I_{ZZ}^{B} \cdot \dot{\omega}_{C,B}^{ZB} \coloneqq \underline{M}_{m}^{ZB} + \left(I_{XX}^{B} - I_{YY}^{B} \right) \cdot \omega_{C,B}^{XB} \cdot \omega_{C,B}^{YB} + m_{m} \cdot P_{m,c}^{XB} \cdot T_{G}^{B}(6) \cdot g_{m}^{ZG}$$

Equation 6.10-24

For more complex models the aerodynamic moment comprises terms due to missile incidence, damping and control surface deflection expressed in the Missile Body frame,

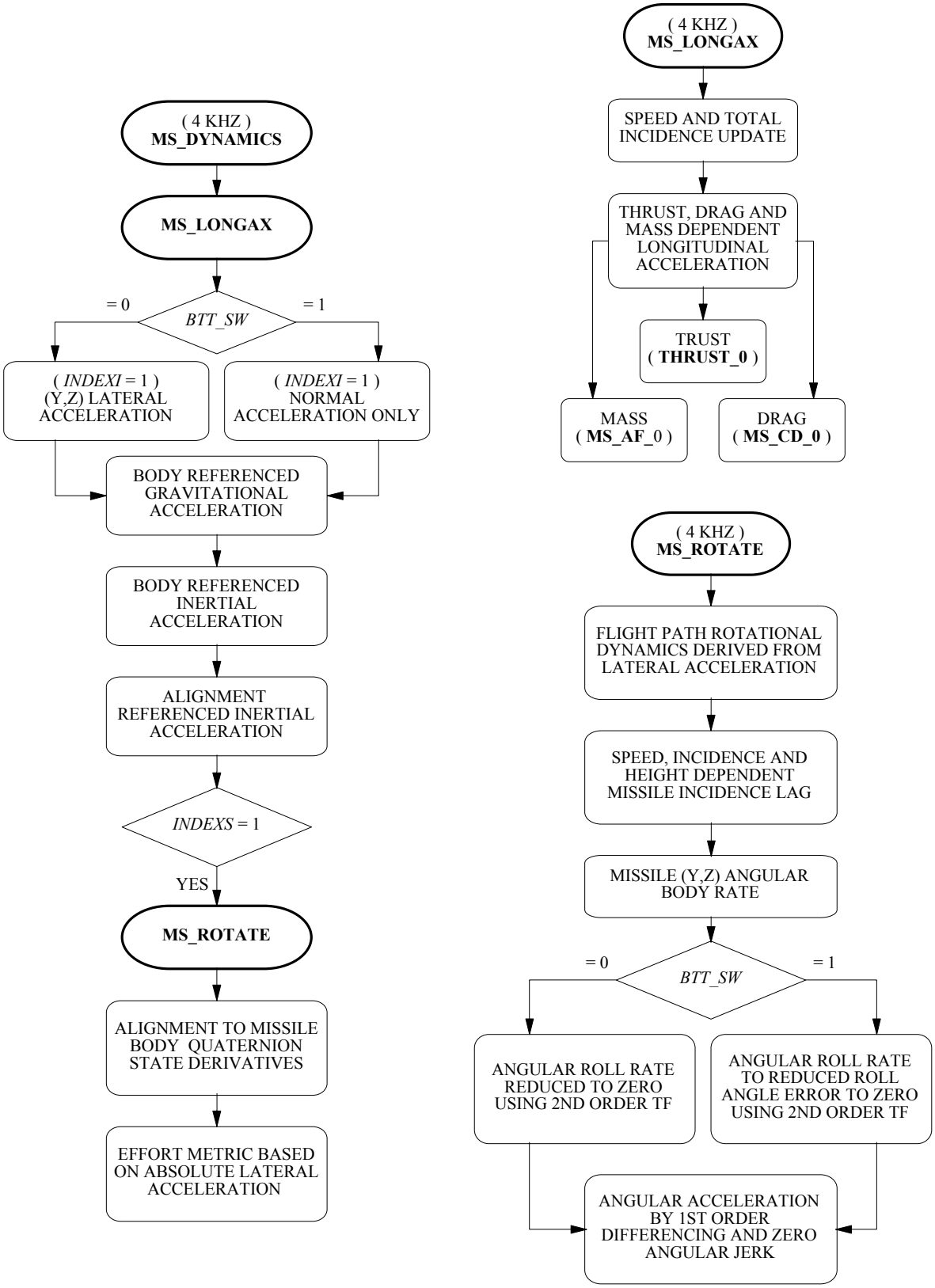

Figure 6-12 : Missile Dynamics

$$\underline{M}_A^B := \underline{M}_v^B + \underline{M}_\omega^B + \underline{M}_\delta^B := \begin{pmatrix} 0 \\ m_w \cdot \dot{P}_{o,m}^{ZB} \\ n_v \cdot \dot{P}_{o,m}^{YB} \end{pmatrix} + \begin{pmatrix} \ell_p \cdot \omega_{A,B}^{XB} \\ m_q \cdot \omega_{A,B}^{YB} \\ n_r \cdot \omega_{A,B}^{ZB} \end{pmatrix} + \begin{pmatrix} \ell_\xi \cdot \xi \\ m_\eta \cdot \eta \\ n_\zeta \cdot \zeta \end{pmatrix}$$

Equation 6.10-25

The control surface deflections are dealt with in §3.11. For an agile missile the derivatives are functions of Mach number, height and lateral acceleration. The generic missile rotational dynamics are simpler and are determined by the speed and incidence dependent incidence lag (T_I) where,

$$\left(T_I^{YB} \quad , \quad T_I^{ZB} \right) := \left(-1 / y_v \quad , \quad 1 / z_w \right)$$

Equation 6.10-26

For BTT missiles,

$$\omega_{A,B}^{YR} := -\left(1 + T_I^{ZB} \cdot s \right) \cdot \frac{\ddot{P}_{o,m}^{ZR}}{\dot{P}_{o,m}^{XB}}$$

Equation 6.10-27

The angular acceleration is determined by differentiating smooth angular rates. The missile orientation quaternion is propagated using the 1st order derivatives followed by normalisation. For STT missiles,

$$\dot{P}_{o,m}^{XB} \cdot \left(\omega_{A,B}^{YB} \quad , \quad \omega_{A,B}^{ZB} \right) :=$$

$$\left(-\left(1 + T_I^{ZB} \cdot s \right) \cdot \ddot{P}_{o,m}^{ZB} \quad , \quad \left(1 + T_I^{YB} \cdot s \right) \cdot \ddot{P}_{o,m}^{YB} \right)$$

Equation 6.10-28

Jerk is also obtained by differences at 4 kHz. The incidence lag for both types of missile control depends on Mach number limited to [1,3] and body incidence limited to ± 40°,

$$\left(\frac{1}{T_I^{YB}} \quad , \quad \frac{1}{T_I^{ZB}} \right) := \varphi_1 \cdot \left(\varphi_2 \quad , \quad \varphi_3 \right) := \frac{5969 \cdot \sqrt{T_S}}{P_S} \cdot \left(\varphi_2 \quad , \quad \varphi_3 \right)$$

Equation 6.10-29

$$\begin{pmatrix} \varphi_2 \\ \cdots \\ \varphi_3 \end{pmatrix} := 0.85 - 0.15 \cdot M_m + \begin{pmatrix} \left(30 - M_m \right) \cdot \left(\Theta_B^{MV} \right)^2 \\ \cdots \\ \left(30 - M_m \right) \cdot \left(\Psi_B^{MV} \right)^2 \end{pmatrix}$$

Equation 6.10-30

Table 6-2 : Sea-Level Missile Incidence Lag (Seconds)

MACH			INCIDENCE (DEGREES)			
NUMBER	0	5	10	20	30	40
1.0	1.429	1.086	0.632	0.236	0.116	0.067
1.5	1.067	0.792	0.446	0.163	0.079	0.046
2.0	0.909	0.655	0.356	0.126	0.061	0.035
2.5	0.842	0.584	0.305	0.105	0.050	0.029
3.0	0.833	0.550	0.273	0.090	0.043	0.026

The variation in incidence lag with Mach number and sea-level incidence is given in Table 6-2. Incidence lag sensitivity with respect to the missile observer states,

$$\frac{\partial T_I^{YB}}{\partial \, {}_{SO}\underline{X}_M} := -\left(T_I^{YB} \right)^2 \cdot \left(\frac{\partial \varphi_1}{\partial \, {}_{SO}\underline{X}_M} \cdot \varphi_2 + \varphi_1 \cdot \frac{\partial \varphi_2}{\partial \, {}_{SO}\underline{X}_M} \right)$$

Equation 6.10-31

$$\frac{\partial T_I^{ZB}}{\partial \, {}_{SO}\underline{X}_M} := -\left(T_I^{ZB} \right)^2 \cdot \left(\frac{\partial \varphi_1}{\partial \, {}_{SO}\underline{X}_M} \cdot \varphi_3 + \varphi_1 \cdot \frac{\partial \varphi_3}{\partial \, {}_{SO}\underline{X}_M} \right)$$

Equation 6.10-32

The sensitivity of incidence lag to geodetic height depends on the change in static air pressure and temperature given in §19,

$$\frac{\partial \varphi_1}{\partial \, {}_{SO}\underline{X}_M} := \left(0_2 \;,\; \frac{5969}{P_S^2} \cdot \left(\frac{P_S}{\sqrt{T_S}} \cdot \frac{\partial T_S}{\partial P_m^{ZG}} - \frac{\partial P_S}{\partial P_m^{ZG}} \right) \;,\; 0_{16} \right)$$

Equation 6.10-33

Decomposing the remaining Jacobians,

$$\frac{\partial \varphi_2}{\partial \, {}_{SO}\underline{X}_M} := \left(0_2 \;,\; \frac{\partial \varphi_2}{\partial P_m^{ZA}} \;,\; \frac{\partial \varphi_2}{\partial \dot{\underline{P}}_m^{A}} \;,\; 0_3 \;,\; \frac{\partial \varphi_2}{\partial Q_A^B} \;,\; 0_6 \right)$$

Equation 6.10-34

$$\frac{\partial \varphi_3}{\partial\, {}_{SO}\underline{X}_M} := \left(0_2 \quad , \quad \frac{\partial \varphi_3}{\partial P_m^{ZA}} \quad , \quad \frac{\partial \varphi_3}{\partial \dot{\underline{P}}_m^{A}} \quad , \quad 0_3 \quad , \quad \frac{\partial \varphi_3}{\partial Q_A^{B}} \quad , \quad 0_6 \right)$$

Equation 6.10-35

The pitch and yaw plane incidence lag variation with geodetic height,

$$\left(\frac{\partial \varphi_2}{\partial P_m^{ZA}} \quad , \quad \frac{\partial \varphi_3}{\partial P_m^{ZA}} \right) := -0.15 - \left(\left(\Theta_B^{MV} \right)^2 \quad , \quad \left(\Theta_B^{MV} \right)^2 \right) \cdot \frac{\partial M_m}{\partial P_m^{ZA}}$$

Equation 6.10-36

The pitch and yaw plane incidence lag variation with linear velocity,

$$\frac{\partial \varphi_2}{\partial \dot{\underline{P}}_m^{A}} := \left(-0.15 - \left(\Theta_B^{MV} \right)^2 \right) \cdot \frac{\partial \Theta_B^{MV}}{\partial \dot{\underline{P}}_m^{A}} + 2 \cdot \left(30 - M_m \right) \cdot \frac{\partial \Theta_B^{MV}}{\partial \dot{\underline{P}}_m^{A}}$$

Equation 6.10-37

$$\frac{\partial \varphi_3}{\partial \dot{\underline{P}}_m^{A}} := \left(-0.15 - \left(\Psi_B^{MV} \right)^2 \right) \cdot \frac{\partial \Psi_B^{MV}}{\partial \dot{\underline{P}}_m^{A}} + 2 \cdot \left(30 - M_m \right) \cdot \frac{\partial \Psi_B^{MV}}{\partial \dot{\underline{P}}_m^{A}}$$

Equation 6.10-38

The pitch and yaw plane incidence lag variation with missile orientation,

$$\left(\frac{\partial \varphi_2}{\partial Q_A^{B}} \quad , \quad \frac{\partial \varphi_3}{\partial Q_A^{B}} \right) := 2 \cdot \left(30 - M_m \right) \cdot \left(\Theta_B^{MV} \cdot \frac{\partial \Theta_B^{MV}}{\partial Q_A^{B}} \quad , \quad \Psi_B^{MV} \cdot \frac{\partial \Psi_B^{MV}}{\partial Q_A^{B}} \right)$$

Equation 6.10-39

The pitch and yaw plane incidence lag variation with missile incidence,

$$\left(\frac{\partial \varphi_2}{\partial \Theta_B^{MV}} \quad , \quad \frac{\partial \varphi_3}{\partial \Psi_B^{MV}} \right) := 2 \cdot \left(30 - M_m \right) \cdot \left(\Theta_B^{MV} \quad , \quad \Psi_B^{MV} \right)$$

Equation 6.10-40

6.11 Discussion

§6 concentrates on the development of a missile simulator in the program infrastructure containing a generic short-range agile missile model. The simulator is designed to accommodate multiple-missiles sharing the target and sensor simulator data, as does the AMIS.

Equations of motion are developed using a full set of normalised aerodynamic derivatives to support the presentation of observer pseudo-measurements in §5. The aerodynamic characteristics of the generic model

are simply defined by height and speed dependent incidence lag implementation of which requires a high state update rate.

The simulator is configured so that missile guidance and autopilots can be stimulated using reference, sensor measurements, or state observer data. STT and BTT lateral autopilots are provided, with a fast roll autopilot for the latter. Limits are imposed on lateral acceleration and angular rate commensurate with motion in a rotating launcher, low speed manoeuvring, and high speed "g" limiting.

The simulator takes a modular approach to guidance law construction providing a test-bed for basic PN and CLOS laws augmented by numerous correction terms. The objective was to separate trajectory optimisation and be able to switch between PN and biased CLOS to study transitions between the two. This approach is rapidly becoming outdated since fusion of ground radar and missile IMU information means pseudo-PN guidance laws can be formulate throughout flight.

The historical development of PN guidance laws provides a useful insight into how analytical trajectory optimisation came to influence the subject. Studying missile trajectories generated by simple cost functions is the ideal starting point for complex cost functions and trajectory optimisation.

Three areas of special interest are considered. The first is PN, and the requirement on the missile state observer to stabilise the seeker preventing missile body motion from cross coupling into the missile sight-line rate. This can severely reduce the acquisition range as the motion of the detector during the stare time smears the IR energy returns. The cross-coupling equations are provided so that the source and characteristics of the parasitic errors can be clearly identified.

The other two areas concern CLOS. Weave frequency estimation accuracy for acceptable performance against weaving targets is presented as a function of the target tracking bandwidth. Finally, CLOS guidance demand corrections are provided when the target is travelling at constant velocity. Clearly target manoeuvre detection is required which may be provided by the IMM filter probabilities up-linked to the missile.

The is little in the way of further work generated by this chapter which in essence supports the main research topics of state observation and trajectory optimisation. The verification of the constant velocity correction, and its interaction with the IMM filter probabilities, is of some academic interest however, such laws are gradually being overtaken by pseudo-PN command generation.

Chapter 7

TRAJECTORY OPTIMISATION

The impetus in missile guidance is to find globally optimum solutions to guidance problems involving complex cost functions using off-line methods such as simulated annealing, or shooting techniques. Although their implementation is relatively simple they require large flight data tables tuned for a nominal missile. Using these tables the guidance commands (trajectory) are updated at regular intervals taking account of the current state estimates. It is difficult to introduce new in-flight constraints into this process without revising the flight tables.

The aforementioned optimisation techniques are unsuitable for on-line optimisation and a return to simpler constrained optimisation techniques is proposed. The work builds on that of Vorley[V.4] – on gradients in function space, and Moody[M.12] – their use for on-line optimisation. §7 starts by describing the process of continually re-optimising a fixed number of controls for the fire solutions, the launch criteria, and in-flight use of controls by the autopilot.

An optimiser state space is selected, the time evolution of the missile and target dynamics defined, together with their variation with respect to the state space and controls. The cost function is built-up of commonly used elements, each activated by a switch that can also acts as a constant scaling normalising their effect on gradient computations.

The TPBVP is defined and reduced to the lesser problem of minimisation of an Hamiltonian function. The missile controls are related to the optimiser state space as required by Pontryagin theory. Discrete formulation of these continuous optimisation equations for a fixed number of controls is based on Euler integration for real-time operation. Search directions and univariate search techniques to reduce the cost without having to bracket the nearest minima are reviewed.

Gradient techniques have proven to be surprisingly robust given a good initial track, here an augmented PN trajectory. The TPBVP solution must also be robust to changes in the smoothed boundary conditions provided by the state observer. The simulation monitors the processing time taken and limits the optimisation process as the controls are required by the autopilot.

7.1 Control Sequence

A conceptual description of the real-time trajectory optimisation process follows. The state observer provides updated missile and target boundary conditions. A set of feasible controls (U) is established that partitions the initial trajectory obtained by propagating the missile boundary conditions to target impact using ATPN and Euler integration. This is the start of the process shown in Figure 7-1. The initial trajectory is updated as the target gets closer until the predicted impact speed exceeds the stable aerodynamic speed (V_S) indicating that the target is reachable.

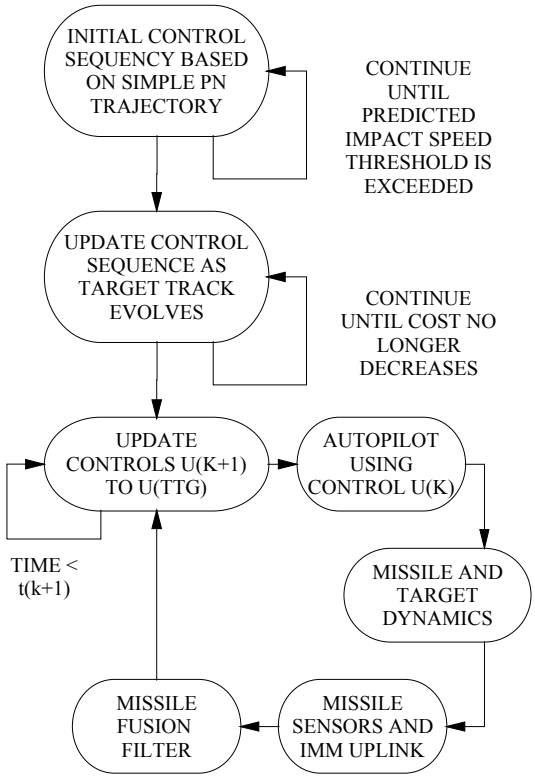

Figure 7-1 : Trajectory Control Update

Once the impact speed is exceeded, gradient projection techniques in function space are used to optimise the controls, launch angle and time-to-impact. Launch is inhibited until the Ghulman conditions for engaging manoeuvring targets presented in §6.5.1.3 are satisfied, and thereafter until the rate of improvement in the PI cost slows and the missile is committed launched. After launch the missile uses each control in turn whilst those remaining are re-optimised subject to the changing boundary conditions and in-flight cost function weights.

The simulation provides a pseudo-real time environment that measures the processing time taken to process the critical functions of the optimisation process using the host clock. It is then possible to assess the trajectory shaping whilst respecting the processing time used, or allow a longer time to determine the fully optimised trajectory.

7.2 Dynamic Model

The position of the target at the impact time (t_F) is propagated from its current position provided by the missile state observer,

$$\begin{pmatrix} \underline{P}_t^A\left(t_F\right) \\ \cdots \\ \dot{\underline{P}}_t^A\left(t_F\right) \end{pmatrix} := \begin{pmatrix} 0_{3x3} & \vdots & t_F \cdot I_3 \\ \cdots & \vdots & \cdots \\ 0_{3x3} & \vdots & 0_{3x3} \end{pmatrix} \cdot \begin{pmatrix} \underline{P}_t^A \\ \cdots \\ \dot{\underline{P}}_t^A \end{pmatrix} + \begin{pmatrix} 0.5 \cdot t_F^2 \cdot I_3 \\ \cdots \\ t_F \cdot I_3 \end{pmatrix} \cdot \ddot{\underline{P}}_t^A$$

Equation 7.2-1

For real-time optimisation the size of the optimiser state vector must be as small as possible. Here missile position, speed and direction, and the launcher orientation with respect to the Alignment frame are used. In literature mass-flow is often included however, when using solid propellant boosters mass can be treated as a quasi-static variable providing the ambient pressure is accounted for in the thrust equation.

$$\underline{X} := \left(P_m^{XA} \;,\; P_m^{YA} \;,\; P_m^{ZA} \;,\; \dot{P}_{o,m} \;,\; \Theta_A^{MV} \;,\; \Psi_A^{MV} \right)^T$$

Equation 7.2-2

These states are propagated from the initial conditions provided by the missile state observer according to the difference equations ($\underline{f}_X$),

$$\underline{X}_{k+1} := \underline{X}_k + \dot{\underline{X}}_k\left(\underline{X}_k, \underline{U}_k, t_k\right) \cdot \Delta t_k \equiv \underline{X}_k + \underline{f}_X \cdot \Delta t_k$$

Equation 7.2-3

Euler integration is the obvious choice, balancing speed and the number of control steps. Runge-Kutta algorithms, although more accurate, impose a greater computation load and require a single-step start up algorithm following a discontinuity in the derivatives. The 1st order Newton-Cotes numerical integration formula (trapezoidal rule), is an alternative to Euler integration with 2nd order convergence and none of the problems associated with higher-order algorithms.

7.2.1 Dynamic Model Propagation Equations

The following parameters, and their derivatives, with respect to the optimiser states are defined in §6 and §20. The time, optimiser states and control dependencies are listed,

- Missile mass $m_m\left(t\right)$
- Missile thrust force $F_T\left(P_m^{ZA}\right)$
- Missile drag force $F_D\left(P_m^{ZA}, \dot{P}_{o,m}, \Theta_B^{MV}, \Psi_B^{MV}\right)$

- Missile lateral lift force $F_L\left(P_m^{ZA} , \dot{P}_{o,m} , \Theta_B^{MV} , \Psi_B^{MV} \right)$
- Gravitational acceleration $g_m^{ZA}\left(P_m^{ZA} \right)$

Defining,

$$\left({}^{147}\underline{\varphi}_A^{MV} \quad , \quad {}^{147}\underline{\varphi}_B^{MV} \quad , \quad {}^{369}\underline{\varphi}_B^{MV} \right) \equiv$$

$$\left(\begin{pmatrix} T_A^{MV}(1) \\ T_A^{MV}(4) \\ T_A^{MV}(7) \end{pmatrix} , \begin{pmatrix} T_B^{MV}(1) \\ T_B^{MV}(4) \\ T_B^{MV}(7) \end{pmatrix} , \begin{pmatrix} T_B^{MV}(3) \\ T_B^{MV}(6) \\ T_B^{MV}(9) \end{pmatrix} \right)$$

Equation 7.2-4

The dynamic states evolve according to the vector functional,

$$\underline{f}_X \coloneqq \left(\underline{f}_P \quad , \quad f_V \quad , \quad f_\Theta \quad , \quad f_\Psi \quad , \quad f_M \right)^T$$

Equation 7.2-5

The missile position with respect to Alignment axes is propagated using,

$$\underline{f}_P \coloneqq \dot{P}_{o,m} \cdot {}^{147}\underline{\varphi}_A^{MV}$$

Equation 7.2-6

Transforming the forces acting along the Missile Body axes through the incidence angles into the Missile Velocity frame, and selecting the missile velocity along $\underline{X}^{MV}$,

$$\underline{F}_m^{MV} \coloneqq T_B^{MV} \cdot \underline{F}_m^B \coloneqq T_B^{MV} \cdot \left(F_T^{XB} + F_D^{XB} \quad , \quad F_L^{YB} \quad , \quad F_L^{ZB} \right)^T$$

Equation 7.2-7

$$f_V \coloneqq m_m^{-1} \cdot \left(\Delta F_m^{XB} \quad , \quad F_L^{YB} \quad , \quad F_L^{ZB} \right) \cdot {}^{147}\underline{\varphi}_B^{MV} + g_m^{ZA} \cdot T_A^{MV}(7)$$

Equation 7.2-8

In which the thrust - drag balance is denoted by,

$$\Delta F_m^{XB} \coloneqq F_T^{XB} + F_D^{XB}$$

Equation 7.2-9

When the missile traces a circle in response to lateral acceleration,

$$m_m \cdot \dot{P}_{o,m} \cdot f_\Theta \;:=\; \underline{F}_m^B \cdot {}^{369}\underline{\varphi}_B^{MV} + m_m \cdot g_m^{ZA} \cdot T_A^{MV}(9)$$

Equation 7.2-10

$$m_m \cdot \dot{P}_{o,m} \cdot T_A^{MV}(9) \cdot f_\Psi \;:=\; \Delta F_m^{XB} \cdot T_B^{MV}(7) + F_L^{YB} \cdot T_B^{MV}(9)$$

Equation 7.2-11

7.2.2 Dynamic Constraint - State Jacobians

The TPBVP solution requires the variation in the dynamic constraints with the optimiser states. For on-line applications analytical derivatives are more efficient than performing functional evaluations and differencing. The automatic computation of partial differentials using Table methods has been studied by Wengert[W.1] and Bellman[B.3]. For the missile position vector,

$$\partial \underline{P}_m^A \,/\, \partial \underline{X} \;:=$$

$$\left(0_{3x3} \;\vdots\; {}^{147}\underline{\varphi}_A^{MV} \;\vdots\; -\dot{P}_{o,m} \cdot {}^{369}\underline{\varphi}_A^{MV} \;\vdots\; \left(-\dot{P}_{o,m} \cdot T_A^{MV}(4) \;,\; \dot{P}_{o,m} \cdot T_A^{MV}(1) \;,\; 0 \right)^T \right)$$

Equation 7.2-12

The missile speed variation with respect to the optimiser states,

$$\partial f_V \,/\, \partial \underline{X} \;:=$$

$$\left(\underline{0}_2^T \;\vdots\; \partial f_V \,/\, \partial P_m^{ZA} \;\vdots\; \partial f_V \,/\, \partial \dot{P}_{o,m} \;\vdots\; -g_m^{ZA} \cdot T_A^{MV}(9) \;\vdots\; 0 \right)$$

Equation 7.2-13

$$\frac{\partial f_V}{\partial P_m^{ZA}} \;:=\; \frac{1}{m_m} \cdot \left(\frac{\partial \underline{F}_m^B}{\partial P_m^{ZA}} \right)^T \cdot {}^{147}\underline{\varphi}_B^{MV} + \frac{\partial g_m^{ZA}}{\partial P_m^{ZA}} \cdot T_A^{MV}(7)$$

Equation 7.2-14

$$\partial f_V \,/\, \partial \dot{P}_{o,m} \;:=\; m_m^{-1} \cdot \left(\partial \underline{F}_m^B \,/\, \partial \dot{P}_{o,m} \right)^T \cdot {}^{147}\underline{\varphi}_B^{MV}$$

Equation 7.2-15

The missile pitch incidence angle variation with respect to optimiser states,

$$\partial f_\Theta \,/\, \partial \underline{X} \;:=\; \left(\underline{0}_2^T \;\vdots\; \frac{\partial f_\Theta}{\partial P_m^{ZA}} \;\vdots\; \frac{\partial f_\Theta}{\partial \dot{P}_{o,m}} \;\vdots\; \frac{\partial f_\Theta}{\partial \Theta_A^{MV}} \;\vdots\; 0 \right)$$

Equation 7.2-16

$$\dot{P}_{o,m} \cdot \left(\partial f_{\Theta} \,/\, \partial P_{o,m}^{ZA} \right) \coloneqq$$

$$m_m^{-1} \cdot \left(\partial \underline{F}_m^B \,/\, \partial P_m^{ZA} \right)^T \cdot {}^{369}\underline{\varphi}_B^{MV} + \left(\partial g_m^{ZA} \,/\, \partial P_{o,m}^{ZA} \right) \cdot T_A^{MV}(9)$$

Equation 7.2-17

$$\dot{P}_{o,m}^2 \cdot \left(\partial f_{\Theta} \,/\, \partial \dot{P}_{o,m} \right) \coloneqq$$

$$-\, m_m^{-1} \cdot \left(\partial \underline{F}_m^B \,/\, \partial \dot{P}_{o,m} \right)^T \cdot {}^{369}\underline{\varphi}_B^{MV} \; + \; g_m^{ZA} \cdot T_A^{MV}(9)$$

Equation 7.2-18

$$\dot{P}_{o,m} \cdot \left(\partial f_{\Theta} \,/\, \partial \Theta_A^{MV} \right) \coloneqq$$

$$m_m^{-1} \cdot \left(\partial \underline{F}_m^B \,/\, \partial \Theta_A^{MV} \right)^T \cdot {}^{369}\underline{\varphi}_B^{MV} \; + \; g_m^{ZA} \cdot T_A^{MV}(7)$$

Equation 7.2-19

The missile yaw incidence angle variation with respect to optimiser states,

$$\partial f_{\Psi} \,/\, \partial \underline{X} \;\coloneqq\; \left(\; \underline{0}_2^T \;\vdots\; \frac{\partial f_{\Psi}}{\partial P_m^{ZA}} \;\vdots\; \frac{\partial f_{\Psi}}{\partial \dot{P}_{o,m}} \;\vdots\; \frac{\partial f_{\Psi}}{\partial \Theta_A^{MV}} \;\vdots\; 0 \; \right)$$

Equation 7.2-20

$$m_m \cdot \dot{P}_{o,m} \cdot T_A^{MV}(9) \cdot \frac{\partial f_{\Psi}}{\partial P_m^{ZA}} \;\coloneqq\; \frac{\partial \Delta F_m^{XB}}{\partial P_m^{ZA}} \cdot T_B^{MV}(7) + \frac{\partial F_L^{YB}}{\partial P_m^{ZA}} \cdot T_B^{MV}(9)$$

Equation 7.2-21

$$m_m \cdot \dot{P}_{o,m} \cdot T_A^{MV}(9) \cdot \frac{\partial f_{\Psi}}{\partial \dot{P}_{o,m}} \;\coloneqq\; \frac{\partial F_D^{XB}}{\partial \dot{P}_{o,m}} \cdot T_B^{MV}(7) + \frac{\partial F_L^{YB}}{\partial \dot{P}_{o,m}} \cdot T_B^{MV}(9) - \frac{f_{\Psi}}{\dot{P}_{o,m}}$$

Equation 7.2-22

$$m_m \cdot \dot{P}_{o,m} \cdot T_A^{MV}(9) \cdot \frac{\partial f_{\Psi}}{\partial \Theta_A^{MV}} \;\coloneqq\; -\frac{T_A^{MV}(7)}{T_A^{MV}(9)} \cdot f_{\Psi} \;\coloneqq\; \tan \Theta_A^{MV} \cdot f_{\Psi}$$

Equation 7.2-23

7.2.3 Dynamic Constraint - Control Jacobians

The optimiser state variation with pitch incidence,

$$\partial \underline{f}_X / \partial \Theta_B^{MV} := \left(\underline{0}_3^T \ \vdots \ \partial f_V / \partial \Theta_B^{MV} \ \vdots \ \partial f_\Theta / \partial \Theta_B^{MV} \ \vdots \ \partial f_\Psi / \partial \Theta_B^{MV} \right)$$

Equation 7.2-24

$$m_m \cdot \left(\partial f_V / \partial \Theta_B^{MV} \right) := \left(\partial \underline{F}_m^B / \partial \Theta_B^{MV} \right)^T \cdot {}^{147}\underline{\varphi}_B^{MV} - \left(\underline{F}_m^B \right)^T \cdot {}^{369}\underline{\varphi}_B^{MV}$$

Equation 7.2-25

$$m_m \cdot \dot{P}_{o,m} \cdot \left(\partial f_\Theta / \partial \Theta_B^{MV} \right) := \left(\partial \underline{F}_m^B / \partial \Theta_B^{MV} \right)^T \cdot {}^{369}\underline{\varphi}_B^{MV} + \left(\underline{F}_m^B \right)^T \cdot {}^{147}\underline{\varphi}_B^{MV}$$

Equation 7.2-26

$$m_m \cdot \dot{P}_{o,m} \cdot \frac{\partial f_\Theta}{\partial \Psi_B^{MV}} := \left(\frac{\partial \underline{F}_m^B}{\partial \Psi_B^{MV}} \right)^T \cdot {}^{369}\underline{\varphi}_B^{MV} - F_D^{XB} \cdot T_B^{MV}(6) + F_L^{YB} \cdot T_B^{MV}(3)$$

Equation 7.2-27

The optimiser state variation with yaw incidence,

$$\partial \underline{f}_X / \partial \Psi_B^{MV} := \left(\underline{0}_3^T \ \vdots \ \partial f_V / \partial \Psi_B^{MV} \ \vdots \ \partial f_\Theta / \partial \Psi_B^{MV} \ \vdots \ \partial f_\Psi / \partial \Psi_B^{MV} \right)$$

Equation 7.2-28

$$m_m \cdot \left(\partial f_V / \partial \Psi_B^{MV} \right) :=$$

$$\left(\partial \underline{F}_m^B / \partial \Psi_B^{MV} \right)^T \cdot {}^{147}\underline{\varphi}_B^{MV} - F_D^{XB} \cdot T_B^{MV}(4) + F_L^{YB} \cdot T_B^{MV}(1)$$

Equation 7.2-29

$$m_m \cdot \dot{P}_{o,m} \cdot T_A^{MV}(9) \cdot \left(\partial f_\Psi / \partial \Theta_B^{MV} \right) :=$$

$$\frac{\partial F_D^{XB}}{\partial \Theta_B^{MV}} \cdot T_B^{MV}(7) + \frac{\partial F_L^{YB}}{\partial \Theta_B^{MV}} \cdot T_B^{MV}(9) - \left(\underline{F}_m^B \right)^T \cdot {}^{147}\underline{\varphi}_B^{MV}$$

Equation 7.2-30

$$m_m \cdot \dot{P}_{o,m} \cdot T_A^{MV}(9) \cdot \left(\partial f_\Psi / \partial \Psi_B^{MV} \right) :=$$

$$\frac{\partial F_D^{XB}}{\partial \Psi_B^{MV}} \cdot T_B^{MV}(7) + \frac{\partial F_L^{YB}}{\partial \Psi_B^{MV}} \cdot T_B^{MV}(9) - \Delta F_m^{XB} \cdot T_B^{MV}(6) + F_L^{YB} \cdot T_B^{MV}(1)$$

Equation 7.2-31

7.2.4 Aerodynamic Derivatives

The aerodynamic characteristics of different missiles tend to be unique. For the generic missile the external forces and moments are ignored, except for lift generated by incidence, thrust, drag and gravity acting through a point.

$$\frac{\partial \underline{F}_m^B}{\partial P_m^{ZA}} := \left(\frac{\partial \underline{F}_T^{XB}}{\partial P_m^{ZA}} + \frac{\partial \underline{F}_D^{XB}}{\partial P_m^{ZA}} \quad , \quad \frac{\partial \underline{F}_L^{YB}}{\partial P_m^{ZA}} \quad , \quad \frac{\partial \underline{F}_L^{ZB}}{\partial P_m^{ZA}} \right)^T$$

Equation 7.2-32

$$\frac{\partial \underline{F}_m^B}{\partial \dot{P}_{o,m}} := \left(\frac{\partial \underline{F}_D^{XB}}{\partial \dot{P}_{o,m}} \quad , \quad \frac{\partial \underline{F}_L^{YB}}{\partial \dot{P}_{o,m}} \quad , \quad \frac{\partial \underline{F}_L^{ZB}}{\partial \dot{P}_{o,m}} \right)^T$$

Equation 7.2-33

$$\frac{\partial \underline{F}_m^B}{\partial \Theta_B^{MV}} := \left(\frac{\partial \underline{F}_D^{XB}}{\partial \Theta_B^{MV}} \quad , \quad \frac{\partial \underline{F}_L^{YB}}{\partial \Theta_B^{MV}} \quad , \quad \frac{\partial \underline{F}_L^{ZB}}{\partial \Theta_B^{MV}} \right)^T$$

Equation 7.2-34

$$\frac{\partial \underline{F}_m^B}{\partial \Psi_B^{MV}} := \left(\frac{\partial \underline{F}_D^{XB}}{\partial \Psi_B^{MV}} \quad , \quad \frac{\partial \underline{F}_L^{YB}}{\partial \Psi_B^{MV}} \quad , \quad \frac{\partial \underline{F}_L^{ZB}}{\partial \Psi_B^{MV}} \right)^T$$

Equation 7.2-35

Lift forces are expressed as a function of the pitch and yaw incidence lags,

$$\left(F_L^{YB} \quad , \quad F_L^{ZB} \right) := m_m \cdot \left(\dot{P}_{o,m} \cdot T_B^{MV}(4) \,/\, T_I^{YB} \quad , \quad \dot{P}_{o,m} \cdot T_B^{MV}(7) \,/\, T_I^{ZB} \right)$$

Equation 7.2-36

Lateral lift force variation due to missile speed,

$$\frac{\partial F_L^{YB}}{\partial \dot{P}_{o,m}} := \frac{m_m}{T_I^{YB}} \cdot \left(T_B^{MV}(4) - \frac{\dot{P}_{o,m}}{T_I^{YB}} \cdot \frac{\partial T_I^{YB}}{\partial \dot{P}_{o,m}} \right)$$

Equation 7.2-37

$$\frac{\partial F_L^{ZB}}{\partial \dot{P}_{o,m}} := \frac{m_m}{T_I^{ZB}} \cdot \left(T_B^{MV}(7) - \frac{\dot{P}_{o,m}}{T_I^{ZB}} \cdot \frac{\partial T_I^{ZB}}{\partial \dot{P}_{o,m}} \right)$$

Equation 7.2-38

Lateral lift force variation due to pitch incidence,

$$\frac{\partial F_L^{YB}}{\partial \Theta_B^{MV}} := -\frac{m_m \cdot \dot{P}_{o,m}}{T_I^{YB}} \cdot \left(T_B^{MV}(6) + \frac{T_B^{MV}(4)}{T_I^{YB}} \cdot \frac{\partial T_I^{YB}}{\partial \Theta_B^{MV}} \right)$$

Equation 7.2-39

$$\frac{\partial F_L^{ZB}}{\partial \Theta_B^{MV}} := -\frac{m_m \cdot \dot{P}_{o,m}}{T_I^{ZB}} \cdot \left(T_B^{MV}(9) + \frac{T_B^{MV}(7)}{T_I^{ZB}} \cdot \frac{\partial T_I^{ZB}}{\partial \Theta_B^{MV}} \right)$$

Equation 7.2-40

Lateral lift force variation due to yaw incidence,

$$\frac{\partial F_L^{YB}}{\partial \Psi_B^{MV}} := \frac{m_m \cdot P_{o,m}}{T_I^{YB}} \cdot \left(T_B^{MV}(1) - \frac{T_B^{MV}(4)}{T_I^{YB}} \cdot \frac{\partial T_I^{YB}}{\partial \Psi_B^{MV}} \right)$$

Equation 7.2-41

$$\left(T_I^{YB}\right)^2 \cdot \frac{\partial F_L^{ZB}}{\partial \Psi_B^{MV}} := -m_m \cdot P_{o,m} \cdot T_B^{MV}(7) \cdot \frac{\partial T_I^{ZB}}{\partial \Psi_B^{MV}}$$

Equation 7.2-42

7.3 Missile Controls

The trajectory is optimised by adjusting a set of admissible controls comprising pitch and yaw incidences, launcher angles, and impact time,

$$\underline{U} \equiv \left(\underline{U}_C \vdots \underline{U}_L \vdots U_T \right)$$

Equation 7.3-1

$$\underline{U} := \left(\underline{\Theta}_B^{MV} , \underline{\Psi}_B^{MV} \vdots \Theta_A^B(0) , \Psi_A^B(0) \vdots t_F \right)$$

Equation 7.3-2

The number of controls must be large enough to accommodate Euler integration and still approach the optimal solution commensurate with real-time operation. Using (N := 100) controls to partition the boost and coast phases,

$$N := N_B + N_C := \frac{t_B}{0.1} + \frac{100 - N_B}{t_F - t_B}$$

Equation 7.3-3

It is important that a boundary between controls coincides with the nominal boost time (t_B). As the autopilot uses the coast phase controls the remainder

split when only half remain to improve integration accuracy as the time-to-go decreases, Moody[M12]. The initial flight controls, and the impact time, are obtained by integrating the missile and target dynamics over the control boundaries using ATPN guidance with the launcher pointing directly at the target. As the impact time is free the duration of the flight coast phase controls are scaled accordingly. The controls are related to the lateral acceleration commands by the incidence lag as shown in Equation 7.2-36,

$$ {}_{OP}\underline{\alpha}_D^B \equiv \left({}^D A_m^{YB} \quad , \quad {}^D A_m^{ZB} \right)^T := m_m^{-1} \cdot \left(F_L^{YB} \quad , \quad F_L^{ZB} \right)^T $$

Equation 7.3-4

7.4 Cost Function

Constrained optimisation is widely studied under the heading of Bolza problems, a combination the Mayer problem for optimising terminal values, and the Lagrangian problem optimising a combination of process variables from the current time to impact,

$$ J := \phi\left(\underline{X}\left(t_F \right), t_F \right) + \int_t^{t_F} L\left(\underline{X}(\tau), \underline{U}_C(\tau), \tau \right) \cdot d\tau $$

Equation 7.4-1

Consider the individual components of the cost function dealing with the terminal state,

$$ \phi := \sum_i \eta_i \cdot \phi_i $$

Equation 7.4-2

Each term in the cost function is scaled by a constant (η_i) to accommodate activation and weighting. The cost is determined in *COST_FUNCTION* that invokes state integration to determine the state, and *OP_MS_DXDT* for the state derivatives over the control steps. The state and control Jacobians associated with each element in the cost function are defined next.

7.4.1 Time to impact

$$ \phi_1 := t_F $$

Equation 7.4-3

$$ \left(\partial\phi_1 / \partial \underline{X} \quad , \quad \partial\phi_1 / \partial \underline{U}_C \right) := \left(\underline{0}_6^T \quad , \quad \underline{0}_2^T \right) $$

Equation 7.4-4

Minimisation of time-to-go on its own results in bang-bang controls at the beginning of the flight as the missile tries to establish a collision course,

Yang[Y.8]. In more practical applications the cost is a balance between impact time, impact speed, miss distance, control effort, etc.

7.4.2 Impact speed

$$\phi_2 \coloneqq -\dot{P}_{o,m}\left(t_F \right)$$

Equation 7.4-5

$$\left(\partial\phi_2 / \partial \underline{X} \quad , \quad \partial\phi_2 / \partial \underline{U}_C \right) \coloneqq \left(\left(\underline{0}_3^T \quad , \quad -1 \quad , \quad \underline{0}_2^T \right) \quad , \quad \underline{0}_2^T \right)$$

Equation 7.4-6

7.4.3 Miss distance

$$\phi_3 \coloneqq \left(P_{m,t}^{XA} \right)^2 + \left(P_{m,t}^{YA} \right)^2 + \left(P_{m,t}^{ZA} \right)^2$$

Equation 7.4-7

$$\underline{P}_{m,t}^{A} \coloneqq \underline{P}_t^A\left(t_F \right) - \underline{P}_m^A\left(t_F \right)$$

Equation 7.4-8

$$\left(\partial\phi_3 / \partial \underline{X} \quad , \quad \partial\phi_3 / \partial \underline{U}_C \right) \coloneqq$$

$$\left(\left(-2 \cdot P_{m,t} \cdot \left(\underline{P}_m^A \right)^T \quad , \quad \underline{0}_3^T \right) \quad , \quad \underline{0}_2^T \right)$$

Equation 7.4-9

7.4.4 Control effort

$$\phi_4 \coloneqq \left(\Psi_B^{MV} \right)^2 + \left(\Theta_B^{MV} \right)^2$$

Equation 7.4-10

$$\left(\partial\phi_4 / \partial \underline{X} \quad , \quad \partial\phi_4 / \partial \underline{U}_C \right) \coloneqq \left(\underline{0}_6 \quad , \quad 2 \cdot \left(\Theta_B^{MV} \quad , \quad \Psi_B^{MV} \right) \right)$$

Equation 7.4-11

7.4.5 Approach angle

Minimising the head-on aspect angle at impact increases the kill probability. For a target travelling towards the missile,

$$\phi_5 \coloneqq \cos^{-1}\left(-\hat{\underline{n}}\left(\dot{\underline{P}}_t^A \right) \bullet {}^{147}\underline{\varphi}_A^{MV} \right)$$

Equation 7.4-12

7.5 Dynamic Constraints

The cost function is minimised subject to the dynamic equality constraints,

$$\underline{X}_k - \underline{X}_{k+1} + \left(\underline{f}_X \right)_k \cdot \Delta t_k \quad := \quad \underline{0}$$

Equation 7.5-1

The high incidence cost is already accounted for in the control effort. An active set strategy is used in conjunction with control hard limiting for the gradients. The remaining constraints are of the form,

$$h\left(\underline{X} \right) \quad \leq \quad c$$

Equation 7.5-2

This can be converted to an equality constraint using a slack variable,

$$s > 0 \quad \Rightarrow \quad h\left(\underline{X} \right) + s^2 - c \quad := \quad \underline{0}$$

Equation 7.5-3

Of the many constraints that may be applied two stand out in importance for air-defence:

7.5.1 Up-link communications

To maintain up-link communication the LOS to the missile must remain within the missile receiver beam width. Assuming that the missile is travelling away from the launcher and the limit for communication purposes is (ξ_C),

$$h_1 \quad := \quad \left(\cos^{-1}\left(\hat{\underline{n}}\left(\underline{P}_m^A \right) \bullet {}^{147}\underline{\varphi}_A^{MV} \right) \right)^2 \quad \leq \quad \xi_C$$

Equation 7.5-4

The cost is squared to heavily penalise excursions beyond the threshold.

7.5.2 Avoidance regions

If the region to be avoided is centred at point (j) and extends spherically a distance R_J,

$$h_2 \quad :=$$

$$-\left(P_{m,j}^{XA} \right)^2 - \left(P_{m,j}^{YA} \right)^2 - \left(P_{m,j}^{ZA} \right)^2 \quad \leq \quad -R_J^2 \quad ; \quad \underline{P}_{m,j}^A \quad := \quad \underline{P}_{o,j}^A - \underline{P}_{o,m}^A$$

Equation 7.5-5

7.6 TPBVP Formulation

Minimising the cost function by adjusting the control sequence is replaced by the simpler problem of minimising a scalar Hamiltonian that depends on boundary conditions only. Thus the constrained TPBVP is reduced to the unconstrained minimisation of a Hamiltonian function. Pontryagin theory is used to reformulate the open-loop solution into a classical control law by relating the controls to state observer parameters, in this case using Equation 7.3-4. The Hamiltonian is formed by combining the cost function, dynamic constraints using Lagrangian multipliers ($\underline{\lambda}$), and inequality constraints using co-state variables ($\underline{\mu}$),

$$H \coloneqq \phi + \underline{\lambda}^T \cdot \underline{f}_X + \underline{\mu}^T \cdot \left(\underline{h} + \underline{s} \otimes \underline{s} - \underline{c} \right)$$

Equation 7.6-1

The Kuhn-Tucker 1st order conditions to be satisfied on an optimum trajectory,

$$\frac{\partial H}{\partial \underline{X}} \coloneqq \frac{\partial \phi}{\partial \underline{X}} + \underline{\lambda}^T \cdot \frac{\partial \underline{f}_X}{\partial \underline{X}} + \underline{\mu}^T \cdot \frac{\partial \underline{h}}{\partial \underline{X}} \coloneqq \underline{0}$$

Equation 7.6-2

$$\frac{\partial H}{\partial \underline{U}} \coloneqq \frac{\partial \phi}{\partial \underline{U}} + \underline{\lambda}^T \cdot \frac{\partial \underline{f}_X}{\partial \underline{U}} + \underline{\mu}^T \cdot \frac{\partial \underline{h}}{\partial \underline{U}} \coloneqq \underline{0}$$

Equation 7.6-3

$$\frac{\partial H}{\partial \underline{\lambda}} \coloneqq \underline{f}_X \coloneqq \underline{0}$$

Equation 7.6-4

$$\frac{\partial H}{\partial \underline{s}} \coloneqq \underline{0} \Rightarrow \underline{\mu}^T \left(\underline{c} - \underline{h} \right) \coloneqq \underline{0}$$

Equation 7.6-5

The optimiser states are propagated using Euler integration over the remaining controls [n(1)N-1], control limits applied, and the Hamiltonian Jacobians determined for each control. For proof of principle the discrete equations that follow involve only the dynamic equality constraints. Modifying the discrete equations in Vorley[V.4] to deal with the remaining controls, the transversality conditions at impact,

$$\underline{\lambda}_{N-1} \coloneqq \left(\partial \phi / \partial \underline{X} \right)_N^T$$

Equation 7.6-6

The Euler-Lagrange equations are propagated backwards to obtain the adjoint variables,

$$k \in \left[N-1(1)n+1 \right] \Rightarrow \underline{\lambda}_{k-1} := \left(I + \Delta t \cdot \left(\frac{\partial \underline{f}_X}{\partial \underline{X}} \right)_k^T \right) \cdot \underline{\lambda}_k$$

Equation 7.6-7

7.7 Gradients

The elements of the reduced gradient,

$$\underline{g} \equiv \left(\frac{\partial H}{\partial \underline{U}} \right)^T := \left(\frac{\partial \phi}{\partial \underline{U}} - \frac{\partial \phi}{\partial \underline{X}} \left(\frac{\partial \underline{f}_X}{\partial \underline{X}} \right)^{-1} \cdot \frac{\partial \underline{f}_X}{\partial \underline{U}} \right)^T$$

Equation 7.7-1

$$k \in \left[n(1)N-1 \right] \Rightarrow \left(\frac{\partial H}{\partial \underline{U}_k} \right)^T := \Delta t \cdot \left(\frac{\partial \underline{f}_k}{\partial \underline{U}_k} \right)^T \cdot \underline{\lambda}_k$$

Equation 7.7-2

$$\left(\frac{\partial H}{\partial \underline{X}_0} \right)^T := \left(I + \Delta t \cdot \left(\frac{\partial \underline{f}_0}{\partial \underline{X}_0} \right)^T \right) \cdot \underline{\lambda}_0$$

Equation 7.7-3

$$\frac{\partial H}{\partial t_N} := \frac{\partial \phi}{\partial t_N} + \frac{1}{N} \cdot \sum_{k:=n}^{N-1} \left(\underline{f}_k^t + t_n \cdot \left(\frac{\partial \underline{f}_k}{\partial t_k} \right)^T \right) \cdot \underline{\lambda}_k$$

Equation 7.7-4

Equation 7.7-3 is applicable when all the controls are available prior to launch and the launcher angles are optimised. If the gradient at a particular step results in a control exceeding the limit, the gradient for that control is set to zero, the control to its limit, and optimisation proceeds over the unbounded set of controls. The gradients with respect to optimiser states, controls and terminal time are provided by *GRADIENT*. This invokes *OP_MS_DXDU* for the variation in state derivatives with respect to the controls, and *OP_MS_DXDX* for their variation with respect to the states. The gradients are scaled in *GRADIENT_SC*, and the direction of steepest descent in *STEEPEST_DD*.

7.8 Search Direction

Rapid initial convergence from the PN trajectory and in response to changing boundary conditions is required. Slow convergence to an optimal trajectory thereafter is less import compared with the ability to respond rapidly to target manoeuvres. The selection of the search direction is a crucial factor in the stability and efficiency of optimisation techniques for minimising the Hamiltonian function. A review of the development of optimisation algorithms is provided by Bazaraa[B.4], including an extensive bibliography.

Techniques for selecting the search direction using derivative information are better suited to the current application, although direct searches are more robust in an off-line capacity. Gradient-based techniques update the system states and controls by taking a step of length (α) in the direction ($\underline{d}$) defined by the inverse Hessian $[B]^{-1}$ and gradient vector ($\underline{g}$),

$$\underline{X}_{k+1} := \underline{X}_k - \underline{d}$$

Equation 7.8-1

$$\underline{X}_{k+1} := \underline{X}_k - \alpha \cdot \left[B \right]^{-1} \cdot \underline{g}$$

Equation 7.8-2

Techniques requiring Hessians such as the class of Variable Metric Methods converge more rapidly than gradient based alternatives. However, they involve numerical differencing of non-linear aerodynamic functions, and possible ill-conditioning if penalty or barrier functions are used. Early optimisation algorithms were prone to premature termination, divergence and cycling. Wolfe introduced three rules associated with the length travelled along the search direction to prevent these effects, conditions that ensure that the magnitude of the gradient ($\underline{g}$) reduces for twice differentiable convex functions.

WOLFE CONDITION 1

$$\underline{g} \bullet \underline{d} = -\underline{g}^T \cdot \left[B \right]^{-1} \cdot \underline{g} > -\varepsilon_1 \cdot \left\| \underline{g} \right\| \cdot \left\| \underline{d} \right\|$$

Equation 7.8-3

This condition ensures that the direction chosen ($\underline{d}$) is close to the initial gradient ($\underline{g}$) by selecting a small value, typically ($\varepsilon_1 := 0.001$).

WOLFE CONDITION 2

$$\left| \underline{g}_{k+1} \bullet \underline{d}_k \right| \leq \varepsilon_2 \cdot \left| \underline{g}_k \bullet \underline{d}_k \right|$$

Equation 7.8-4

This condition ensures that the step length chosen results in a new gradient that is > 0 but < ($\varepsilon_2 := 0.5$) with respect to the initial gradient.

WOLFE CONDITION 3

$$H\left(\underline{X}_k\right) - H\left(\underline{X}_{k+1}\right) \;\geq\; -\varepsilon_3 \cdot \alpha \cdot \left(\underline{d}_k \bullet \underline{g}_k\right)$$

Equation 7.8-5

This condition ensures that the function value is less than that its initial value using ($\varepsilon_3 := 0.0001$) to prevent cycling. With this value the function must be reduced by 0.01% of the linear prediction. This condition is automatically satisfied in Steepest Descent if ($\varepsilon_1 := 1$ and $\varepsilon_2 := 0$).

7.8.1 Newton - Raphson Method

For Steepest Descent, [B] is replaced by the identity matrix [I]. This is the simplest of the gradient-based algorithms and is used to initialise many other more complex algorithms. Minimisation in function space using an inexact line search is conceptually simple, computationally efficient, robust away from an optimum solution. Improvement at each step is generally assured and accommodating control constraints is simple. Detrimentally, convergence close to an optimal solution is slow and prone to "zig-zagging", although this should not be a problem given continually changing boundary conditions.

7.8.2 Conjugate Gradient Method

Conjugate Gradient methods are often selected as an alternative to Newton-Raphson methods if Hessians are unavailable. The method searches along "n-1" conjugate directions following a steepest-decent step,

$$\left(k \neq j\right) \wedge \left(k, j\right) \in \left[1\left(1\right)n\right] \;\Rightarrow\; \underline{d}_k^T \cdot \left[G\right] \cdot \underline{d}_j \;:=\; 0$$

Equation 7.8-6

$$k \in \left[1\left(1\right)n-1\right] \;\Rightarrow\; \underline{d}_k \;:=\; \underline{g}_k + \beta_k \cdot \underline{d}_{k-1}$$

Equation 7.8-7

The use of inexact line searches can lead to slow convergence. For non-quadratic functions convergence takes more than (n) iterations and the process must be restarted when (k := n), generally using a steepest-decent step. *CONJ_GRADIENT* uses an implementation of Shanno's Conjugate Gradient method recommended by Vorley[V.4], a memoryless quasi-Newton algorithm modified for constraints in conjunction with a Fibonacci search. This algorithm is used to examine alternative directions when the cost reduction using the steepest-descent method begins to slow.

7.9 Univariate Search and Termination

For locating local minima, directed searches and polynomial fitting techniques are generally superior to methods based on function evaluations that have a linear rate of convergence. Univariate minimisation for this application is performed in the presence of constraining hyper-planes bounding the feasible region. Methods that requiring data beyond a constraining plane must limit the step length to stay in the feasible region even if the minimum lies beyond it. The cost function is thus a complex curve close to a boundary, particularly if penalty functions are used.

7.9.1 Fibonacci

FIBONA_LS performs a Fibionacci univariate line search minimising a convex cost function along a conjugate gradient direction, a combination that ensures stability of the optimisation process. It uses a fixed number of function evaluations to locate the minimum given a specified uncertainty bound - note apriori knowledge of the number of function evaluations is required. This method gives the optimal interval reduction for a given number of function evaluations.

7.9.2 Armijo

ARMIJO_LS performs an Armijo inexact line search guaranteeing a minimum reduction in the function and hence convergence,

$$\underline{X}_{k+1} = \underline{X}_k - \left(0.5\right)^m \cdot \left[B\right]^{-1} \cdot \underline{g}$$

Equation 7.9-1

(m) must satisfy Wolfe Condition 3, whilst (m-1) does not, starting with a Newton step when (m) is zero. Bazaraa[B.4] provides a proof of convergence when this technique is used to search in the steepest-descent direction.

7.10 Algorithm Implementation

Figure 7-2 encapsulates the major elements of the optimisation algorithm. The cycle is packed into the duration of the next control step before it is used by the missile autopilot. Any “spare” time is used for cost reduction and control updates. During line searches the boundary conditions remain unchanged. The steepest-descent direction, selected for its simplicity with an Armijo search to determine step length (α), results in the control update,

$$\underline{U}_{k+1} := \underline{U}_k - \alpha \cdot \frac{\partial H}{\partial \underline{U}_k}$$

Equation 7.10-1

As the steepest-decent cost reduction slows, a conjugate gradient search direction is used to explore cost reductions normal to the steepest-decent

direction using a Fibonacci search to determine step length (α) resulting in a control update,

$$\underline{U}_{k+1} \coloneqq \underline{U}_k - \alpha \cdot \Xi_k$$

Equation 7.10-2

$$\Xi_k \coloneqq \left(\frac{\partial H}{\partial \underline{U}_k} \right)^T - \left(\frac{\frac{\partial H}{\partial \underline{U}_k} \cdot \left(\frac{\partial H}{\partial \underline{U}_k} \right)^T}{\frac{\partial H}{\partial \underline{U}_{k-1}} \cdot \left(\frac{\partial H}{\partial \underline{U}_{k-1}} \right)^T} \right) \cdot \Xi_{k-1}$$

Equation 7.10-3

OP_LIMITS limits the control change allowed between iterations improving the stability of the optimisation process. Gradient scaling is crucial for good performance since for this application the parameters involved used have a large dynamic range. To accelerate line searches experience indicates that the number of cost evaluations in any direction should be ≤ 5, Moody[M.12]. Post launch no stopping conditions are required since the controls are used by the autopilot. If the optimisation is terminated without completion the previous controls and gradients are re-instating.

7.11 Trajectory Optimisation Simulator

The optimisation simulator shown in Figure 7-3 is embedded in the missile simulator. The modules performing the optimisation functions in this figure are highlighted in bold and placed in parentheses. The numbers identifying certain blocks represent the order in which the functions are performed.

Setting *GU_DM_TP* to zero activates the missile trajectory optimisation bypassing the conventional guidance laws. The optimiser defaults and initialisation are performed by *D_OPTIMER* and *I_OPTIMISER*, even if the facility is not subsequently activated. The TPBVP can be formulated using either reference or missile state observer data. Counting numerical operations to establish the processor load is inaccurate and fails to account for overheads associated with data communication, storage and algorithm control etc. Instead, the simulation increments a process timer latched to the hosts Central Processing Unit clock. Scaling the process timer controls the amount of processing power available to the optimiser. As the scale factor increases more processing time is allowed until eventually a near-optimal result is obtained that is very-nearly equivalent to static re-optimisation.

7.12 Discussion

The guidance module in the missile simulator provides the building blocks for PN and CLOS guidance laws. If none are selected the program invokes on-line trajectory optimisation. The optimisation process is latched to the host's processor clock to study the effect of limiting the available processing time. For example if the next control to be taken by the autopilot last for 0.5 s re-optimisation of the missile controls is allowed for precisely this amount of time. For this to be meaningful the algorithms must be written efficiently. Critical parameters must be stored at the beginning of each cycle in case the re-optimisation is prematurely terminated. Because the algorithms are to be executed in real-time, global optimisation algorithms currently in favour such as simulated annealing and shooting methods are inappropriate. Given the recent increase in computing capacity some of the simpler early optimisation techniques have been selected.

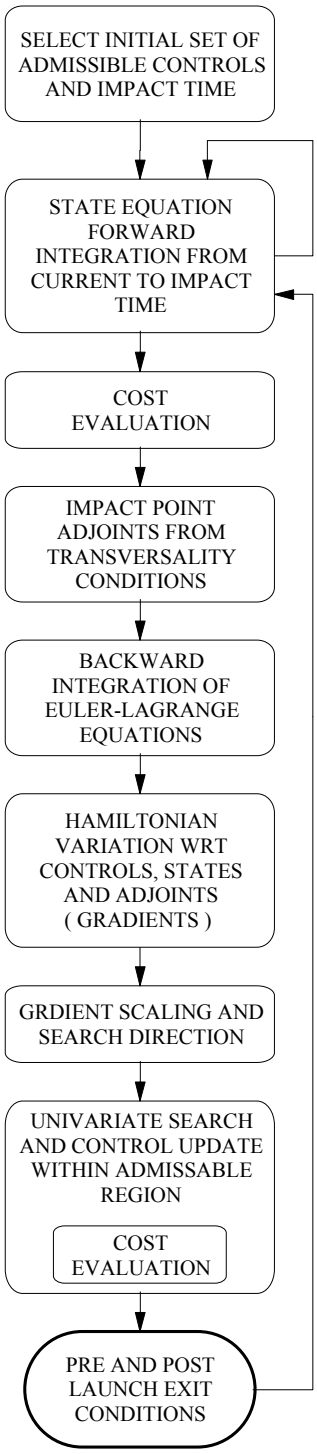

Figure 7-2

Optimisation Flowchart

Gradient techniques have proven to be robust for real-time optimisation given a reasonable set of initial controls, Moody[M.12]. Propagating the dynamic equations using ATPN with the missile initially pointing at the target providing the initial trajectory. The optimiser state space selected to define the missile dynamics was Cartesian position, speed and direction with respect to the earth referenced Alignment frame. The terms in the cost function and adjoined dynamic constraints can be weighted depending on target characteristics providing a more flexible system. Gradient projection in function-space along the direction of steepest-descent with an Armijo univariate search minimising the cost function is the primary algorithm. If cost reduction stalls a conjugate directions are explored using an exact Fibonnacci search. The line search step-length is doubled, or halved, depending on cost function values to accelerate the search for a local minimum.

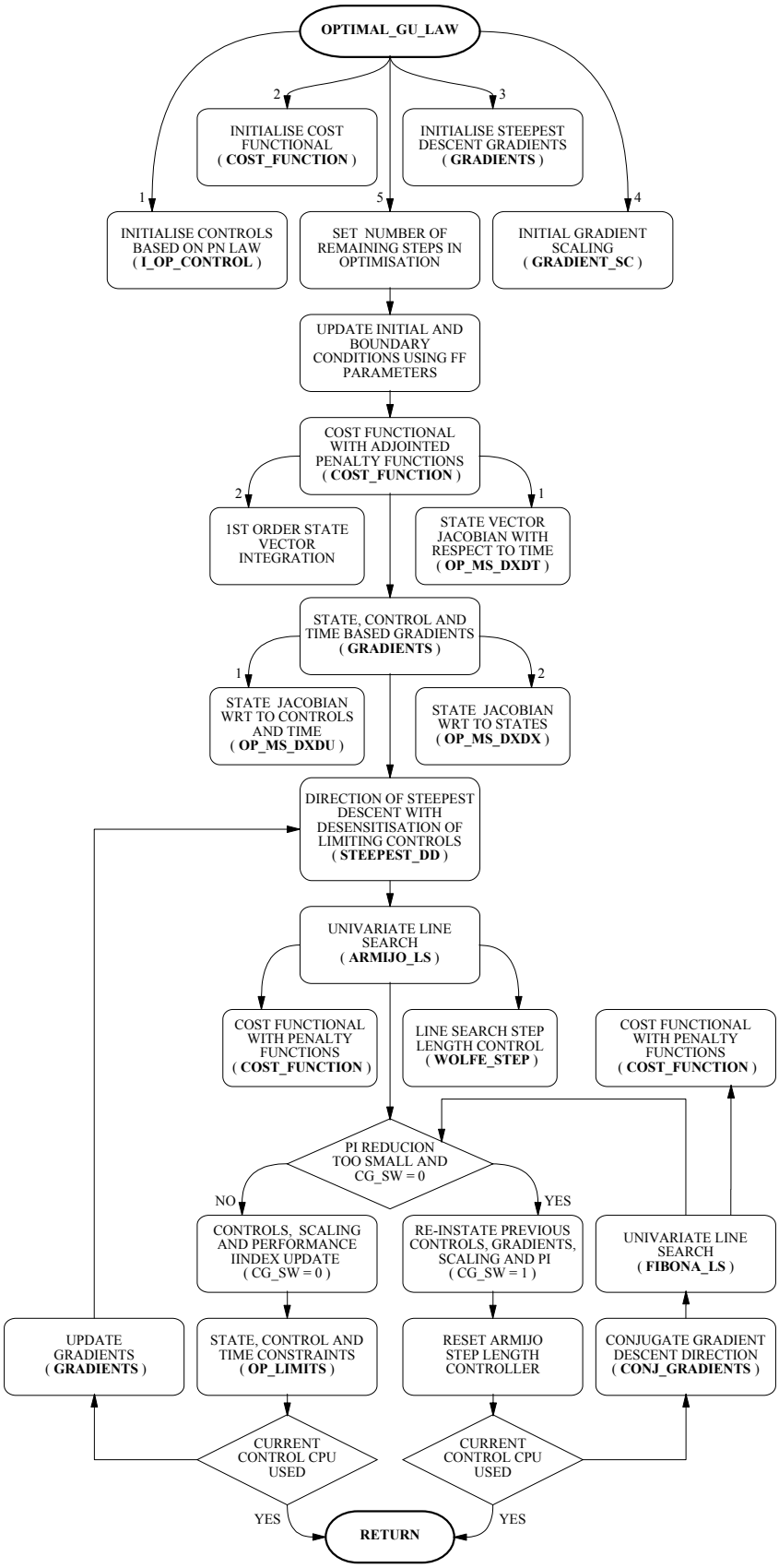

Figure 7-3 : Trajectory Optimisation Simulator

Changes in the controls are limited between optimisation cycles to make the optimisation process more robust. These controls are then converted into guidance demands for fire control, launcher steering and in-flight manoeuvring. Validation of the optimiser can be undertaken once the noise characteristics associated with the boundary conditions provided by the state observers are known. This work will:

- Consider each contribution to the cost function in turn and compare the trajectory produced by the optimiser, wherever possible with analytic results, and with the baseline results presented in this document.
- Quantify any increase in target capture region compared with conventional guidance alternatives.
- Investigate the convergence rate from the initial trajectory and review other alternatives such as keeping the controls at zero and pointing the launcher at the predicted intercept point.
- Assess convergence rates as a function of processor load to determine if on-line optimisation is feasible with current processors.
- Systematically add cost function elements and dynamic constraints to determine if in combination they prevent the optimiser from converging to a sensible solution. If so, can the cost weights be re-balanced, or be made trajectory dependent, to avoid the conflicts.

Chapter 8

SIMULATION

This chapter expands on the growing role of simulation in the context of modern weapon systems design that was started in the Introduction. Reliance on simulation for performance assessment and application software testing is discussed in conjunction with the AMIS.

The discussion then focuses on the simulation infrastructure that was designed to support dynamical models with state integration, in particular the simulators described in previous chapters. Interaction between the simulators is considered in the context of data communication between models, internal and external data handling facilities.

The program infrastructure is described with the aid of flowcharts capturing the functionality provided and the hierarchical control exercised over key elements. In the first instance the simulation decomposes, as do most simulations, into initialisation and in-run functions. Initialisation comprises general and application specific internal default data, followed by external user characterisation, in the main associated with system clocks and output file handling.

The I/O file control structure, and the content of the files, is presented in the form of a user guide. This covers the mandatory data required, and the scope for user defined changes to the default data during initialisation and in-run. Of particular interest is the automated hardcopy data output, and the selection of data for MATLAB post-processing. The in-run structure is more rudimentary, covering integration algorithms and structure supporting the dynamic models and associated state machine.

The interactive program controller, data visualisation and statistical tracking, data change facility, in-run graphics and wire frame presentation are designed as separate facilities to be used in simulations containing a central variable store. These facilities are described, and in the case of the wire frame model, characterisation for this application.

8.1 The Role of Simulation

The current expectation of a Customer is to fund a limited number of trials thereby obtaining sufficient data to validate a sophisticated simulation. The simulation is then used to provide performance assessments over the entire missile and launcher operation envelope. After delivery of a weapon system these simulations are often used to assess proposed enhancements leading to mid-life updates.

Sub-system models capable of delivering accurate performance predictions for modern weapon systems are usually highly complex. The multinational nature of today's weapon programs means that validated sub-system models are often provided by sub-contractors. Whilst produced with contractually agreed interfaces, and to an agreed accuracy, they all too often ignore computational load when used at the system performance level. The solution to this is a simulation that supports alternative sub-system models with different levels of complexity.

Automatic weapon selection with the highest kill probability from a range of ordnance demands communication between the launcher and the missile through high bandwidth digital links. No longer can simulations be isolated to the missile, or the launcher, they must encompass pre-launch targeting, fire solutions, and post launch communication in multiple target environments. As a consequence both simulation cost and development duration have increased. By taking advantage of the synergy between weapon systems this may be reduced, particularly in the air-launched environment where a single aircraft may support a number of missile types.

Missile software is becoming so complex that it must be tested in a simulation capable of stimulating embedded missile code. The downside is how to verify that the application software replicates algorithms designed to meet the weapon system technical requirements. Alternatively, application software can be modelled independently and used to generate input stimuli and reference outputs. This data is then used to verify that application software is functioning correctly using an off-line test harness that proves only that isolated test entities are functioning correctly. Further testing is needed on target processors, or HWIL facilities, to resolve timing and integration issues. These are interim solutions awaiting reliable automatic code generation from simulation models used to prove the design.

8.2 The Scope of Modern Simulation

The office of the US Secretary for Defense is supporting an initiative whereby simulation is used to reduce risk prior to Contract issue, the first project being the JSF. The aim of this initiative is to identify conflicting system requirements, assess requirements against risk, capability vs affordability, and the development of large system architectures.

The complexity of modern missiles is radically altering the role of simulation. Historically, relatively simple simulations were required for proof of principle, and limited provision of performance data. This would be undertaken during a development phase lasting perhaps 6-8 years encompassing HWIL testing, captive carry data analysis and live firing telemetry. Today's weapons have operational capacities beyond the available funds to support live firing proof of performance. Thus simulation has become an indispensable tool for design proving aimed at reducing program development to 4-5 years, and for supporting weapon qualification. Simulations validated against HWIL and a limited number of flight trials are now Contract deliverable items, their results being used to support certification over the entire flight envelope.

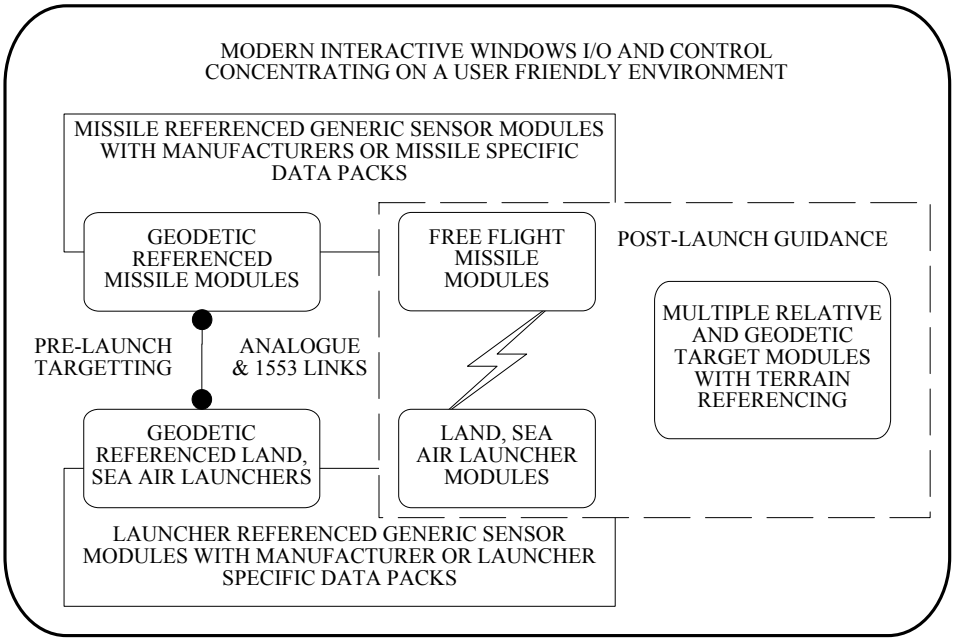

Figure 8-1 : Integrated Simulation Concept

Post-launch 6 DoF missile simulations, with little or no interaction with the launcher, tend to dominate during the bid and development stages of a weapon system. The increase in pre-launch functionality, and in-flight guidance of air-launched missiles, demands more of today's simulations. Although the two phases of an engagement still tend to be treated in isolation, the time is fast approaching when the pre-launch simulation will be the tool of choice containing a free-flight phase. This reversal of dominance is being driven by the TFA of medium and long-range missiles, rear hemisphere targeting of short-range air-to-air missiles, and launcher fly-out models allied to fire control solutions. Figure 8-1 captures the essence of this role reversal with pre and post launch phases contained within a single entity. The digital and analogue data links between the launcher and missile being modelled so that the ability to transmit digital messages to the missile once launched is retained.

8.3 The AMIS Philosophy

Increased functionality, validation, maintenance and configuration control of simulations is becoming a limiting factor preventing significant reductions in development times. Fundamental change is required in the approach to weapon system simulation design. Simulations based on the concept shown Figure 8-2 are required capable of supporting different launchers and missiles, embedded in a common reference environment.

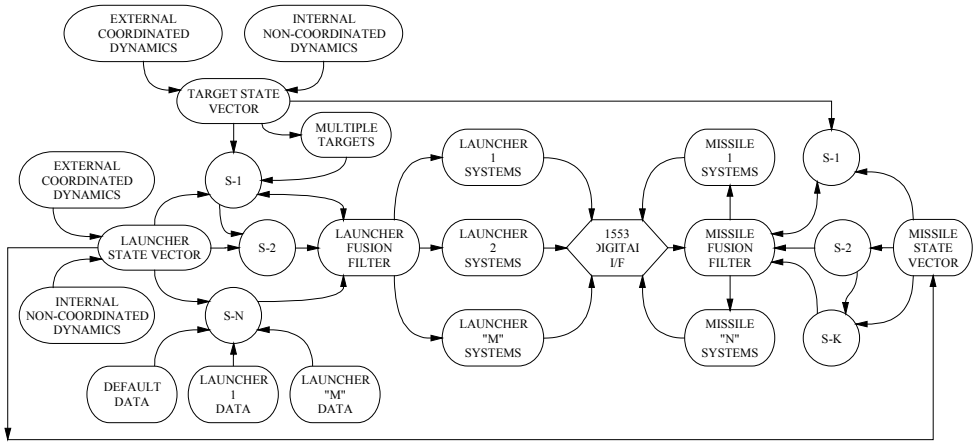

Figure 8-2 : Multiple Launcher and Missile Concept

Their complexity is such that the use of a GUI is essential to shorten learning curves by reducing control and data presentation to a process of selection from drop down menus in a Windows environment.

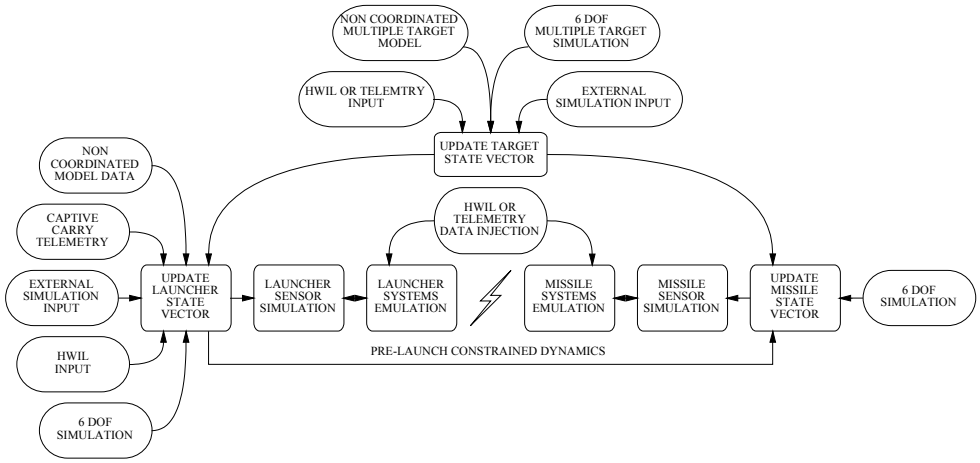

Figure 8-3 : Stimuli for the Multiple Launcher and Missile Concept

The AMIS was developed with the capacity for adding modules representing air, sea and land launchers and missiles, isolated as required by national and commercial security considerations. In the AMIS the generic systems are pitted against terrain referenced targets, non co-ordinated targets with respect to the launcher, and co-ordinate targets visualised as wire frame models as shown in Figure 8-3.

A suite of sensor models denoted by (S-*) is provided in the launcher and missile, activated depending on application. The launcher and missile sensor suites can be loaded with application specific data representative of particular weapon systems, data that can be changed during initialisation or interactively during program execution. The sensor suites operate in a common reference environment that is controlled using a Windows interface with menu and button selections invoking performance, design and analysis tools.

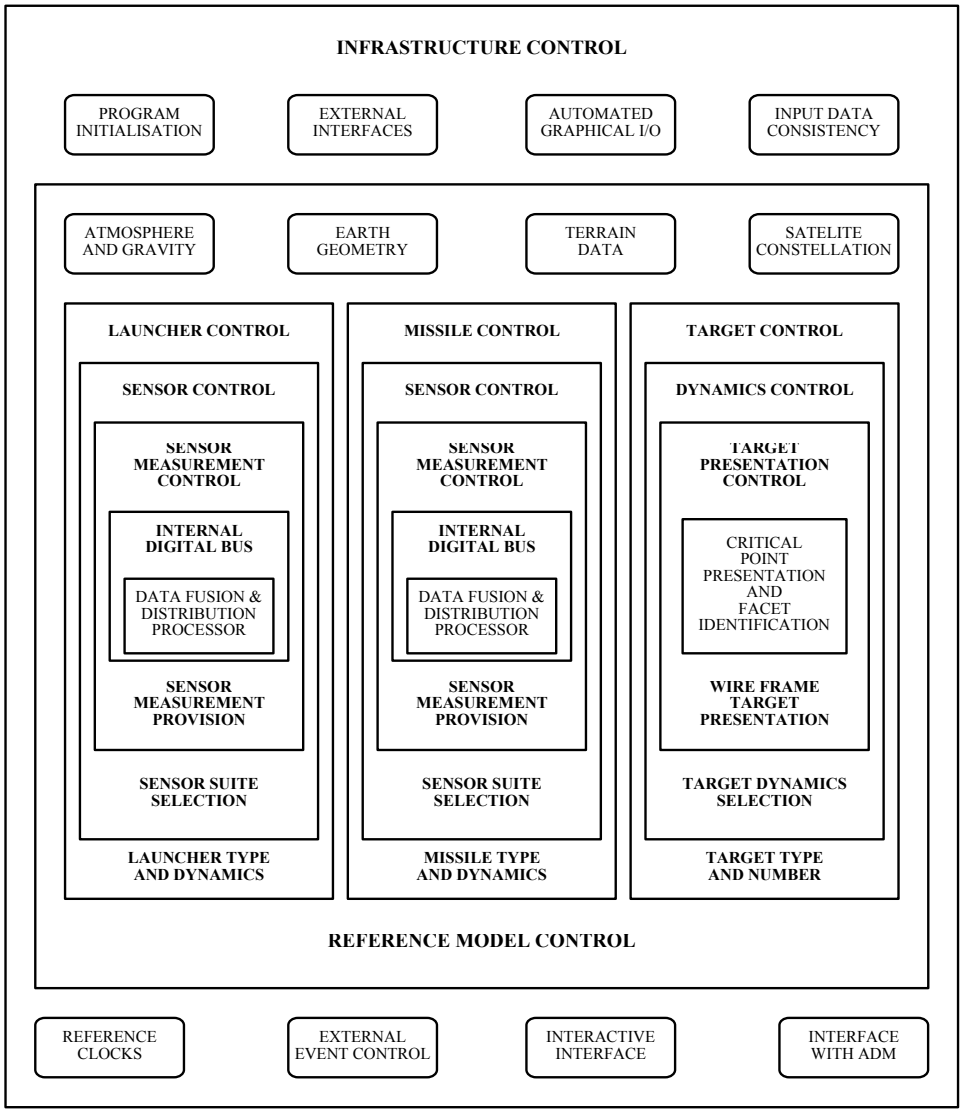

Figure 8-4 : Launcher, Missile and Target Functional Decomposition

The AMIS decomposes naturally into the infrastructure shown in Figure 8-4 dealing with initialisation, I/O facilities, external interfaces and non-core facilities controlled from the top most level. The core models in this common reference environment comprise launcher, missile and targets, with space based satellite constellation and terrain referencing facilities.

Having philosophised over an integrated approach to weapon system development, the remainder of §8 focuses on the simulation infrastructure provided for this research from which the AMIS was developed.

8.4 The Research Simulation Infrastructure

The program is a single entity whose modular design supports a number of simulators embedded in the infrastructure at the level of state derivative provision:

- Target trajectory simulator with airframe visualisation
- Sensor simulator
- Target state observation
- Missile state observation
- Missile model with conventional guidance
- Missile model with trajectory optimisation

The hierarchical nature of these "simulators", each incorporating the functionality of those preceding it, and the program controls isolating them, are shown in Figure 8-5.

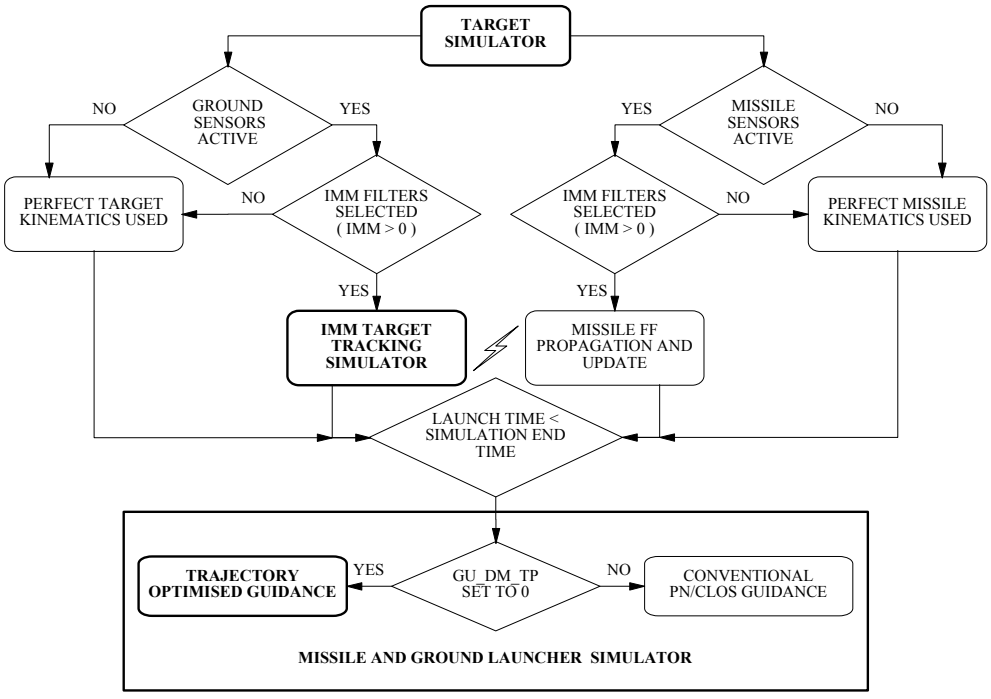

Figure 8-5 : Application Software - Embedded Simulators

The algorithms, isolating controls, pre-requisite and default data for each simulator are dealt with in detail in §2 to §7.

8.5 Internal Data Communication between Software Modules

Communication between modules, other than utilities, is performed using a global pool of variables, the "global common block (GCB). These data are defined in isolated code segments, compiled into the relevant modules using the *INCLUDE* statement, and include variable definitions, scaling factors and units used for automated I/O. The major program variables required for data logging and windows display are contained in the GCB defined in code segment *COMMON.FTN*. Here variables are mapped to a location in a 64 bit real vector, or a 32 bit integer vector. Logical and character types are not supported since they require conversion for automated I/O purposes. This code segment also contains an initialisation flag, typed utility functions, work variables, vectors and matrices that are available for local use in each module containing it. Data is automatically "SAVED" between invocations. The use of a GCB, contrary to the usual software ethos based on argument lists, was adopted to promote:

- Rapid software development
- Consistent use of unique variable names and units
- Use of general plotting, printing and data management facilities
- Interactively changing variables prior to, and during, execution
- Interactive parameter browsing and plotting facilities

Supporting the GCB are subsidiary common blocks dealing with data transfer between modules comprising localised functionality, or parameters that are not required for data logging, or windows visualisation. These additional common blocks have the extension "*.FTN", their purpose being:

- `COMAER`: Missile aerodynamics and their derivatives
- `COMCNG`: User defined in-run change data
- `COMGEN`: Transformation matrices, random seeds, etc.
- `COMGPS`: GPS sensor local common block
- `COMMAP`: DLMS map data
- `COMOPT`: Missile trajectory optimisation data
- `COMSFF`: Tracking and Missile Observer data
- `COMTWF`: Target wire frame model data
- `COMWIN`: FORTRAN / C++ interface data
- `PRIPLO`: Automated printing and plotting data

Where practicable these files contain data structures identical to those used in the GCB to facilitate transfer between them as designs evolve.

8.5.1 Global Common Block Consistency Checking

Stand-alone software has been developed to check the GCB code segment. The software checks for consistency, multiple mappings to a single common block variable, multiple use of common block locations, and text alignment. The latter is important as the text is read and decomposed by the simulation for automated printing, graphics, and windows interface presentation, where field widths are critical. The program is stored in CMS group [SUPPORT] and comprises two source modules and a DEC DCL command file:

COMMON_CHECKER.FOR
CB_SORT.FOR
COMMON_CHECKER.COM

The command file builds an executable image directly from the CMS library, assigns the common block file to input channel 10, runs the image, and deletes both the image and all files used to build the program. Three ASCII data files are produced:

FOR016.DAT
A data file produced in response to variables failing the tests.

FOR017.DAT
List of variable names, units, and scaling factors ordered by their position in the GCB real and integer vectors (their ID number).

ORDERED_COMMON_BLOCK.DAT
List of variable names, location, units and definition ordered alphabetically.

Similar consistency checks are carried out during simulation initialisation. If errors are detected at this stage the program is terminated by setting *ISTOP* to 1, with a diagnostic message written to the Data Logging file described later.

8.6 Simulation Infrastructure Control

SIMULATOR controls the program infrastructure invoking *DF_CONTROL* that in turn controls the loading of pre-set default data, as shown in Figure 8-6. The stored information is sufficient to run the program in conjunction with control data provided by the user. The data is loaded ignoring later restrictions imposed on program functionality by the user, and includes:

- I/O data channel identifiers
- Threshold for comparing real values
- Integration order set to 2, and the integration state range [1(1)28]
- Initial value of in-run real and integer common block change indices
- Number of lines per page to the Data Logging file
- Commonly used constants and unit conversions

- Mathematical constants and WGS84 geodetic constants
- System clock initialisation
- Windows refresh rates
- Bi-modal distribution factors (see §22.2.4.3)

Program controls are customised using data read by *INPUT_DATA* from the external control data file as described in §8.6.4. Default initialisation ends by activating separate modules to load target, sensor, missile and trajectory optimisation data. The program is initialised by *IN_CONTROL*, starting with the system clocks and the printing and plotting facility (PRIPLO). The data from an external characterisation data file is read and used to overwrite previously loaded defaults with application specific data, as described in §8.6.5. If any data fails its consistency checks these are recorded and the program continues with the initialisation irrespective of the models that are to be used. If any input data faults are recorded, or inconsistencies detected in the user requirements during the initialisation process, the program is terminated with diagnostics so that the faults can be rectified. Uniquely numbered termination conditions are written to the Data Logging file described in §8.6.8.

After initialisation the 16 kHz master timing loop is invoked. GMT and simulation reference times are updated using integer counter *INDEXS* to preserve accuracy. The system clocks are updated at the master clock rate so that precise timing can be achieved in *CLOCK_UPDATE*. User specified in-run real and integer variable changes are monitored and activated at the appropriate time by *R_CB_CHANGE* and *I_CB_CHANGE* respectively. Changes are applied at 1 kHz so the activation time provided should be commensurate if quantisation is to be avoided. Control is then passed to one of the Runge-Kutta state integrators (*RK_**) that propagate the reference state vector at 4 kHz. The integration order is selected by setting the value of *INTORD* whose value is reflected in the integration module names. This parameter defaults to 2nd order integration however, it can be changed during program initialisation and program execution. After each integration step, if the termination flag *ISTOP* has been set by the application models a controlled shut down is initiated. The program ends by processing the MATLAB graphics and formatted data requested.

8.6.1 Reference State Vector Integration

State propagation is controlled by *DX_CONTROL*, as shown in shown in Figure 8-7. The integration process defined in §22.2.2 starts by resetting the integration *INDEXI* to 1 that identifies which pass of the state derivative is being executed. Data output from *OUT_CONTROL* is invoked immediately the 1st state derivative computation in each integration period so that all data can be displayed and recorded at the current time. The process increases time locally, performs additional state derivative computations, updates the integration index, and finally collates the weighted state data.

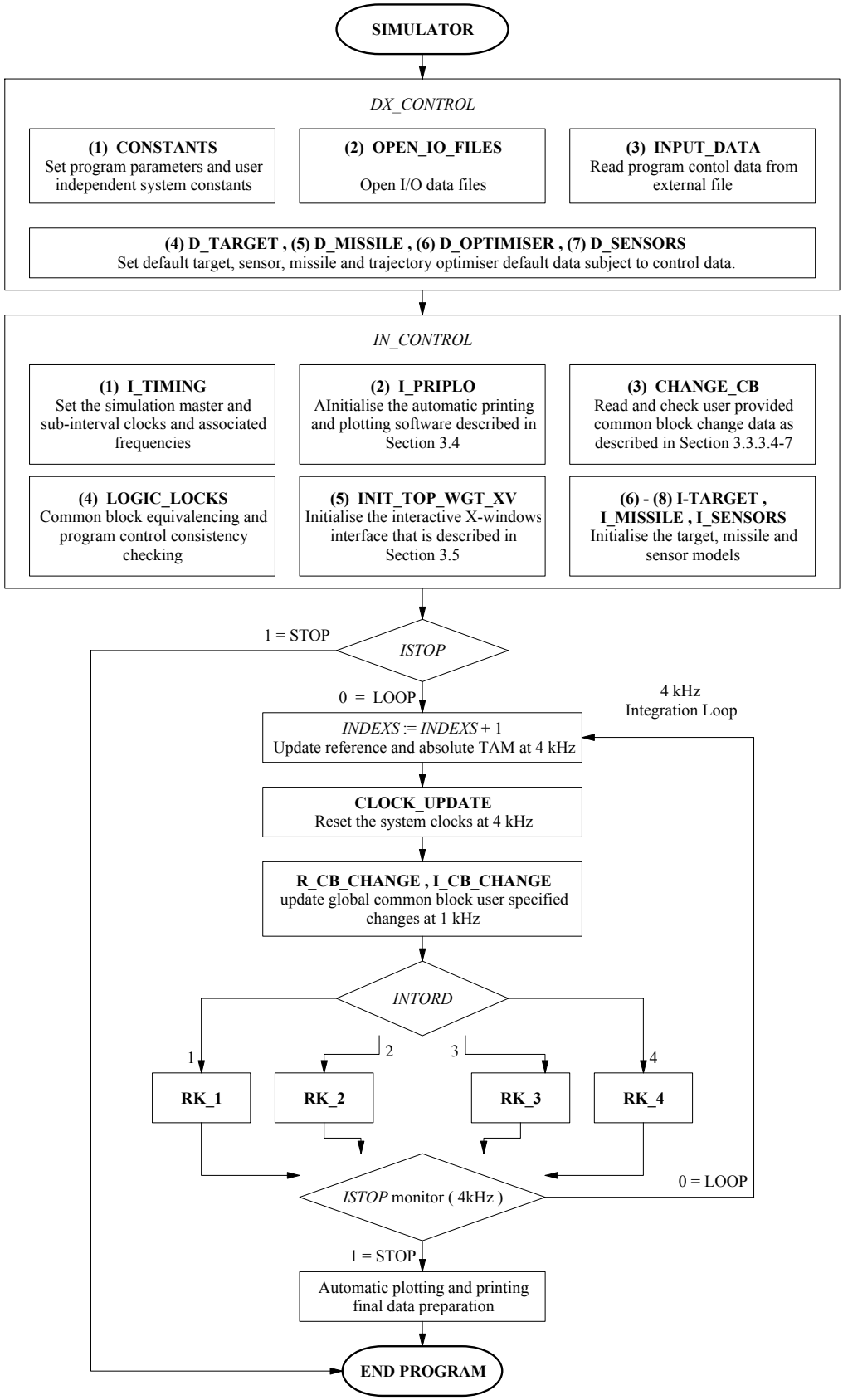

Figure 8-6 : Simulation Top-Level Infrastructure

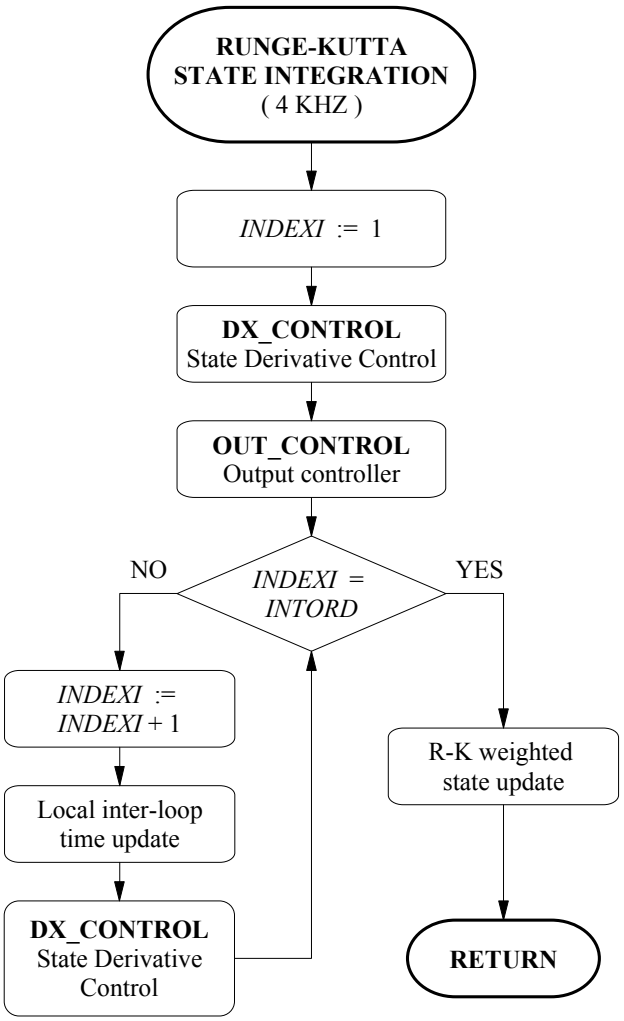

Figure 8-7

Simulation Infrastructure
State Integration Control

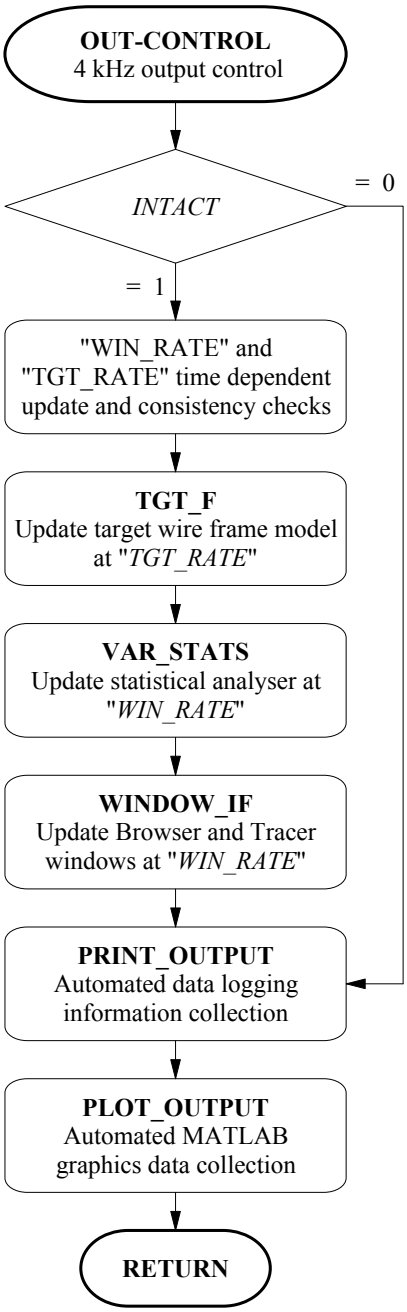

Figure 8-8

Simulation Infrastructure
Output Control

8.6.2 Output Control

OUT_CONTROL in Figure 8-8 performs the following functions providing data up to a maximum rate of 4 kHz:

- Updates the Windows interface described in §8.7 if (*INTACT* := 1), and starts the on-line statistical analyser on request.
- When automated ASCII data logging is requested (*NPRINT* > 0) the functions described in §8.6.5.1 are performed.
- When MATLAB automated data logging is requested (*NPLOT* > 0) the functions described in §8.6.5.2 are performed.

8.6.3 Simulation I/O Data Files

The infrastructure supports two user interfaces. The first involves program control by pre-defined external data files for precise initiation and time stamping of events. The second is an interactive interface using DEC X-windows dealt with in §8.7. The program first requests a 9-character string via channel *LUNSCR* containing the name of the I/O files to be accessed or created. The user responds via channel *LUNINT* and *OPEN_IO_FILES* opens the required I/O data files. Initialisation follows using the following ASCII input data files via the channels identified:

- Control ASCII data file (LUNDAT : Ch. 11)
- Characterisation ASCII data file (LUNOVR : Ch. 12)
- Monte-Carlo ASCII data file (master seed) (LUNMON : Ch. 23)
- GCB ASCII source code (LUNCOM : Ch. 18)

If any of these files are missing the program stops. The simulation then reads the following external data files on request:

- Digital Terrain Elevation Data (LUNMAP : Ch. 10)
- Target wire frame co-ordinates (LUNTWF : Ch. 72)

The following output data files are automatically provided:

- ASCII Data Logging file (LUNOUT : Ch. 16)
- Simulation progress data to a monitor (LUNSCR : Ch. 6)

The following output data files are provided on request:

- Monte-Carlo ASCII data file (updated master seed) (LUNMON : Ch. 23)
- MATLAB graphics ASCII data file (LUNMTB : Ch. 24)
- Temporary binary data file for formatted printing (LUNPRT : Ch. 15)
- Temporary binary data file for MATLAB plotting (LUNPLO : Ch. 14)

- Terminal miss statistics ASCII data file (LUNMDT : Ch. 22)

One of the most time consuming tasks when developing a simulation is that of preparing data in the correct format for output post-processing and presentation. A generic I/O facility has been developed around the GCB to provide a generic data tracking, change and logging facility. The automated printing and plotting modules can be used to place a diagnostic trace on any GCB variable at a frequency of up to 4 kHz. The facility is initialised by *I_PRIPLO* invoking modules that extract the character strings associated with variable location, name, definition, units and scaling direct from the GCB source code. These data are used for common block diagnostic checking, automated plotting and printing, and presentation of data in the Windows interface. If output has been requested, *OUT_CONTROL* invokes *PLOT_OUTPUT* and *PRINT_OUTPUT* that collect and scale the data, and write it to temporary data files. As the simulation closes these files are processed by *FINAL_PRINTING* and *FINAL_PLOTING* sending print data to the Data Logging file, and plot data to the MATLAB graphics file. Whereas the AMIS interfaces with several graphical packages, the research program only provides MATLAB graphics data for post processing.

8.6.4 Control Data File

The ASCII Control data file read by *INPUT_DATA* has a 9-character name with the extension *"*.DAT"*. Logical pointer *DAT_LOC* defines the location of this file.

An example of a Control data file:

```
FIVE LINES IN WHICH TO PUT
A HEADER OR DESCRIPTION
BLOCK FOR THE CURRENT
SIMULATION RUN, EACH LINE IS
RESTRICTED TO 80 CHARACTERS

SIMULATION END TIME
112.0
INITIALISING RANDOM SEED
54321
ACTIVATE MONITOR OUTPUT
1
ACTIVATE INTERACTIVE INPUT MODE
1
TARGET WIRE FRAME TYPE
2
TARGET TRAJECTORY
3
SENSOR SUITE (PHD = 294)
0
SENSOR MEASUREMENTS AVAILABLE
33424270,30
MISSILE GYROSCOPE
0,0,0
MISSILE ACCELEROMETER
0,0,0
MISSILE BAROMETER
0,0,0
MISSILE RADAR ALTIMETER
0,0,0
MISSILE NAVSTAR GPS
0,0,0
MISSILE SEEKER
0,0,0,0
MISSILE FINS
0,0,0
MISSILE GPS
0,0,0
GB RADAR
0,0,0,0
GB HMS
0,0,0
MISSILE AIR DATA
0,0,0
IMM FILTER TYPE
0
MISSILE TYPE
0
MISSILE LAUNCH TIME
30.0
MISSILE GUIDANCE LAW TYPE
2
```

The file contains 5 records, each an 80-character string that may be used to describe the function of the data to follow, and assist configuration control since this data is written directly to the Data Logging file. In the example given, the title is followed by a series of 80-character strings preceding the data it describes.

8.6.5 Characterisation Data

The Characterisation data file, whose location is defined by the logical pointer *OVR_LOC*, has the same 9-character name as the Control data file, with the extension "OVR". The data is partitioned into 6 sections:

- Automatic data trace/printing required
- Automatic MATLAB plotting required
- Initialisation real GCB changes required
- Initialisation integer GCB changes required
- In-Run real GCB changes required
- In-Run integer GCB changes required

An example of a Characterisation data file:

```
1                                ! PRINTING VARIABLES
0.0,2.0,20
5
R0001,I0146,R1453,R1454,R1428
1                                ! PLOTTING VARIABLES
0.0,2.0,400
5
R0001,I0146,R1453,R1454,R1428
35   ,    4.000D+1
234  ,    0.000D+0
0    ,    0.0D+0                 ! [R] INITIAL CHANGE DELIMITER
16   ,    8
17   , 1000
0    ,    0                      ! [I] INITIAL CHANGE DELIMITER
1.00 ,  250 ,  5.0000D+0
1.50 ,  250 ,  3.5355D+0
0.00 ,    0 ,  0.0D+0            ! [R] IN-RUN CHANGE DELIMITER
0.50 ,  405 ,  3
1.00 ,  653 ,  1
0.00 ,    0 ,  0                 ! [I] IN-RUN CHANGE DELIMITER
```

8.6.5.1 Automatic Printing

The program contains printing and plotting facilities that can place a diagnostic trace on any GCB variable at frequencies up to 4 kHz. This facility is referred to as PRIPLO. The number of graphical and diagnostic traces that can be activated simultaneously is limited to 100, a limit applied to graphical and diagnostic traces separately. The traces requested for printing and plotting can be different if so desired. Up to 10 mutually

exclusive recording periods can be defined for both with different output frequencies.

PRIPLO can be controlled via the Windows interface overriding the user specified logging periods provided. Under windows control the data specified in this file is logged at *WIN_RATE*. The format of the input data in the Characterisation Data file is:

```
2
0.0,0.8,1000
1.0,1.5,400
14
R0001,I0002,R0003,R0004,I0005,R0006,R0007,I0008,R0009,R0010
R0001,R0011,R0012,I0013
```

The first line specifies the number of data logging periods limited to the range [1(1)10]. The next 2 records specify the data logging start and end times in seconds, and the data output frequency. The fourth record specifies the number of data items to follow in the range [1(1)100]. The remaining lines contain the common block type, "R" for real variables, "I" for integers, followed by 5-digit strings delimited by commas listing the GCB array locations required. The number of variables on each line is limited to 10 and each line must be filled before starting the next. Automatic printing is de-activated by setting the number of data logging periods to zero. The variable *NPRINT* is then set to zero and no further lines of data must be specified in the input file. The name of the variables selected, and their units are written to the Data Logging file as headers on each page of output. Thereafter the scaled data is listed for the periods, and at the rates specified.

8.6.5.2 Automatic Plotting

The format for MATLAB automated plotting is identical to that for printing although the number of periods, time slices and variables may be different. The first variable on each line defining the data to be plotted should be the reference time (R0001). Failure to conform to this standard does not prevent automatic plotting however, the data will be plotted against the first variable specified in the list. The ASCII data file produced is described in §8.6.9. This is read and manipulated by the MATLAB GUI.

8.6.5.3 Real Common Block Initialisation Changes

Real GCB changes to be processed during program initialisation are specified as records containing location and value. For example, “35,4.0” will overwrite the real GCB location RV(35) with the value 4.0D+0. The delimiter record identifying the last of the real changes is “0,0.0”. This data is read by *CHANGE_CB* that checks the input data to ensure that:

- The variable to be changed is in the range [1(1)*RV_MAX*]
- A simulation variable is mapped to that location

- The location it is not mapped to a change inhibited variable

If any of these tests fail the simulation sets *ISTOP* to 1, and informs the user of a data error in the Data Logging file.

8.6.5.4 Integer Common Block Initialisation Changes

Integer GCB changes to be processed during initialisation are dealt with in exactly the same way as changes to real data. For example, "35,4" will overwrite the integer GCB location IV(35) with the value 4. The delimiter record identifying the last of the integer changes is "0,0". *CHANGE_CB* checks the data using integer array range [1(1)*IV_MAX*].

8.6.5.5 Real Common Block In-Run Changes

Up to 200 real GCB changes during program execution can be specified. Each record contains the change time, variable location and its new value. For example, "1.0,35,4.0" overwrites GCB location RV(35) with the value 4 at 1 s. The data in each record is loaded into separate real arrays *TCHNGR*, *LCHNGR* and *VCHNGR* respectively, the number of records is counted and the value *L_LINDEX* set. The delimiter record identifying completion of the real changes is "0.0,0,0.0". The data read in by *CHANGE_CB* are checking to ensure that:

- The common block location is in the range [1(1)*RV_MAX*]
- A variable is mapped to the location specified
- The location it is not mapped to a change inhibited variable
- The time at which the variable is to be changed is greater than zero
- The change times are in monotonically increasing order

If test fails *ISTOP* is set to 1 and the error is recorded in the Data Logging file. If the number of GCB changes processed is less than *L_LINDEX R_CB_CHANGE* continues to interrogate the monotonically increasing change times at 1 kHz, executing those due. Multiple changes at a common time are permissible. For accurate execution changes must be specified to an accuracy of 0.001 s, those that are not are automatically rounded.

8.6.5.6 Integer Common Block In-Run Changes

Up to 200 integer GCB changes are dealt with in the same way as the real changes. For example, "1.0,35,4" overwrites location IV(35) with the value 4 at 1 s. The delimiter record identifying completion of the integer common block changes is "0.0,0,0". *CHANGE_CB* performs the same tests using array boundary [1(1)*IV_MAX*], loading the data into real arrays *TCHNGI*, *LCHNGI* and *VCHNGI* respectively, with the number of changes in *N_LINDEX*.

8.6.6 Monte-Carlo Facility

The Monte-Carlo facility is activated if the master seed in the Control data file is set to zero. The program then opens an existing ASCII data file residing in a location defined by logical pointer *MON_LOC* with the I/O data file name and the extension "MON". This file contains the master seed for the first program execution. The program reads the seed and updates it ready for the next program execution before closing the file. The program does not re-initialise itself as this leads to poor structure and proving difficulties, problems that are avoided by executing the simulation under external control. Command file *MCARLO.COM* runs the simulation in a loop, directing the output from each execution to the area identified by *MON_LOC*. Monte-Carlo operation is invoked by a single instruction containing the number of executions and the 9-character name of the input data files, for example:

@MCARLO 5 TESTFL001 < Carriage Return >

A *MCARLO.LOG* file is written to the output location containing the time stamp and number of each program run. The Data Logging file header block in §8.6.8 can then be correlated with the program execution number and the master seed so that individual runs can be repeated in isolation.

8.6.7 Digital Terrain Elevation Data

The radar altimeter model requires digital map data processed as described in §22.7. The map processing software reads the digital map data residing in a location defined by the logical pointer *MAP_LOC*.

8.6.8 Data Logging File and Self Diagnostic Reporting

This data file with the I/O name, and extension "OUT", is written to a location defined by logical pointer *OUT_LOC* and records input data errors and significant time stamped events. It also captures the automated printing output, and the termination conditions if the missile is launched and passes close enough to the target. Diagnostic checks are performed on the input data during initialisation to trap user input errors that would cause the program to stop prematurely. Further logical interlocks are provided to prevent the selection of mutually exclusive program combinations, a facility that has been refined through user fault reporting. If faults are detected the simulation is terminated after initialisation is complete, with diagnostic messages and remedies written to this file; a facility that is a great help to the less experienced user.

8.6.9 MATLAB Graphics Data

The simulation infrastructure is a shell containing facilities for inputting and outputting data produced within a clocked integration process. A cost effective approach to I/O is to provide data in a form that is compatible with a dedicated graphics package like MATLAB. MATLAB contains a

comprehensive array of time series analysis tools and graphics facilities complementing those provided in the simulation. The simulation provides an ASCII output data file with the I/O name and extension "MTB" in a location defined by the logical pointer *MTB_LOC* for analysis using MATLAB. Initially two header records are written to this file, the first is a list of variable names, the second their units extracted from the GCB text file. The data records are then written at the prescribed time and frequency, for example:

```
        TIME          CR_PH_SH          CR_TH_SH          I_PHI_SH
[  SECONDS]      [  DEGREES]       [  DEGREES]       [  DEGREES]
0.00000E+00       0.12561E-2        0.12000E+1        0.12551E-2
0.12500E-01       0.13761E-2        0.12600E+1        0.13753E-2
          ⋮                 ⋮                 ⋮                 ⋮
0.10000E+10       0.14961E-2        0.13300E+1        0.14951E-2
```

The internal SI representation of the data is multiplied by the GCB scaling factor prior to output. A MATLAB graphical user interface (GUI) has been created to manipulating the data provided by the research simulation and the AMIS. MATLAB reads the data in these files, creating a vector for each output variable, denoted by the original variable name, and a complimentary vector of units.

8.7 Interactive X-Windows Interface

Competition to secure fixed price contracts has reduced the development period of missile systems even though the complexity of the modern weapon systems has increased. Simulations such as the AMIS, developed to cope with this increase in functionality, must also address the problem of longer learning curves by automating as many of the housekeeping functions as possible. Simulations now include a level of functionality that cannot be controller entirely by external data files alone if rapid development, analysis, and system assessment is required. To do so would inevitably lead to excessive learning curves, limit testing, reduce scenario generation and their analysis. An interactive windows interface enhances user control and on-line data presentation, maximising its potential for rapid development and fault finding.

The windows I/F here provides an easy to use "front end" to the core model, thereby reducing the time taken for familiarisation. Combining the windows I/F with a GCB makes all the program variables accessible for automated I/O, statistical analysis and interactive change during program execution. Interactive control over the program means that it can be stepped at any one of the clock rates provided, a valuable tool for detailed algorithm analysis and sub-system interactions.

For this application the Windows interactive and visualisation software is written in "C++", a language ideally suited to graphical presentations, utilising MOTIF X-18 library functions. The interactive interface with the FORTRAN core models controls the flow of data to and from the visualisation software using a mouse. The windows are dynamically linked,

i.e. an operation in one is reflected in the others taking into account initialisation and in-run changes initiated by external data file. Dynamic linkage between the windows is limited to *RUN*, *STEP* and *STOP* buttons shown in Figure 8-9. When initialisation is complete program control is passed to the Windows interface if *INTACT* is set to 1, otherwise external data is used. When using the windows I/F any changes specified in the user's input data files are processed and their effect on the system observed.

Each window is created during program initialisation using separate resource files (*.RES) accessed by setting the logical pointer *RES_LOC*. The windows I/F is constructed using data file *GENWINDOWS.DAT* residing in the user's top-level directory. The research simulation contains three windows: target wire frame modelling, parameter visualisation and parameter tracing. The flexibility of these facilities is a tribute to Mr. P. Heath and his input to the design process. Once the windows are activated they must be de-activated using the control buttons provided and not by the window manager as this terminates the simulation without final diagnostic data processing.

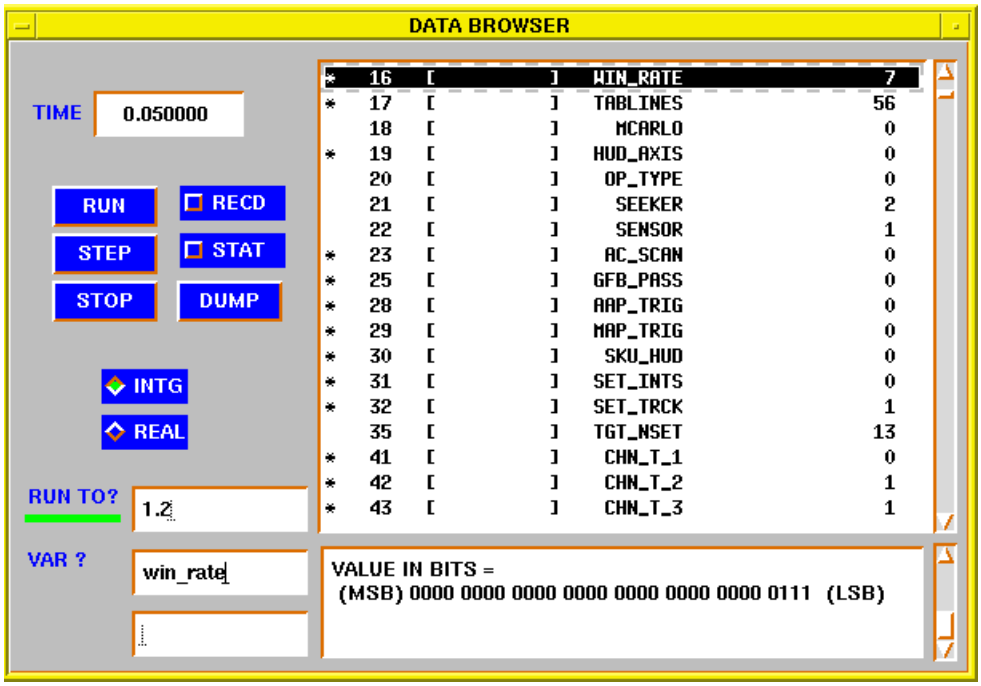

Figure 8-9 : Browser Control Window

The *RUN* button instructs the simulation to run continuously without passing control back to the windows I/F unless interrupted using either the *STEP* or *STOP* buttons. The *STEP* button interrupts the simulation, passing control back to the windows I/F after each processing period. The *STOP* button instructs the simulation to terminate at the end of the current integration loop and prepare all the requested diagnostic data. The windows refresh rate is controlled by *OUT_CONTROL*. Until the missile is within 1 km of the target, the data viewing windows refresh rate is determined by

WIN_RATE, and target wire frame visualisation by *TGT_RATE*, initially set to 20 Hz and 10 Hz respectively. Between 1 km and 100 m the refresh rate for all the windows passes to *END_RATE* initially set to 50 Hz. Thereafter, and until the point of closest approach, the windows refresh rate is fixed at 1 kHz. The user may change the initial setting of *WIN_RATE*, *TGT_RATE* and *END_RATE* to any of the clocks provided between 1 Hz and 4 kHz (clocks 2 to 23 defined in §22.2.1). If a value is entered outside this range they are reset to their initialisation values.

8.7.1 Parameter Visualisation Window

Using a GCB makes it possible to display and change most of the simulation data during program execution. The window shown in Figure 8-9 has been designed to display GCB variables, their definitions and units. When the simulation is in *STEP* mode the scrollable parameter area lists all the GCB variables. The real and integer variables are partitioned and displayed by activating the radio box *REAL* or *INTG* buttons using the left mouse button. The program converts its internal data representation into the units displayed in the sub-windows. Parameters are displayed in GCB order, with the first page visible without scrolling. If a parameter is selected using the left-hand mouse button it remains as the first variable displayed on subsequent presentations until another is selected. When a parameter is selected the scrollable text output area below displays its definition, current value, units, and in the case of integers, their 32-bit pattern. The simulation time is updated at the windows refresh rate and is permanently displayed in a sub-window. It is presented with an accuracy that is consistent with the precise value of the clocks provided.

8.7.1.1 *RUN TO ?* Facility

When paused in *STEP* mode this facility allows the user to enter a future time at which the simulation should re-enter *STEP* mode. Once the field has been selected using the left mouse button, and a valid time keyed in followed by <Carriage Return>, a green indicator bar is displayed. When this time is reached the simulation re-enters *STEP* mode, the indicator disappears, and the future time text field is cleared. If the time entered has already passed, the indicator light immediately disappears and the text field is cleared.

8.7.1.2 *VAR ?* Facility

When paused in *STEP* mode this facility allows the user to search through the GCB for a variable by name. Once the field has been selected using the left mouse button, a variable is keyed in followed by <Carriage Return>. The program then searches through the GCB for it. Once found the scrollable parameter selection area is refreshed and the variable displayed at the top. If the variable requested is not in the GCB a message to this effect is displayed in the scrollable text output area.

8.7.1.3 Parameter Change Facility

When paused in *STEP* mode this facility allows the user to change any variable in the simulation that is not write protected. If a parameter is selected in the scrollable parameter selection area, the cursor automatically jumps to this field (bottom left box). If a new value is keyed in followed by <Carriage Return> the GCB variable selected is updated and displayed in the scrollable parameter selection area. If the left-hand mouse button is clicked over any other button within the window prior to entering the <Carriage Return> the variable value remains unchanged. Invalid entries, or changes to write protected variables, are rejected and a message to this effect is written to the scrollable text output area.

8.7.1.4 RECD Facility

This facility records unanticipated events. Activating this button changes it to green and starts the printing and plotting data facility (PRIPLO). The user provided time periods and frequencies in the external Characterisation file are ignored and the data requested is output at *WIN_RATE*.

8.7.1.5 *STAT* Facility

The interactive collection of statistical data on any variable is desirable when dealing with stochastic variables.

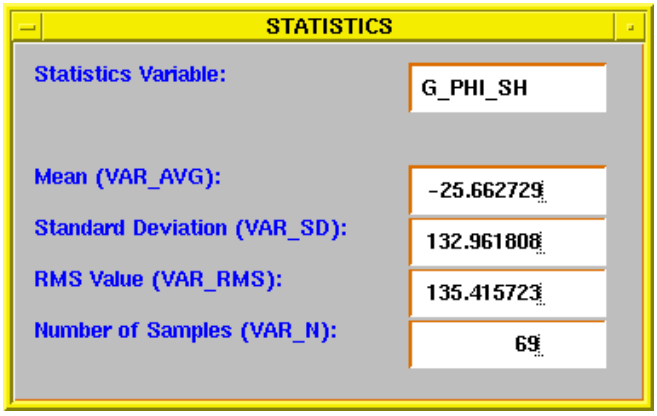

Figure 8-10 : Statistical Analyser Window

Activating the *STAT* button changes its indicator light to green, forces the simulation to enter step mode, and activates the pop-up window shown in Figure 8-10. This window contains a text field, selected for input using the left mouse button, into which any real GCB variable name can be keyed in followed by <Carriage Return>. The text is left justified, converted to upper-case characters, and variable statistics are collated at the windows refresh rate. If the variable name is not found the string in the text field is replaced by a warning message to this effect. When the simulation is re-started the mean, standard deviation and rms values are computed by *VAR_STATS* as defined in §22.2.7. Each time this window is activated all previous data is cleared except for the variable name. However, statistics

for this parameter will not be collated until the text field has been re-selected followed by <Carriage Return>. The variable in the text field can be changed without de-activating the window, or even returning to step mode. If the variable trace is changed the program automatically re-initialises the statistical data presented.

8.7.1.6 DUMP Facility

Activating this button writes the entire contents of the GCB to the Data Logging file capturing the system status at a particular time before returning to normal operation. Because of the GCB size this facility must be used sparingly.

8.7.2 Parameter Trace Window

Whereas the Parameter Visualisation is used to observe GCB variables on a frame-to-frame basis with the program in *STEP* mode, the Parameter Tracer can be used to view a variable "continuously" for anomalous behaviour whilst in *RUN* mode.

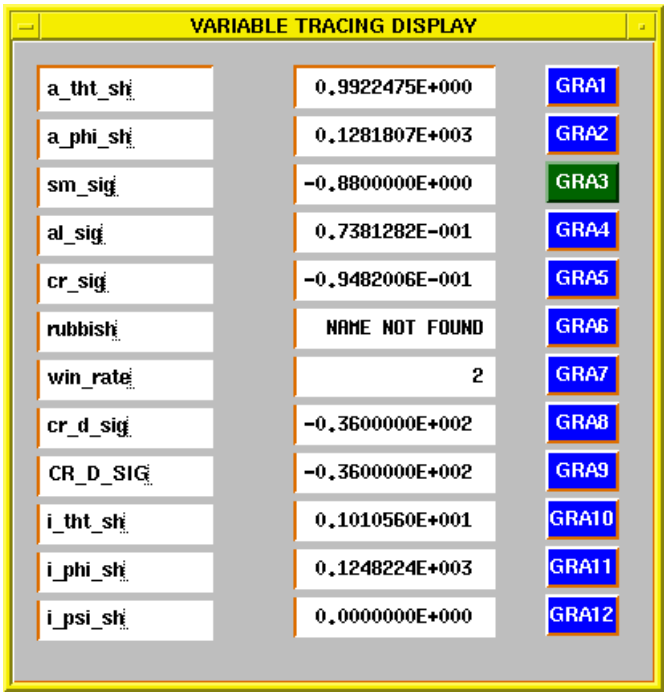

Figure 8-11 : Parameter Trace Window

The window shown in Figure 8-11 uses the same search and display logic to display up to 12 GCB variables refreshed at the windows update rate. Using the left-hand mouse button to select one of the text fields a variable name is keyed in followed by <Carriage Return>. The program searches the GCB for the variable and displays its value in the output field in the units shown in the Parameter Visualisation window. If the variable name is not found a message to that effect is written in the text output field. A variable name can be keyed in with the simulation in any mode. To remove a variable, the

field is re-selecting, the cursor is placed at the end of the text, and the delete key is used. There are 12 graph control buttons labelled *GRA1* to *GRA12* selected using the left-hand mouse button. These buttons invoke separate pop-up windows for each variable containing a revolving time base graph, automatically scaled and presented in display units; an example of which is shown in Figure 8-12.

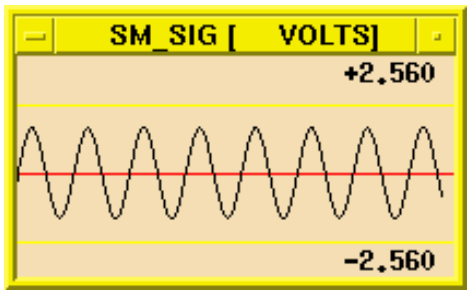

Figure 8-12 : Rolling Graphics Window

A new point is drawn on the graph at the windows refresh rate. Each graph is scaled to display the maximum value of the input signal. If the current limit is exceeded the graph is re-scaled and a "↓" symbol is displayed above the upper limit guide and the scale values increased by a factor of 2. When a *GRA* button is de-activated the graph automatically disappears and all limits are reset if re-activated.

8.7.3 Target Wire Frame Window

Critical points associated with target designation and tracking are dipicted on a wire frame representation of the following targets:

- Backfire (I_BACKFIRE)
- F106 (I_F106)
- F15 (I_F15)
- Flanker (I_FLANKER)
- Flogger (I_FLOGGER)
- Fulcrum (I_FULCRUM)

The simulation modules shown in brackets above are used to initialise the selected wire frame target model. Embedding the initialisation modules in the target visualisation software allows the user to change the target type interactively. The facet co-ordinates are defined in data files with the extension "*.GEO", taking the name listed above. The facets are drawn in order, starting with those whose range is greatest along the LOS. This hidden facet layering technique removes lines that would naturally be hidden from view, as shown in Figure 8-13. The range to the target from the origin of the viewing axis chosen is displayed at the bottom of the window together with the image processing state (unused).

8.7.3.1 Control Menu

The *CONTROL* menu provides the usual *RUN*, *STEP* and *STOP* controls and a ZOOM facility. This toggles between a target viewed in perspective

with the red viewing circle expanded to the size of the window (as shown in Figure 8-13), and a view in which the target is enlarged to fill the window.

8.7.3.2 Aim Point Menu

The AIMPOINTS menu provides a list of critical points that can be displayed, all turned off by default. Next to each aim-point is an indicator, the colour of which corresponds to the colour of the symbol displayed when selected using the left-hand mouse button. The key to these symbols and their colours is given in the Table 8-1. The first two symbols are the position of the viewing axis and the reference point of the target (t) at its range from the viewing axis origin.

8.7.3.3 Axis Button

This *AXIS* button controls the target view. The left-hand mouse button is used to toggle between the viewing options thereby setting *AXISVIEW*. The target body is aligned with Target Velocity axes (target reference) and is presented with respect to the viewing axis at the target range. The user is provided with 5 aim-point sets that depend on *AXISVIEW* cycled by clicking on the AXIS button. Characterisation of the sets is listed in Table 8-2 to Table 8-6. The red circle is centred on the reference axis, and its diameter depends on the viewpoint:

- Radar beam-width or target-missile differential angle,

$$R_{C1} := \max\left(\xi_{TBW}, \xi_T^M \right)$$

Equation 8.7-1

- Radar beam-width, combined IMM estate, and the individual IMM filter estimates of the angle between the Alignment and Target frames,

$$R_{C2} := \max\left(\xi_{TBW}, {}_{IMM}\hat{\xi}_A^T, \hat{\xi}_A^{T1}, \hat{\xi}_A^{T2}, \hat{\xi}_A^{T3}, \hat{\xi}_A^{T4} \right)$$

Equation 8.7-2

- Seeker beam width, Missile Velocity, Seeker Head, and estimated Missile Body, Missile Velocity and Seeker angles,

$$R_{C3} := \max\left(\xi_{SBW}, \xi_A^{MV}, \xi_A^H, \hat{\xi}_A^B, \hat{\xi}_A^{MV}, \hat{\xi}_A^S \right)$$

Equation 8.7-3

- Seeker beam width, Missile Velocity, Seeker Head, and equivalent estimated angles,

$$R_{C4} := \max\left(\xi_{SBW}, \xi_B^{MV}, \xi_B^H, \hat{\xi}_B^{MV}, \hat{\xi}_B^S \right)$$

Equation 8.7-4

- Seeker beam width and Seeker Head angles,

$$R_{C5} := \max\left(\xi_{SBW} , \xi_B^S \right)$$

Equation 8.7-5

Sensor beam-width was added enable the user to manually adjust the view.

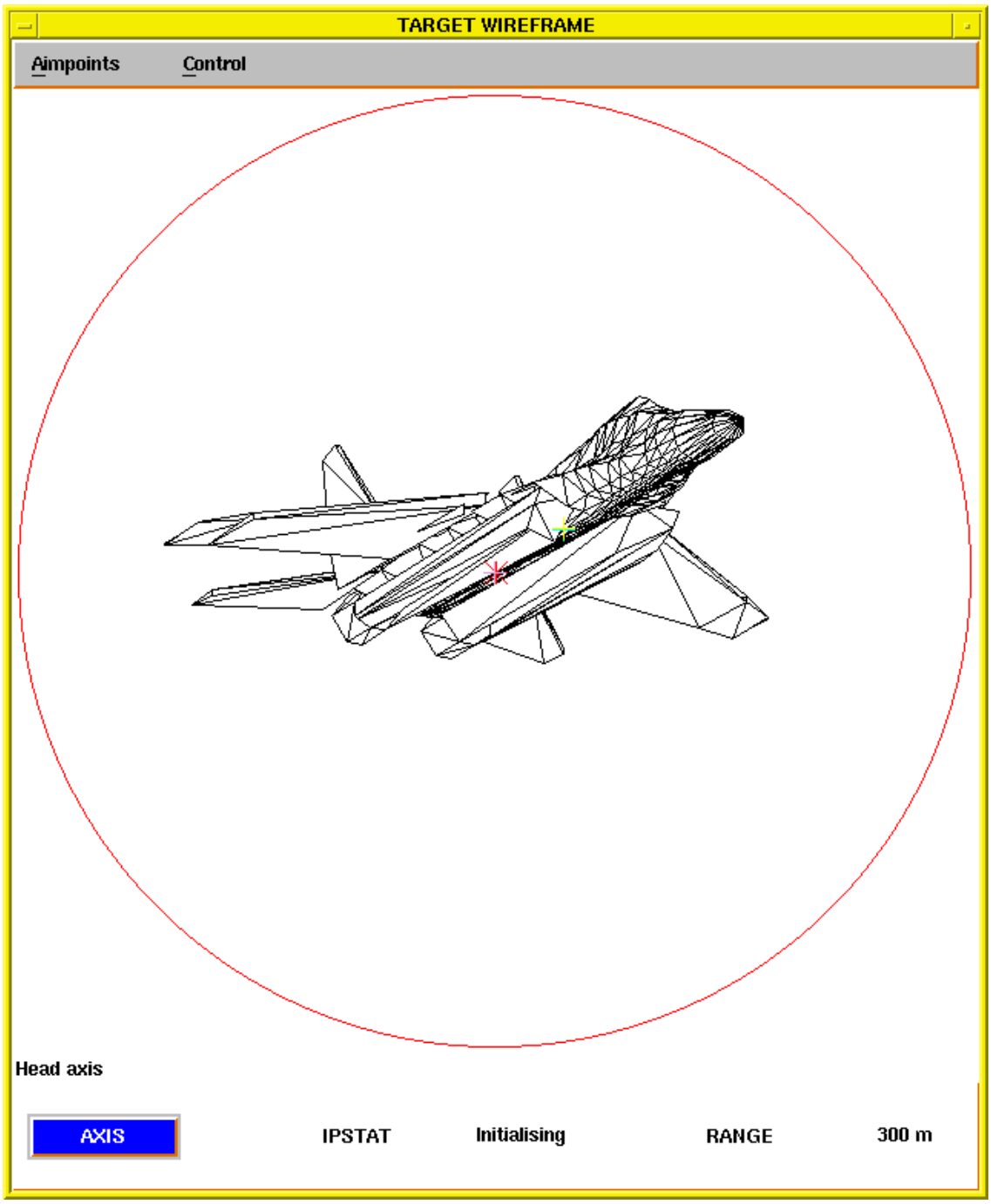

Figure 8-13 : Target Wire Frame Viewer

Table 8-1 : Generic Target Views and Superimposed Points

AIM-POINT	COLOUR	SYMBOL	DESCRIPTION
VIEWING AXIS	red	X	Viewing LOS axis at target range
TARGET REFERENCE	blue	+	Target wire frame reference point
CIRCULAR MARKER	red	O	Application specific circular indicator
AIMPOINT 1	green	◊	Arbitrary X-axis 1 at the target range
AIMPOINT 2	light blue	□	Arbitrary X-axis 2 at the target range
AIMPOINT 3	yellow	∇	Arbitrary X-axis 3 at the target range
AIMPOINT 4	black	Δ	Arbitrary X-axis 4 at the target range
AIMPOINT 5	purple	X	Arbitrary X-axis 5 at the target range
SET ALL			sets all the aim-points on
CLEAR ALL			sets all the aim-points off

Table 8-2 : Radar Tracking View (*AXISVIEW* := 0)

AIM-POINT	LOS	ALIGNMENT AXIS REFERENCED
VIEWING AXIS	$E_A^T(\pi, 0, 0)$	Target LOS axes
TARGET REFERENCE	$E_A^T(\pi, 0, 0)$	Target LOS axes
TARGET DIRECTION	E_A^{TV}	Target Velocity axes
TARGET RANGE	P_t^{XT}	Target LOS range
CIRCULAR MARKER	$(\underline{X}^T, R_{C1})$	
AIMPOINT 1	$\tilde{E}_A^T(\pi, 0, 0)$	Measured Target LOS orientation
AIMPOINT 2	$\hat{E}_A^T(\pi, 0, 0)$	Estimated Target LOS orientation
AIMPOINT 3	$E_A^M(\pi, 0, 0)$	Missile LOS orientation
AIMPOINT 4	$\tilde{E}_A^M(\pi, 0, 0)$	Measured Missile LOS orientation
AIMPOINT 5	$\hat{E}_A^M(\pi, 0, 0)$	Estimated Missile LOS orientation

Table 8-3 : Target Tracking View (*AXISVIEW* := 1)

AIM-POINT	LOS	ALIGNMENT AXIS REFERENCED
VIEWING AXIS	$E_A^T(\pi, 0, 0)$	Target LOS axes
TARGET REFERENCE	$E_A^T(\pi, 0, 0)$	Target LOS axes
TARGET DIRECTION	E_A^{TV}	Target Velocity axes
TARGET RANGE	P_t^{XT}	Target LOS range
CIRCULAR MARKER	$(\underline{X}^T, R_{C2})$	
AIMPOINT 5	$\hat{E}_A^T(\pi, 0, 0)$	IMM optimum target tracking orientation
AIMPOINT 1	$\hat{E}_A^{T1}(\pi, 0, 0)$	Target tracking model 1 – Target LOS
AIMPOINT 2	$\hat{E}_A^{T2}(\pi, 0, 0)$	Target tracking model 2 – Target LOS
AIMPOINT 3	$\hat{E}_A^{T3}(\pi, 0, 0)$	Target tracking model 3 – Target LOS
AIMPOINT 4	$\hat{E}_A^{T4}(\pi, 0, 0)$	Target tracking model 4 – Target LOS

Table 8-4 : Missile Body View (*AXISVIEW* := 2)

AIM-POINT	LOS	ALIGNMENT AXIS REFERENCED
VIEWING AXIS	E_A^B	Missile Body axes
TARGET REFERENCE	E_A^S	Seeker LOS axes
TARGET DIRECTION	E_A^{TV}	Target Velocity axes
TARGET RANGE	P_t^{XS}	Seeker LOS range
CIRCULAR MARKER	$(\underline{X}^S, R_{C3})$	
AIMPOINT 1	E_A^{MV}	Missile Velocity axis orientation
AIMPOINT 2	E_A^H	Seeker Head axis orientation
AIMPOINT 3	$\hat{E}_A^B$	Missile Body axis orientation
AIMPOINT 4	$\hat{E}_A^{MV}$	Missile Velocity axis orientation
AIMPOINT 5	$\hat{E}_A^S$	Target LOS axis orientation

Table 8-5 : Missile Seeker Head View (*AXISVIEW* := 3)

AIM-POINT	LOS	MISSILE BODY AXIS REFERENCED
VIEWING AXIS	E_B^S	Seeker LOS axes
TARGET REFERENCE	E_B^S	Seeker LOS axes
TARGET DIRECTION	E_B^{TV}	Target Velocity axes
TARGET RANGE	P_t^{XS}	Seeker LOS range
CIRCULAR MARKER	$\left(\underline{X}^S , R_{C4} \right)$	
AIMPOINT 1	$\widetilde{E}_B^S$	Missile Body to Seeker LOS orientation
AIMPOINT 2	E_B^{MV}	Missile Body to Velocity axis orientation
AIMPOINT 3	E_B^H	Missile Body to Seeker Head axis orientation
AIMPOINT 4	$\hat{E}_B^{MV}$	Missile Body - Velocity orientation
AIMPOINT 5	$\hat{E}_B^S$	Missile Body to Seeker LOS orientation

Table 8-6 : Lateral Acceleration View (*AXISVIEW* := 4)

AIM-POINT	LOS	MISSILE BODY AXIS REFERENCED
VIEWING AXIS	E_B^{MV}	Missile Velocity axes
TARGET REFERENCE	E_B^S	Seeker LOS axes
TARGET DIRECTION	E_B^{TV}	Target Velocity axes
TARGET RANGE	P_t^{XS}	Seeker LOS range
CIRCULAR MARKER	$\left(\underline{X}^S , R_{C5} \right)$	
AIMPOINT 1		$E_B^* := \left(\xi_B^S \quad 0 \quad \tan^{-1}\left(\frac{{}^D A_{o,m}^{YB}}{{}^D A_{o,m}^{ZB}} \right) \right)$
AIMPOINT 2		$E_B^* := \left(\xi_B^S \quad 0 \quad \tan^{-1}\left(\frac{\ddot{P}_{o,m}^{YB}}{\ddot{P}_{o,m}^{ZB}} \right) \right)$
AIMPOINT 3		
AIMPOINT 4		
AIMPOINT 5		

8.8 Discussion

The program infrastructure described is the basis for several MBDA simulations, the main one being the AMIS. Exploiting synergies between applications using a common infrastructure has reduced development time-scales, costs and learning curves. The approach promotes standardisation, development of transportable utilities, and the use of common graphical support facilities. These are rapidly mature products with an expanding user base, feedback from which continues to shape their development.

The software was developed on a DEC ALPHA 610 supporting the Open-VMS operating system hosting:

- AXP Version 7.1 Operating System
- Version 7.0 FORTRAN compiler
- Version 1.3A-0 "C++" compiler

The infrastructure, application models and utilities were written in FORTRAN 77 (ANSI x 3.9.1978, ISO 1539-1980(E)), and the interactive interface in “C” (ANSI X3.159-1989). These languages were selected to exploit the benefits of “C” for on-screen visualisation and interactive control, and FORTRAN for its flexibility and rapid code development. DEC VAX dependent extensions to FORTRAN 77 are used. Proprietary software, other than MOTIF, is not used. The software was configured using the DEC Code Management System.

The infrastructure comprises hierarchical control modules divorcing system control from the application models. It can host any dynamic model which it controls by external data files and an interactive windows interface. Both have proven to be invaluable, the former for performance work, and the latter for rapid learning and model development. Interactive controls make it possible to step through the program on a frame-to-frame basis at any of the clock rates provided, return to continuous running, or stop in a controlled fashion retaining all diagnostic data up to that point. Capturing externally defined data in the windows was a design driver for this interface. The “run”, “step” and “stop” controls used in separate windows are dynamically linked, an operation in one being reflected in the others.

Communication with utility modules is in most cases by argument, and by a global data pool between infrastructure and application modules. The latter is paramount for interactive analysis, debugging, and on-line statistical analysis, facilities that would be impossible to implement otherwise. Control parameters are implemented as integers rather than booleans, to avoid difficulties with the automated I/O and visualisation facilities. Vectors and matrices are decomposed into their individual elements for similar reasons, although both may be used in the software.

External command files are used to invoke the simulation in Monte-Carlo mode. This form of control requires no internal variable re-setting, and is superior to multiple "runs" generated by a single execution of the simulation that can hinder program modularity and reduce code clarity.

The original design had additional output files supporting a number of post analysis applications. As the program evolved only two survived: the output of formatted records to hardcopy, and a MATLAB interface so as to exploit the latter's extensive analysis tools. The MATLAB interface is particularly useful for Monte-Carlo ensemble analysis.

Chapter 9

PERFORMANCE

This chapter contains the results of studies undertaken for software verification and algorithm validation. They are preceded by description of a conceptual air-defence scenario in terms of the event sequence linking the functionality defined in preceding chapters. Target tracking, trajectory optimisation, launch, and subsequent flight stages, are related to simulation parameters controlling the phase transitions. Tracking and guidance performance metrics used in these, and future studies, are defined using some of the results presented in §5.10 and §22.13.

The first two studies explore the performance of PN and CLOS stimulated using reference data. Their basic forms and augmentations are used against crossing and weaving targets that manoeuvre a short time before impact. The purpose of the studies:

- Verify the program infrastructure, launcher, target and missile simulators
- Establish performance baselines for later studies involving PN, CLOS and optimised guidance laws
- Select a guidance law for initialising the trajectory optimiser

The third study was a tuning exercise for the IMM filters. Idealised target trajectories were used to generate polar measurements corrupted by Gaussian noise typical of modern phased-array tracking radar. The purpose of the study:

- Verify the tracking simulator, its controls and structure, target parameters and covariance extraction
- Select process noise levels for tracking under ideal conditions
- Investigate measurement processing order, observability, and the stability of filters with inappropriate dynamics

9.1 Air-to-Air Engagement Scenario

Figure 9-1 shows an event sequence that is typical for a surface-to-air engagement. These reflect the key processes involving all the simulators described in this document: target and sensor simulation, target tracking, trajectory optimisation, missile launch and state observation. Conventional missile guidance and target observer tuning presented in this chapter use the complex and idealised target trajectories designed for the purpose.

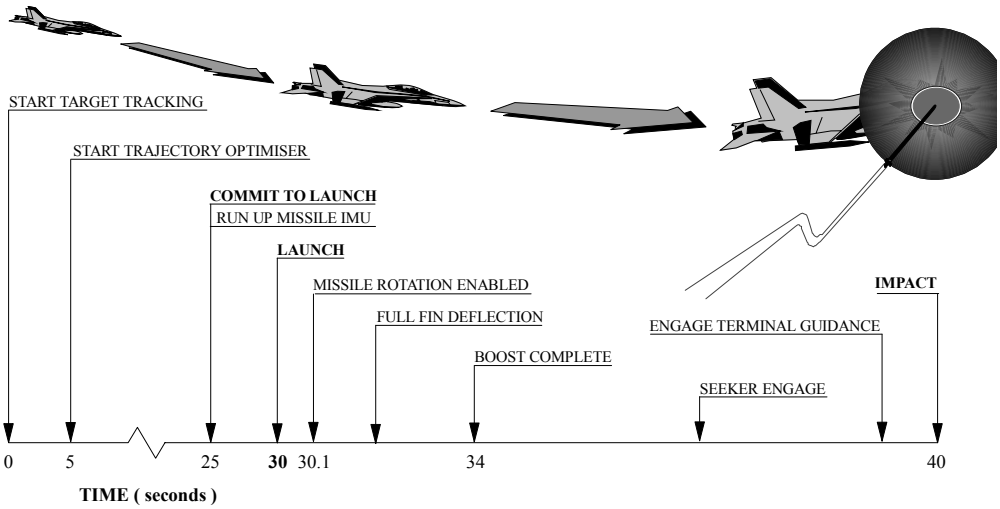

Figure 9-1 : Surface-to-Air Simulation Scenario

The times quoted in Figure 9-1 are approximate. The missile launch time is fixed at 30 s rather than optimally selected using the trajectory optimiser. The radar measurements are processed by the target state observer from the start at time (t := 0 s).

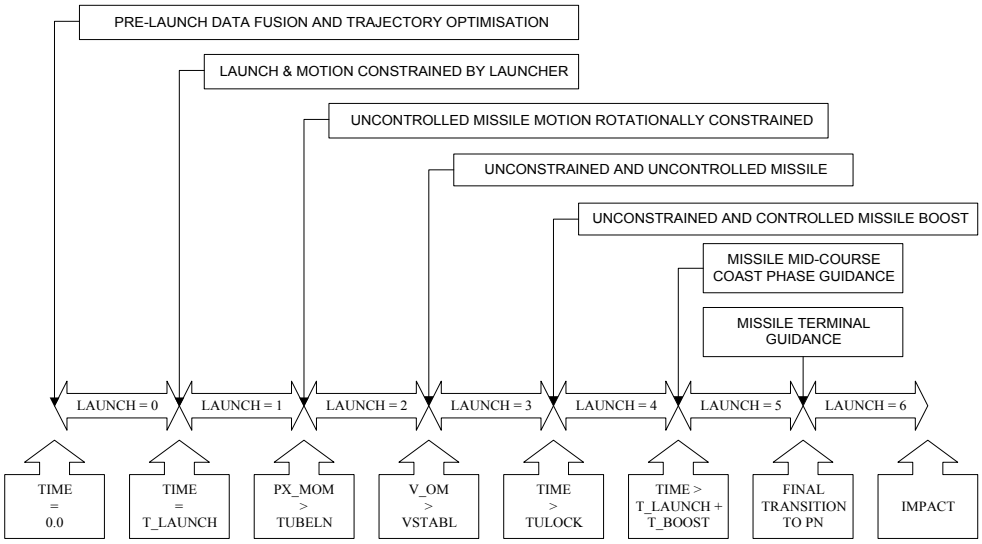

Figure 9-2 : Missile Launch sequence

All the trajectories start with the target at constant velocity for the first 5 s to allow time for the tracking filters to converge. After 5 s target manoeuvres start, the trajectory optimiser is activated, and the launcher is steered using target state observer data. The missile IMU is activated 5 s before launch. The seeker powers-up at launch with its gimbals locked - once the launch transients are over its gimbals are released and its detector activated. When the missile is committed to launch its observer is initialised via a data link from the target (radar) data processor to the launcher.

The missile observer then processes valid tracks and plots, characterising the IMU prior to launch, and thereafter providing "optimal" data as the missile passes through it various flight phases and terminal guidance. The event sequence is controlled in the simulation by the irreversible *LAUNCH* flag; the phases of flight and transition conditions are shown in Figure 9-2.

9.1.1 Flight Phase 0

Pre-launch operation starting at (t := 0) and up to missile launch, comprising radar tracking, target state observation, launcher training and missile initialisation and IMU characterisation.

$$t < t_L \quad \Rightarrow \quad LAUNCH \quad := \quad 0$$

Equation 9.1-1

Trajectory optimisation is invoked after 5 s after the target state observer has converged. The missile IMU is activated 5 s before launch, communication between the radar, launcher and missile is established, and the on-board state observer is initialised. Conceptually, the trajectory optimiser is duplicated in the launcher as part of the fire control software. When the missile observer is initialised the boundary conditions and optimal control sequence is loaded into the missile trajectory optimiser.

9.1.2 Flight Phase 1

Booster ignition, first motion, and constrained flight in a rotating launcher until the missile has travelled the length of the launcher (L_T).

$$\left(P_m^{XM} \leq L_T \right) \wedge \left(t \geq t_L \right) \Rightarrow \quad LAUNCH \quad := \quad 1$$

Equation 9.1-2

9.1.3 Flight Phase 2

Missile roll control is active but no lateral acceleration demands are applied until a stable flight speed (V_S) is reached. The missile dynamics during this phase are determined by thrust, drag and gravity induced forces alone. Tube launched munitions often undergo an upward pitch motion resulting in a height droop until their speed has built up.

$$\left(P_m^{XM} > L_T \right) \wedge \left(\dot{P}_{o,m} < V_S \right) \Rightarrow LAUNCH := 2$$

Equation 9.1-3

For BTT the fins are unlocked for roll control as the missile clears the tube however, pitch plane manoeuvring is delayed until aerodynamic control is established.

9.1.4 Flight Phase 3

Although the missile has reached a stable speed, controlled lateral motion is prevented until the fins are unlocked as part of a safe launch and arming sequence.

$$\left(t < t_L + t_F \right) \wedge \left(\dot{P}_{o,m} \geq V_S \right) \Rightarrow LAUNCH := 3$$

Equation 9.1-4

9.1.5 Flight Phase 4

The missile manoeuvres in response to lateral acceleration demands whilst boosting.

$$\left(t < t_L + t_B \right) \wedge \left(t_B > t_F \right) \wedge \left(\dot{P}_{o,m} \geq V_S \right) \Rightarrow LAUNCH := 4$$

Equation 9.1-5

9.1.6 Flight Phase 5

Boosting is complete and coasting mid-course guidance is established.

$$t \geq t_L + t_B \Rightarrow LAUNCH := 5$$

Equation 9.1-6

9.1.7 Flight Phase 6

Seeker activation (t_{TG}) seconds after launch resulting in target acquisition. In conventional engagements this would indicate a transition from mid-course to terminal guidance.

$$t \geq t_{TG} \Rightarrow LAUNCH := 6$$

Equation 9.1-7

9.2 Performance Metrics

The performance metrics used are miss distance, impact speed, impact time, and control effort, denoted by PI_M, PI_S, PI_T and PI_E respectively. The first three are self-explanatory. The effort metric is dependent on the demanded missile lateral acceleration that is closely linked to the energy expended,

$$LAUNCH \leq 3 \Rightarrow PI_E := 0$$

Equation 9.2-1

$$LAUNCH \geq 4 \Rightarrow PI_E := \frac{1}{4000} \cdot \sum \left(\left(\ddot{P}_{o,m}^{YB} \right)^2 + \left(\ddot{P}_{o,m}^{ZB} \right)^2 \right)$$

Equation 9.2-2

This metric is applied when the missile is fully controlled. The summation is performed at the simulation integration rate. For each target tracking filter, and the combined IMM output, a normalised distance metric is provided. For example, the position error along $\underline{X}^A$ for the i'th filter,

$${}^{i}PI_{PX} := \left| {}^{i}\hat{P}_t^{XA} - {}^{i}P_t^{XA} \right| \Big/ \sqrt{\left({}^{i}\hat{P}_t^{XA} - {}^{i}P_t^{XA} \right)}$$

Equation 9.2-3

The metrics associated with each individual axis are referred to graphically as *TMPX_AOT*, the "P" being replaced by "V" and "A", and "X" by "Y" and "Z" as appropriate. Spherical errors, denoted by (PI_P), (PI_V) and (PI_A), are referred to as *TG_P_MET* , *TG_P_SIG* etc. For the i'th filter the true and estimated spherical position errors are,

$$\left({}^{i}PI_P \quad , \quad E\left({}^{i}PI_P \right) \right) :=$$

$$\left(\sqrt{\frac{1}{3} \cdot \sum_{j:=X,Y,Z} \left({}^{i}\hat{P}_t^{jA} - {}^{i}P_t^{jA} \right)^2} \quad , \quad \sqrt{\frac{1}{3} \cdot \sum_{j:=X,Y,Z} E\left({}^{i}\hat{P}_t^{iA} - {}^{i}P_t^{jA} \right)} \right)$$

Equation 9.2-4

Normalised spherical errors are referred to graphically as *TG_PNMET*, the "P" being replaced by "V" and "A" as appropriate. The i'th filter the normalised spherical position error,

$${}^{i}\overline{PI}_P := \prod_{i:=X,Y,Z} \left(\left| \hat{P}_t^{iA} - P_t^{iA} \right| \Big/ E\left(\hat{P}_t^{iA} - P_t^{iA} \right) \right)$$

Equation 9.2-5

The Eigen observability metric (PI_C) is the Condition Number (CN) defined in §5.10.9. This is identified by *F1_E_MET* on the graphs, the number identifying the IMM filter.

9.3 PN Performance

The simulation cases when referring to PN and CLOS performance against targets 3 (crossing) and 7 (weave) are listed in Being clear in context, the use of the identifier (SO), and the observer kinematic type have been dropped. At this stage sensor error states are not included in the filter – this being an alternative to calibrating the IMU whilst the missile is in the launcher. On-line bias, misalignment and scale factor is made possible due to measurement duality and shaped trajectories. The ideal is a combination of both, characterising the IMU biases before launch which are then fixed, and estimating the IMU scale factors and other sensor errors in-flight.

Table 5-1 at the end of §9.4. The 1st column in this table identifies the simulation case referred to in the text. The 2nd column is the data file name for configuration purposes.

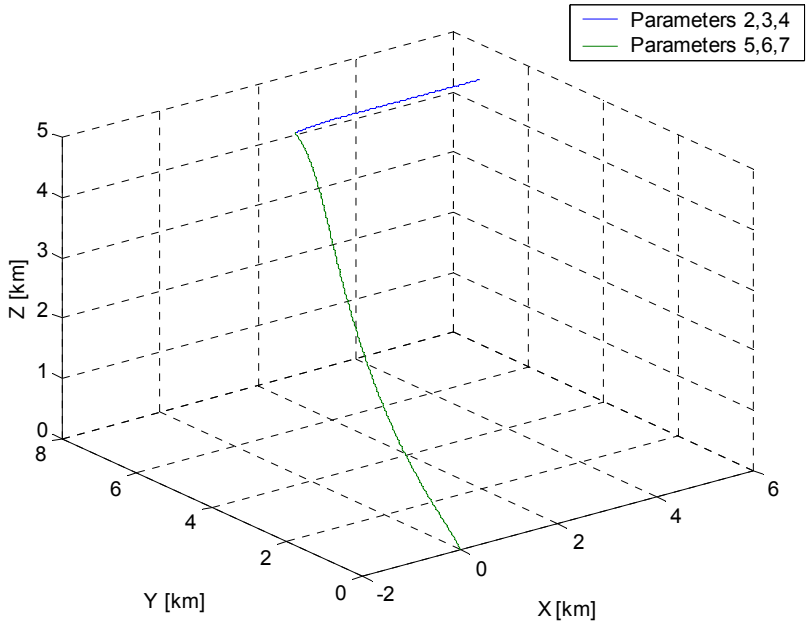

Figure 9-3 : Missile ATPN Track (Target Trajectory 3)

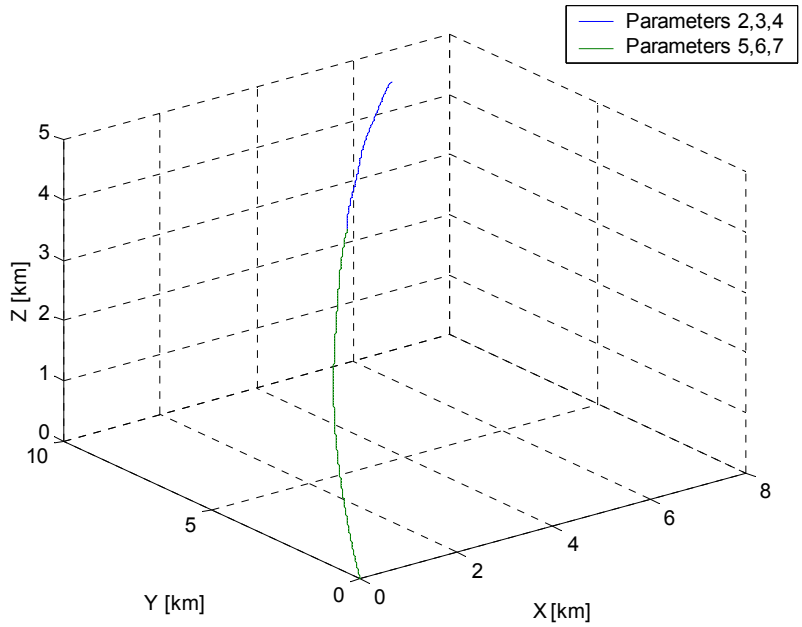

Figure 9-4 : Missile ATPN Track (Target Trajectory 7)

The post-launch missile and target trajectories against these targets are shown in Figure 9-3 and Figure 9-4 respectively. The key refers to Parameters (2-4) and (5-7) - the target and missile Cartesian position in the Alignment frame. The missile is guided using ATPN with low and high-speed G-limiting and a 2nd order autopilot as defined in §6. The missile guidance laws were stimulated using reference inputs by-passing the sensors and state observers, hence no Monte Carlo analysis. PN against a non-manoeuvring, crossing target and a weaving target sets the performance baseline (PN01 and PN10). In these cases target avoidance, missile and target acceleration compensation are deactivated.

Consider the crossing target (PN01) - from Being clear in context, the use of the identifier (SO), and the observer kinematic type have been dropped. At this stage sensor error states are not included in the filter – this being an alternative to calibrating the IMU whilst the missile is in the launcher. On-line bias, misalignment and scale factor is made possible due to measurement duality and shaped trajectories. The ideal is a combination of both, characterising the IMU biases before launch which are then fixed, and estimating the IMU scale factors and other sensor errors in-flight.

Table 5-1 the baseline miss distance was 0.2 m, with an impact speed of 896 m/s, and an effort of 32. If the target performs an avoidance manoeuvre 2 s before impact (PN02 vs PN01) the miss distance increases to 0.7 m, the impact speed falls to 819 m/s and the effort doubles. ATPN with a gain of 4, missile and target acceleration compensation, and LOS to missile body scaling (PN07 vs PN01) marginally improves miss distance and impact speed, although the effort required rises to 45, a 40% increase compared with the baseline case.

The effect of varying the gain by [2(1)6] on performance is shown parametrically in Figure 9-5 to Figure 9-8 (PN03 to PN09). The results are as expected and giving confidence in the fidelity of the generic missile model. These results would suggest a gain of 2.8 - 3.5 for optimal impact speed with minimum miss distance and effort. From the review of guidance laws a gain of 4 maximises the target no-escape zone for manoeuvring targets without inducing excessive fin noise. These results demonstrate how miss distance alone can be misleading as the trends show a falling impact speed as the gain increases even though the miss distance continues to decrease slowly.

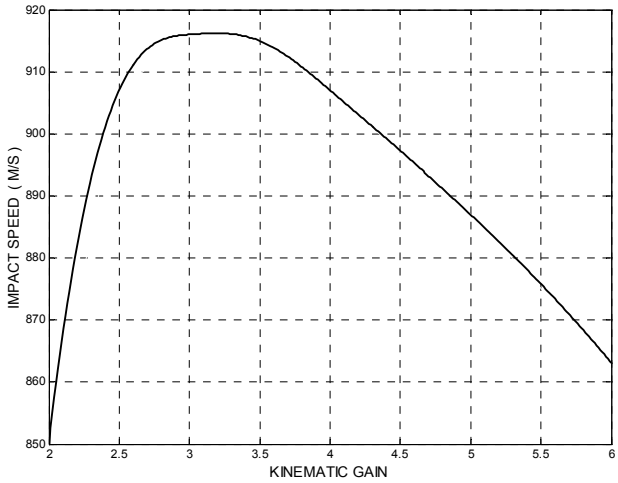

Figure 9-5 : Impact Speed vs PN Gain

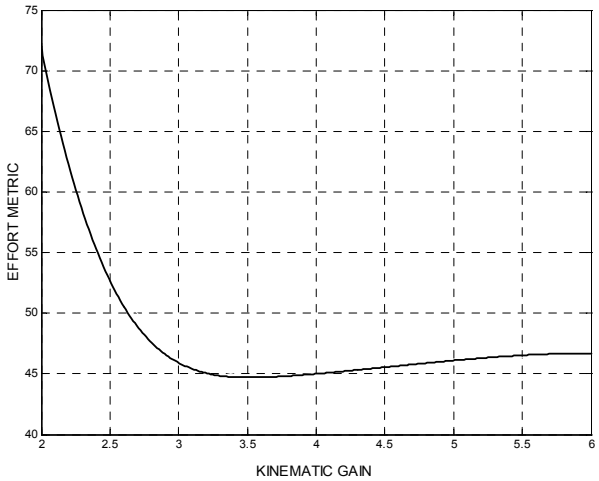

Figure 9-6 : Effort vs PN Gain

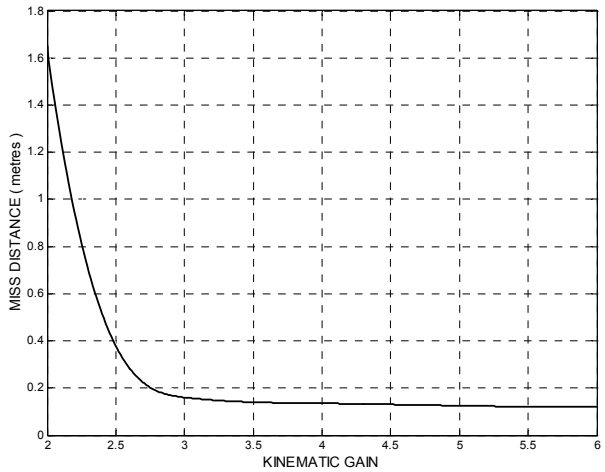

Figure 9-7 : Miss Distance vs PN Gain

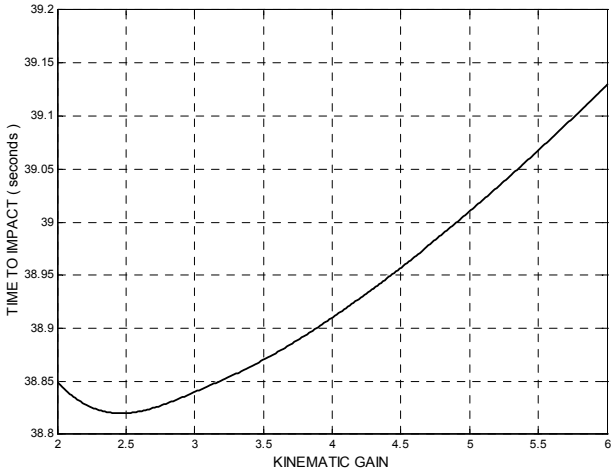

Figure 9-8 : Flight time vs PN Gain

Cases PN01 (blue), PN02 (green) and PN07 (red) are compared in Figure 9-9 to Figure 9-12. The traces terminate just before impact with respect to the shortest flight time. PN02 (no compensation) shows the typical LOS rate increase and lateral acceleration limiting when the missile is close to impact with a commensurate drop in impact speed. Performance is much the same until the target manoeuvres and target acceleration compensation improves the terminal flight profile maintaining the impact speed.

The performance in cases PN03 (gain := 2 - green), PN07 (gain := 4 - blue) and PN09 (gain := 6 - red) are compared in Figure 9-13 to Figure 9-16. With the target is flying at constant velocity, reducing the rate at which the a collision course is established by dropping the gain to 2 reduces incidence and hence improves missile speed. However, if the target manoeuvres guidance is clearly inadequate and control saturation ensues. Increasing the gain to 6 rapidly establishes the impact geometry at the expense of speed and higher incidence eventually resulting in a reduced impact speed of

863 m/s. Increasing the guidance bandwidth so that the missile can respond rapidly to target manoeuvres is detrimental in the non-manoeuvring case. Clearly the choice of gain is dependent on manoeuvring levels and hence the up-linked IMM filter probabilities.

PN performance and gain selection against weaving targets is fundamentally different. Target compensation induced LOS rates as guidance tries to establish the a non-existent constant velocity geometry, were so severe the compensation was switched off until the missile achieved Mach 2 at (launch + 2 s). Baseline performance with a gain of 4 and no acceleration compensation (PN10 - blue) is compared with (PN11 - green) no target compensation, and (PN14 - red) delayed target compensation in Figure 9-17 to Figure 9-20. There is little difference in the performance without target acceleration. Target compensation against weaving targets is clearly detrimental with excessive LOS rate oscillations throughout the flight.

Care is required when quoting miss distance and impact speed against weaving targets. The weave phase, and to a lesser extent the target lateral acceleration, must be treated as stochastic variables in a Monte Carlo analysis for definitive results. This deficiency was highlighted in the discussion on targets in §2. The results here are sufficient to demonstrate the fundamental difference in approach between constant velocity and weaving targets. The performance using different gains PN12 (gain := 2: green), PN14 (gain := 4: blue) and PN16 (gains := 6: red) is compared in Figure 9-21 to Figure 9-24. The trends are similar to previous results with the higher bandwidth inducing larger oscillations at the expense of a 50 m/s reduction in impact speed. These results show the importance of weave detection, as distinct from lateral manoeuvre detection. Ideally the target acceleration compensation must be removed and the gain reduced as the target weaves. Low bandwidth is preferable against weaving targets so as to track the underlying trajectory until close to impact. Close to the target the bandwidth must be increased to remove the heading error dependent on the phase of the target relative to its fundamental trajectory.

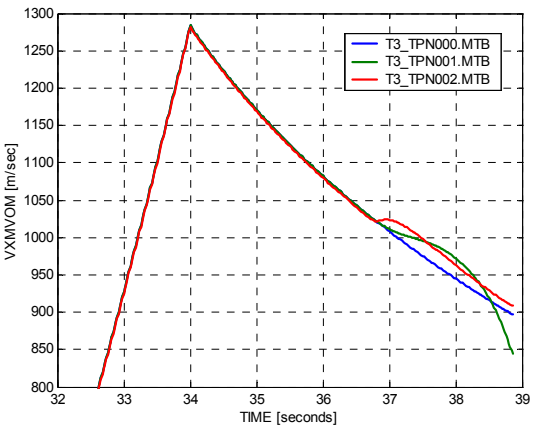

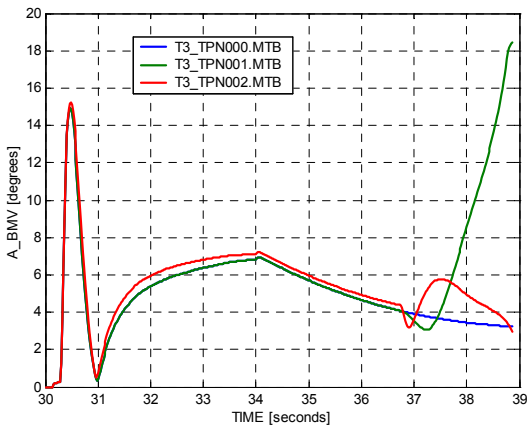

Figure 9-9
Speed (Trajectory 3)

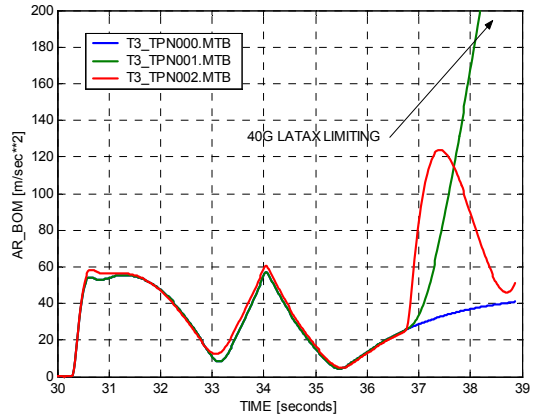

Figure 9-10
Body Incidence (Trajectory 3)

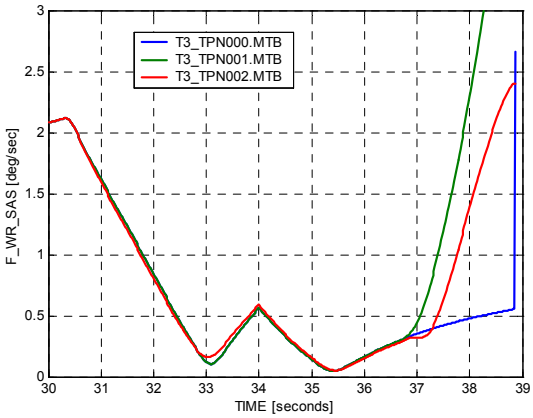

Figure 9-11
Lateral Acceleration (Trajectory 3)

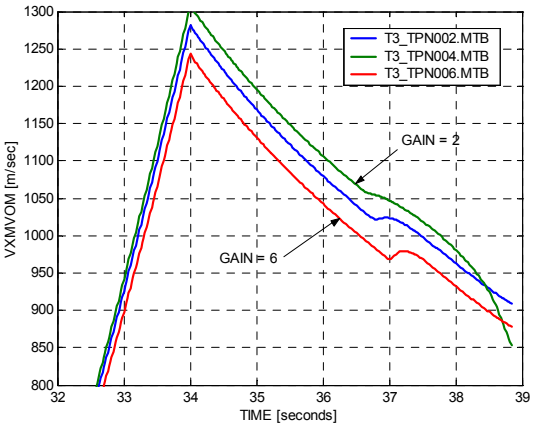

Figure 9-12
Seeker LOS Rate (Trajectory 3)

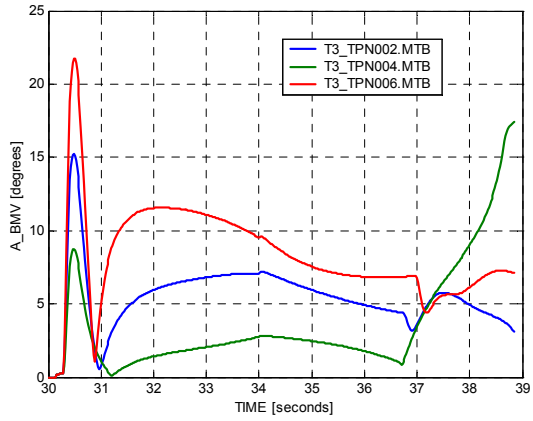

Figure 9-13
Speed (Trajectory 3)

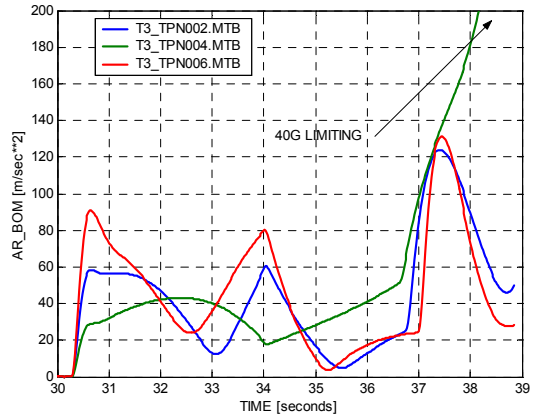

Figure 9-14
Body Incidence (Trajectory 3)

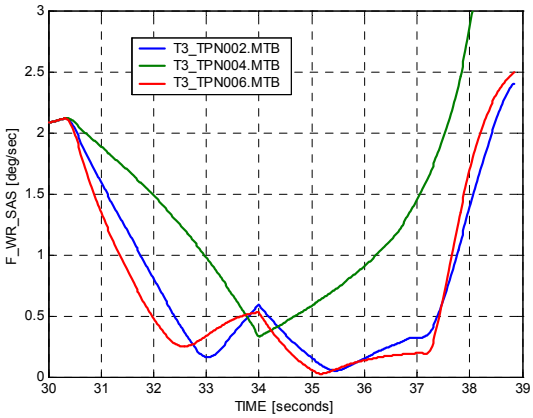

Figure 9-15
Lateral Acceleration (Trajectory 3)

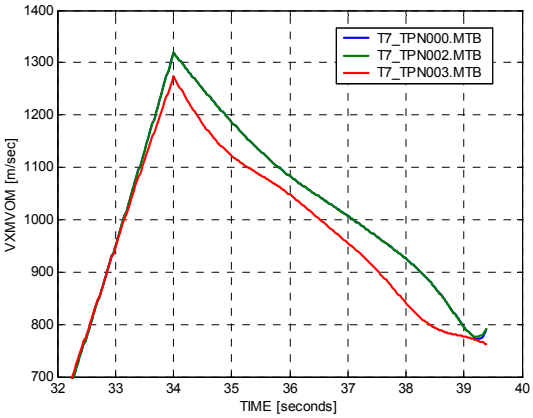

Figure 9-16
Seeker LOS Rate (Trajectory 3)

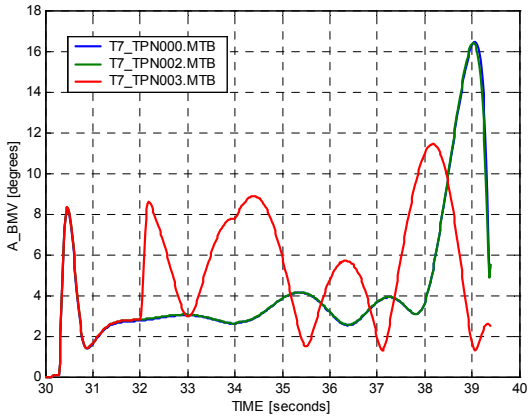

Figure 9-17
Speed (Trajectory 7)

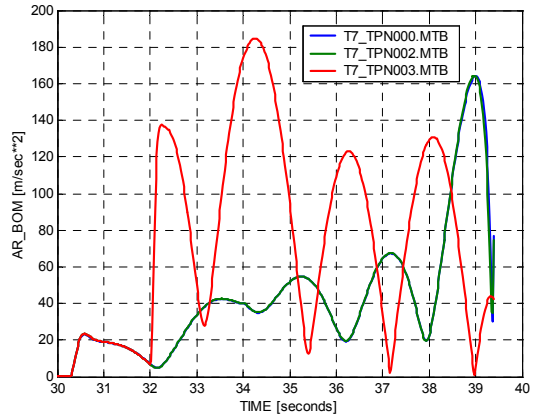

Figure 9-18
Body Incidence (Trajectory 7)

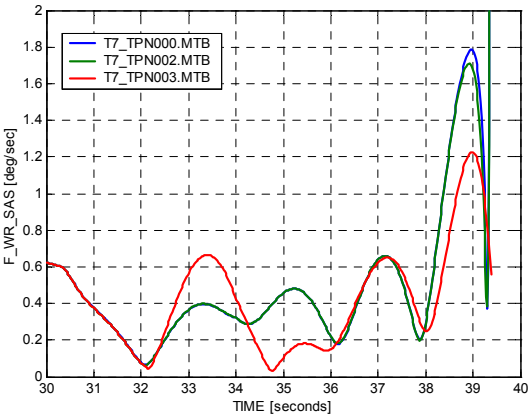

Figure 9-19
Lateral Acceleration (Trajectory 7)

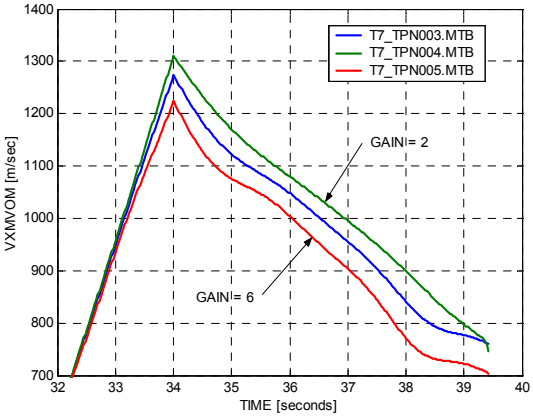

Figure 9-20
Seeker LOS Rate (Trajectory 7)

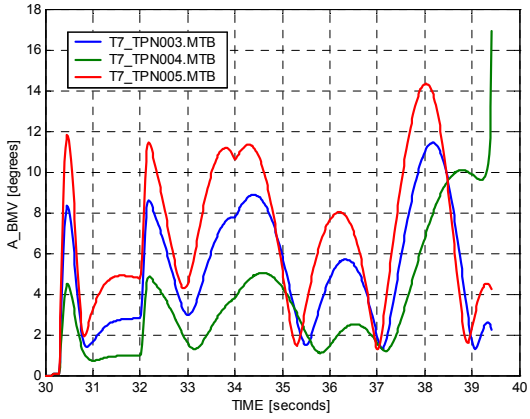

Figure 9-21
Speed (Trajectory 7)

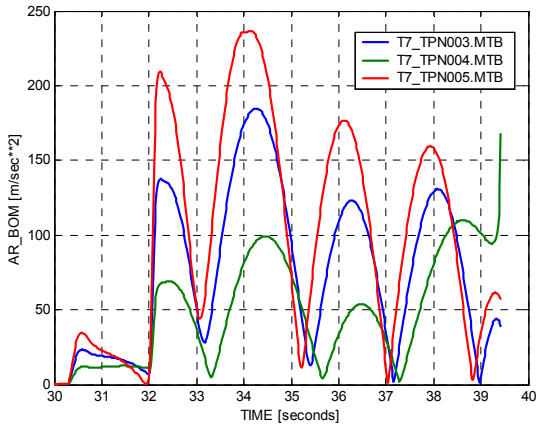

Figure 9-22
Body Incidence (Trajectory 7)

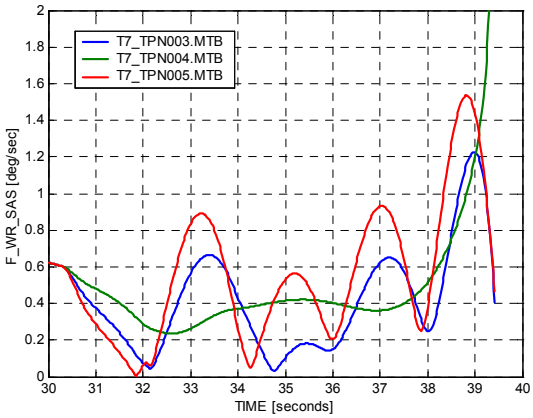

Figure 9-23
Lateral Acceleration (Trajectory 7)

Figure 9-24
Seeker LOS Rate (Trajectory 7)

9.4 CLOS Performance

The missile trajectories against Targets 3 and 7 are shown in Figure 9-25 and Figure 9-26 respectively. CLOS guidance is used with compensation terms included using the same autopilot as was used for the previous PN performance assessment.

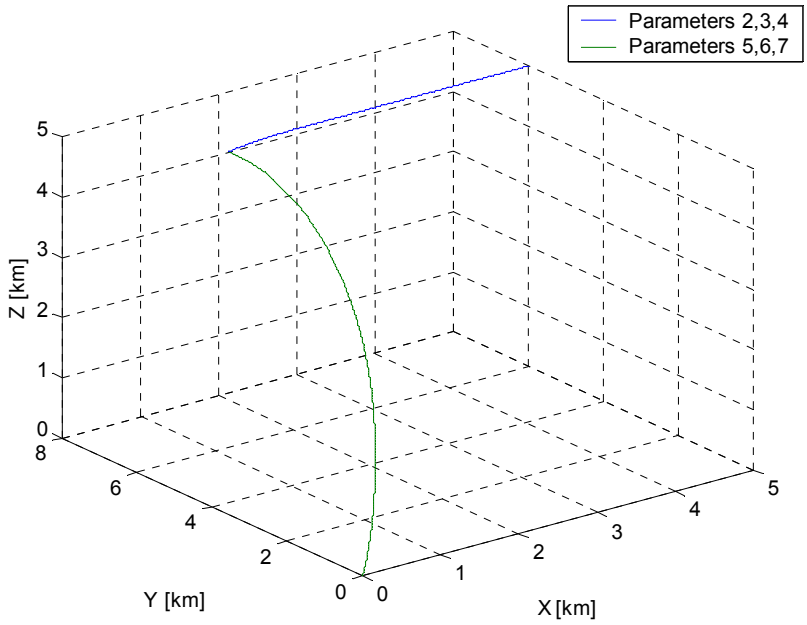

Figure 9-25 : CLOS Track (Target Trajectory 3)

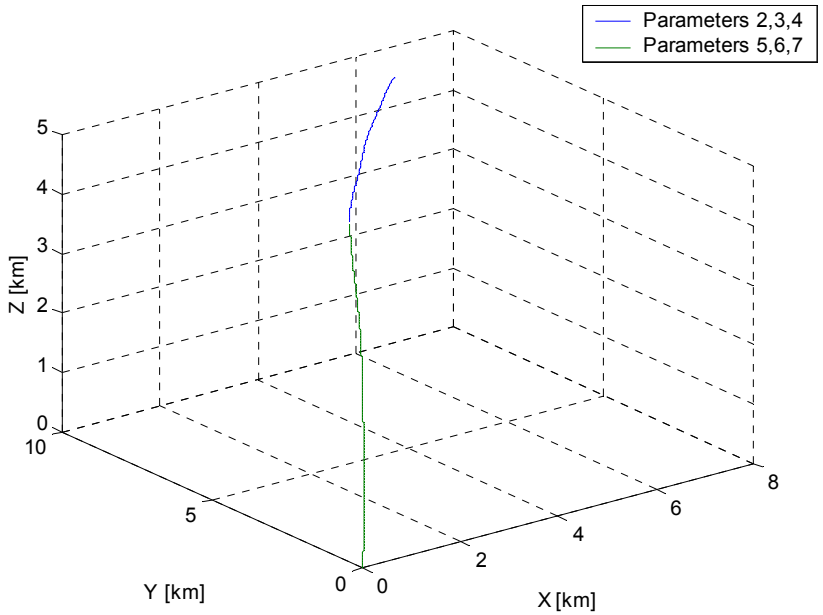

Figure 9-26 : CLOS Track (Target Trajectory 7)

The baseline performance for Target 3 contains no body-to-beam, missile or target acceleration compensation (CL01 - blue). This is compared with (CL02 - green), the same with a target avoidance manoeuvre with 2 s to impact, and (CL03 - red) fully compensated with target manoeuvre, in Figure 9-27 to Figure 9-30.

Baseline performance is typically poor without the compensation terms that remove boost phase oscillations and increasing missile speed. Compare the cases in which the target manoeuvres prior to impact. The compensation reduces the miss distance from 11 m to 5 m with less effort at the expense of impact speed that drops from 695 m/s to 671 m/s. The performance of CLOS compared with PN in respect of miss distance demonstrates why PN is preferred for terminal guidance, particularly for long-range engagements.

Now consider CLOS performance against a weaving target by comparing (CL04 - blue) with no compensation, and (CL05 - green) with compensation in Figure 9-31 to Figure 9-34. Apart from the aforementioned oscillations during the boost phase that are removed by the compensation, the performance of the two is similar.

The miss distance of 0.7 m is fortuitous, a reflection of the weave phase, although the beam stiffness was sufficient to track the weave expending slightly less energy as in the equivalent PN case. The missile is less responsive and better able to follow the underlying trajectory upon which the target weave is superimposed. From these results CLOS performs better against weaves than relatively high bandwidth PN, which fares better against constant velocity for which it is designed and manoeuvring targets.

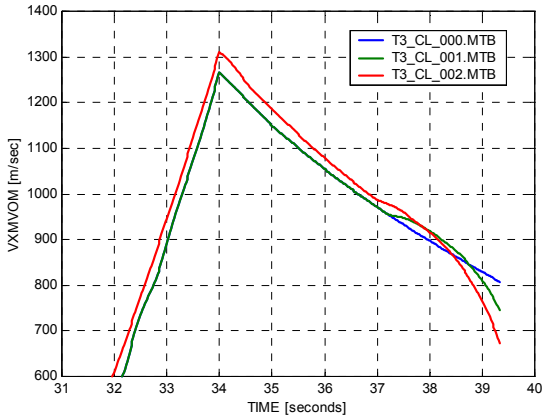

Figure 9-27
Speed (Trajectory 3)

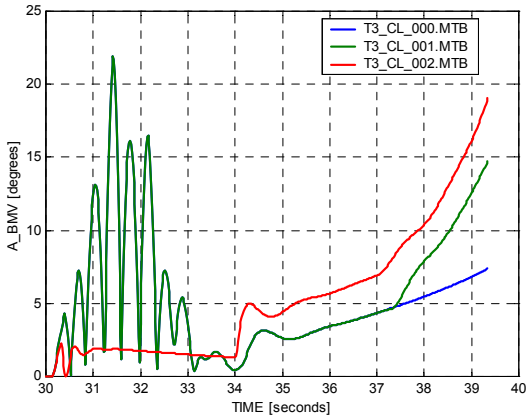

Figure 9-28
Body Incidence (Trajectory 3)

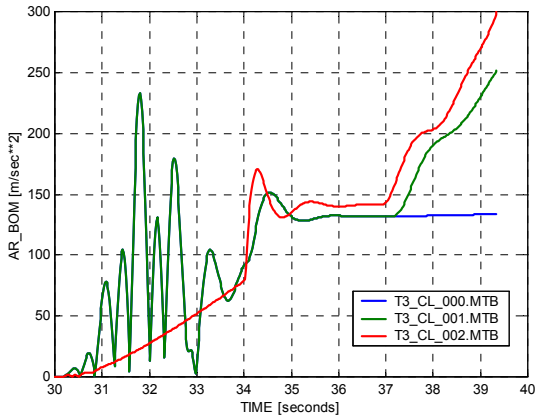

Figure 9-29
Lateral Acceleration (Trajectory 3)

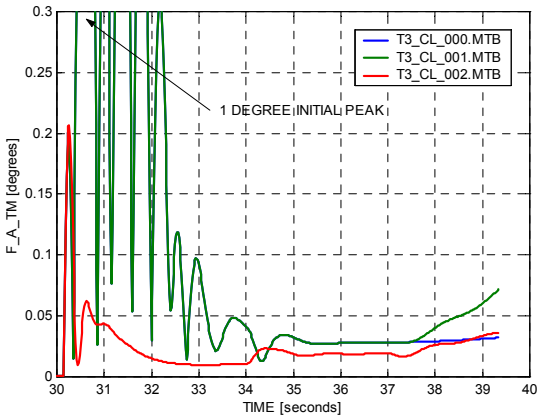

Figure 9-30
Differential Angle (Trajectory 3)

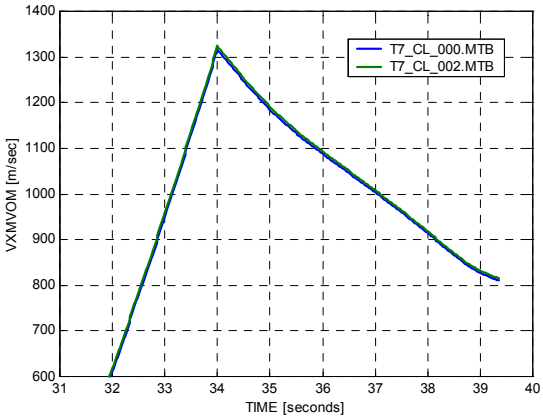

Figure 9-31
Speed (Trajectory 7)

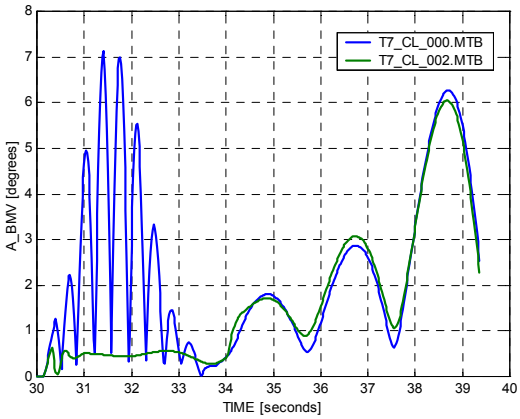

Figure 9-32
Body Incidence (Trajectory 7)

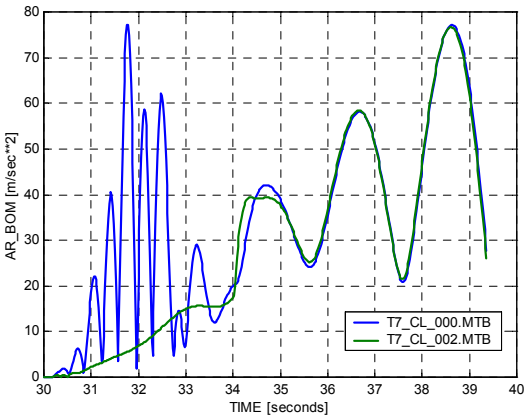

Figure 9-33
Lateral Acceleration (Trajectory 7)

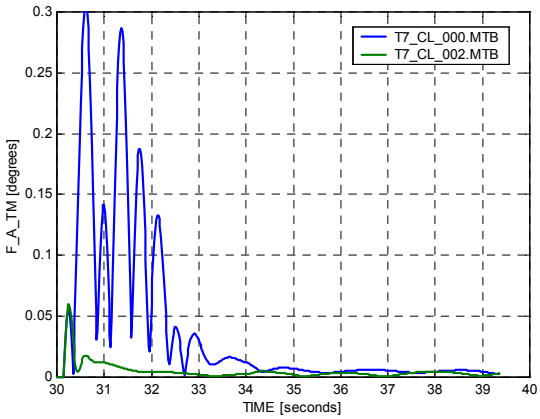

Figure 9-34
Differential Angle (Trajectory 7)

Chapter 9 / Performance

Table 9-1 : Simulation Test Cases, Data Files and Performance

Code	Filename	Speed (m/s)	Time (s)	Miss (m)	Effort	DESCRIPTION AND RUN CHARACTERISTICS
PN01	T3_TPN000	896	38.86	0.23	32.0	TPN: no missile or target acceleration compensation: target trajectory 3 with no target avoidance close to impact: PN gain = 4
PN02	T3_TPN001	819	38.92	0.74	63.8	TPN: no missile or target acceleration compensation: target trajectory 3, target avoidance 2s to impact: PN gain = 4
PN03	T3_TPN004	850	38.85	1.65	72.1	PN07 : PN gain := 2.0
PN04	Not retained	910	38.82	0.19	52.7	PN07 : PN gain := 2.5
PN05	T3_TPN003	915	38.84	0.21	45.9	PN07 : PN gain := 3.0
PN06	Not retained	914	38.87	0.13	44.7	PN07 : PN gain := 3.5
PN07	T3_TPN002	907	38.91	0.13	45.0	ATPN: full compensation: target trajectory 3: target avoidance 2s to impact: PN gain := 4.0
PN08	T3_TPN005	887	39.01	0.13	46.1	PN07 : PN gain := 5.0
PN09	T3_TPN006	863	39.13	0.12	46.7	PN07 : PN gain := 6.0
PN10	T7_TPN000	795	39.39	0.33	45.1	TPN: no missile or target acceleration compensation : target trajectory 7: PN gain = 4
PN11	T7_TPN002	796	39.40	0.17	44.9	TPN: missile but no target acceleration compensation : target trajectory 7: PN gain = 4
PN12	T7_TPN004	732	39.43	0.29	50.7	PN14 : PN gain = 2
PN13	Not retained	760	39.52	0.29	62.4	PN14 : PN gain = 3
PN14	T7_TPN003	721	39.65	0.23	76.4	TPN: missile acceleration compensation but no target acceleration compensation until 2s after launch: target trajectory 7: PN gain = 4
PN15	Not retained	706	39.77	0.15	88.0	PN14 : PN gain = 5
PN16	T7_TPN005	672	39.96	0.14	98.0	PN14 : PN gain = 6
CL01	T3_CL_000	801	39.42	4.51	106.1	CLOS: no body-to-beam, missile or target acceleration compensation: target trajectory 3, no target avoidance
CL02	T3_CL_001	695	39.54	11.06	123.4	CLOS: no body-to-beam, missile or target acceleration compensation: target trajectory 3, target avoidance 2s to impact
CL03	T3_CL_002	671	39.35	5.05	115.3	CLOS: body-to-beam, missile and target acceleration compensation: target trajectory 3, target avoidance 2s to impact
CL04	T7_CL_000	809	39.40	0.69	34.7	CLOS: no body-to-beam, missile or target acceleration compensation: target trajectory 7
CL05	T7_CL_002	815	39.37	0.69	29.2	CLOS: body-to-beam, missile and target acceleration compensation: target trajectory 7

Chapter 9 / Performance

9.5 IMM Filter Tuning and Verification

Discrete filters can only approximate the actual continuous target dynamics. Even using perfect measurements in a state space matched to the dynamics of the target, a discrete filter still requires process noise to compensate for piecewise continuous velocity or acceleration models. This is important when tracking long-range targets using high frequency measurement updates as the state covariance can become unacceptably small.

The IMM filters were verified and tuned using idealised target trajectories suited to their dynamics as described in §2.4. The filters were updated at 10 Hz using radar range, range-rate, and angle measurements corrupted by 10 m, 4 m/s and 3 mrad (1σ) noise respectively. Monte Carlo analysis was performed using 50 runs. Performance metrics were computed after each measurement update and ensemble analysis provided between 10 s and 30 s, the onset and cessation of the manoeuvres.

When tracking targets whose dynamics are radically different to those assumed Kalman Filters can become ill-conditioned without the injection of sufficient process noise. IMM filter re-initialisation should be performed at a rate commensurate with the evolution of the individual filter dynamics for discrimination purposes. This process is only effective when the innovation statistics reflect the filter's inherent dynamics i.e. only low levels of process noise can be used. It is therefore important that the filters with inappropriate dynamics remain stable over the re-initialisation interval.

9.5.1 Acceleration Filter Tuning

A target turning in the Alignment frame was tracked using the acceleration filter with process noise levels ranging from 0.1 $m^2/s^4/Hz$ to 100 $m^2/s^4/Hz$. The maximum position error from the ensemble results at each update as a function of the process noise is shown in Figure 9-35.

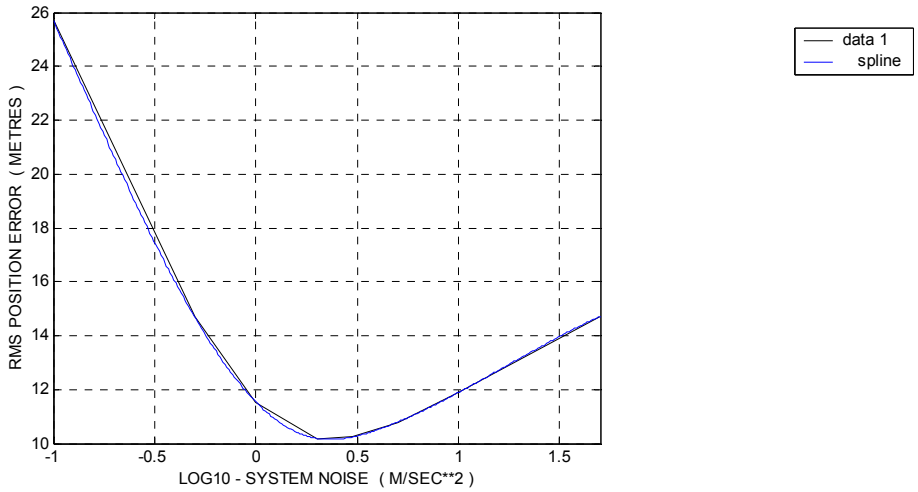

Figure 9-35 : Acceleration Filter Maximum Position Error

Initially the position error falls as the noise increases to 2.5 $m^2/s^4/Hz$, compensating for model mismatch caused by filter digitisation. Thereafter the filter is increasingly de-sensitised to the measurements and the error begins to increase. Figure 9-36 shows the time taken for the filter to estimate the target acceleration as a function of the system noise. The response time is the time from manoeuvre onset to the peak overshoot. The filter took 0.6 s to 1.5 s to respond using noise in the range [1,10] $m^2/s^4/Hz$. Tracking accuracy and manoeuvre detection are mutually exclusive and the selection of system noise level is a trade-off between the two.

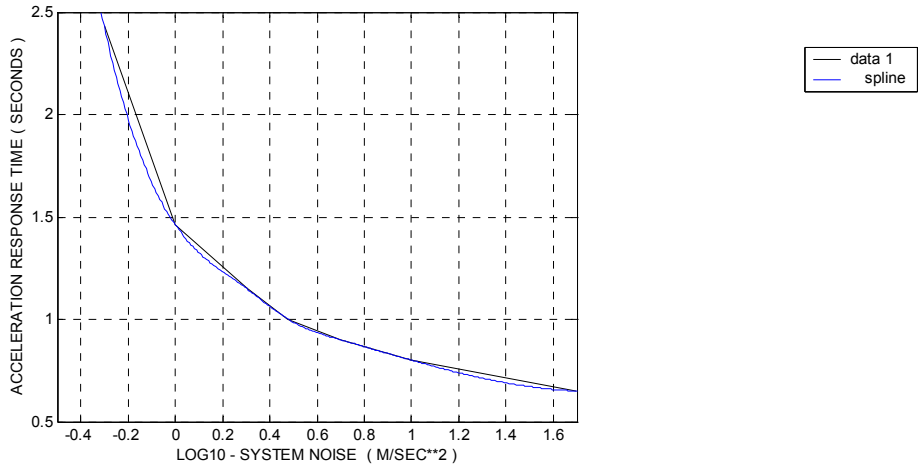

Figure 9-36 : Acceleration Filter Time to Peak Acceleration Overshoot

Figure 9-37 shows the acceleration error (PI_A) during the turns as a function of time for noise of 1 $m^2/s^4/Hz$ (blue), 3 $m^2/s^4/Hz$ (green) and 10 $m^2/s^4/Hz$ (red). Using 10 $m^2/s^4/Hz$ noise the changes in acceleration that occur at 10 s, 17 s and 24 s are hardly detectable and the error is typically 12 m/s^2. As the noise is reduced the steady-state performance improves, the acceleration errors dropping to 2 m/s^2, although the filter is now less responsive to changing acceleration levels.

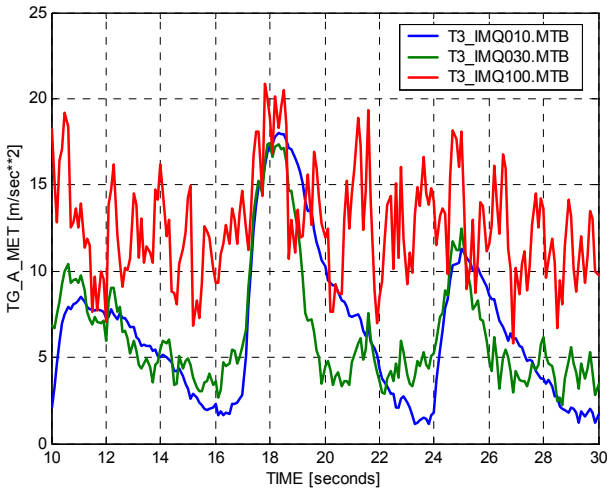

Figure 9-37 : Acceleration Filter Acceleration Error (PI_A)

This effect is clearer if one considers the normalised acceleration error shown in Figure 9-38. Using noise levels of 1 $m^2/s^4/Hz$ the filter is tuned to the steady-state turn (normalised error close to 1). The changes in the acceleration levels are now distinct, compared with 10 $m^2/s^4/Hz$ when they are hardly detectable. This is why the mode transition probabilities in the IMM must inject noise when a transient is detected using the Singer filter.

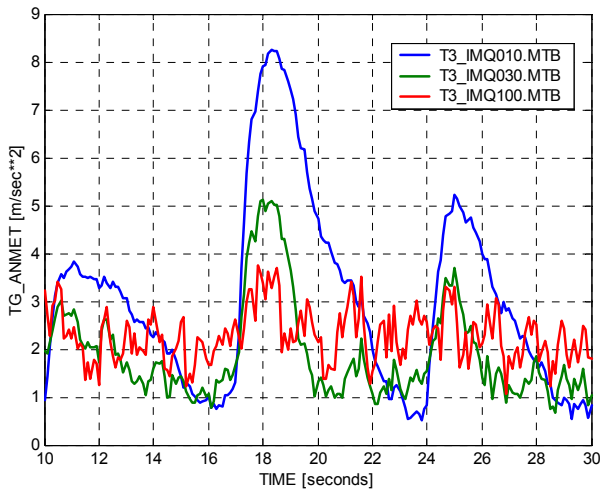

Figure 9-38 : Acceleration Filter Normalised Acceleration Error ($\overline{PI}_A$)

IMM performance is more accurate than other types of stochastic filter following a mode change, Li[L.36]. This can be inferred from these results as 3 $m^2/s^4/Hz$ provides a faster settling time to the steady-state than does 1 $m^2/s^4/Hz$. Once a new mode or acceleration level has been established it is clearly important to purge the noise from the system so as to reduce the steady state error.

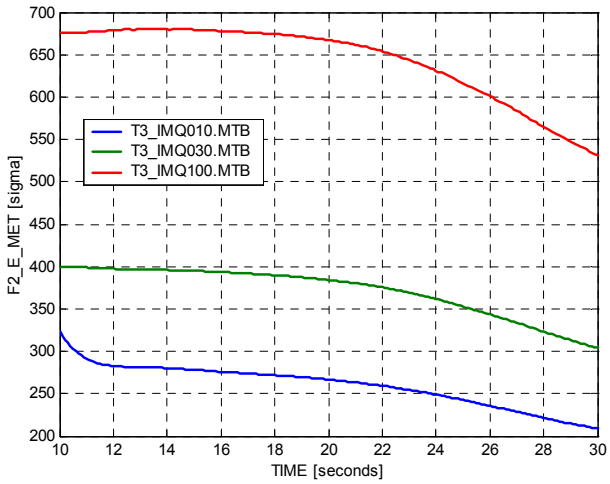

Figure 9-39 : Acceleration Filter Conditioning Number

Figure 9-39 shows that the Conditioning Number (CN) increases with the system noise level. The filter becomes less observable, confirming that high

values of CN are not always a reliable indicator of accuracy, nor even stability, Daum[D.2]. Noise of 1 $m^2/s^4/Hz$ was finally selected. The actual position and acceleration errors compared with filter expectations are shown in Figure 9-40. The position error is reasonably matched to the expectation, although the steady state acceleration error is lower than filter expectation indicating some over damping.

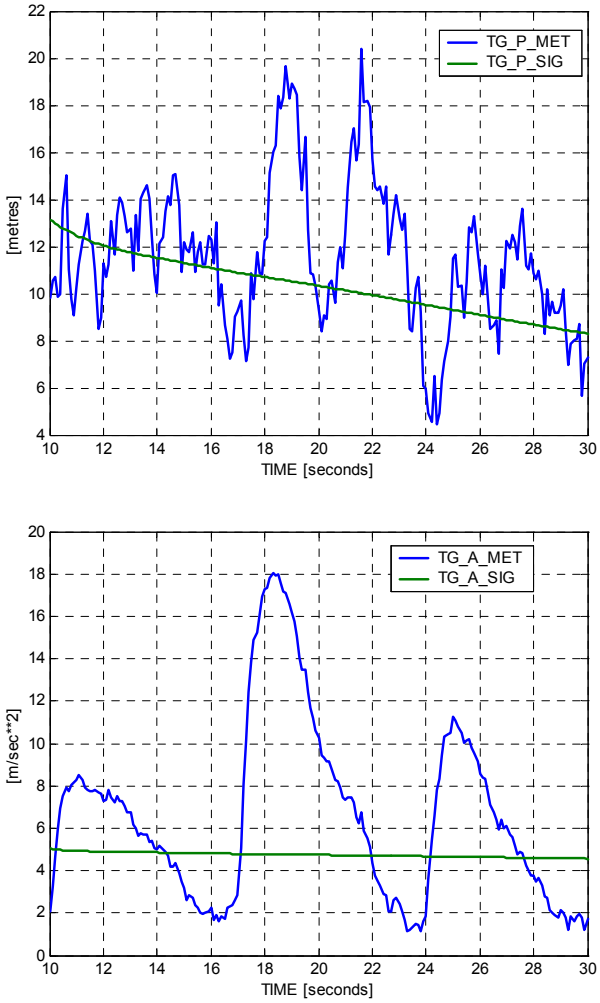

Figure 9-40 : Tuned Acceleration Filter

Position and Acceleration Errors (PI_P) and (PI_A)

This performance was compared with that using the Joseph covariance update, and serially processing combinations of radar range, range-rate and angle measurements. There was very little improvement in performance at the current 10 Hz measurement update rate. One concludes that using 64 bit arithmetic and linearisation between serial measurement updates removes any sensitivity that may have existed. These techniques, together with iteration and 2^{nd} order filtering, are only expected to make a significant impact if the radar update rate reduces significantly to say 1 Hz.

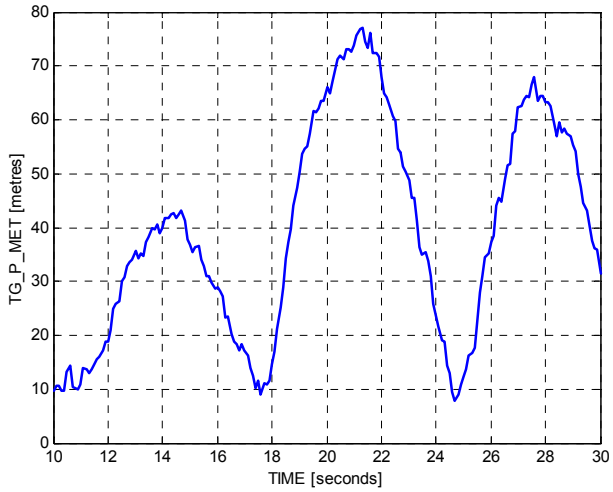

Figure 9-41 : Acceleration Filter Position Error (PI_P)

The tuned acceleration filter was used to track the target "U" turn designed for Singer model tuning. The position error shown in Figure 9-41 indicates that whilst the filter does not track the manoeuvre, the errors approaching the actual acceleration of the target, it remains stable.

9.5.2 Velocity Filter Tuning

The velocity filter was used to track a constant speed crossing target using system noise levels of (0.2, 1, 3, 10) $m^2/s^4/Hz$. The CN is shown in Figure 9-42, and the position and velocity errors in Figure 9-43. A noise level of 1 $m^2/s^4/Hz$ was selected, a compromise between minimising the steady state error and observability.

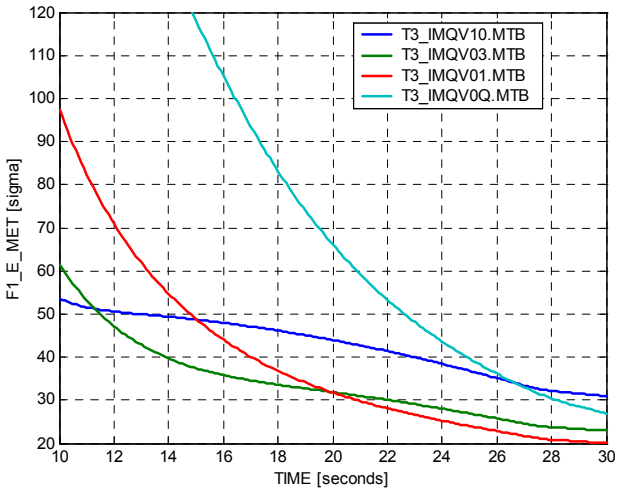

Figure 9-42 : Velocity Filter Conditioning Number

Figure 9-44 shows the position and velocity errors when the noise is set to 1 $m^2/s^4/Hz$ compared with filter expectations. There is a concern that the

crude initialisation introduces errors that are initially outside expectation that take upwards of 4 s to decay.

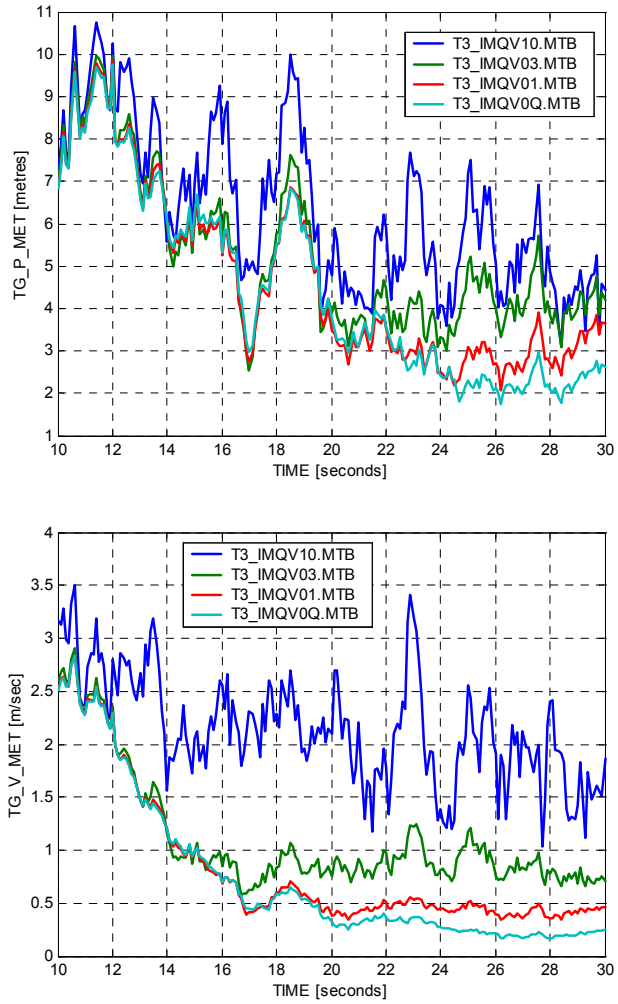

Figure 9-43

Velocity Filter - Position and Velocity Errors, (PI_P) and (PI_V)

The gradual reduction in the errors, and the improvement in observability as indicated by the CN, is due to the relative position of the target with respect to the radar. The closest approach to the radar occurs at approximately 30 s when range-rate measurements are most effective.

The velocity filter position error when tracking a target performing a "U" turn designed for Singer filter tuning is shown in Figure 9-45. Although the performance is poor the velocity filter by remains stable.

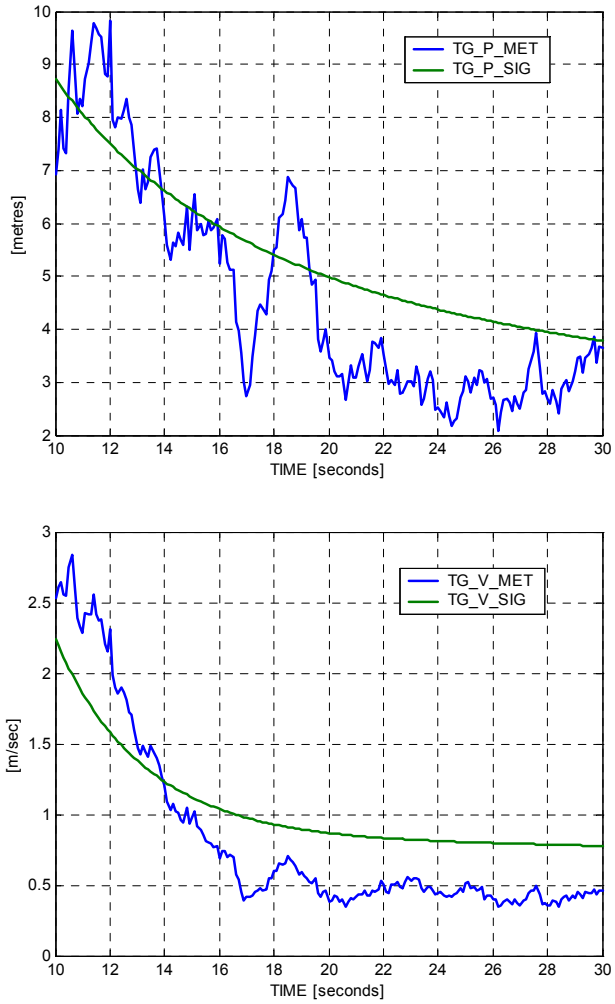

Figure 9-44

Tuned Velocity Filter - Position and Velocity Errors, (PI_P) and (PI_V)

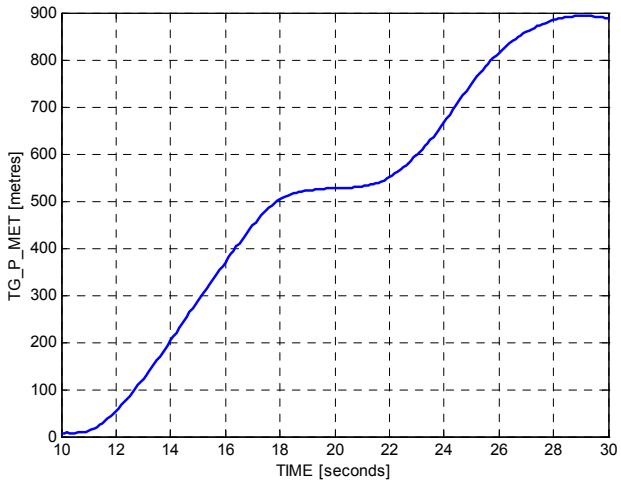

Figure 9-45 : Velocity Filter Position Error (PI_P)

9.5.3 Singer Filter Tuning

The Singer filter system noise was not tuned, it was set to 80 m/s^2 representing a sustained 9 g manoeuvre (5 g in each Cartesian axis). Figure 9-46 and shows the position and acceleration errors when tracking the "U" turn test trajectory. The injection of large amounts of process noise means that the tracking errors remain high, with mean PVA errors over the 20 s sampling interval of 19 ± 3 m, 54 ± 14 m/s and 83 ± 19 m/s^2 respectively.

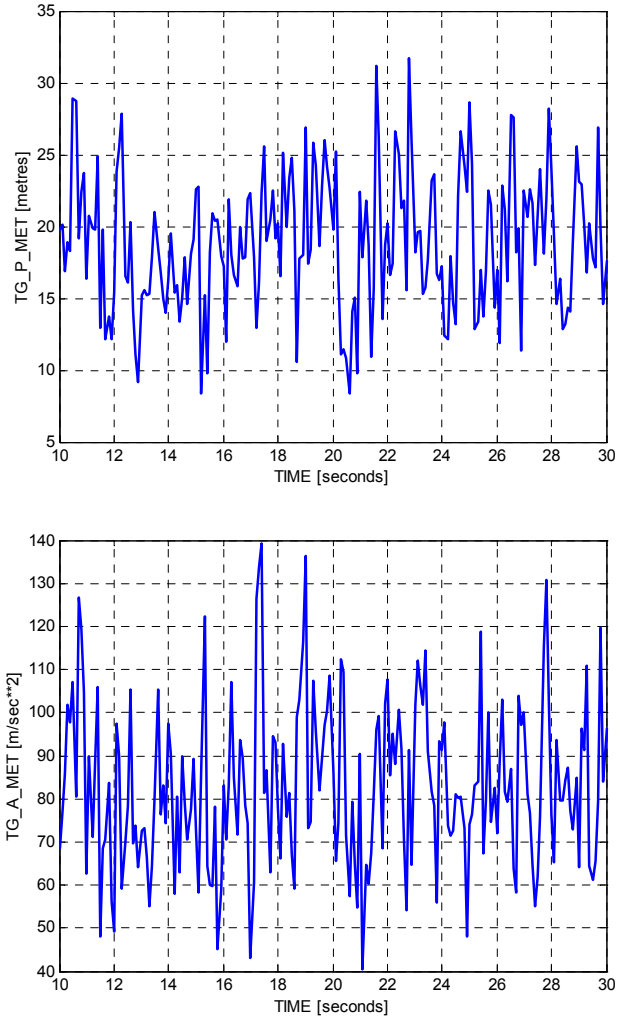

Figure 9-46

Singer Filter - Position and Acceleration Errors, (PI_P) and (PI_A)

These results reinforce the comments of Mazor[M.2] that the classical use of filters with large amounts of system noise make them oblivious to small dynamic changes, whereas hybrid systems such as the IMM are expected to remain responsive.

9.6 Discussion

The studies undertaken so far have proven the simulation infrastructure, target, tracking and missile simulators. The reference and state observer parameters listed in §22.3 were verified, as was the launcher, in-tube and free flight missile dynamics, in particular the low speed thresholds applied for stability when using the simplified generic model.

A study of PN and CLOS guidance laws provides a performance baseline against which other guidance laws and trajectory optimisation can be judged. The laws, stimulated by reference data, were used to stimulate the guidance laws and a STT autopilot whilst engaging Target 3 (crossing) and Target 7 (weaving GOT) with an avoidance manoeuvre 2 s from impact.

The IMM filters are tuned in isolation to determine suitable system noise levels when tracking targets with matching dynamics using range, range-rate and angle measurements corrupted by Gaussian noise.

9.6.1 PN Study

The ATPN guidance law from §6 was selected on the basis of this study trajectory optimisation initialisation. For the crossing target a gain of 3 to 3.5 results in maximum impact speed and minimum effort. The miss distance dropped sharply as the gain increases from 2 to 3, and only marginally thereafter as expected. It is known that miss distance and control effort minimisation against manoeuvring targets requires a gain of 4 to maximise the no escape region.

PN performance against weaving targets was poor but improved as the gain, and hence bandwidth, were reduced. The implication being that PN performance can be improved given target manoeuvre discrimination, perhaps using the IMM filter probabilities, or the output from the missile state observer. For example, make the PN gain a function of the IMM weave filter probability with an upper threshold of 0.5,

$$\lambda_m := 4 \cdot \left(1 - {}_{UL}\mu_4 \Big|_0^{0.5} \right)$$

Equation 9.6-1

This places the onus on the IMM to properly reflect the dynamic mode of the system. At low speeds, target acceleration compensated PN performs badly as it tries to establish a collision course against the weaving target. This form of compensation should be introduced as a function of Mach number limited to a value of 1.

9.6.2 CLOS Study

The CLOS study showed how important missile longitudinal acceleration and body-to-beam compensation are, particularly at low speed and when boosting. The miss distances achieved with the fully compensated guidance law were 3 times larger than the PN equivalents. A feature of CLOS is the increase in miss distance with range, hence the need for a seeker and a terminal guidance phase at long-range.

Under ideal conditions the beam stiffness used allowed the missile to follow the weaving target LOS indicating, as did PN, that range-to-go bandwidth control is required if control effort is to be minimised.

9.6.3 Tracking Filter Tuning Study

Velocity, acceleration and Singer filter performance against idealised targets was investigated; work is ongoing with the weave filter. System noise levels for the VA filters were set at 1 $m^2/s^4/Hz$ and 1 $m^2/s^6/Hz$ respectively to accommodate digitisation errors.

Using the low bandwidth acceleration filter, the normalised acceleration error rapidly exceeded the expected 3σ error in response to changes in target acceleration. This is ideal, both for IMM discrimination, and for later manoeuvre detection. By comparison, when a new constant acceleration regime is established the filter recovers slowly taking 2 s to 3 s. This is why the IMM filter transition probabilities are set to inject system noise under these circumstances.

Changing the measurement processing order made no difference to the tracking errors using a 10 Hz data rate. Using the most accurate measurement first, with re-linearisation, is only expected to improve accuracy at lower data rates.

The low bandwidth Singer filter as expected provided little measurement filtering with PVA errors of the order of 20 m, 50 m/s and 80 m/s^2. However, changes in the target flight regime associated with avoidance manoeuvring are expected to be short. During such periods the velocity and acceleration filters remained stable, if inaccurate, when tracking targets with a different dynamic model.

Chapter 10

CONCLUSIONS

Research Obective :

Select, develop and integrate algorithms for a "fifth" generation air-defence missile system using on-line trajectory optimisation, multiple-model target tracking and centralised state observation with distributed sensor track and plot fusion.

The process of algorithm selection and systems integration is complete and the relevant equations presented using a common nomenclature. A simulation has been created to support generic target and sensor models stimulating multiple-model target tracking, data up-link, and missile state observer. The estimates of target and missile data stimulate conventional guidance laws and trajectory optimisation. The process of model verification, technique validation and tuning is in progress and some initial results from this programme are presented.

The work was decompose into the following functional blocks that is typical for an air-defence weapon system:

- Targets (§2)
- Sensors (§3)
- State Observation (§4 and §5)
- Missile Guidance (§6 and §7)
- Simulation and Proving (§8 and §9)

Future weapon systems will be expected to use increasing computing capacities to maintain kill probabilities against agile targets whilst expanding their operational footprint. This requires advanced sensors, state observation, and advanced missile guidance techniques. Current "smart" weapons have reached the stage that proving can only be afforded using simulations underpinned by a limited number of flight trials. These conclusions gather together comments made in the discussion to be found at the end each chapter.

10.1 Nomenclature

A mathematical nomenclature has been developed so that algorithms from different research areas can be presented in a common framework, and to promote a consistent approach to simulation variablea. During this research the nomenclature evolved and was adopted for use on several major MBDA projects where refinement of its basic tenants continues. It has proven robust and capable of supporting systems comprising of multiple targets, launchers, missiles and defended assets.

10.2 Simulation

A simulation infrastructure has been created capable of supporting any model requiring state integration. For transportability, and compatibility with a range of host systems, it was developed as a self-contained entity. The following infrastructure facilities are particularly important for the rapid development and proving of algorithms:

- Interactive program control and data visualisation with access to a global data pool.
- A comprehensive library of utilities dealing with common mathematical operations.
- A data link to MATLAB for post processing and graphical presentation.

This infrastructure is used on several MBDA programmes for terrain following navigation, transfer alignment, and pre-launch studies involving air-launched munitions from various fighter aircraft. This expanding user group has accelerated software verification, and the refinement of the facilities provided. This software is now considered to be mature. As a test-bed for this research it supports a number of hierarchical simulators:

- Targets
- Sensors
- Target tracking
- Missile state observation
- Missile guidance (conventional and trajectory optimisation)

The simulators utilise reference, sensor or state observer data, depending on their level in the hierarchy. The reference, target tracking and missile observer states are the same by design. Copying the reference state into the observer state produces identical copies of the comprehensive set of parameters listed in §22.3, thereby stimulated algorithms indirectly with reference data.

10.3 Targets

The target simulator generates trajectories using elemental acceleration models activated and characterised either interactively or by external data. Stationary, crossing and head-on targets are initialised depending on the user input data, subject thereafter to acceleration demands filtered to produce realistic target dynamics. The elemental models comprise earth and target velocity referenced, piecewise constant acceleration, sinusoidal and square weaves. Specific models have been embedded in the simulator for IMM filter tuning, and for performance comparisons.

10.4 Sensors

Sensors were selected for their enduring impact on future weapon system development. They are broadly categorised as either earth referencing, or targeting instruments:

- IMU gyroscope and accelerometers
- Barometric and radar altimeters
- RF and IR sensors (Radar and seekers)
- Missile fin transducers
- NAVSTAR global positioning
- Helmet mounted sights
- Air data derived from Pitot tube and temperature detectors

A system level approach provides models that capture the essential characteristics of an instrument commensurate with its output bandwidth. Each sensor model is self-contained extracting its input from the reference state to promote cloning, and transportation to other applications. Any combination of characteristic errors can be superimposed on the reference input, the measurements passing through a 1553 digital interface.

Inertial IMU sensors provide absolute and incremental measurements at 800Hz characterised as mechanical, optical, or solid state devices. The generation of accurate reference inputs from earth referenced data for distributed master/slave IMU in the presence of body flexure is explored. The radar altimeter model relies on digital map error characterisation for nap-of-the-earth navigation. The GPS model provides 1 Hz or 10 Hz earth referenced position and velocity data rather than pseudo-measurements, data that depends on the geometry of the satellites selected for triangulation, and subject to errors such as selective availability. The ground based radar and missile seeker can be characterised as RF and IR devices and both have detectors encased in yaw-pitch gimbals that can be locked for strap-down applications.

10.5 State Observation

The tracking simulator comprises IMM re-initialisation and combination of constant velocity and acceleration, Singer and weave filter, the structure permitting the introduction of additional filters. An earth-referenced Cartesian frame was selected, assuming that extreme target manoeuvres are short. Transition probabilities were selected to inflate the filter covariances when the target regime changes. IMM re-initialisation occurs at 1 Hz, and combination at the 10 Hz up-link rate. Radar range, range-rate and angle measurements are serially processed by conventional EKFs; the simulator provides iterated EKF and 2nd order alternatives.

Low bandwidth filters are used so that changes in the target dynamics are readily observed. In isolation, manoeuvre detection was better than (onset + 1 s), with a (cessation + 4 s) recovery time. The velocity and acceleration filters remained stable when tracking targets for which they were not designed. Weave filter tuning and an assessment of its performance against Targets 3 and 7 is ongoing.

The IMM state, covariance, and filter probabilities are up-linked with radar missile range, range-rate and angle measurements to the missile state observer. The IMM state and covariance, based on the propagated filter state without measurement update, is also up-linked for correlated track fusion.

The missile EKF state observer operates in the same state space as the target tracker, and is updated by up-link data, gyroscope, accelerometer and seeker measurements. The process model is simple and is propagated at rates commensurate with seeker control and autopilot requirements. Stability is provided by 400 Hz gyroscope measurements (the one critical sensor), and accumulated accelerometer data processed at 100 Hz. The missile observer uses track fusion to absorb up-link target data. Pseudo-measurements are used to characterise the process model target and missile dynamics. This approach promotes flexibility: multi-rate processing for load alleviation, prioritisation, and the use of manoeuvre dependent dynamics based on the IMM filter probabilities.

10.6 Missile Simulation

The missile simulator supports a number of missile models one being the generic, point mass missile used for this research. The generic model is designed for stable flight from a rotating launcher using lateral acceleration and incidence limiting. The missile linear and angular motion is determined by its height and speed dependent incidence lag, lateral accelerations being applied in the direction determined by 2nd order STT and BTT autopilots.

10.7 Missile Guidance

The missile simulator constructs guidance commands from basic TPN, PPN and CLOS, introducing augmentations on requested. The infrastructure, targets and missile model were verified using augmented TPN and CLOS guidance against a crossing and a weaving target (Targets 3 and 7). Against crossing targets the optimal PN gain was 2.5-3 minimising the miss distance and effort, as expected. For weaving targets, bandwidth reduction according to IMM filter probabilities is proposed providing that the IMM can accurately discriminate between weaves and other types of target motion.

10.8 Trajectory Optimisation

Trajectory optimisation is performed in pseudo real-time for examining the effect of limited processing on convergence from an initial trajectory, and in response to changing boundary conditions. Pre-launch, a PN trajectory is updated until the target is reachable. The optimiser then updates a fixed number of controls from the initial state passing optimum pointing angles to the launcher. In-flight, a dwindling number of controls are re-optimised, scaled to accommodate the varying impact time, and split when the processing load halves.

The optimisation algorithm uses Steepest Descent and an Armijo line search to minimise the Hamiltonian formed by adjoining dynamic equality and inequality constraints to the cost function. Control limits are applied using an active set strategy. As cost reduction slows, conjugate directions are explored at intervals using a Fibonacci line search.

10.9 Future Research

Although a great deal has been accomplished, the scale of the research is ambitious and a considerable amount of simulation code verification and system proving remains. The near-term evolution of this work is presented in §11.

Chapter 11

FUTURE RESEARCH

Whilst laying the foundations for an advanced air-defence missile guidance system, references are made in the discussion sections to areas warranting further work, or in the case of the simulators useful additions to existing models. Observations of this type throughout the report are collected together and presented here.

For targets, sensors and the simulation infrastructure the focus is on extending the current facilities to make their generic design applicable to a wider range of research topics. This process culminates in a brief review of synergies between this simulation and the MBDA Aircraft and Missile Integration Simulation that was developed from it.

When radical changes are proposed to proven elements in existing weapon systems so as to increase their capability, continuity of design is essential. Inevitably, integration of the various functions, their verification, and eventual validation, requires a considerable amount of work well beyond that already presented. This is reflected in the recommendations for further work that follows.

11.1 Targets

- Randomise the phase offset of the elemental weave models.
- Provide the goal-orientated target with a moveable aim-point rather than the current missile launcher/radar, expressing its acceleration dynamics in the Alignment frame.
- Introduce an elemental model for the iterative solution of pursuit - evasion games subject to typical target limitations.
- Introduce a target reference frame defining its initial state, and angular acceleration dynamics, with respect to the Alignment frame. Place a target on the X-axis of this frame with linear LOS acceleration dynamics.

11.2 Sensors

Inertial Sensors

- Introduce a facility for modelling zero-mean angular rate and acceleration vibration rectification. Automatically generated a state space model driven by Gaussian noise that matches a smooth power spectrum defined at a number of frequencies.

Radar Altimeters

- Provide a sea-surface for sea-states in the range [0,7] using internationally accepted sea-spectra and a wide-beam error model.

Radar and Seekers

- Clone the detector error models so that that can be executed in parallel for 2-colour sensor fusion.
- Review the effect of frequency agility, multipath and clutter models, capturing their effect on the sensor measurements at the system level.

NAVSTAR GPS

- Determining satellite positions directly from Ephemeris data to compliment the idealised method based on a symmetrical 24 satellite constellation.
- Extend the earth and self-screening models to include satellite rejection when the local terrain impinges on the missile seeker LOS.

Air-Data Sensors

- Add a magnetometer error model and attitude extraction software.

11.3 Target State Observation

- Assess the stability of IMM tracking filters at 0.5 Hz and 1 Hz, repeating the filter tuning study presented in §9. Re-examine the measurement processing order and the benefits of iterating the EKF measurement update.

- Implement Li's robust IMM formulation that avoids bounding the filter transition probabilities and assess its benefits for typical target trajectories.
- Investigate the IMM re-initialisation rate when using high frequency measurement to establish the time it takes for the dynamic characteristics of a particular filter to emerge.
- Active set maintenance is proposed linked to generic types, reducing the computational load by using EKF incremental updates proposed by Hanlon.
- Explore Bootstrap and Particle filter formulations that combine individual filter outputs whilst preserving covariance higher order moments that are crudely approximated by the IMM using a Gaussian distribution.
- Establish filter probability thresholds for identify the start and end of target manoeuvres, and if possible discriminate between the type of manoeuvre.

11.4 Missile State Observation

- Assess if computing a covariance correction to account for non-optimal quaternion state normalisation is justified.
- Quantify the destabilising effect of treating high frequency IMM track data as measurements, and at what up-link rate can the correlation be ignored.
- Assess the robustness of IMM filter probabilities as manoeuvre detectors for conventional guidance enhancements and pseudo-measurement control.
- Quantify the residual error levels in the missile IMU sensors after a ground calibration subject to launcher rotation and vibration.

11.5 Trajectory Optimisation

- Compare the trajectories produced by each element of the cost function with analytic results, and the baseline results presented in §9.
- Quantify increases in target capture regions.
- Investigate convergence rates for alternative algorithms.
- Assess convergence rates as a function of processor load.
- Assess optimiser stability as characterised noise on the boundary conditions increases.
- Explore cost function combinations that prevent optimiser convergence and if such conflicts can be avoided by cost weight re-balancing, or by making the weights trajectory dependent.

11.6 Weapon System Simulation

Consider the future of the simulation created during this research and the AMIS spawned from it. The author hopes to develop the AMIS as a research tool that shares models with the simulators described here to create a combined pre- and post launch facility.

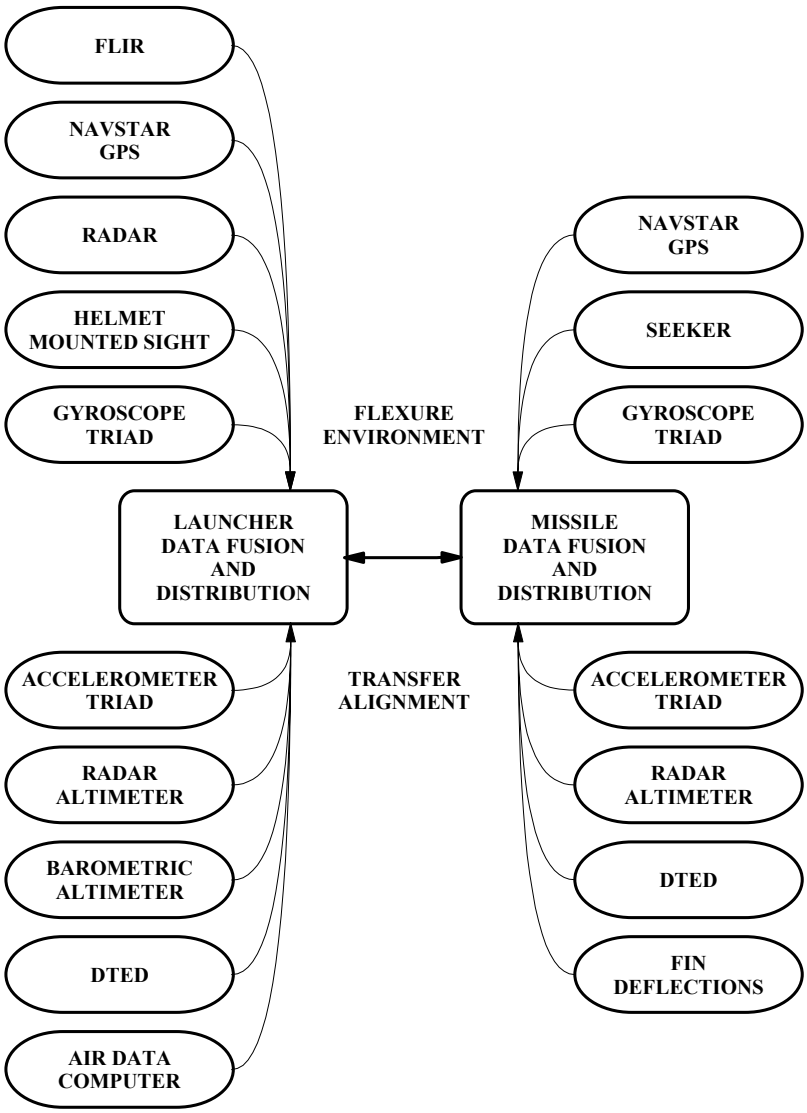

Figure 11-1 : AMIS Launcher and Missile Sensors

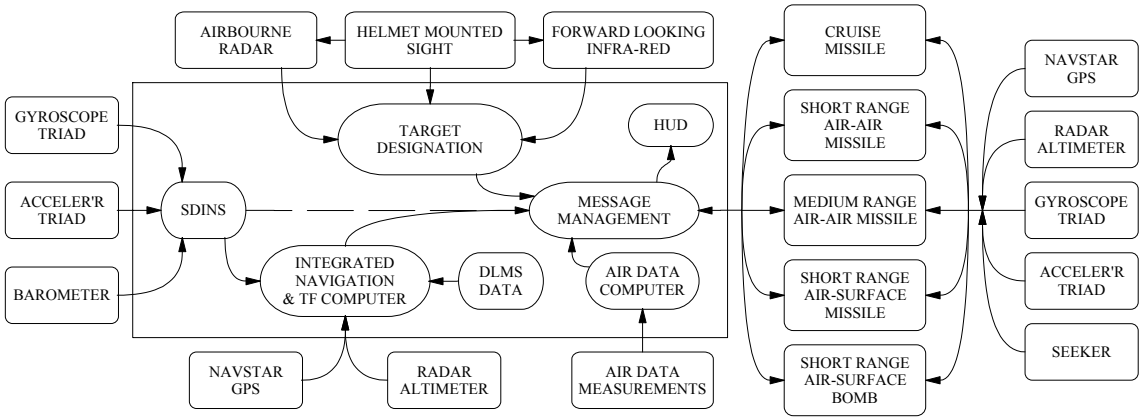

Figure 11-2 : AMIS Air-Launched Future Functionality

To build on, and expand, the many synergies existing between the two, and other MBDA products that share this software, thereby supporting an expanding used community.

Figure 11-1 captures the core of the AMIS concept with multiple launchers and missiles supported by a suite of generic sensors, models characterised internally, or by the user, for particular applications. Launchers with access to a target state observer similar to the one developed here. Likewise the generic missile with a state observer providing targeting and dynamic data required for conventional guidance and on-line trajectory optimisation. For air-launched applications it will support the systems shown in Figure 11-2 comprising integrated inertial navigation, air data and targeting. To provide a simulation capable of undertaking complex targeting and missile guidance, data fusion, and transfer alignment studies in a realistic vibration environment.

12 REFERENCES

References preceded by " # " have been cited from other references.

MBDA references are not available to the general public

A

A.1 ARCHER S.M., SWORDER D.D., "Selection of the Guidance Variable for a Re-Entry Vehicle", AIAA J. Guidance and Control, Vol. 2, No. 2, 1979, pp. 130-138.

A.2 #ADLER F.P., "Missile Guidance by 3D Proportional Navigation", J. Applied Physics, No. 27, 1956, pp. 500-507.

A.3 ANDRISANI D., KUHL F.P., GLEASON D., "A Nonlinear Tracker Using Attitude Measurements", IEEE AES, Vol. 22, No. 5, 1986, pp. 533-539.

A.4 ARCASOY C.C., "The $\alpha-\beta-\gamma$ Tracking Filter with a Noisy Jerk as the Maneuver Model - Frequency Domain Solution", IEEE AES, Vol. 32, No. 3, 1996, pp. 1170-1173.

A.5 ARCASOY C.C., OUYANG G., "Analytical Solution of Tracking Filter with a Noisy Jerk as Correlated Target Maneuver Model", IEEE AES, Vol. 33, No. 1, 1997, pp. 347-353.

B

B.1 BECKER K., "Closed-Form Solution of Pure Proportional Navigation", IEE AES, Vol. 26, No. 3, 1990, pp. 526-533.

B.2 #BEN-ASHER J., YAESH I., "Optimal Guidance with Reduced Sensitivity to Time-to-go Estimation Errors", J. Guidance, Vol. 20, No. 1, 1997, pp. 158-163.

B.3 #BELLMAN R., KAGIWADA H., KALABA R., "Wengert's Numerical Method for Partial Derivatives, Orbit Determination, and Quasilinearization", Mommun. ACM, No. 8, 1965, pp. 231-232.

B.4 BAZARAA M.S., SHERALI H.D., SHETTY C.M., “Nonlinear Programming- Theory and Algorithms”, 1993 (2nd Edition), John Wiley & Sons.

B.5 BAR-SHALOM Y., LI X-R, “Multitarget-Multisensor Tracking – Principles and Techniques”, ISSN 0895-9110.

B.6 BLACKMAN S.S., “Multiple-Target Tracking with Radar Applications”, Artech House Inc., ISBN 0-89006-179-3.

B.7 #BIERMAN G.J., “Measurement Updating using U-D Factorisation”, Automatica, Vol. 12, 1976, pp. 375-382.

B.8 BERG R.F., “Estimation and Prediction for Maneuvering Target Trajectories”, IEEE AC., Vol. 28, No. 3, 1983, pp. 294-304.

B.9 #BLOM H.A.P., HOGENDOORE R.A., Van DOORN B.A., “Design od Multi-Target Tracking System for Advanced Air Traffic Control”, Multi-Target – Multi-Sensor Tracking Applications and Advances”, Chapter 2, Vol. 2, Norwood House, 1992.

B.10 BARTON D.K., “Modern Radar System Analysis”, Published by the George Washington University - Continuing Engineering Education, Course No. 1136, 1989.

B.11 BORDEN B.H., MUMFORD M.L., “A Statistical Glint/Radar Cross Section Target Model”, IEEE AES, Vol. 19, No. 5, 1983, pp. 781-785.

B.12 BURKS D.G., GRAF E.R., FAHEY M.D., “A High-Frequency Analysis of Radome-Induced Radar Pointing Error”, IEEE AP, Vol. 30, No. 5, 1982.

C

C.1 COCHRAN J.E., HAYNES D.A., “Constrained Initial Guidance Algorithm”, AIAA J. Guidance and Control, Vol. 13, No. 2, 1990, pp. 193-197.

C.2 COCHRAN J.E., NO T.S., THAXTON D.G., “Analytical Solutions to a Guidance Problem”, AIAA J. Guidance and Control, Vol. 14, No. 1, 1991, pp. 117-122.

C.3 CHAKRAVARTHY A., GHOSE D., “Capturability of Realistic Generalized True Proportional Navigation”, IEEE AES, Vol. 32, No. 1, 1996, pp. 407-418.

C.4 CARVALHO H., DEL MORAL P., MONIN A. SALUT G., "Optimal Nonlinear Filtering in GPS/INS Integration", IEEE AES, Vol. 33, No. 3, 1997, pp. 835-849.

C.5 CHANG C., TABACZYNSKI J.A., "Application of State Estimation to Target Tracking", IEEE AC., Vol. 29, No. 2, 1984, pp. 98-109.

C.6 #CARLSON N.A., "Fast Triangulation Formulation of the Square Root Filter", A.I.A.A, Vol. 11, No. 9, 1973.

C.7 CHEN B., TUGNAIT J.K., "Multisensor Tracking of a Maneuvering Target in Clutter Using IMMPDA Fixed-Lag Smoothing", IEEE AES, Vol. 36, No. 3, 2000, pp. 983-991.

C.8 COLLINSON R.P.G., "Introduction to Avionics", ISBN 0-412-48250-9, 1996.

C.9 CHOUKROUN D., BAR-ITZHACK I.Y., OSHMAN Y., "A Novel Quaternion Kalman Filter", AIAA Guidance, Navigation and Control Conference and Exhibition, Monterey, California, 5-8 August 2002.

D

D.1 DHAR A., GHOSE D., "Capture Region for a Realistic TPN Guidance Law", IEEE AES, Vol. 29, No. 3, 1993, pp. 995-1003.

D.2 DUFLOS E., PENEL P., VANHEEGHE P., "3D Guidance Law Modelling", IEEE AES, Vol. 35, No. 1, 1999, pp. 72-83.

D.3 DAUM F.E., FITZGERALD R.J.,"Decoupled Kalman Filters for Phased Array Radar Tracking", IEEE AC., Vol. 28, No. 3, 1983, pp. 269-282.

D.4 DAEIPOUR E., BLAIR W.D., BAR-SHALOM Y., "Bias Compensation and Tracking with Monopulse Radars in the Presence of Multipath", IEEE AES, Vol. 33, No. 3, 1997, pp. 863-881.

D.5 DURIS C.S., MOURSUND D.G., "Elementary Theory and Applications of Numerical Methods", New York,: McGraw-Hill, 1967.

D.6 DAILEY D.J., BELL B.M., "A Method for GPS Positioning", IEEE AES, Vol. 32, No. 3, 1996, pp. 1148-1154.

E

E.1 ERRINGTON I., "The application of Steady State Kalman Filters for Obtaining Good Position, Velocity and Acceleration Estimates", MBDA Report BT 13015.

F

F.1 FOX J.E., “A CLOS Design Procedure for IMPACT”, MBDA Report BT 17774, 1985.

F.2 FOSSIER M.W., The Development of Radar Homing Missiles”, AIAA J. Guidance and Control, Vol. 7, No. 6, 1984, pp. 641-651.

F.3 FAROOQ M., BRUDER S., “Information Type Filters for Tracking a Maneuvering Target”, IEEE AES, Vol. 26, No. 3, 1990, pp. 441-454.

F.4 FEESS W.A. et. al., “GPS Satellite-to-User Range Accuracies: A Calibration Experiment”, J. ION, Vol. 34, No. 3, pp. 229-249.

F.5 FEESS W.A., STEPHENS S.G., “Evaluation of GPS Ionosperic Time-Delay Model”, IEEE AES, Vol. 23, No. 3, pp. 332-338.

F.6 FITZGERALD R.J., “Analytic Track Solutions with Range-Dependent Errors”, IEEE AES, Vol. 36, No. 1, pp. 343-348.

G

G.1 GARNELL P., EAST D.J., “Guided Weapon Control Systems”, Pergamon Press, ISBN 0-08-019691-8, 1977.

G.2 #GHOSE D., “On the Generalisation of True Proportional Navigation”, IEEE AES, Vol. 30, No. 2, 1994, pp. 545-555.

G.3 GUELMAN M., “The Closed-Form Solution of True Proportional Navigation”, IEEE AES, Vol. 12, No. 4, 1976, pp. 472-482.

G.4 GHOSE D., “True Proportional Navigation with Manoeuvring Target”, IEEE AES, Vol. 30, No. 1, 1994, pp. 229-237.

G.5 #GUELMAN M., “A qualitative study of Proportional Navigation”, IEEE AES, Vol. 7, No. 3, 1971, pp. 637-643.

G.6 #GUELMAN M., “Proportional Navigation with a manoeuvring target”, IEEE AES, Vol. 8, No. 3, 1972, pp. 364-371.

G.7 GHAWGHAWE S.N., GHOSE D., “Pure Proportional Navigation against Time Varying Target Maneuvers”, IEEE AES, Vol. 32, No. 4, 1996, pp. 1336-1346.

G.8 #GUELMAN M., “A Qualitative Study of Proportional Navigation”, IEEE AES, Vol. 7, No. 3, 1971, pp. 637-643.

G.9 #GUELMAN M., “Proportional Navigation with Maneuvering Target”, IEEE AES, Vol. 8, No. 2, 1972, pp. 364-371.

G.10 GUELMAN M., IDAN M., GOLAN O.M., “Three-Dimensional Minimum Energy Guidance”, IEEE AES, Vol. 31, No. 2, 1995, pp. 835-841.

G.11 GREEN A., SHINAR J., GUELMAN M., “Game Optimal Guidance Law Synthesis for Short Range Missiles”, AIAA J. Guidance and Control, Vol. 15, No. 1, 1992, pp. 191-197.

G.12 GELB A., “Applied Optimal Estimation”, ISBN 0-262-20027-9.

G.13 GHOLSON N.H., MOOSE R.L., “Maneuvering Target Tracking Using Adaptive State Estimation”, IEEE AES, Vol. 13, No. 3, 1977, pp. 310-317.

G.14 GUU J., WEI C., “Maneuvering Target Tracking Using IMM Method at High Measurement Frequency”, IEEE AES, Vol. 27, No. 3, pp. 514-519.

G.15 GRIFFIN G.C., MAYBECK P.S., “MMAE/MMAC Control for Bending with Multiple Uncertainty Parameters”, IEEE AES, Vol. 33, No. 3, pp. 903-911.

G.16 GOAD C.C., “Optimal Filtering of Pseudoranges and Phases from Single-Frequency GPS Receivers”, J. ION, Vol. 37, No. 3, pp. 249-272.

G.17 GREENSPAN R.L., DONNA J.I., “Measurement Errors in GPS Observables”, J. ION, Vol. 33, No. 4, pp. 319-334.

G.18 GRIME S., DURRANT-WHYTE H.F., “Data Fusion in Decentralised Sensor Networks”, Control Eng. Practice, Vol. 2, No. 5, 1994, pp. 849-863.

H

H.1 HUTT R., “A Brief Review of Homing Guidance Laws and Their Applications”, MBDA Report BT 29890, Issue 1, 1994.

H.2 HA I., HUR J., KO M., SONG T, “Performance Analysis of PNG Laws for Randomly Maneuvering Targets”, IEEE AES, Vol. 26, No. 5, 1990, pp. 713-721.

H.3 HOLDER E.J., SYLVESTER V.B., “An Analysis of Modern versus Classical Homing Guidance”, IEEE AES, Vol. 26, No. 4, 1990, pp. 599-605.

H.4 HULL D.G., SPEYER J.L., TSENG C.Y., “Maximum-Information Guidance for Homing Missiles”, AIAA J. Guidance and Control, Vol. 8, No. 4, 1985, pp. 494-497.

H.5 #HULL D.G., RADKE J.J., MACK R.E., “Time-to-Go Prediction of Homing Missiles Based on Minimum Time Intercepts”, J. Guidance, Vol. 14, No. 5, 1991, pp. 865-871.

H.6 HANLON P.D., MAYBECK P.S., “Interrelationship of Single-Filter and Multiple-Model Adaptive Algorithms”, IEEE AES, Vol. 34, No. 3, pp. 934-945.

H.7 HEWER G.A., MARTIN R.D., ZEH J., “Robust Preprocessing for Kalman Filtering of Glint Noise”, IEEE AES, Vol. 23, No. 1, 1987, pp. 120-128.

H.8 HANLON P.D., MAYBECK P.S., “Characterisation of Kalman Filter Residuals in the Presence of Mis-modelling”, IEEE AES, Vol. 36, No. 1, 2000, pp. 114-130.

H.9 HELFERTY J.P., “Improved Tracking of Maneuvering Targets: The Use of Turn-Rate Distributions for Acceleration Modelling”, IEEE AES, Vol. 32, No. 4, 1996, pp. 1355-1361.

H.10 HOULES A., BAR-SHALOM Y.,”Multisensor Tracking of a Maneuvering Target in Clutter”, IEEE AES, Vol. 25, No. 2, 1989, pp. 176-188.

H.11 HAM F.M., BROWN R.G., “Observability, Eigenvalues and Kalman Filtering”, IEEE AES, Vol. 19, No. 2, 1983, pp. 269-273.

H.12 HOFFMAN S.A., BLAIR W.D., “Comments on The $\alpha-\beta-\gamma$ Tracking Filter with Noisy Jerk as the Maneuver Model”, IEEE AES, Vol. 30, No. 3, 1994, pp. 925-928.

H.13 HIGGINS W.T., MOSSMAN D.C., McCLURG J.L., “Satellite Selection for the Global Positioning System”, AIAA J. Guidance and Control, Vol. 6, No. 6, pp. 472-475.

I

I.1 IEEE Standard Specification Format Guide & Test Procedure for Single-Axis Laser Gyros”, IEEE Std 647-1995.

J

J.1 JARMARK B., “A Missile Duel Between Two Aircraft”, AIAA J. Guidance and Control, Vol. 8, No. 4, 1985, pp. 508-513.

J.2 JULIER S.J., UHLMANN J.K., DURRANT-WHYTE H.F., “A New Approach for Filtering Non-Linear Systems”, American Control Conference, Seattle, Washington, 1995.

K

K.1 KIM Y.S., CHO H.S., BIEN Z., “A New Guidance Law for Homing Missiles”, AIAA J. Guidance and Control, Vol. 8, No. 3, 1985, pp. 402-404.

K.2 KIRUBARAJAN T., BAR-SHALOM Y., PATTIPATI K.R., KADAR I., “Ground Target Tracking with Variable Structure IMM Estimator”, IEEE AES, Vol. 36, No. 1, 2000, pp. 26-44.

K.3 KALMAN R.E., “a New Approach to Linear Filtering and Prediction Problems”, Trans. ASME, Vol. 82D, 1960, pp. 34-45.

K.4 KERR T.H., “Streamlining Measurement Iteration for EKF Target Tracking”, IEEE AES, Vol. 27, No. 2, 1991, pp. 408-421.

K.5 KYGER D.W., MAYBECK P.S., “Reducing Lag in Virtual Displays Using Multiple Model Adaptive Estimation”, IEEE AES, Vol. 34, No. 4, 1998, pp. 1237-1247.

K.6 KERR T.H., “Fallacies in Computational Testing of Matrix Positive Definiteness-Semidefiniteness”, IEEE AES, Vol. 26, No. 2, 1990, pp. 415-421.

K.7 #KALATA P.R., “The Tracking Index: A generalised parameter for αβ and αβγ Target Tracers”, IEEE AES, Vol. 20, No. 2, 1984, pp. 174-182.

K.8 KIHARA M., OKADA T., “A Satellite Selection Method and Accuracy for the Global Positioning System”, J. ION, Vol. 31, No. 1, pp. 8-20.

K.9 KAO M.H., ELLER D.H., “Multiconfigurational Kalman Filter Design for High-Performance GPS Navigation”, IEE AC., Vol. 28, No. 3, 1983, pp. 304-314.

K.10 KLOBUCHAR J.A., “Ionospheric Time-Delay Algorithm for Single Frequency GPS Users”, IEEE AES, Vol. 23, No. 3, pp. 325-331.

L

L.1 #LOCKE A.S., “Guidance”, Princeton, N.J. Van Nostrand, 1955.

L.2 LOOZE D.P., HSU J.Y., GRUNBERG D., “Investigation of the Use of Acceleration Estimates by Endgame Guidance Laws”, AIAA J. Guidance and Control, Vol. 13, No. 2, 1990, pp. 198-206.

L.3 LEE G.K.F., “Estimation of the Time-to-Go Parameter for Air-to-Air Missiles”, J. Guidance, Control and Dynamics, Vol. 8, No. 2, 1985, pp. 262-266.

L.4 LEE G.T., LEE J.G., “Improved Command to Line-of-Sight for Homing Guidance”, IEEE AES, Vol. 31, No. 1, 1995, pp. 506-510.

L.5 LI X.R., ZHANG Y., “Numerically Robust Implementation of Multiple-Model Algorithms”, IEEE AES, Vol. 36, No. 1, 2000, pp. 266-278.

L.6 LONGBIN M., XIAOQUAN S., YIYU Z., KANG S.Z., “Unbiased Converted Measurements for Tracking”, IEEE AES, Vol. 34, No. 3, 1998, pp. 1023-1027.

L.7 LERRO D., BAR-SHALOM Y., “Tracking with Debiased Consistent Converted Measurements Versus EKF”, IEEE AES, Vol. 29, No. 3, 1993, pp. 1015-1022.

L.8 LOBBIA R., KENT M., “Data Fusion of Decentralised Local Tracker Outputs”, IEEE AES, Vol. 30, No. 3, 1994, pp. 787-798.

L.9 LAMBERT W.D., SWICK C.H., "Formulas and Tables for the Computation of Geodetic Positions of the International Ellipsoid", Special Publication 200, U.S. Coast and Geodetic Survey, Washington, 1935, pp. 26.

L.10 LAWRENCE A., “Modern Inertial Technology - Navigation, Guidance and Control”, ISBN 0-387-97868-2, 1993.

M

M.1 MAHAPATRA P.R., SHUKLA U.S., “Accurate Solution of Proportional Navigation for Maneuvering Targets”, IEEE AES, Vol. 25, No. 1, 1989, pp. 81-89.

M.2 MAZOR E., AVERBUCH A., BAR-SHALOM Y., DAYAN J., “Interacting Multiple Model Methods in Target Tracking: A Survey”, IEEE AES, Vol. 34, No. 1, 1998, pp. 103-123.

M.3 #MAGILL D.T.,”Optimal Adaptive Estimation of Sampled Stochastic Processes”, IEEE AC., Vol. 10, 1965, pp. 434-439.

M.4 MAYBECK P.S. MERCIER D.E., “A Target Tracker Using Spatially Distributed Infrared Measurements”, IEEE AC., Vol. 25, No. 2, 1980, pp. 222-225.

M.5 MASRELIEZ C.J., MARTIN R.D., “Robust Bayesian Estimation for the Linear Model and Robustifying the Kalman Filter”, IEEE AC., Vol. 22, No. 3, 1977, pp. 361-371.

M.6 MAHAPATRA P.R., MEHROTRA K., “Mixed Co-ordinate Tracking of Generalized Maneuvering Targets Using Acceleration and Jerk”, IEEE AES, Vol. 36, No. 3, 2000, pp. 992-1000.

M.7 #MASRELIEZ C.J., “Approximate Non-Gaussian Filtering with linear State and Observation Relations”, IEEE AC., Vol. 20, 1975, pp. 107-110.

M.8 MOOSE R.L., “An Adaptive State Estimation Solution to the Maneuvering Target Problem”, IEEE AC., Vol. 20, 1975, pp. 359-362.

M.9 MOOSE R.L., VANLANDINGHAM H.F., McCABE D.H., “Modeling and Estimation for Tracking Maneuvering Targets”, IEEE AES, Vol. 15, No. 3, 1979, pp. 448-457.

M.10 MILLER K.S., LESKIW, “Nonlinear Estimation with Radar Observations”, IEEE AES, Vol. 18, No. 2, 1982, pp. 192-200.

M.11 MOODY L., “Terrain Referenced Navigation Studies - Typical FRG DTED Map Errors and their Characterisation”, MBDA Report BT 23745, DCS No. 9844586, August 1988.

M.12 MOODY L., “Closed Loop Missile Trajectory Optimisation”, MBDA report DCS No. 9844585, March 1986.

N

N.1 NOONAN C.A, EVERETT M.E., FREEDMAN R.C., “Sensor Data Fusion for Air-to-Air Situation Awareness Beyond Visual Range”, AGARD Conference Proceedings 539, 1993.

N.2 NESLINE F.W., ZARCHAN P., “A new Look at Classical vs Modern Homing Missile Guidance”, AIAA J. Guidance and Control, Vol. 4, No. 1, 1981.

N.3 NISHIMURA T., “Modelling Errors in Kalman Filters”, AGARD 139, 1970, pp. 89-103.

N.4 NABAA N., BISHOP R.H., “Validation and Comparison of Coordinated Turn Aircraft Maneuver Models”, IEEE AES, Vol. 36, No. 1, 2000, pp. 250-259.

N.5 NESLINE F.W., ZARCHAN P., “Digital Homing Guidance - Stability vs Performance Tradeoffs”, AIAA J. Guidance and Control, Vol. 8, No. 2, 1985, pp. 255-261.

N.6 NESLINE F.W., ZARCHAN P., “Why Modern Controllers can go Unstable in Practice”, AIAA J. Guidance and Control, Vol. 7, No. 4, 1984, pp. 495-500.

N.7 NESLINE F.W., ZARCHAN P., “Line-of-Sight Reconstruction for Faster Homing Guidance”, AIAA J. Guidance and Control, Vol. 8, No. 1, 1985, pp. 3-8.

N.8 NATO (MAS): NAVSTAR GPS System Characteristics, STANAG 4294, May 1993.

N.9 NAVSTAR GPS, Papers published in Navigation, Institute of Navigation, Vol. 1, 1980 revised edition.

O

O.1 OH J-H., HA I-J., “Capturability of the 3D Pure PNG Law”, IEEE AES, Vol. 35, No. 2, 1999, pp. 491-502.

O.2 OHMURO T., “A Decoupled Kalman Tracker using LOS Coordinates”, Proc. of the International Symposium on Noise and Clutter Rejection in Radars”, IEEE AES, Vol. 24, No. 3, 1984, pp. 451-455.

O.3 OHTSUKA K., “Better M Sequence Design for Parameter Identification based on EKF”, IEE Proc. Control Theory Appl., Vol. 145, No. 1, 1998, pp. 92-96.

O.4 OLSON D.K., “Converting Earth-Centred, Earth-Fixed Coordinates to Geodetic Coordinates”, IEEE AES, Vol. 32, No. 1, 1996, pp. 473-476.

P

P.1 Proceedings of the Symposium International - Tactical Missiles, Paris, November 1998, Page 0.33.

P.2 PASTRICK H.L., SELTZER S.M., WARREN M.E., “Guidance Laws for Short-Range Tactical Missiles”, AIAA J. Guidance and Control, Vol. 4, No. 2, 1981, pp. 98-108.

P.3 PFLEGHAAR W., “The General Class of Optimal Proportional Navigation”, AIAA J. Guidance and Control, Vol. 8, No. 1, 1985, pp. 144-147.

P.4 PRICE C.F., WARREN R.S., GELB A., VANDER-VELDE W.E., “Evaluation of Homing Guidance Laws using the CovarianceAnalysis Describing Function Technique”, NWC TP 5522, pp. 73-93.

P.5 PULFORD G., La SCALA B., “A survey of Manoeuvring Target Tracking Methods and their Applicability to Over-the –Horizon Radar”, Department of Electrical and Electronic Engineering, University of Melbourne and the Co-operative Research Centre for Sensor Signal and Information Processing, July 1996.

P.6 PARK S.T., LEE J.G., “Design of a Practical Tracking Algorithm with Radar Measurements”, IEEE AES, Vol. 34, No 4, 1998, pp. 1337-1367.

P.7 PARKINSON W.B., GILBERT S.W., “NAVSTAR: Global Positioning System - Ten Years Later”, IEEE Proc., Vol. 71, No 10, 1993, pp. 1177-1186.

P.8 PAO L.Y., “Measurement Reconstruction Approach for Distributed Multisensor Fusion”, J. Guidance, Vol. 19, No. 4, 1996, pp. 842-847.

Q

Q.1 QUIGLEY A.L.C., HOLMES J.E., “The Development of Algorithms for the Formation and Updating of Tracks”, Admiralty Surface Weapons Establishment, Report Number WP-XBC-7512, 1975.

R

R.1 RUSNAK I., “Discrete Optimal Guidance for High-Order Missile and Maneuvering Target”, IEEE AES, Vol. 27, No. 6, 1991, pp. 870-872.

R.2 RUSNAK I., “Advanced Guidance Laws for Acceleration-Constrained Missile, Randomly Maneuvering Target and Noisy Measurements”, IEEE AES, Vol. 32, No. 1, 1996, pp. 456-464.

R.3 RUSNACK I., “Optimal Guidance for High Order Maneuvering Target and High Order Missile”, Proc. of IEEE International Conference on Control and Applications, 1989, Paper TP-1-7, pp. 1-2.

R.4 RUSNAK I., MEIR L., “Optimal Guidance for Acceleration Constrained Missile and Maneuvering Target”, IEEE AES, Vol. 26, No. 4, 1990, pp. 618-624.

R.5 RAO M.N., “New Analytical Solutions for Proportional Navigation”, AIAA J. Guidance and Control, Vol. 16, No. 3, 1993, pp. 591-594.

R.6 REW D-Y., TAHK M-J., CHO H., “Short-Time Stability of Proportional Navigation Guidance Loop”, IEEE AES, Vol. 32, No. 3, 1996, pp. 1107-1114.

R.7 RUSNAK I., “Optimal Guidance Laws with Uncertain Time-of-Flight”, IEEE AES, Vol. 36, No. 2, 2000, pp. 721-725.

R.8 RIGGS T., “Linear Optimal Guidance for Short Range Air-to-Air Missiles”, Proc. of National Aerospace and Electronics Conference, 1979, pp. 772-779.

R.9 RODDY D.J., IRWIN G.W., “Fixed-Wing-Angle BTTT Control”, IEEE Proc., Part D, Vol. 133, No. 3, 1986, pp. 111-120.

R.10 RTCA, “Minimum Operational Standards for Airborne Supplemental Navigation Equipment Using GPS”, Radio Technical Commission for Aeronautics, SC-159, Document 208, Appendix K, (1991).

R.11 RODDY D.J., IRWIN G.W., WILSON H., “Optimal Controllers for Bank-to-Turn CLOS Guidance”, IEE Proc., Part D, Vol. 131, No. 4, pp. 109-116.

R.12 RODDY D.J., IRWIN G.W., WILSON H., “Approaches to Roll-Loop Design for BTT CLOS Guidance”, IEEE Proc., Part D, Vol. 132, 1985, pp. 268-276.

R.13 #RICKER G.C., WILLIAMS J.R., “Adaptive Tracking Filter for Manoeuvring Targets”, IEEE AES, Vol. 14, No. 1, 1978, pp. 448-455.

R.14 RAO K.D., “An Approach for Accurate GPS Navigation with SA”, IEEE AES, Vol. 34, No. 2, 1998, pp. 695-698.

S

S.1 SHULKA U.S., MAHAPATRA P.R., “The Proportional Navigation Dilemma - Pure or True?”, IEEE AES, Vol. 26, No. 2, 1990, pp. 382-392.

S.2 SHULKA U.S., MAHAPATRA P.R., “Generalized Linear Solution of Proportional Navigation”, IEEE AES, Vol. 24, No. 3, 1988, pp. 231-238.

S.3 SONG S-H, HA I-J, “A Lyapunaov-Like Approach to Performance Analysis of 3-Dimensional Pure PNG Laws”, IEEE AES, Vol. 30, No. 1, 1994, pp. 238-248.

S.4 SHULKA U.S., MAHAPATRA P.R., “Optimisation of Biased Proportional Navigation”, IEEE AES, Vol. 25, No. 1, 1989, pp. 73-80.

S.5 SHINAR J., GUELMAN M., SILBERMAN G., GREEN A., “On Optimal Missile Avoidance – A Comparison between Optimal Control and Differential Game Solutions”, AIAA Paper No. WA-6-2, Guidance and Control Conference - Minneapolis, August 1988.

S.6 SONG T.L., UM T.Y., “Practical Guidance for Homing Missiles with Bearings only Measurements”, IEEE AES, Vol. 32, No. 1, 1996, pp. 434-442.

S.7 SONG T.L., “Target Adaptive Guidance for Passive Homing Missiles”, IEEE AES, Vol. 33, No. 1, 1997, pp. 312-316.

S.8 #SHINAR J., ROTSZTEIN Y., BEZNER E., “Analysis of 3D Optimal Evasion with Linearised Kinematics”, J. Guidance, Control and Dynamics, No. 2, 1979, pp. 353-360.

S.9 SPEYER J.L., CRUES E.Z., “Approximate Optimal Atmospheric Guidance Law for Aeroassisted Plane-Change Maneuvers”, AIAA J. Guidance and Control, Vol. 13, No. 5, 1990, pp. 792-801.

S.10 SPEYER J.L., HULL D.G., TSENG S.W., LARSON S.W., “Estimation Enhancement by Trajectory Modulation for Homing Missiles”, AIAA J. Guidance and Control, Vol. 7, No. 2, 1984, pp. 167-174.

S.11 STEPANIAK M.J., MAYBECK P.S., “MMAE -Based Control Redistribution Applied to the VISTA F-16”, Vol. 34, No. 4, pp. 1249-1259.

S.12 SONG T.L., AHN J.Y., PARK C., “Suboptimal Filter Design with Pseudomeasurements for Target Tracking”, IEEE AES, Vol. 24, No. 1, 1988, pp. 28-39.

S.13 SPEYER J.L., KIM K.D., TAHK M., “Passive Homing Missile Guidance Law Based on New Target Maneuver Models”, AIAA J. Guidance and Control, Vol. 13, No. 5, 1990, pp. 803-812.

S.14 SONG T.L., SPEYER J.L., “A Stochastic Analysis of a Modified Gain Extended Kalman Filter with Applications to Estimation with Bearings Only Measurements”, IEEE AC., Vol. 30, No. 10, 1985, pp. 940-949.

S.15 SINGER R.A., “Estimating Optimal Tracking Filter Performance for Manned Maneuvering Targets', IEEE AES, Vol. 6, No. 4, 1970, pp. 473-483.

S.16 SUDANO J.J., “Maneuver-Driven α–β and α–β–γ Tracking Filters”, IEEE AES, Vol. 31, No. 1, 1995, pp. 341-357.

S.17 SUDANO J.J., “The Alpha-Beta-Gamma Tracking Filter with a Noisy Jerk as the Maneuver Model”, IEEE AES, Vol. 29, No. 2, 1993, pp. 578-580.

S.18 SOLOMON D.L., “Covariance Matrix for α–β–γ Filtering”, IEEE AES, Vol. 21, No. 1, 1985, pp. 157-159.

S.19 STEIN B.A., “Satellite Selection Criteria During Altimeter Aiding of GPS”, J. ION, Vol. 32, No. 2, pp. 149-157.

S.20 SCALES L.E., “Introduction to Non-linear Optimisation”, ISBN 0-333-32553-2, Macmillan Publishers Ltd., 1985.

S.21 SAMMONS J.M., BALAKRISHNAN S., SPEYER J.L., HULL D.G., “Development and Comparison of Optimal Filters”, USAF/University of Texas, Report No. AFATL-TR-79-87, ADB044665, 1979, pp. 1-143.

S.22 #SINGER R.A., KANYUCK A.J., “Computer Control of Multiple Site Correlation”, Automatica, Vol. 7, 1971, pp. 455-463.

T

T.1 TAHK M., SPEYER J.L., “Target Tracking Problems Subject to Kinematic Constraints”, IEEE AC., Vol. 35, No. 3, 1990, pp. 324-326.

T.2 TRUNK G.V., “Optimal Number of Phased Array Faces and Signal Processors for Horizon Surveillance”, IEEE AES, Vol. 33, No. 3, 1999, pp. 1002-1006.

U

V

V.1 VERGEZ P.L., LIEFER R.K., “Target Acceleration Modeling for Tactical Missile Guidance”, AIAA J. Guidance and Control, Vol. 7, No. 3, 1984, pp. 315-321.

V.2 VATHSAL S., RAO M.N., “Analysis of Generalised Guidance Laws for Homing Missiles”, IEEE AES, Vol. 31, No. 2, pp. 514-520.

V.3 VORLEY D.H., “Theoretical Analysis of VLSW Performance against Weaving Targets”, MBDA Report BT28348, 1991.

V.4 VORLEY D.H., “Trajectory Optimisation by Gradients in Function Space”, MBDA Report BT 17309, 1984.

W

W.1 #WENGERT R., “A Simple Automatic Derivative Evaluation Program”, Commun. ACM, No. 7, 1964, pp. 463-464.

W.2 WHEATON B.J., MAYBECK P.S., “Second-Order Acceleration Models for an MMAE Target Tracker”, IEEE AES, Vol. 31, No. 1, 1995, pp. 151-167.

W.3 WILLSKY A.S., “A Survey of Design Methods for Failure Detection in Dynamic Systems”, Automatica, Vol. 12, 1976, pp. 601-611.

W.4 WU W., CHANG D., “Maneuvering Target Tracking with Colored Noise”, IEEE AES, Vol. 32, No. 4, 1996, pp. 1311-1319.

W.5 WU W., “Tracking with Glint Noise”, IEEE AES, Vol. 29, No. 1, 1993, pp. 174-185.

W.6 WEINER M.M., “Noise Factor and Antenna Gains in the Signal/noise Equation for Over-the-Horizon Radar”, IEEE AES, Vol. 27, No. 6, 1991, pp. 886-890.

W.7 WONG R.V.C., SCHWARZ K.P., CANNON M.E., “High-Accuracy Kinematic Positioning by GPS-INS”, J. ION, Vol. 35, No. 2, pp. 275-286.

X

Y

Y.1 #YANG C, YEH F., CHEN J., “The Closed Form Solution of Generalised Proportional Navigation”, Journal of Guidance, Control and Dynamics, Part 10, March-April, 1987, pp. 216-218.

Y.2 YUAN P., CHERN J., “Solutions of True Proportional Navigation for Maneuvering and Nonmaneuvering Targets”, AIAA J. Guidance and Control, Vol. 15, No. 1, 1992, pp. 268-271.

Y.3 YUAN P., HSU S., “Solutions of Generalised Proportional Navigation with Maneuvering and Nonmaneuvering Targets”, IEEE AES, Vol. 31, No. 1, 1995, pp. 469-474.

Y.4 YUAN P., “Optimal Guidance of Proportional Navigation”, IEEE AES, Vol. 33, No. 3, 1997, pp. 1007-1011.

Y.5 YANG C-D., YANG C-C., “Analytical Solution of 3D True Proportional Navigation”, IEEE AES, Vol. 32, No. 4, 1996, pp.1509-1522.

Y.6 YANG C-D., YANG C-C., “Unified Approach to Proportional Navigation”, IEEE AES, Vol. 33, No. 2, 1997, pp. 557-567.

Y.7 YANG C., HSIAO F., YEH F., “Generalized Guidance Law for Homing Missiles”, IEEE AES, Vol. 25, No. 2, 1989, pp. 197-212.

Y.8 YANG C., YEH F., “Optimal Proportional Navigation”, AIAA J. Guidance and Control, Vol. 11, No. 4, 1988, pp. 375-377.

Y.9 YANG S.M., HUANG N.H., “Application of H Control to Pitch Autopilot of Missiles”, IEEE AES, Vol. 32, No. 1, 1996, pp. 426-433.

Z

Z.1 ZWILLINGER D., “Standard Mathematical Tables and Formulae”, LCCN 0-8493-2479-3, CRC Press, 30th Edition, 1996.

Z.2 ZHANG Y., LI X.R., “Detection and Diagnosis of Sensor and Actuator Failures using IMM Estimator”, IEEE AES, Vol. 34, No. 4, 1998, pp. 1293-1312.

Z.3 ZHU J., “Conversion of Earth-Centred Earth-Fixed to Geodetic Coordinates”, IEEE AES, Vol. 30, No. 3, 1994, pp. 957-961.

13 BIBLIOGRAPHY

A

A.6 AIDALA V., HAMMEL S.E., "Utilisation of Modified Polar Coordinates for Bearings Only Tracking", IEEE AC., Vol. 28, No. 3, 1983, pp. 283-294.

A.7 AKISHITA S., KUROSAKI R., OKADA K., HIRATA T., "Theoretical Prediction of Roll Moment on Wing Controlled Missile", J. Aircraft, Vol. 23, No. 11, 1986, pp. 808-813.

A.8 ALGRAIN M.C., SANIIE J., "Estimation of 3-D Angular Motion Using Gyroscopes and Linear Accelerometers", IEEE AES, Vol. 27, No. 6, 1991, pp. 910-920.

A.9 ALHAKEEM S., VARSHNEY P.K., "A Unified Approach to the Design of Decentralised Detection Systems", IEEE AES, Vol. 31, No. 1, 1995, pp. 9-20.

A.10 ALSPACH D.L., SORENSON H.W.,"Nonlinear Bayesian Estimation Using Gaussian Sum Approximations", IEEE AC., Vol. 17, No. 4, 1972, pp. 439-447.

A.11 AMOROSO F., MONZINGO R.A., "Adaptive A/D Converter for Improved DS/SS Jam Resistance", IEEE AES, Vol. 34, No. 3, 1998, pp. 810-815.

A.12 ANANDA M.P., BERNSTEIN H., FEESS W.A., PAUGSTAT T.C., "Global Positioning System (GPS) Autonomous user System", J. ION, Vol. 35, No. 2, pp. 197-207.

A.13 ARDEMA M.D., RAJAN N., "Separation of Time Scales in Aircraft Trajectory Optimisation", AIAA J. Guidance and Control, Vol. 8, No. 2, 1985, pp. 275-278.

A.14 AUSTIN F., FALCO M., HINZ H., LEWIS M., "Game Theory for Automated Maneuvering During Air-to-Air Combat", AIAA J. Guidance and Control, Vol. 13, No. 6, 1990, pp. 1143-1149.

A.15 #ASHER R.B., MATASZEWSKI J.P., "Optimal Guidance with Maneuvering Targets", J. Spacecraft, Vol. 11, No. 2, 1974, pp. 204-206.

B

B.13 BABA Y., YAMAGUCHI M., HOWE R.M., "Generalized Guidance Law for Collision Courses", J. Guidance, Control and Dynamics, Vol. 16, No. 3, 1993, pp. 511-516.

B.14 BAHETI R.S., "Efficient Approximation of a Kalman Filter for Target Tracking", IEEE AES, Vol. 22, No 1, 1986, pp. 9-14.

B.15 BANCROFT S., "An Algebraic Solution of the GPS Equations", IEEE AES, Vol. 21, No. 7, pp. 56-59.

B.16 BARHETI R.S., "Efficient Approximation of Kalman Filter for Target Tracking", IEEE AES, Vol. 22, No. 1, 1986, pp. 8-14.

B.17 BAR-ITZHACK I.Y., "Modeling of Certain Strapdown Heading-Sensitive Errors in INS Error Models", AIAA J. Guidance and Control, Vol. 8, No. 1, 1985, pp. 142-144.

B.18 BAR-ITZHACK I.Y., BERMAN N., "Control Theoretic Approach to Inertial Navigation Systems", J. Guidance, Vol. 11, No. 3, 1988, pp. 237-245.

B.19 BAR-SHALOM Y., "The Effect of the Common Process Noise on the Two Sensor Fused-Track Covariance", IEEE AES, Vol. 22, No. 6, 1986, pp. 803-805.

B.20 BAR-SHALOM Y., BIRMIWAL K., "Variable Dimension Filter for Maneuvering Target Tracking", IEEE AES, Vol. 18, No. 5, 1982, pp. 621-629.

B.21 BEINER L., "Optimal Re-Entry Maneuvers with Bounded Lift Control", AIAA J. Guidance and Control, Vol. 10, No. 4, 1987, pp. 321-329.

B.22 BEN-ASHER J.Z., CLIFF E.M., "Optimal Evasion Against a Proportionally Guided Pursuer", AIAA J. Guidance and Control, Vol. 12, No. 4, 1989, pp. 598-600.

B.23 BEN-ASHER J.Z., CLIFF E.M., KELLEY H.J., "Optimal Evasion with a Path-Angle Constraint and Against Two Pursuers", AIAA J. Guidance and Control, Vol. 11, No. 4, 1988, pp. 300-304.

B.24 BENDER D.J., "The Open Loop Transfer Matrix of an Estimator Controller", IEEE AES, Vol. 23, No. 2, 1987, pp. 158-167.

B.25 BERIZZI F., DIANI M., "Multipath Effects on ISAR Image Reconstruction", IEEE AC., Vol. 34, No. 2, 1998, pp. 645-654.

B.26 BEST R.A., NORTON J.P., “A New Model and Efficient Tracker for a Target with Curvilinear Motion”, IEEE AES, Vol. 33, No. 3, 1999, pp. 1030-1037.

B.27 BETTS J.T., HUFFMAN P., “Application of Sparse Nonlinear Programming to Trajectory Optimisation”, AIAA J. Guidance and Control, Vol. 15, No. 1, 1992, pp. 198-206.

B.28 BILIMORIA K.D., CLIFF E.M., “Singular Trajectories in Airplane Cruise-Dash Optimisation”, AIAA J. Guidance and Control, Vol. 12, No. 3, 1989, pp. 304-310.

B.29 BLAIR W.D., “Fixed Gain Two-Stage Estimators for Tracking Maneuvering Targets”, IEEE AES, Vol. 29, No. 3, 1993, pp. 1004-1014.

B.30 BLAIR W.D., BAR-SHALOM Y., “Tracking Maneuvering Targets with Multiple Sensors: Does More Data Always Mean Better Estimates”, IEEE AES, Vol. 32, No. 1, 1996, pp. 450-456.

B.31 BODDY D.J., IRWIN G.W., FLEMING R.J., “Linear Quadratic Approach to Optimal Control and Estimation in Bank-to-Turn CLOS Guidance”, Queen's University, Belfast, U.K.

B.32 BREAKWELL J.V., SPEYER J.L., BRYSON A.E., “Optimisation and Control of Nonlinear Systems Using the Second Variation”, J.S.I.A.M., Control Series A, Vol. 1, No. 2, 1963.

B.33 BRIERLEY S.D., LONGCHAMP R., “Application of Sliding-Mode Control to Air-Air Interception Problem”, IEEE AES, Vol. 26, No. 2, 1990, pp. 306-325.

B.34 BRUMBACK B.D., SRINATH M.D., “A Fault-Tolerant Multisensor Navigation System Design”, IEEE AES, Vol. 23, No. 6, 1987, pp. 738-755.

B.35 BRUMBAUGH R.W., “Aircraft Model for the AIAA Controls Design Challenge”, J. Guidance, Control and Dynamics, Vol. 17, No. 4, 1994, pp. 747-752.

B.36 BRYSON A.E., DENHAM W.F., “A Steepest Ascent Method for Solving Optimum Programming Problems”, J. Applied Mechanics, Trans. of the ASME, 1962, pp. 247-257.

B.37 BRYSON A.E., HO Y., “Applied Optimal Control”, John Wiley & Sons, ISBN 0 470 11481-9, 1975.

B.38 BUNDAY B.D., GARSIDE G.R., “Optimisation Methods in Pascal”, Published by Edward Arnold, ISBN 0-7131-3615-4, 1987.

B.39 BREIDT F.J., CARRIQUIRY A.L., “Highest Density Gates for Target Tracking”, Vol. 36, No. 1, 2000, pp. 47-55.

B.40 BECKER J.C., “Fusion of Data from the Object-Detecting Sensors of an Autonomous Vehicle”, IEEE International Conference on Intelligent Transportation Systems, 1999.

B.41 BISHOP R.H., ANTOULAS A.C., “Non Linear Approach to the Aircraft Tracking Problem”, J. Guidance, Vol. 17, No. 5, 1994, pp. 1124-1130.

C

C.10 CADRE J.P., TREMOIS O., “Properties and Performance of Extended Target Motion Analysis”, IEEE AES, Vol. 32, No. 1, 1996, pp. 66-82.

C.11 CARRINGTON C.K., JUNKINS J.L., “Optimal Nonlinear Feedback Control for Spacecraft Attitude Maneuvers”, AIAA J. Guidance and Control, Vol. 9, No. 1, 1986, pp. 99-107.

C.12 CASTELLA F.R., DUNNEBACKE F.G., “Analytical Results for the X,Y Kalman Tracking Filter”, IEEE AES, Vol. 20, No. 6, 1974, pp. 891-895.

C.13 CHADWICK W.R., “Miss Distance of Proportional Navigation Missile with Varying Velocity”, AIAA J. Guidance and Control, Vol. 8, No. 5, 1984, pp. 662-665.

C.14 CHAER W.S., BISHOP R.H., GHOSH J., “Hierarchical Adaptive Kalman Filtering for Interplanetary Orbit Determination”, IEEE AES, Vol. 34, No. 3, 1998, pp. 883-895.

C.15 CHAN Y.T., HU A.G.C., PLANT J.B., “A Kalman Filter Based Tracking Scheme with Input Estimation”, IEEE AES, Vol. 15, No. 2, 1979, pp. 237-244.

C.16 CHAN Y.T., PLANT J.B., BOTTOMLEY J.R.T., “A Kalman Tracker with a Simple Input Estimator”, IEEE AES, Vol. 18, No. 2, 1982, pp. 235-241.

C.17 CHEN B., TUGNAIT J.K., “Multisensor Tracking of a Maneuvering Target in Clutter Using IMMPDA Fixed-Lag Smoothing”, IEEE AES, Vol. 36, No. 3, 2000, pp. 983-991.

C.18 CHAUDHURI S., KARANDIKAR S.S., “Recursive Methods for the Estimation of Rotation Quaternions”, IEEE AES, Vol. 32, No. 2, 1996, pp. 846-854.

C.19 CHEN G., “A Simple Treatment for Suboptimal Kalman Filtering in Case of Measurement Data Missing”, IEEE AES, Vol. 26, No. 2, 1990, pp. 413-415.

C.20 CHEN G., CHUI C.K., "A Modified Adaptive Kalman Filter for Real Time Applications", IEEE AES, Vol. 27, No. 1, 1991, pp. 149-153.

C.21 CHEN G., WANG J., SHIEH L.S., "Interval Kalman Filtering", IEEE AES, Vol. 33, No. 1, 1997, pp. 250-258.

C.22 CHENG V.H.L., GUPTA N.K., "Advanced Midcourse Guidance for Air-to-Air Missiles", AIAA J. Guidance and Control, Vol. 9, No. 2, 1986, pp. 135-142.

C.23 CHENG V.H.L., MENON P.K.A. , GUPTA N.K., BRIGGS M.M., "Reduced Order Pulse-Motor Ignition Control Logic", AIAA J. Guidance and Control, Vol. 10, No. 4, 1987, pp. 343-350.

C.24 CHENG V.H.L., GUPTA N.K., Advanced Midcourse Guidance for Air-to-Air Missiles", AIAA J. Guidance and Control, Vol. 9, No. 2, 1986, pp. 135-141.

C.25 CHICHKA D.F., SHANKAR U.J., CLIFF E.M., KELLEY H.J., "Cruise-Dash-Climb Analysis of an Airbreathing Missile", AIAA J. Guidance and Control, Vol. 11, No. 4, 1988, pp. 293-299.

C.26 CHOWDHRY R.S., CLIFF E.M., FREDERICK H.L., "Optimal Rigid-Body Motions", AIAA J. Guidance and Control, Vol. 14, No. 2, 1991, pp. 383-390.

C.27 CHUNG D., LEE J.G., PARK C.G., PARK H.W., "Strapdown INS Error Model for Multiposition Alignment", IEEE AES, Vol. 32, No. 4, 1996, pp. 1362-1366.

C.28 CLOUTIER J.R., LIN C.F., YANG C., "Enhanced Variable Dimension Filter for Maneuvering Target Tracking", IEEE AES, Vol. 29, No. 3, 1993, pp. 786-796.

C.29 COOK G.F., "NAVSTAR GPS for Sea and Air Navigation", J. Navigation, Vol. 36, No. 3, pp. 341-358.

C.30 COPPS E.M., "An Aspect of the Role of the Clock in a GPS Receiver", J. ION, Vol. 31, No. 3, pp. 233-242.

C.31 CONTE E., LOPS M., RICCI G., "Asymptotically Optimum Radar Detection in Compound Gaussian Clutter", IEEE AES, Vol. 31, No. 2, pp. 617-624.

C.32 CORBAN J.E., CALISE A.J., FLANDO G.A., "Trajectory Optimisation and Guidance Law Development for Transatmospheric Vehicles", Proc. of IEEE International Conference on Control and Applications, 1989, Paper WA-6-3, pp. 1-6.

C.33 CORTINA E., OTERO D., D'ATTELLIS C.E., "Maneuvering Target Tracking Using Extended Kalman Filter", IEEE AES, Vol. 27, No. 1, 1991, pp. 155-158.

C.34 CORBAN J.E., CALISE A.J., FLANDRO G.A., "Rapid Near-Optimal Aerospace Plane Trajectory Generation and Guidance", AIAA J. Guidance and Control, Vol. 14, No. 6, 1991, pp. 1181-1190.

C.35 CRAGGS J.W., "Calculus of Variations", Published by George Allen & Unwin LTD., ISBN 0 04 517009 6, 1973.

C.36 CUONG H.T., TROESCH A.W., BIRDSALL T.G., "The Generation of Digital Random Time Histories", Ocean Engineering, Vol. 9, No. 6, pp. 581-588.

C.37 COLLINSON R.P.G., "Introduction to Avionics", Chapman & Hall, ISBN 0-412-48250-9, 1996.

C.38 CARLSON N.A., Federated Square Root Filter for Decentralised Parallel Processes", IEEE AES, Vol. 26, No. 3, 1990, pp. 517-525.

C.39 CHANG K-C., BAR-SHALOM Y., "Joint Probabilistic Data Association for Multitarget Tracking with Possibly Unresolved Measurements and Maneuvers", IEEE AC., Vol. 29, No. 7, 1984, pp. 585-594.

C.40 CHANG K-C., CHONG C-Y., BAR-SHALOM Y., "Joint Probabilistic Data Association IN Distributed Sensor Networks", IEEE AC., Vol. 31, No. 10, 1986, pp. 889-897.

D

D.7 DAILEY D.J., BELL B.M., "A Method for GPS Positioning", IEEE AES, Vol. 32, No. 3, 1996, pp. 1148-1154.

D.8 DAMIANI T.R., HEMESATH N.B., "Choosing the Best Solution to the GPS Integrity and Coverage Issues", J. ION, Vol. 35, No. 2, pp. 217-237.

D.9 DENHAM W.F., PINES S., "Sequential Estimation when Measurement Function Nonlinearity is Comparable to Measurement Error", AIAA, Vol. 4, No. 6, 1966, pp. 1071-1076.

D.10 DMITRIYEV S.P., STEPANOV O.A., SHEPEL S.V., "Nonlinear Filtering Methods Application in INS Alignment", IEEE AES, Vol. 33, No. 1, 1997, pp. 260-271.

D.11 DISTEFANO N., "Dynamic Programming and the Solution of the Biharmonic Equation", Ineternational Journal for Numerical Methods in Engineering, Vol. 3, 1971, pp. 199-213.

D.12 DOUGHERTY J.J., EL-SHERIEF H., SIMON D.J., WHITMER G.A., "GPS Modeling Aerospace Vehicle Navigation Systems", IEEE AES, Vol. 31, No. 2, pp. 695-704.

D.13 DRAIM J.E., "A Common-Period Four-Satellite Continuous Coverage Constellation", J. Guidance, Vol. 10, No. 5, pp. 492-499.

D.14 DRAKOPOULOS E., LEE C.C, "Optimum Multisensor Fusion of Correlated Local Decisions", IEEE AES, Vol. 27, No. 4, 1991, pp. 593-606.

D.15 DURHAM W., "Constrained Control Allocation", J. Guidance, Control and Dynamics, Vol. 16, No. 4, 1993, pp. 717-725.

D.16 VAN DIERENDONCK A.J., RUSSELL S.S., KOPITZKE E.R., BIRNBAUM M., "The GPS Navigation Message", Global Position System, J. ION, Vol. 1, 1980, revised edition.

D.17 DOYLE R.S., HARRIS C.J., "Multi-Sensor Data Fusion for Helicopter Guidance using Neuro-fuzzy Estimation Algorithms", Aeronatical Journal, June, 1996, pp. 241-251.

E

E.2 EASTWOOD R.A., "An Integrated GPS/ GLONASS Receiver", J. ION, Vol. 37, No. 2, pp. 141-151.

E.3 EDWARDS F.G., LOOMIS P.V.W., "Civil Helicopter Operations Using Differential GPS", J. ION, Vol. 32, No. 3, pp. 233-253.

E.4 EIDE P., MAYBECK P., "An MMAE Failure Detection System for the F-16", IEEE AES, Vol. 32, No. 3, 1996, pp. 1125-1135.

E.5 EISLER G.R., HULL D.G., "Optimal Descending, Hypersonic Turn to Heading", AIAA, J. Guidance and Control, Vol. 10, No. 3, 1987, pp. 255-261.

E.6 EL-FATTAH Y.M., "Recursive Self-Tuning Algorithm for Adaptive Kalman Filtering", IEE Proc., Vol. 130, Part D, No. 6, 1983, pp. 341-344.

E.7 ENGE P.K., OLSON K.E., "Medium Frequency Broadcast of Differential GPS Data", IEEE AES, Vol. 26, No. 4, pp. 607-617.

E.8 ERSHOV A.A., “Robust Filtering Algorithms”, Automatic Remote Control, Vol. 3, No. 7, 1978, pp. 68-73.

E.9 ERSHOV A.A., LIPSTER R.Sh., “Robust Kalman Filter in Descrete Time”, Automatic Remote Control, Vol. 39, No. 3, 1978, pp. 60-69.

F

F.7 FANG J.C., WAN D.J., “A Fast Initial Alignment Method for Strapdown Inertial Navigation System on Stationary Base”, IEEE AES, Vol. 32, No. 4, 1996, pp. 1501-1505.

F.8 FARIDANI H.M., “Performance of Kalman Filter with Missing Measurements”, Automatica, Vol. 22, No. 1, 1986, pp. 117-120.

F.9 FARINA D.J., FLAM R.P., “A Self-Normalizing Gradient Search Adaptive Array Algorithm”, IEEE AES, Vol. 27, No. 6, 1991, pp. 901-905.

F.10 FITZGERALD R.J.,”Simple Tracking Filters: Steady-State Filtering and Smoothing Performance”,IEEE AES, Vol. 16, No. 6, 1980, pp. 860-864.

F.11 FITZGERALD R.J., “Simple Tracking Filters: Closed-Form Solutions”, IEEE AES, Vol. 17, No. 6, 1981, pp. 781-785.

F.12 FLEMING R.J., IRWIN G.W., “Filter Controllers for Bank-to-Turn CLOS Guidance”, IEEE Proc., Part D, Vol. 134, No. 1, 1987, pp. 17-25.

F.13 FREDRIC M.H., BROWN R.G., “Observability, Eigenvalues, and Kalman Filtering”, IEEE AES, Vol. 19, No 2, 1983.

F.14 FOGEL E., GAVISH M., “Nth-Order Dynamics Target Observability from Angle Measurements”, IEEE AES, Vol. 24, No. 3, 1988, pp. 305-308.

F.15 FORTE I., SHINAR J., “Can a Mixed Guidance Strategy Improve Missile Guidance”, AIAA J. Guidance and Control, Vol. 11, No. 1, 1988, pp. 53-59.

F.16 FARRELL J.L., “Strapdown Inertial Navigation System Requirements Omposed by Synthetic Aperture Radar”, AIAA J. Guidance and Control, Vol. 8, No. 4, 1985, pp. 433-439.

G

G.19 GANGAAS D., BRUCE K.R., BLIGHT J.D., LY U., “Applications of Modern Synthesis to Aircraft Control: Three case Studies”, IEEE AC., Vol. 31, No. 11, 1986, pp. 995-1013.

G.20 GARDNER B.E., CANNON R.H., BRYSON A.E., “Time Invariant Conrollers for Target Tracking”, AIAA J. Guidance and Control, Vol. 10, No. 4, 1987, pp. 330-337.

G.21 GAVISH M., FOGEL E., “Effect of Bias on Bearing-Only Target Location”, IEEE AES, Vol. 26, No. 1, 1990, pp. 22-25.

G.22 GAWTHROP P.J., “Self-Tuning PID Controllers: Algorithms and Implementation”, IEEE AC., Vol. 31, No. 3, pp. 201-209.

G.23 GAZIT R., “Digital Tracking Filters with High Order Correlated Measurement Noise”, IEEE AES, Vol. 33, No. 1, 1997, pp. 171-176.

G.24 GE H., TUFTS D.W., “Estimating the Frequencies of Two Sinusoids Using Only Phase Angles of Complex-Valued Data”, IEEE Trans. on Signal Processing, Vol. 41, No. 5, 1993, pp. 1982-1986.

G.25 GEFEN M., “Sensitivity of Estimation Errors Caused by not Updating Gains in Simple Tracking Filters”, Proc. of IEEE International Conference on Control and Applications, 1989, Paper RA-1-5, pp. 1-2.

G.26 GILBERT E.G., HOWE R.M., LU P., VINH N.X., “Optimal Aeroassisted Intercept Trajectories at Hyperbolic Speeds”, AIAA J. Guidance and Control, Vol. 14, No. 1, 1991, pp. 123-131.

G.27 GRAY R.L., “A Pure-Cartesian Formulation for Tracking Filters”, IEEE AES, Vol. 29, No. 3, 1993, pp. 749-754.

G.28 GREEN G.B., MASSATT P.D., RHODUS N.W., “The GPS 21 Primary Satellite Constellation”, J. ION, Vol. 36, No. 1, pp. 9-24.

G.29 GREGORIOU G., “CEP Calculations for a Rocket with Different Control Systems”, AIAA J. Guidance and Control, Vol. 11, No. 3, 1988, pp. 193-198.

G.30 GREWAL M.S., HENDERSON V.D., MIYASAKO R.S., “Application of Kalman Filtering to the Calibration and Alignment of Inertial Navigation Systems”, IEEE AC., Vol. 36, No. 1, pp. 4-13.

G.31 GRIMBLE M.J., “Observations-Weighted Minimum-Variance Control of Nonlinear Systems”, IEE Proc., Vol. 133, No. 4, pp. 172-176.

G.32 GUELMAN M., MOSHE I., ODED M.G., “Three Dimensional Minimum Energy Guidance”, IEEE AES, Vol. 31, No. 2, pp. 835-841.

G.33 GUTMAN P., CWIKEL M., “An Algorithm to Find Maximal State Constraint Sets for Discrete-Time Linear Dynamical Systems with Bounded Controls and States”, IEEE AC., Vol. 32, No. 3, 1987, pp. 251-254.

G.34 GUTMAN P., VELGER M., "Tracking Targets Using Adaptive Kalman Filtering", IEEE AES, Vol. 26, No. 5, 1990, pp. 691-699.

G.35 GUSTAFSON J.A., "Flexible Spacestructure Control via Moving Bank Multiple Model Algorithms", IEEE AES, Vol. 30, No. 3, 1994, pp. 750-757.

G.36 GUSTAFSON D.E., "Linear Minimum Variance Filters Applied to Carrier Tracking", IEEE AC., Vol. 21, No. 1, 1976, pp. 65-73.

G.37 #GUELMAN M., "Missile Acceleration in Proportional Navigation", IEEE AES, Vol. 9, No. 2, 1973, pp. 462-463.

G.38 #GUELMAN M., SHINAR J., GREEN A., "Qualitative Study of Planar Pursuit-Evasion Game in the Atmosphere", AIAA Paper No. 88-4158, Guidance and Control Conference - Minneapolis, August 1988.

H

H.14 HA T.T., ROBERTSON R.C., "Geostationary Satellite Navigation Systems", IEEE AES, Vol. 23, No. 2, pp. 247-253.

H.15 HALEVI Y., "Optimal Observers for Systems With Colored Noises", Proc. of IEEE International Conference on Control and Applications, 1989, Paper WA-5-3, pp. 1-4.

H.16 O'HALLARON D.R., BAHETI S., "Fast Mapping of a Kalman Filter on Warp", SPIE Real Time Signal Processing XI, Vol. 977, pp. 196-205.

H.17 HAMMEL S.E., AIDALA V.J., "Observability Requirements for 3D Tracking via Angle Measurements", IEEE AES, Vol. 21, No. 2, 1985, pp. 200-207.

H.18 HAMPTON R.L.T., COOKE J.R., "Unsupervised Tracking of Maneuvering Vehicles", IEEE AES, Vol. 9, No. 2, 1973, pp. 197-207.

H.19 HARGRAVES C.R., PARIS S.W., "Direct Trajectory Optimisation Using Nonlinear Programming and Collocation", AIAA J. Guidance and Control, Vol. 10, No. 4, 1987, pp. 338-342.

H.20 HASHEMIPOUR H.R., LAUB A.J., "Kalman Filtering for Second-Order Models", AIAA J. Guidance and Control, Vol. 11, No. 2, 1988, pp. 181-186.

H.21 HEPNER S.A., GEERING H.P., "Observability Analiysis for Target Maneuver Estimation vis Bearing-Only and Bearing-Rate-Only Measurements", AIAA J. Guidance and Control, Vol. 13, No. 6, 1990, pp. 977-983.

H.22 HEIN G.W., BAUSTERT G., EISSFELLER B., LANDAU H., "High-Precision Kinematic GPS Differential Positioning and Integration of GPS with a Ring Laser Strapdown Inertial System", J. ION, Vol. 36, No. 1, pp. 77-97.

H.23 HYSLOP G., GERTH D. KRAEMER, "GPS/INS Integration on the Standoff Land Attack Missile (SLAM)", IEEE AES Magazine, July 1990, pp. 29-33.

H.24 HODGES D.H., CALISE A.J., BLESS R.R., LEUNG M., "A Weak Hamiltonian Finite Element Method for Optimal Guidance of an Advanced Launch Vehicle", Proceedings of the IEEE (Piscataway, NJ), Vol. 3, Paper No. FA5-11:45, pp. 2037-2043.

H.25 HOLM S., "Optimum FFT-Based Frequency Acquisition with Application to COSPAS-SARSAT", IEEE AES, Vol. 29, No. 2, 1993, pp. 464-475.

H.26 HONG L., WANG W., LOGAN M., DONOHUE T., "Comments on True Proportional Navigation with Maneuvering Target", IEEE AES, Vol. 33, No. 1, 1997, pp. 273-281.

H.27 HONG L., JUNG Y., "Optimal Scheduling of Track Updates in Phased Array Radars", IEEE AES, Vol. 34, No. 3, 1998, pp. 1016-1022.

H.28 HORAK D.T., "System Failure Isolation in Dynamic Systems", AIAA J. Guidance and Control, Vol. 13, No. 6, 1990, pp. 1075-1082.

H.29 HOSTETLER L.D., "Nonlinear Kalman Filtering Techniques for Terrain-Aided Navigation", IEEE AC., Vol. 28, No. 3, pp. 315-308.

H.30 HOUGH M.E., "Explicit Guidance Along an Optimal Space Curve", AIAA J. Guidance and Control, Vol. 12, No. 4, 1989, pp. 495-504.

H.31 HULL D.G., KITE P.C., SPEYER J.L., "New Target Models for Homing Guidance", Proc. of AIAA Guidance and Control Conference (New York), 83-2166, 1983, pp. 22-29.

H.32 HULL D.G., SPEYER J.L., GREENWELL W.M., "Adaptive Noise Estimation for Homing Missiles", AIAA J. Guidance and Control, Vol. 7, No. 3, 1984, pp. 322-328.

H.33 HURD W.J., STATMAN J.I., VILNROTTER V.A., "High Dynamic GPS Receiver using Maximum Likelihood Estimation and Frequency Tracking", IEEE AES, Vol. 23, No. 4, pp. 425-437.

H.34 HURRAB K., WINTER H., "Gyro Accuracy Requirements in a Strapdown INS with GPS Aiding for RPV Missions", AGARD Report No. 147, Vol. IID, Study No. 4.

H.35 HUSSAIN A.M., "Multisensor Distributed Sequential Detection", IEEE AES, Vol. 30, No. 3, 1994, pp. 698-708.

H.36 HUTCHINS R.G., SWORDER D.D., "Image Fusion Algorithms for Tracking Maneuvering Targets", AIAA J. Guidance and Control, Vol. 15, No. 1, 1992, pp. 175-184.

H.37 HWANG P.Y.C., BROWN R.G., "GPS Navigation: Combining Pseudorange with Continuous Carrier Phase using a Kalman Filter", J. ION, Vol. 37, No. 2, pp. 181-196.

H.38 #HULL D.G., SPEYER J.L., BURRIS D.B., "Linear-Quadratic Guidance Law for Dual Control of Homing missiles", J. Guidance, Vol. 13, No. l, 1990, pp. 137-144.

H.39 HANLON P.D., MAYBECK P.S., "Multiple-Model Adaptive Estimation Using a Residual Correlation Kalman Filter Bank", IEEE AES, Vol. 36, No. 2, 2000, pp. 393-406.

H.40 HASHEMIPOUR H.R., ROY S., LAUB A.J., "Decentralised Structures for Parallel Kalman Filtering", IEEE AC., Vol. 33, No. 1, 1988, pp. 88-93.

I

I.2 IEEE Standard Inertial Sensor Terminology, IEEE Std 528-1984.

I.3 IEEE Standard Specification Format Guide and Test procedure for Single Degree of Freedom Rate Integrating Gyros".

I.4 IMADO F., KURODA T., MIWA S., "Optimal Midcourse Guidance for Medium-Range Air-to-Air Missiles", AIAA J. Guidance and Control, Vol. 13, No. 4, 1990, pp. 603-608.

I.5 IIGUNI Y., AKIYOSHI H., ADACHI N., "An Intelligent Landing System Based on a Human Skill Model", IEEE AES, Vol. 34, No. 3, 1998, pp. 877-882.

I.6 IMADO F., KURODA T., MIWA S., "Optimal Thrust Control of a Missile with a Pulse Motor", AIAA J. Guidance and Control, Vol. 14, No. 2, 1991, pp. 377-382.

I.7 IRWIN G.W., FLEMING R.J., "Analysis of Coloured Filter Controllers for Bank-to-Turn CLOS Guidance", IEE Proc., Vol. 135, Part D, No. 8, 1988, pp. 486-492.

I.8 ISAACS D., "Algorithms for Sequential Optimisation of Control Systems", Academic Press, Advances in Controls Systems - Theory and Applications, 1966.

I.9 IVERS W.D., MUDIE J.D., "Towing Long Cables at Slow Speeds: A Three Dimensional Dynamic Model", MTS Journal, Vol. 7, No. 3, 1973, pp. 23-31.

J

J.3 JAZWINSKI A.H., "Stochastic Processes and Filtering Theory", Academic Press Inc., Mathematics in Science and Engineering, Vol. 64, LCCC 71-84150, 1970.

J.4 JIANG Y.F., LIN Y.P., "Error Analysis of Quaternion Transformations", IEEE AES, Vol. 27, No. 4, 1991, pp. 634-639.

J.5 JILKOV V.P., ANGELOVA D.S., SEMERDJIEV TZ.A., "Design and Comparison of Mode-Set Adaptive IMM Algorithms for Maneuvering Target Tracking", IEEE AES, Vol. 35, No. 1, 1999, pp. 343-350.

J.6 JOHNSTON S.L., "An Approach for Accurate GPS Navigation with SA", IEEE AES, Vol. 34, No. 2, pp. 695-699.

J.7 JORDAN S.K., "Effects of Geodetic Uncertainties on a Damped Inertial Navigation System", IEEE AES, Vol. 9, No. 5, pp. 741-752.

J.8 JUNKINS J.L., BANG H., "Maneuver and Vibration Control of Hybrid Coordinate Systems Using Lyapunov Stability Theory", J. Guidance, Control and Dynamics, Vol. 16, No. 4, 1993, pp. 668-676.

K

K.11 KABAMBA P.T., LONGMAN R.W., JIAN-GUO S., "A Homotopy Approach to the Feedback Stabilisation of Linear Systems", AIAA J. Guidance and Control, Vol. 10, No. 5, 1987, pp. 422-431.

K.12 KALABA R., SPINGARN K., "Automatic Solution of Nth-Order Optimal Control Problems", IEEE AES, Vol. 21, No. 3, 1985, pp. 345-350.

K.13 KELLY R.J., "Additional Results on Reducing Geometrical Dilution of Precision using Ridge Regression", IEEE AES, Vol. 26, No. 4, pp. 677-681.

K.14 KATZIR S., CLIFF E.M., LUTZE F.H., "An Approach to Near Optimal Guidance On-Booard Calculations", Proc. of IEEE International Conference on Control and Applications, 1989, Paper TP-1-1, pp. 1-7.

K.15 KAYTON M., "Navigation: Ships to Space", IEEE AES, Vol. 24, No. 5, 1988, pp. 474-519.

K.16 KENDRICK J.D., MAYBECK P.S., REID J.G., "Estimation of Aircraft Motion Using Orientation Measurements", IEEE AES, Vol. 17, No. 2, 1981, pp. 254-259.

K.17 KERR T.H., "Critique of some Neural Network Architectures and Claims for Control and Estimation", IEEE AES, Vol. 34, No. 2, 1998, pp. 406-418.

K.18 KERR T., "Decentralized Filtering and Redundancy Management for Multisensor Navigation", IEEE AES, Vol. 23, No. 1, pp. 83-119.

K.19 KIHARA M., OKADA T., "A Satellite Selection Method and Accuracy for the Global Positioning System", J. ION, Vol. 31, No. 1, pp. 8-20.

K.20 KIM E.T., ANDRISANI D., "Design of a Robust Estimator for Target Tracking", J. Guidance and Control, Vol. 16, No. 3, 1992, pp. 595-597.

K.21 KIM B.S., LEE J.G., HAN H.S., "Biased PNG Law for Impact with Angular Constraint", IEEE AES, Vol. 34, No. 1, 1998, pp. 275-287.

K.22 KIM K.D., SPEYER J.L., TAHK M., "Target Maneuver Models for Tracking Estimators", Proc. of the IEEE International Conference on Control and Applications, Paper RA-1-7, New York, 1989.

K.23 KIRLIN R.L., MOGHADDAMJOO A., "Robust Adaptive Kalman Filter for Systems with Unknown Step Inputs and Non-Gaussian Measurement Errors", IEEE ASSP, Vol. 34, No. 2, 1986, pp. 252-263.

K.24 KITSON F.L., GRIFFITHS L.J., "Design and Analysis of Recursive Periodically Time Varying Digital Filters with Highly Quantized Coefficients", IEEE Trans. on Acoustics, Speech and Signal Processing, Vol. 36, No. 5, 1988, pp. 674-684.

K.25 KLEIN L.A., "A Boolean Algebra Approach to Multiple Sensor Voting Fusion", IEEE AES, Vol. 29, No. 2, 1993, pp. 317-327.

K.26 KRAUSE L.O., "A Direct Solution to GPS-Type Navigation Equations", IEEE AES, Vol. 23, No. 2, pp. 225-231.

K.27 KOIFMAN M., MERHAV S.J., "Autonomously Aided Strapdown Attitude Reference System", AIAA J. Guidance and Control, Vol. 14, No. 6, 1991, pp. 1164-1172.

K.28 KOVACEVIC F., “Microprocessor Control of Rocket Flight Stabilization”, Microprocessors and Microsystems, Vol. 11, No. 6, 1987, pp. 330-336.

K.29 KUMAR R., KELLEY H.J., “Singular Optimal Atmospheric Rocket Trajectories”, AIAA J. Guidance and Control, Vol. 11, No. 4, 1988, pp. 305-312.

K.30 KOCH W., “Fixed-Interval Retrodiction Approach to Bayesian IMM-MHT for Maneuvering Multiple Targets”, IEEE AES, Vol. 36, No. 1, 2000, pp. 2-14.

K.31 KIM K.B., KIM M-J, CHOI J.W., “Modified Receding Horizontal Guidance Law with Information on Small Accurate Time-to-Go”, IEEE AES, Vol. 36, No. 2, 2000, pp. 725-729.

K.32 KRONHAMN T.R., Geometric Illustration of the Kalman Filter Gain and Covariance Update Algorithms”, IEEE Control Systems Magazine, May 1985, pp. 41-43.

L

L.11 LARGE E., “Optimal Flight Paths for a Winged Supersonic Rocket Vehicle”, Aeronautical Journal, December 1978, pp. 517-522.

L.12 LASSITER E.M., PARKINSON B., “The Operational Status of NAVSTAR/GPS”, J. Navigation, Vol. 30, No. 1, pp. 35-47.

L.13 LEFFERTS R.E., “Alpha-Beta Filters in Polar Coordinates with Acceleration Corrections”, IEEE AES, Vol. 24, No. 6, 1988, pp. 693-699.

L.14 LEE A.Y., “Optimal Autorotation Descent of a Helicopter with Control and State Inequality Constraints”, AIAA J. Guidance and Control, Vol. 13, No. 5, 1990, pp. 922-924.

L.15 LEE G.T., LEE J.G., ROH Y.K., PARK C.G., “Modeling Quaternion Errors in SDINS: Computer Frame Approach”, IEEE AES, Vol. 34, No. 1, 1998, pp. 289-299.

L.16 LEE Y.C., “New Concept for Independent GPS Integrity Monitoring”, J. ION, Vol. 35, No. 2, pp. 239-253.

L.17 LEE Y.C., “Ground Monitoring Schemes for GPS Integrity Channel”, IEEE AES, Vol. 26, No. 3, pp. 481-489.

L.18 LEFAS C.C., “Real-Time Wind Estimation and Tracking with Transponder Downlinked Airspeed and Heading Data”, IEEE AES, Vol. 23, No. 2, 1987, pp. 169-173.

L.19 LEFAS C.C, “Using Roll-Angle Measurements to Track Aircraft Maneuvers”, IEEE, Vol. 20, No. 6, 1984, pp. 672-681.

L.20 LENNEN G.R., DALY P., “A NAVSTAR GPS C/A Code Digital Receiver”, J. ION, Vol. 36, No. 1, pp. 115-125.

L.21 LEONDES C.T. (ED.), “Advances in Control Systems - Theory and Applications”, Vol. 4, 1966, Academic Press.

L.22 LEONDES C.T. (Ed.), “Control and Dynamic Systems”, Academic Press, LCCC No. 64-8027, 1973.

L.23 LERRO D., BAR-SHALOM Y., “Interacting Multiple Model Tracking with Target Amplitude Feature”, IEEE AES, Vol. 29, No. 2, 1993, pp. 494-509.

L.24 LEVA J.L., “An Alternative Closed-Form Solution to the GPS Pseudo-RAnge Equations”, IEEE AES, Vol. 32, No. 4, 1996, pp. 1430-1439.

L.25 LEVANON N., “Radar Principles”, J. Wiley & Sons, ISBN 0-471-85881-1, 1988.

L.26 LI X.R., Y. BAR-SHALOM, “A Recursive Multiple Model Approach to Noise Identification”, IEEE AES, Vol. 30, No. 3, 1994, pp. 671-683.

L.27 LI X.R., “Optimal Selection of Estimatee for Multiple-Model Estimation with Uncertain Parameters”, IEEE AES, Vol. 34, No. 2, 1998, pp. 653-656.

L.28 LI X.R., Y. BAR-SHALOM, “Detection Threshold Selection for Tracking Performance Optimisation”, IEEE AES, Vol. 30, No. 3, 1994, pp. 742-749.

L.29 LI X.R., ZHANG Y., ZHI X., “Multiple-Model Estimation with Variable Structure Part III: Model-Group Switching Algorithm”, IEEE AES, Vol. 35, No. 1, 1999, pp. 225-240.

L.30 LI X.R., ZHANG Y., ZHI X., “Multiple-Model Estimation with Variable Structure Part IV: Design and Evaluation of Model-Group Switching Algorithm”, IEEE AES, Vol. 35, No. 1, 1999, pp. 242-253.

L.31 LIANG D.F., CHRISTENSEN G.S., “Exact and Approximate State Estimation for Nonlinear Dynamic Systems”, Automatica, Vol. 11, 1975, pp. 603-612.

L.32 LIN C.F., LEE S.P., “Robust Missile Autopilot Design Using a Generalized Singular Optimal Control Technique”, AIAA J. Guidance and Control, Vol. 8, No. 4, 1985, pp. 498-507.

L.33 LIN C.F., SHAFROTH M.W., “A Comparative Evaluation of Some Maneuvering Target Tracking Algorithms”, Proc. of AIAA Guidance and Control Conference (Gatlinburg), Paper 83-2168, 1983, pp. 39-56.

L.34 LIN C., TSAI L.L., “Analytical Solution of Optimal Trajectory-Shaping Guidance”, AIAA J. Guidance and Control, Vol. 10, No. 1, 1987, pp. 61-66.

L.35 LIN C., “A New Failure Detection Approach and its Application to GPS Autonomous Integrity Monitoring”, IEEE AES, Vol. 31, No. 1, 1995, pp. 499-506.

L.36 LI X.R., ZHANG Y., “Multiple-Model Estimation with Variable Structure Part V: Likely-Model Set Algorithm”, IEEE AES, Vol. 36, No. 2, 2000, pp. 448-465.

L.37 LOVREN N., PIEPER J.K., “A Strapdown Inertial Navigation System for the Flat-Earth Model”, IEEE AES, Vol. 33, No. 1, 1997, pp. 214-223.

L.38 LOVREN N., PIEPER J.K., “Error Analysis of Direction Cosines and Quaternion Parameters Techniques for Aircraft Attitude Determination”, IEEE AES, Vol. 34, No. 3, 1998, pp. 983-989.

L.39 LU P., “Inverse Dynamics Approach to Trajectory Optimisation for an Aerospace Plane”, J. Guidance, Control and Dynamics, Vol. 16, No. 4, 1993, pp. 726-732.

L.40 LUPASH L.O., A New Algorithm for the Computation of the Geodetic Coodinates as a Function of Earth-Centred Earth-Fixed Coordinates”, AIAA J. Guidance and Control, Vol. 8, No. 6, 1985, pp. 787-789.

L.41 LUSE D.W., KHALIL H.K., “Frequency Domain Results for Systems with Slow and Fast Dynamics”, IEEE AC., Vol. 30, No. 12, pp. 1171-1178.

L.42 LEE H., TAHK M-J., “Generalized Input-Estimation Technique for Tracking Maneuvering Targets”, IEEE AES, Vol. 35, No. 4, 1999, pp. 1388-1402.

L.43 LI T., SETHI I.K., “Optimal Multiple Level Decision Fusion with Distributed Sensors”, IEEE AES, Vol. 29, No. 4, 1993, pp. 1252-1259.

M

M.13 MAGUIRE L.P., IRWIN G.W., “Transputer Implementation of Kalman Filters”, IEE Proc., Part D, Vol. 138, No. 4, 1991, pp. 355-362.

M.14 MARTIN K.W., SUN M.T., “Adaptive Filters Suitable for Real-Time Spectral Analysis”, IEEE CAS, Vol. 33, No. 2, 1986, pp. 218-229.

M.15 MAYBECK P.S., JENSEN R.L., HARNLY D.A., “An Adaptive Extended Kalman Filter for Target Image Tracking”, IEEE AES, Vol. 17, No. 2, 1981, pp. 173-180.

M.16 MAYNE D.Q., POLAK E., "An Exact Penalty Function Algorithm for Control Problems with State and Control Constraints", IEEE AC., Vol. 32, No. 5, 1987, pp. 380-387.

M.17 MATTIN R.B., "Derivation of the Inertial Navigation System Equations", Prepared by the Inertial Guidance of Europe, 1962.

M.18 McAULAY R.J., DENLINGER E., "A Decision-Directed Adaptive Tracker", IEEE AES, Vol. 9, No. 2, 1973, pp. 229-236.

M.19 MEHRA R.K., "On the Identification of Variances and Adaptive Kalman Filtering", Proc. Joint Automatic Control Conference, 1969, pp. 494-503.

M.20 MENON P.K.A., BRIGGS M.M., "Near-Optimal Midcourse Guidance for Air-to-Air Missiles", AIAA J. Guidance and Control, Vol. 13, No. 4, 1990, pp. 596-608.

M.21 MENON P.K.A., CHENG V.H.L., LIN C.A., BRIGGS M.M., "High Performance Missile Synthesis with Trajectory and Propulsion System Optimisation", J. Spacecraft, Vol. 24, No. 6, 1987, pp. 552-557.

M.22 MERIAM J.L., KRAIGE L.G., "Engineering Mechanics, Volume 2 - Dynamics", John Wiley & Sons, 1987.

M.23 MIELE A., WANG T., MELVIN W.W., "Optimisation and Acceleration Guidance of Flight Trajectories in a Windshear", AIAA J. Guidance and Control, Vol. 10, No. 4, 1987, pp. 368-377.

M.24 MIWA S., IMADO F., KURODA T., "Clutter Effect on the Miss Distance of a Radar Homing Missile", AIAA J. Guidance and Control, Vol. 11, No. 4, 1988, pp. 336-342.

M.25 MOOK D.J., SHYU I., "Nonlinear Aircraft Tracking Filter Utilizing Control Variable Estimation", AIAA J. Guidance and Control, Vol. 15, No. 1, 1992, pp. 228-237.

M.26 MOOSE R.L., "Passive Range Estimation of an Underwater Maneuvering Target", IEEE ASSP, Vol. 35, No. 3, 1987, pp. 274-285.

M.27 MOOSE R.L.,"Modeling and Estimation for Tracking Maneuvering Targets", IEEE AES, Vol. 15, No. 3, 1979, pp. 448-456.

M.28 MOOSE R.L., CAPUTI J., "A Convergence Analysis of a Passive Underwater Tracking System with Nonlinear Feedback", IEEE ASSP, Vol. 34, No. 6, 1986, pp. 1401-1409.

M.29 MOOSE R.L., DAILEY T.E., "Adaptive Underwater Target Tracking Using Passive Multipath Time-Delay Measurements", IEEE ASSP, Vol. 33, No. 4, 1985, pp. 777-786.

M.30 MUEHLDORF E.I., “The Intersection of a Loxodrome with a Great Circle”, IEEE AES, Vol. 26, No. 2, 1990, pp. 410-412.

M.31 #MAGILL D.T.,”Optimal Adaptive Estimation of Sampled Stochastic Processes”, IEEE AC., Vol. 10, 1965, pp. 434-439.

M.32 McGINNITY S., IRWIN G.W., “Multiple Model Bootstrap Filter for Maneuvering Target Tracking”, IEEE AES, Vol. 36, No. 3, 2000, pp. 1006-1012.

N

N.10 NAIDU D.S., HIBLEY J.L., CHARALAMBOUS C.D., “Neighboring Optimal Guidance for Aeroassisted Orbital Transfer”, IEEE AES, Vol. 29, No. 3, 1993, pp. 656-663.

N.11 NAIDU D.S., PRICE D.B., “Time-Scale Synthesis of a Closed-Loop Discrete Optimal Control System”, AIAA J. Guidance and Control, Vol. 10, No. 5, 1987, pp. 417-421.

N.12 NAUTIYAL A., “Algorithm to Generate Geodetic Coordimates from Earth-Centered Earth-Fixed Coordimates”, J. Guidance, Vol. 11, No. 3, 1982, pp. 281-283.

N.13 NESLINE F.W., NESLINE M.L., “How Autopilot Requirements Constrain the Aerodynamic Design of Homing Missiles”, AIAA, TA7-8:30, pp. 716-730.

N.14 NISHIMURA T., “On the aPriori Information in Sequential Estimation Problems”, IEEE AC., Vol. 11, No. 2, 1966, pp. 197-204.

O

O.5 O'HALLARON D.R., BAHETI S., “Fast Mapping of a Kalman Filter on Warp”, SPIE Real Time Signal Processing XI, Vol. 977, pp. 196-205.

O.6 OHMURO T., “A Decoupled Kalman Tracker Using LOS Coordinates”, Proc. of the Internaltional Symposium on Noise and Clutter Rejection in Radars and Image Sensors, 1984, pp. 451-455.

O.7 OLSON D.K., “Calculation of Geodetic Coordinates from Earth-Centred, Earth-Fixed Coordinates”, AIAA J. Guidance and Control, Vol. 11, No. 2, 1988, pp. 188-190.

P

P.1 PAINTER J.H., KERSTETTER D., JOWERS S., "Reconciling Steady State Kalman and Alpha-Beta Filter Design", IEEE AES, Vol. 26, No. 6, 1990, pp. 986-991.

P.2 PARKINSON B.W., AXELRAD, "Autonomous GPS Integrity Monitoring using the Pseudorange Residual", J. ION, Vol. 35, No. 2, pp. 255-271.

P.3 PASSERIEUX J.M., van CAPPEL D, "Optimal Observer Maneuver for Bearings-Only Tracking", IEEE AES, Vol. 34, No 3, 1998, pp. 777-788.

P.4 PATTON R.J., WILLCOX S.W., WINTER J.S., "Parameter-Insensitive Technique for Aircraft Sensor Fault Analysis", AIAA J. Guidance and Control, Vol. 10, No. 4, 1987, pp. 359-367.

P.5 PAU L.Y., "Knowledge Representation Approaches in Sensor Fusion", Automatica, Vol. 25, No. 2, 1989, pp. 207-214.

P.6 PEARSON F., "Map Projections - Theory and Applications", ISBN 0-8493-6888-X.

P.7 PRATT A.R., "G-Effects on Oscillator Performance in GPS Receivers", J. ION, Vol. 36, No. 1, pp. 63-75.

P.8 PRUSSING J.E., CHIU J., "Optimal Multiple Impulse Time Fixed Rendezvous Between Circular Orbits", AIAA J. Guidance and Control, Vol. 9, No. 1, 1986, pp. 17-22.

P.9 PRUSSING J.E., WELLNITZ L.J., HECKATHORN W.G., "Optimal Impulsive Time-Fixed Direct-Ascent Interception", AIAA J. Guidance and Control, Vol. 12, No. 4, 1989, pp. 487-494.

P.10 PUKKILA T.M., KRISHNAIAH P.R., "On the Use of Autoregressive Order Determination Criteria in Univariate White Noise Tests", IEEE ASSP, Vol. 36, No. 5, 1988, pp. 764-773.

R

R.15 RAMACHANDRA K.V., "Analytical Results for a Kalman Tracker Using Position and Rate Measurements", IEEE AES, Vol. 19, No. 5, 1983, pp. 776-778.

R.16 RAMACHANDRA K.V., "Optimal Steady State Position, Velocity, and Acceleration Estimation Using Noisy Sampled Position Data", IEEE AES, Vol. 23, No. 5, 1987, pp. 705-708.

R.17 RAMACHANDRA K.V., MOHAN B.R., GEETHA B.R., "A Three-State Kalman Tracker Using Position and Rate Measurements", IEEE AES, Vol. 29, No. 1, 1993, pp. 215-221.

R.18 RAMACHANDRA K.V., SRINIVASAN V.S., "Steady State Results for the X, Y, Z, Kalman Tracking Filter", IEEE AES, Vol. 13, No. 4, 1977, pp. 419-423.

R.19 RANGASWAMY M., WEINER D., OZTURK A., "Computer Generation of Correlated Non-Gaussian Radar Clutter", IEEE AES, Vol. 31, No. 1, pp. 106-115.

R.20 RAO M.N., "Analytical Solution of Optimal Trajectory-Shaping Guidance", AIAA J. Guidance and Control, Vol. 12, No. 4, 1989, pp. 600-601.

R.21 RAO S.S., "Optimisation Theory and Applications", Wiley Eastern Ltd., ISBN 0 85226 756 8, 1989.

R.22 RAOL J.R., SINHA N.K., "On the Orbit Determination Problem", IEEE AES, Vol. 21, No. 3, pp. 274-291.

R.23 REHAK M., BENAROYA H., "Simulation of a Random Differential Equation", J. Guidance, Vol. 11, No. 2, pp. 173-178.

R.24 RHODES I.B., "A Parallel Decomposition for Kalman Filters", IEEE AC., Vol. 35, No. 3, 1990, pp. 322-324.

R.25 RICKER G.G., WILLIAMS J.R., "Adaptive Tracking Filter for Maneuvering Targets", IEEE AES, Vol. 14, No. 1, 1978, pp. 185-193.

R.26 ROBBINS J.E., "Reference Trajectories from GPS Measurements", J. ION, Vol. 35, No. 1, pp. 89-103.

R.27 RODGERS R.S., "Continuous-Time ECV and ECA Track Filters with Colored Measurement Noise", IEEE AES, Vol. 26, No. 4, 1990, pp. 663-666.

R.28 ROECKER J.A., "Track Monitoring When Tracking With Multiple 2-D Passive Sensors", IEEE AES, Vol. 27, No. 6, pp. 872-876.

R.29 ROME H.J., "Low-Orbit Navigation Concepts", J. ION, Vol. 35, No. 3, pp. 371-390.

R.30 ROTH Z.S., XU H., "Effects of Modeling Errors on the Stability and Innovations Moments of Kalman Filters", Proc. of IEEE International Conference on Control and Applications, 1989, Paper wp-5-8, pp. 1-2.

R.31 RUSNAK I., "Closed-Form Solution for the Kalman Filter Gains of Time-Varying Systems", IEEE AES, Vol. 34, No. 2, 1998, pp. 635-638.

R.32 RONG LI X., ZHANG Y., "Numerically Robust Implementation of Multiple-Model Algorithms", IEEE AES, Vol. 36, No. 1, 2000, pp. 266-278.

S

S.23 SACHS G., LESCH K., "Periodic Maximum Range Cruise with Singular Control", AIAA J. Guidance and Control, Vol. 16, No. 4, 1992, pp. 790-793.

S.24 SAHA R.K., "An efficient Algorithm for Multisensor Track Fusion", IEEE AES, Vol. 34, No. 1, pp. 200-210.

S.25 SANGSUK-IAM S., BULLOCK T.E.,"Behaviour of the Discrete-Time Kalman Filter Under Incorrect Noise Covariances", Proc. of the 26th Conference on Decision and Control, Los Angeles, CA, December 1987, pp. 1594-1599.

S.26 SATIN A.L., LEONDES C.T., "Ensembling Clocks of the Global Positioning Systems", IEEE AES, Vol. 26, No. 1, pp. 84-87.

S.27 SAVAGE P.G., "Strapdown Inertial Systems - Strapdown Sensors", AGARD LS Paper 95, 2-1, May 1978.

S.28 SENNOTT J.W., PIETRASZEWSKI D., "Experimental Measurement and Characterization of Ionospheric and Multipath Errors in Differential GPS", J. ION, Vol. 34, No. 2, pp. 160-173.

S.29 SHEFER M., SHEMESH S., VALD M., "Optimal Guidance and Control of Anti-Ballistic Missiles", Proc. of IEEE International Conference on Control and Applications, 1989, Paper TP-1-5, pp. 1-6.

S.30 SCHIERMAN J.D., ANDRISANI D., "Linear Helicopter Trackers Using Attitude Measurements", AIAA J. Guidance and Control, Vol. 13, No. 6, pp. 929-935.

S.31 SEYWALD H., "Trajectory Optimisation Based on Differential Inclusion", J. Guidance, Control and Dynamics, Vol. 17, No. 3, 1994, pp. 480-487.

S.32 SEYWALD H., CLIFF E.M., "Goddard Problem in Presence of a Dynamic Pressure Limit", J. Guidance, Control and Dynamics, Vol. 16, No. 4, 1993, pp. 776-781.

S.33 SEYWALD H., KUMAR R.R., "Singular Control in Minimum Time Spacecraft Reorientation", J. Guidance, Control and Dynamics, Vol. 16, No. 4, 1993, pp. 686-694.

S.34 SHAKERI M., PATTIPATI K.R., KLEINMAN D.L., Optimal Measurement Scheduling for State Estimation", Vol. 31, No. 2, 1995, pp. 716-729.

S.35 SHEU S.R., LEE J.Y., WANG J.F., "A VLSI Architecture for the Maneuvering Target Tracking Filter", International Journal of Mini and Microcomputers, Vol. 9, No 2, 1987, pp. 50-55.

S.36 SHIBATA M., "Error Analysis Strapdown Inertial Navigation Using Quaternions", AIAA J. Guidance and Control, Vol. 9, No. 3, 1986, pp. 379-381.

S.37 SHINAR J., "Zeroth-Order Feedback Strategies for Medium-Range Interception in a Horizontal Plane", AIAA J. Guidance and Control, Vol. 8, No. 1, 1985, pp. 9-15.

S.38 SHINAR J., GUELMAN M., SILBERMAN G., GREEN A., "Optimal Missile Avoidance - a Comparison Between Optimal Control and Differential Game Solutions", Proc. of IEEE International Conference on Control and Applications, 1989, Paper WA-6-2, pp. 1-7.

S.39 SINGER R.A., BEHNKE K.W., "Real-Time Tracking Filter Evaluation and Selection for Tactical Applications", IEEE AES, Vol. 7, No. 1, 1971, pp. 100-110.

S.40 SINHA N.K., PUTHENPURA S., "Choice of the Sampling Interval for the Identification of Continuous-Time Systems from Samples of Input/Output Data", IEE Proc., Vol. 132, Part. D, No. 6, pp. 263-267.

S.41 SIOURIS G.M., CHEN G., WANG J., "Tracking an Incoming Ballistic Missile Using an Extended Interval Kalman Filter", IEEE AES, Vol. 33, No. 1, 1997, pp. 232-239.

S.42 SMITH R., SPEYER J.L., "An Adaptive Flight Control System Based on an Explicit Parameter Identification Technique", Proc. of IEEE International Conference on Control and Applications, 1989, Paper WP-1-2, pp. 1-5.

S.43 SONG T.L., AHN J.Y. UM T.Y., " A Passive Tracking Filter for Missile Capture", IEEE AES, Vol. 26, No. 5, 1990, pp. 867-875.

S.44 SORENSON H.W., ALSPACH D.L., "Recursive Bayesian Estimation using Gaussian Sums", Automatica, Vol. 7, 1971, pp. 465-479.

S.45 SORENSON H.W., STUBBERUD A.R., "Non-linear Filtering by Approximation of the a posteriori Density", J. Control, Vol. 8, No. 1, 1968, pp. 33-51.

S.46 SPALL J.C., "Implementation of the Simultaneous Perturbation Algorithm for Stochastic Optimization", IEEE AES, Vol. 34, No. 3, 1998, pp. 817-822.

S.47 SPEYER J.L., CRUES E.Z., "On-Line Aircraft State and Stability Derivative Estimation Using Modified-Gain Extended Kalman Filter", AIAA J. Guidance and Control, Vol. 10, No. 3, 1987, pp. 262-268.

S.48 SPEYER J.L., GUSTAFSON D.E., "An Approximation for Estimation in Linear Systems with Parameter Uncertainty", IEEE AC., Vol. 20, No. 6, 1975, pp. 354-359.

S.49 SPEYER J.L., HULL D.G., "Comparison of Several Extended Kalman Filter Formulations for Homing Missile Guidance", Proc. of AIAA Guidance and Control Conference, Massachusetts, August 1988.

S.50 SPINGARN K., WEIDEMANN H.L., "Linear Regression Filtering and Prediction for Tracking Maneuvering Aircraft Targets", IEEE AES, Vol. 8, November 1972, pp. 800-810.

S.51 STATMAN J.I., "Simplified Solution for a Class of Fading Memory Filters", IEEE AES, Vol. 23, No. 3, 1987, pp. 355-360.

S.52 STURZA M.A., "GPS Navigation Using Three Satellites and a Precise Clock", J. ION, Vol. 30, No. 2, 1983, pp. 146-156.

S.53 SUN J.L., "How to Perform Differentiations on Matrices", AIAA J. Guidance and Control, Vol. 13, No. 5, 1990, pp. 924-926.

S.54 SWERLING P., PETERMAN W.L., "Radar Measurement Accuracy for Fluctuating Targets", IEEE AES, Vol. 27, No. 6, 1991, pp. 868-870.

S.55 SWERLING P., "Radar Probability of Detection for Some Additional Fluctuating Target Cases", IEEE AES, Vol. 33, No. 2, 1997, pp. 698-709.

S.56 SWORDER D.D., KENT M., VOJAK R., HUTCHINS R.G., "Renewal Models for Maneuvering Targets", IEEE AES, Vol. 31, No. 1, 1995, pp. 138-150.

S.57 SWORDER D.D., WELLS G.R., "Guidance Laws for Aerodynamically Controlled Re-entry Vehicles", J. Spacecraft, Vol. 14, No. 2, 1977, pp. 111-117.

S.58 #SONG T-L, SPEYER J., "The Modified Gain Extended Kalman Filter and Parameter Identification in Linear Systems", Automatica, Vol. 22, No. 1, 1986.

S.59 #SONG T-L, LEE D-G, "Effective Filtering of Target Glint", IEEE AES, Vol. 36, No. 1, 2000, pp. 234-240.

T

T.3 TANG Y.M., BORRIE J.A., "Missile Guidance Based on Kalman Filter Estimation of Target Maneuver", IEEE AES, Vol. 20, No. 6, 1984, pp. 736-741.

T.4 TAZARTES D.A., MARK J.G., "Integration of GPS Receivers into Existing Inertial Navigation Systems", J. ION, Vol. 35, No. 1, pp. 105-119.

T.5 TEMPLEMAN A.B.,"A Steepest Gradient Method for Optimum Structural Design", International Journal for Numerical Methods in Engineering Vol. 3, 1971, pp. 249-259.

T.6 TENNEY R.R., HEBBERT R.S., SANDELL N.R.,"A Tracking Filter for Maneuvering Sources", IEEE AC., Vol. 22, 1977, pp. 246-251.

T.7 THOMOPOULOS S.C.A., BOUGOULIAS D.K., WANN C., "Dignet: An Unsupervised-Learning Cluster Algorithm for Clustering and Data Fusion", IEEE AES, Vol. 31, No. 1, 1995, pp. 21-38.

T.8 THORNTON C.L., BIERMAN G.J., "UDU^T Covariance Factorisation for Kalman Filtering", Academic Press Inc., 1980, ISBN 0-12-012716-4. pp. 177-250.

T.9 THORP J.S., "Optimal Tracking of Maneuvering Targets", IEEE AES, Vol. 9, No. 4, 1973, pp. 512-519.

T.10 TSAI C., KURZ L., "An Adaptive Robustizing Approach to Kalman Filtering", Automatica, Vol. 19, No. 3, 1983, pp. 279-288.

T.11 TSENG H.C., "Ship-Mounted Satellite Tracking Antenna with Fuzzy Logic Control", IEEE AES, Vol. 34, No. 2, 1998, pp. 639-645.

T.12 TYLEE J.L., HARDTLA J.W., "Adaptive Guidance for Future Launch Vehicles", AIAA, Paper 88-4124-CP, 1988, pp. 609-617.

U

U.1 UPADHYAY T., COTTERILL S., DEATON A.W., "Autonomous GPS/INS Navigation Experiment for Space Transfer Vehicle", IEEE AES, Vol. 29, No. 3, 1993, pp. 772-785.

U.2 UM T.Y., LEE J.G., PARK S-T, PARK C.G., "Noise Covariances Estimation for Systems with Bias States", IEEE AES, Vol. 36, No. 1, 2000, pp. 226-232.

V

V.5 VIAN J.L., MOORE J.R., “Trajectory Optimisation with Risk Minimisation for Military Aircraft”, AIAA J. Guidance and Control, Vol. 12, No. 3, 1989, pp. 311-317.

V.6 VIETS K.J., “Independent Ground Monitor Coverage of GPS Satellites”, IEEE AES, Vol. 23, No. 5, pp. 678-685.

V.7 VISSER H.G., SHINAR J., “First-Order Corrections in Optimal Feedback Control of Singularly Perturbed Nonlinear Systems”, IEEE AC., Vol. 31, No. 5, 1986, pp. 387-393.

V.8 VISSER H.G., SHINAR J., “A Highly Accurate Feedback Approximation for Horizontal Variable-Speed Interceptions”, AIAA J. Guidance and Control, Vol. 9, No. 6, 1986, pp. 691-698.

W

W.8 WALTZ E., LLINAS J., “Multisensor Data Fusion”,Artech House Inc., ISBN 0-89006-277-3, 1990.

W.9 WANG P.K.C., “Non-linear Guidance Laws for Automatic Orbit Rendezous”, J. Control, Vol. 42, No. 3, 1985, pp. 651-670.

W.10 WANG H., KIRUBARAJAN T., BAR-SHALOM Y. “Precision Large Scale Air Traffic Surveillance Using IMM/Assignment Estimators”, IEEE AES, Vol. 35, No. 1, 1999, pp. 255-265.

W.11 WANG T.C., VARSHNEY P.K., “A Tracking Algorithm for Maneuvering Targets”, IEEE AES, Vol. 29, No. 3, 1993, pp. 910-924.

W.12 WEI M., SCHWARZ K.P., “A Strapdown Inertial Algorithm Using an Earth-Fixed Cartesian Frame”, J. ION, Vol. 37, No. 2, pp. 153-167.

W.13 WEISS H., “Quaternion Based Rate/Attitude Tracking System with Application to Gimbal Attitude Control”, J. Guidance, Control and Dynamics, Vol. 16, No. 4, 1993, pp. 609-616.

W.14 WEISS J.L., UPADHYAY T.N., TENNEY R., “Finite Computable Filters for Linear Systems Subject to Time Varying Model Uncertainty”, Proc. of the National AES Conference, May 1983, pp. 349-355.

W.15 WERTZ J.R., “Spacecraft Attitude Determination and Control”, D. Reidel Publishing Co., ISBN 90-277-0959-9, 1986.

W.16 WEST-VUKOVICH G., SCHERZINGER J.Z.B., BURKE H.R.S., "The Honeywell/DND Helicopter Navigation System (HINS) IEEE AES Magazine, March 1989, pp. 18-27.

W.17 WHITE N.A., MAYBECK P.S. DeVILBISS S.L., "Detection of Interference/Jamming and Spoofing in a DGPS-Aided Inertial System", IEEE AES, Vol. 34, No. 4, 1998, pp. 1208-1216.

W.18 WILLMAN W.W., "Effects of Strapdown Seeker Scale-Factor Uncertainty on Optimal Guidance", AIAA J. Guidance and Control, Vol. 11, No. 3, 1988, pp. 199-206.

W.19 WILLNER D., "Kalman Filter Algorithms for a Multi-Sensor System", Procs. IEEE Conference on Decision & Control (Clearwater, Florida), December 1976, pp. 570-574.

W.20 WILLIAMS D.E., FREIDLAND B., MADIWALE A.N., "Modern Control Theory for Design of Autopilots for Bank-to-Turn Missiles", AIAA J. Guidance and Control, Vol. 10, No. 4, 1987, pp. 378-386.

W.21 WINDALL W.S., KELLEY J.F., "JTIDS Relative Navigation with Measurement Sharing: Design and Performance", IEEE AES, Vol. 22, No. 2, pp. 146-154.

W.22 WINGROVE R.C., RABY J.S., "Trajectory Optimisation Using Fast-Time Repetitive Computation", Proceedings - Fall Joint Computer Conference, 1966, pp. 799-808.

W.23 WOOLFSON M.S., "An Evaluation of Manoeuvre Detector Algorithms", GEC Journal of Research, Vol. 3, No. 3, 1985, pp. 181-190.

W.24 WONG R.V.C., SCHWARZ K.P., CANNON M.E., "High Accuracy Kinematic Positioning by GPS-INS", USA ION, Vol. 35, No. 2, 1987.

W.25 WU W., "Target Tracking with Glint Noise", IEEE AES, Vol. 29, No. 1, 1993, pp. 174-185.

W.26 WU W., KUNDU A., "Kalman Filtering in Non-Gaussian Environment using Efficient Score Function Approximation", IEEE, Paper No. CH2692-2/89/0000-0413$1.00, 1989, pp. 413-416.

W.27 WU W., "Maximum Likelihood Identification of Glint Noise", IEEE AES, Vol. 32, No. 1, 1996, pp. 41-51.

W.28 WANG F., LITVA J., LO T., BOSSE E., LEUNG H., "Feature-Mapping Data Fusion", IEE Proc. Radar, Sonar and Navigation, Vol. 143, No. 2, 1996, pp. 65-70.

W.29 WATSON G.A., BLAIR W.D., “Interacting Acceleration Compensation Algorithm for Tracking Maneuvering Targets”, IEEE AES, Vol. 31, No. 3, 1995, pp. 1152-1158.

X

X.1 XIHENG H., “FF-Pade Method of Model Reduction in Frequency Domain”, IEEE AC., Vol. 32, No. 3, pp. 243-248.

Y

Y.10 YAKOWITZ S.J., “The Stagewise Kuhn-Tucker Condition and Differential Dynamic Programming”, IEEE AC., Vol. 31, No. 1, 1986, pp. 25-67.

Y.11 YANG S.M., “Analysis of Optimal Midcourse Guidance Law”, IEEE AES, Vol. 32, No. 1, 1996, pp. 419-425.

Y.12 YANG C-D., YANG C-C., “Optimal Pure Proportional Navigation for Maneuvering Targets”, IEEE AES, Vol. 33, No. 3, 1997, pp. 949-957.

Y.13 YANG Z., “Partical Velocity Estimation Using Kalman Filtering”, IEEE AES, Vol. 21, No. 3, 1985, pp. 407-419.

Y.14 YUEH W.R., LIN C., “Guidance Performance Analysis with In-Flight Radome Error Calibration”, AIAA J. Guidance and Control, Vol. 8, No. 5, 1985, pp. 666-669.

Z

Z.4 ZELINSKI A., KLEINLE B., “Design of a Minature High Precision Ovenised Oscillator for GPS Receivers”, J. ION, Vol. 36, No. 4, pp. 379-395.

Z.5 ZHU Y., “Efficient Recursive State Estimator for Dynamic Systems without Knowledge of Noise Covariances”, IEEE AES, Vol. 35, No. 1, 1999, pp. 102-113.

Z.6 ZHUANG W., TRANQUILLA J., “Modeling and Analysis for the GPS Pseudo-Range Observable”, IEEE AES, Vol. 31, No. 2, pp. 739-751.

APPENDIX A

14 GEOMETRIC POINTS

The Glossary reflects the breadth of the work undertaken and imposes a common framework within which algorithms from various disciplines can be expressed. The generic nature of the definitions therein, and their relationship with the naming convention adopted for simulation work, must be customised, starting with the definition of the critical points associated with the air defence application. The geometric points defined here are usually associated with the origin of the Frames-of-Reference dealt with in Appendix B.

Although terrestrial vehicle dynamics are the main consideration, the use of inertial motion sensors, and a GPS constellation, means that an inertial reference must be established for long-range vehicles; a reference which provides a general platform for dynamics of a point with respect to inertial space.

Only the geometrical points listed in Table 14-1 are used when defining vectors. When selecting notation for geometric points (i , j , k) are reserved for use as mathematical indices.

Table 14-1 : Geometric Points

POINT	DESCRIPTION	
b	Target-missile intercept point	
c	Missile centre of gravity	
d	Missile position on the Earth's ellipsoid	
e	Target position on the Earth's ellipsoid	
f	Missile position on the Earth's surface	
g	GPS receiver reference point	
m	Seeker (missile) reference point	
o	Earth fixed launcher and ground radar position	
p	General point	
q	Intersection of LGA verticals and the equatorial plane	
r	Earth's geometric centre	
s	NAVSTAR GPS satellite reference points	
t	Target centroid - nominal observation point	
u	Missile IMU reference point	
w	Target position on the Earth's surface	

14.1 Geometric Earth Centre

Point (r) is the intersection of a line between the Earth's poles and its equatorial plane. It is assumed that this point moves with constant linear velocity with respect to the distant stars.

14.2 Local Geoid Centre

Point (q) is the intersection of a geodetic vertical through a generic point (p) and the Earth's equatorial plane. The geodetic centre of the Earth (q) moves in the equatorial plane and is always at, or a short distance away from, the geometric Earth centre (r).

14.3 Earth Referenced Launcher Position

Point (o) is the intersection of a geodetic vertical through point (m) and the Earth's surface at time (t := 0). Point (o) is defined by its geodetic latitude, longitude, and height with respect to the WGS-84 geoid. If these co-ordinates are set to zero the missile is launched from the intersection of the Equatorial Plane and Greenwich meridian on the Earth's equipotential surface. This data is then transformed into the Alignment Frame commensurate with the simulation state vector. For convenience, at launch, points (o), (d) and (m) are coincident and at rest on the Earth's surface.

14.4 **NAVSTAR GPS Reference Points**

The set of 24 reference points $\{n_i\}$ of the satellites comprising the NAVSTAR GPS constellation.

14.5 **Missile Centre of Gravity**

Point (c) is the missile centre-of-gravity in a locally uniform gravitational field that lies on its longitudinal axis of rotation. During the boost phase this point moves along the longitudinal axis as fuel is expended. When the missile is treated as a point mass points (c), (u) and (m) are coincident.

14.6 **Missile IMU Reference Point**

Point (u) is the IMU reference point on the missile's longitudinal axis.

14.7 **Missile GPS Receiver Reference Point**

Point (g) is the NAVSTAR GPS reference point that lies on the upper surface of the vehicle in the longitudinal plane spanned by $\underline{X}^B$ and $\underline{Z}^B$.

14.8 **Seeker (Missile) Reference Point**

Point (m) is the seeker gimbals centre of rotation that lies on the missile longitudinal axis. This point also acts as the electronic centre for the detector and is also the missile's reference point. When the missile is treated as a point mass points (c), (u) and (m) are coincident.

14.9 **Missile Geodetic Position**

Point (d) is the intersection of a geodetic vertical through point (m) and the WGS-84 geoid.

14.10 **Missile Ground Position**

Point (f) is the intersection of a geodetic vertical through point (m) and the ground represented by 3rd order DTED interpolation centred about point (d).

14.11 **Target Reference Point**

Point (t) is the target reference point when it is treated as a point mass. It is also used as the observation point for the radar and seeker models in the absence of measurement glint.

14.12 **Target Impact Point**

Point (b) is the point at which the missile and target collide.

APPENDIX B

15 FRAMES OF REFERENCE

The Frames-of-Reference (frames) located at the key geometrical points defined in Appendix A are defined here. Frames fall into 3 groups: Earth referenced including the Celestial (Inertial) and satellite frames, missile, and target located frames. Frames are key in the specification of vectors and frame related matrices such as the state vector covariances introduced in the Glossary, relating the generic nomenclature therein to the air-defence application.

All the frames listed in Figure 15-1 are defined by orthogonal vectors ($\underline{X}$, $\underline{Y}$, $\underline{Z}$), notation reserved for principal axis identifiers. Transformation between frames requires only proper (right-handed) rotations.

Table 15-1 : Frames of Reference

SYMBOL	POINT	DESCRIPTION	
A	o	Alignment Frame	
B	m	Missile Body Frame	
C	r	Celestial (Inertial) Frame	
E	r	Earth Centred, Earth Fixed Frame	
G	p	Local Geodetic Frame	
H	m	Seeker Head Frame	
I	p	Local Inertial Frame	
L	g	Missile to GPS Satellite LOS Frames	
M	o	Missile LOS Frame	
MB	o	Radar Missile Beam Frame	
MU	u	Missile IMU Frame	
MV	m	Missile Velocity Frame	
O	r	NAVSTAR GPS Orbital Frames	
R	m	Missile Rolled Body Frame	
S	m	Seeker LOS Frame	
T	o	Target LOS Frame	
TB	o	Radar Target Beam Frame	
TD	o	Radar Planar Array Boresight Frame	
TV	t	Target Velocity Frame	

15.1 Celestial Frame

The Celestial frame (C) in Figure 15-1, referred to as the geocentric-equatorial, or Earth-Centred-Inertial (ECI) axes, is a non-rotating, Earth centred frame whose origin moves with constant linear velocity with respect to the distant stars. This frame is a set of Earth-Centred, Earth fixed axes established at a reference time and is the frame in which inertial sensors such as gyroscopes and accelerometers operate. Terrestrial missile flights are of short duration compared with the Earth's rotation around the Sun, and the precession of the equinoxes, and therefore the celestial axes can be used as inertial axes for long-range missiles.

The Earth's orbital plane, which includes the centre of the sun, is called the plane of the ecliptic which is inclined at ($\zeta := 24.66°$) to the equatorial plane defined by the equator. The intersection of these two planes defines the vernal and autumnal equinoxes, the vernal equinox being $\underline{X}^C$ which points towards the first point in Aries, nominally a fixed point in space. $\underline{Z}^C$ passes through the north pole. Although this frame is considered to be inertial for

this application, $\underline{Z}^C$ in fact describes a circle with a period of some 26,000 years caused by lunar/solar induced torque on the Earth's equatorial bulge.

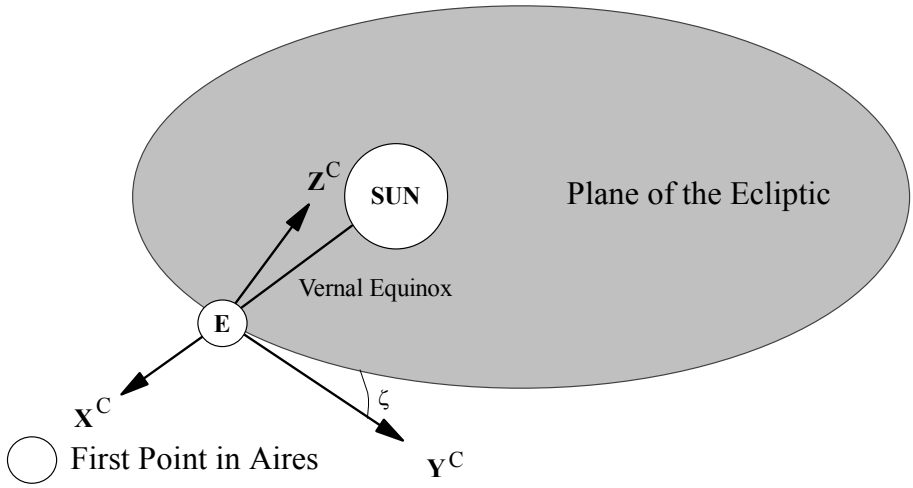

Figure 15-1 : Celestial Frame of Reference

The Local Inertial frame (I) is a translated Celestial frame located at the general point (p) that will depend on application.

15.2 NAVSTAR GPS Orbital Frames

The 6 GPS Satellite Orbital frames (O), one of which is shown in Figure 15-2, are Earth centred, and remain stationary with respect to the Celestial frame. $\underline{X}^O$ and $\underline{Y}^O$ span the satellite orbital plane in which the line of nodes NN' is defined by the intersection between the orbital and equatorial planes. $\underline{X}^O$ passes through the satellite ascending node (N), and $\underline{Z}^O$ is normal to the orbital plane.

The right ascension of the ascending node (Ω) is the angle measured from $\underline{X}^C$ to $\underline{X}^O$ in the equatorial plane. The orbital planes are inclined at ($\iota := 55°$) to the equatorial plane with the position of a particular satellite around its orbit defined by the Mean Anomoly (M), measured clockwise about $\underline{Z}^O$ from the ascending node.

15.3 Missile to Satellite LOS Frames

The 24 Missile-Satellite LOS frames (L) are located at the missile GPS receiver reference point (g). The $\underline{X}^L$ point to each satellite whilst the $\underline{Y}^L$ are contained in a plane parallel to the equatorial plane.

15.4 Earth Centred, Earth Fixed Frame

The Earth-Centred, Earth-Fixed (ECEF) frame (E) shown in Figure 15-3 is located at the Earth's geometric centre (r) and rotates with the Earth. $\underline{X}^E$ lies in the equatorial plane and passes through the line of zero longitude defined

by the poles and Greenwich (London). $\underline{Z}^E$ passes through the north pole. In 1984 the International Earth Rotation Service created the WGS 84 standard comprising the zero reference meridian and axis of rotation that define $\underline{X}^C$ and $\underline{Z}^C$.

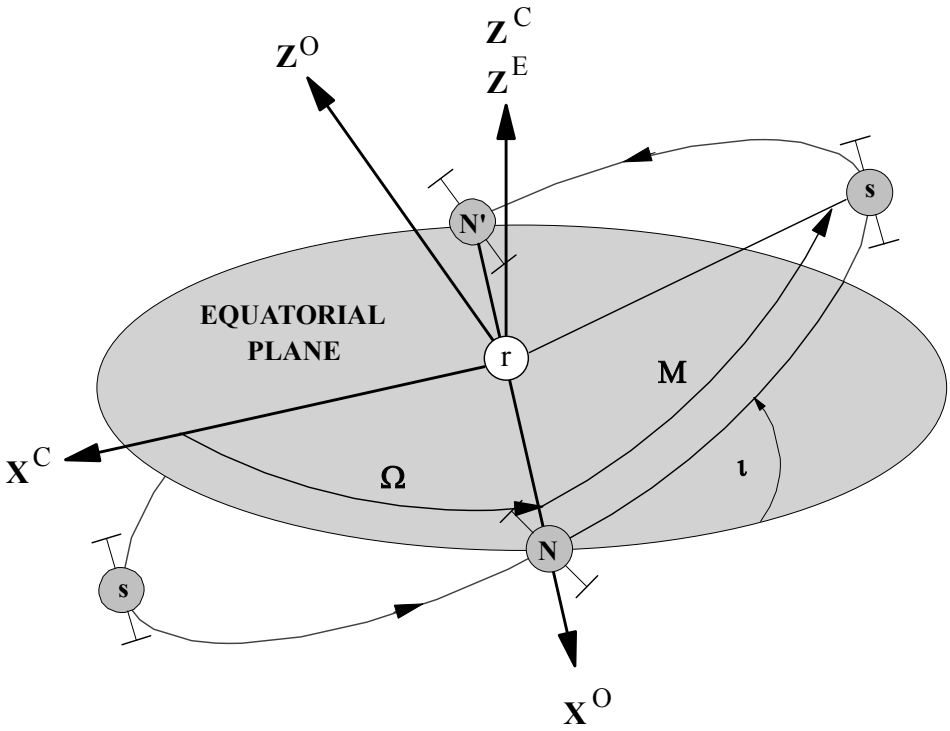

Figure 15-2 : Celestial and GPS Satellite Orbital Frames

15.5 Alignment Frame

The Alignment Frame (A), shown in Figure 15-3, is fixed with respect to the Earth at point (o). $\underline{X}^A$ is an easterly tangent to the Earth's surface parallel to the equatorial plane. $\underline{Z}^A$ lies along the ray from the Earth geometric centre (r) through point (o). $\underline{Y}^A$ lies in the local meridian plane spanned by $\underline{Z}^E$ and $\underline{Z}^A$ pointing in a northerly direction.

15.6 Local Geodetic Axes

Generic LGA (G), an example of which is shown in Figure 15-3, are located a general point (p) above the Earth's surface. $\underline{Z}^G$ points away from the Earth along the bi-normal vector to the tangent plane at the Earth's equipotential surface. $\underline{X}^G$ lies parallel to an easterly tangent at the Earth's surface. $\underline{Y}^G$ points north in the local meridian plane spanned by $\underline{Z}^E$ and $\underline{Z}^G$. The geodetic vertical of the LGA located at point (m) passes through point (d) on the WGS-84 geoid, and point (f) on the Earth's surface.

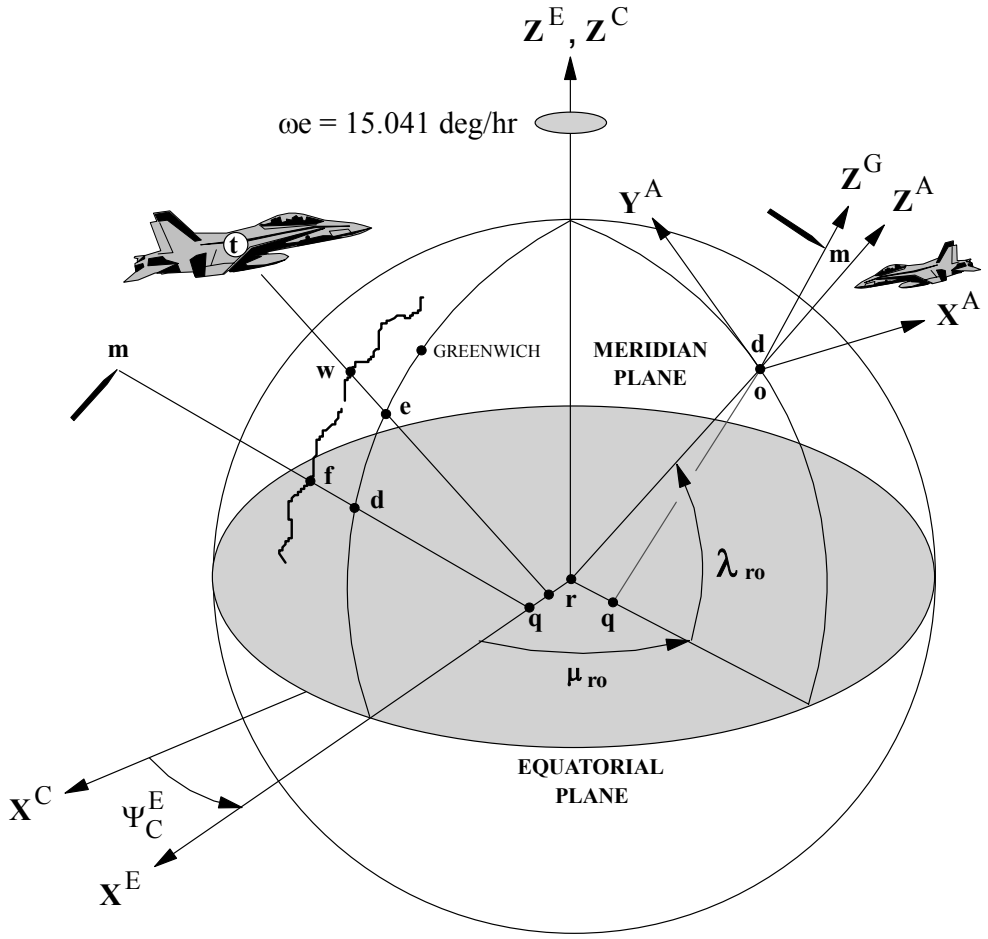

Figure 15-3 : Alignment and Earth Fixed Frames

15.7 Missile LOS Frame

The Missile LOS frame (M) shown in Figure 15-4 is located at point (o), coincident with the launcher and ground radar reference position. $\underline{X}^M$ is the LOS from (o) through point (m). $\underline{Z}^M$ points upwards and is normal to the plane spanned by $\underline{X}^M$ and $\underline{Z}^A$. Y^M remains parallel to the plane spanned by $\underline{X}^A$ and $\underline{Y}^A$.

15.8 Missile Body Frame

The Missile Body frame (B) shown in Figure 15-4 is fixed in the missile at point (m). $\underline{X}^B$ points forward along the missile's longitudinal centre-line, $\underline{Y}^M$ right and $\underline{Z}^M$ downwards when the missile is flying straight and level.

15.9 Missile Velocity Frame

The Missile Velocity frame (MV) is located at point (m) and is rotated through YP angles with respect to the Missile Body frame such that $\underline{X}^{MV}$ points along the missile velocity vector. When $\underline{X}^B$ and $\underline{X}^{MV}$ are aligned when the missile flies straight and level.

15.10 **Missile IMU Frame**

The Missile IMU frame (MU) is located at point (u), the point to which all its inertial sensors are referred. The MU frame is rotated through YPR angles with respect to the Missile Body frame such that it is aligned with the principal IMU sensor input axes.

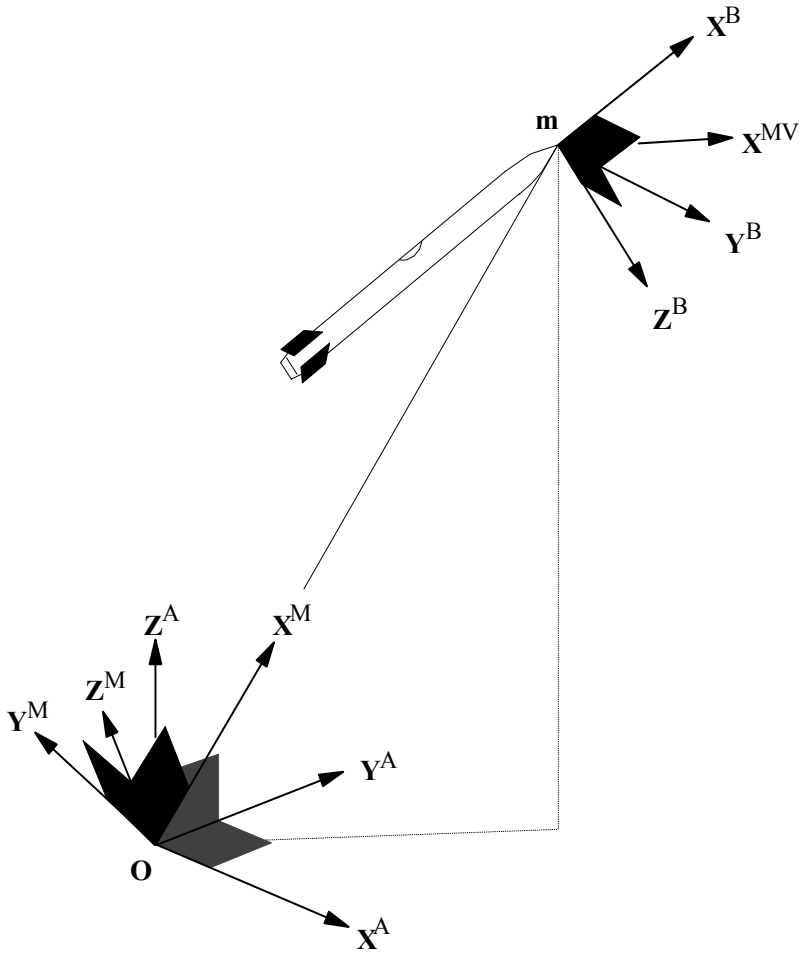

Figure 15-4 : Missile Frames of Reference

15.11 **Seeker LOS Frame**

The Seeker LOS frame (S) shown in Figure 15-5 is located at point (m) and are rotated through YP angles with respect to the Missile Body frame until $\underline{X}^S$ passes through point (t). When the Missile Body and Seeker LOS frames are aligned, and the missile flies straight and level, $\underline{Y}^S$ and $\underline{Z}^S$ point right and down respectively.

15.12 **Seeker Head Frame**

The Seeker Head frame (H) is located at point (m) and is defined by the angular displacement of the YP gimbals with respect to the Missile Body frame. $\underline{X}^H$ points along the seeker boresight normal to the detector, and is

the centre of the main RF beam. $\underline{Y}^H$ and $\underline{Z}^H$ span the seeker detector plane that is bi-normal to $\underline{X}^H$. When the gimbals are locked, or at rest, the Seeker Head frame and Missile Body axes are coincident.

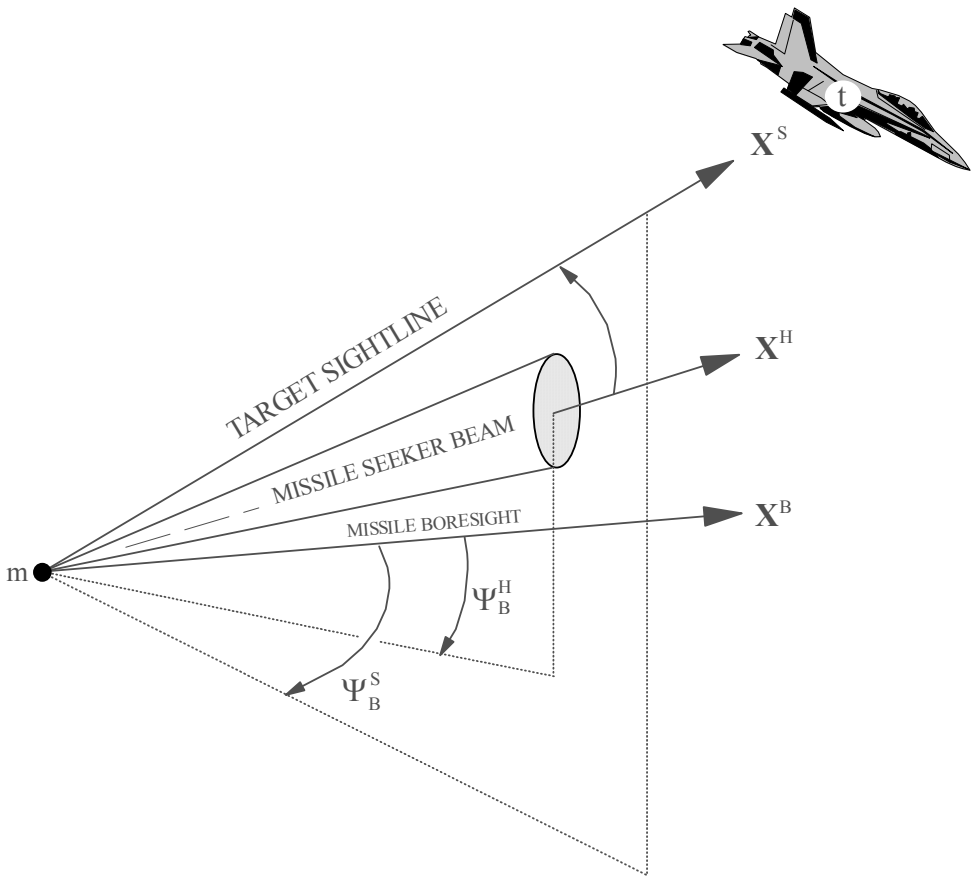

Figure 15-5 : Missile – Target Relative Frames of Reference

15.13 Missile Rolled Frame

The Missile Rolled frame (R) is located at point (m) and is subject to a roll rotation about $\underline{X}^B$ such that $\underline{Z}^R$ points along the total lateral acceleration demand vector.

15.14 Target LOS Frame

The Target LOS frame (T) shown in Figure 15-6 is located at point (o). $\underline{X}^T$ is a vector from (o) through the target at point (t). $\underline{Z}^T$ points upwards and is normal to the plane spanned by $\underline{X}^T$ and $\underline{Z}^A$. $\underline{Y}^T$ remains parallel to the plane spanned by $\underline{X}^A$ and $\underline{Y}^A$.

15.15 Target Body Frame

The Target Body frame (TB) shown in Figure 15-6 is located at point (t). $\underline{X}^{TB}$ points forward along the target's longitudinal centreline, $\underline{Y}^{TB}$ right and $\underline{Z}^{TB}$ down when the target flies straight and level. Although the target is

generally considered to be a point mass, the orientation of the wire frame target model is defined with respect to target body axes.

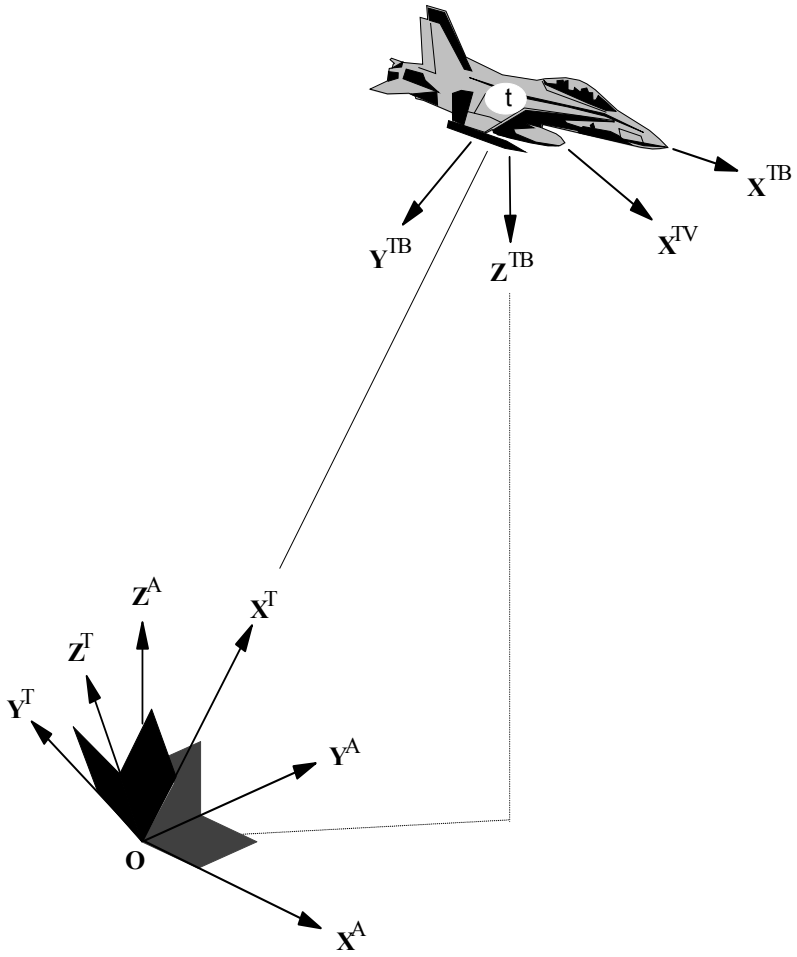

Figure 15-6 : Target Frames of Reference

15.16 Target Velocity Frame

The Target Velocity frame (TV) is located at point (t) and is rotated through YP angles with respect to the Target Body frame such that $\underline{X}^{TV}$ points along the target velocity vector. When the target is flying straight and level the Target Velocity and Target Body frames are coincident with $\underline{Y}^{TV}$ and $\underline{Z}^{TV}$ point right and down respectively.

15.17 Radar Boresight Axes

Radar boresight axes (TD) shown in Figure 15-7 are located at point (o), the centre of the planar array spanned by $\underline{Y}^{TD}$ and $\underline{Z}^{TD}$. $\underline{X}^{TD}$ is a bi-normal vector pointing outwards from the array and $\underline{Y}^{TD}$ remains in the plane spanned by $\underline{X}^{A}$ and $\underline{Y}^{A}$.

15.18 **Radar-Target Beam Axis**

The Radar-Target Beam frame (TB) shown in Figure 15-7 is located at point (o). $\underline{X}^{TB}$ is rotated through YP angles with respect to the Radar Boresight frame defining the centre of the RF beam illuminating the target.

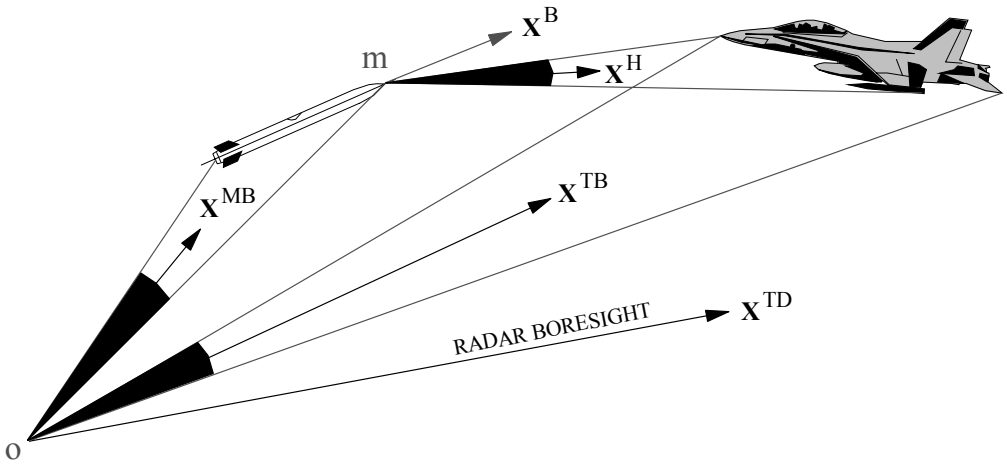

Figure 15-7 : Tracking Radar and Missile Seeker Frames

15.19 **Radar-Missile Beam Axes**

The Radar-Missile Beam axes (MB) shown in Figure 15-7, located at point (o), are rotated through YP angles with respect to the Radar Boresight frame until $\underline{X}^{MB}$ passes through the centre of the RF beam illuminating the missile.

APPENDIX C

16 AXIS TRANSFORMS

The orientation of forces and moments acting at a point are expressed in different Frames of Reference in terms of direction cosines. The transformation matrices defined here using either elemental Euler rotations, or the four-parameter method of quaternions described in §22.9 to avoid the singularity that occurs at pitch angles of ± 90°. Additional notation is introduced to deal with the set of 12 possible Euler angle triplets, although only the yaw-pitch-roll and roll-pitch-yaw variants are considered for the current application. Small angle approximations, the Euler skew-symmetric form and its memory mapping using the FORTRAN computer language are presented.

The transformations between Cartesian, Spherical and UVR co-ordinates with respect to a given frame are explored. The UVR co-ordinate system is of particular interest since phased-array radar usually provide measurements comprising 2 direction cosines (U and V) and range; rarely do they output bearing, elevation and range directly.

Finally, the primary axis transforms used in this application are defined, i.e. transforms that cannot be expressed as the product of two or more direction cosine matrices. When defining algorithms any transform used should be related to a combination of these primary cases. Of particular interest is the relationship between direction cosines defined using trigonometric functions and those described using Cartesian linear position and velocity parameters with their associated singularities.

16.1 Euler Rotations

Expressing vectors in more than one frame requires the application of a matrix transformation from Cartesian frame (A) to Cartesian frame (B). Three proper Euler rotations are required to bring frame (A) into coincidence with frame (B). The following rotations are applied in strict order; a yaw about $\underline{Z}^A$, a pitch about axis $\underline{Y}$', and a roll about axis $\underline{X}$" which is equivalent to axis $\underline{X}^B$. The Euler rotations about the intermediate axes are as follows:

- A proper yaw rotation through angle Ψ about $\underline{Z}^A$ to produce an intermediate set of axes $\underline{X}'\underline{Y}'\underline{Z}'$, where $\underline{Z}'$ is coincident with $\underline{Z}^A$.
- A proper pitch rotation through angle Θ about $\underline{Y}'$ to produce an intermediate set of axes $\underline{X}''\underline{Y}''\underline{Z}''$, where $\underline{Y}'$ is coincident with $\underline{Y}''$.
- A proper roll rotation through angle Φ about $\underline{X}''$ to produce axes $\underline{X}^B\underline{Y}^B\underline{Z}^B$, where $\underline{X}''$ is coincident with $\underline{X}^B$.

Pitch angles refer exclusively to proper Euler rotations about a vector in, and measured with respect to, the plane spanned by ($\underline{X}^A$,$\underline{Y}^A$). In the text it is permissible to refer to the negative Euler pitch angle as elevation. In mathematical definitions only Euler pitch angles are used to avoid confusion with the terminology reserved for one of the Spherical Polar co-ordinates. The elementary Euler rotations are therefore,

$$\left\{ \left[\Psi \right] , \left[\Theta \right] , \left[\Phi \right] \right\} :=$$

$$\left\{ \begin{bmatrix} c\Psi & , & s\Psi & , & 0 \\ -s\Psi & , & c\Psi & , & 0 \\ 0 & , & 0 & , & 1 \end{bmatrix} , \begin{bmatrix} c\Theta & , & & , & -s\Theta \\ & , & 1 & , & \\ s\Theta & , & & , & c\Theta \end{bmatrix} , \begin{bmatrix} 1 & , & 0 & , & 0 \\ 0 & , & c\Phi & , & s\Phi \\ 0 & , & -s\Phi & , & c\Phi \end{bmatrix} \right\}$$

Equation 16.1-1

In this equation "s" represents the sine function, and "c" the cosine function. When analysing dynamic systems it is convenient to refer to a set of Euler angles as an ordered triplet, for example, the Euler angles transforming vectors from frame (A) to frame (B),

$$\underline{E}_A^B := \begin{pmatrix} \Phi_A^B & \Theta_A^B & \Psi_A^B \end{pmatrix}$$

Equation 16.1-2

Euler triplets are not vectors, they are merely useful terminology when dealing with 3D angular quantities. However, to be consistent with the treatment of frame co-ordinates as "vectors" the underlining notation associated with vectors is used. Combining these transformations in strict

YPR order (yaw rotation is applied first) results in a matrix that transforms the components of a vector in frame (A) to those in frame (B),

$$T_A^B \coloneqq \left[\Phi_A^B\right] \cdot \left[\Theta_A^B\right] \cdot \left[\Psi_A^B\right]$$

Equation 16.1-3

$$T_A^B \coloneqq \begin{bmatrix} c\Theta \cdot c\Psi & , & c\Theta \cdot s\Psi & , & -s\Theta \\ s\Phi \cdot s\Theta \cdot c\Psi - c\Phi \cdot s\Psi & , & c\Phi \cdot c\Psi + s\Phi \cdot s\Theta \cdot s\Psi & , & s\Phi \cdot c\Theta \\ s\Phi \cdot s\Psi + c\Phi \cdot s\Theta \cdot c\Psi & , & c\Phi \cdot s\Theta \cdot s\Psi - s\Phi \cdot c\Psi & , & c\Phi \cdot c\Theta \end{bmatrix}$$

Equation 16.1-4

Whereas a quaternion has one normalisation condition, direction cosine matrices have 6; the sum of squares of each row and column must equal 1. This example given is 1 of 12 combinations of elemental rotations. The majority of angular transformations for this application are carried out using ordered YPR rotations. If another Euler combination is used it is identified explicitly. For example, the RPY Euler triplet would be,

$${}^{RPY}\underline{E}_A^B \equiv \left({}^{RPY}\Phi_A^B \;,\; {}^{RPY}\Theta_A^B \;,\; {}^{RPY}\Psi_A^B \right)$$

Equation 16.1-5

The resulting direction cosine matrix is ${}^{RPY}T_A^B$. This transform is the only other one of interest as it to deals with seeker detectors with an outer roll gimbal,

$${}^{RPY}T_A^B \coloneqq \left[\Psi\right] \cdot \left[\Theta\right] \cdot \left[\Phi\right]$$

Equation 16.1-6

$${}^{RPY}T_A^B \coloneqq$$

$$\begin{bmatrix} c\Theta \cdot c\Psi & , & s\Phi \cdot s\Theta \cdot c\Psi + c\Phi \cdot s\Psi & , & s\Phi \cdot s\Psi - c\Phi \cdot s\Theta \cdot c\Psi \\ -c\Theta \cdot s\Psi & , & c\Phi \cdot c\Psi + s\Phi \cdot s\Theta \cdot s\Psi & , & c\Phi \cdot s\Theta \cdot s\Psi + s\Phi \cdot c\Psi \\ s\Theta & , & -s\Phi \cdot c\Theta & , & c\Phi \cdot c\Theta \end{bmatrix}$$

Equation 16.1-7

When it is necessary to identify the order of elemental rotations the prefixed superscript shown here is used. If the prefix is omitted (YPR) is assumed.

When referring to individual direction cosines the notation is consistent with the *FORTRAN* array mapping structure.

$$T_A^B \;:=\; \begin{bmatrix} T(1) & , & T(4) & , & T(7) \\ T(2) & , & T(5) & , & T(8) \\ T(3) & , & T(6) & , & T(9) \end{bmatrix}$$

Equation 16.1-8

This is equivalent to,

$$T_A^B \;\equiv\; \begin{bmatrix} T(1,1) & , & T(1,2) & , & T(1,3) \\ T(2,1) & , & T(2,2) & , & T(2,3) \\ T(3,1) & , & T(3,2) & , & T(3,3) \end{bmatrix}$$

Equation 16.1-9

If the full notation becomes laborious when dealing with direction cosines it is permissible to drop the frame reference providing that the meaning of the transform is clearly defined. Since transformations defined by direction cosines result in orthogonal matrices,

$$T_B^A \;\equiv\; \left[\, T_A^B \,\right]^T \;\equiv\; \left[\, T_A^B \,\right]^{-1}$$

Equation 16.1-10

16.2 Small Angle Approximations

When the angular rotation between frames is small the transformation matrix reduces to a skew symmetric form using small angle approximations highlighted by the delta notation. A transformation defined by small angular rotations decomposes into the identity matrix and an anti-symmetric matrix defined by an Euler triplet,

$$\Delta T_A^B \;:=\; \left[\, I_3 - \Delta \underline{E}_A^B \times \,\right] \;\equiv\; \begin{bmatrix} 1 & , & \Delta\Psi_A^B & , & -\Delta\Theta_A^B \\ -\Delta\Psi_A^B & , & 1 & , & \Delta\Phi_A^B \\ \Delta\Theta_A^B & , & -\Delta\Phi_A^B & , & 1 \end{bmatrix}$$

Equation 16.2-1

$$\underline{X}^{B} \;\coloneqq\; \Delta T_{A}^{B} \cdot \underline{X}^{A} \;\equiv\; \left[\, I_3 - \Delta \underline{E}_{A}^{B} \times \right] \cdot \underline{X}^{A}$$

Equation 16.2-2

$$\left[\, \Delta \underline{E}_{A}^{B} \times \right] \;\equiv\; \begin{bmatrix} 0 & , & -\Delta\Psi_{A}^{B} & , & \Delta\Theta_{A}^{B} \\ \Delta\Psi_{A}^{B} & , & 0 & , & -\Delta\Phi_{A}^{B} \\ -\Delta\Theta_{A}^{B} & , & \Delta\Phi_{A}^{B} & , & 0 \end{bmatrix}$$

Equation 16.2-3

Consider a misalignment in the transformation from frame (A) to frame (B),

$$T_{A}^{\tilde{B}} \;\coloneqq\; \Delta T_{B}^{\tilde{B}} \cdot T_{A}^{B} \;\coloneqq\; \left[\, I_3 - \Delta \underline{E}_{B}^{\tilde{B}} \times \right] \cdot T_{A}^{B}$$

Equation 16.2-4

$$T_{A}^{B} \;\coloneqq\; -\Delta T_{B}^{\tilde{B}} \cdot T_{A}^{\tilde{B}} \;\coloneqq\; \left[\, I_3 + \Delta \underline{E}_{B}^{\tilde{B}} \times \right] \cdot T_{A}^{\tilde{B}}$$

Equation 16.2-5

This use of the skew symmetric form using the positive sign is not advised; reversal of the frame identifier is preferred,

$$T_{A}^{B} \;\coloneqq\; \left[\, I_3 - \Delta \underline{E}_{\tilde{B}}^{B} \times \right] \cdot T_{A}^{\tilde{B}}$$

Equation 16.2-6

16.3 Euler Angles as a Function of Direction Cosines

Euler angles are obtained from the transformation matrix direction cosines. For example, for a YPR Euler triplet where $\Theta_{A}^{B} \in \left]-\pi/2\,,\,\pi/2\right[$,

$$E_{A}^{B} \;\coloneqq\; \left(\tan^{-1}\left(\frac{T_8}{T_9} \right) \;,\; \sin^{-1}\left(-T_7 \right) \;,\; \tan^{-1}\left(\frac{T_4}{T_1} \right) \right)$$

Equation 16.3-1

The implementation of this equation must accommodate zero pitch and roll angles when defining the arc-tangent function.

16.4 Transformation Between Co-ordinate Systems

16.4.1 Co-ordinate Systems

Three types of co-ordinates are defined for dealing with the position of points in E^3 with respect to a frame: Rectangular, Spherical Polar and UVR. Using generic co-ordinates for specifying algorithms is permissible providing that they have been previously defined using the full notation and their scope is clearly identified. Cartesian, Spherical Polar and Radar UVR co-ordinate systems are denoted by (C), (S) and (R) respectively.

16.4.2 Cartesian (Rectangular) Co-ordinates

The position of (p) in Rectangular co-ordinates with respect to frame (A) located at (a),

$$\left(x \;,\; y \;,\; z \right) \equiv \left(P_{a,b}^{XA} \;,\; P_{a,b}^{YA} \;,\; P_{a,b}^{ZA} \right)$$

Equation 16.4-1

The position of a point in E^3 is only equal to Rectangular co-ordinates since these are measured in a direction coincident with the unit vectors defining the frame. Rectangular co-ordinates form a vector in its strictest sense, whereas all other co-ordinates are defined in terms of ordered sets (triplets in E^3).

16.4.3 Spherical Polar Co-ordinates

If frame (B) located at point (p) is rotated through Euler YP angles such that $\underline{X}^B$ passes through point (p) the polar co-ordinates with respect to frame (A),

$$\left(P_{a,b} \;,\; \Theta_A^B \;,\; \Psi_A^B \right) :=$$

$$\left(\sqrt{\underline{P}_b^A \bullet \underline{P}_b^A} \;,\; -\tan^{-1}\left(\frac{P_b^{ZA}}{P_b^{hA}} \right) \;,\; \tan^{-1}\left(\frac{P_b^{YA}}{P_b^{XA}} \right) \right)$$

Equation 16.4-2

The inverse transformation from Spherical Polar to Cartesian co-ordinates,

$$\underline{P}_b^A := \left(P_{a,b} \cdot c\Psi_A^B \cdot c\Theta_A^B \;,\; P_{a,b} \cdot s\Psi_A^B \cdot c\Theta_A^B \;,\; -P_{a,b} \cdot s\Theta_A^B \right)^T$$

Equation 16.4-3

16.4.4 UVR Co-ordinates

The relationship between the position of point (p) in UVR and Rectangular co-ordinates is,

$$\left(u \;,\; v \;,\; r \right) \coloneqq \left(\hat{\underline{n}}^{YB}\left(\underline{P}_p^A \right) \;,\; \hat{\underline{n}}^{ZB}\left(\underline{P}_p^A \right) \;,\; P_{a,p} \right)$$

Equation 16.4-4

If the radar is orientated such that its planar array is spanned by $\underline{Y}^B$ and $\underline{Z}^B$, the co-ordinates (u,v) are the normalised projection of $P_{a,b}$ onto the array.

16.4.5 Transformations Between Frames and Co-ordinates Types

The notation [T] is reserved for rotational transformations (not translation) of vectors expressed in two Cartesian frames, (A) and (B), in which case,

$$\underline{V}^{B|C} \coloneqq T_{A|C}^{B|C} \cdot \underline{V}^{A|C}$$

Equation 16.4-5

The vertical bar differentiates between the frame on the left and the co-ordinate system on the right. When using the Cartesian co-ordinates it is permissible to simplify the notation to,

$$\underline{V}^B \coloneqq T_A^B \cdot \underline{V}^A$$

Equation 16.4-6

Vector function ($\underline{c}$) is used to denote conversion of position between co-ordinates systems when expressed in the same frame,

$$\underline{P}^{A|S} \coloneqq \underline{c}_C^S \left(\underline{P}^{A|C} \right)$$

Equation 16.4-7

Although (S) and (R) are strictly ordered triplets they are conventionally denoted as vectors. To avoid confusion with components of a position vector in (C) the co-ordinate type is specified for (S) and (R), for example,

$$\underline{P}^A \equiv \underline{P}^{A|C} \coloneqq \underline{c}_R^C \left(\underline{P}^{A|R} \right)$$

Equation 16.4-8

The Jacobian associated with co-ordinate conversion is thus,

$$C_{A|C}^{A|S}(i,j) \coloneqq \frac{\partial \underline{c}_C^S \left(\underline{P}_{a,b}^{A|C} \right)}{\partial \underline{P}_{a,b}^{A|C}} \equiv \frac{\partial c_C^{iS} \left(\underline{P}_{a,b}^{A|C} \right)}{\partial P_{a,b}^{jA|C}}$$

Equation 16.4-9

16.5 Simulation Naming Convention

The naming convention for Euler angles taking frame (A) to frame (B) is *E_AB* with components *E_PHI_AB*, *E_THT_AB* and *E_PSI_AB*. Euler rate and acceleration triplets are DE_AB and D2E_AB with components (*DPH_AB*, *DTH_AB*, *DPS_AB*) and (*D2PHAB*, *D2THAB*, *D2PSAB*) respectively. The notation for transformation matrices is *TRATOB* representing the reference transform from frame (A) to frame (B). If the axes are denoted using two characters then the notation is modified to *TRABTC* in the case of a transform from frame (AB) to frame (C).

16.6 Satellite Orbital to Celestial Transformations

Index (i) refers to the indexed set of 6 GPS satellite orbital planes whose ascending nodes are equally spaced around the equator. The ascending node of the 1st plane is located 30° from $\underline{X}^C$. Rotating $\underline{X}^O$ clockwise about $\underline{Z}^C$ with respect to $\underline{X}^C$ defines the yaw angle,

$$i = [1(1)6] \Rightarrow \eta_i := \frac{\pi}{6} \cdot (2 \cdot i - 1)$$

Equation 16.6-1

There follows a constant clockwise 55° rotation about the $\underline{X}^O$ that brings the $\underline{X}^O$ into the satellite orbital plane,

$$E_C^O(i) := (11 \cdot \pi / 36 \quad , \quad 0 \quad , \quad \eta_i)$$

Equation 16.6-2

The transforms from the Satellite Orbital frames to the Celestial frame (TROTOC) are obtained by substituting these Euler angles into Equation 16.1-4 and transposing the resulting direction cosine matrix,

$$T_O^C(i) := \begin{bmatrix} \cos\eta_i & , & -0.5736 \cdot \sin\eta_i & , & 0.8192 \cdot \sin\eta_i \\ \sin\eta_i & , & 0.5736 \cdot \cos\eta_i & , & -0.8192 \cdot \cos\eta_i \\ 0 & , & 0.8192 & , & 0.5736 \end{bmatrix}$$

Equation 16.6-3

The 3rd column of direction cosines in this equation is superfluous since by definition every satellite travels in one of the six satellite orbital planes. There are no position or velocity components along the $\underline{Z}^O$.

16.7 Celestial to Satellite LOS Transformations

The Euler triplet defining the transform from the Celestial to each of the Satellite LOS frames (TRCTOL) located at the missile receiver point (g),

$$\left(i := [1(1)6] \right) \wedge \left(j := [1(1)4] \right) \Rightarrow$$

$$E_C^L(i,j) := \left(0 \quad , \quad -\tan^{-1}\left(\frac{P_{g,s}^{ZC}(i,j)}{P_{g,s}^{hC}(i,j)} \right) \quad , \quad \tan^{-1}\left(\frac{P_{g,s}^{YC}(i,j)}{P_{g,s}^{XC}(i,j)} \right) \right)$$

Equation 16.7-1

Index (j) refers to a particular satellite in orbital plane (i). When the roll angle is zero the transformation matrix reduces to,

$$T_C^L := \begin{bmatrix} \cos\Theta_C^L \cos\Psi_C^L & , & \cos\Theta_C^L \sin\Psi_C^L & , & -\sin\Theta_C^L \\ -\sin\Psi_C^L & , & \cos\Psi_C^L & , & 0 \\ \sin\Theta_C^L \cos\Psi_C^L & , & \sin\Theta_C^L \sin\Psi_C^L & , & \cos\Theta_C^L \end{bmatrix}$$

Equation 16.7-2

16.8 Celestial to Earth Transformation

$\underline{Z}^E$ rotates clockwise about $\underline{Z}^C$ at 15.041°/hr. At midnight GMT the yaw angle between $\underline{X}^C$ and $\underline{X}^E$ is 30°. The Euler triplet defining the transform from Celestial to Earth axes in terms of the time after midnight (t_M),

$$E_C^E := \left(0 \quad , \quad 0 \quad , \quad \frac{\pi}{6} + \omega_{C,E}^{ZE} \cdot t_M \right)$$

Equation 16.8-1

The transform from the Celestial to Earth frame (TRCTOE) is obtained by substituting these Euler angles into Equation 16.1-4.

16.9 Earth to Alignment Transformation

The Earth and Alignment frames are fixed with respect to the Earth. The transform between the two is time invariant and defined by the Euler triplet,

$$E_E^A := \left(\frac{\pi}{2} - \lambda_{r,o} \quad , \quad 0 \quad , \quad \frac{\pi}{2} + \mu_{r,o} \right)$$

Equation 16.9-1

The geocentric longitude and latitude at point (o) are,

$$\left(\mu_{r,o} \quad , \quad \lambda_{r,o} \right) \coloneqq \left(\tan^{-1}\left(P_o^{YE} \,/\, P_o^{XE} \right) \quad , \quad \tan^{-1}\left(P_o^{ZE} \,/\, P_o^{hE} \right) \right)$$

Equation 16.9-2

The transform from the Earth to Alignment frame (TRETOA) is obtained by substituting the Euler angles into Equation 16.1-4. Introducing the functional form from LGA to direction cosines for this transform,

$$T_E^A \coloneqq \varphi_{LGA}^{DC}\left(\mu_{r,o} \quad , \quad \lambda_{r,o} \right)$$

Equation 16.9-3

$$T_E^A \coloneqq \begin{bmatrix} -\sin\mu_{r,o} & , & \cos\mu_{r,o} & , & 0 \\ -\sin\lambda_{r,o}\cdot\cos\mu_{r,o} & , & -\sin\lambda_{r,o}\cdot\sin\mu_{r,o} & , & \cos\lambda_{r,o} \\ \cos\lambda_{r,o}\cdot\cos\mu_{r,o} & , & \cos\lambda_{r,o}\cdot\sin\mu_{r,o} & , & \sin\lambda_{r,o} \end{bmatrix}$$

Equation 16.9-4

16.10 LGA to Earth Position Vector Transformation

The position of a point (p) with respect to Earth axes is determined from its geodetic orientation with respect to the Earth frame, and its altitude along the geodetic vertical through point (d),

$$\underline{P}_p^E \coloneqq \begin{pmatrix} \left(P_{r,d} + P_{d,p}^{ZG} \right)\cdot\cos\mu_p\cdot\cos\lambda_p \\ \left(P_{r,d} + P_{d,p}^{ZG} \right)\cdot\sin\mu_p\cdot\cos\lambda_p \\ \left(\left(1-e^2 \right)\cdot P_{r,d} + P_{d,p}^{ZG} \right)\cdot\sin\lambda_p \end{pmatrix}$$

Equation 16.10-1

The Earth's eccentricity (e) and the WGS84 values for the Earth's semi-major and semi-minor radii (R_A and R_B) are defined in §18.1.

16.11 Earth to LGA Transformation

A review of a number of "exact" and iterative techniques developed by Paul, Heikkinen, Barbee, Borkowski, and Zhu for the inverse transformation from ECEF to LGA axes is provided by Zhu[Z.4]. Although the most accurate of the non-iterative techniques for near-Earth studies is Heikkinen's method, Olsen's iterative algorithm taken from [0.7] has been selected and defined in §22.5.4.

Using a 64 bit computation to convert from LGA to ECEF co-ordinates, and converting back using Olsen's algorithm, results in errors of the order of:

Geodetic Longitude error

Less than 2.6×10^{-14} degrees in the range [-179.92°,179.92°], rising to 0.143° over and up to, but not including, 180°

Geodetic Latitude error

Less than 1.3×10^{-14} degrees in the range [-89.96°,89.96°], rising to 0.070° over and up to, but not including, 90°

Geodetic height error

Less than 4×10^{-9} metres in the range [-1,20] km

There is a singularity at the poles in the plane of the meridian through Greenwich, and another on the equatorial plane at 180° longitude. The Euler angles defining the orientation missile referenced LGA with respect to the ECEF frame expressed in terms of geodetic longitude and latitude are,

$$E_E^G := \left(\frac{\pi}{2} - \lambda_d \quad , \quad 0 \quad , \quad \frac{\pi}{2} + \mu_d \right)$$

Equation 16.11-1

The transform from the Earth frame to the LGA (TRETOG) is obtained by substituting these Euler angles into Equation 16.1-4,

$$T_E^G := \varphi_{LGA}^{DC} (\mu_d \quad , \quad \lambda_d)$$

Equation 16.11-2

The Euler triplet and the transform from ENU to NED LGA are,

$$E_{ENU}^{NED} = \left(\pi \quad , \quad 0 \quad , \quad \frac{\pi}{2} \right) \Rightarrow T_{ENU}^{NED} := \begin{bmatrix} 0 & , & 1 & , & 0 \\ 1 & , & 0 & , & 0 \\ 0 & , & 0 & , & -1 \end{bmatrix}$$

Equation 16.11-3

In NED axes pitching upwards is a positive quantity, and negative in ENU axes. Height is usually positive upwards when presented at a human interface that is inconsistent with NED axes.

16.12 Alignment to Missile Body Transformation

The transform from the Alignment frame to the Missile Body frame (TRATOB) is defined using a quaternion to avoid discontinuities as the missile pitch angle approaches 90°.

16.13 Alignment to Missile and Target LOS Transformations

The Euler triplet defining the orientation of the Missile LOS frame with respect to the Alignment frame,

$$E_A^M := \left(0 \;,\; -\tan^{-1}\left(P_m^{ZA} \,/\, P_m^{hA} \right) \;,\; \tan^{-1}\left(P_m^{YA} \,/\, P_m^{XA} \right) \right)$$

Equation 16.13-1

The transform from the Alignment to the Missile LOS frame (TRATOM) is obtained by substituting these Euler angles into Equation 16.1-4,

$$T_A^M := \begin{bmatrix} \cos\Theta_A^M \cdot \cos\Psi_A^M & , & \cos\Theta_A^M \cdot \sin\Psi_A^M & , & -\sin\Theta_A^M \\ -\sin\Psi_A^M & , & \cos\Psi_A^M & , & 0 \\ \sin\Theta_A^M \cdot \cos\Psi_A^M & , & \sin\Theta_A^M \cdot \sin\Psi_A^M & , & \cos\Theta_A^M \end{bmatrix}$$

Equation 16.13-2

In terms of Cartesian position with respect to the Alignment frame,

$$T_A^M := \begin{bmatrix} \dfrac{P_m^{XA}}{P_{o,m}} & , & \dfrac{P_m^{YA}}{P_{o,m}} & , & \dfrac{P_m^{ZA}}{P_{o,m}} \\ -\dfrac{P_{o,m}^{YA}}{P_m^{hA}} & , & \dfrac{P_{o,m}^{XA}}{P_m^{hA}} & , & 0 \\ -\dfrac{P_m^{XA} \cdot P_m^{ZA}}{P_m^{hA} \cdot P_{o,m}} & , & -\dfrac{P_m^{YA} \cdot P_m^{ZA}}{P_m^{hA} \cdot P_{o,m}} & , & \dfrac{P_m^{hA}}{P_{o,m}} \end{bmatrix}$$

Equation 16.13-3

The singularity when the elevation is ($\pm\pi$) must be accounted for. If the slant range is close to zero, a rare occurrence in this application,

$$P_u^C < 5 \;\Rightarrow\; T_A^M := I_3$$

Equation 16.13-4

Not so rare is a near-zero horizontal range for high diving targets,

$$\left(P_m^M > 5 \right) \wedge \left(P_m^{hM} < 5 \right) \Rightarrow T_A^M := \begin{pmatrix} 0 & , & 0 & , & 1 \\ 1 & , & 0 & , & 0 \\ 0 & , & 1 & , & 0 \end{pmatrix}$$

Equation 16.13-5

Introducing the functional form,

$$T_A^M := \varphi_{XYZ}^{DC}\left(\underline{P}_m^A , 5 \right)$$

Equation 16.13-6

The transform from the Alignment to Target LOS frame is (TRATOT),

$$T_A^T := \varphi_{XYZ}^{DC}\left(\underline{P}_t^A , 5 \right)$$

Equation 16.13-7

16.14 Alignment to Missile and Target Velocity Transformations

The Euler triplet defining the orientation of the Missile Velocity frame with respect to the Alignment frame,

$$E_A^{MV} = \left(0 , -\tan^{-1}\left(\dot{P}_m^{ZA} / \dot{P}_m^{hA} \right) , \tan^{-1}\left(\dot{P}_m^{YA} / \dot{P}_m^{XA} \right) \right)$$

Equation 16.14-1

The transform from the Alignment to Missile Velocity frame (TRATMV),

$$T_A^{MV} := \varphi_{XYZ}^{DC}\left(\underline{\dot{P}}_c^A , 5 \right)$$

Equation 16.14-2

The same equations can be used for the orientation of the Target Velocity frame with respect to the Alignment frame. The transform from the Alignment to Target LOS frame (TRATTV),

$$T_A^{TV} := \varphi_{XYZ}^{DC}\left(\underline{\dot{P}}_t^A , 5 \right)$$

Equation 16.14-3

Consider the YP Euler angle Jacobians associated with the Alignment to Missile Velocity frame transform, that apply in general,

$$\frac{\partial T_A^{MV}}{\partial \Theta_A^{MV}} := \begin{bmatrix} -T_A^{MV}(3) & , & -T_A^{MV}(6) & , & -T_A^{MV}(9) \\ 0 & , & 0 & , & 0 \\ -T_A^{MV}(1) & , & -T_A^{MV}(4) & , & -T_A^{MV}(7) \end{bmatrix}$$

Equation 16.14-4

$$\frac{\partial T_A^{MV}}{\partial \Psi_A^{MV}} := \begin{bmatrix} -T_A^{MV}(4) & , & -T_A^{MV}(1) & , & 0 \\ -T_A^{MV}(5) & , & -T_A^{MV}(2) & , & 0 \\ -T_A^{MV}(6) & , & -T_A^{MV}(3) & , & 0 \end{bmatrix}$$

Equation 16.14-5

16.15 Missile Body to Missile IMU Transformation

The IMU sensor outputs are pre-processed and referred to a common frame located at a reference point in the INU. The orientation of the Missile IMU frame with respect to the Missile Body frame is defined by the Euler triplet,

$$E_A^{AU} := \left(\Phi_A^{AU} , \Theta_A^{AU} , \Psi_A^{AU} \right)$$

Equation 16.15-1

The transform from the Missile Body to Missile IMU frame (TRBTMV) is obtained by substituting these Euler angles into Equation 16.1-4. In most applications the IMU and its sensors are aligned with Missile Body axes for convenience, in which case, the transform is the identity matrix. In practice, the IMU is skewed by a combination of sensor-to-case non-orthogonality and misalignment errors, and the case with respect to Missile Body axes.

16.16 Missile Body to Missile Velocity Transformation

The compound transform from the Missile Body to Missile Velocity frame,

$$T_B^{MV} := T_A^{MV} \cdot T_B^A$$

Equation 16.16-1

This Euler triplet is related to the missile incidence angles as follows,

$$E_B^{MV} := \left(0 , \Theta_B^{MV} , \Psi_B^{MV} \right)$$

Equation 16.16-2

The velocity of the missile along the Missile Body axes,

$$\underline{\dot{P}}^{B}_{o,m} \coloneqq T^{B}_{MV} \cdot \underline{\dot{P}}^{MV}_{o,m}$$

Equation 16.16-3

$$\underline{\dot{P}}^{B}_{o,m} \coloneqq \dot{P}_{o,m} \cdot \left(c\Theta^{MV}_{B} \cdot c\Psi^{MV}_{B} \quad , \quad c\Theta^{MV}_{B} \cdot s\Psi^{MV}_{B} \quad , \quad -s\Theta^{MV}_{B} \right)^{T}$$

Equation 16.16-4

The exact relationship between the two sets of angles being,

$$\begin{pmatrix} \alpha^{MV}_{B} \\ \beta^{MV}_{B} \\ \gamma^{MV}_{B} \end{pmatrix} \coloneqq \begin{pmatrix} -\tan^{-1}\left(\tan\Theta^{MV}_{B} \cdot \sec\Psi^{MV}_{B} \right) \\ \Psi^{MV}_{B} \\ -\tan^{-1}\left(\cot\Theta^{MV}_{B} \cdot \sin\Psi^{MV}_{B} \right) \end{pmatrix}$$

Equation 16.16-5

When the missile incidence is small,

$$\left(\alpha^{MV}_{B} \quad , \quad \beta^{MV}_{B} \quad , \quad \gamma^{MV}_{B} \right) \coloneqq \left(-\Theta^{MV}_{B} \quad , \quad \Psi^{MV}_{B} \quad , \quad -\Psi^{MV}_{B} \,/\, \Theta^{MV}_{B} \right)$$

Equation 16.16-6

In terms of the velocity along the Missile Body axes,

$$\left(\alpha^{MV}_{B} \quad , \quad \beta^{MV}_{B} \quad , \quad \gamma^{MV}_{B} \right) \coloneqq$$

$$\left(\tan^{-1}\left(\frac{\dot{P}^{ZB}_{o,m}}{\dot{P}^{XB}_{o,m}} \right) \quad , \quad \tan^{-1}\left(\frac{\dot{P}^{YB}_{o,m}}{\dot{P}^{XB}_{o,m}} \right) \quad , \quad \tan^{-1}\left(\frac{\dot{P}^{YB}_{o,m}}{\dot{P}^{ZB}_{o,m}} \right) \right)$$

Equation 16.16-7

The incidence variation with respect to missile velocity and the orientation of the Missile Body frame with respect to the Alignment frame,

$$\frac{\partial\Theta^{MV}_{B}}{\partial\underline{\dot{P}}^{A}_{o,m}} \coloneqq \left(\dot{P}^{vB}_{o,m} \right)^{-2} \cdot \left(\dot{P}^{ZB}_{o,m} \cdot \frac{\partial\dot{P}^{XB}_{o,m}}{\partial\underline{\dot{P}}^{A}_{o,m}} - \dot{P}^{XB}_{o,m} \cdot \frac{\partial\dot{P}^{ZB}_{o,m}}{\partial\underline{\dot{P}}^{A}_{o,m}} \right)$$

Equation 16.16-8

$$\frac{\partial\Theta^{MV}_{B}}{\partial Q^{B}_{A}} \coloneqq \left(\dot{P}^{vB}_{o,m} \right)^{-2} \cdot \left(\dot{P}^{ZB}_{o,m} \cdot \frac{\partial\dot{P}^{XB}_{o,m}}{\partial Q^{B}_{A}} - \dot{P}^{XB}_{o,m} \cdot \frac{\partial\dot{P}^{ZB}_{o,m}}{\partial Q^{B}_{A}} \right)$$

Equation 16.16-9

$$\frac{\partial \Psi_B^{MV}}{\partial \underline{\dot{P}}_{o,m}^{A}} := \left(\dot{P}_{o,m}^{hB} \right)^{-2} \cdot \left(\dot{P}_{o,m}^{XB} \cdot \frac{\partial \dot{P}_{o,m}^{YB}}{\partial \underline{\dot{P}}_{o,m}^{A}} - \dot{P}_{o,m}^{ZB} \cdot \frac{\partial \dot{P}_{o,m}^{XB}}{\partial \underline{\dot{P}}_{o,m}^{A}} \right)$$

Equation 16.16-10

$$\frac{\partial \Theta_B^{MV}}{\partial Q_A^B} := \left(\dot{P}_{o,m}^{hB} \right)^{-2} \cdot \left(\dot{P}_{o,m}^{XB} \cdot \frac{\partial \dot{P}_{o,m}^{YB}}{\partial Q_A^B} - \dot{P}_{o,m}^{ZB} \cdot \frac{\partial \dot{P}_{o,m}^{XB}}{\partial Q_A^B} \right)$$

Equation 16.16-11

The variation in velocity in Missile Body axes with respect to velocity in the Alignment frame,

$$\partial \underline{\dot{P}}_{o,m}^{B} \Big/ \partial \underline{\dot{P}}_{o,m}^{A} := T_A^B$$

Equation 16.16-12

The variation in velocity in Missile Body axes with respect to the Alignment frame orientation,

$$\frac{\partial \dot{P}_{o,m}^{XB}}{\partial Q_A^B} := \left(2 \cdot \begin{pmatrix} q_0 & , & q_3 & , & -q_2 \\ q_1 & , & q_2 & , & q_3 \\ -q_2 & , & q_1 & , & -q_0 \\ -q_3 & , & q_0 & , & q_1 \end{pmatrix} \cdot \underline{\dot{P}}_{o,m}^{A} \right)^T$$

Equation 16.16-13

$$\frac{\partial \dot{P}_{o,m}^{YB}}{\partial Q_A^B} := \left(2 \cdot \begin{pmatrix} -q_3 & , & q_0 & , & q_1 \\ q_2 & , & -q_1 & , & q_0 \\ q_1 & , & q_2 & , & q_3 \\ -q_0 & , & -q_3 & , & q_2 \end{pmatrix} \cdot \underline{\dot{P}}_{o,m}^{A} \right)^T$$

Equation 16.16-14

$$\frac{\partial \dot{P}^{ZB}_{o,m}}{\partial Q^{B}_{A}} := \left(2 \cdot \begin{pmatrix} q_2 & , & -q_1 & , & q_0 \\ q_3 & , & -q_0 & , & q_1 \\ q_0 & , & q_3 & , & -q_2 \\ q_1 & , & q_2 & , & -q_3 \end{pmatrix} \cdot \underline{\dot{P}}^{A}_{o,m} \right)^{T}$$

Equation 16.16-15

The missile incidence is the absolute angle between $\underline{X}^{B}$ and $\underline{X}^{MV}$ axes,

$$\xi^{MV}_{B} := \cos^{-1}\left(\frac{\dot{P}^{XB}_{o,m}}{\dot{P}_{o,m}} \right) \equiv \tan^{-1}\left(\cos \alpha^{MV}_{B} \cdot \tan \beta^{MV}_{B} \right)$$

Equation 16.16-16

The variation in incidence with velocity and Alignment frame orientation,

$$\frac{\partial \xi^{MV}_{B}}{\partial \underline{\dot{P}}^{A}_{o,m}} := \frac{\dot{P}^{XB}_{o,m} \cdot \underline{\dot{P}}^{A}_{o,m} - \dot{P}^{2}_{o,m} \cdot \left(T^{B}_{A}(1) \quad , \quad T^{B}_{A}(4) \quad , \quad T^{B}_{A}(7) \right)^{T}}{\dot{P}^{2}_{o,m} \cdot \sqrt{\dot{P}^{2}_{o,m} - \left(\dot{P}^{XB}_{o,m} \right)^{2}}}$$

Equation 16.16-17

$$\frac{\partial \xi^{MV}_{B}}{\partial Q^{B}_{A}} := \frac{2}{\sqrt{\dot{P}^{2}_{o,m} - \left(\dot{P}^{XB}_{o,m} \right)^{2}}} \cdot \begin{pmatrix} q_2 \cdot \dot{P}^{ZA}_{o,m} - q_3 \cdot \dot{P}^{YA}_{o,m} \\ q_3 \cdot \dot{P}^{ZA}_{o,m} - q_2 \cdot \dot{P}^{YA}_{o,m} \\ 2 \cdot q_2 \cdot \dot{P}^{XA}_{o,m} - q_1 \cdot \dot{P}^{YA}_{o,m} + q_0 \cdot \dot{P}^{ZA}_{o,m} \\ 2 \cdot q_3 \cdot \dot{P}^{XA}_{o,m} - q_0 \cdot \dot{P}^{YA}_{o,m} - q_1 \cdot \dot{P}^{ZA}_{o,m} \end{pmatrix}$$

Equation 16.16-18

16.17 Alignment to Seeker LOS Transformation

The Euler triplet defining the orientation of the Seeker LOS frame with respect to the Missile Body frame,

$$E^{S}_{A} := \left(\pi \quad , \quad -\tan^{-1}\left(\frac{P^{ZA}_{m,t}}{P^{hA}_{m,t}} \right) \quad , \quad \tan^{-1}\left(\frac{P^{YA}_{m,t}}{P^{XA}_{m,t}} \right) \right)$$

Equation 16.17-1

$$\underline{P}^{A}_{m,t} := \underline{P}^{A}_{t} - \underline{P}^{A}_{m}$$

Equation 16.17-2

The transform from the Alignment to Seeker LOS frame (TRATOS) is obtained by substituting these Euler angles into Equation 16.1-4 and expanding the trigonometric functions with respect to this position vector as is done in Equation 16.13-3.

16.18 Missile Body to Seeker Head Transformation

When the Seeker Head frame is rotates with respect to Missile Body axes using an inner pitch and an outer roll gimbal, ignoring missile body flexure,

$$E^{H}_{B} := \left(\Phi^{H}_{B} \;,\; \Theta^{H}_{B} \;,\; 0 \right)$$

Equation 16.18-1

The transform from Seeker Head to Missile Body frame (TRBTOH) is obtained by substituting these Euler angles into Equation 16.1-4,

$$T^{H}_{B} := \begin{bmatrix} \cos\Theta^{H}_{B} & \sin\Phi^{H}_{B}\cdot\sin\Theta^{H}_{B} & -\cos\Phi^{H}_{B}\cdot\sin\Theta^{H}_{B} \\ 0 & \cos\Phi^{H}_{B} & \sin\Phi^{H}_{B} \\ \sin\Theta^{H}_{B} & -\sin\Phi^{H}_{B}\cdot\cos\Theta^{H}_{B} & \cos\Phi^{H}_{B}\cdot\cos\Theta^{H}_{B} \end{bmatrix}$$

Equation 16.18-2

For seekers with inner pitch and outer yaw gimbals the orientation of the Seeker Head frame with respect to the Missile Body frame,

$$E^{H}_{B} := \left(0 \;,\; \Theta^{H}_{B} \;,\; \Psi^{H}_{B} \right)$$

Equation 16.18-3

The transformation matrix from the Seeker Head to Missile Body frame,

$$T^{H}_{B} := \begin{bmatrix} \cos\Theta^{H}_{B}\cdot\cos\Psi^{H}_{B} & \cos\Theta^{H}_{B}\cdot\sin\Psi^{H}_{B} & -\sin\Theta^{H}_{B} \\ -\sin\Psi^{H}_{B} & \cos\Psi^{H}_{S} & 0 \\ \sin\Theta^{H}_{B}\cdot\cos\Psi^{H}_{B} & \sin\Theta^{H}_{B}\cdot\sin\Psi^{H}_{B} & \cos\Theta^{H}_{B} \end{bmatrix}$$

Equation 16.18-4

16.19 LGA to Alignment Transformation

The compound transform from LGA to the Alignment frame,

$$T_G^A := T_E^A \cdot T_G^E$$

Equation 16.19-1

The orientation of the Alignment frame with respect to LGA at the missile position (d) at time (t := 0), is defined by a roll rotation about $\underline{X}^G$ which lies in the range [0 , 0.19325] degrees,

$$E_G^A(0) := \left(\left(\frac{R_A - R_B}{R_A} \right) \cdot \sin(2 \cdot \lambda_d) \quad , \quad 0 \quad , \quad 0 \right)$$

Equation 16.19-2

The transform from the Alignment to missile LGA at this time (TRGTOA) is given by substituting these Euler angles into Equation 16.1-4.

APPENDIX D

17 POINT MASS DYNAMICS

Appendices A to C provide a framework for defining the position of points, and the transformation of the forces and moments acting on them, that produce changes in their linear and angular velocity, acceleration and jerk. Some commonly used dynamical relationships are revisited and expressed in terms of the globally applied nomenclature. The approach is purposely generic since these dynamics occur in many aspects of the work concerning the absolute motion of the launcher, missile and target, and the relative motion between each. The presentation of the relationships using the global nomenclature provides insight to the terms that appear when developing conventional missile guidance laws, and when using trajectory optimisation.

To avoid confusion with specific frames and vectors, two general axis systems "I" and "R" are used. "I" represents a stationary reference frame located at point (a) and "R" a general set of rotating axes located at a different point (b) as shown in Figure 17-1.

The relationship between Euler triplets and body rates is explored first, followed by transformation matrix time derivatives, and the extraction of average angular rates from the evolution of direction cosines. These relationships are key when deriving the velocity, acceleration and jerk of a point, and their reduced forms when the Euler roll angle is ignored.

17.1 Transformation from Angular to Euler Rates

The transform from Euler to angular rates is given by the vector sum of the angular velocity components about the intermediate Euler axes.

$$\underline{\omega}_{I,R}^{R} := \begin{pmatrix} -\sin\Theta_I^R \\ \sin\Phi_I^R \cdot \cos\Theta_I^R \\ \cos\Phi_I^R \cdot \cos\Theta_I^R \end{pmatrix} \cdot \dot{\Psi}_I^R + \begin{pmatrix} 0 \\ \cos\Phi_I^R \\ -\sin\Phi_I^R \end{pmatrix} \cdot \dot{\Theta}_I^R + \begin{pmatrix} 1 \\ 0 \\ 0 \end{pmatrix} \cdot \dot{\Phi}_I^R$$

Equation 17.1-1

$$\underline{\omega}_{I,R}^{R} := \begin{pmatrix} 1 & , & 0 & , & -\sin\Theta_I^R \\ 0 & , & \cos\Phi_I^R & , & \sin\Phi_I^R \cdot \cos\Theta_I^R \\ 0 & , & -\sin\Phi_I^R & , & \cos\Phi_I^R \cdot \cos\Theta_I^R \end{pmatrix} \cdot \dot{E}_I^R$$

Equation 17.1-2

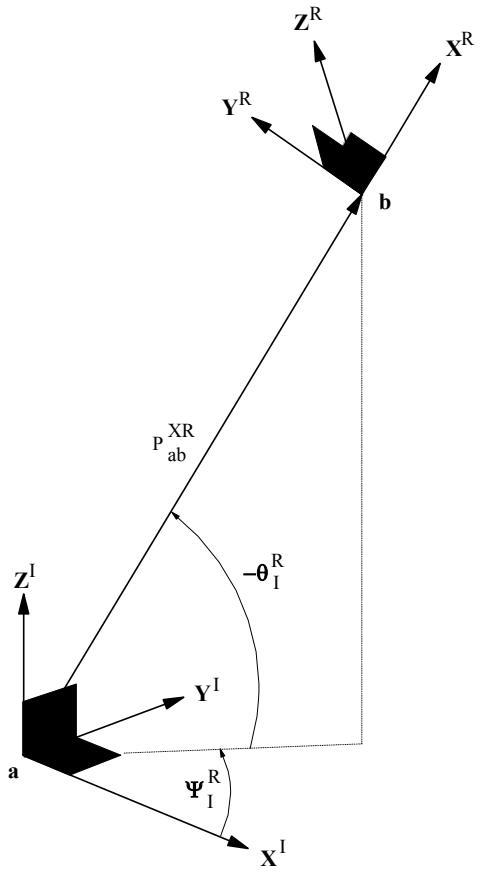

Figure 17-1 : Inertial and Rotating Frames of Reference

17.2 Transformation Time Derivatives

Consider the transform from frame (I) to frame (R) at time (t), and again (Δt) seconds later,

$$T_I^R(t+\Delta t) \coloneqq T_I^R(t, t+\Delta t) \cdot T_I^R(t)$$

Equation 17.2-1

If the rotation of frame (R) during the time (Δt) is small,

$$T_I^R(t+\Delta t) \coloneqq \left(I_3 - \left[\Delta E_{R(t)}^{R(t+\Delta t)} \times\right]\right) \cdot T_I^R(t)$$

Equation 17.2-2

Replacing the Euler angle triplet with average body rate over Δt,

$$\frac{T_I^R(t+\Delta t) - T_I^R(t)}{\Delta t} \coloneqq -\left[\underline{\omega}_{I,R}^R \times\right] \cdot T_I^R(t)$$

Equation 17.2-3

As Δt tends to zero, the transformation matrix derivative at time (t),

$$\dot{T}_I^R \coloneqq -\left[\underline{\omega}_{I,R}^R \times\right] \cdot T_I^R$$

Equation 17.2-4

Consider a 2nd rotating frame (C), and using the same process,

$$\dot{T}_C^I \coloneqq T_C^I \cdot \left[\underline{\omega}_{I,C}^C \times\right]$$

Equation 17.2-5

The time rate of change of the transform between the two rotating frames,

$$T_C^R \coloneqq T_I^R \cdot T_C^I$$

Equation 17.2-6

$$\dot{T}_C^R \coloneqq \dot{T}_I^R \cdot T_C^I + T_I^R \cdot \dot{T}_C^I$$

Equation 17.2-7

$$\dot{T}_C^R \coloneqq -\left[\omega_{I,R}^R \times\right] \cdot T_I^R \cdot T_C^I + T_I^R \cdot T_C^I \cdot \left[\omega_{I,C}^C \times\right]$$

Equation 17.2-8

$$\dot{T}_C^R \;:=\; -\left[\,\omega_{I,R}^R\times\right]\cdot T_C^R + T_C^R\cdot\left[\,\omega_{I,C}^C\times\right]$$

Equation 17.2-9

$$\dot{T}_C^R \;:=\; -\left[\,\omega_{R,C}^R\times\right]\cdot T_C^R \;:=\; T_C^R\cdot\left[\,\omega_{R,C}^R\times\right]$$

Equation 17.2-10

Using additional rotating frames (D) and (E), other useful results, verifiable by matrix element expansion, are,

$$T_R^C\cdot\left[\,\omega_{C,R}^R\times\right] \;:=\; T_R^C\cdot\left[\,\underline{\omega}_{C,R}^R\times\right]\cdot T_C^R$$

Equation 17.2-11

$$\left[\,\omega_{C,D}^R\times\right] \;:=\; \left[\,\omega_{C,R}^R\times\right] + \left[\,\omega_{R,D}^R\times\right]$$

Equation 17.2-12

$$-\left[\,\omega_{C,R}^R\times\right]^3 \;:=\; \omega_{C,R}^2\cdot\left[\,\omega_{C,R}^R\times\right]$$

Equation 17.2-13

$$-\left[\,\omega_{C,R}^R\times\right]^T \;:=\; \left[\,\omega_{C,R}^R\times\right]$$

Equation 17.2-14

$$\left[\,\omega_{C,R}^R\times\right]\cdot\left[\,\omega_{D,E}^R\times\right] \;:=\; \left(\left[\,\omega_{D,E}^R\times\right]\cdot\left[\,\omega_{C,R}^R\times\right]\right)^T$$

Equation 17.2-15

17.3 Average Angular Rates From Direction Cosines

The average angular rate of frame (R) with respect to a frame (I), over a time interval (Δt), is derived from the direction cosines between them at time (t) and ($t+\Delta t$).

$$\dot{T}_I^R \;:=\; -\left[\,\underline{\omega}_{I,R}^R\times\right]\cdot T_I^R$$

Equation 17.3-1

The transform at time ($t+\Delta t$) is obtained from,

$$T_I^R\left(t+\Delta t\right) \;:=\; \exp\left(-\left[\,\underline{\omega}_{I,R}^R\times\right]\cdot\Delta t\right)\cdot T_I^R\left(t\right)$$

Equation 17.3-2

Expanding the exponential function as an infinite series,

$$T_I^R\left(t+\Delta t\right)\cdot T_R^I\left(t\right) \;:=\; I_3 + \sum_{n:=1}^{\infty}\left(\frac{1}{n!}\cdot\left(-\left[\,\underline{\omega}_{I,R}^R\times\,\right]\right)^n\cdot\Delta t^{\,n}\right)$$

Equation 17.3-3

Collecting even and odd powers, and expressing them as power series expansions of sine and cosine functions,

$$T_I^R\left(t+\Delta t\right)\cdot T_R^I\left(t\right) :=$$

$$I_3 - \omega_{I,R}^{-1}\cdot\left[\,\underline{\omega}_{I,R}^R\times\,\right]\cdot\sin\left(\omega_{I,R}\cdot\Delta t\right) + \omega_{I,R}^{-2}\cdot\left[\,\underline{\omega}_{I,R}^R\times\,\right]^2\cdot\left(1-\cos\left(\omega_{I,R}\cdot\Delta t\right)\right)$$

Equation 17.3-4

Expanding and equating the appropriate direction cosines,

$$T_I^R\left(t+\Delta t\right)\cdot T_R^I\left(t\right) - T_I^R\left(t\right)\cdot T_R^I\left(t+\Delta t\right) :=$$

$$-2\cdot\omega_{I,R}^{-1}\left[\,\underline{\omega}_{I,R}^R\times\,\right]\cdot\sin\left(\omega_{I,R}\cdot\Delta t\right)$$

Equation 17.3-5

The average angular rate of the rotating frame with respect to the reference axes over the time interval (Δt) is therefore,

$$\overline{\underline{\omega}}_{I,R}^R \;:=\; \frac{\underline{\Lambda}_I^R\cdot\sin^{-1}\left(\Lambda_I^R\right)}{\Lambda_I^R\cdot\Delta t}$$

Equation 17.3-6

$$2\cdot\underline{\Lambda}_I^R \;:=$$

$$\left(\Delta T_I^R\left(6\right)-T_R^I\left(8\right)\;,\;\Delta T_I^R\left(7\right)-T_R^I\left(3\right)\;,\;\Delta T_I^R\left(2\right)-T_R^I\left(4\right)\right)^T$$

Equation 17.3-7

17.4 Inertial Velocity Vector

The inertial velocity of point (b) with respect to point (a) is,

$$\underline{V}_b^I \;:=\; \dot{T}_R^I\cdot\underline{P}_{a,b}^R + T_R^I\cdot\dot{\underline{P}}_{a,b}^R$$

Equation 17.4-1

Substituting for the transformation matrix derivatives,

$$\underline{V}_b^I \coloneqq T_R^I \cdot \left(\underline{\dot{P}}_{a,b}^R + \underline{\omega}_{I,R}^R \times \underline{P}_{a,b}^R \right)$$

Equation 17.4-2

Expressing the absolute velocity in terms of its components with respect to the rotating frame,

$$\underline{V}_{a,b}^R \coloneqq \underline{\dot{P}}_{a,b}^R + \underline{\omega}_{I,R}^R \times \underline{P}_{a,b}^R$$

Equation 17.4-3

The individual velocity components in the rotating frame (R) are,

$$V_{a,b}^{XR} \coloneqq \dot{P}_{a,b}^{XR} + \omega_{I,R}^{YR} \cdot P_{a,b}^{ZR} - \omega_{I,R}^{ZR} \cdot P_{a,b}^{YR}$$

Equation 17.4-4

$$V_{a,b}^{YR} \coloneqq \dot{P}_{a,b}^{YR} + \omega_{I,R}^{ZR} \cdot P_{a,b}^{XR} - \omega_{I,R}^{XR} \cdot P_{a,b}^{ZR}$$

Equation 17.4-5

$$V_{a,b}^{ZR} \coloneqq \dot{P}_{a,b}^{ZR} + \omega_{I,R}^{XR} \cdot P_{a,b}^{YR} - \omega_{I,R}^{YR} \cdot P_{a,b}^{XR}$$

Equation 17.4-6

Replacing the body rates with the time rate of change of the Euler angles,

$$V_{a,b}^{XR} \coloneqq$$

$$\dot{P}_{a,b}^{XR} + \dot{\Psi}_I^R \cdot \left(P_{a,b}^{ZR} \cdot s\Phi_I^R - P_{a,b}^{YR} \cdot c\Phi_I^R \right) \cdot c\Theta_I^R + \dot{\Theta}_I^R \cdot \left(P_{a,b}^{YR} \cdot s\Phi_I^R + P_{a,b}^{ZR} \cdot c\Phi_I^R \right)$$

Equation 17.4-7

$$V_{a,b}^{YR} \coloneqq$$

$$\dot{P}_{a,b}^{YR} + \dot{\Psi}_I^R \cdot \left(P_{a,b}^{XR} \cdot c\Phi_I^R \cdot c\Theta_I^R + P_{a,b}^{ZR} \cdot s\Theta_I^R \right) - \dot{\Theta}_I^R \cdot P_{a,b}^{XR} \cdot s\Phi_I^R + \dot{\Phi}_I^R \cdot P_{a,b}^{ZR}$$

Equation 17.4-8

$$V_{a,b}^{ZR} \coloneqq$$

$$\dot{P}_{a,b}^{ZR} + \dot{\Psi}_I^R \cdot \left(P_{a,b}^{YR} \cdot s\Theta_I^R - P_{a,b}^{XR} \cdot s\Phi_I^R \cdot c\Theta_I^R \right) - \dot{\Theta}_I^R \cdot P_{a,b}^{XR} \cdot c\Phi_I^R + \dot{\Phi}_I^R \cdot P_{a,b}^{YR}$$

Equation 17.4-9

Setting the Euler roll angle to zero gives,

$$V_{a,b}^{XR} := \dot{P}_{a,b}^{XR} - \Psi_I^R \cdot P_{a,b}^{YR} \cdot \cos\Theta_I^R + \dot{\Theta}_I^R \cdot P_{a,b}^{ZR}$$

Equation 17.4-10

$$V_{a,b}^{YR} := \dot{P}_{a,b}^{YR} + \dot{\Psi}_I^R \cdot \left(P_{a,b}^{XR} \cdot \cos\Theta_I^R + P_{a,b}^{ZR} \cdot \sin\Theta_I^R \right)$$

Equation 17.4-11

$$V_{a,b}^{ZR} := \dot{P}_{a,b}^{ZR} + \dot{\Psi}_I^R \cdot P_{a,b}^{YR} \cdot \sin\Theta_I^R - \dot{\Theta}_I^R \cdot P_{a,b}^{XR}$$

Equation 17.4-12

When point (b) is forced to lie on $\underline{X}^R$ its velocity with respect to point (a),

$$\underline{V}_{a,b}^R := \left(\dot{P}_{a,b}^{XR} \quad \dot{\Psi}_I^R \cdot P_{a,b} \cdot \cos\Theta_I^R \quad -\dot{\Theta}_I^R \cdot P_{a,b} \right)^T$$

Equation 17.4-13

17.5 Inertial Acceleration Vector

Differentiating inertial velocity to obtain inertial acceleration of point (b) with respect to point (a),

$$\underline{A}_{a,b}^I := \dot{T}_R^I \cdot \left(\underline{\dot{P}}_{a,b}^R + \underline{\omega}_{I,R}^R \times \underline{P}_{a,b}^R \right) + T_R^I \cdot \left(\underline{\ddot{P}}_{a,b}^R + \underline{\dot{\omega}}_{I,R}^R \times \underline{P}_{a,b}^R + \omega_{I,R}^R \times \underline{\dot{P}}_{a,b}^R \right)$$

Equation 17.5-1

Substituting for the transformation matrix derivatives,

$$\underline{A}_{a,b}^R := \underline{\ddot{P}}_{a,b}^R + 2 \cdot \underline{\omega}_{I,R}^R \times \underline{\dot{P}}_{a,b}^R + \underline{\dot{\omega}}_{I,R}^R \times \underline{P}_{a,b}^R + \underline{\omega}_{I,R}^R \times \underline{\omega}_{I,R}^R \times \underline{P}_{a,b}^R$$

Equation 17.5-2

The acceleration in frame (R) expressed in terms of the angular body rates,

$$A_{a,b}^{XR} := \ddot{P}_{a,b}^{XR} + 2 \cdot \left(\omega_{I,R}^{YR} \cdot \dot{P}_{a,b}^{ZR} - \omega_{I,R}^{ZR} \cdot \dot{P}_{a,b}^{YR} \right) + \varphi_{PX} \left(\underline{P}_{a,b}^R \right)$$

Equation 17.5-3

$$\varphi_{PX} :=$$

$$-\left(\omega_{IR}^{rR} \right)^2 \cdot P_{ab}^{XR} + \left(\omega_{IR}^{XR} \cdot \omega_{IR}^{YR} - \dot{\omega}_{IR}^{ZR} \right) \cdot P_{ab}^{YR} + \left(\omega_{IR}^{XR} \cdot \omega_{IR}^{YR} + \dot{\omega}_{IR}^{ZR} \right) \cdot P_{ab}^{ZR}$$

Equation 17.5-4

$$A_{a,b}^{YR} \coloneqq \ddot{P}_{a,b}^{YR} + 2 \cdot \left(\omega_{I,R}^{ZR} \cdot \dot{P}_{,b}^{XR} - \omega_{I,R}^{XR} \cdot \dot{P}_{a,b}^{ZR} \right) + \varphi_{PY} \left(\underline{P}_{a,b}^{R} \right)$$

Equation 17.5-5

$$\varphi_{PY} \coloneqq$$

$$\left(\omega_{I,R}^{XR} \cdot \omega_{I,R}^{YR} + \dot{\omega}_{I,R}^{ZR} \right) \cdot P_{a,b}^{XR} - \left(\omega_{I,R}^{vR} \right)^2 \cdot P_{a,b}^{YR} + \left(\omega_{I,R}^{YR} \cdot \omega_{I,R}^{ZR} - \dot{\omega}_{I,R}^{XR} \right) \cdot P_{a,b}^{ZR}$$

Equation 17.5-6

$$A_{a,b}^{ZR} \coloneqq \ddot{P}_{a,b}^{ZR} + 2 \cdot \left(\omega_{I,R}^{XR} \cdot \dot{P}_{a,b}^{Y} - \omega_{I,R}^{YR} \cdot \dot{P}_{a,b}^{X} \right) + \varphi_{PZ} \left(\underline{P}_{a,b}^{R} \right)$$

Equation 17.5-7

$$\varphi_{PZ} \coloneqq$$

$$\left(\omega_{I,R}^{XR} \cdot \omega_{I,R}^{ZR} - \dot{\omega}_{I,R}^{YR} \right) \cdot P_{a,b}^{XR} + \left(\omega_{I,R}^{YR} \cdot \omega_{I,R}^{ZR} + \dot{\omega}_{I,R}^{XR} \right) \cdot P_{a,b}^{YR} - \left(\omega_{I,R}^{hR} \right)^2 \cdot P_{a,b}^{ZR}$$

Equation 17.5-8

Replacing the body rates with Euler rates with a zero Euler roll angle,

$$A_{a,b}^{XR} \coloneqq$$

$$\ddot{P}_{a,b}^{XR} - 2 \cdot \left(\dot{P}_{a,b}^{YR} \cdot \dot{\Psi}_{I}^{R} \cdot c\Theta_{I}^{R} - \dot{P}_{a,b}^{ZR} \cdot \dot{\Theta}_{I}^{R} \right) + \varphi_{XX} \left(\underline{P}_{a,b}^{R} \right) + \varphi_{XYZ} \left(\underline{P}_{a,b}^{R} \right)$$

Equation 17.5-9

$$\varphi_{XX} \coloneqq -P_{a,b}^{XR} \cdot \left(\dot{\Psi}_{I}^{R} \right)^2 \cdot \cos^2 \Theta_{I}^{R} - P_{a,b}^{XR} \cdot \left(\dot{\Theta}_{I}^{R} \right)^2$$

Equation 17.5-10

$$\varphi_{XYZ} \coloneqq -P_{a,b}^{YR} \cdot \ddot{\Psi}_{I}^{R} \cdot \cos\Theta_{I}^{R} + P_{a,b}^{ZR} \cdot \left(\ddot{\Theta}_{I}^{R} - \left(\dot{\Psi}_{I}^{R} \right)^2 \cdot \sin\Theta_{I}^{R} \cdot \cos\Theta_{I}^{R} \right)$$

Equation 17.5-11

$$A_{a,b}^{YR} \coloneqq$$

$$\ddot{P}_{a,b}^{YR} + 2 \cdot \dot{\Psi}_{I}^{R} \cdot \left(\dot{P}_{a,b}^{XR} c\Theta_{I}^{R} + \dot{P}_{a,b}^{ZR} \cdot s\Theta_{I}^{R} \right) + \varphi_{YX} \left(\underline{P}_{a,b}^{R} \right) + \varphi_{YYZ} \left(\underline{P}_{a,b}^{R} \right)$$

Equation 17.5-12

$$\varphi_{YX} \coloneqq P_{a,b}^{XR} \cdot \left(\ddot{\Psi}_{I}^{R} \cdot \cos\Theta_{I}^{R} - 2 \cdot \dot{\Theta}_{I}^{R} \cdot \dot{\Psi}_{I}^{R} \cdot \sin\Theta_{I}^{R} \right)$$

Equation 17.5-13

$$\varphi_{YYZ} := -P_{a,b}^{YR} \cdot \left(\dot{\Psi}_I^R \right)^2 + P_{a,b}^{ZR} \cdot \left(\ddot{\Psi}_I^R + 2 \cdot \dot{\Psi}_I^R \cdot \dot{\Theta}_I^R \cdot \cos\Theta_I^R \right)$$

Equation 17.5-14

$$A_{a,b}^{ZR} :=$$

$$\ddot{P}_{a,b}^{ZR} - 2 \cdot \left(\dot{P}_{a,b}^{YR} \cdot \dot{\Psi}_I^R \cdot s\Theta_I^R + \dot{P}_{a,b}^{XR} \cdot \dot{\Theta}_I^R \right) + \varphi_{ZX} \left(\underline{P}_{a,b}^R \right) + \varphi_{ZYZ} \left(\underline{P}_{a,b}^R \right)$$

Equation 17.5-15

$$\varphi_{ZX} := -P_{a,b}^{XR} \cdot \left(\dot{\Psi}_I^R \right)^2 \cdot \sin\Theta_I^R \cdot \cos\Theta_I^R - P_{a,b}^{XR} \cdot \ddot{\Theta}_I^R$$

Equation 17.5-16

$$\varphi_{ZYZ} := -P_{a,b}^{YR} \cdot \ddot{\Psi}_I^R \cdot \sin\Theta_I^R - P_{a,b}^{ZR} \cdot \left(\dot{\Theta}_I^R \right)^2 - P_{a,b}^{ZR} \cdot \left(\dot{\Psi}_I^R \right)^2 \cdot \sin^2 \Theta_I^R$$

Equation 17.5-17

When point (b) lies on $\underline{X}^R$ its acceleration with respect to point (a),

$$A_{a,b}^{XR} := \ddot{P}_{a,b}^{XR} - P_{a,b}^{XR} \cdot \left(\dot{\Psi}_I^R \right)^2 \cdot \cos^2 \Theta_I^R + P_{a,b}^{XR} \cdot \left(\dot{\Theta}_I^R \right)^2$$

Equation 17.5-18

$$A_{a,b}^{YR} := \left(2 \cdot \dot{\Psi}_I^R \cdot \dot{P}_{a,b}^{XR} + P_{a,b}^{XR} \cdot \ddot{\Psi}_I^R \right) \cdot \cos\Theta_I^R - 2 \cdot P_{a,b}^{XR} \cdot \dot{\Theta}_I^R \cdot \dot{\Psi}_I^R \cdot \sin\Theta_I^R$$

Equation 17.5-19

$$A_{a,b}^{ZR} := -2 \cdot \dot{P}_{a,b}^{XR} \cdot \dot{\Theta}_I^R - P_{a,b}^{XR} \cdot \left(\dot{\Psi}_I^R \right)^2 \cdot \sin\Theta_I^R \cdot \cos\Theta_I^R - P_{a,b}^{XR} \cdot \ddot{\Theta}_I^R$$

17.6 Inertial Rate of Change of Acceleration Vector

Differentiating inertial acceleration gives inertial jerk of point (b) with respect to point (a) expressed in frame (R),

$$\underline{J}_{a,b}^R := \dddot{\underline{P}}_{a,b}^R + 3 \cdot \underline{\omega}_{I,R}^R \times \ddot{\underline{P}}_{a,b}^R + 3 \cdot \left(\left[\underline{\omega}_{I,R}^R \times \right]^2 + \left[\dot{\underline{\omega}}_{I,R}^R \times \right] \right) \cdot \dot{\underline{P}}_{a,b}^R + \varphi_J \cdot \underline{P}_{a,b}^R$$

Equation 17.6-1

$$\varphi_J :=$$

$$\left[\ddot{\underline{\omega}}_{I,R}^R \times \right] + 2 \cdot \left(\left[\underline{\omega}_{I,R}^R \times \right] \cdot \left[\dot{\underline{\omega}}_{I,R}^R \times \right] + \left[\dot{\underline{\omega}}_{I,R}^R \times \right] \cdot \left[\underline{\omega}_{I,R}^R \times \right] \right) + \left[\underline{\omega}_{I,R}^R \times \right]^3$$

Equation 17.6-2

Replacing the body rates with Euler rates with a zero Euler roll angle,

$$J_{a,b}^{XR} := \ddot{P}_{a,b}^{XR} - 3 \cdot \dot{P}_{a,b}^{XR} \cdot \left(\left(\dot{\Psi}_I^R \right)^2 \cdot \cos^2 \Theta_I^R + \left(\dot{\Theta}_I^R \right)^2 \right) + 3 \cdot P_{a,b}^{XR} \cdot \varphi_{JX}$$

Equation 17.6-3

$$\varphi_{JX} := -\dot{\Psi}_I^R \cdot \left(\ddot{\Psi}_I^R \cdot \cos\Theta_I^R - \dot{\Theta}_I^R \cdot \dot{\Psi}_I^R \cdot \sin\Theta_I^R \right) \cdot \cos\Theta_I^R + \ddot{\Theta}_I^R \cdot \dot{\Theta}_I^R$$

Equation 17.6-4

$$J_{a,b}^{YR} :=$$

$$3 \cdot \ddot{P}_{a,b}^{XR} \cdot \dot{\Psi}_I^R \cdot c\Theta_I^R + 3 \cdot \dot{P}_{a,b}^{XR} \cdot \left(\Psi_I^R \cdot c\Theta_I^R - 2 \cdot \dot{\Theta}_I^R \cdot \dot{\Psi}_I^R \cdot s\Theta_I^R \right) + P_{a,b}^{XR} \cdot \varphi_{JY}$$

Equation 17.6-5

$$\varphi_{JY} :=$$

$$\ddot{\Psi}_I^R - 3 \cdot \left(\dot{\Theta}_I^R \right)^2 \cdot \dot{\Psi}_I^R - \left(\dot{\Psi}_I^R \right)^3 \cdot c\Theta_I^R + 3 \cdot \left(\ddot{\Psi}_I^R \cdot \dot{\Theta}_I^R + \dot{\Psi}_I^R \cdot \ddot{\Theta}_I^R \right) \cdot s\Theta_I^R$$

Equation 17.6-6

$$J_{a,b}^{ZR} :=$$

$$-3 \cdot \ddot{P}_{a,b}^{XR} \cdot \dot{\Theta}_I^R - 3 \cdot \dot{P}_{a,b}^{XR} \cdot \left(\ddot{\Theta}_I^R + \dot{\Psi}_I^R \cdot s\Theta_I^R \cdot c\Theta_I^R \right) + P_{a,b}^{XR} \cdot \left(\varphi_{JZ\Theta} + \varphi_{JZ\Psi} \right)$$

Equation 17.6-7

$$\varphi_{JZ\Theta} := -\ddot{\Theta}_I^R + \dot{\Theta}_I^R \cdot \left(3 \cdot \left(\dot{\Psi}_I^R \right)^2 + \left(\dot{\Theta}_I^R \right)^2 \right)$$

Equation 17.6-8

$$\varphi_{JZ\Psi} := 3 \cdot \dot{\Psi}_I^R \cdot \left(\ddot{\Psi}_I^R \cdot \sin\Theta_I^R + \dot{\Psi}_I^R \cdot \dot{\Theta}_I^R \cdot \cos\Theta_I^R \right) \cdot \cos\Theta_I^R$$

Equation 17.6-9

APPENDIX E

18 EARTH GEOMETRY

Most terrestrially based weapon systems are wholly endo-atmospheric, the navigation of launchers, missiles and targets taking place with respect to the Earth. For medium and long-range navigation the Earth must be considered as an ellipsoid not a sphere, and for highly accurate systems such as GPS as a local geoid. Accurate earth geometry is crucial when deriving the input to height sensors whose measurements are used in integrated navigation systems.

General ellisoidal geometry is used to determine the earth radius at a point on its equi-potential surface. The local radii of curvature in the plane parallel to the equatorial plane, and in the east-west plane containing the geodetic vertical, are derived and approximations made to accommodate the height of a point above the Earth's surface. These generic equations are characterised using a particular geoid defined by its semi-major and semi-minor radii; the simulation is based on the WGS 84 ellipsoid.

Whilst there is always the temptation to reduce the earth's geometry to a simple sphere. This is a false economy when producing simulations described in this research. Even local area defence missile systems with relatively short ranges compared with the cruise missiles contain navigation systems requiring more sophisticated earth models.

18.1 General Ellipsoidal Geometry

This research involves terrestrial motion of targets, missiles and satellite constellations relative to the Earth. The Earth's mass (M) is 5.977×10^{24} kg a distance of 1.496×10^{11} m from the Sun, travelling at an average orbital speed of 29.7859 km/s. Its Siderial rate of rotation (ω_e) is $7.2921151487 \times 10^{-5}$ rad/s (15.0410671786 °/hr) resulting in a centripetal acceleration of 0.00594 m/s^2. The molten nature of the Earth, and its rotation, results in an oblate spheroid.

For short-range missile engagements it is usually adequate to ignore the Earth's curvature and rate of rotation. When the missile includes an IMU for guidance purposes a rotating spherical Earth model is sometimes used. For accurate long-range navigation the Earth must be treated as an ellipsoid (Figure 18-1).

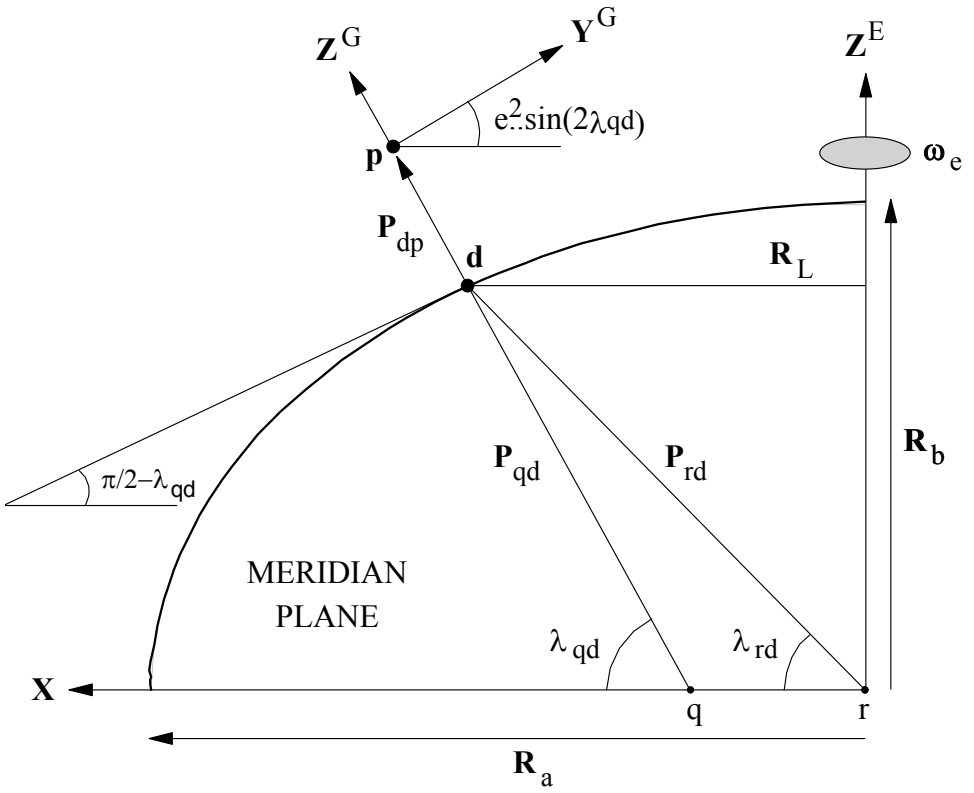

Figure 18-1 : Ellipsoid Meridian Plane Geometry

Highly accurate navigation systems such as GPS replace the general ellipsoid with local elliptical patches, each modelling a particular area on the Earth's surface. Figure 18-1 shows the meridian plane defined by a point (p) above the Earth's surface and $\underline{Z}^C$. The equatorial and polar radii (R_A and R_B) from NATO STANAG 4294 are given in Table 18-1.

The transform between different ellipsoids involves translation, rotation, and in some cases scale factor. The process is performed using Helmert or Molodenskii transforms that are beyond the scope of this work. The simulation is based on the USA DoD WGS 84 co-ordinate system used by NAVSTAR GPS, and by the DLMS for referencing digital maps.

Table 18-1 : Local Earth Reference Ellipsoids

ELLIPSOID	SEMI-MAJOR AXIS (R_A)	SEMI-MINOR AXIS (R_B)	DATE	AREA
Clarke	6 378 206	6 356 584	1866	North America
Clarke	6 378 249	6 356 480	1880	France,North Africa
International	6 378 388	6 356 912	1924	Europe
Mod Airey (OS)	6 378 563	6 356 257	1936	Great Britain
Krassowski	6 378 245	6 356 836	1940	Russia
WGS 72	6 378 135	6 356 751	1972	USA DoD
WGS 84	6 378 137	6 356 752	1984	USA DoD (GPS)

The variation in the Earth radii with latitude derived in the following sub-sections is shown in Figure 18-2.

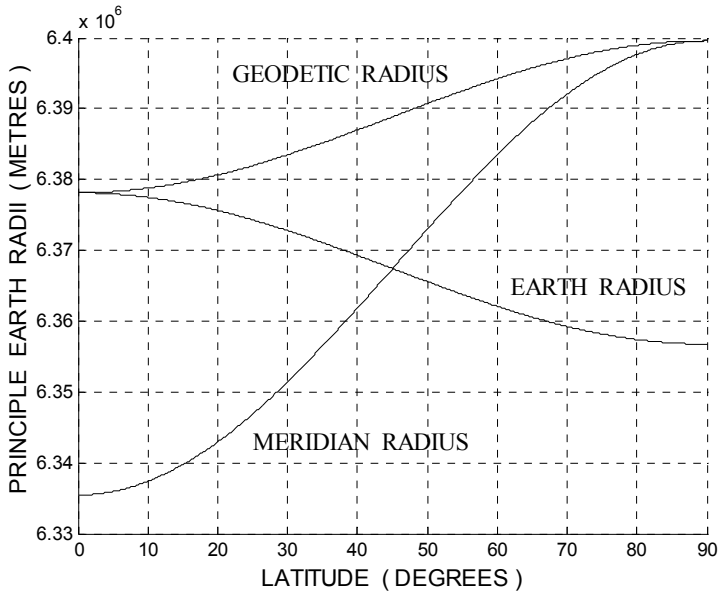

Figure 18-2 : Principle Earth Radii for Navigation

The geocentric radius ($R_{r,d}$) is a function of the polar and meridian radii (R_{pd}) and (R_{md}).

$$P_{r,d} := \sqrt{R_{pd}^2 \cdot \sin^2 \lambda_d + R_{md}^2 \cdot \cos^2 \lambda_d}$$

Equation 18.1-1

When dealing with terrestrial navigation over long distances the term Nautical mile is often used which is equivalent to 1 arc-second, or 1852 m.

18.2 General Ellipsoidal Analysis

The Earth's flattening at the poles due to its rotation,

$$f := 1 - \frac{R_B}{R_A} := 0.0033528107$$

Equation 18.2-1

The geocentric latitude of the missile (λ_{rd}) is the angle between the equatorial plane and a vector from the Earth centre (r) through points (p), and by definition (d) on the Earth's surface. The angle between the equatorial plane and a vector from point (q) through point (p) defines the geodetic latitude (λ_d). The angle between these latitude,

$$\lambda_d - \lambda_{rd} := 3.373 \times 10^{-3} \cdot \sin\left(2 \cdot \lambda_d\right) + 5.672 \times 10^{-6} \cdot \sin\left(4 \cdot \lambda_d\right)$$

Equation 18.2-2

Earth eccentricity expressed in terms of flattening and elliptical radii,

$$e^2 := 1 - \left(\frac{R_B}{R_A}\right)^2 := 2 \cdot f - f^2 := 0.00669438$$

Equation 18.2-3

From Figure 18-1,

$$\begin{pmatrix} x \\ z \end{pmatrix} := P_{r,d} \cdot \begin{pmatrix} \cos\lambda_{rd} \\ \sin\lambda_{rd} \end{pmatrix} := P_{r,d} \cdot \begin{pmatrix} \cos\lambda_{rd} \\ x \cdot \tan\lambda_{rd} \end{pmatrix}$$

Equation 18.2-4

The ellipsoid representing the Earth's equipotential surface is,

$$1 := \left(\frac{x}{R_A}\right)^2 + \left(\frac{z}{R_B}\right)^2$$

Equation 18.2-5

Differentiating with respect to (x) and expressing the result in terms of eccentricity,

$$\frac{dz}{dx} := -\frac{x}{z} \cdot \left(\frac{R_B}{R_A}\right)^2 := \frac{x}{z} \cdot \left(e^2 - 1\right)$$

Equation 18.2-6

(dx/dz) is deduced from the tangent plane to the surface at point (d). This plane is tilted at an angle of tan ($\pi/2 - \lambda$) to the equatorial plane, hence as (x) increases, (z) decreases and the rate of change of (x) with respect to (z) is negative,

$$\frac{dz}{dx} := -\cot\lambda_d$$

Equation 18.2-7

Equating and rearranging these equations,

$$z := x \cdot \left(1 - e^2\right) \cdot \tan\lambda_d$$

Equation 18.2-8

$$\tan\lambda_{rd} := \left(1 - e^2\right) \cdot \tan\lambda_d$$

Equation 18.2-9

Differentiating again with respect to (x**)** again, and substituting for (dz/dx),

$$\frac{d^2z}{dx^2} := \frac{1}{z} \cdot \left(e^2 - 1\right) \cdot \left(1 - \frac{x}{z} \cdot \frac{dz}{dx}\right)$$

Equation 18.2-10

$$\frac{d^2z}{dx^2} := \frac{1}{z} \cdot \left(e^2 - 1\right) \cdot \left(1 + \left(1 - e^2\right) \cdot \frac{x^2}{z^2}\right)$$

Equation 18.2-11

Substituting for (x^2/z^2) and then for resulting cotangent function,

$$\frac{d^2z}{dx^2} := \frac{e^2 - 1 - \cot^2\lambda_d}{z} := \frac{1}{z} \cdot \left(e^2 \cdot \sin^2\lambda_d - 1\right) \cdot \operatorname{cosec}^2\left(\lambda_d\right)$$

Equation 18.2-12

Starting with the trigonometric identities,

$$\sec\lambda_{rd} := \sqrt{1 + \tan^2\lambda_{rd}}$$

Equation 18.2-13

$$\cos\lambda_{r,d} := \frac{1}{\sqrt{1 + \tan^2\lambda_{rd}}} \approx \frac{1}{\sqrt{1 + \left(1 - e^2\right)^2 \cdot \tan^2\lambda_d}}$$

Equation 18.2-14

$$\cos\lambda_{rd} := \frac{1}{\sqrt{1+\left(1-2\cdot e^2\right)\cdot\tan^2\lambda_d}}$$

Equation 18.2-15

Replacing ($\sec\lambda_d$) assuming that ($\tan\lambda_{rd} \approx \tan\lambda_d$),

$$\cos\lambda_{rd} := \frac{1}{\sqrt{\sec^2\lambda_d - 2\cdot e^2\cdot\tan^2\lambda_d}} := \cos\lambda_d\cdot\left(1+e^2\cdot\sin^2\lambda_d\right)$$

Equation 18.2-16

Substituting from this equation into the following trigonometric identity,

$$\sin^2\lambda_{rd} := 1-\cos^2\lambda_{rd} := 1-\left(1+e^2\cdot\sin^2\lambda_d\right)^2\cdot\cos^2\lambda_d$$

Equation 18.2-17

Expanding ignoring powers of (e) greater than 2,

$$\sin^2\lambda_{rd} := 1-\left(1+2\cdot e^2\cdot\sin^2\lambda_d\right)\cdot\cos^2\lambda_d$$

Equation 18.2-18

$$\sin^2\lambda_{rd} := \left(1-2\cdot e^2\cdot\cos^2\lambda_d\right)\cdot\sin^2\lambda_d$$

Equation 18.2-19

$$\sin^2\lambda_{rd} := \left(1-e^2\cdot\cos^2\lambda_d\right)\cdot\sin^2\lambda_d$$

Equation 18.2-20

18.3 Geocentric Earth Radius

The geocentric radius is the distance from point (r) to point (p). Substituting for (x) and (z) in the general equation for an ellipsoid,

$$1 := P_{r,d}^2\cdot\left(\frac{\cos^2\lambda_{rd}}{R_a^2}+\frac{\sin^2\lambda_{rd}}{R_b^2}\right)$$

Equation 18.3-1

Re-arranging and taking the positive root of this equation,

$$P_{r,d} := \frac{R_A}{\sqrt{\cos^2\lambda_{rd}+\left(R_A/R_B\right)^2\cdot\sin^2\lambda_{rd}}}$$

Equation 18.3-2

Introducing eccentricity and expanding ignoring powers of (e) > 2,

$$P_{r,d} := \frac{R_A}{\sqrt{\cos^2 \lambda_{rd} + \frac{\sin^2 \lambda_{rd}}{1 - e^2}}} := \frac{R_A}{\sqrt{\cos^2 \lambda_{rd} + \left(1 + e^2\right) \cdot \sin^2 \lambda_{rd}}}$$

Equation 18.3-3

Replacing geocentric latitude, and expanding ignoring powers of (e) > 2,

$$P_{r,d} := \frac{R_A}{\sqrt{1 + e^2 \cdot \sin^2 \lambda_{rd}}}$$

Equation 18.3-4

Expanding to 1st order, replacing geocentric with geodetic latitude,

$$P_{r,d} := R_A \cdot \sqrt{1 - e^2 \cdot \sin^2 \lambda_d}$$

Equation 18.3-5

Lambert[L.9] provides a more accurate value for the Earth radius,

$$P_{r,d} := R_A \cdot \left(0.998320047 + \Delta P_{r,d}\right)$$

Equation 18.3-6

$$\Delta P_{r,d} := 1.683494 \times 10^{-3} \cdot \cos\left(2 \cdot \lambda_d\right) + 3.549 \times 10^{-6} \cdot \cos\left(4 \cdot \lambda_d\right) + \cdots$$

Equation 18.3-7

The variation of the Earth radius with geodetic latitude,

$$\frac{\partial P_{r,d}}{\partial \lambda_d} := -\frac{P_{r,d} \cdot e^2 \cdot \sin \lambda_d \cdot \cos \lambda_d}{1 + e^2 \cdot \sin^2 \lambda_d}$$

Equation 18.3-8

Relating this expression to the geodetic velocity at point (d),

$$\frac{\partial P_{r,d}}{\partial \underline{\dot{P}}_m^G} := \frac{\partial P_{r,d}}{\partial \lambda_d} \cdot \frac{\partial \lambda_d}{\partial \underline{\dot{P}}_m^G} := \left(0 \quad , \quad \frac{1}{R_{\lambda d}} \quad , \quad 0\right)^T \cdot \frac{\partial P_{r,d}}{\partial \lambda_d}$$

Equation 18.3-9

18.4 Earth Curvature in the Plane of the Geodetic Vertical

Curvature at point (d) normal to the local meridian plane,

$$R_L := P_{r,d} \cdot \cos \lambda_{rd}$$

Equation 18.4-1

Replacing geocentric latitude with the geodetic latitude,

$$R_L := P_{r,d} \cdot \left(1 + e^2 \cdot \sin^2 \lambda_d \right) \cdot \cos \lambda_d$$

Equation 18.4-2

The Earth's polar radius at point (p),

$$R_{pd} := R_L \cdot \sec \lambda_d$$

Equation 18.4-3

Substituting for the horizontal radius,

$$R_{pd} := P_{r,d} \cdot \left(1 + e^2 \cdot \sin^2 \lambda_d \right)$$

Equation 18.4-4

$$R_{pd} := R_a \cdot \left(1 + e^2 \cdot \sin^2 \lambda_d \right) \cdot \sqrt{1 - e^2 \cdot \sin^2 \lambda_d}$$

Equation 18.4-5

$$R_{pd} \approx \frac{R_A}{\sqrt{1 - e^2 \cdot \sin^2 \lambda_d}}$$

Equation 18.4-6

The polar radius of curvature at the point (p), close to the Earth's surface,

$$R_{\mu d} := R_{pd} + P_{d,m}^{ZG}$$

Equation 18.4-7

The variation of the Earth polar radius with geodetic latitude in (m/rad),

$$\frac{\partial R_{pd}}{\partial \lambda_d} := \frac{R_{pd} \cdot e^2 \cdot \sin \lambda_d \cdot \cos \lambda_d}{1 - e^2 \cdot \sin^2 \lambda_d}$$

Equation 18.4-8

18.5 Earth Curvature in the Plane of the Meridian

Curvature in the meridian at point (d) from the standard curvature equation,

$$R_{md} := \left(\frac{d^2 z}{dx^2} \right)^{-1} \cdot \sqrt{1 + \left(\frac{dz}{dx} \right)^2}$$

Equation 18.5-1

Substituting for the derivatives and expanding the cotangent function,

$$R_{md} := \frac{z \cdot \sin^2 \lambda_d \cdot \sqrt{\left(1 + \cot^2 \lambda_d \right)^3}}{1 - e^2 \cdot \sin^2 \lambda_d} := \frac{z \cdot \operatorname{cosec} \lambda_d}{1 - e^2 \cdot \sin^2 \lambda_d}$$

Equation 18.5-2

Combining like terms after substituting for (z) and the Earth radius,

$$R_{md} := \frac{P_{r,d} \cdot \left(1 - e^2 + e^2 \cdot \sin^2 \lambda_d \right)}{1 - e^2 \cdot \sin^2 \lambda_d} := \frac{R_A \cdot \left(1 - e^2 + e^2 \cdot \sin^2 \lambda_d \right)}{\sqrt{1 - e^2 \cdot \sin^2 \lambda_d}}$$

Equation 18.5-3

Expanding ignoring powers of (e) > 2,

$$R_{md} := \frac{R_A \cdot \left(1 - e^2 + e^2 \cdot \sin^2 \lambda_d \right)}{\sqrt{1 - e^2 \cdot \sin^2 \lambda_d}}$$

Equation 18.5-4

$$R_{md} := \frac{R_A \cdot \left(1 - e^2 \right)}{\left(1 - e^2 \cdot \sin^2 \lambda_d \right) \cdot \sqrt{1 - e^2 \cdot \sin^2 \lambda_d}} := \frac{R_A \cdot \left(1 - e^2 \right)}{\sqrt{\left(1 - e^2 \cdot \sin^2 \lambda_d \right)^3}}$$

Equation 18.5-5

Curvature in the meridian at point (p) close to the Earth's surface,

$$R_{\lambda d} := R_{md} + P_{d,m}^{ZG}$$

Equation 18.5-6

The variation of the meridian radius with latitude in (m/rad),

$$\frac{\partial R_{md}}{\partial \lambda_d} := \frac{3 \cdot R_{md} \cdot e^2 \cdot \sin \lambda_d \cdot \cos \lambda_d}{1 - e^2 \cdot \sin^2 \lambda_d}$$

Equation 18.5-7

APPENDIX F

19 ATMOSPHERIC PROPERTIES

Aerodynamic forces and moments acting on a point are often presented in normalised form with respect to the local air density and speed. Their variation with geodetic height is dealt with using functions involving Mach number, air density and speed of sound, both locally and at sea-level. Air-data sensors are a direct example of a system requiring these atmospheric characteristics, and the local air temperature.

This section provides standard expressions for the variation of air density, pressure, temperature, Mach number and the speed of sound with geodetic height and speed. The height variation encompasses the Troposphere (-1 km to 11 km), Stratosphere (11 km to 20 km) and the Chemosphere (20 km to 32 km). The data provided is based on standard equations taken from Collinson[C.8].

Missile trajectory optimisation depends on the variation of the external forces and moments acting on it, and therefore the atmospheric parameter gradients presented here. For optimisation purposes discontinuities in the atmospheric parameter gradients are removed by expressing variations in terms of accurate approximating polynomials.

19.1 **Static Air Pressure**

$$P_{d,p}^{ZG} \in [-900, 11\,000] \Rightarrow P_S := P_{so} \cdot \left(1 - L_t \cdot \frac{P_{d,p}^{ZG}}{T_{so}}\right)^{g_o / L_t \cdot R_g}$$

Equation 19.1-1

$$P_{d,p}^{ZG} \in]11\,000, 20\,000] \Rightarrow$$

$$P_S := P_S(11\,000) \cdot \exp\left(-\frac{g_o \cdot \left(P_{d,p}^{ZG} - 11\,000\right)}{L_t \cdot R_g}\right)$$

Equation 19.1-2

$$P_{d,p}^{ZG} \in]20\,000, 32\,000] \Rightarrow$$

$$P_S := P_S(20000) \cdot \left(1 + L_c \cdot \frac{P_{d,p}^{ZG} - 20000}{T_t}\right)^{g_o / L_t \cdot R_g}$$

Equation 19.1-3

L_t	:=	Tropospheric lapse rate	:=	0.0065	deg K/m
L_c	:=	Chemospheric rise rate	:=	1.0×10^{-3}	deg K/m
P_{so}	:=	Static pressure at sea level	:=	101,325	N/m^2
T_{so}	:=	Static temperature at sea level	:=	288.15	deg K
T_t	:=	Tropopause temperature	:=	216.65	deg K
g_o	:=	Gravity at sea level	:=	9.80665	m/s^2
R_g	:=	Gas constant (air)	:=	287.0529	J/deg K/kg

Inserting these data into the static air pressure equations,

$$P_p^{ZG} \in [-900, 11\,000] \Rightarrow$$

$$P_S := 101325 \cdot \left(1 - 2.25577 \times 10^{-5} \cdot P_p^{ZG}\right)^{5.255879}$$

Equation 19.1-4

$$P_p^{ZG} \in \left]11\,000, 20\,000\right] \Rightarrow$$

$$P_S := 22632 \cdot \exp\left(-1.576885 \times 10^{-4} \cdot \left(P_p^{ZG} - 11\,000\right)\right)$$

Equation 19.1-5

$$P_p^{ZG} \in \left]20\,000, 32\,000\right] \Rightarrow$$

$$P_S := \frac{5\,474.82}{\left(1 + 4.61574 \times 10^{-6} \cdot \left(P_p^{ZG} - 20\,000\right)\right)^{34.163215}}$$

Equation 19.1-6

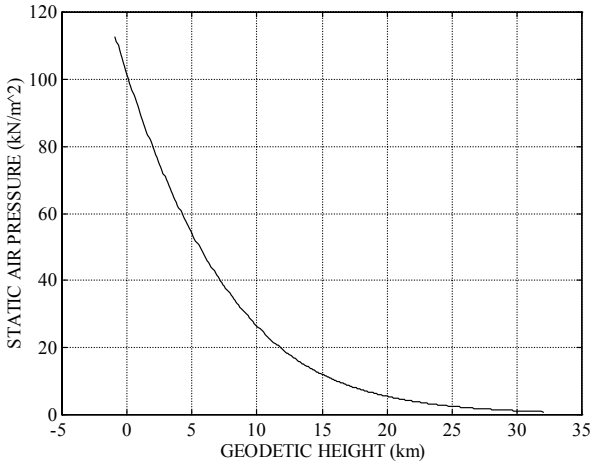

Figure 19-1 : Static Air Pressure vs Height

The sea-level gravitational acceleration used here is an approximation to the actual gravity that is a function of geodetic height. When solving trajectory optimisation problems using gradients a continuous function is preferred. For the static pressure a 4th degree polynomial is the best balance between efficiency and accuracy with errors in the range [-150,100] N/m^2,

$$P_S :=$$

$$101370 + \left(-12 + \left(563.02 + \left(-12.117 + 0.099324 \cdot P_p^{ZG}\right) \cdot P_p^{ZG}\right) \cdot P_p^{ZG}\right) \cdot P_p^{ZG}$$

Equation 19.1-7

To avoid numerical problems the height is input in (km). Likewise, the rate of change in pressure with geodetic height is approximated using a cubic polynomial resulting in errors in the range ± 0.1 N/m,

$$\partial P_S \,/\, \partial P_p^{ZG} \;:=$$

$$-12 + \left(1.1259 - \left(0.03651 - 4.0327 \times 10^{-4} \cdot P_p^{ZG} \right) \cdot P_p^{ZG} \right) \cdot P_p^{ZG}$$

Equation 19.1-8

19.2 Static Air Temperature

The change in static temperature with geodetic height,

$$P_p^{ZG} \in [-900, 11\,000\,] \Rightarrow$$

$$T_S := T_{so} - L_t \cdot P_p^{ZG} := 288.15 - 0.0065 \cdot P_p^{ZG}$$

Equation 19.2-1

$$P_p^{ZG} \in \,]11\,000, 20\,000\,] \Rightarrow T_S := T_t := 216.65$$

Equation 19.2-2

$$P_p^{ZG} \in \,]20\,000, 32\,000\,] \Rightarrow$$

$$T_S := T_t + L_c \cdot \left(P_p^{ZG} - 20\_000 \right) := 216.65 + 0.001 \cdot \left(P_p^{ZG} - 20\_000 \right)$$

Equation 19.2-3

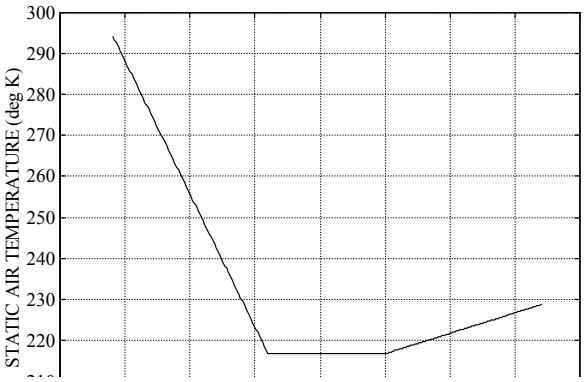

Figure 19-2 : Static Air Temperature vs Height

The rate of change of static temperature with geodetic height,

$$P_p^{ZG} < 11\,000 \Rightarrow \partial T_S \,/\, \partial P_p^{ZG} := -0.0065$$

Equation 19.2-4

$$P_p^{ZG} \in [\, 11\,000 , 20\,000 \,] \Rightarrow \partial T_S \,/\, \partial P_p^{ZG} := 0$$

Equation 19.2-5

$$P_p^{ZG} > 20\,000 \Rightarrow \partial T_S \,/\, \partial P_p^{ZG} := 0.001$$

Equation 19.2-6

19.3 Air Density

The air density is given by the gas law (sea-level air density is 1.225 kg/m^3),

$$\rho_A := \frac{P_S}{R_g \cdot T_S}$$

Equation 19.3-1

The cubic polynomial approximation with errors in the range ± 0.01kg/m^3,

$$\rho_A :=$$

$$1.2231 + \left(-0.11477 + \left(3.7188 \times 10^{-3} - 4.1034 \times 10^{-5} \cdot P_p^{ZG} \right) \cdot P_p^{ZG} \right) \cdot P_p^{ZG}$$

Equation 19.3-2

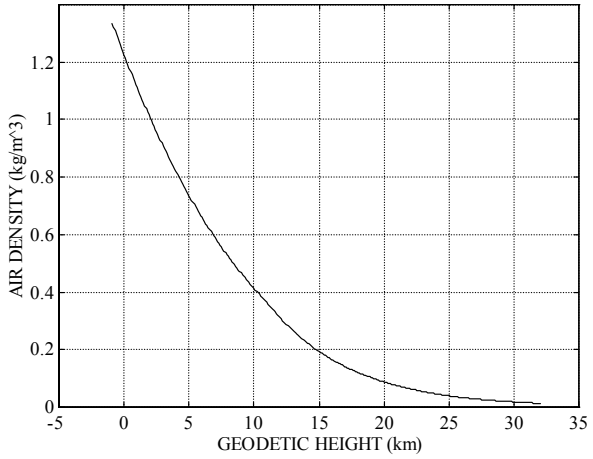

Figure 19-3 : Air Density vs Height

Deriving a polynomial approximation for the air density variation with height using curve fitting to the original equations results in a discontinuity due to the static temperature since,

$$\frac{\partial \rho_A}{\partial P_p^{ZG}} := \frac{1}{R_g \cdot T_S} \cdot \left\{ \frac{\partial P_S}{\partial P_p^{ZG}} - \frac{P_S}{T_S} \cdot \frac{\partial T_S}{\partial P_p^{ZG}} \right\}$$

Equation 19.3-3

The polynomial approximation is therefore derived by direct differentiation of Equation 19.3-2,

$$\partial \rho_A \,/\, \partial P_p^{ZG} \;\coloneqq\; -0.11477 + \left(7.4376 \times 10^{-3} - 1.231 \times 10^{-4} \cdot P_p^{ZG} \right) \cdot P_p^{ZG}$$

Equation 19.3-4

19.4 Speed of Sound in Air

The speed of sound in air (at sea level the speed of sound is 340.294 m/s),

$$V_A \;\coloneqq\; \sqrt{1.4 \cdot R_g \cdot T_S}$$

Equation 19.4-1

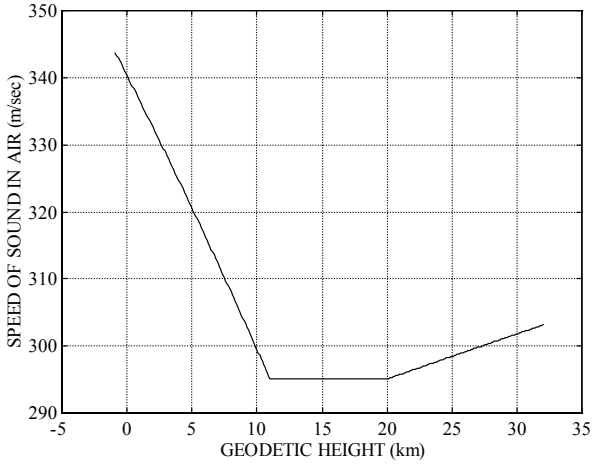

Figure 19-4 : Speed of Sound in Air vs Height

19.5 Mach Number

The Mach number associated with the speed of sound in air,

$$M_p \;\coloneqq\; \frac{\dot{P}_{o,p}}{V_A} \;\coloneqq\; \frac{0.0498539 \cdot \dot{P}_{o,p}}{\sqrt{T_S}}$$

Equation 19.5-1

The Mach Number variation with speed, velocity and geodetic height below 11 km,

$$\frac{\partial M_p}{\partial \underline{\dot{P}}_p^G} \;\coloneqq\; \frac{0.0498539}{\sqrt{T_S}} \cdot \frac{\partial \dot{P}_{d,p}}{\partial \underline{\dot{P}}_p^G} \;\coloneqq\; \frac{M_p \cdot \underline{\dot{P}}_p^G}{\dot{P}_{d,p}^2}$$

Equation 19.5-2

$$\frac{\partial M_p}{\partial P_p^{ZG}} := -\frac{0.0498539 \cdot \dot{P}_{d,p}}{2 \cdot \sqrt{T_S^3}} \cdot \frac{\partial T_S}{\partial P_p^{ZG}} := -\frac{0.024927 \cdot M_p}{T_S} \cdot \frac{\partial T_S}{\partial P_p^{ZG}}$$

Equation 19.5-3

APPENDIX G

20 GRAVITY

The motion of a body is determined by aerodynamic forces and moments, and by gravitational forces acting at its mass centre. The variation in gravity with respect to latitude and height are therefore a key element in the trajectory optimisation state equations. Indeed, they dominate the exo-atmospheric dynamics of a conventionally controlled missile coasting at heights above some 20 km.

The gravitational acceleration acting on a point mass moving close to the Earth's surface in a uniform gravitational field is considered. The gravitational force at this point is a combination of the Earth attraction, as dictated by Newton's universal law of gravitation, and centripetal acceleration due to Earth rotation.

Gravitational acceleration is derived in LGA together with its variation with geodetic height and latitude. The effects of introducing approximations for nap-of-the-earth navigation are explored, as are the implications of Newton's universal law of gravitation when determining the position of satellites based on Keplerian orbital parameters.

20.1 Absolute Gravitational Acceleration

The dominant gravitational acceleration component acting at a point is the local gravity vector (g) shown in Figure 20-1 acting through the geodetic centre (q). The local gravity vector comprises mass attraction between the vehicle and the Earth, and centripetal acceleration caused by Earth rotation that acts parallel to its equatorial plane. The Earth's equatorial bulge causes the local gravitational vector to deviate from the local geodetic vertical by up to 0.15 mrad. The gravitational acceleration at point (p) in inertial space,

$$\underline{G}_p \;:=\; \underline{g}_p + \underline{\omega}_{C,E} \times \underline{\omega}_{C,E} \times \left(\underline{P}_{r,d} + \underline{P}_{d,p} \right)$$

Equation 20.1-1

The gravitational acceleration acting at the Earth's surface directly below point (p),

$$\underline{G}_d \;:=\; \underline{g}_d + \underline{\omega}_{C,E} \times \underline{\omega}_{C,E} \times \underline{P}_{r,d}$$

Equation 20.1-2

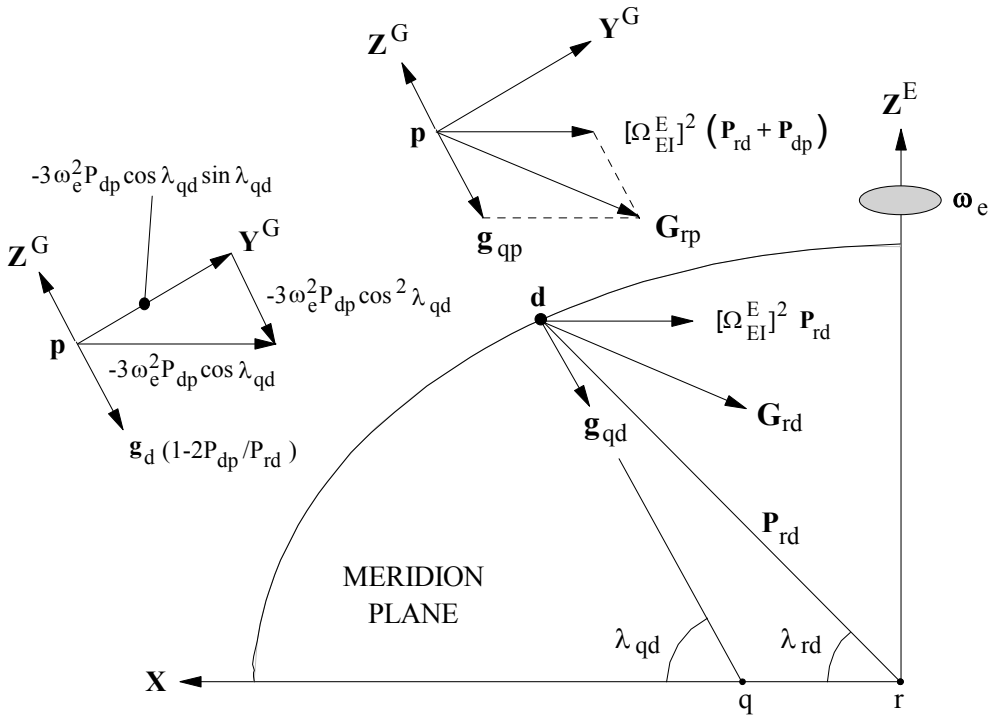

Figure 20-1 : Near Earth Gravitational Acceleration Components

20.2 Local Gravitational Acceleration

Combining the equations in §20.1 gives an expression for local gravitation acceleration acting at (p) that is independent of earth radius,

$$\underline{g}_p \;\coloneqq\; \underline{g}_d + \underline{G}_p - \underline{G}_d - \underline{\omega}_{C,E} \times \underline{\omega}_{C,E} \times \underline{P}_{d,p}$$

Equation 20.2-1

Newton's universal law of gravitation states that the mutually attractive force (F) acting along a vector between two homogeneous masses a distance ($P_{r,p}$) apart,

$$F \;\coloneqq\; \frac{G \cdot M \cdot m}{P_{r,p}^2} \;\Rightarrow\; \underline{\ddot{P}}_{r,d} \;\coloneqq\; -\frac{G \cdot M \cdot \underline{P}_{r,d}}{P_{r,p}^3}$$

Equation 20.2-2

($\underline{G}$) is the universal gravitational constant 6.673 x 10^{-11} $m^3/(kg.s^2)$, (m) the vehicle mass referenced to point (p), and (M) is the Earth's mass. For near-earth studies $P_{d,p} << P_{r,p}$, and assuming that the unit vectors point in the same direction, the absolute gravitational acceleration at points (p) and (d),

$$\left(G \cdot M \right) \cdot \hat{\underline{G}}_d \;\coloneqq\; m \cdot \left(P_{r,d} + P_{d,p} \right)^2 \cdot \underline{G}_p \;\cong\; m \cdot P_{r,d}^2 \cdot \underline{G}_d$$

Equation 20.2-3

The ratio of these two vectors is thus,

$$\underline{G}_p \;\coloneqq\; \varphi_1 \cdot \underline{G}_d$$

Equation 20.2-4

For accurate long-range, and high-altitude short-range, applications the following expression for (φ_1) is recommended,

$$\varphi_1 \;\coloneqq\; \left(\frac{P_{r,d}}{P_{r,d} + P_{d,p}} \right)^2$$

Equation 20.2-5

For less accurate short-range and near-earth applications this function may be reduced with care to,

$$\varphi_1 \;\approx\; 1 - \left(2 \cdot P_{d,p} \;/\; P_{r,d} \right)$$

Equation 20.2-6

From Equation 20.2-3, substituting for the absolute gravity vectors,

$$\underline{g}_p \;\coloneqq\; \underline{g}_d \cdot \varphi_1 - \underline{\omega}_{C,E}^E \times \underline{\omega}_{C,E}^E \times \underline{P}_{d,p} - 2 \cdot \frac{P_{d,p}}{P_{r,d}} \cdot \left(\underline{\omega}_{C,E}^E \times \underline{\omega}_{C,E}^E \times \underline{P}_{r,d} \right)$$

Equation 20.2-7

The components of gravity are required in LGA. If ($\underline{\hat{n}}_*$) are unit vectors parallel to the Equatorial Plane, originating at points (d) and (p), and acting in the direction of the centripetal acceleration as shown in Figure 20-1,

$$\underline{\omega}^E_{C,E} \times \underline{\omega}^E_{C,E} \times \underline{P}_{r,d} := \left(\omega_e^2 \cdot P_{r,d} \cdot \cos\lambda_{r,d} \right) \bullet \underline{\hat{n}}_d$$

Equation 20.2-8

$$\underline{\omega}^E_{C,E} \times \underline{\omega}^E_{C,E} \times \underline{P}_{d,p} := \left(\omega_e^2 \cdot P_{d,p} \cdot \cos\lambda_{r,p} \right) \bullet \underline{\hat{n}}_p$$

Equation 20.2-9

Replacing the geocentric latitude with the geodetic latitude,

$$\underline{\omega}^E_{C,E} \times \underline{\omega}^E_{C,E} \times \underline{P}_{r,d} := \left(\omega_e^2 \cdot P_{r,d} \cdot \cos\lambda_d \right) \bullet \underline{\hat{n}}_d$$

Equation 20.2-10

$$\underline{\omega}^E_{C,E} \times \underline{\omega}^E_{C,E} \times \underline{P}_{d,p} := \left(\omega_e^2 \cdot P_{d,p} \cdot \cos\lambda_d \right) \bullet \underline{\hat{n}}_p$$

Equation 20.2-11

Substituting for the cross-products and expressing the centripetal acceleration in local (NED) geodetic axes,

$$\underline{g}^G_p := \underline{g}^G_d \cdot \varphi_l - \left(3 \cdot \omega_e^2 \cdot P_{d,p} \cdot \cos\lambda_d \right) \cdot \left(\sin\lambda_d \quad 0 \quad \cos\lambda_d \right)^T$$

Equation 20.2-12

Similarly, in (ENU) geodetic axes,

$$\underline{g}^G_p := -\underline{g}^G_d \cdot \varphi_l + \left(3 \cdot \omega_e^2 \cdot P_{d,p} \cdot \cos\lambda_d \right) \cdot \left(0 \quad -\sin\lambda_d \quad \cos\lambda_d \right)^T$$

Equation 20.2-13

The 1980 International Gravity Formula provides the gravitational acceleration acting at the Earth's surface along the local geodetic vertical as a function of the geodetic latitude,

$$g^{ZG}_d := 9.78049 \cdot \left(1 + 0.0052884 \cdot \sin^2\left(\lambda_d \right) - 5.9 \cdot 10^{-6} \cdot \sin^2\left(2 \cdot \lambda_d \right) \right)$$

Equation 20.2-14

Compare this with the 1967 gravity formula,

$$g^{ZG}_d := 9.780318 \cdot \left(1 + 5.3026 \cdot 10^{-3} \cdot \sin^2\lambda_d + \Delta g_d \right)$$

Equation 20.2-15

$$\Delta g_d := -5.85\cdot 10^{-6}\cdot \sin^2\left(2\cdot\lambda_d\right) - 3.2\cdot 10^{-8}\cdot \sin^2\lambda_d\cdot\sin^2\left(2\cdot\lambda_d\right)$$

Equation 20.2-16

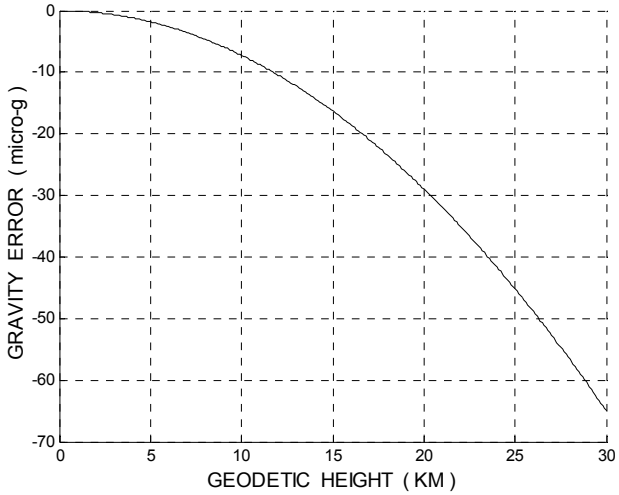

Figure 20-2 : Gravity Error

For short-range applications the geodetic gravitational acceleration in the Alignment frame is a good approximation to the geodetic value. The LGA and Alignment frames are closely aligned as the tilt between them over the distances involved is small.

20.3 Gravitational Anomalies

Figure 20-2 shows the gravitational acceleration error as a function of geodetic height at 53° latitude if Equation 20.2-6 is used rather than the more accurate expression in Equation 20.2-5. When doubly integrated over a long period of time the height error can be substantial, for example, an error of 2 km is induced at 20 km after 1 hr.

The variation in gravity with geodetic height using the more accurate expression for the gravitational acceleration,

$$\partial g_p^{ZG} \,/\, \partial P_p^{ZG} := -2\cdot g_p^{ZG}\cdot\left(P_{r,d} + P_{d,p}\right)^{-1}$$

Equation 20.3-1

For short-range applications,

$$\partial g_p^{ZG} \,/\, \partial P_p^{ZA} \cong \partial g_p^{ZG} \,/\, \partial P_p^{ZG}$$

Equation 20.3-2

Ignoring small terms involving the earth rate the only significant variation in gravity with latitude is,

$$\frac{\partial g_p^{ZG}}{\partial \lambda_d} := 0.10372 \cdot \varphi_l \cdot \sin \lambda_d \cdot \cos \lambda_d$$

Equation 20.3-3

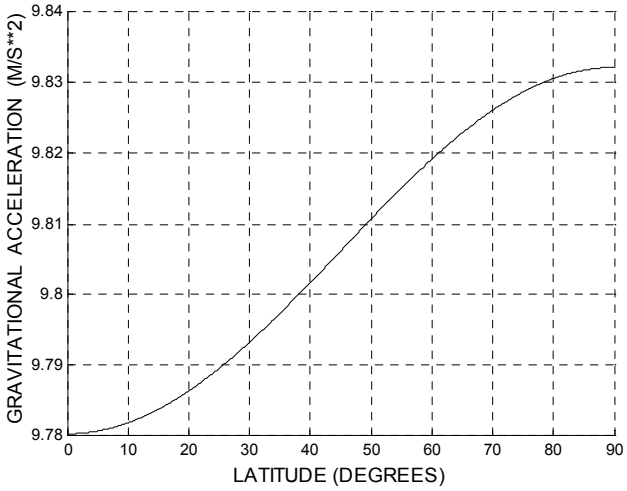

Figure 20-3 : Gravity vs Latitude

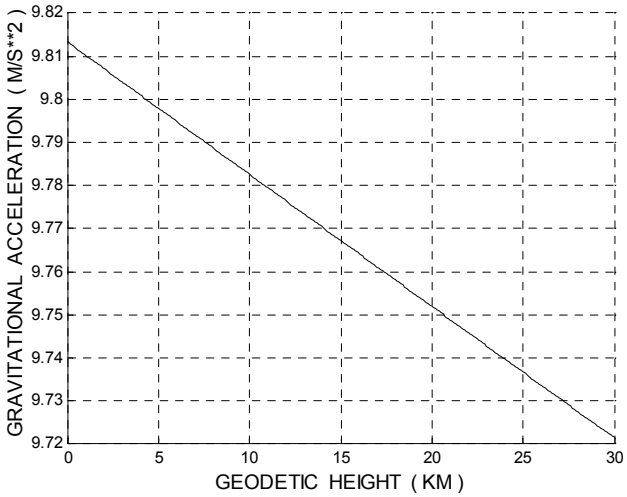

Figure 20-4 : Gravity vs Height

The variation in gravitational acceleration with latitude and geodetic height is shown in Figure 20-3 and Figure 20-4 respectively. At a latitude of 45° the gravitational acceleration at sea-level is 9.8067m/s^2.

APPENDIX H

21 STEADY STATE TRACKING FILTERS

When stochastic filtering was first introduced processor load constraints often resulted in the use of fixed gain "Kalman" filters tuned for "simple" targets. According to Sudano[S.16] the originator of the fixed gain filter was Sklansky in 1957. In 1962 Benedict & Bordner developed the constant velocity $\alpha-\beta$ tracker. Since then others such as Kalata, Solomon, Arcasoy and Vorley have all advanced the subject. The ground tracker in this application is a bank of target tracking EKFs within an IMM structure. If the system and measurement noise uncertainty (σ_S) and (σ_M) remain constant these filters reduce to $\alpha-\beta-\gamma$ filters with the following dynamics:

- Piecewise constant acceleration input to a velocity filter
- Piecewise constant jerk input to an acceleration filter
- Manoeuvre dependent 1st order Gauss-Markov filter (dog-leg)
- Manoeuvre dependent 2nd order Gauss-Markov filter (weaving)

Under these conditions the steady state filter covariances (C^{∞}) are determined from the Ricatti equation, Arcasory[A.4],

$$C^{\infty} := \Phi \cdot C \cdot \Phi^T - \Phi \cdot C \cdot H^T \cdot \left(H \cdot C \cdot H^T + R \right)^{-1} \cdot H \cdot C \cdot \Phi^T + \Gamma \cdot Q \cdot \Gamma^T$$

The steady state gain being,

$$K := \frac{C \cdot H^T}{H \cdot C \cdot H^T + R}$$

An appreciation of the equivalent fixed gain KF provides an insight into the quasi-static behaviour of the ground tracker. These type of fixed gain filters are often employed in radar and seekers to smooth the measurements and provide higher dynamic estimates required for gimbal/beam steering and missile guidance.

21.1 Introduction

Kalata[K.7] produced an α–β filter in 1984 which minimised the sum of the expected PV errors for a filter driven by piecewise constant acceleration. He also introduced the tracking index (TI) concept that has become a key element in selecting static filter gains. Sudano[S.17] was responsible for the α–β–γ filter driven by piecewise continuous jerk minimising expected PVA error in 1993. The constant acceleration dynamics was replaced by manoeuvre driven filters first by Sudano[S.16] (1st order Gauss-Markov in 1995), and by Vorley[V.3] (2nd order Gauss-Markov in 1991). In these cases the filter gains are complex functions of the TI requiring iterative numerical solution, the TI representing the ratio of system to measurement noise, balancing measurement smoothing with accurate tracking.

21.2 Constant Velocity Filter

An α–β filter with states {$\underline{X}$,d($\underline{X}$)/dt}, minimising the Performance Index used by Kalata[K.7],

$$J := \min \sum \left(E\left(\Delta X^2\right) + \Delta t^2 \cdot E\left(\Delta \dot{X}^2\right)\right)$$

Equation 21.2-1

Resulting in the recursive state equations,

$$X_{k+1} := \left(1-\alpha\right)\cdot\left(X_k + \dot{X}_k \cdot \Delta t\right) + \alpha \cdot X_I(k)$$

Equation 21.2-2

$$\dot{X}_{k+1} := \frac{\beta}{\Delta t}\cdot\left(X_I(k) - X_k\right) + \left(1-\beta\right)\cdot\dot{X}_k$$

Equation 21.2-3

Kalata also introduced the tracking index (TI) on which the filter gains in many subsequent papers on this subject rely. The TI relates the uncertainty in the X-state (σ_S) to the uncertainty in the measurement of that state (σ_M),

$$TI := \frac{\sigma_S \cdot \Delta t^2}{\sigma_M}$$

Equation 21.2-4

The noise characteristics, and the update rate of the filter (Δt), define the tracking index from which the gains are computed. The filter gains are a function of the number of measurements processed (n), Quigley[Q.1],

$$(\alpha \quad , \quad \beta) := \frac{(2\cdot(2\cdot n-1) \quad , \quad 6)}{n\cdot(n+1)}$$

Equation 21.2-5

These gains are identical to those in a KF given infinite initial covariances, the measurement uncertainties are constant, no system noise, nor any correlation between the state errors. Under these conditions the tracking uncertainty immediately after a measurement update are again from Quigley[Q.1],

$$E(X^2) := \frac{2\cdot\sigma_M^2\cdot(2\cdot n-1)}{n\cdot(n+1)} \xrightarrow{\text{large n}} \frac{4\cdot\sigma_M^2}{n}$$

Equation 21.2-6

$$E(X,\dot{X}) := \frac{6\cdot\sigma_M^2}{n\cdot(n+1)\cdot\Delta t} \xrightarrow{\text{large n}} \frac{6\cdot\sigma_M^2}{n\cdot\Delta t}$$

Equation 21.2-7

$$E(\dot{X}^2) := \frac{12\cdot\sigma_M^2}{n\cdot(n^2-1)\cdot\Delta t^2} \xrightarrow{\text{large n}} \frac{12\cdot\sigma_M^2}{n\cdot\Delta t^2}$$

Equation 21.2-8

The PV estimates provided by these approximations are accurate to 10% and 6% after 8 and 3 measurements respectively, Fitzgerald[F.6]. If (τ) is the time after the n^{th} measurement update the state error propagates according to,

$$E(X^2) := \frac{2\cdot\sigma_M^2}{n\cdot(n+1)}\cdot\left\{2\cdot n-1+\frac{6\cdot\tau}{\Delta t}\cdot\left(1+\frac{\tau}{\Delta t\cdot(n-1)}\right)\right\}$$

Equation 21.2-9

As (t) approaches (Δt) this equation provides the uncertainty in the state immediately before the n^{th} measurement is processed,

$$E(X^2) := \frac{2\cdot(2\cdot n-1)\cdot\sigma_M^2}{(n-1)\cdot(n-2)}$$

Equation 21.2-10

21.3 Constant Acceleration Filter

For targets moving in circular arcs, the PI of the constant acceleration filter originally used by Sudano[S.17],

$$J := \min \sum \left(E\left(\Delta X^2 \right) + \Delta t^2 \cdot E\left(\Delta \dot{X}^2 \right) \cdot + \Delta t^4 \cdot E\left(\Delta \ddot{X}^2 \right) \right)$$

Equation 21.3-1

Resulting in the recursive state equations from Soloman[S.18],

$$X_{k+1} := (1-\alpha) \cdot \left(X_k + \dot{X}_k \cdot \Delta t + \frac{\ddot{X}_k \cdot \Delta t^2}{2} \right) + \alpha \cdot X_I(k)$$

Equation 21.3-2

$$\dot{X}_{k+1} := \frac{\beta}{\Delta t} \cdot \left(X_I(k) - X_k \right) + (1-\beta) \cdot \dot{X}_k + \left(1 - \frac{\beta}{2} \right) \cdot \ddot{X}_k \cdot \Delta t$$

Equation 21.3-3

$$\ddot{X}_{k+1} := \frac{\gamma}{\Delta t} \cdot \left(\frac{X_I(k) - X_k}{\Delta t} - \dot{X}_k \right) + \left(1 - \frac{\gamma}{2} \right) \cdot \ddot{X}_k$$

Equation 21.3-4

The gains arising from the steady-state, least-squares solution of the KF equations for constant acceleration and measurement variance,

$$(\alpha \ , \ \beta \ , \ \gamma) := \frac{\left(9 \cdot n^2 - 9 \cdot n + 6 \ , \ 18 \cdot (2 \cdot n - 1) \ , \ 30 \right)}{n \cdot (n+1) \cdot (n+2)}$$

Equation 21.3-5

The tracking index in this case is,

$$TI := \frac{\sigma_S \cdot \Delta t^3}{\sigma_M} := \frac{\gamma}{\sqrt{1-\alpha^2}}$$

Equation 21.3-6

The state covariances,

$$E\left(X^2 \right) := \left(2 \cdot \alpha \cdot \chi_1 - \beta^2 \cdot (6 \cdot \alpha - 4) + \alpha \cdot \beta \cdot \gamma \right) \cdot \chi_3$$

Equation 21.3-7

$$\Delta t \cdot E\left(X, \dot{X} \right) := \left(\beta \cdot (2 \cdot \alpha - \beta) \cdot (2 \cdot \beta - \gamma) \right) \cdot \chi_3$$

Equation 21.3-8

$$\Delta t^2 \cdot E\left(X, \ddot{X} \right) := \left(2 \cdot \gamma \cdot \left(\chi_1 - \beta^2 \right) - \beta \cdot \gamma^2 \right) \cdot \chi_3$$

Equation 21.3-9

$$\Delta t^2 \cdot E\left(\dot{X}^2 \right) := \left(2 \cdot \gamma^2 \cdot \left(2 - \alpha \right) + 4 \cdot \beta^2 \cdot \left(\beta - \gamma \right) \right) \cdot \chi_3$$

Equation 21.3-10

$$\Delta t^3 \cdot E\left(\dot{X}, \ddot{X} \right) := \left(4 \cdot \beta^2 \cdot \gamma - 2 \cdot \beta \cdot \gamma^2 \right) \cdot \chi_3$$

Equation 21.3-11

$$\Delta t^4 \cdot E\left(\ddot{X}^2 \right) := 4 \cdot \beta \cdot \gamma^2 \cdot \chi_3$$

Equation 21.3-12

Where,

$$\chi_1 := 2 \cdot \left(\alpha \cdot \beta - \gamma \right) + \alpha \cdot \gamma$$

Equation 21.3-13

$$\chi_2 := 2 \cdot \left(2 - \alpha \right) - \beta$$

Equation 21.3-14

$$\chi_3 := \frac{E\left(X_I \right)}{\chi_1 \cdot \chi_2}$$

Equation 21.3-15

Steady-state filters are a balance between tracking accuracy and noise suppression hence the choice of (α) is application dependent, and something of an art-form. The following emprical relationship is often used to set the filter gains instead of Equation 21.3-5,

$$\alpha := \left(\frac{b}{b+1} \right)^{1/3} \quad \text{where} \quad b := \frac{\ddot{P}_{o,t} \ \Delta t^2}{2 \cdot P_{o,t} \cdot \sigma_M}$$

Equation 21.3-16

Errington[E.1] suggests that (α) should be tuned to the maximum lateral acceleration capability of the target (A_{MAX}),

$$\left(\alpha \ , \ \beta \ , \ \gamma \right) :=$$

$$\left(\sqrt{\frac{A_{MAX} \cdot \Delta t^2}{2 \cdot \sigma_M + A_{MAX} \cdot \Delta t^2}} \ , \ \left(\frac{\alpha}{4} + \frac{\beta}{8} \right)^2 \ , \ \frac{\beta^2}{2 \cdot \alpha} \right)$$

Equation 21.3-17

Now consider the constant acceleration filter in the frequency domain,

$$\hat{X}(s) := \left(\frac{\omega_E \cdot \left(2 \cdot s^2 + 2 \cdot \omega_E \cdot s + \omega_E^2 \right)}{\left(s + \omega_E \right) \cdot \left(s^2 + \omega_E \cdot s + \omega_E^2 \right)} \right) \cdot \tilde{X}$$

Equation 21.3-18

$$\hat{\dot{X}}(s) := \left(\frac{s \cdot \left(2 \cdot \omega_E^2 \cdot s + \omega_E^3 \right)}{\left(s + \omega_E \right) \cdot \left(s^2 + \omega_E \cdot s + \omega_E^2 \right)} \right) \cdot \tilde{X}$$

Equation 21.3-19

$$\hat{\ddot{X}}(s) := \left(\frac{s^2 \cdot \omega_E^3}{\left(s + \omega_E \right) \cdot \left(s^2 + \omega_E \cdot s + \omega_E^2 \right)} \right) \cdot \tilde{X}$$

Equation 21.3-20

When expressing filter gains in terms of the Butterworth frequency (ω_E), the filter poles are identical and constrained to lie on the unit circle with a damping of 0.5. Its relationship with the KF and equivalent α–β–γ gains,

$$K := \left(\alpha \quad , \quad \frac{\beta}{\Delta t} \quad , \quad \frac{\gamma}{\Delta t^2} \right)$$

Equation 21.3-21

$$\left(\alpha \quad , \quad \beta \quad , \quad \gamma \right) :=$$

$$\left(1 - \exp\left(-2 \cdot \omega_E \cdot \Delta t \right) \quad , \quad 2 \cdot \left(2 - \alpha \right) - 4 \cdot \sqrt{1 - \alpha} \quad , \quad \frac{\beta^2}{4 \cdot \alpha} \right)$$

Equation 21.3-22

The relationship between the tracking index and butterworth frequency (ω_E),

$$\omega_E := \sqrt[3]{\frac{\sigma_S}{\sigma_M \cdot \Delta t}}$$

Equation 21.3-23

21.4 First Order Correlated Noise Filter

Arcasory[A.5] extended their work to include 1st order Gauss-Markov dynamics driven by piecewise continuous jerk. Using the same PI as in §21.2,

$$TI := 6 \cdot \left(1 - \tau_c^2 \cdot \Delta t + \frac{\tau_c}{2} \cdot \Delta t^2 - \tau_c^3 \cdot \exp\left(\frac{-\Delta t}{\tau_c} \right) \right) \cdot \frac{\sigma_S}{\sigma_M}$$

Equation 21.4-1

The optimal α–β–γ gains are complicated functions of the TI requiring the solution of a quartic function that are given in the paper by Arcasoy.

21.5 Second Order Correlated Filter

Sudano[S.16] extended his work to include 2nd order Gauss-Markov dynamics driven by piecewise continuous jerk. Using the PI defined in §21.2 the analysis resulted in a tracking index of,

$$TI := \frac{\dot{A}_{max} \cdot \Delta t}{\sigma_M}$$

Equation 21.5-1

The optimal α–β–γ gains are again complicated functions of this TI and its functional constraints and are given in the paper by Sudano. A more pragmatic approach to weaving targets based on stability criteria was taken by Vorley[V.3] using a fixed gain implementation of the 2nd order Markov model requiring the estimated target weave frequency (ω_W) resulting in the following equations in the frequency domain

$$\hat{X}(s) := \left(\frac{2 \cdot \omega_E \cdot s^2 + 2 \cdot \omega_E^2 \cdot s + \left(\omega_E^3 + \omega_E \cdot \omega_W^2 \right)}{s^3 + 2 \cdot \omega_E \cdot s^2 + \left(2 \cdot \omega_E^2 + \omega_W^2 \right) \cdot s + \left(\omega_E^3 + \omega_E \cdot \omega_W^2 \right)} \right) \cdot \tilde{X}$$

Equation 21.5-2

$$\hat{\dot{X}}(s) := \left(\frac{2 \cdot \omega_E^2 \cdot s + \left(\omega_E^3 - \omega_E \cdot \omega_W^2 \right)}{s^3 + 2 \cdot \omega_E \cdot s^2 + \left(2 \cdot \omega_E^2 + \omega_W^2 \right) \cdot s + \left(\omega_E^3 + \omega_E \cdot \omega_W^2 \right)} \right) \cdot \tilde{X}$$

Equation 21.5-3

$$\hat{\ddot{X}}(s) := \left(\frac{\left(\omega_E^3 - \omega_E \cdot \omega_W^2 \right) \cdot s^2 - 2 \cdot \omega_E^2 \cdot \omega_W^2 \cdot s}{s^3 + 2 \cdot \omega_E \cdot s^2 + \left(2 \cdot \omega_E^2 + \omega_W^2 \right) \cdot s + \left(\omega_E^3 + \omega_E \cdot \omega_W^2 \right)} \right) \cdot \tilde{X}$$

Equation 21.5-4

The equivalent discrete formulation with initialisation conditions,

$$\chi_1(k+1) := \chi_1(k) + \chi_2(k) \cdot \Delta t$$

Equation 21.5-5

$$\chi_2(k+1) := \chi_2(k) + \chi_3(k) \cdot \Delta t$$

Equation 21.5-6

$$\chi_3(k+1) := \chi_3(k) - (\varphi_2 - X_I(k)) \cdot \Delta t$$

Equation 21.5-7

$$\varphi_2 :=$$

$$\left(\omega_E^3 + \omega_E \cdot \omega_W^2\right) \cdot \chi_1(k) + \left(2 \cdot \omega_E^2 + \omega_W^2\right) \cdot \chi_2(k) + 2 \cdot \omega_E \cdot \chi_3(k)$$

Equation 21.5-8

$$X_{k+1} := -2 \cdot \omega_E^2 \cdot \omega_W^2 \cdot \chi_2(k+1) + \left(\omega_E^3 - \omega_E \cdot \omega_W^2\right) \cdot \chi_3(k+1)$$

Equation 21.5-9

$$\dot{X}_{k+1} := \left(\omega_E^3 - \omega_E \cdot \omega_W^2\right) \cdot \chi_2(k+1) + 2 \cdot \omega_E^2 \cdot \chi_3(k+1)$$

Equation 21.5-10

$$\ddot{X}_{k+1} :=$$

$$\left(\omega_E^3 + \omega_E \cdot \omega_W^2\right) \cdot \chi_1(k+1) + 2 \cdot \omega_E \cdot \left(\omega_E \cdot \chi_2(k+1) + \chi_3(k+1)\right)$$

Equation 21.5-11

$$\chi_2(k) := \frac{\left(\omega_E^3 - \omega_E \cdot \omega_W^2\right) \cdot \dot{X}_I(k) - 2 \cdot \omega_E^2 \cdot \ddot{X}_I(k)}{\left(\omega_E^3 - \omega_E \cdot \omega_W^2\right)^2 - 4 \cdot \omega_E^4 \cdot \omega_W^2}$$

Equation 21.5-12

$$\chi_3(k) := \frac{\ddot{X}_I(k) + 2 \cdot \omega_E^2 \cdot \omega_W^2 \cdot \chi_2(k)}{\omega_E^3 - \omega_E \cdot \omega_W^2}$$

Equation 21.5-13

$$\chi_1(k) := \frac{X_I(k) - 2 \cdot \omega_E^2 \cdot \chi_2(k) - 2 \cdot \omega_E \cdot \chi_3(k)}{\omega_E^3 + \omega_E \cdot \omega_W^2}$$

Equation 21.5-14

APPENDIX I

22 SIMULATION UTILITIES

Utility software is rarely afforded the importance it deserves when starting out to create research simulations on the scale described in this document. Often a proprietary source is used, or in haste utilities are ignored and disparate groups will forge software devoid of common facilities. The use of proprietary software limits portability, and hence a product's potential, as different host processors may not support a particular product, or the Customer may be unwilling to acquire the necessary software licences.

These difficulties have been avoided by creating a software library containing utilities customised to suite the combined disciplines within this application. Customised utilities are generally simpler, and often quicker, than more general utilities that contain facilities that are not applicable but are non-the-less executed. It also means that the method of data transfer between the utilities and core models can be controlled. In this respect the use of the "global" common block (GCB) is severely restricted as this defeats the principle of transferable modules; augment lists being the preferred mode of data transfer.

The utility software forms the backbone of this research simulation, and by inheritance the AMIS. The design ethos for both was such that if the same function was performed more than once it was classified as generic requiring a utility. In most cases this has resulted in utilities comprising single, simple functions. The utility software modules are stored by functional group. The downside of creating a separate utility library is the cost of testing. Fortunately, as this software has been used in the development of MBDA products it has received a considerable amount of testing.

22.1 Utility CMS Groups

22.1.1 General Utilities

CMS group [GENERAL]

General utilities comprise 23 system clocks ranging from 1Hz to 8kHz split from a 16 kHz Master Clock; Runge-Kutta state integration (order 1-4); function gradients; random number generators (Normal, Uniform, Rayleigh and Bi-normal); statistical analysis package used by the interactive interface; function and surface interpolation modules.

System Clock Update	Time and Date Stamp
Runge-Kutta Integration	Recursive Statistical Analyser
Real Variable Comparator	Integer Word Bit Manipulation
Random Number Generator	1D Linear Interpolation
PRBS Initialisation	2D Bi-Linear Interpolation
Normal Distributed Variables	Numerical Differentiation
Bi-modally Distributed Variables	ASCII to Integer Re-formatting
Uniformly Distributed Variables	Convex Surface Testing
Rayleigh Distributed Variables	Integer Word Single Bit Delay
Simulation PRBS Noise Sequences	

22.1.2 WGS 84, Target and Missile Data

CMS group [GEOMETRY]

Simulation speed has been sacrificed to provide commonly used point-mass kinematics. This information is refreshed at a rate in excess of any practical system implementation so as to promote rapid algorithm development. The data is derived from the reference states and, where possible, from state observer output. The simulation variables relating to this data have been selected as prescribed in the Glossary with those derived from the observer states prefixed by"F_".

Closest Approach Detection and Reporting	Missile Kinematics
Geodetic Referenced Parameters	Missile/Target Relative Inertial Kinematics
Target Kinematics	Relative Missile and Target Kinematics

22.1.3 Axis Transformations

CMS group [AXTRAN]

These utilities deal with the conversion between Cartesian and Polar co-ordinates, and transformation matrix direction cosines. They cover the projection of vectors onto the principal planes of a frame, and the angle subtended by the rotation of one frame with respect to another.

Cartesian to Euler YP Transformation	Transformation x Skew Matrix Product
Cartesian to Euler RP Transformation	Vector Projection onto Reference Planes
Euler YP to Euler RP Transformation	Euler YP to Solid Angle Transformation
Euler RP to Euler YP Transformation	Euler RP to Solid Angle Transformation
Euler YP to Cartesian Transformation	Differential Angle
Euler RP to Cartesian Transformation	Transformation Angle
Euler YPR to DC Transformation	Differential Angular Rate
Euler RPY to DC Transformation	Given's Transformations
DC to Euler YPR Transformation	Euler YPR Small Angle Transform Approx.
Cartesian to DC Transformation,	Cartesian Direction Cosine Jacobian
DC to Cartesian Transformation	Euler YPR Direction Cosine Jacobian
Skew x Transformation Matrix Product	

22.1.4 Point Mass Kinematics

CMS group [KINEMATICS]

These utilities deal with the dynamics of a particle with respect to a given frame of reference, and conversion between Euler and angular kinematic data.

Propagation of Linear Dynamic States	Angular to Euler (YPR) Rates
Propagation of Angular Dynamic States	Euler to Angular Accelerations
Average Angular Rates from Direction Cosines	Angular to Euler Accelerations
Dynamics of a Point in Inertial Space	Cartesian to Euler Rates
Euler to Angular Rates	Cartesian to Euler Acceleration

22.1.5 Earth, Atmosphere & Gravity

CMS group [EARTH]

These utilities provide those earth characteristics that that ae required when describing the dynamics of vehicles moving with respect to the Earth, and the transformation between the Earth frame and LGA.

Atmospheric Parameters	Conversion from ECEF to WGS84 Co-ordinates
Earth Curvature Parameters	Conversion from WGS84 to ECEF Co-ordinates
Gravitational Acceleration	

22.1.6 Digital Map Data Extraction

CMS group [MAPS]

These utilities provide the height of the ground and local ground slopes needed for nap-of-the-Earth navigation, radar altimeters over land, and

terrain following NAVSTAR GPS satellite obscuration models. They process MBDA(UK) reformatted DLMS map data.

Map Data Initialisation	Map Data Interpolation
Map Square Selection	

22.1.7 Digital Filters

CMS group [FILTERS]

These utilities provide a toolbox of filters and like functions, i.e. limiters, quantisers, interface functions, etc. required for digital systems modelling.

Digital First Order Lag Filters	Digital Interface 2s Complement Wrap Filter
Digital First Order Lead Filters	Real Parameter Limiting
Digital Lead-Lag Filters	Integer Parameter Limiting
Digital Integration Filters	Parameter Quantisation
Digital Notch Filters	Time Delay
Digital Second Order Lag Filters	Covariance Matrix Transformation
Digital $\alpha-\beta-\gamma$ Filters	State Transition Matrix
Tuned Digital $\alpha-\beta-\gamma$ Filters	Angular Range Limiter
Digital $\alpha-\beta-\gamma$ Filter Covariances	Rate Limiter
Analogue to Digital Converter Noise	Digital State Space Update
Digital to Analogue Converter Noise	Parameter Range Check
Digital Interface Filter	Digital Butterworth Filters

22.1.8 Matrix Utilities

CMS group [MATRICES]

Matrix utilities undertake the majority of the number crunching in much the same way as in MATLAB. The generic approach to matrix computations for rapid algorithm development ignores sparseness and is therefore less efficient than it might be in some cases. They include utilities for the extraction and insertion of sub-matrices, and manipulation of covariance matrices often required in practical stochastic filtering.

Constant x Matrix Product	Matrix Transpose
Matrix Addition	Matrix Unity
Matrix Determinant	Matrix x Vector Product
Matrix Image	Matrix Zero
Matrix Initialisation	Skew Symmetric Matrix Squared from a Vector
Matrix Inversion	Matrix Element-by-Element Product
Matrix Product	Matrix Symmetry
Matrix Product (Pre-Multiplier Transposed)	Matrix Positive Define Testing

Matrix Product (Post-Multiplier Transposed)	Matrix of Correlation Coefficients
Matrix Product (Pre & Post Transposed)	Matrix Eigen Analysis
Matrix Subtraction	Matrix Insertion
Matrix Trace	Matrix Extraction

22.1.9 Quaternion Utilities

CMS group [QUATERNIONS]

These utilities manipulate quaternions in the context of frames, time rate of change, and gradients with respect to their individual scalar and vector components.

Quaternion Conjugation	Quaternion Propagation by Euler Angle Increments
YPR Euler Angles to Quaternions	Quaternion Transformation Matrix
Quaternion Product	Quaternion Vector Transform
Quaternion Normalisation	Quaternion from Direction Cosines
Quaternion Propagation	Direction Cosine Jacobians
Quaternion Error Propagation	

22.1.10 Trigonometric Functions

CMS group [TRIG]

When developing algorithms the host mathematical library is usually the source of the trigonometrical functions used. For application software faster computation of these functions is often required, albeit with a reduced accuracy. These utilities give a reasonable level of accuracy with minimal computational effort.

Sine Approximation	Arc-cosine Approximation
Cosine Approximation	Arc-tangent Approximation (Single Argument)
Tangent Approximation	Arc-tangent Approximation (Two Arguments)
Arc-sine Approximation	

22.1.11 Vector utilities

CMS group [VECTORS]

These utilities complement the matrix utilities, although the latter are often used a dimension set to one. Vector utilities have a lower computational loop overhead and are design so that a subset of a vector can be manipulated in isolation.

Angle Between Vectors	Vector X-Z Magnitude

Constant x Vector Product	Vector Negation
Vector Addition	Vector Subtraction
Vector Cross Product	Vector Triple Product
Scalar Product	Vector Zero
Vector Image	Vector Summation
Vector Magnitudes	Vector Extraction from a Matrix
Vector Spherical Magnitude	Vector Insertion
Vector X-Y Magnitude	Vector Extraction
Vector Y-Z Magnitude	

22.1.12 Covariance Extraction

CMS group [COVARS]

State observation analysis requires utilities for determining the uncertainty in parameters that are functions of the state, i.e. covariance extraction. The utilities provided determine the uncertainty in commonly used parameters that are a function of the state observer. They perform covariance transformation from one representation, or frame, to another; and provide performance metrics that are covariance data dependent.

Quaternion to Euler angle Variance Transform	Pitch Rate Uncertainty
Range Uncertainty	Differential Angle Uncertainty
Range Rate Uncertainty	Differential Angular Rate Uncertainty
Yaw Angle Uncertainty	Polar to Cartesian Covariance Conversion
Pitch Angle Uncertainty	Covariance Matrix Main Diagonal Extraction
Velocity Vector Yaw Angle Uncertainty	Covariance Matrix Eigenvalue Metric
Velocity Vector Pitch Angle Uncertainty	Covariance Tracking Metric
Yaw Rate Uncertainty	Mahalanobis Distance Metric
	Circular Error Probable (CEP) Metric

22.2 General Utilities

22.2.1 System Clock Update

Provision for up to 50 system clocks of which 23 are currently in use, each initialised to a different cyclic rate in *CONSTANTS*. The Master Clock runs at 16 kHz from which the sub-system clocks are derived. Thus the simulation reference time interval (Δt_R) has a fixed value of 62.5 μs. To prevent time quantisation only clocks that are 16 kHz dividers are permitted.

Table 22-1 : Simulation Clock Frequencies

CLOCK (n)	RATE ω_C (Hz)	CLOCK (n)	RATE ω_C (Hz)	CLOCK (n)	RATE ω_C (Hz)
1	8000	9	400	17	20
2	4000	10	200	18	10
3	3200	11	125	19	8
4	2000	12	100	20	5
5	1600	13	80	21	4
6	1000	14	50	22	2
7	800	15	40	23	1
8	500	16	25	*NUPDAT* := 23	

The clocks are synchronised during initialisation so that their leading edges are aligned. When the clocks are reset this represents their leading edge to which all simulation models are latched. During initialisation the clock rates in Table 22-1 are converted into the number of simulation reference cycles in *I_TIMING*. These indices control the clock reset and are stored in the 2nd column of array *UPDATE*(n,2) U(n,2), where (n) is the clock identifier. For the time period after initialisation [0 , Δt_R [,

$$U(n,1)_{k:=1} := 1$$

Equation 22.2-1

$$\omega_{CLK} < \text{nint}\left(1 / \Delta t_R\right) \Rightarrow U(n,2) := \text{nint}\left(\frac{1}{\omega_{CLK} \cdot \Delta t_R}\right)$$

Equation 22.2-2

$$\omega_C \geq \text{nint}\left(1 / \Delta t_R\right) \Rightarrow U(n,2) := \text{nint}\left(1 / \Delta t_R\right)$$

Equation 22.2-3

Vector *TUPDAT*(n) T(n) remains constant once initialised and contains the time interval between clock leading edges,

$$T(n) := \Delta t_R \cdot U(n,2)$$

Equation 22.2-4

At the start of each 16 kHz reference cycle the clocks are updated in *CLOCK_UPDATE*. For the time period t(k-1) to t(k), a duration of (Δt_R),

$$U(n,1)_{k-1} = U(n,2) \Rightarrow U(n,1)_k := 1$$

Equation 22.2-5

$$U(n,1)_{k-1} < U(n,2) \Rightarrow U(n,1)_k := U(n,1)_{k-1} + 1$$

Equation 22.2-6

22.2.2 Runge-Kutta Integration

Four Runge-Kutta integration modules, *RK_1*, *RK_2*, *RK_3* and *RK_4* are provided, the number referring to the integration order. By default the reference state vector is propagated using *RK_2*, which can be interactively changed by setting the order of *INTORD* to a value in the range [1(1)4]. For this application the reference-state vector and associated state derivative vector are listed in Table 5-1. The state vector is partitioned so that sub-sets can be propagated depending on the embedded simulator invoked, e.g. when undertaking target trajectory analysis only the target states are required. The partitioning of the state vector is controlled by setting [*NSTATL*(1)*NSTATH*] defaulting to the entire state vector [1(1)28] if no user input is received.

State integration takes place over the reference time interval *TIMSTP* (Δt_R). Each integration routine calls *DX_CONTROL* the state derivative controller. The state derivatives are updated using a state vector appropriate to the sub-interval time; the stage of the Runge-Kutta algorithm identified by *INDEXI* in the range [1(1)4]. At the start of an integration step, after the state derivatives have been determined, *OUTPUT_CONTROL* is called. The simulation output is captured at a time (t) in the integration process when all the data exists at a common time. Thereafter the integration algorithm propagates the state vector from time (t) to time ($t+\Delta t_R$). The reference state vector is propagated using either:

22.2.2.1 First Order Integration (RK_1)

$$\underline{X}(t + \Delta t_R) := \underline{X}(t) + \dot{\underline{X}}(\underline{X}(t), t)$$

Equation 22.2-7

22.2.2.2 Second Order Integration (RK_2)

$$\underline{X}(t + \Delta t_R) := \underline{X}(t) + 2^{-1} \cdot \Delta t_R \cdot \varphi_1$$

Equation 22.2-8

$$\varphi_1 \coloneqq \dot{\underline{X}}\left(\underline{X}\left(t\right), t\right) + \dot{\underline{X}}\left(\underline{X}\left(t\right) + \dot{\underline{X}}\left(\underline{X}\left(t\right), t\right) \cdot \Delta t_R\ , t + \Delta t_R\right)$$

Equation 22.2-9

22.2.2.3 Third Order Integration (RK_3)

$$\underline{X}\left(t + \Delta t_R\right) \coloneqq \underline{X}\left(t\right) + 6^{-1} \cdot \Delta t_R \cdot \varphi_2$$

Equation 22.2-10

$$\varphi_2 \coloneqq \dot{\underline{X}}\left(\underline{X}\left(t\right), t\right) + 4 \cdot \xi + \dot{\underline{X}}\left(\underline{X}\left(t\right) + \Delta t_R \cdot \left(2 \cdot \xi - \dot{\underline{X}}\left(\underline{X}\left(t\right), t\right)\right), t\right)$$

Equation 22.2-11

$$\xi \coloneqq \dot{\underline{X}}\left(\underline{X}\left(t\right) + 2^{-1} \cdot \Delta t_R \cdot \dot{\underline{X}}\left(\underline{X}\left(t\right), t\right), t + 2^{-1} \cdot \Delta t_R\right)$$

Equation 22.2-12

22.2.2.4 Fourth Order Integration (RK_4)

$$\underline{X}\left(t + \Delta t\right) \coloneqq \underline{X}\left(t\right) + 6^{-1} \cdot \Delta t_R \cdot \varphi_3$$

Equation 22.2-13

$$\varphi_3 \coloneqq \dot{\underline{X}}\left(\underline{X}\left(t\right), t\right) + \cdots$$

$$\cdots + 2 \cdot \left(\dot{\underline{X}}\left(\xi_1, t + 2^{-1} \cdot \Delta t_R\right) + \dot{\underline{X}}\left(\xi_2, t + 2^{-1} \cdot \Delta t_R\right)\right) + \dot{\underline{X}}\left(\xi_3, t + \Delta t_R\right)$$

Equation 22.2-14

$$\xi_1 \coloneqq \underline{X}\left(t\right) + 2^{-1} \cdot \Delta t_R \cdot \dot{\underline{X}}\left(t\right)$$

Equation 22.2-15

$$\xi_2 \coloneqq \underline{X}\left(t\right) + 2^{-1} \cdot \Delta t_R \cdot \dot{\underline{X}}\left(\xi_1, t + 2^{-1} \cdot \Delta t_R\right)$$

Equation 22.2-16

$$\xi_3 \coloneqq \underline{X}\left(t\right) + \Delta t_R \cdot \dot{\underline{X}}\left(\xi_2, t + \Delta t_R\right)$$

Equation 22.2-17

22.2.3 Real Variable Comparator

Function *R_T* tests the equality of real variables by taking the absolute difference between (A) and a reference value (B) returning zero if the result is ≤ (C), or 1 otherwise.

$$y \coloneqq \mathbf{R\_T}\left(A, B, C\right)$$

Equation 22.2-18

$$\left| A - B \right| \leq C \quad \Rightarrow \quad y \quad := \quad 0$$

Equation 22.2-19

$$\left| A - B \right| > C \quad \Rightarrow \quad y \quad := \quad 1$$

Equation 22.2-20

For 64 bit arithmetic threshold (C) := 10^{-15}, and 10^{-8} for 32 bit arithmetic.

22.2.4 Random Number Generator

RANDOM initialises and updates 1000 unique Pseudo-Random Binary Sequences (PRBS), returning a randomly distributed real variable (y) from the sequence identified by (N), where N [1(1)1000].

$$y \quad := \quad \textbf{RANDOM} \left(N , M , A , B \right)$$

Equation 22.2-21

The function seeds each PRBS with an odd integer number de-correlated from the previous seed. Four statistical distributions are available characterised using (A) and (B), and selected by setting (M) as follows:

- M := 0 : Gaussian Distribution
- M := 1 : Bi-modal Gaussian Distribution
- M := 2 : Uniform Distribution
- M := 3 : Rayleigh Distribution

The function first tests (M). If it is not in the range [0(1)3] a fault report is written to the ASCII output file and the simulation is terminated. A fault is reported and the simulation stopped if the master seed (S_0) provided by the user is set to zero in the external data file.

22.2.4.1 PRBS Initialisation

The Master Seed (S_0) is read from external data file (*.DAT) into *ISEED*, the transfer effected using the GCB, converted if necessary to an integer, and stored in *ISEED0*. *ISEED* is then changed during the initialisation of a 1000 element vector *SIGNV* that contains randomly numbers from the normal distribution N (B := 0 , A := 1) generated by *GAUSS*:

$$N \left(B , A \right) \quad \equiv \quad \textbf{GAUSS} \left(S , A , B , C \right)$$

Equation 22.2-22

$$65539 \cdot S_{i-1} < 0 \quad \Rightarrow \quad S_i \quad := \quad 65539 \cdot S_{i-1} + 2147483648$$

Equation 22.2-23

$$65539 \cdot S_{i-1} \geq 0 \quad \Rightarrow \quad S_i \coloneqq 65539 \cdot S_{i-1}$$

Equation 22.2-24

$$C \coloneqq A \cdot \left(\left[\sum_{i:=1}^{12} \left(S_i \cdot 4.656613 \cdot 10^{-10} \right) \right] - 6 \right) + B$$

Equation 22.2-25

GAUSS returns a Gaussian distributed random variable (C) from the pdf,

$$p(C) \coloneqq \frac{1}{A \cdot \sqrt{2 \cdot \pi}} \cdot \exp\left(-\frac{(C - B)^2}{2 \cdot A^2} \right)$$

Equation 22.2-26

The exponential represents a scaling so that the cumulative probability, the integral of p(C) over $C \in [-\infty,\infty]$, is 1; the peak of p(C) being $1/\sqrt{2\pi}$ at (B). The following special values are useful when analysing stochastic filters,

$$p(C \in [-1,1]) \coloneqq 0.6837$$

Equation 22.2-27

$$p(C \in [-2,2]) \coloneqq 0.9545$$

Equation 22.2-28

$$p(C \in [-3,3]) \coloneqq 0.9973$$

Equation 22.2-29

When initialising *SIGNV* the seed from *GAUSS* is used,

$$S_0(1) \coloneqq S_0$$

Equation 22.2-30

$$k \in [1(1)999] \quad \Rightarrow \quad S_0(k+1) \coloneqq S_{12}(k)$$

Equation 22.2-31

GAUSS uses integer overflow to generate random numbers and must be compiled with overflow checking disabled. Initialisation of the random number generator is completed by taking $S_{12}(1000)$ and using it to seed 1000 sequences stored in vector *IRAND*. During this process the seeds returned by *GAUSS* are manipulated as follows,

$$S_0(1001) \coloneqq S_{12}(1000)$$

Equation 22.2-32

$$\left(S_{12}\left(k \right)+1 \right) \in \left\{ \text{odd integers} \right\} \Rightarrow S_0\left(k+1 \right) := S_{12}\left(k \right)+1$$

Equation 22.2-33

$$\left(S_{12}\left(k \right)+1 \right) \in \left\{ \text{even integers} \right\} \Rightarrow S_0\left(k+1 \right) := S_{12}\left(k \right)+2$$

Equation 22.2-34

If Monte-Carlo mode is invoked $S_0(2001)$ is written to an external ASCII file to be used as the Master Seed for the next program execution.

22.2.4.2 Normal Distributed Variables

When (M := 0) *RANDOM* using *GAUSS* to refresh the random seed in *IRAND*(N) and obtain the next value of (C) in the PRBS identified by (N) taken from the Gaussian distribution N(B,A),

$$\textbf{GAUSS}\left(\text{IRAND}\left(N \right), A, B, C \right)$$

Equation 22.2-35

22.2.4.3 Bi-modally Distributed Variables

When (M := 1) *RANDOM* returns a value from a bi-modal distribution, i.e. a Gaussian distribution reflected about zero, with median values at (B) and a standard deviation about each of (A). Using N(B,A) there is a small but finite statistical probability at zero. The process is the same as for normally distributed variables, however,

$$C := C \cdot \text{sign}\left(1, \mathit{SIGNV}\left(N \right) \right)$$

Equation 22.2-36

22.2.4.4 Uniformly Distributed Variables

When (M := 2) *RANDOM* uses *UNIFORM* to return a uniformly distributed random variable (C) in the range [A,B], whilst updating seed *IRAND*(N).

$$\textbf{UNIFORM}\left(\text{IRAND}\left(N \right), A, B, C, \text{LUNOUT} \right)$$

Equation 22.2-37

$$65539 \cdot S_i < 0 \Rightarrow S_{i+1} := 65539 \cdot S_i + 2147483648$$

Equation 22.2-38

$$65539 \cdot S_i \geq 0 \Rightarrow S_{i+1} := 65539 \cdot S_i$$

Equation 22.2-39

$$C := A + S_{i+1} \cdot 4.656613 x 10^{-10} \cdot (B - A)$$

Equation 22.2-40

The uniformly distributed variable (C) is taken from the pdf,

$$C \in [A,B] \Rightarrow p(C) := (B - A)^{-1}$$

Equation 22.2-41

$$C \notin [A,B] \Rightarrow p(C) := 0$$

Equation 22.2-42

UNIFORM generates random numbers using integer overflow and must be compiled without overflow checking. If (AB) a fault report is written to the ASCII output file (channel *LUNOUT*) and the simulation is terminated.

22.2.4.5 Rayleigh Distributed Variables

When (M := 2) *RANDOM* uses *RAYLEIGH* to return a Rayleigh distributed random variable (C) defined by (A), (B) is not used, whilst updating seed *IRAND*(N).

RAYLEIGH (*IRAND*(N) , A , C)

Equation 22.2-43

RAYLEIGH invokes *UNIFORM* to update the seed and provide a uniformly distributed random variable in the range $[10^{-15},1-10^{-15}]$, denoted in the following equations by U[0,1] for convenience, transformed into a Rayleigh distributed random variable,

$$C := \sqrt{-2 \cdot \ln(U[0,1])}$$

Equation 22.2-44

The Rayleigh distributed variable (C) is taken from the pdf,

$$C > 0 \Rightarrow p(C) := \frac{C}{A^2} \cdot \exp\left(-\frac{C^2}{2 \cdot A^2}\right)$$

Equation 22.2-45

$$C \leq 0 \Rightarrow p(C) := 0$$

Equation 22.2-46

22.2.5 Time and Date Stamp

TIME_DATE extracts the time and date from the host operating system using the DEC *SYSDATE* and *SYSTIME* functions.

$$y := \textbf{TIME\_DATE}\ (\ TIMDAT\ )$$

Equation 22.2-47

TIMDAT is a 20 character string comprising:

- Date characters [1(1)9]
- Space character [10]
- Time characters [11(1)18]

A flag indicating that this function has been correctly executed is returned in the function name, in which case (y := 1).

22.2.6 Recursive Statistical Analyser

VAR_STATS samples the GCB real variable whose vector location is identified by *VAR_STAT*. It returns the number of samples used in the statistical analysis (*VAR_N*), the sample mean (*VAR_AVG*), standard deviation (*VAR_SD*), and rms value (*VAR_RMS*). The interface between *VAR_STATS* and the simulation is the GCB. The recursive values of the statistical outputs are derived using,

$$\left\{ \overline{X}_N \ , \ Y \right\} := \left\{ \frac{1}{N} \cdot \sum_{k:=1}^{N} \left(X_k \cdot S \right) \ , \ \frac{1}{N} \cdot \sum_{k;=1}^{N} \left(X_k \cdot S \right)^2 \right\}$$

Equation 22.2-48

$$Y - \overline{X}_N^2 > 10^{-15} \ \Rightarrow \left\{ \begin{array}{l} \left(\sigma_X \right)_N := \sqrt{Y - \overline{X}_N^2} \\ \\ \left(rms_X \right)_N := \sqrt{Y} \end{array} \right\}$$

Equation 22.2-49

$$Y - \overline{X}_N^2 \leq 10^{-15} \ \Rightarrow \left\{ \begin{array}{l} \left(\sigma_X \right)_N := 0 \\ \\ \left(rms_X \right)_N := 0 \end{array} \right\}$$

Equation 22.2-50

(S) is a scaling factor applied by PRIPLO when converting simulation parameters from SI into engineering units. Recursive analysis is controlled by *ST_FLAG*. When set to 1 the variable is sampled and statistical analysis

performed at the interactive windows refresh rate (*WIN_RATE*). When set to 0 the statistics are not updated and remain constant until re-initialisation. Re-initialised occurs under the following conditions:

$$\left(\left(\mathrm{F_k} = 0\right) \wedge \left(\mathrm{F_{k-1}} = 1\right)\right) \vee \left(\left(\mathrm{F_k} = \mathrm{F_{k-1}}\right) \wedge \left(\mathrm{V_k} \neq \mathrm{V_{k-1}}\right)\right) \Rightarrow$$

$$\left(\mathrm{N}, \overline{\mathrm{X}}, \mathrm{Y}, \sigma_{\mathrm{x}}, \mathrm{rms_X}\right) := \underline{0}_5$$

Equation 22.2-51

If (*VAR_STAT* $\notin$ [1(1)max]), where "max" is the size of the real GCB, the statistical computations are suspended, re-commence only when the range check is satisfied.

22.2.7 Integer Word Bit Manipulation

UT_COMB takes a 32 bit integer (X) and returns it with bits [j(1)j+n-1] set to the integer value (Z), the remaining bits are unchanged.

$$\mathrm{y} := \textbf{UT\_COMB}\left(\mathrm{X}, \mathrm{N}, \mathrm{J}, \mathrm{Z}, \mathrm{LUNOUT}, \mathrm{ISTOP}\right)$$

Equation 22.2-52

$$\mathrm{y}\left[0\left(1\right)\mathrm{j}-1\right] := \mathrm{X}\left[0\left(1\right)\mathrm{j}-1\right]$$

Equation 22.2-53

$$\mathrm{y}\left[\mathrm{j}\left(1\right)\mathrm{j}+\mathrm{n}-1\right] := \mathrm{Z}$$

Equation 22.2-54

$$\mathrm{y}\left[\mathrm{j}+\mathrm{n}\left(1\right)31\right] := \mathrm{X}\left[\mathrm{j}+\mathrm{n}\left(1\right)31\right]$$

Equation 22.2-55

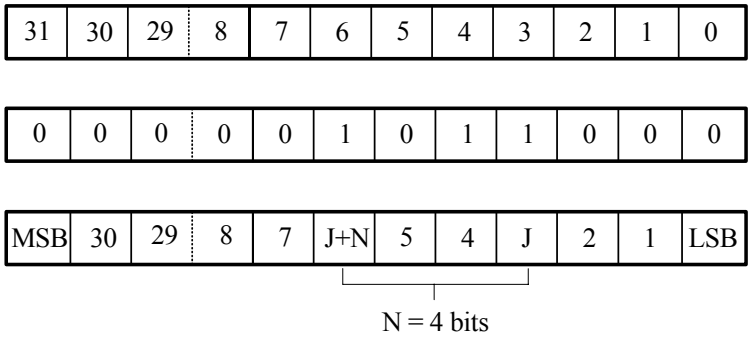

Figure 22-1 : Integer Word BIT Manipulation

Figure 22-1 shows the effect of this utility on word (X) that is initially zero, although any value could be used, invoked by,

$$y \;:=\; \textbf{UT\_COMB}\left(X, 4, 3, 11, \text{LUNOUT}, \text{ISTOP} \right)$$

Equation 22.2-56

In this example (n := 4) bits are modified, starting with bit (j := 3) and the value 11 inserted. The remaining bits [0(1)2] and [7(1)31] are unchanged. The flag *ISTOP* is set after delivering a diagnostic message to the ASCII data file via channel *LUNOUT* when,

$$\left(N < 1 \right) \vee \left(J < 1 \right) \vee \left(Z < 1 \right) \vee \left(N > \left(31 - J + 1 \right) \right) \vee \left(Z > 2^N \right)$$

$$\Rightarrow \quad ISTOP \;:=\; 1$$

Equation 22.2-57

22.2.8 One Dimensional Linear Interpolation

TB_1 takes a set of (n) variably spaced {(X,Y)} co-ordinates with the independent variable (X) arranged in monotonically increasing order. Given the independent variable (X_P) the function returns the dependent variable (Y_P) using linear interpolation, without extrapolation beyond the table boundary, as shown in Figure 22-2.

$$Y_p \;:=\; \textbf{TB\_1}\left(\{X\}, \{Y\}, N, X_P, \text{LUNOUT}, \text{ISTOP} \right)$$

Equation 22.2-58

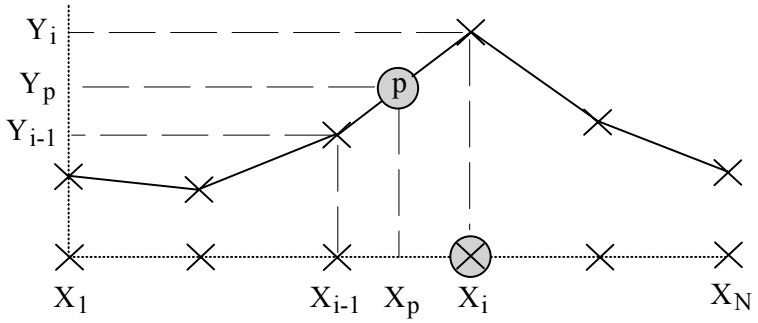

Figure 22-2 : One Dimensional Interpolation

The following input data consistency check is applied.

$$X_P \notin \left[X_1, X_N \right] \;\Rightarrow\; ISTOP \;:=\; 1$$

Equation 22.2-59

If a fault is detected a report is written to the ASCII output file via communication channel *LUNOUT* and *ISTOP* is set. On passing this input range check,

$$Y_P := \left(\frac{X_i - X_P}{X_i - X_{i-1}} \right) \cdot Y_{i-1} + \left(1 - \frac{X_i - X_P}{X_i - X_{i-1}} \right) \cdot Y_i$$

Equation 22.2-60

22.2.9 Two Dimensional Bi-Linear Interpolation

TB_2 takes a set of (n,m) variably spaced (X,Y,Z) co-ordinates with the independent variables (X,Y) arranged in monotonically increasing order. Given independent variables (X_P,Y_P) the function returns the dependent variable (Z_p) using bi-linear interpolation, without extrapolation beyond the table boundaries, as shown in Figure 22-3.

$$Z_p := \textbf{TB\_2} \left(\{X\}, \{Y\}, \{Z\}, N, M, X_P, Y_P, \text{LUNOUT}, \text{ISTOP} \right)$$

Equation 22.2-61

The following input data consistency check is applied.

$$\left(X_P \notin [X_1, X_N] \right) \vee \left(Y_P \notin [Y_1, Y_M] \right) \Rightarrow ISTOP := 1$$

Equation 22.2-62

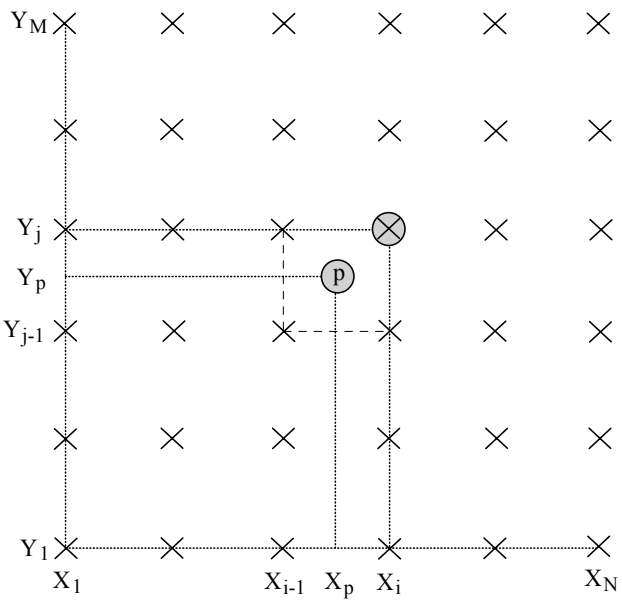

Figure 22-3 : Two Dimensional Interpolation

If a fault is detected a report is written to the ASCII output file via channel *LUNOUT* and *ISTOP* is set. On passing the input range check,

$$\xi_1 \;:=\; \varphi_X \cdot Z_{i-1,\,j-1} + \left(1 - \varphi_X \right) \cdot Z_{i,\,j-1}$$

Equation 22.2-63

$$\xi_2 \;:=\; \varphi_X \cdot Z_{i-1,\,j} + \left(1 - \varphi_X \right) \cdot Z_{i,\,j}$$

Equation 22.2-64

$$Z_P \;:=\; \varphi_Y \cdot \xi_1 + \left(1 - \varphi_Y \right) \cdot \xi_2$$

Equation 22.2-65

$$\left\{ \varphi_X \;,\; \varphi_Y \right\} \;:=\; \left\{ \left(\frac{X_i - X_P}{X_i - X_{i-1}} \right) \;,\; \left(\frac{Y_i - Y_P}{Y_i - Y_{i-1}} \right) \right\}$$

Equation 22.2-66

22.2.10 Numerical Differentiation

DY_BY_DX takes five evenly spaced values (Y_{-2},Y_{-1},Y_0,Y_1,Y_2), the interval between them (ΔX), and the order of the difference equation required (I_{ORD}) in the range [1(1)3], and returns the slope at (X_0).

$$\dot{\varphi}\left(X_0 \right) \;:=\; \textbf{DY\_BY\_DX} \left(I_{ORD} , Y_{-2} , Y_{-1} , Y_0 , Y_1 , Y_2 , \Delta X \right)$$

Equation 22.2-67

$$I_{ORD} = 1 \;\Rightarrow\; \Delta X \cdot \dot{\varphi}\left(X_0 \right) \;:=\; Y_0 - Y_{-1}$$

Equation 22.2-68

$$I_{ORD} = 2 \;\Rightarrow\; 2 \cdot \Delta X \cdot \dot{\varphi}\left(X_0 \right) \;:=\; Y_{+1} - Y_{-1}$$

Equation 22.2-69

$$I_{ORD} = 3 \;\Rightarrow\; 12 \cdot \Delta X \cdot \dot{\varphi}\left(X_0 \right) \;:=\; Y_{-2} - 8 \cdot Y_{-1} + 8 \cdot Y_{+1} - Y_{+2}$$

Equation 22.2-70

22.2.11 ASCII to Integer Re-formatting

C_TO_I takes a 5 character string (X) representing a number in the range [1(1)9999] including leading blanks, and returns a 32 bit integer value in the range [0(1)9999].

$$y \;:=\; \textbf{C\_TO\_I} \left(X \right)$$

Equation 22.2-71

The algorithm used converts the text, including leading blanks, into an integer in the aforementioned range,

$$y \;:=\; \sum_{i:=2}^{5} \left(\mathrm{ICHAR}\left(X_i \right) - 48 \right) \cdot \delta \cdot 10^{5-i}$$

Equation 22.2-72

(i) is the position of each character in the string, (i := 1) being the first character and (i := 5) the last. *ICHAR* returns the numerical value of the ASCII input. (δ) is defined by,

$$\mathrm{ICHAR}\left(X_i \right) = \text{"blank"} \;\Rightarrow\; \delta \;:=\; 0$$

Equation 22.2-73

$$\mathrm{ICHAR}\left(X_i \right) \neq \text{"blank"} \;\Rightarrow\; \delta \;:=\; 1$$

Equation 22.2-74

22.2.12 Convex Surface Testing

CONVEX returns a flag indicating whether the n-dimensional hyper-surface in (n+1)-dimensional hyper-space resulting in the input (X) compared with the positive threshold (T) is concave, convex, or flat.

$$y \;:=\; \mathbf{CONVEX}\left(X, T \right)$$

Equation 22.2-75

$$X \leq T \;\Rightarrow\; y \;:=\; -1$$

Equation 22.2-76

$$X \in \left] -T, T \right[\;\Rightarrow\; y \;:=\; 0$$

Equation 22.2-77

$$X \geq T \;\Rightarrow\; y \;:=\; +1$$

Equation 22.2-78

22.2.13 Integer Word Single Bit Delay

BIT_DELAY returns integer input (X) with the value of bit (m) delayed by (t_D) seconds.

$$y \;:=\; \mathbf{BIT\_DELAY}\left(X, M, t_D, \Delta t, N \right)$$

Equation 22.2-79

TIME_DELAY with arguments (X_I , t_D , Δt , N) delays the value of bit (m) shown in Figure 22-4,

$$\left(\text{bit } X\left(M \right) \text{ set} \right) \Rightarrow X_I := 1$$

Equation 22.2-80

$$\left(\text{bit } X\left(M \right) \neg \text{set} \right) \Rightarrow X_I := 0$$

Equation 22.2-81

$$y = X \left\{ \begin{array}{|c|c|c|} \hline \text{bits [31 , M+1]} \\ \text{unchanged} \end{array} \right. \left. \begin{array}{|c|} \hline \text{bit [M(t)] =} \\ \text{bit [M(t-t}_D\text{)]} \end{array} \right. \left. \begin{array}{|c|} \hline \text{bits [M-1 , 0]} \\ \text{unchanged} \end{array} \right\}$$

Figure 22-4 : Bit Manipulation

22.3 WGS 84, Target and Missile Data

The simulation utilises many target and missile dynamic parameters that are derived from the reference state vector. Although these parameters can be derived in-situ as a need arises, their computation is centralised so that they are easier control and modify. The modules involved in this process are not strictly utilities since they have been developed for a specific purpose. However, they demonstrate how the utilities are combined to generate the kinematic parameters required.

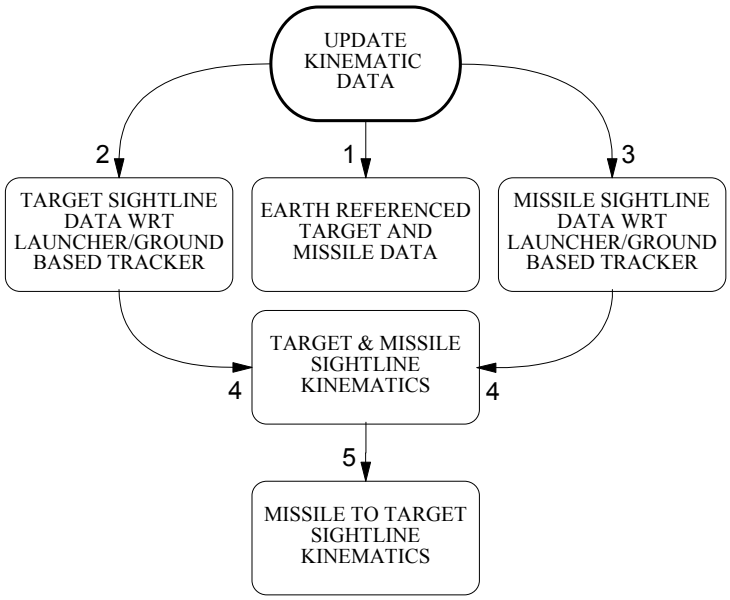

Figure 22-5 : Kinematic Data Precedence

The kinematic generator modules must be executed in the hierarchical order indicated by numbered arrows in Figure 22-5. Each module has two separate forms, one based on reference state data, the other on observer state vector. All parameters are derived, from reference data at 4 kHz the state integration rate, and from observer data at 400 Hz. This is simpler than implementing multi-rate logic.

22.3.1 Missile Closest Approach Detection and Reporting

C_A*PPROACH* monitors the *LAUNCH* flag at the state integration rate. After missile launch, range-to-go is interrogated and the *STOP_MONITOR* activated to test the following program termination conditions:

- Missile speed < 200 m/s
- Closing speed < 200 m/s
- Range-to-go < 1000 m and Seeker LOS angular rate > 10,000°/s

If any of these conditions are true before impact the program is put into a controlled shut down to obtain any requested data output, and the reason written to the Data Logging file. Similarly, if the range-to-go increases indicating that the missile has passed close to, or through, the target, the following closest approach logic is activated:

- The existing ASCII data file *MISS_RESULTS.DAT* is opened containing the previous miss distance data using communication channel *LUNMDT*,
- The following data is written to this file as a record:
  - Date and time stamp for the current simulation run
  - Simulation time at impact
  - Closest approach (P_K)

$$P_K := 2^{-1} \cdot \left(P_{m,t}(t) - P_{m,t}(t - \Delta t) \right)$$

Equation 22.3-1

  - Missile speed at impact
  - Missile lateral acceleration effort from controlled free-flight to impact
- The simulation time and miss distance are also written to the general ASCII output file via channel *LUNOUT*,
- The stop flag *ISTOP* is set that terminates the program.

22.3.2 Geodetic Referenced Parameters

The following modules provide the WGS-84 related data listed in Table 22-2,

- **WG_GEOMETRY** (reference state)
- **FF_WG_GEOMETRY** (observer state)

22.3.3 Target Kinematics

The following modules provide the target data listed in Table 22-3,

- **TG_GEOMETRY** (reference state)
- **FF_TG_GEOMETRY** (observer state)

22.3.4 Missile Kinematics

The following modules provide the missile data listed in Table 22-4 (pre-launch), Table 22-5 (post-launch) and Table 22-6 those data common to both phases,

- **MS_GEOMETRY** (reference state)
- **FF_MS_GEOMETRY** (observer state)

These modules also provide a flag indicating which missile flight phase is currently in effect.

22.3.5 Missile and Target Relative Inertial Kinematics

The following modules provide the relative missile and target data listed in Table 22-7. This data is provided with respect to the coincident launcher and ground based tracker located at point (o).

- **TM_GEOMETRY** (reference state)
- **FF_TM_GEOMETRY** (observer state)

22.3.6 Relative Missile and Target Kinematics

The following modules provide the relative missile to target sight-line dynamic data listed in Table 22-8.

- **ST_GEOMETRY** (reference state)
- **FF_ST_GEOMETRY** (observer state)

These provide missile time-to-go depending on LOS range and range rate,

$$\dot{P}_{m,t} > V_S \Rightarrow t_{GO} := P_{m,t}^{XS} \cdot \dot{P}_{m,t}^{-1}$$

Equation 22.3-2

$$\dot{P}_{m,t} \leq V_S \Rightarrow t_{GO} := 0$$

Equation 22.3-3

(V_S) is the threshold for stable missile flight required by the aerodynamic model and has a default value of 80 m/s.

Table 22-2 : Geodetically Referenced Parameters

SYM	UTILITY	ARG	DEFINITION
E_C^E	N/A	Ψ_C^E	Celestial to ECEF axes Euler triplet
T_C^E	N/A	E_C^E	Celestial to ECEF axis transform
T_C^A	M_PRODUCT	T_C^E , T_A^E	Celestial to alignment axis transform
$\underline{P}_{o,m}^E$	M_PRODUCT_AT	T_E^A , $\underline{P}_m^A$	Missile position wrt (o) in ECEF axes
$\underline{P}_m^E$	M_ADD	$\underline{P}_o^E$, $\underline{P}_{o,m}^E$	Missile position wrt (r) in ECEF axes
$\mu_m, \lambda_m, P_{d,m}^{GZ}$	ECEF_WGS_84	$\underline{P}_m^E$	Missile longitude, latitude & geodetic height
$P_{r,d}$, $R_{\mu d}, R_{\lambda d}$	EARTH_RADII	R_A , R_B , λ_d	WGS 84 Earth radius below missile position; E/W and N/S Earth radii at the point on the Earth's surface below the missile
$R_{\mu m}, R_{\lambda m}$	EARTH_RADII	$R_{\mu d}$, $R_{\lambda d}$	WGS 84 E/W & N/S Earth radii at the missile
E_E^G	N/A	λ_d	LGA Euler triplet wrt ECEF axes
T_E^G	DC_TO_YPR	E_E^G	ECEF to LGA transform
$\underline{\omega}_{C,E}^A$	M_PRODUCT	T_E^A , $\underline{\omega}_{C,E}^E$	Earth's Siderial rate in Alignment axes
$\underline{\omega}_{C,E}^G$	M_PRODUCT	T_E^G , $\underline{\omega}_{C,E}^E$	Earth's Siderial rate in LGA
P_S, T_S, σ_A	ATMOSPHERE	$P_{d,m}^{GZ}$	Missile air pressure, temperature and density
g_m^{ZG}	GRAVITY	λ_m , $P_{d,m}^{GZ}$	Missile gravitational acceleration wrt LGA
g_d^{ZG}	GRAVITY	λ_m , $P_{d,m}^{GZ}$	Gravity at sea-level under missile wrt LGA
$\underline{g}_m^A$	M_PRODUCT_AT M_PRODUCT	T_E^G , T_E^G , $\underline{g}_m^G$	Missile gravitational acceleration in Alignment axes
$\underline{P}_m^C$	M_PRODUCT_AT	T_C^E , $\underline{P}_m^E$	Missile position wrt (r) in Celestial axes
$\underline{P}_{r,m}^A$	M_PRODUCT	T_E^A , $\underline{P}_m^E$	Missile position wrt (r) in Alignment axes
$\underline{\dot{P}}_{o,m}^E$	M_PRODUCT_AT	T_E^A , $\underline{\dot{P}}_m^A$	Missile velocity wrt (o) in ECEF axes
$\underline{P}_{r,m}^B$	M_PRODUCT	T_E^B , $\underline{P}_{r,m}^A$	Missile position wrt (r) in Missile Body axes
$\underline{\omega}_{C,E}^B$	M_PRODUCT	T_A^B , $\underline{\omega}_{C,E}^A$	Earth's Siderial rate in Missile Body axes
$\underline{\omega}_{C,B}^B$	M_ADD	$\underline{\omega}_{C,E}^B$, $\underline{\omega}_{A,B}^B$	Missile angular rate in Missile Body axes

Table 22-3 : Target Kinematics

SYM	UTILITY	ARG	DEFINITION
$P_{o,t}$	V_S_MAG	$\underline{P}_t^A$	Target range with respect to missile launcher
P_t^{hA}	V_H_MAG	$\underline{P}_t^A$	Target ground range from missile launcher
$\dot{P}_t^{hA}$	V_H_MAG	$\underline{\dot{P}}_t^A$	Target velocity wrt (o) over the ground
E_A^T	XYZ_TO_YP	$\underline{P}_t^A$	Target LOS orientation wrt Alignment axes
E_A^{TV}	XYZ_TO_YP	$\underline{\dot{P}}_t^A$	Target Velocity orientation wrt Alignment axes
T_A^T	DC_TO_YPR	E_A^T	Alignment to Target LOS axis transform
T_A^{TV}	DC_TO_YPR	E_A^{TV}	Alignment to Target Velocity axis transform
T_T^{TV}	M_PRODUCT_BT	T_A^{TV} , T_A^T	Target LOS to Target Velocity axis transform
E_T^{TV}	YPR_TO_DC	T_T^{TV}	Target Velocity orientation wrt Target LOS axes
ξ_T^{TV}	ABS_ANG	E_T^{TV}	Absolute target velocity wrt Target LOS angle
$\underline{\dot{P}}_{o,t}^{TV}$	M_PRODUCT	T_A^{TV} , $\underline{\dot{P}}_t^A$	Target velocity wrt (o) in Target Velocity axes
$\underline{\dot{P}}_t^T$	M_PRODUCT	T_A^T , $\underline{\dot{P}}_t^A$	Target velocity wrt (o) in Target LOS axes
$\underline{\ddot{P}}_t^T$	M_PRODUCT	T_A^T , $\underline{\ddot{P}}_t^A$	Target acceleration wrt (o) in Target LOS axes
T_{TV}^{TB}	XYZ_TO_DC	$\underline{\dot{P}}_{o,t}^{TV}$	Target Velocity to Target Body axis transform
E_{TV}^{TB}	YPR_TO_DC	T_{TV}^{TB}	Target Body orientation wrt Target Velocity axes
$\dot{E}_A^T$	DX_TO_DE	$\underline{P}_t^A$, $\underline{\dot{P}}_t^A$	Target LOS Euler rates wrt Alignment axes
$\ddot{E}_A^T$	D2X_TO_D2E	$\underline{P}_t^A$, $\underline{\dot{P}}_t^A$, $\underline{\ddot{P}}_t^A$	Target LOS Euler accel'n wrt Alignment axes
$\underline{\omega}_{A,T}^T$	DE_TO_W	$\dot{E}_A^T$, E_A^T	Target LOS angular rate wrt Alignment axes
$\underline{\dot{\omega}}_{A,T}^T$	D2E_TO_DW	$\ddot{E}_A^T$, $\dot{E}_A^T$, E_A^T	Target LOS angular accel'n wrt Alignment axes
$\dot{E}_A^{TV}$	DX_TO_DE	$\underline{\dot{P}}_t^A$, $\underline{\ddot{P}}_t^A$	Target Velocity Euler rates wrt Alignment axes
$\underline{\omega}_{A,TV}^{TV}$	DE_TO_W	$\dot{E}_A^{TV}$, E_A^{TV}	Target Velocity angular rate wrt Alignment axes
$\underline{\omega}_T^{TV}$	M_PRODUCT_AT	T_T^{TV} , $\underline{\omega}_{A,TV}^{TV}$	Target Velocity angular rate wrt Target LOS axes
$\underline{\omega}_{A,T}^A$	M_PRODUCT_AT	T_A^T , $\underline{\omega}_{A,T}^T$	Target LOS angular rate wrt Alignment axes

Table 22-4 : Missile Kinematics (Pre-launch)

SYM	UTILITY	ARG	DEFINITION
$P_{o,m}$	V_S_MAG	$\underline{P}_m^A$	Missile range with respect to launcher
T_A^B	Q_TO_DC	Q_A^B	Alignment to Missile Body axis transform
E_A^B	DC_TO_YPR	T_A^B	Alignment to Missile Body axis transform
$\dot{\underline{P}}_{o,m}^B$	M_PRODUCT	T_A^B , $\dot{\underline{P}}_m^A$	Missile Velocity wrt (o) in Missile Body axes
$\ddot{\underline{P}}_{o,m}^B$	M_PRODUCT	T_A^B , $\ddot{\underline{P}}_m^A$	Missile acceleration wrt (o) in Missile Body axes
T_C^B	M_PRODUCT	T_C^A , T_A^B	Celestial to Missile Body axis transform
E_A^M	N/A		Missile LOS orientation wrt Alignment axes
$\underline{P}_m^A$	YP_TO_XYZ	$P_{o,m}$, E_A^M	Missile position wrt (o) in Alignment axes
$\dot{E}_A^M$	M_IMAGE	$\dot{E}_A^B$	Missile LOS Euler rate wrt Alignment axes
$\ddot{E}_A^M$	M_IMAGE	$\ddot{E}_A^B$	Missile LOS Euler accel'n wrt Alignment axes
$\underline{\omega}_{A,M}^M$	M_IMAGE	$\underline{\omega}_{A,B}^B$	Missile LOS angular rate wrt Alignment axes
$\dot{\underline{\omega}}_{A,M}^M$	M_IMAGE	$\dot{\underline{\omega}}_{A,B}^B$	Missile LOS angular accel'n wrt Alignment axes
E_B^{MV}	M_ZERO		Missile incidence
E_A^{MV}	M_IMAGE	E_A^B	Missile Velocity orientation wrt Alignment axes
T_B^{MV}	DC_TO_YPR	E_B^{MV}	Missile Body to Missile Velocity axis transform
T_A^{MV}	DC_TO_YPR	E_A^{MV}	Alignment to Missile Velocity axis transform

The remaining missile parameters are common to both

pre-launch and post launch – see Table 22-6.

Table 22-5 : Missile Kinematics (Post-launch)

SYM	UTILITY	ARG	DEFINITION
$P_{o,m}$	V_S_MAG	$\underline{P}_m^A$	Missile range with respect to launcher
T_A^B	Q_TO_DC	Q_A^B	Alignment to Missile Body axis transform
E_A^B	DC_TO_YPR	T_A^B	Alignment to Missile Body axis transform
$\dot{\underline{P}}_{o,m}^B$	M_PRODUCT	T_A^B , $\dot{\underline{P}}_m^A$	Missile Velocity wrt (o) in Missile Body axes
$\ddot{\underline{P}}_{o,m}^B$	M_PRODUCT	T_A^B , $\ddot{\underline{P}}_m^A$	missile acceleration wrt (o) in Missile Body axes
T_C^B	M_PRODUCT	T_C^A , T_A^B	Celestial to Missile Body axis transform
E_A^M	XYZ_TO_YP	$\underline{P}_m^A$	Missile LOS orientation wrt Alignment axes
$\dot{E}_A^M$	DX_TO_DE	$\underline{P}_m^A$, $\dot{\underline{P}}_m^A$	Missile LOS Euler rates wrt Alignment axes
$\ddot{E}_A^M$	D2X_TO_D2E	$\underline{P}_m^A, \dot{\underline{P}}_m^A, \ddot{\underline{P}}_m^A$	Missile LOS Euler accel'n wrt Alignment axes
$\underline{\omega}_{A,M}^M$	DE_TO_W	$\dot{E}_A^M$, E_A^M	Missile LOS angular rate wrt Alignment axes
$\dot{\underline{\omega}}_{A,M}^M$	D2E_TO_DW	$\ddot{E}_A^M$, $\dot{E}_A^M$, E_A^M	Missile LOS angular accel'n wrt Alignment axes
E_B^{MV}	XYZ_TO_YP	$\dot{\underline{P}}_{o,m}^B$	Missile incidence
T_B^{MV}	DC_TO_YPR	E_B^{MV}	Missile Body to Velocity axis transform
T_A^{MV}	YPR_TO_DC	T_B^{MV} , T_A^B	Alignment to Missile Velocity axis transform
E_A^{MV}	YPR_TO_DC	T_A^{MV}	Missile Velocity orientation wrt Alignment axes

The remaining missile parameters are common to both

pre-launch and post launch – see Table 22-6.

Table 22-6 : Missile Kinematics (Pre-Launch and Post-launch)

SYM	UTILITY	ARG	DEFINITION
T_A^M	DC_TO_YPR	E_A^M	Alignment to Missile LOS axis transform
$\underline{\dot{P}}_m^M$	M_PRODUCT	T_A^M , $\underline{\dot{P}}_m^A$	Missile velocity wrt (o) in Missile LOS axes
$\underline{\dot{P}}_{o,m}^E$	M_PRODUCT_AT	T_E^A , $\underline{\dot{P}}_m^A$	Missile velocity wrt (o) in ECEF axes
$\underline{\dot{P}}_{d,m}^G$	M_PRODUCT	T_A^G , $\underline{\dot{P}}_{o,m}^E$	Missile Velocity in LGA axes at (m)
$\dot{E}_A^B$	W_TO_DE	E_A^B , $\underline{\omega}_{A,B}^B$	Missile Body angular velocity wrt Align't axes
$\ddot{E}_A^B$	DW_TO_D2E	E_A^B , $\underline{\omega}_{A,B}^B$, $\underline{\dot{\omega}}_{A,B}^B$	Missile Body angular accel'n wrt Alignment axes
$\underline{\omega}_{C,B}^B$	M_ADD	$\underline{\omega}_{C,E}^B$, $\underline{\omega}_{A,B}^B$	Missile inertial angular rate wrt Celestial axes
T_B^{MV}	YPR_TO_DC	T_A^{MV} , T_A^B	Missile Body to Velocity axis transform
T_M^{MV}	M_PRODUCT_BT	T_A^{MV} , T_A^M	Missile LOS to Velocity axis transform
T_M^B	M_PRODUCT_BT	T_A^B , T_A^M	Missile LOS to Missile Body axis transform
$\dot{P}_{o,m}$	V_S_MAG	$\underline{\dot{P}}_m^A$	Missile velocity wrt (o)
$\underline{g}_m^B$	M_PRODUCT	T_E^G , T_E^G , g_m^{ZG}	Gravity wrt (m) in Missile Body axes
$\underline{P}_{r,m}^B$	M_PRODUCT	T_E^B , $\underline{P}_{r,m}^A$	Missile position wrt (r) in Missile Body axes
$\underline{\omega}_{C,E}^B$	M_PRODUCT	T_A^B , $\underline{\omega}_{C,E}^A$	Earth's Siderial rate in Missile Body axes
$\underline{\omega}_{C,B}^B$	M_ADD	$\underline{\omega}_{C,E}^B$, $\underline{\omega}_{A,B}^B$	Missile inertial angular rate in missile body axes
E_M^{MV}	YPR_TO_DC	T_M^{MV}	Missile velocity orientation wrt missile LOS axes
E_M^B	YPR_TO_DC	T_M^B	Missile body orientation wrt missile LOS
P_m^{hA}	V_H_MAG	$\underline{P}_m^A$	Missile horizontal ground range from launcher
$\dot{P}_m^{hA}$	V_H_MAG	$\underline{\dot{P}}_m^A$	Missile horizontal speed in Alignment plane
$\dot{P}_{d,m}^{hG}$	V_H_MAG	$\underline{\dot{P}}_{o,m}^G$	Missile velocity over the ground in LGA
M_m	N/A	$V_{o,m}^{XMV}$, T_S	Missile Mach Number
ξ_B^{MV}	ABS_ANG	E_B^{MV}	Missile incidence
ξ_A^{MV}	ABS_ANG	E_A^{MV}	Missile LOS to velocity vector angle
ξ_M^{MV}	ABS_ANG	E_M^{MV}	Alignment to missile velocity vector angle
ξ_M^B	ABS_ANG	E_M^B	Missile LOS to velocity vector angle
$\ddot{P}_{o,m}^{rB}$	V_R_MAG	$\underline{\ddot{P}}_{o,m}^B$	Missile lateral acceleration wrt body axes

Table 22-7 : Missile and Target Ground-Based Relative Kinematics

SYM	UTILITY	ARG	DEFINITION
$\underline{\dot{P}}^{A}_{m,t}$	M_SUBTRACT	$\underline{\dot{P}}^{A}_{t}$, $\underline{\dot{P}}^{A}_{m}$	Target velocity wrt missile in Alignment axes
T^{B}_{T}	M_PRODUCT_BT	T^{B}_{A} , T^{T}_{A}	Target LOS to Missile Body transform
T^{MV}_{T}	M_PRODUCT_BT	T^{MV}_{A} , T^{T}_{A}	Target LOS to Missile Velocity transform
T^{M}_{T}	M_PRODUCT_BT	T^{M}_{A} , T^{T}_{A}	Target LOS to missile LOS transform
T^{TV}_{B}	M_PRODUCT_BT	T^{TV}_{A} , T^{B}_{A}	Missile Body to Target Velocity transform
$\underline{\dot{P}}^{T}_{m,t}$	M_PRODUCT	T^{T}_{A} , $\underline{\dot{P}}^{T}_{m,t}$	Target velocity wrt (m) in Target LOS axes
$\underline{P}^{T}_{o,m}$	M_PRODUCT	T^{T}_{A} , $\underline{P}^{A}_{m}$	Missile position wrt (o) in Target LOS axes
$\underline{\dot{P}}^{T}_{o,m}$	M_PRODUCT	T^{T}_{A} , $\underline{\dot{P}}^{A}_{m}$	Missile velocity wrt (o) in Target LOS axes
$\underline{\ddot{P}}^{MV}_{o,t}$	M_PRODUCT	T^{MV}_{A} , $\underline{\ddot{P}}^{A}_{t}$	Target velocity wrt (o) in Missile Velocity axes
E^{B}_{T}	YPR_TO_DC	T^{B}_{T}	Missile Body orientation wrt Target LOS axes
E^{MV}_{T}	YPR_TO_DC	T^{MV}_{T}	Missile Velocity orientation wrt Target LOS axes
E^{M}_{T}	YPR_TO_DC	T^{M}_{T}	Target to Missile LOS orientation
E^{TV}_{B}	YPR_TO_DC	T^{TV}_{B}	Missile Body to Target Velocity orientation
$\underline{\omega}^{T}_{A,M}$	M_PRODUCT_AT	T^{M}_{T} , $\underline{\omega}^{M}_{A,M}$	Missile LOS angular rate wrt target LOS axes
$\underline{\omega}^{T}_{T,M}$	M_PRODUCT_AT	$\underline{\omega}^{T}_{A,M}$, $\underline{\omega}^{T}_{A,T}$	Missile LOS angular rate wrt Target LOS axes
ξ^{MV}_{T}	ABS_ANG	E^{MV}_{T}	Target LOS to Missile Velocity angle
ξ^{M}_{T}	ABS_ANG	E^{M}_{T}	Target LOS to Missile LOS angle

Table 22-8 : Relative Missile and Target Kinematics

SYM	UTILITY	ARG	DEFINITION
$P_{m,t}$	V_S_MAG	$\underline{P}_t^S$	Missile seeker to target range
E_A^S	XYZ_TO_YP	$\underline{P}_{m,t}^A$	Seeker LOS orientation wrt Alignment axes
T_A^S	DC_TO_YPR	E_A^S	Alignment to Seeker LOS transform
T_S^{TV}	M_PRODUCT_BT	T_A^{TV} , T_A^S	Seeker LOS to Target Velocity transform
$\dot{\underline{P}}_t^S$	M_PRODUCT	T_A^S , $\dot{\underline{P}}_{m,t}^A$	Target velocity wrt (m) in Seeker LOS axes
$\dot{\underline{P}}_{o,m}^S$	M_PRODUCT	T_A^S , $\dot{\underline{P}}_m^A$	Missile velocity wrt (o) in Seeker LOS axes
E_S^{TV}	YPR_TO_DC	T_S^{TV}	Seeker LOS to Target Velocity transform
$\dot{E}_A^S$	DX_TO_DE	$\underline{P}_{m,t}^A$, $\dot{\underline{P}}_{m,t}^A$	Seeker LOS Euler rates wrt Alignment axes
$\underline{\omega}_{A,S}^S$	DE_TO_W	$\dot{E}_A^S$, E_A^S	Seeker LOS angular rate wrt Alignment
T_B^S	M_PRODUCT_BT	T_A^S , T_A^B	Missile Body to Seeker LOS transform
T_S^T	M_PRODUCT_BT	T_A^T , T_A^S	Seeker LOS to target LOS transform
T_S^{TV}	M_PRODUCT_BT	T_A^{TV} , T_A^S	Seeker LOS to Target Velocity transform
T_M^S	M_PRODUCT_BT	T_A^M , T_A^S	Missile LOS to Seeker LOS transform
T_{MV}^S	M_PRODUCT_BT	T_A^{MV} , T_A^S	Missile Velocity to Seeker LOS transform
E_B^S	YPR_TO_DC	T_B^S	Seeker LOS orientation wrt Missile Body axes
E_S^T	YPR_TO_DC	T_S^T	Target LOS orientation wrt Seeker LOS axes
E_S^{TV}	YPR_TO_DC	T_S^{TV}	Target Velocity orientation wrt Seeker LOS axes
E_M^S	YPR_TO_DC	T_M^S	Missile LOS orientation wrt Seeker LOS axes
E_{MV}^S	YPR_TO_DC	T_{MV}^S	Seeker LOS orientation wrt Missile Velocity axes
$\underline{\omega}_{A,B}^S$	M_PRODUCT	T_B^S , $\underline{\omega}_{A,B}^B$	Missile Body angular rate in Seeker LOS axes
$\underline{\omega}_{B,S}^S$	M_SUBTRACT	$\underline{\omega}_{A,S}^S$, $\underline{\omega}_{A,B}^S$	Seeker LOS angular rate wrt Missile Body axes
$\dot{E}_B^S$	W_TO_DE	$\underline{\omega}_{B,S}^S$, E_B^S	Seeker LOS Euler rate wrt Missile Body axes
$\underline{\omega}_{A,TV}^S$	M_PRODUCT_AT	T_{TV}^S , $\underline{\omega}_{A,TV}^{TV}$	Target Velocity angular rate in Seeker LOS axes
$\ddot{\underline{P}}_{o,t}^S$	M_PRODUCT	T_A^S , $\ddot{\underline{P}}_{o,t}^A$	Target acceleration wrt (o) in Seeker LOS axes
$\ddot{\underline{P}}_{o,t}^B$	M_PRODUCT_AT	T_A^S , $\ddot{\underline{P}}_{o,t}^S$	Target acceleration wrt (o) in Missile Body axes

SYM	UTILITY	ARG	DEFINITION
E_A^H	YPR_TO_DC	$E_B^H > T_B^H$	Transform from Missile Body to Seeker Head axes
	M_PRODUCT	$T_B^H \cdot T_A^B > T_A^H$	Transform from Alignment to Seeker Head axes
	DC_TO_YPR	T_A^H	Seeker Head orientation wrt Alignment axes
ξ_S^T	ABS_ANG	E_S^T	Target LOS wrt Seeker LOS angle
ξ_S^{TV}	ABS_ANG	E_S^{TV}	Target Velocity wrt Seeker LOS angle
ξ_B^S	ABS_ANG	E_B^S	Seeker LOS wrt Missile Body angle
ξ_M^S	ABS_ANG	E_M^S	Seeker LOS to Missile LOS angle
ξ_{MV}^S	ABS_ANG	E_{MV}^S	Seeker LOS wrt Missile Velocity angle
ξ_A^H	ABS_ANG	E_A^H	Seeker Head wrt Alignment angle
$\omega_{A,S}^{rS}$	V_R_MAG	$\underline{\omega}_{A,S}^{rS}$	Missile angular rate normal to Seeker LOS axes

22.4 Axis Transformations

Consider the two Cartesian frames (A) and (B) shown in Figure 15-2 with a common origin at point (a), and $\underline{X}^B$ passing through point (b). The position of (b) with respect to (a), expressed in frame A, is denoted by vector ($\underline{P}_b^A$).

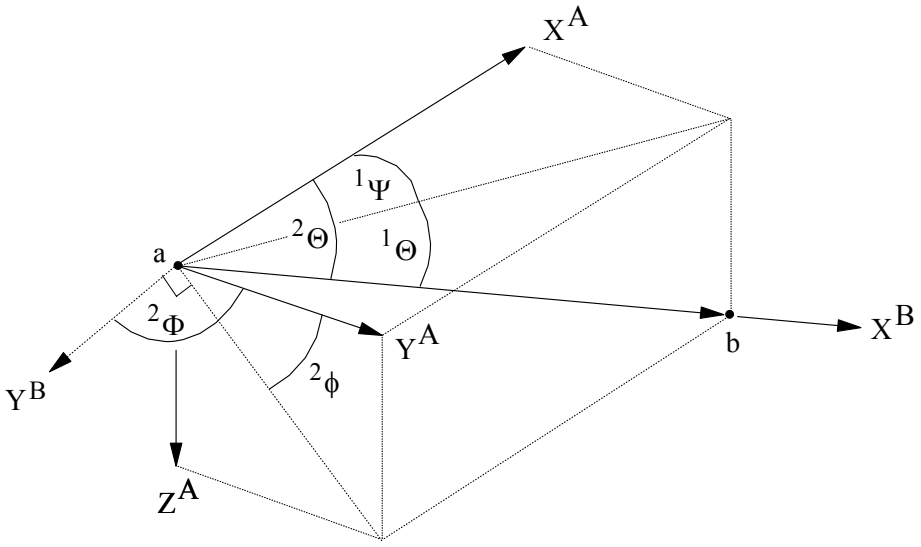

Figure 22-6 : YPR and RPY Euler Triplet Definition

Euler triplets defining the orientation of frame (B) with respect to frame (A),

$$ {}^{YPR}E_A^B \equiv {}^1E_A^B \quad \text{(roll angle redundant)} $$

Equation 22.4-1

$$ {}^{RPY}E_A^B \equiv {}^2E_A^B \quad \text{(yaw angle redundant)} $$

Equation 22.4-2

Since the YPR Euler triplet is the most commonly used its prefix has been dropped when the meaning of an equation is clear in context.

22.4.1 Cartesian to Euler YP Transformation

XYZ_TO_YP takes the position of point (b) with respect to point (a) expressed in frame (A), and returns the YPR Euler triplet representing the orientation of frame (B) with respect to frame (A).

$$ \mathbf{XYZ\_TO\_YP}\left(\underline{P}_b^A, E_A^B\right) \equiv \varphi_X^E\left(\underline{P}_b^A\right) $$

Equation 22.4-3

$$ \Delta := 10^{-15} $$

Equation 22.4-4

$$E_A^B \coloneqq \left(0 \quad , \quad -\tan^{-1}\left(P_b^{ZA} \,/\, P_b^{hA} \right) \quad , \quad \tan^{-1}\left(P_b^{YA} \,/\, P_b^{XA} \right) \right)$$

Equation 22.4-5

$$\left(\left| P_b^{XA} \right| < \Delta \right) \wedge \left(\left| P_b^{YA} \right| < \Delta \right) \wedge \left(\left| P_b^{ZA} \right| < \Delta \right) \Rightarrow E_A^B \coloneqq \underline{0}_3$$

Equation 22.4-6

$$\left(\left(\left| P_b^{XA} \right| < \Delta \right) \wedge \left(\left| P_b^{YA} \right| < \Delta \right) \right) \wedge \left(\left| P_b^{ZA} \right| \geq \Delta \right) \Rightarrow$$

$$E_A^B \coloneqq \left(0 \quad , \quad -\pi / 2 \quad , \quad 0 \right)$$

Equation 22.4-7

E_ANGLES determines the orientation of frame (B) from the linear velocity and acceleration of point (b) expressed in ENU geodetic axes (A) assuming zero incidence and a non-zero roll angle,

$$\textbf{E\_ANGLES}\left(\underline{A}_b^A , \underline{V}_b^A , g_b^{ZA} , E_A^B \right) \equiv \varphi_{LD}^E \left(\underline{A}_b^A , \underline{V}_b^A , g_b^{ZA} \right)$$

Equation 22.4-8

The linear velocity and acceleration of point (b) with respect to point (a), and the local gravitational acceleration at (b), determine the Euler triplet,

$$E_A^B \coloneqq \left(\Phi_A^B \quad , \quad -\tan^{-1}\left(V_b^{ZA} \,/\, V_b^{hA} \right) \quad , \quad \tan^{-1}\left(V_b^{YA} \,/\, V_b^{XA} \right) \right)$$

Equation 22.4-9

$$\underline{A}_b^C \coloneqq T_A^C\left(0 \quad \Theta_A^B \quad \Psi_A^B \right) \cdot \left(A_b^{XA} \quad , \quad A_b^{YA} \quad , \quad A_b^{ZA} + g_b^{ZA} \right)^T$$

Equation 22.4-10

$$\left(\left| A_b^{YC} \right| > \Delta \right) \vee \left(\left| A_b^{ZC} \right| > \Delta \right) \Rightarrow \overline{\Phi}_A^B \coloneqq -\tan^{-1}\left(A_b^{YC} \,/\, A_b^{ZC} \right)$$

Equation 22.4-11

$$\left(\left| A_b^{YC} \right| \leq \Delta \right) \wedge \left(\left| A_b^{ZC} \right| \leq \Delta \right) \Rightarrow \overline{\Phi}_A^B \coloneqq 0$$

Equation 22.4-12

$$A_b^{YB} \geq 0 \Rightarrow \Phi_A^B \coloneqq \overline{\Phi}_A^B + \pi$$

Equation 22.4-13

$$A_b^{YB} < 0 \Rightarrow \Phi_A^B \coloneqq \overline{\Phi}_A^B - \pi$$

Equation 22.4-14

22.4.2 Cartesian to Euler RP Transformation

XYZ_TO_RP takes the position of point (b) with respect to point (a) in frame (A) and returns the RPY Euler triplet representing the orientation of frame (B) with respect to (A) with a positive pitch angle.

$$\mathbf{XYZ\_TO\_RP}\left(\underline{P}_b^A\ ,\ {}^{RPY}E_A^B\right) \equiv \varphi_{XYZ}^{RP}\left(\underline{P}_b^A\ ,\ {}^{RPY}E_A^B\right)$$

Equation 22.4-15

$${}^{RPY}E_A^B := \left(2^{-1}\cdot\pi + \tan^{-1}\left(P_b^{ZA} \,/\, P_b^{YA}\right)\ ,\ \tan^{-1}\left(P_b^{rA} \,/\, P_b^{XA}\right)\ ,\ 0\right)$$

Equation 22.4-16

$$\left(\left|P_{ab}^{YB}\right| < 10^{-15}\right) \wedge \left(\left|P_{ab}^{ZB}\right| < 10^{-15}\right) \Rightarrow {}^{RPY}E_A^B := \underline{0}_3$$

Equation 22.4-17

22.4.3 Euler YP to Euler RP Transformation

Module *YP_TO_RP* takes the YPR Euler triplet defining the orientation of frame (B) with respect to frame (A) and returns the equivalent RPY Euler triplet such that the pitch angle is positive.

$$\mathbf{YP\_TO\_RP}\ \left(E_A^B\ ,\ {}^{RPY}E_A^B\right) \equiv \varphi_{YP}^{RP}\left(\Psi_A^B\ ,\Theta_A^B\right)$$

Equation 22.4-18

$$y := \frac{\pi}{2} + \tan^{-1}\left(-\tan\left(\Theta_A^B\right)\cdot\cos ec\left(\Psi_A^B\right)\right)$$

Equation 22.4-19

$$y > \pi \Rightarrow {}^{RPY}\Phi_A^B := -2\cdot\pi + y$$

Equation 22.4-20

$$y \in \left]-\pi\ ,\pi\right] \Rightarrow {}^{RPY}\Phi_A^B := y$$

Equation 22.4-21

$$y \le -\pi \Rightarrow {}^{RPY}\Phi_A^B := 2\cdot\pi + y$$

Equation 22.4-22

$${}^{RPY}\Theta_A^B := \cos^{-1}\left(\cos\left(\Theta_A^B\right)\cdot\cos\left(\Psi_A^B\right)\right)$$

Equation 22.4-23

$$ {}^{RPY}\Psi_A^B := 0 $$

Equation 22.4-24

$$ \left(\left| \Psi_A^B \right| < 10^{-15} \right) \wedge \left(\left| \Theta_A^B \right| < 10^{-15} \right) \Rightarrow {}^{RPY}E_A^B := \underline{0}_3 $$

Equation 22.4-25

22.4.4 Euler RP to Euler YP Transformation

RP_TO_YP takes the RPY Euler triplet defining the orientation of frame (B) with respect to frame (A) and returns the equivalent YPR Euler triplet.

$$ \textbf{RP\_TO\_YP} \left({}^{RPY}E_A^B , E_A^B \right) \equiv \varphi_{RP}^{YP} \left({}^{RPY}\Phi_A^B , {}^{RPY}\Theta_A^B \right) $$

Equation 22.4-26

$$ E_A^B := \begin{pmatrix} 0 \\ \sin^{-1}\left(\sin\left({}^{RPY}\Theta_A^B \right) \cdot \cos\left({}^{RPY}\Phi_A^B \right) \right) \\ \tan^{-1}\left(\tan\left({}^{RPY}\Theta_A^B \right) \cdot \sin\left({}^{RPY}\Phi_A^B \right) \right) \end{pmatrix} $$

Equation 22.4-27

$$ \left(\left| {}^{RPY}\Phi_A^B \right| < 10^{-15} \right) \wedge \left(\left| {}^{RPY}\Theta_A^B \right| < 10^{-15} \right) \Rightarrow E_A^B := \underline{0}_3 $$

Equation 22.4-28

22.4.5 Euler YP to Cartesian Transformation

YP_TO_XYZ takes the distance from point (a) to point (b), and the YPR Euler triplet defining the orientation of frame (B) with respect to frame (A), and returns the position of (b) with respect to (A).

$$ \textbf{YP\_TO\_XYZ} \left(P_{a,b} , E_A^B , \underline{P}_b^A \right) \equiv \varphi_E^X \left(P_{a,b} , E_A^B \right) $$

Equation 22.4-29

22.4.6 Euler RP to Cartesian Transformation

RP_TO_XYZ takes the distance from point (a) to point (b), and the RPY Euler triplet defining the orientation of frame (B) with respect to frame (A), and returns the Cartesian position of (b) with respect to (A).

$$ \textbf{RP\_TO\_XYZ} \left(P_{a,b} , {}^{RPY}E_A^B , \underline{P}_b^A \right) $$

Equation 22.4-30

$$\underline{P}_b^A \;:=\; P_{a,b} \cdot \left(\cos\Theta_A^B \;,\; \sin\Theta_A^B \cdot \sin\Phi_A^B \;,\; -\sin\Theta_A^B \cdot \cos\Phi_A^B \right)^T$$

Equation 22.4-31

22.4.7 Euler YPR to Direction Cosine Transformation

YPR_TO_DC takes an Euler triplet defining the orientation of frame (B) with respect to frame (A), and returns the transformation matrix from Equation 16-4.

$$\mathbf{YPR\_TO\_DC} \left(E_A^B \,, T_A^B \right) \;\equiv\; \varphi_E^{DC} \left(E_A^B \right)$$

Equation 22.4-32

If any Euler angle is $< 10^{-15}$ a reduced set of equations is computed using the two remaining Euler rotations. In strict order,

$$\left| \Phi_A^B \right| \le 10^{-15} \;\Rightarrow\; T_A^B \;:=\; \begin{bmatrix} c\Theta_A^B \cdot c\Psi_A^B & c\Theta_A^B \cdot s\Psi_A^B & -s\Theta_A^B \\ -\sin\Psi_A^B & \cos\Psi_A^B & 0 \\ s\Theta_A^B \cdot c\Psi_A^B & s\Theta_A^B \cdot s\Psi_A^B & c\Theta_A^B \end{bmatrix}$$

Equation 22.4-33

$$\left| \Theta_A^B \right| \le 10^{-15} \;\Rightarrow\; T_A^B \;:=\; \begin{bmatrix} \cos\Psi_A^B & \sin\Psi_A^B & 0 \\ -c\Phi_A^B \cdot s\Psi_A^B & c\Phi_A^B \cdot c\Psi_A^B & s\Phi_A^B \\ s\Phi_A^B \cdot s\Psi_A^B & -s\Phi_A^B \cdot c\Psi_A^B & c\Phi_A^B \end{bmatrix}$$

Equation 22.4-34

$$\left| \Psi_A^B \right| \le 10^{-15} \;\Rightarrow\; T_A^B \;:=\; \begin{bmatrix} \cos\Theta_A^B & 0 & -\sin\Theta_A^B \\ s\Phi_A^B \cdot s\Theta_A^B & c\Phi_A^B & s\Phi_A^B \cdot c\Theta_A^B \\ c\Phi_A^B \cdot s\Theta_A^B & -s\Phi_A^B & c\Phi_A^B \cdot c\Theta_A^B \end{bmatrix}$$

Equation 22.4-35

22.4.8 Euler RPY to Direction Cosine Transformation

RPY_TO_DC takes a RPY Euler triplet representing the orientation of frame (B) with respect to frame (A), and returns the transformation matrix.

$$\mathbf{RPY\_TO\_DC}\left({}^{RPY}E_A^B\,,T_A^B\right) \equiv \varphi_{RP}^{XYZ}\left({}^{RPY}E_A^B\,,T_A^B\right)$$

Equation 22.4-36

$$T_A^B :=$$

$$\begin{bmatrix} c\Theta_A^B\cdot c\Psi_A^B & , & s\Phi_A^B\cdot s\Theta_A^B\cdot c\Psi_A^B + c\Phi_A^B\cdot s\Psi_A^B & , & s\Phi_A^B\cdot s\Psi_A^B - c\Phi_A^B\cdot s\Theta_A^B\cdot c\Psi_A^B \\ -c\Theta_A^B\cdot s\Psi_A^B & , & c\Phi_A^B\cdot c\Psi_A^B + s\Phi_A^B\cdot s\Theta_A^B\cdot s\Psi_A^B & , & c\Phi_A^B\cdot s\Theta_A^B\cdot s\Psi_A^B + s\Phi_A^B\cdot c\Psi_A^B \\ s\Theta_A^B & , & -s\Phi_A^B\cdot c\Theta_A^B & , & c\Phi_A^B\cdot c\Theta_A^B \end{bmatrix}$$

Equation 22.4-37

If one of the Euler angles is $< 10^{-15}$ a reduced set of equations is computed using the remaining two Euler rotations. In strict order,

$$\left|\Phi_A^B\right| \le 10^{-15} \Rightarrow T_A^B := \begin{bmatrix} c\Theta_A^B\cdot c\Psi_A^B & , & s\Psi_A^B & , & -s\Theta_A^B\cdot c\Psi_A^B \\ -c\Theta_A^B\cdot s\Psi_A^B & , & c\Psi_A^B & , & s\Theta_A^B\cdot s\Psi_A^B \\ \sin\Theta_A^B & , & 0 & , & \cos\Theta_A^B \end{bmatrix}$$

Equation 22.4-38

$$\left|\Theta_A^B\right| \le 10^{-15} \Rightarrow T_A^B := \begin{bmatrix} c\Psi_A^B & , & c\Phi_A^B\cdot s\Psi_A^B & , & s\Phi_A^B\cdot s\Psi_A^B \\ -s\Psi_A^B & , & c\Phi_A^B\cdot c\Psi_A^B & , & s\Phi_A^B\cdot c\Psi_A^B \\ 0 & , & -\sin\Phi_A^B & , & \cos\Phi_A^B \end{bmatrix}$$

Equation 22.4-39

$$\left|\Psi_A^B\right| \le 10^{-15} \Rightarrow T_A^B := \begin{bmatrix} c\Theta_A^B & , & s\Phi_A^B\cdot s\Theta_A^B & , & -c\Phi_A^B\cdot s\Theta_A^B \\ 0 & , & \cos\Phi_A^B & , & \sin\Phi_A^B \\ s\Theta_A^B & , & -s\Phi_A^B\cdot c\Theta_A^B & , & c\Phi_A^B\cdot c\Theta_A^B \end{bmatrix}$$

Equation 22.4-40

22.4.9 Direction Cosines to Euler YPR Transformation

DC_TO_YPR takes the transformation matrix from frame (A) to frame (B) and extracts the YPR Euler triplet.

$$\mathbf{DC\_TO\_YPR}\left(T_A^B, E_A^B\right) \equiv \varphi_{DC}^E\left(T_A^B\right)$$

Equation 22.4-41

$$\Phi_A^B := \tan^{-1}\left(T_A^B(8) / T_A^B(9)\right)$$

Equation 22.4-42

$$T_A^B(7) \le 0.999999 \Rightarrow \Theta_A^B := \sin^{-1}\left(-T_A^B(7)\right)$$

Equation 22.4-43

$$T_A^B(7) > 0.999999 \Rightarrow$$

$$\Theta_A^B := \sin^{-1}\left(-0.999999 \cdot \text{sign}\left(1, T_A^B(7)\right)\right)$$

Equation 22.4-44

$$\Psi_A^B := \tan^{-1}\left(T_A^B(4) / T_A^B(1)\right)$$

Equation 22.4-45

22.4.10 Cartesian to Direction Cosine Transformation,

XYZ_TO_DC takes the Cartesian position of point (b) with respect to point (a) both expressed in frame (A). The utility returns the transformation matrix from (A) to frame (B), where (B) is orientated with respect to (A) such that the Euler roll angle is zero using the results of §16.13 with point (m) replaced by the generic point (b).

$$\mathbf{XYZ\_TO\_DC}\left(\underline{P}_b^A, T_A^B\right) \equiv \varphi_X^{DC}\left(\underline{P}_b^A\right)$$

Equation 22.4-46

22.4.11 Direction Cosines to Cartesian Transformation

DC_TO_XYZ takes the transformation matrix from frame (A) to frame (B) and returns the Cartesian components of a unit vector emanating from point (a) whose projection passes through point (b).

$$\mathbf{DC\_TO\_XYZ}\left(T_A^B, \underline{P}_b^A, k\right) \equiv \varphi_{DC}^X\left(T_A^B\right)$$

Equation 22.4-47

$$i \in \{(1:X),(2:Y),(3:Z)\} \Rightarrow \left\{\begin{array}{l} k = 0 \Rightarrow P_b^{iA} := T_A^B(1,i) \\ \\ k \ne 0 \Rightarrow P_b^{iA} := T_A^B(i,1) \end{array}\right\}$$

Equation 22.4-48

22.4.12 Skew x Transformation Matrix Product

SM_X_DC takes a [3,3] matrix [A], and a 3-vector (V), and returns their [3x3] matrix product [B].

$$\mathbf{SM\_X\_DC}\ \left([A], \underline{V}, [B] \right)$$

Equation 22.4-49

$$B := -[\underline{V}\times] \cdot A$$

Equation 22.4-50

$$B := \begin{bmatrix} a_{21}\cdot V^Z - a_{31}\cdot V^Y & , & a_{22}\cdot V^Z - a_{32}\cdot V^Y & , & a_{23}\cdot V^Z - a_{33}\cdot V^Y \\ a_{31}\cdot V^X - a_{11}\cdot V^Z & , & a_{32}\cdot V^X - a_{12}\cdot V^Z & , & a_{33}\cdot V^X - a_{13}\cdot V^Z \\ a_{11}\cdot V^Y - a_{21}\cdot V^X & , & a_{12}\cdot V^Y - a_{22}\cdot V^X & , & a_{13}\cdot V^Y - a_{23}\cdot V^X \end{bmatrix}$$

Equation 22.4-51

22.4.13 Transformation x Skew Matrix Product

DC_X_SM takes a [3,3] matrix [A], and a 3-vector (V), and returns their [3x3] matrix product [B].

$$\mathbf{DC\_X\_SM}\ \left([A], \underline{V}, [B] \right)$$

Equation 22.4-52

$$B := A \cdot [\underline{V}\times]$$

Equation 22.4-53

$$B := \begin{bmatrix} a_{13}\cdot V^Y - a_{12}\cdot V^Z & , & a_{11}\cdot V^Z - a_{13}\cdot V^X & , & a_{12}\cdot V^X - a_{11}\cdot V^Y \\ a_{23}\cdot V^Y - a_{22}\cdot V^Z & , & a_{21}\cdot V^Z - a_{23}\cdot V^X & , & a_{22}\cdot V^X - a_{21}\cdot V^Y \\ a_{33}\cdot V^Y - a_{32}\cdot V^Z & , & a_{31}\cdot V^Z - a_{33}\cdot V^X & , & a_{32}\cdot V^X - a_{31}\cdot V^Y \end{bmatrix}$$

Equation 22.4-54

22.4.14 Vector Projection onto Reference Planes

XYZ_TO_RAD takes the Cartesian position of point (b) with respect to point (a), expressed in frame (A), and returns the projection of the vector onto the principal planes of frame (A) as determined by (k).

$$y := \textbf{XYZ\_TO\_RAD}\left(\underline{P}_b^A , k \right)$$

Equation 22.4-55

$$k = 1 \Rightarrow y := \sqrt{\left(P_b^{XA} \right)^2 + \left(P_b^{YA} \right)^2}$$

Equation 22.4-56

$$k = 2 \Rightarrow y := \sqrt{\left(P_b^{YA} \right)^2 + \left(P_b^{ZA} \right)^2}$$

Equation 22.4-57

$$k = 3 \Rightarrow y := \sqrt{\left(P_b^{XA} \right)^2 + \left(P_b^{ZA} \right)^2}$$

Equation 22.4-58

22.4.15 Euler YP to Solid Angle Transformation

ANG_ERR_YP takes Euler triplets defining the orientation of frames (B) and (C) with respect to frame (A), and returns the smallest angle between them.

$$\xi_B^C := \textbf{ANG\_ERR\_YP}\left(E_A^B , E_A^C \right)$$

Equation 22.4-59

$$y := \sin\Theta_A^B \cdot \sin\Theta_A^C + \cos\Theta_A^B \cdot \cos\Theta_A^C \cdot \cos\left(\Psi_A^B - \Psi_A^C \right)$$

Equation 22.4-60

$$|y| \le 1 \Rightarrow \xi_B^C := \cos^{-1}\left(y \right)$$

Equation 22.4-61

$$|y| > 1 \Rightarrow \xi_B^C := \cos^{-1}\left(\text{sign}\left(1 , y \right) \right)$$

Equation 22.4-62

22.4.16 Euler RP to Solid Angle Transformation

ANG_ERR_RP takes two RPY Euler triplets defining the orientation of frames (B) and (C) with respect to frame (A), and returns the smallest angle between them.

$$\xi_B^C := \textbf{ANG\_ERR\_RP}\left({}^{RPY}E_A^B , {}^{RPY}E_A^C \right)$$

Equation 22.4-63

$$y := \sin\Theta_A^B \cdot \sin\Theta_A^C + \sin\Theta_A^B \cdot \sin\Theta_A^C \cdot \cos\left(\Phi_A^B - \Phi_A^C\right)$$

Equation 22.4-64

$$|y| \le 1 \Rightarrow \xi_B^C := \cos^{-1}(y)$$

Equation 22.4-65

$$|y| > 1 \Rightarrow \xi_B^C := \cos^{-1}(\text{sign}(1, y))$$

Equation 22.4-66

22.4.17 Differential Angle

V_ANGLE returns the differential angle between position vectors from point (a), the origin of a common frame (A), through points (b) and (c).

$$\textbf{V\_ANGLE}\left(\underline{P}_b^A, \underline{P}_c^A, \xi_B^C\right)$$

Equation 22.4-67

$$y := \cos^{-1}\left(\frac{\underline{P}_b^A \bullet \underline{P}_c^A}{P_{a,b} \cdot P_{a,c}}\right)$$

Equation 22.4-68

22.4.18 Transformation Angle

ABS_ANG takes a YPR Euler triplet defining the orientation of frame (B) with respect to a frame (A), and returns the angle from $\underline{X}^A$ to $\underline{X}^B$.

$$\xi_A^B := \textbf{ABS\_ANG}\left(E_A^B\right)$$

Equation 22.4-69

$$y := \cos\Theta_A^B \cdot \cos\Psi_A^B$$

Equation 22.4-70

$$|y| \le 1 \Rightarrow \xi_A^B := \cos^{-1}(y)$$

Equation 22.4-71

$$|y| > 1 \Rightarrow \xi_A^B := \cos^{-1}(\text{sign}(1, y))$$

Equation 22.4-72

22.4.19 Differential Angular Rate

DA_RATE takes the PV of points (b) and (c) with respect to frame (A) at point (a), and returns the differential angular rate between the two vectors.

$$\dot{\xi}_B^C := \textbf{DA\_RATE}\left(\underline{P}_b^A , \underline{V}_b^A , \underline{P}_c^A , \underline{V}_c^A \right)$$

Equation 22.4-73

$$\dot{\xi}_B^C := \cot \xi_B^C \cdot \left(\frac{\underline{P}_b^A \bullet \underline{V}_b^A}{P_{a,b}^2} + \frac{\underline{P}_c^A \bullet \underline{V}_c^A}{P_{a,c}^2} \right) - \frac{\csc \xi_B^C \cdot \left(\underline{P}_c^A \bullet \underline{V}_b^A + \underline{P}_b^A \bullet \underline{V}_c^A \right)}{P_{a,b} \cdot P_{a,c}}$$

Equation 22.4-74

$$\dot{\xi}_B^C := -\csc \xi_B^C \cdot \left(\varphi_1 + \varphi_2 + \left(\dot{\Psi}_A^B - \dot{\Psi}_A^C \right) \cdot \cos \Theta_A^B \cdot \cos \Theta_A^C \cdot \sin \left(\Psi_A^B - \Psi_A^C \right) \right)$$

Equation 22.4-75

$$\varphi_1 := \dot{\Theta}_A^B \cdot \left(\cos \Theta_A^B \cdot \sin \Theta_A^C - \sin \Theta_A^B \cdot \cos \Theta_A^C \cdot \cos \left(\Psi_A^B - \Psi_A^C \right) \right)$$

Equation 22.4-76

$$\varphi_2 := \dot{\Theta}_A^C \cdot \left(\sin \Theta_A^B \cdot \cos \Theta_A^C - \cos \Theta_A^B \cdot \sin \Theta_A^C \cdot \cos \left(\Psi_A^B - \Psi_A^C \right) \right)$$

Equation 22.4-77

22.4.20 Given's Transformations

GIVENS takes a YPR Euler triplet defining the orientation of frame (B) with respect to frame (A) using a single rotation about one of the principal axes of (A), and returns the transformation matrix identified by (k).

$$\textbf{GIVENS}\left(E_A^B , T_A^B , k \right)$$

Equation 22.4-78

$$k = 1 \Rightarrow T_A^B\left(\Phi_A^B \right) := \begin{bmatrix} \cos \Psi_A^B & , & \sin \Psi_A^B & , & 0 \\ -\sin \Psi_A^B & , & \cos \Psi_A^B & , & 0 \\ 0 & , & 0 & , & 1 \end{bmatrix}$$

Equation 22.4-79

$$k = 2 \Rightarrow T_A^B\left(\Theta_A^B \right) := \begin{bmatrix} \cos \Theta_A^B & , & 0 & , & -\sin \Theta_A^B \\ 0 & , & 1 & , & 0 \\ \sin \Theta_A^B & , & 0 & , & \cos \Theta_A^B \end{bmatrix}$$

Equation 22.4-80

$$k = 3 \Rightarrow T_A^B\left(\Phi_A^B\right) := \begin{bmatrix} 1 & , & 0 & , & 0 \\ 0 & , & \cos\Phi_A^B & , & \sin\Phi_A^B \\ 0 & , & -\sin\Phi_A^B & , & \cos\Phi_A^B \end{bmatrix}$$

Equation 22.4-81

22.4.21 Euler YPR Small Angle Transform Approximation

YPR_TO_ADC takes a YPR Euler triplet of small rotations representing the orientation of frame (B) with respect to frame (A), and returns a transformation matrix using the results of §16.2.

$$\textbf{YPR\_TO\_ADC}\left(E_A^B, \Delta T_A^B\right)$$

Equation 22.4-82

22.4.22 Cartesian Direction Cosine Jacobian,

X_DC_JACOB takes the position of point (b) with respect to point (a) expressed in frame (A), and the transform from (A) to frame (B). It returns the Jacobian of the transform, where (B) is orientated with respect to (A) such that the Euler roll angle is zero.

$$\textbf{X\_DC\_JACOB}\left(\underline{P}_b^A, T_A^B, \partial T_A^B / \partial \underline{P}_b^A\right)$$

Equation 22.4-83

The Jacobian elements with respect to P^{XA},

$$P_{a,b} \cdot \partial T_A^B(1) / \partial P_b^{XA} := 1 - \left(P_b^{XA} / P_{a,b}\right)^2$$

Equation 22.4-84

$$P_{a,b}^3 \cdot \partial T_A^B(4) / \partial P_b^{XA} := -P_b^{YA} \cdot P_b^{XA}$$

Equation 22.4-85

$$P_{a,b}^3 \cdot \partial T_A^B(7) / \partial P_b^{XA} := -P_b^{XA} \cdot P_b^{ZA}$$

Equation 22.4-86

$$\left(P_b^{hA}\right)^3 \cdot \partial T_A^B(2) / \partial P_b^{XA} := P_b^{XA} \cdot P_b^{YA}$$

Equation 22.4-87

$$P_b^{hA} \cdot \partial T_A^B(5) / \partial P_b^{XA} := 1 - \left(P_b^{XA} / P_b^{hA} \right)^2$$

Equation 22.4-88

$$\partial T_A^B(8) / \partial P_b^{XA} := 0$$

Equation 22.4-89

$$P_b^{hA} \cdot P_{a,b} \cdot \partial T_A^B(3) / \partial P_b^{XA} := P_b^{ZA} \cdot \left(\left(P_b^{XA} \right)^2 \cdot \varphi_1 - 1 \right)$$

Equation 22.4-90

$$\varphi_1 := \frac{1}{\left(P_b^{hA} \right)^2} + \frac{1}{\left(P_{a,b} \right)^2}$$

Equation 22.4-91

$$P_b^{hA} \cdot P_{a,b} \cdot \partial T_A^B(6) / \partial P_b^{XA} := P_b^{ZA} \cdot P_b^{YA} \cdot P_b^{XA} \cdot \varphi_1$$

Equation 22.4-92

$$P_{a,b} \cdot \partial T_A^B(9) / \partial P_b^{XA} := \frac{P_b^{XA}}{P_b^{hA}} - \frac{P_b^{hA} \cdot P_b^{XA}}{P_{a,b}^2}$$

Equation 22.4-93

Expressing the transform components in terms of the direction cosines,

$$\frac{\partial T_A^B}{\partial P_b^{XA}} := \begin{bmatrix} \frac{1 - T_1^2}{P_{a,b}} & , & -\frac{T_1 \cdot T_4}{P_{a,b}} & , & -\frac{T_1 \cdot T_7}{P_{a,b}} \\ -\frac{T_2 \cdot T_5}{P_b^{hA}} & , & \frac{1 - T_5^2}{P_b^{hA}} & , & 0 \\ \frac{T_7}{P_b^{hA}} \cdot \left(T_1^2 + T_5^2 - 1 \right) & , & T_5 \cdot T_7 \cdot \left(\frac{T_4}{P_{a,b}} - \frac{T_2}{P_b^{hA}} \right) & , & \frac{T_5 - T_1 \cdot T_9}{P_{a,b}} \end{bmatrix}$$

Equation 22.4-94

The Jacobian elements with respect to P^{YA},

$$P_{a,b}^3 \cdot \partial T_A^B(1) / \partial P_b^{YA} := -P_b^{YA} \cdot P_b^{XA}$$

Equation 22.4-95

$$P_{a,b} \cdot \partial T_A^B(4) / \partial P_b^{YA} := 1 - \left(P_b^{YA} / P_{a,b} \right)^2$$

Equation 22.4-96

$$P_{a,b}^3 \cdot \partial T_A^B(7) / \partial P_b^{YA} := -P_b^{ZA} \cdot P_b^{YA}$$

Equation 22.4-97

$$P_b^{hA} \cdot \partial T_A^B(2) / \partial P_b^{YA} := \left(P_b^{YA} / P_b^{hA} \right)^2 - 1$$

Equation 22.4-98

$$\left(P_b^{hA} \right)^3 \cdot \partial T_A^B(5) / \partial P_b^{YA} := -P_b^{YA} \cdot P_b^{XA}$$

Equation 22.4-99

$$\partial T_A^B(8) / \partial P_b^{YA} := 0$$

Equation 22.4-100

$$P_b^{hA} \cdot P_{a,b} \cdot \partial T_A^B(3) / \partial P_b^{YA} := P_b^{ZA} \cdot P_b^{YA} \cdot P_b^{XA} \cdot \varphi_1$$

Equation 22.4-101

$$P_b^{hA} \cdot P_{a,b} \cdot \partial T_A^B(6) / \partial P_b^{YA} := P_b^{ZA} \cdot \left(\left(P_b^{YA} \right)^2 \cdot \varphi_1 - 1 \right)$$

Equation 22.4-102

$$P_{a,b} \cdot \partial T_A^B(9) / \partial P_b^{YA} := \frac{P_b^{XA}}{P_b^{hA}} - \frac{P_b^{hA} \cdot P_b^{Y}}{P_{a,b}^2}$$

Equation 22.4-103

Expressing the transform components in terms of the direction cosines,

$$\frac{\partial T_A^B}{\partial P_b^{YA}} := \begin{bmatrix} \frac{\partial T_4}{\partial P_b^{XA}} & , & \frac{1 - T_4^2}{P_{a,b}} & , & -\frac{T_4 \cdot T_7}{P_{a,b}} \\ \frac{T_2^2 - 1}{P_b^{hA}} & , & -\frac{\partial T_2}{\partial P_b^{XA}} & , & 0 \\ -T_2 \cdot T_7 \cdot \left(\frac{T_1}{P_{a,b}} + \frac{T_5}{P_b^{hA}} \right) & , & \frac{T_7}{P_b^{hA}} \cdot \left(T_2^2 + T_4^2 - 1 \right) & , & \frac{T_5 + T_2 \cdot T_9}{P_{a,b}} \end{bmatrix}$$

Equation 22.4-104

The Jacobian elements with respect to P^{ZA},

$$P_{a,b}^{3} \cdot \partial T_{A}^{B}(1) / \partial P_{b}^{ZA} := -P_{b}^{ZA} \cdot P_{b}^{XA}$$

Equation 22.4-105

$$P_{a,b}^{3} \cdot \partial T_{A}^{B}(4) / \partial P_{b}^{ZA} := -P_{b}^{ZA} \cdot P_{b}^{YA}$$

Equation 22.4-106

$$P_{a,b} \cdot \partial T_{A}^{B}(7) / \partial P_{b}^{ZA} := 1 - \left(P_{b}^{ZA} / P_{a,b} \right)^{2}$$

Equation 22.4-107

$$\left(P_{b}^{hA} \right)^{3} \cdot \partial T_{A}^{B}(2) / \partial P_{b}^{ZA} := P_{b}^{YA} \cdot P_{b}^{ZA}$$

Equation 22.4-108

$$\left(P_{b}^{hA} \right)^{3} \cdot \partial T_{A}^{B}(5) / \partial P_{b}^{ZA} := -P_{b}^{XA} \cdot P_{b}^{ZA}$$

Equation 22.4-109

$$\partial T_{A}^{B}(8) / \partial P_{b}^{ZA} := 0$$

Equation 22.4-110

$$P_{b}^{hA} \cdot P_{a,b} \cdot \partial T_{A}^{B}(3) / \partial P_{b}^{ZA} := P_{b}^{XA} \cdot \left(\left(P_{b}^{ZA} \right)^{2} \cdot \varphi_{1} - 1 \right)$$

Equation 22.4-111

$$P_{b}^{hA} \cdot P_{a,b} \cdot \partial T_{A}^{B}(6) / \partial P_{b}^{ZA} := P_{b}^{YA} \cdot \left(\left(P_{b}^{ZA} \right)^{2} \cdot \varphi_{1} - 1 \right)$$

Equation 22.4-112

$$P_{a,b} \cdot \partial T_{A}^{B}(9) / \partial P_{b}^{ZA} := \frac{P_{b}^{ZA}}{P_{b}^{hA}} - \frac{P_{b}^{hA} \cdot P_{b}^{ZA}}{P_{a,b}^{2}}$$

Equation 22.4-113

Expressing the transform components in terms of the direction cosines,

$$\frac{\partial T_A^B}{\partial P_b^{ZA}} := \begin{bmatrix} \frac{\partial T_7}{\partial P_b^{XA}} & , & \frac{\partial T_7}{\partial P_b^{YA}} & , & \frac{1-T_7^2}{P_{a,b}} \\ -\frac{T_2 \cdot P_b^{ZA}}{\left(P_b^{hA}\right)^2} & , & \frac{T_5}{T_2} \cdot \frac{\partial T_2}{\partial P_b^{ZA}} & , & 0 \\ \frac{T_1}{P_b^{hA}} \cdot \left(\left(\frac{P_b^{ZA}}{P_b^{hA}} \right)^2 + T_7^2 - 1 \right) & , & \frac{T_4}{T_1} \cdot \frac{\partial T_3}{\partial P_b^{ZA}} & , & T_3 \cdot \left(\frac{1}{P_b^{hA}} - \frac{T_9}{P_{a,b}} \right) \end{bmatrix}$$

Equation 22.4-114

22.4.23 Euler YPR Direction Cosine Jacobian

E_DC_JACOB takes the transform from frame (A) to frame (B) and returns its Jacobian with respect to the YPR Euler angles defining the orientation between the two frames.

$$\mathbf{E\_DC\_JACOB}\left(E_A^B, T_A^B, \partial T_A^B / \partial E_A^B\right)$$

Equation 22.4-115

$$\frac{\partial T_A^B}{\partial \Psi_A^B} := \begin{bmatrix} -T_A^B(4) & , & T_A^B(1) & , & 0 \\ -T_A^B(5) & , & T_A^B(2) & , & 0 \\ -T_A^B(6) & , & T_A^B(3) & , & 0 \end{bmatrix}$$

Equation 22.4-116

$$\frac{\partial T_A^B}{\partial \Theta_A^B} := \begin{bmatrix} -s\Theta_A^B \cdot c\Psi_A^B & , & -s\Theta_A^B \cdot s\Psi_A^B & , & -c\Theta_A^B \\ s\Phi_A^B \cdot c\Theta_A^B \cdot c\Psi_A^B & , & s\Phi_A^B \cdot c\Theta_A^B \cdot s\Psi_A^B & , & -s\Phi_A^B \cdot s\Theta_A^B \\ c\Phi_A^B \cdot c\Theta_A^B \cdot c\Psi_A^B & , & c\Phi_A^B \cdot c\Theta_A^B \cdot s\Psi_A^B & , & -c\Phi_A^B \cdot s\Theta_A^B \end{bmatrix}$$

Equation 22.4-117

$$\frac{\partial T_A^B}{\partial \Phi_A^B} := \begin{bmatrix} 0 & , & 0 & , & 0 \\ T_A^B(3) & , & T_A^B(6) & , & T_A^B(9) \\ -T_A^B(2) & , & -T_A^B(5) & , & -T_A^B(8) \end{bmatrix}$$

Equation 22.4-118

22.5 Point Mass Kinematics

22.5.1 Propagation of Linear Dynamic States

L_X_PROP takes the current PVAJ of point (b) with respect to point (a) at time (t) with respect to and in frame (A), and propagates them over the time interval (Δt) assuming that jerk is piecewise continuous.

$$\mathbf{L\_X\_PROP}\left(\underline{P}_b^A , \underline{V}_b^A , \underline{A}_b^A , \underline{J}_b^A , \Delta t \right)$$

Equation 22.5-1

$$\underline{P}_b^A\left(t + \Delta t \right) := \underline{P}_b^A + \Delta t \cdot \left(\underline{V}_b^A + 2^{-2} \cdot \Delta t \cdot \left(\underline{A}_b^A + 3^{-2} \cdot \Delta t \cdot \underline{J}_b^A \right) \right)$$

Equation 22.5-2

$$\underline{V}_b^A\left(t + \Delta t \right) ;= \underline{V}_b^A + \Delta t \cdot \left(\underline{A}_b^A + 2^{-2} \cdot \Delta t \cdot \underline{J}_b^A \right)$$

Equation 22.5-3

$$\underline{A}_b^A\left(t + \Delta t \right) := \underline{A}_b^A + \Delta t \cdot \underline{J}_b^A$$

Equation 22.5-4

22.5.2 Propagation of Angular Dynamic States

A_X_PROP takes a quaternion representing the orientation of frame (B) with respect to frame (A), the angular velocity of (B) with respect to (A), acceleration and jerk at time (t), and propagates them over the time interval (Δt) assuming that angular jerk is piecewise continuous.

$$\mathbf{A\_X\_PROP}\left(Q_A^B , \underline{\omega}_{A,B}^B , \dot{\underline{\omega}}_{A,B}^B , \ddot{\underline{\omega}}_{A,B}^B , \Delta t \right)$$

Equation 22.5-5

$$Q_A^B\left(t + \Delta t \right) := Q_A^B + \Delta t \cdot \dot{Q}_A^B$$

Equation 22.5-6

$$\underline{\omega}_{A,B}^B\left(t + \Delta t \right) := \underline{\omega}_{A,B}^B + \Delta t \cdot \left(\dot{\underline{\omega}}_{A,B}^B + 2^{-2} \cdot \Delta t \cdot \ddot{\underline{\omega}}_{A,B}^B \right)$$

Equation 22.5-7

$$\dot{\underline{\omega}}_{A,B}^B\left(t + \Delta t \right) := \dot{\underline{\omega}}_{A,B}^B + \Delta t \cdot \ddot{\underline{\omega}}_{A,B}^B$$

Equation 22.5-8

22.5.3 Average Angular Rates from Direction Cosines

AVG_W_RATES takes the transform defining the orientation of frame (B) with respect to frame (A) at time (t - Δt) and again at time (t), and returns the average angular rate over time interval (Δt).

$$\textbf{AVG\_W\_RATES}\left(T_A^B\left(t-\Delta t \right), T_A^B, \underline{\omega}_{A,B}^B, \Delta t \right)$$

$$\equiv \overline{\varphi}_{AR}\left(T_A^B\left(t-\Delta t \right), T_A^B \right)$$

Equation 22.5-9

The transformation over time (Δt) is,

$$\Delta T\left(t \right) := T_A^B\left(t-\Delta t \right)\cdot T_A^B\left(t \right)$$

Equation 22.5-10

$$2\cdot\underline{\Lambda} := \left(\Delta T\left(6 \right)-\Delta T\left(6 \right) \;,\; \Delta T\left(7 \right)-\Delta T\left(7 \right) \;,\; \Delta T\left(2 \right)-\Delta T\left(2 \right) \right)^T$$

Equation 22.5-11

$$\Lambda \geq 10^{-12} \Rightarrow \Lambda\cdot\Delta t\cdot\underline{\omega}_{A,B}^B := \underline{\Lambda}\cdot\sin^{-1}\left(\Lambda \right)$$

Equation 22.5-12

$$\Lambda < 10^{-12} \Rightarrow \underline{\omega}_{A,B}^B = \underline{0}_3$$

Equation 22.5-13

22.5.4 Dynamics of a Point in Inertial Space

Consider a general point (p) moving with respect to frame (B) that is itself in motion with respect to the non-rotating frame (A). *PTM_DYNAMICS* provides the inertial velocity and acceleration of point (p), expressed in (B).

PTM_DYNAMICS

$$\left(\underline{A}_{a,b}^B, \underline{V}_{a,b}^B, \dot{\underline{\omega}}_{A,B}^B, \underline{\omega}_{A,B}^B, \underline{P}_{b,p}^B, \dot{\underline{P}}_{b,p}^B, \ddot{\underline{P}}_{b,p}^B, k, \underline{A}_{a,p}^B, \underline{V}_{a,p}^B \right)$$

Equation 22.5-14

If (p) is moving with respect to (B) then (k = 0) and,

$$\underline{V}_{a,p} := \underline{V}_{a,b} + \dot{\underline{P}}_{b,p} + \underline{\omega}_{A,B}\times\underline{P}_{b,p}$$

Equation 22.5-15

$$\underline{A}_{a,p} :=$$

$$\underline{A}_{a,b} + \ddot{\underline{P}}_{b,p} + \underline{\omega}_{A,B} \times \underline{V}_{a,b} + 2 \cdot \underline{\omega}_{A,B} \times \dot{\underline{P}}_{b,p} + \dot{\underline{\omega}}_{A,B} \times \underline{P}_{b,p} + \underline{\omega}_{A,B} \times \underline{\omega}_{A,B} \times \underline{P}_{b,p}$$

Equation 22.5-16

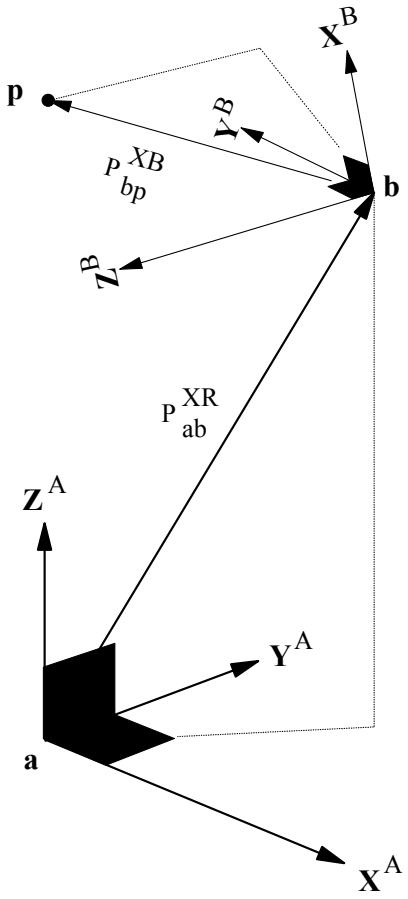

Figure 22-7 : Dynamics of a Point in E^3

If point (p) is stationary with respect to frame (B) then (k = 1) and,

$$\underline{V}_{a,p} := \underline{V}_{a,b} + \underline{\omega}_{A,B} \times \underline{P}_{b,p}$$

Equation 22.5-17

$$\underline{A}_{a,p} := \dot{\underline{V}}_{a,b} + \underline{\omega}_{A,B} \times \underline{V}_{a,b} + \dot{\underline{\omega}}_{A,B} \times \underline{P}_{b,p} + \underline{\omega}_{A,B} \times \underline{\omega}_{A,B} \times \underline{P}_{b,p}$$

Equation 22.5-18

Expanding the acceleration equation assuming that points (b) and (p) are fixed in a rigid body, expressing the result in frame (B),

$$A_{a,p}^{XB} \coloneqq \dot{V}_{a,b}^{XB} + \omega_{A,B}^{YB} \cdot V_{a,b}^{ZB} - \omega_{A,B}^{ZB} \cdot V_{a,b}^{YB} + \underline{P}_{b,p}^{B} \otimes \begin{pmatrix} -\left(\omega_{A,B}^{YB}\right)^2 - \left(\omega_{A,B}^{ZB}\right)^2 \\ \omega_{A,B}^{XB} \cdot \omega_{A,B}^{YB} - \dot{\omega}_{A,B}^{ZB} \\ \dot{\omega}_{A,B}^{YB} + \omega_{A,B}^{XB} \cdot \omega_{A,B}^{ZB} \end{pmatrix}$$

Equation 22.5-19

$$A_{a,p}^{YB} \coloneqq \dot{V}_{a,b}^{YB} + \omega_{A,B}^{ZB} \cdot V_{a,b}^{XB} - \omega_{A,B}^{XB} \cdot V_{a,b}^{ZB} + \underline{P}_{b,p}^{B} \otimes \begin{pmatrix} \dot{\omega}_{A,B}^{ZB} + \omega_{A,B}^{XB} \cdot \omega_{A,B}^{YB} \\ -\left(\omega_{A,B}^{XB}\right)^2 - \left(\omega_{A,B}^{ZB}\right)^2 \\ \omega_{A,B}^{YB} \cdot \omega_{A,B}^{ZB} - \dot{\omega}_{A,B}^{XB} \end{pmatrix}$$

Equation 22.5-20

$$A_{a,p}^{ZB} \coloneqq \dot{V}_{a,b}^{ZB} + \omega_{A,B}^{XB} \cdot V_{a,b}^{YB} - \omega_{A,B}^{YB} \cdot V_{a,b}^{XB} + P_{b,p}^{B} \otimes \begin{pmatrix} \omega_{A,B}^{XB} \cdot \omega_{A,B}^{ZB} - \dot{\omega}_{A,B}^{YB} \\ \dot{\omega}_{A,B}^{XB} + \omega_{A,B}^{YB} \cdot \omega_{A,B}^{ZB} \\ -\left(\omega_{A,B}^{XB}\right)^2 - \left(\omega_{A,B}^{YB}\right)^2 \end{pmatrix}$$

Equation 22.5-21

If point (p) is lies on $\underline{X}^B$, as is common in missile kinematics,

$$A_{a,p}^{XB} \coloneqq \dot{V}_{a,b}^{XB} + \omega_{A,B}^{YB} \cdot V_{a,b}^{ZB} - \omega_{A,B}^{ZB} \cdot V_{a,b}^{YB} - P_{b,p}^{XB} \cdot \left(\left(\omega_{A,B}^{YB}\right)^2 + \left(\omega_{A,B}^{ZB}\right)^2 \right)$$

Equation 22.5-22

$$A_{a,p}^{YB} \coloneqq \dot{V}_{a,b}^{YB} + \omega_{A,B}^{ZB} \cdot V_{a,b}^{XB} - \omega_{A,B}^{XB} \cdot V_{a,b}^{ZB} + P_{b,p}^{XB} \cdot \left(\dot{\omega}_{A,B}^{ZB} + \omega_{A,B}^{XB} \cdot \omega_{A,B}^{YB} \right)$$

Equation 22.5-23

$$A_{a,p}^{ZB} \coloneqq \dot{V}_{a,b}^{ZB} + \omega_{A,B}^{XB} \cdot V_{a,b}^{YB} - \omega_{A,B}^{YB} \cdot V_{a,b}^{XB} - P_{b,p}^{XB} \cdot \left(\dot{\omega}_{A,B}^{YB} - \omega_{A,B}^{XB} \cdot \omega_{A,B}^{ZB} \right)$$

Equation 22.5-24

22.5.5 Euler to Angular Rates

DE_TO_W takes a YPR Euler triplet defining the orientation and angular rate of frame (B) with respect to frame (A), and its time rate of change, and returns the angular rate vector.

$$\mathbf{DE\_TO\_W}\left(\dot{E}_A^B, E_A^B, \omega_{A,B}^B\right) \equiv \varphi_{DE}^W\left(\dot{E}_A^B, E_A^B\right)$$

Equation 22.5-25

$$\underline{\omega}_{A,B}^B := \begin{pmatrix} \dot{\Phi}_A^B - \dot{\Psi}_A^B \cdot \sin\Theta_A^B \\ \dot{\Psi}_A^B \cdot \sin\Phi_A^B \cdot \cos\Theta_A^B + \dot{\Theta}_A^B \cdot \cos\Phi_A^B \\ \dot{\Psi}_A^B \cdot \cos\Phi_A^B \cdot \cos\Theta_A^B - \dot{\Theta}_A^B \cdot \sin\Phi_A^B \end{pmatrix}$$

Equation 22.5-26

If the roll angle is zero,

$$\underline{\omega}_{A,B}^B := \left(-\dot{\Psi}_A^B \cdot \sin\Theta_A^B \quad , \quad \dot{\Theta}_A^B \quad , \quad \dot{\Psi}_A^B \cdot \cos\Theta_A^B\right)^T$$

Equation 22.5-27

22.5.6 Angular to Euler (YPR) Rates

W_TO_DE takes the angular rate of frame (B) with respect to frame (A), and Euler triplet representing the orientation between the two, and returns the Euler rate of frame (B) with respect to frame (A).

$$\mathbf{W\_TO\_DE}\left(\underline{\omega}_{A,B}^B, E_A^B, \dot{E}_A^B\right) \equiv \varphi_W^{DE}\left(\underline{\omega}_{A,B}^B, E_A^B\right)$$

Equation 22.5-28

$$\dot{E}_A^B := \begin{pmatrix} \omega_{A,B}^{XB} + \dot{\Psi}_A^B \cdot \sin\Theta_A^B \\ \omega_{A,B}^{YB} \cdot \cos\Phi_A^B - \omega_{A,B}^{ZB} \cdot \sin\Phi_A^B \\ \left(\omega_{A,B}^{YB} \cdot \sin\Phi_A^B + \omega_{A,B}^{ZB} \cdot \cos\Phi_A^B\right) \cdot \sec\Theta_A^B \end{pmatrix}^T$$

Equation 22.5-29

If the roll angle is zero,

$$\dot{E}_A^B := \left(\omega_{A,B}^{ZB} \cdot \tan\Theta_A^B \quad , \quad \omega_{A,B}^{YB} \quad , \quad \omega_{A,B}^{ZB} \cdot \sec\Theta_A^B\right)$$

Equation 22.5-30

22.5.7 Euler to Angular Accelerations

D2E_TO_DW takes an Euler triplet representing the orientation of frame (B) with respect to frame (A), and its Euler rate and acceleration, and returns the angular acceleration.

$$\textbf{D2E\_TO\_DW}\left(\ddot{E}_A^B , \dot{E}_A^B , E_A^B , \underline{\dot{\omega}}_{A,B}^B \right)$$

Equation 22.5-31

$$\dot{\omega}_{A,B}^{XB} := \ddot{\Phi}_A^B - \ddot{\Psi}_A^B \cdot \sin\Theta_A^B - \dot{\Psi}_A^B \cdot \dot{\Theta}_A^B \cdot \cos\Theta_A^B$$

Equation 22.5-32

$$\dot{\omega}_{A,B}^{YB} := \begin{pmatrix} \ddot{\Theta}_A^B + \ddot{\Psi}_A^B \cdot \dot{\Phi}_A^B \cdot \cos\Theta_A^B \\ \ddot{\Psi}_A^B \cdot \cos\Theta_A^B - \left(\dot{\Phi}_A^B + \dot{\Psi}_A^B \cdot \sin\Theta_A^B \right) \cdot \dot{\Theta}_A^B \end{pmatrix}^T \cdot \begin{pmatrix} \cos\Phi_A^B \\ \sin\Phi_A^B \end{pmatrix}$$

Equation 22.5-33

$$\dot{\omega}_{A,B}^{ZB} := \begin{pmatrix} \ddot{\Psi}_A^B \cdot \cos\Theta_A^B - \left(\dot{\Phi}_A^B + \dot{\Psi}_A^B \cdot \sin\Theta_A^B \right) \cdot \dot{\Theta}_A^B \\ -\ddot{\Theta}_A^B - \dot{\Psi}_A^B \cdot \dot{\Phi}_A^B \cdot \cos\Theta_A^B \end{pmatrix}^T \cdot \begin{pmatrix} \cos\Phi_A^B \\ \sin\Phi_A^B \end{pmatrix}$$

Equation 22.5-34

If the roll angle is zero,

$$\underline{\dot{\omega}}_{A,B}^B := \begin{pmatrix} -\ddot{\Psi}_A^B \cdot \sin\Theta_A^B - \dot{\Psi}_A^B \cdot \dot{\Theta}_A^B \cdot \cos\Theta_A^B \\ \ddot{\Theta}_A^B \\ \ddot{\Psi}_A^B \cdot \cos\Theta_A^B - \dot{\Theta}_A^B \cdot \dot{\Psi}_A^B \cdot \sin\Theta_A^B \end{pmatrix}$$

Equation 22.5-35

22.5.8 Angular to Euler Accelerations

DW_TO_D2E takes an Euler triplet representing the orientation of frame (B) with respect to frame (A), and its angular velocity and acceleration, and returns the Euler angle acceleration.

$$\textbf{DW\_TO\_D2E}\left(\ddot{E}_A^B , E_A^B , \underline{\omega}_{A,B}^B , \underline{\dot{\omega}}_{A,B}^B \right)$$

Equation 22.5-36

$$\ddot{\Psi}_A^B := \left(\dot{\omega}_{A,B}^{YB} \cdot \sin\Phi_A^B + \dot{\omega}_{A,B}^{ZB} \cdot \cos\Phi_A^B + \varphi_1 \right) \cdot \sec\Theta_A^B$$

Equation 22.5-37

$$\varphi_1 := \begin{pmatrix} \omega_{AB}^{YB} \cdot \cos\Phi_A^B - \omega_{AB}^{ZB} \cdot \sin\Phi_A^B \\ \left(\omega_{AB}^{YB} \cdot \sin\Phi_A^B + \omega_{AB}^{ZB} \cdot \cos\Phi_A^B \right) \cdot \tan\Theta_A^B \end{pmatrix}^T \cdot \begin{pmatrix} \dot{\Phi}_A^B \\ \dot{\Theta}_A^B \end{pmatrix}$$

Equation 22.5-38

$$\ddot{\Theta}_A^B := \left(\dot{\omega}_{A,B}^{YB} - \omega_{A,B}^{ZB} \cdot \dot{\Phi}_A^B \right) \cdot \cos\Phi_A^B - \left(\dot{\omega}_{A,B}^{ZB} + \omega_{A,B}^{YB} \cdot \dot{\Phi}_A^B \right) \cdot \sin\Phi_A^B$$

Equation 22.5-39

$$\ddot{\Phi}_A^B := \dot{\omega}_{A,B}^{XB} + \ddot{\Psi}_A^B \cdot \sin\Theta_A^B + \dot{\Psi}_A^B \cdot \dot{\Theta}_A^B \cdot \cos\Theta_A^B$$

Equation 22.5-40

If the roll angle is zero,

$$\ddot{E}_A^B := \begin{pmatrix} \dot{\omega}_{A,B}^{ZB} + \omega_{A,B}^{ZB} \cdot \omega_{A,B}^{YB} \cdot \tan\Theta_A^B \cdot \sec\Theta_A^B \\ \dot{\omega}_{A,B}^{YB} \\ -\ddot{\Psi}_A^B \cdot \sin\Theta_A^B - \dot{\Psi}_A^B \cdot \dot{\Theta}_A^B \cdot \cos\Theta_A^B \end{pmatrix}^T$$

Equation 22.5-41

22.5.9 Cartesian to Euler Rates

DX_TO_DE takes the PV of point (b) with respect to point (a), the origins of frames (A) and (B) respectively, and returns the Euler rate of (B) with respect to (A) assuming that the Euler roll angle is zero.

$$\textbf{DX\_TO\_DE}\left(\dot{E}_A^B , \underline{P}_b^A , \underline{V}_b^A \right) \equiv \varphi_{DX}^{DE}\left(\underline{P}_b^A , \underline{V}_b^A \right)$$

Equation 22.5-42

$$\dot{\Phi}_A^B := 0$$

Equation 22.5-43

$$\dot{\Theta}_A^B := \frac{\varphi_1}{P_{a,b}^2} \cdot \left(\frac{P_b^{ZA}}{P_b^{hA}} \right) - \frac{V_b^{ZA} \cdot P_b^{hA}}{P_{a,b}^4}$$

Equation 22.5-44

$$\left(P_b^{hA} \right)^2 \cdot \dot{\Psi}_A^B := \varphi_2$$

Equation 22.5-45

$$\varphi_1 \coloneqq P_b^{XA} \cdot V_b^{XA} + P_b^{YA} \cdot V_b^{YA}$$

Equation 22.5-46

$$\varphi_2 \coloneqq P_b^{XA} \cdot V_b^{YA} - P_b^{YA} \cdot V_b^{XA}$$

Equation 22.5-47

E_RATES takes the VAJ of point (b) with respect to point (a), the gravitational acceleration at (b), and the orientation of frame (B) with respect to ENU LGA (A), returning the Euler rate, assuming zero incidence.

$$\mathbf{E\_RATES}\left(E_A^B , \underline{V}_b^A , \underline{A}_b^A , \underline{J}_b^A , g_b^{ZA} , \dot{E}_A^B \right)$$

Equation 22.5-48

$$\dot{\Psi}_A^B \equiv \dot{\Psi}_A^C \coloneqq \frac{V_b^{XA} \cdot A_b^{YA} - V_b^{YA} \cdot A_b^{XA}}{V_b^{hA}}$$

Equation 22.5-49

$$\dot{\Theta}_A^B \equiv \dot{\Theta}_A^C \coloneqq \frac{V_b^{ZA} \cdot \left(V_b^{XA} \cdot A_b^{XA} + V_b^{YA} \cdot A_b^{YA} \right)}{V_{a,b}^{hA} \cdot V_{a,b}^2} - \frac{V_b^{hA} \cdot A_b^{ZA}}{V_{a,b}^2}$$

Equation 22.5-50

$$\underline{A}_b^C \coloneqq T_A^C\left(0 \quad \Theta_A^C \quad \Psi_A^C \right) \cdot \left(A_b^{XA} \quad , \quad A_b^{YA} \quad , \quad A_b^{ZA} + g_b^{ZA} \right)^T$$

Equation 22.5-51

$$\underline{J}_b^C \coloneqq T_A^C\left(0 \quad \Theta_A^C \quad \Psi_A^C \right) \cdot \underline{J}_b^A$$

Equation 22.5-52

$$\varphi_3 \coloneqq J_b^{YC} + \dot{\Psi}_A^C \cdot \left(T_A^C(2) \cdot A_b^{YA} - T_A^C(5) \cdot A_b^{XA} \right)$$

Equation 22.5-53

$$\varphi_4 \coloneqq \dot{\Psi}_A^C \cdot \left(T_A^C(3) \cdot A_b^{YA} - T_A^C(6) \cdot A_b^{XA} \right) + \dot{\Theta}_A^C \cdot A_b^{XC} + J_b^{ZC}$$

Equation 22.5-54

$$\left(\left| A_b^{YC} \right| > 10^{-15} \right) \vee \left(\left| A_b^{ZC} \right| > 10^{-15} \right) \Rightarrow$$

$$\left(A_b^{rC} \right)^2 \cdot \Phi_A^B \coloneqq A_b^{YC} \cdot \varphi_4 - A_b^{ZC} \cdot \varphi_3$$

Equation 22.5-55

$$\left(\left| A_b^{YC} \right| \le 10^{-15} \right) \wedge \left(\left| A_b^{ZC} \right| \le 10^{-15} \right) \Rightarrow \Phi_A^B := 0$$

Equation 22.5-56

22.5.10 Cartesian to Euler Acceleration

D2X_TO_D2E takes the PVA of point (b) with respect to point (a), the origins of frames (A) and (B) respectively, returning the Euler acceleration of (B) with respect to (A), assuming that the Euler roll angle is zero.

$$\textbf{D2X\_TO\_D2E}\left(\ddot{E}_A^B , \underline{P}_b^A , \underline{V}_b^A , \underline{A}_b^A \right)$$

Equation 22.5-57

$$\left(P_{a,b}^{hA} \right)^2 \cdot \ddot{\Psi}_A^B := \dot{\varphi}_2 - 2 \cdot \varphi_1 \cdot \varphi_2 \cdot \left(P_{a,b}^{hA} \right)^{-4}$$

Equation 22.5-58

$$P_{a,b}^2 \cdot \ddot{\Theta}_A^B :=$$

$$-2 \cdot \dot{\Theta}_A^B \cdot \left(\underline{P}_b^A \bullet \underline{V}_b^A \right) + \frac{P_b^{ZA}}{P_b^{hA}} \cdot \left(\dot{\varphi}_1 - \left(\frac{\varphi_1}{P_b^{hA}} \right)^2 \right) - A_b^{ZA} \cdot P_b^{hA}$$

Equation 22.5-59

$$\varphi_1 := P_b^{XA} \cdot V_b^{XA} + P_b^{YA} \cdot V_b^{YA}$$

Equation 22.5-60

$$\varphi_2 := P_b^{XA} \cdot V_b^{YA} - P_b^{YA} \cdot V_b^{XA}$$

Equation 22.5-61

$$\dot{\varphi}_1 := P_b^{XA} \cdot A_b^{XA} + P_b^{YA} \cdot A_b^{YA} + \left(V_b^{hA} \right)^2$$

Equation 22.5-62

$$\dot{\varphi}_2 := P_b^{XA} \cdot A_b^{YA} - P_b^{YA} \cdot A_b^{XA}$$

Equation 22.5-63

22.6 Earth, Atmosphere and Gravity

22.6.1 Atmospheric Parameters

ATMOSPHERE provides atmospheric data at point (p), directly above point (d) on the Earth's surface, as a function of geodetic height [-0.9,32] km. The speed of sound (V_A), static air pressure (P_S), static air temperature (T_S), and air density (σ_A) defined in §19.1-5 are returned.

$$\textbf{ATMOSPHERE}\left(P_{d,p}^{ZG} , V_A , P_S , T_S , \rho_A , \text{LUNOUT} , \text{ISTOP} \right)$$

Equation 22.6-1

If the geodetic height is outside the given range a warning is written to the formatted output file via channel *LUNOUT*, and the *ISTOP* flag set to 1.

22.6.2 Earth Curvature Parameters

EARTH_RADII takes the WGS 84 geodetic latitude of point (d) on the Earth's surface (λ_d), and its equatorial and polar radii, returning the geocentric radius ($P_{r,d}$), E/W and N/S curvatures (R_{pd} , R_{md}) from §18.3-5.

$$\textbf{EARTH\_RADII}\left(\lambda_d , P_{r,d} , R_{p,d} , R_{md} \right)$$

Equation 22.6-2

22.6.3 Gravitational Acceleration

GRAVITY takes the geodetic height of point (p), its geodetic latitude, and the radius of the Earth at point (d) directly beneath, returning the gravitational acceleration from §20.

$$g_p^{ZG} := \textbf{GRAVITY}\left(P_{d,p}^{ZG} , \lambda_d , P_{r,d} , k \right)$$

Equation 22.6-3

When (k = 0) an accurate gravity function is used, otherwise the simplified model is used.

22.6.4 Conversion from ECEF to WGS84 Co-ordinates

ECEF_TO_WGS84 takes the ECEF position of point (p) which lies on the geodetic vertical intersecting the Earth's geoid at point (d), and returns its WGS84 Geodetic co-ordinates using Olsen's[O.4] algorithm.

$$\textbf{ECEF\_TO\_WGS84}\left(\underline{P}_p^E , \mu_d , \lambda_d , P_{d,p}^{ZG} , \text{LUNOUT} \right) \equiv \varphi_E^G\left(\underline{P}_p^E \right)$$

Equation 22.6-4

Starting with the Earth's principal radii and eccentricity defined in §18.1,

$$\left(\xi_1 \quad , \quad \xi_2 \quad , \quad \xi_3 \right) := \left(R_A \cdot e^2 \quad , \quad \xi_1^2 \quad , \quad 0.5 \cdot \xi_1 \cdot e^2 \right)$$

Equation 22.6-5

$$\left(\xi_4 \quad , \quad \xi_5 \quad , \quad \xi_6 \right) := \left(0.4 \cdot \xi_2^2 \quad , \quad \xi_1 + \xi_3 \quad , \quad 1 - e^2 \right)$$

Equation 22.6-6

If the distance from the Earth's centre (r) to (p) is < 100 km a warning message is sent to the output file via channel *LUNOUT*.

$$P_{r,p} < 10^5 \Rightarrow \left(\mu_p \quad , \quad \lambda_p \quad , \quad P_{d,p}^{ZG} \right) := \left(0 \quad , \quad 0 \quad , \quad R_A \right)$$

Equation 22.6-7

Providing this inequality is false, i.e. $P_{r,p} \geq 10^5$,

$$\left(\xi_7 \quad , \quad \xi_8 \quad , \quad \xi_9 \quad , \quad \xi_{10} \right) :=$$

$$\left(\left(\frac{P_{r,p}^{ZE}}{P_{r,p}} \right)^2 \quad , \quad \frac{\left(P_{r,p}^{hE} \right)^2}{P_{r,p}} \quad , \quad \frac{\xi_2}{P_{r,p}} \quad , \quad \xi_3 - \left(\frac{\xi_4}{P_{r,p}} \right) \right)$$

Equation 22.6-8

If $\xi_8 > 0.3$ then,

$$\xi_{11} := \frac{\left| P_p^{ZE} \right|}{P_{r,p}} \cdot \left(1 + \frac{\xi_8 \cdot \left(\xi_1 + \xi_9 + \xi_7 \cdot \xi_{10} \right)}{P_{r,p}} \right)$$

Equation 22.6-9

$$\lambda'_p := \xi_{12} := \sin^{-1}\left(\xi_{11} \right)$$

Equation 22.6-10

else $\xi_8 \leq 0.3$,

$$P_{r,p} \cdot \xi_{12} := \left| P_p^{hE} \right| \cdot \left(1 - \frac{\xi_7 \cdot \left(\xi_5 - \xi_9 + \xi_8 \cdot \xi_{10} \right)}{P_{r,p}} \right)$$

Equation 22.6-11

$$\lambda'_p := \cos^{-1}\left(\xi_{12} \right)$$

Equation 22.6-12

$$\xi_{11} := \sqrt{1 - \xi_{12}^2}$$

Equation 22.6-13

Endif . Whereupon,

$$\left(\xi_{13} \;,\; \xi_{14} \;,\; \xi_{15} \;,\; \xi_{16} \right) :=$$

$$\left(1 - e \cdot \xi_{11}^2 \;,\; R_a \,/\, \sqrt{\xi_{13}} \;,\; \xi_6 \cdot \xi_{14} \;,\; P_p^{hE} - \xi_{14} \cdot \xi_{12} \right)$$

Equation 22.6-14

$$\left(\xi_{17} \;,\; \xi_{18} \right) := \left(\left| P_p^{ZE} \right| - \xi_{15} \cdot \xi_{11} \;,\; \xi_{12} \cdot \xi_{16} + \xi_{11} \cdot \xi_{17} \right)$$

Equation 22.6-15

$$\left(\xi_{19} \;,\; \xi_{20} \right) := \left(\xi_{12} \cdot \xi_{17} - \xi_{11} \cdot \xi_{16} \;,\; \frac{\xi_{19}}{\xi_{15} \cdot \xi_{13}^{-1} + \xi_{18}} \right)$$

Equation 22.6-16

The geodetic co-ordinates are given by,

$$\left(\mu_p \;,\; \lambda_p \;,\; P_{d,p}^{ZG} \right) :=$$

$$\left(\tan^{-1}\left(P_p^{YE} \,/\, P_p^{XE} \right) \;,\; \left(\lambda'_p + \xi_{20} \right) \cdot \operatorname{sign}\left(1, P_p^{ZE} \right) \;,\; \xi_{18} + 2^{-1} \cdot \xi_{19} \cdot \xi_{20} \right)$$

Equation 22.6-17

22.6.5 Conversion from WGS84 to ECEF Co-ordinates

WGS84_TO_ECEF takes the co-ordinates of point (p) on the geodetic vertical intersecting the Earth's geoid at (d), returning its ECEF position.

$$\textbf{WGS84\_TO\_ECEF}\left(\mu_d , \lambda_d , P_{d,p}^{ZG} , \underline{P}_p^{E} \right)$$

Equation 22.6-18

$$\underline{P}_p^{E} := \begin{pmatrix} \left(R_{r,d} + P_{d,p}^{ZG} \right) \cdot \cos\mu_p \cdot \cos\lambda_p \\ \left(R_{r,d} + P_{d,p}^{ZG} \right) \cdot \sin\mu_p \cdot \cos\lambda_p \\ \left(\left(1 - e^2 \right) \cdot R_{r,d} + P_{d,p}^{ZG} \right) \cdot \sin\lambda_p \end{pmatrix}$$

Equation 22.6-19

22.7 Digital Map Data Extraction

The map data extraction modules manipulate MBDA reformatted DLMS WGS 84 DTED data, derived from 1:50,000 scale paper maps, and stored as 1° digitised map squares. The DTED contains height points every 100 m over the ground. These points are extracted and manipulated by the map handling modules shown in Figure 22-8.

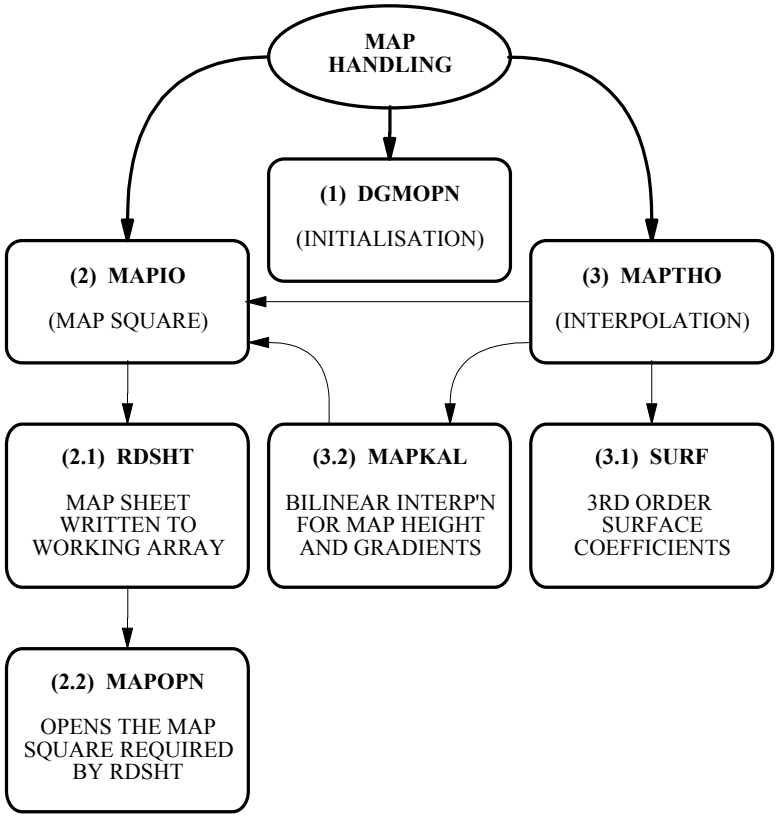

Figure 22-8 : Map Handling Structure

Map handling is initialised by a single call to *DGMOPN*. Thereafter, *MAPIO* and *MAPTHO* extract the ground height, E/W and N/S gradients at a given WGS 84 latitude and longitude.

22.7.1 Map Data Initialisation

DGMOPN is called once during simulation initialisation and provides the map scaling depending on the WGS 84 latitude of a general point (p).

$$\mathbf{DGMOPN}\ \left(\lambda_p \right)$$

Equation 22.7-1

The path to the digital map data is established by assigning data channel *LUNMAP* to the map square storage area.

22.7.2 Map Square Selection

MAPIO opens the map square containing the current geodetic position of (p), and thereafter, as directed by *MAPTHO*.

$$\textbf{MAPIO}\ \left(\mu_P , \lambda_P \right)$$

Equation 22.7-2

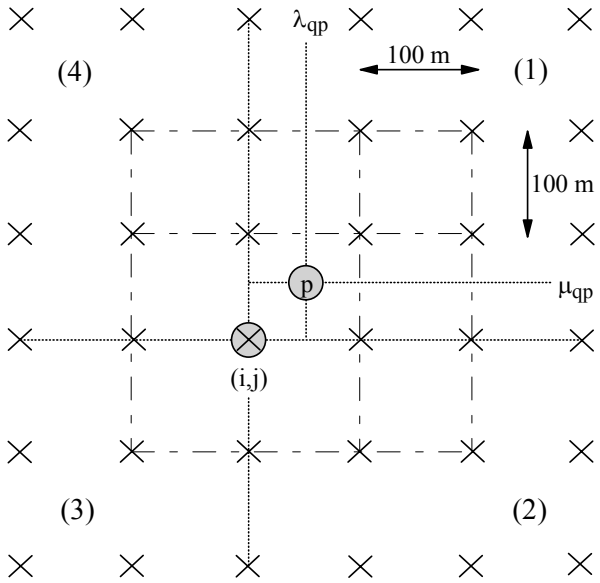

Figure 22-9 : Map Height Ordinates

Equi-distant 100 m map height ordinates are loaded into the working map array. In Figure 22-9 map square (1) is loaded first containing point (p), map squares being identified by their bottom-left hand corner (i,j).

22.7.3 Map Data Interpolation

MAPTHO takes the position (p), and returns the height of the ground at point (f) directly below, together with the E/W and N/S ground slopes there.

$$\textbf{MAPTHO}\ \left(\mu_p , \lambda_p , P_{f,p}^{ZG} , \frac{\partial P_{f,p}^{ZG}}{\partial \mu_p} , \frac{\partial P_{f,p}^{ZG}}{\partial \lambda_p} \right)$$

Equation 22.7-3

16 map heights are extracted in the square {(i,j):i,j = [-1(1)2]}, starting with those which fall in the map square (1) containing (p). Nearby maps are accessed to collect ordinates from squares (2) to (4) by calling *MAPIO*. When the ordinates defining the 300 m patch have been extracted a 3rd order bi-cubic spline is fitted by *SURF* and interpolation used to extract the map height and ground slopes at (p) in *MAPKAL*. The map data extracted contain random triangulation and digitisation errors that differ between map sources and digitisation techniques used.

22.8 Digital Filters

The author would like to acknowledge the work of Dr. R. Stirling in the conversion of continuous filters in the Laplace domain to the digital domain using bi-linear transforms.

Digital filters functional forms are used in the text that operate on a scalar argument (φ_{XYZ}), or a vectorised input ($\underline{\varphi}_{XYZ}$). If a scalar argument is given in a vector function it applies to all the elements of the vector input.

When using the functional form it is assumed that the update rate is provided in-situ. Digital filters should be used with an update frequency at least 10x the bandwidth of their continuous counterpart so as to maintain accuracy.

22.8.1 Digital First Order Lag Filters

D_LAG propagates up to 150 digital lags over time interval (Δt), with time varying bandwidth (ω_C).

$$y := \mathbf{D\_LAG}\left(X_I, \Delta t, t_C, N, I\right) \equiv \varphi_{DlL}\left(X_I, 1/\omega_C\right)$$

Equation 22.8-1

These filters are the discrete equivalent to the continuous transfer function:

$$y(s) := \frac{X_I}{1 + s \cdot t_C}$$

Equation 22.8-2

$$\chi_k := \chi_{k-1} + \left(\frac{X_I(k-1) - 2 \cdot \chi_{k-1}}{\Delta t + 2 \cdot t_C}\right) \cdot \Delta t$$

Equation 22.8-3

$$\chi_0 := \chi_{-1} := 2^{-1} \cdot X_I$$

Equation 22.8-4

$$y_k := \chi_k + \chi_{k-1}$$

Equation 22.8-5

If (I := 1), and on first use, the filter is re-initialised without integration using input (X_I). Each filter is identified by a unique number (N).

22.8.2 Digital First Order Lead Filters

D_LEAD propagates up to 50 digital leads over time interval (Δt), with time varying bandwidth (ω_C).

$$y := \textbf{D\_LEAD}\left(X_I , \Delta t , t_C , N , I \right) \equiv \varphi_{LD}\left(X_I , 1 / \omega_C \right)$$

Equation 22.8-6

These filters are the discrete equivalent to the continuous transfer function:

$$y(s) := \left(\frac{t_C \cdot s}{1 + t_C \cdot s} \right) \cdot X_I$$

Equation 22.8-7

$$\chi_k := \chi_{k-1} + \left(\frac{X_I(k-1) - 2 \cdot \chi_{k-1}}{\Delta t + 2 \cdot t_C} \right) \cdot \Delta t$$

Equation 22.8-8

$$\chi_0 := \chi_{-1} := 2^{-1} \cdot X_I$$

Equation 22.8-9

$$y_k := X_I(k) - \chi_k - \chi_{k-1}$$

Equation 22.8-10

If (I := 1), and on first use, the filter is re-initialised without integration using input (X_I). Each filter is identified by a unique number (N).

22.8.3 Digital Lead-Lag Filters

D_LEAD_LAG propagates up to 50 digital lead-lags over time interval (Δt), with time varying characteristics.

$$y := \textbf{D\_LEAD\_LAG}\left(X_I , \Delta t , t_N , t_D , N , I \right)$$

$$\equiv \varphi_{DLL}\left(X_I , 1 / \omega_N , 1 / \omega_D \right)$$

Equation 22.8-11

These filters are the discrete equivalent to the continuous transfer function:

$$y(s) := \left(\frac{1 + s \cdot t_N}{1 + s \cdot t_D} \right) \cdot X_I$$

Equation 22.8-12

$$\chi_k := \chi_{k-1} + \left(\frac{X_I(k-1) - 2 \cdot \chi_{k-1}}{\Delta t + 2 \cdot t_D} \right) \cdot \Delta t$$

Equation 22.8-13

$$\chi_0 := \chi_{-1} := 2^{-1} \cdot X_I$$

Equation 22.8-14

$$y_k := (t_N / t_D) \cdot X_I(k-1) - ((t_N / t_D) - 1) \cdot (\chi_k + \chi_{k-1})$$

Equation 22.8-15

If (I := 1), and on first use, the filter is re-initialised without integration using input (X_I). Each filter is identified by a unique number (N).

22.8.4 Digital Integration Filters

D_INTEG propagates up to 50 digital integrators over time interval (Δt), with a time varying gain, starting from an initial state (X_0).

$$y := \textbf{D\_INTEG} (X_O , X_I , \Delta t , t_C , N , I) \equiv \varphi_{DI} (X_I , t_C)$$

Equation 22.8-16

These filters are the discrete equivalent to the continuous transfer function:

$$y(s) := X_0 + \left(\frac{X_I}{s \cdot t_C} \right)$$

Equation 22.8-17

$$\chi_k := \chi_{k-1} + \left(\frac{X_I(k-1)}{2 \cdot t_C} \right) \cdot \Delta t$$

Equation 22.8-18

$$\chi_0 := \chi_{-1} := 0.5 \cdot X_I$$

Equation 22.8-19

$$y_k := \chi_k + \chi_{k-1}$$

Equation 22.8-20

If (I := 1), and on first use, the filter is re-initialised without integration using input (X_I). Each filter is identified by a unique number (N).

22.8.5 Digital Notch Filters

D_NOTCH propagates up to 50 digital notches over time interval (Δt), with time varying characteristics.

$$y := \textbf{D\_NOTCH}\left(X_I , \Delta t , t_{N1} , t_{N2} , t_{D1} , t_{D2} , N , I \right) \equiv \varphi_{DN}\left(X_I , t_{N1} , t_{N2} , t_{D1} , t_{D2} \right)$$

Equation 22.8-21

These filters are the discrete equivalent to the continuous transfer function:

$$y(s) := \left(\frac{1 + t_{N1} \cdot s + t_{N2} \cdot s^2}{1 + t_{D1} \cdot s + t_{D2} \cdot s^2} \right) \cdot X_I$$

Equation 22.8-22

$$\xi_4 \cdot \chi_k := X_I(k-1) \cdot \xi_3 - \xi_5 \cdot \chi_{k-1} - \xi_6 \cdot \chi_{k-2}$$

Equation 22.8-23

$$y_k := \chi_{k-2} + \xi_3^{-1} \cdot \left(\xi_1 \cdot \chi_k + \xi_2 \cdot \chi_{k-1} \right)$$

Equation 22.8-24

$$\xi_1 := 1 + \left(2 \cdot t_{N1} / \Delta t \right) + \left(4 \cdot t_{N2} / \Delta t^2 \right)$$

Equation 22.8-25

$$\xi_2 := 2 \cdot \left(1 - \left(4 \cdot t_{N2} / \Delta t^2 \right) \right)$$

Equation 22.8-26

$$\xi_3 := 1 - \left(2 \cdot t_{N1} / \Delta t \right) + \left(4 \cdot t_{N2} / \Delta t^2 \right)$$

Equation 22.8-27

$$\xi_4 := 1 + \left(2 \cdot t_{D1} / \Delta t \right) + \left(4 \cdot t_{D2} / \Delta t^2 \right)$$

Equation 22.8-28

$$\xi_5 := 2 \cdot \left(1 - \left(4 \cdot t_{D2} / \Delta t^2 \right) \right)$$

Equation 22.8-29

$$\xi_6 := 1 - \left(2 \cdot t_{D1} / \Delta t \right) + \left(4 \cdot t_{D2} / \Delta t^2 \right)$$

Equation 22.8-30

$$\chi_{-1} := \frac{\xi_3 \cdot X_I \cdot (\xi_4 - \xi_1)}{\xi_4 \cdot (\xi_2 + \xi_3) - \xi_1 \cdot (\xi_5 + \xi_6)}$$

Equation 22.8-31

$$\xi_1 \cdot \chi_0 = X_I \cdot \xi_3 - \chi_{-1} \cdot (\xi_2 + \xi_3)$$

Equation 22.8-32

If (I := 1), and on first use, the filter is re-initialised without integration using input (X_I). Each filter is identified by a unique number (N).

22.8.6 Digital Second Order Lag Filters

D_2_LAG propagates up to 100 digital 2nd order lags over time interval (Δt), with time varying characteristics.

$$y := \textbf{D\_2\_LAG}(X_I, \Delta t, \zeta, \omega_n, N, I) \equiv \varphi_{D2L}(X_I, \zeta, \omega_n)$$

Equation 22.8-33

These filters are the discrete equivalent to the continuous transfer function:

$$y(s) := \left(\frac{\omega_n^2}{s^2 + 2 \cdot \zeta \cdot \omega_n \cdot s + \omega_n^2}\right) \cdot X_I$$

Equation 22.8-34

$$\chi_k := \chi_{k-1} + \xi_1^{-1} \cdot (X_I(k-1) - \xi_2 \cdot \chi_{k-1} - \xi_3 \cdot \chi_{k-2})$$

Equation 22.8-35

$$y_k := \chi_k + 2 \cdot \chi_{k-1} + \chi_{k-2}$$

Equation 22.8-36

$$\xi := 2 / (\omega_N \cdot \Delta t)$$

Equation 22.8-37

$$\xi_1 := 1 + \xi \cdot (\xi + 2 \cdot \zeta)$$

Equation 22.8-38

$$\xi_2 := 2 \cdot (1 - \xi^2)$$

Equation 22.8-39

$$\xi_3 := 1 + \xi \cdot (\xi - 2 \cdot \zeta)$$

Equation 22.8-40

$$\chi_{-1} \coloneqq \chi_{-2} \coloneqq \left(\frac{\xi_1 - 1}{3 \cdot \xi_1 - \xi_2 - \xi_3} \right) \cdot X_I$$

Equation 22.8-41

If (I := 1), and on first use, the filter is re-initialised without integration using input (X_I). Each filter is identified by a unique number (N).

22.8.7 Digital α–β–γ Filters

D_ABG propagates 50 α–β–γ filters with time varying gains (α,β,γ). The input (X_I) is returned filtered (F_X) together with its 1st and 2nd derivatives (F_DX and F_D2X) using the equations given in §21.2.

$$\mathbf{D\_ABG} \left(t , X_I , DX_I , D2X_I , \alpha , \beta , \gamma , F\_X , F\_DX , F\_D2X , N , I \right)$$

Equation 22.8-42

The provision of current time (t) allows for variable update rates, the time interval for filter propagation being determined for each channel (N),

$$\Delta t \coloneqq t - t_{k-1}$$

Equation 22.8-43

If argument (I) is set to 1, and on first use, the filter is re-initialised using the input (X_I) and its 1st and 2nd derivatives. Each filter is identified by a unique number (N).

22.8.8 Tuned Digital α–β–γ Filters

T_ABG propagates 50 weave frequency (ω_W) tuned α–β–γ filters using 1st order integration with time varying gains based on the filter bandwidth (ω_E). The input (X_I) is returned filtered (F_X) together with its 1st and 2nd derivatives (F_DX and F_D2X) using the equations given in §21.4.

$$\mathbf{T\_ABG} \left(t , X_I , DX_I , D2X_I , \omega_E , \omega_W , F\_X , F\_DX , F\_D2X , N , I \right)$$
$$\equiv$$
$${}^{WT}\varphi_{\alpha\beta\gamma} \left(X_I , \omega_E , \omega_W \right)$$

Equation 22.8-44

If (I := 1), and on first use, the filter is initialised using input (X_I) and its 1st and 2nd derivatives. Each filter is identified by a unique number (N).

22.8.9 Digital α–β–γ Filter Covariances

ABG_COVARS takes a set of α–β–γ filter gains at time (t), and the input variance ($E(X_I)$), and returns a [3,3] covariance matrix [P] using the equations given in §20.2.

$$\mathbf{ABG\_COVARS}\left(t , \langle X_I \rangle , \alpha , \beta , \gamma , [P] , N , I \right)$$

Equation 22.8-45

Each filter is identified by a unique number (N).

22.8.10 Analogue to Digital Converter Noise

ADC_NOISE takes input (X_I) and adds uniformly distributed random noise in (N_B) least significant bits, quantised to one least significant bit (ΔQ). *RANDOM* provides the uniform random noise via data channel (N_S). The quantisation function is denoted by *Q*(…).

$$y \coloneqq \mathbf{ADC\_NOISE}\left(X_I , N_B , \Delta Q , I_{BS} \right)$$

$$\equiv {}^{AD}\varphi_{QN}\left(X_I , {}^{AD}N_B , {}^{AD}X_{LL} , {}^{AD}X_{UL} \right)$$

Equation 22.8-46

$$\Delta Q \le 0 \Rightarrow y \coloneqq X_I$$

Equation 22.8-47

$$\left(\Delta Q > 0 \right) \wedge \left(N_B \le 0 \right) \Rightarrow y \coloneqq Q\left(X_I , \Delta Q , 1 , \Delta Q_N \right)$$

Equation 22.8-48

$$\left(\Delta Q > 0 \right) \wedge \left(N_B > 0 \right) \Rightarrow y \coloneqq Q\left(X_I , 2^{N_B} \cdot \Delta Q , 2 , Q_N \right) + \varphi_1$$

Equation 22.8-49

$$\varphi_1 \coloneqq \operatorname{sign}\left(Q\left(U\left(0 , \left(2^{N_B} - 1 \right) \cdot \Delta Q \right) \right) , X_I \right)$$

Equation 22.8-50

The input is returned unaltered if (ΔQ) is zero. If the number of noise bits (N_B) is zero the input is quantised by rounding.

22.8.11 Digital to Analogue Converter Noise

DAC_NOISE takes input (X_I) and adds uniformly distributed random noise in (N_B) least significant bits, quantised to one least significant bit (ΔQ). *RANDOM* provides the uniform random noise via data channel (N_S). The quantisation function is denoted by *Q*(…).

$$y \coloneqq \textbf{DAC\_NOISE}\left(X_I , N_B , \Delta Q , I_{BS} \right)$$

$$\equiv \ {}^{DA}\varphi_{QN}\left(X_I , {}^{DA}N_B , {}^{DA}X_{LL} , {}^{DA}X_{UL} \right)$$

Equation 22.8-51

$$\Delta Q \le 0 \ \Rightarrow \ y \coloneqq X_I$$

Equation 22.8-52

$$\left(\Delta Q > 0 \right) \wedge \left(N_B \le 0 \right) \ \Rightarrow \ y \coloneqq Q\left(X_I , \Delta Q , 1 , \Delta Q_N \right)$$

Equation 22.8-53

$$\left(\Delta Q > 0 \right) \wedge \left(N_B > 0 \right) \ \Rightarrow \ y \coloneqq Q\left(X_I , 2^{N_B} \cdot \Delta Q , 2 , Q_N \right) + \varphi_1$$

Equation 22.8-54

$$\varphi_1 \coloneqq \text{sign}\left(Q\left(U\left(0 , \left(2^{N_B} - 1 \right) \cdot \Delta Q \right) \right) , X_I \right)$$

Equation 22.8-55

The input is returned unaltered if (ΔQ) is zero. If the number of noise bits (N_B) is zero the input is quantised by rounding.

22.8.12 Digital Interface Filter

IF_1553 takes input to the data bus (X_I), and returns the delayed, range limited, 2s complement wrapped, and quantised output.

$$y \coloneqq \textbf{IF\_1553}\left(X_I , E , X_L , X_U , N_B , N_{TD} , N_{CK} , ID \right)$$

Equation 22.8-56

The input (X_I) passes through the following processes in order, starting with rounding quantisation,

$$E(27) \ \Rightarrow \ X_I' \coloneqq \textbf{QUANTISE}\left(X_I , \frac{X_U - X_L}{2^{N_B} - 1} , 1 , I_W \right)$$

$$\equiv \ {}^{IF}\varphi_Q\left(X_I , {}^{IF}N_B , {}^{IF}X_{LL} , {}^{IF}X_{UL} \right)$$

Equation 22.8-57

$$\neg E(27) \ \Rightarrow \ X_I' \coloneqq X_I$$

Equation 22.8-58

E(27) represents bit 27 of the integer (E) controlling the addition of errors. The quantised result is range limited, or wrapped, to the interface range.

$$E(28) \wedge (\neg E(29)) \Rightarrow$$

$$X_I'' := \textbf{R\_LIMITER}\left(X_I', X_L, X_U\right) \equiv {}^{IF}\varphi_{LIM}\left(X_I, {}^{IF}X_L, {}^{IF}X_U\right)$$

Equation 22.8-59

$$E(29) \Rightarrow X_I'' := \textbf{IF\_2CW}\left(X_I', X_L, X_U\right)$$

Equation 22.8-60

$$E(28) \wedge (\neg E(29)) \Rightarrow X_I'' := X_I'$$

Equation 22.8-61

This result is time delayed by an integer number of transmission intervals.

$$E(30) \vee (U(N_{CK},1) = 1) \Rightarrow$$

$$y := \textbf{TIME\_DELAY}\left(X_I'', N_{TD} \cdot T(N_{CK}), T(N_{CK}), ID\right)$$
$$\equiv$$
$$\equiv {}^{IF}\varphi_{TD}\left(X_I, {}^{IF}N_{TD}\right)$$

Equation 22.8-62

$$\neg E(30) \Rightarrow y := X_I''$$

Equation 22.8-63

The transmission interval (T ≡ *TUPDAT*), and the clock (U ≡ *UPDATE*), are as defined in §22.2.1, with clock number (N_{CK}). For a symmetric range about zero, a number of interface bits (N_B), and a least significant bit (ΔQ), the upper and lower limits are,

$$X_L := -\left(2^{N_B-1}\right) \cdot \Delta Q$$

Equation 22.8-64

$$X_U := \left(\left(2^{N_B-1}\right) - 1\right) \cdot \Delta Q$$

Equation 22.8-65

The range,

$$X_U - X_L := \left(2^{N_B} - 1\right) \cdot \Delta Q$$

Equation 22.8-66

22.8.13 Digital Interface 2s Complement Wrap Filter

IF_2CW takes input (X_I) and wraps it into the range [X_L,X_U] emulating a 2s complement implementation.

$$y \coloneqq \textbf{IF\_2WC}\left(X_I , X_L , X_U \right)$$

Equation 22.8-67

$$X_I \in \left[X_L , X_U \right] \Rightarrow y \coloneqq X_I$$

Equation 22.8-68

$$y = X_I \rightarrow X_I - X_U + X_L \quad \text{until } X_I \le X_L$$

Equation 22.8-69

$$y = X_I \rightarrow X_I + X_U - X_L \quad \text{until } X_I \ge X_U$$

Equation 22.8-70

This algorithm wraps inputs into a symmetric range about zero and cannot be used for unsigned input representations in the range [0,X_U].

22.8.14 Parameter Limiting

R_LIMITER limits the real valued input (X_I) to the range [X_L,X_U].

$$y \coloneqq \textbf{R\_LIMITER}\left(X_I , X_L , X_U \right) \equiv \varphi_{RL}\left(X_I , X_{LL} , X_{UL} \right)$$

Equation 22.8-71

$$X_I \in \left]-\infty , X_L \right] \Rightarrow y \coloneqq X_L$$

Equation 22.8-72

$$X_I \in \left] X_L , X_U \right[\Rightarrow y \coloneqq X_I$$

Equation 22.8-73

$$X_I \in \left[X_U , \infty \right[\Rightarrow y \coloneqq X_U$$

Equation 22.8-74

I_LIMITER limits the integer input (X_I) to the range [X_L(1)X_U] using the same logic.

$$y \coloneqq \textbf{I\_LIMITER}\left(X_I , X_L , X_U \right) \equiv \varphi_{IL}\left(X_I , X_{LL} , X_{UL} \right)$$

Equation 22.8-75

22.8.15 Parameter Quantisation

QUANTISE quantises input (X_I) to a resolution of (ΔQ) using rounding if the value of (N) is set to 1, otherwise by truncation. The number of quantised steps comprising the input is returned as (N_Q).

$$y \;:=\; \textbf{QUANTISE}\left(X_I , \Delta Q , N , N_Q \right) \;\equiv\; \varphi_Q \left(X_I , \Delta Q \right)$$

Equation 22.8-76

$$\Delta Q \le 0 \;\Rightarrow\; \left\{ \begin{array}{l} y \;:=\; X_I \\ \\ N_Q \;:=\; 0 \end{array} \right\}$$

Equation 22.8-77

$$\Delta Q > 0 \;\Rightarrow\; \left\{ \begin{array}{l} N = 1 \;\Rightarrow\; N_Q \;:=\; \text{nint}\left(X_I / \Delta Q \right) \\ \\ N \ne 1 \;\Rightarrow\; N_Q \;:=\; \text{int}\left(X_I / \Delta Q \right) \\ \\ y \;:=\; N_Q \cdot \Delta Q \end{array} \right\}$$

Equation 22.8-78

22.8.16 Time Delay

TIME_DELAY takes up to 400 variables and returns their value (t_D) seconds ago. The maximum delay is 1000 times the function update period (Δt).

$$y \;:=\; \textbf{TIME\_DELAY}\left(X_I , t_D , \Delta t , N \right) \;\equiv\; \varphi_{TD} \left(X_I , t_D \right)$$

Equation 22.8-79

If the time delay is < 0.5*Δt, the input is returned unaltered.

$$t_D < 0.5 \cdot \Delta t \;\Rightarrow\; y \;:=\; X_I$$

Equation 22.8-80

For precise operation, the update frequency and the time delay are forced to be consistent during initialisation, or when (t_D) changes during execution.

$$m \in \left[1(1)1000 \right] \;\Rightarrow\; m \;:=\; \text{nint}\left(\frac{t_D}{\Delta t} + 1 \right)$$

Equation 22.8-81

$$t_D := m \cdot \Delta t$$

Equation 22.8-82

$$k \in [1(1)m] \Rightarrow X(k) := X_I$$

Equation 22.8-83

$$k \in [m(-1)2] \Rightarrow X(k) := X(k-1)$$

Equation 22.8-84

$$X(1) := X_I$$

Equation 22.8-85

$$y := X(m)$$

Equation 22.8-86

After initialisation the output remains constant at the input value for (t_D) s. The time increment and time delay may be different for each input parameter. The parameter channels are identified by a unique number (N).

22.8.17 Covariance Matrix Transformation

COVARIANCE_TM takes a covariance matrix in frame (A), the transform from (A) to frame (B), and returns the covariance matrix in (B).

$$\textbf{COVARIANCE\_TM}\ \left(C^A , T_A^B , C^B \right)$$

Equation 22.8-87

$$C^B := C_A^B \cdot P^A \cdot C_B^A$$

Equation 22.8-88

22.8.18 State Transition Matrix

STATE_TM takes state matrix [A] of dimension (N) and returns the state transition matrix [Φ] using series approximation of order (k) limited to the range [1(1)3], over time interval (Δt).

$$\textbf{STATE\_TM}\ \left([A], [\Phi], N, \Delta t, k \right)$$

Equation 22.8-89

$$\Phi := I_3 + \frac{\Delta t^{\,k}}{k!} \cdot [A]^k$$

Equation 22.8-90

22.8.19 Angular Range Wrapping

PI_WRAP takes an angle (X) and maps it onto the range [-π ,π].

$$y \coloneqq \textbf{PI\_WRAP}\left(X \right)$$

Equation 22.8-91

$$\xi_0 \coloneqq X$$

Equation 22.8-92

$$\xi_k \notin \left[-\pi , \pi \right] \Rightarrow \xi_{k+1} \coloneqq \xi_k - 2 \cdot \pi \cdot \text{sign}\left(1 , \xi_k \right)$$

Equation 22.8-93

$$\xi_k \in \left[-\pi , \pi \right] \Rightarrow \xi_{k+1} \coloneqq \xi_k$$

Equation 22.8-94

When in range,

$$\xi_{k+1} \in \left[-\pi , \pi \right] \Rightarrow y \coloneqq \xi_{k+1}$$

Equation 22.8-95

22.8.20 Rate Limiter

RATE_LIMIT takes 50 inputs (X), their input rate limits (DXL), and time increment between updates (Δt), returning the rate-limited input and a flag indicating whether the input has been rate-limited.

$$y \coloneqq \textbf{RATE\_LIMIT}\left(X , DXL , \Delta t , LIMIT , N \right) \equiv \varphi_{RL}\left(X_I , \dot{X}_L \right)$$

Equation 22.8-96

$$X_{-1} \coloneqq X_0$$

Equation 22.8-97

$$\left| X_i - X_{i-1} \right| \leq \dot{X}_L \cdot \Delta t \Rightarrow \left\{ \begin{array}{c} y \coloneqq X_i \\ \\ y \coloneqq LIMIT \end{array} \right\}$$

Equation 22.8-98

$$\left| X_i - X_{i-1} \right| > \dot{X}_L \cdot \Delta t \quad \Rightarrow \quad \left\{ \begin{array}{c} y := X_i + \dot{X}_L \cdot \Delta t \cdot \text{sign}\left(X_i - X_{i-1} \right) \\ \\ \text{LIMIT} := 1 \end{array} \right\}$$

Equation 22.8-99

Each rate limiting function is identified by (N).

22.8.21 Digital State Space Update

D_STATESPACE takes in state-space matrices A(N,N), B(N,I), C(O,I) and D(O,I), and input and state vectors $\underline{U}$(I) and $\underline{X}$(N) at time (t_k), where (N), (I) and (O) represent the number of states, inputs and outputs. It returns the updated state vector at time (t_{k+1}), and the output vector $\underline{Y}$(O) at time (t_k).

$$\textbf{D\_STATESPACE}\left([A], [B], [C], [D], \underline{X}, \underline{U}, \underline{Y}, N, I, O \right)$$

Equation 22.8-100

$$\underline{X}_{k+1} := A_k \cdot \underline{X}_k + B_k \cdot \underline{U}_k$$

Equation 22.8-101

$$\underline{Y}_{k+1} := C_k \cdot \underline{X}_k + D_k \cdot \underline{U}_k$$

Equation 22.8-102

22.8.22 Parameter Range Check

RANGE_CHECK takes input (X), and returns a flag indicating if the parameter is in the range specified by the upper and lower limits [L , U].

$$y := \textbf{RANGE\_CHECK}\left(X, L, U \right)$$

Equation 22.8-103

$$X \in [L, U] \quad \Rightarrow \quad y := 0$$

Equation 22.8-104

$$X \in]L, U[\quad \Rightarrow \quad y := 1$$

Equation 22.8-105

22.8.23 Digital Butterworth Filters

D_BUTTER propagates up to 50 digital low pass Butterworth filters of order (M), with a -3dB break frequency of (ω_B) over time interval (Δt), and time varying characteristics.

$$y := \textbf{D\_BUTTER}\left(t , X_I , M , \omega_B , N , I \right) \equiv \varphi_{AA}\left(X_I , M , \omega_B \right)$$

Equation 22.8-106

$$\Delta t := t_k - t_{k-1}$$

Equation 22.8-107

These filters provide a magnitude squared frequency response in the continuous domain,

$$\left| G(s) \right|^2 := \left(1 + \left(\frac{s}{j \cdot \omega_B} \right)^{2 \cdot M} \right)^{-1}$$

Equation 22.8-108

The digital state space equivalent for filters of order M := [2(1)4] utilise the state-space update utility with the following arguments,

D_STATESPACE

$$\left(\left[A(M,M) \right] , \left[B(M,1) \right] , \left[C(1,M) \right] , \left[D \right] , X_I , \underline{0}_M , y_k , M , 1 , 1 \right)$$

Equation 22.8-109

D_BUTTER then returns y := y_k and $[X(M)]_{k+1}$ from,

$$X_{k+1} := 2^{-1} \cdot \omega_B \cdot \Delta t \cdot Z_k \cdot I_M \cdot A_k \cdot X_k + \sqrt{\Delta t} \cdot \omega_B \cdot Z_k \cdot B_k \cdot X_I$$

Equation 22.8-110

$$y_k := \sqrt{\Delta t} \cdot C_k \cdot Z_k \cdot X_k + \omega_B \cdot C_k \cdot Z_k \cdot B_k \cdot X_I$$

Equation 22.8-111

For the 2nd order Butterworth filter,

$$k = 2 \Rightarrow \left\{ A , B , C \right\} :=$$

$$\left\{ \begin{bmatrix} -\sqrt{2} & -1 \\ 1 & 0 \end{bmatrix} , \begin{pmatrix} 1 \\ 0 \end{pmatrix} , \begin{pmatrix} 0 \\ 1 \end{pmatrix}^T \right\}$$

Equation 22.8-112

For the 3rd order Butterworth filter,

$$k = 3 \Rightarrow \{ A , B , C \} :=$$

$$\left\{ \begin{bmatrix} -1 & 0 & 0 \\ 1 & -1 & -1 \\ 0 & 1 & 0 \end{bmatrix} , \begin{pmatrix} 1 \\ 0 \\ 0 \end{pmatrix} , \begin{pmatrix} 0 \\ 0 \\ 1 \end{pmatrix}^T \right\}$$

Equation 22.8-113

For the 4th order Butterworth filter,

$$k = 4 \Rightarrow \{ A , B , C \} :=$$

$$\left\{ \begin{bmatrix} -1.847759065 & -1 & 0 & 0 \\ 1 & 0 & 0 & 0 \\ 0 & 1 & -0.765366865 & -1 \\ 0 & 0 & 1 & 0 \end{bmatrix} , \begin{pmatrix} 1 \\ 0 \\ 0 \\ 0 \end{pmatrix} , \begin{pmatrix} 0 \\ 0 \\ 0 \\ 1 \end{pmatrix}^T \right\}$$

Equation 22.8-114

$$Z_k := \left(I_M - 2^{-1} \cdot \omega_B \cdot \Delta t \cdot A_k \right)^{-1}$$

Equation 22.8-115

The argument (I) is to be used for filter re-initialisation. This has not been implemented in the current utility function and the input should always be set to zero. Each filter is identified by a unique number (N).

22.9 Matrix Utilities

22.9.1 Constant x Matrix Product

CXM_PRODUCT takes a constant (A) and matrix [B(n,m)], and returns their product [C].

$$\mathbf{CXM\_PRODUCT}\left(A , [B] , [C] , n , m \right)$$

Equation 22.9-1

$$\left(i \in [1(1)n] \right) \wedge \left(j \in [1(1)m] \right) \Rightarrow c_{ij} := a \cdot b_{ij}$$

Equation 22.9-2

22.9.2 Matrix Addition

M_ADD takes matrices [A(n,m)] and [B(n,m)], and returns the sum [C].

$$\mathbf{M\_ADD}\left([A] , [B] , [C] , n , m \right)$$

Equation 22.9-3

$$\left(i \in [1(1)n] \right) \wedge \left(j \in [1(1)m] \right) \Rightarrow c_{ij} := a_{ij} + b_{ij}$$

Equation 22.9-4

22.9.3 Matrix Determinant

M_DETER inserts matrix [A(n,n)] where n ∈ [1(1)m] into the upper left partition of a matrix shell of dimension (m), returning the determinant of the partition.

$$y := \mathbf{M\_DETER}\left(m , [A] , n \right)$$

Equation 22.9-5

$$y \equiv \det[A] := \sum_{i,j := 1}^{n} \left(a_{ij} \cdot (-1)^{i+j} \cdot \min\text{or}\left(a_{ij} \right) \right)$$

Equation 22.9-6

22.9.4 Matrix Image

M_IMAGE takes matrix [A(n,m)], and returns an exact copy of it in [B].

$$\mathbf{M\_IMAGE}\left([A] , [B] , n , m \right)$$

Equation 22.9-7

$$\left(i := [1(1)n] \right) \wedge \left(j := [1(1)m] \right) \Rightarrow b_{ij} := a_{ij}$$

Equation 22.9-8

M_I_IMAGE deals with an integer matrix [A(n,m)] in the same manner.

22.9.5 Matrix Initialisation

M_INITIAL takes constant (A) and returns matrix [B(n,m)] with its elements set to (A).

$$\textbf{M\_INITIAL}\ (A, [B], n, m)$$

Equation 22.9-9

$$\left(i := [1(1)n] \right) \wedge \left(j := [1(1)m] \right) \Rightarrow b_{ij} := a$$

Equation 22.9-10

22.9.6 Matrix Inversion

M_INVERSE inserts matrix [A(n,n)] where $n \in [1(1)m]$ into the upper left partition of a matrix shell of dimension (m), returning the inverse of the partition in [B(n,n)].

$$\textbf{M\_INVERSE}\ ([A], [B], m, n)$$

Equation 22.9-11

$$\left(i := [1(1)m] \right) \wedge \left(j := [1(1)m] \right) \Rightarrow [B] \equiv [A]^{-1} := \frac{\mathrm{cof}(a_{ij})}{\det[A]}$$

Equation 22.9-12

22.9.7 Matrix Product

M_PRODUCT takes matrices [A(n,m)] and [B(m,p)], and returns their product in [C(n,p)].

$$\textbf{M\_PRODUCT}\ ([A], [B], [C], n, m, p)$$

Equation 22.9-13

$$\left(i := [1(1)n] \right) \wedge \left(j := [1(1)p] \right) \Rightarrow c_{ij} := \sum_{k:=p}^{m} \left(a_{ik} \cdot b_{kj} \right)$$

Equation 22.9-14

22.9.8 Matrix Product (Pre-Multiplier Transposed)

M_PRODUCT_AT takes matrices [A(n,m)] and [B(n,p)], and returns their product $[A]^T [B]$ in [C(m,p)].

M_PRODUCT_AT ([A] , [B] , [C] , n , m , p)

Equation 22.9-15

$$(i := [1(1)n]) \wedge (j := [1(1)p]) \Rightarrow c_{ij} := \sum_{k:=p}^{n} (a_{ki} \cdot b_{kj})$$

Equation 22.9-16

22.9.9 Matrix Product (Post-Multiplier Transposed)

M_PRODUCT_BT takes matrices [A(n,m)] and [B(p,m)], and returns their product $[A] [B]^T$ in [C(n,p)].

M_PRODUCT_BT ([A] , [B] , [C] , n , m , p)

Equation 22.9-17

$$(i := [1(1)n]) \wedge (j := [1(1)p]) \Rightarrow c_{ij} := \sum_{k:=p}^{m} (a_{ik} \cdot b_{jk})$$

Equation 22.9-18

22.9.10 Matrix Product (Pre and Post-Multipliers Transposed)

M_PRODUCT_AT_BT takes matrices [A(n,m)] and [B(p,n)], and returns their product $[A]^T [B]^T$ in [C(m,p)].

M_PRODUCT_AT_BT ([A] , [B] , [C] , n , m , p)

Equation 22.9-19

$$(i := [1(1)n]) \wedge (j := [1(1)p]) \Rightarrow c_{ij} := \sum_{k:=p}^{n} (a_{ki} \cdot b_{jk})$$

Equation 22.9-20

22.9.11 Matrix Subtraction

M_SUBTRACT takes matrices [A(n,m)] and [B(n,m)], returning [A] - [B] in [C(n,m)].

M_SUBTRACT ([A] , [B] , [C] , n , m)

Equation 22.9-21

$$\left(i := [1(1)n] \right) \wedge \left(j := [1(1)m] \right) \Rightarrow c_{ij} := a_{ij} - b_{ij}$$

Equation 22.9-22

22.9.12 Matrix Trace

M_TRACE takes matrix [A(n,n)], and returns its trace.

$$y := \textbf{M\_TRACE}\left([A], n \right) \equiv tr[A] := \sum_{i:=1}^{n} \left(a_{ii} \right)$$

Equation 22.9-23

22.9.13 Matrix Transpose

M_TRANSPOSE takes matrix [A(n,m)], returning its transpose in [B(m,n)].

$$\textbf{M\_TRANSPOSE}\left([A], [B], n, m \right)$$

Equation 22.9-24

$$\left(i := [1(1)n] \right) \wedge \left(j := [1(1)m] \right) \Rightarrow b_{ji} := a_{ij}$$

Equation 22.9-25

22.9.14 Matrix Unity

M_UNITY returns the identity matrix [A(n,n)] whose diagonal elements are set to one, and its off-diagonal elements to zero.

$$\textbf{M\_UNITY}\left([A], n \right)$$

Equation 22.9-26

Using the Kronecker delta,

$$\left(i := [1(1)n] \right) \wedge \left(j := [1(1)n] \right) \Rightarrow a_{ij} := \delta_{ij}$$

Equation 22.9-27

22.9.15 Matrix x Vector Product

MXV_PRODUCT takes matrix [A(n,m)], and vector (B) of dimension (m), and returns their product [A] . B in vector (C) of dimension (n).

$$\textbf{MXV\_PRODUCT}\left([A], \underline{B}, \underline{C}, n, m \right)$$

Equation 22.9-28

$$i \in [1(1)n] \Rightarrow c_i := \sum_{k:=1}^{n} (a_{ik} \cdot b_k)$$

Equation 22.9-29

22.9.16 Matrix Zero

M_ZERO takes a real matrix [A(n,m)] and returns it with its elements set to zero.

M_ZERO ([A] , n , m)

Equation 22.9-30

$$(i := [1(1)n]) \wedge (j := [1(1)m]) \Rightarrow a_{ij} := 0$$

Equation 22.9-31

M_I_ZERO takes integer matrix [A(n,m)] and returns it with its elements set to zero using the same logic.

22.9.17 Skew Symmetric Matrix Squared from a Vector

SM_SQUARED takes 3-vector (A), and returns an equivalent squared skew-symmetric matrix [B(3,3)].

SM_SQUARED (A , [B])

Equation 22.9-32

$$B := \begin{bmatrix} -a_2^2 - a_3^2 & , & a_1 \cdot a_2 & , & a_1 \cdot a_3 \\ b_{1,2} & , & -a_1^2 - a_3^2 & , & a_1 \cdot a_2 \\ b_{1,3} & , & b_{2,3} & , & -a_1^2 - a_2^2 \end{bmatrix}$$

Equation 22.9-33

22.9.18 Matrix Element-by-Element Product

M_E_PROD takes matrices [A(n,m)] and [B(n,m)], and returns their elemental product in [C(n,m)].

M_E_PROD ([A] , [B] , [C] , n , m)

Equation 22.9-34

$$(i := [1(1)n]) \wedge (j := [1(1)m]) \Rightarrow c_{ij} := a_{ij} \cdot b_{ij}$$

Equation 22.9-35

22.9.19 Matrix Symmetry

M_SYMMETRIC takes a near-symmetric matrix [P(n,n)], and returns it with its off-diagonal elements symmetric using the method determined by (k).

$$\mathbf{M\_SYMMETRY}\left(\left[P\right], n, k\right)$$

Equation 22.9-36

For the case where the lower triangular matrix is loaded into the upper triangular matrix,

$$\left(k = 0\right) \wedge \left(i \in \left[1(1)n-1\right]\right) \wedge \left(j \in \left[1+1(1)m\right]\right) \Rightarrow$$

$$p(i,j) := p(j,i)$$

Equation 22.9-37

For the case where the average value of the upper and lower off-diagonal elements are loaded into the respective triangular matrices,

$$\left(k \neq 0\right) \wedge \left(i \in \left[1(1)n-1\right]\right) \wedge \left(j \in \left[1+1(1)m\right]\right) \Rightarrow$$

$$\left\{ \begin{array}{l} p(i,j) := 0.5 \cdot \left(p(i,j) + p(j,i)\right) \\ p(j,i) := p(i,j) \end{array} \right\}$$

Equation 22.9-38

22.9.20 Matrix Positive Define Testing

M_POSDEF takes covariance matrix [C(n,n)], and returns a value > 0 when it is ill-conditioned, otherwise zero. A non-zero value indicates the type of ill-conditioning. If k > 0 [C] is returned after forcing positive-definiteness.

$$y := \mathbf{M\_POSDEF}\left(\left[C\right], n, k\right)$$

Equation 22.9-39

First test the main diagonal for zero, or negative terms,

$$\left(i \in \left[1(1)n\right]\right) \wedge \left(c(i,i) < 10^{-8}\right) \Rightarrow y := 2$$

Equation 22.9-40

The 2nd stage is to apply the off-diagonal correlation test,

$$\left(i \in [1(1)n-1] \right) \wedge \left(j \in [i+1(1)n] \right) \wedge \left(c(i,j)^2 > c(i,i) \cdot c(j,j) \right)$$

$$\Rightarrow \quad y \coloneqq 4$$

Equation 22.9-41

If (k > 0), [C] is returned positive definite using,

$$\left(c(i,i) \le 10^{-8} \right) \wedge \left(i \in [1(1)n] \right) \Rightarrow c^*(i,i) \coloneqq |c(i,i)|$$

Equation 22.9-42

$$\left(i \in [1(1)n-1] \right) \wedge \left(j \in [i+1(1)n] \right) \Rightarrow$$

$$c^*(i,j) \coloneqq \frac{c(i,j)^2}{c^*(i,i) \cdot c^*(j,j)}$$

Equation 22.9-43

$$c^*(j,i) \coloneqq c^*(i,j)$$

Equation 22.9-44

22.9.21 Matrix of Correlation Coefficients

M_CORREL takes covariance matrix [C(n,n)] and returns [R] whose upper triangular partition contains correlation coefficients in the range [0,1].

$$\textbf{M\_CORREL}\ ([C],[R],n,LUN)$$

Equation 22.9-45

$$\left(i \in [1(1)n-1] \right) \wedge j \in [i+1(1)n] \Rightarrow$$

$$\left\{ \begin{array}{c} \left(c(i,i) \ne 0 \right) \wedge \left(c(j,j) \ne 0 \right) \Rightarrow r(i,j) \coloneqq \dfrac{c(i,j)}{\sqrt{c(i,i) \cdot c(j,j)}} \\ \\ \left(c(i,i) = 0 \right) \vee \left(c(j,j) = 0 \right) \Rightarrow r(i,j) \coloneqq 1 \end{array} \right\}$$

Equation 22.9-46

The correlation coefficients are written to the output file through *LUNOUT*.

22.9.22 Matrix Eigen Analysis

M_EIGEN takes a full rank square matrix [C] of dimension (n), and returns the eigenvalues in vector (V) and eigenvectors in matrix [M] using Jacobi's method of annihilation.

$$\mathbf{M\_EIGEN}\left([C], \underline{V}, [M], n, m, SUM \right)$$

Equation 22.9-47

The algorithm ends after 30 iterations and the sum of the off-diagonal terms (*SUM*), a measure of the process accuracy, is provided. If ($SUM < 10^{-10}$) after fewer iterations the algorithm is terminated and (m) contains the number of iterations used. If ($m := 30$) the results of the modal analysis should be used with care.

22.9.23 Matrix Insertion

M_INSERT takes matrices [A(i,j)] and [B(k,l)], returning [A] with [B] inserted in it starting at element (m,n).

$$\mathbf{M\_INSERT}\left([A], [B], i, j, k, l, m, n \right)$$

Equation 22.9-48

$$\left(i := [1(1)k] \right) \wedge \left(j := [1(1)l] \right) \Rightarrow$$

$$a(i+m-1, j+n-1) := b(i, j)$$

Equation 22.9-49

22.9.24 Matrix Extraction

M_EXTRACT takes matrix [A(i,j)], returning matrix [B(k,l)] extracted from it, starting at element (m,n).

$$\mathbf{M\_EXTRACT}\left([A], [B], i, j, k, l, m, n \right)$$

Equation 22.9-50

$$\left(i := [1(1)k] \right) \wedge \left(j := [1(1)l] \right) \Rightarrow$$

$$b(i, j) := a(i+m-1, j+n-1)$$

Equation 22.9-51

22.10 Quaternion Utilities

The author would like to acknowledge P.H. Jones, R.E. Daisley and J.D. Stanley for the many interesting and rigorous discussions concerning Quaternions, in particularly their evolution using gyroscope incremental angle data.

22.10.1 Quaternion Conjugation

Q_CONJ takes a quaternion representing the transformation from frame (A) to frame (B), and returns its conjugate quaternion representing the transformation from (B) to (A).

$$\mathbf{Q\_CONJ}\left(Q_A^B , Q_B^A \right)$$

Equation 22.10-1

$$Q_B^A \coloneqq \left(q_A^B \quad -\underline{q}_A^B \right)$$

Equation 22.10-2

22.10.2 YPR Euler Angles to Quaternions

E_TO_Q takes a Euler triplet representing the orientation of frame (B) with respect to frame (A) and provides the equivalent quaternion.

$$\mathbf{E\_TO\_Q}\left(E_A^B , Q_A^B \right) \equiv \varphi_E^Q\left(E_A^B \right)$$

Equation 22.10-3

The relationship between quaternion components and Euler angles is given by the following half angle equations.

$$Q_A^B \coloneqq Q_\Phi \otimes Q_\Theta \otimes Q_\Psi$$

Equation 22.10-4

$$Q_A^B \coloneqq \begin{bmatrix} \cos\left(\Phi_A^B/2\right) \\ \sin\left(\Phi_A^B/2\right) \\ 0 \\ 0 \end{bmatrix} \otimes \begin{bmatrix} \cos\left(\Theta_A^B/2\right) \\ 0 \\ \sin\left(\Theta_A^B/2\right) \\ 0 \end{bmatrix} \otimes \begin{bmatrix} \cos\left(\Psi_A^B/2\right) \\ 0 \\ 0 \\ \sin\left(\Psi_A^B/2\right) \end{bmatrix}$$

Equation 22.10-5

Expanding,

$$q_A^B(0) := c\left(\frac{\Phi_A^B}{2}\right)\cdot c\left(\frac{\Theta_A^B}{2}\right)\cdot c\left(\frac{\Psi_A^B}{2}\right) + s\left(\frac{\Phi_A^B}{2}\right)\cdot s\left(\frac{\Theta_A^B}{2}\right)\cdot s\left(\frac{\Psi_A^B}{2}\right)$$

Equation 22.10-6

$$q_A^B(1) := s\left(\frac{\Phi_A^B}{2}\right)\cdot c\left(\frac{\Theta_A^B}{2}\right)\cdot c\left(\frac{\Psi_A^B}{2}\right) - c\left(\frac{\Phi_A^B}{2}\right)\cdot s\left(\frac{\Theta_A^B}{2}\right)\cdot s\left(\frac{\Psi_A^B}{2}\right)$$

Equation 22.10-7

$$q_A^B(2) := c\left(\frac{\Phi_A^B}{2}\right)\cdot s\left(\frac{\Theta_A^B}{2}\right)\cdot c\left(\frac{\Psi_A^B}{2}\right) + s\left(\frac{\Phi_A^B}{2}\right)\cdot c\left(\frac{\Theta_A^B}{2}\right)\cdot s\left(\frac{\Psi_A^B}{2}\right)$$

Equation 22.10-8

$$q_A^B(3) := c\left(\frac{\Phi_A^B}{2}\right)\cdot c\left(\frac{\Theta_A^B}{2}\right)\cdot s\left(\frac{\Psi_A^B}{2}\right) - s\left(\frac{\Phi_A^B}{2}\right)\cdot s\left(\frac{\Theta_A^B}{2}\right)\cdot c\left(\frac{\Psi_A^B}{2}\right)$$

Equation 22.10-9

22.10.3 Quaternion Product

Q_PRODUCT takes quaternions representing the orientation of frame (B) with respect to frame (B), and frame (C) with respect to (B), and returns the quaternion product representing the transformation from (A) to (C).

$$\textbf{Q\_PRODUCT}\ \left(\ Q_A^B\ ,\ Q_B^C\ ,\ Q_A^C\ \right)$$

Equation 22.10-10

The product of two quaternions is,

$$Q_B^C \otimes Q_A^B\ :=$$

$$\left(\ q_B^C(0)\cdot q_A^B(0) - \underline{q}_B^C \bullet \underline{q}_A^B\ \ ,\ \ q_B^C(0)\cdot \underline{q}_A^B + \underline{q}_B^C \cdot q_A^B(0) - \underline{q}_B^C \times \underline{q}_A^B\ \right)$$

Equation 22.10-11

Expanding,

$$q_A^C(0) := q_B^C(0)\cdot q_A^B(0) - q_B^C(1)\cdot q_A^B(1) - q_B^C(2)\cdot q_A^B(2) - q_B^C(3)\cdot q_A^B(3)$$

Equation 22.10-12

$$q_A^C(1) := q_B^C(0)\cdot q_A^B(1) + q_B^C(1)\cdot q_A^B(0) + q_B^C(3)\cdot q_A^B(2) - q_B^C(2)\cdot q_A^B(3)$$

Equation 22.10-13

$$q_A^C(2) := q_B^C(0)\cdot q_A^B(2) + q_B^C(2)\cdot q_A^B(0) - q_B^C(3)\cdot q_A^B(1) + q_B^C(1)\cdot q_A^B(3)$$

Equation 22.10-14

$$q_A^C(3) := q_B^C(0)\cdot q_A^B(3) + q_B^C(3)\cdot q_A^B(0) + q_B^C(2)\cdot q_A^B(1) - q_B^C(1)\cdot q_A^B(2)$$

Equation 22.10-15

22.10.4 Quaternion Normalisation

A quaternion of unit magnitude satisfies the normalisation condition:

$$\| Q \|^2 := 1 := q_0^2 + \underline{q} \bullet \underline{q}$$

Equation 22.10-16

Propagating a quaternion over time leads to errors and this condition is no longer satisfied. *Q_NORMAL* takes in quaternion (Q) and normalises it, returning the corrected quaternion (^{C}Q).

$$\textbf{Q\_NORMAL}\ (\ Q\ ) \equiv \varphi_{NORM}^{Q}\ (\ Q\ )$$

Equation 22.10-17

From Equation 22.10-16,

$$\| Q \|^2 := (\ 1+\xi\ )^2 \cong 1 + 2\cdot\xi$$

The corrected quaternion is related to the input by,

$$Q \cong (\ 1+\xi\ )\cdot {}^C Q$$

Equation 22.10-18

Therefore,

$${}^C Q \cong 2\cdot Q \Big/ \left(1 + \| Q \|^2 \right)$$

Equation 22.10-19

22.10.5 Quaternion Propagation

The orientation of frame (B) with respect to frame (A) can be propagated between time (t) and (t+Δt) using quaternion multiplication,

$$Q_A^B\left(t+\Delta t\right) \;:=\; \left(\dot{Q}_A^B\cdot\Delta t\right)\otimes Q_A^B \;:=\; \Delta Q_A^B\otimes Q_A^B$$

Equation 22.10-20

Over time period (Δt) the rotating frame moves through an angle ($\omega_{AB}.\Delta t$) about a vector defined by the direction cosines ($\underline{\omega}_{A,B}/\omega_{A,B}$). If the angular rate remains constant over this period the quaternion representing the rotation,

$$\Delta Q_A^B \;:=\; \left(\cos\left(\frac{\Delta t}{2}\cdot\omega_{A,B}^B\right)\;,\;\frac{\underline{\omega}_{A,B}^B}{\omega_{A,B}^B}\cdot\sin\left(\frac{\Delta t}{2}\cdot\omega_{A,B}^B\right)\right)$$

Equation 22.10-21

$$\Delta Q_A^B \;:=\; \begin{pmatrix} 1-\dfrac{1}{8}\cdot\left(\omega_{A,B}^B\cdot\Delta t\right)^2+\ldots \\ \dfrac{\underline{\omega}_{A,B}^B}{\omega_{A,B}^B}\cdot\left(\dfrac{1}{2}-\dfrac{1}{48}\cdot\left(\omega_{A,B}^B\cdot\Delta t\right)^2+\ldots\right)\cdot\Delta t \end{pmatrix}$$

Equation 22.10-22

The general expression for propagating a quaternion over time interval (Δt),

$$\left(Q_A^B\right)_{k+1} \;:=\; Q_A^B \;+\; \sum_{n:=1}^{N}\left(\frac{\Delta t^n}{n+1}\cdot\begin{bmatrix} 0 & \vdots & -\left(\underline{\omega}_{A,B}^B\right)^T \\ \ldots & \vdots & \ldots \\ \underline{\omega}_{A,B}^B & \vdots & -\left[\,\underline{\omega}_{A,B}^B\times\,\right] \end{bmatrix}^n\cdot Q_A^B\right)$$

Equation 22.10-23

Q_RATE takes a quaternion representing the transformation from frame (A) to frame (B), and the angular velocity vector of (B) with respect to (A). It returns the quaternion time rate of change representing the rate of rotation of (B) with respect to (A), using 1st order of approximation.

$$\mathbf{Q\_RATE}\left(Q_A^B\,,\underline{\omega}_{A,B}^B\,,\dot{Q}_A^B\right)$$

Equation 22.10-24

$$2\cdot\dot{Q}_A^B \;:=\; \left(-\underline{\omega}_{A,B}^B\bullet\underline{q}_A^B\;\;,\;\;q_A^B(0)\cdot\underline{\omega}_{A,B}^B-\underline{\omega}_{A,B}^B\times\underline{q}_A^B\right)$$

Equation 22.10-25

$$\dot{Q}_A^B \coloneqq \frac{1}{2} \cdot \begin{pmatrix} 0 & , & -q_A^B(1) & , & -q_A^B(2) & , & -q_A^B(3) \\ 0 & , & q_A^B(0) & , & -q_A^B(3) & , & q_A^B(2) \\ 0 & , & q_A^B(3) & & q_A^B(0) & , & -q_A^B(1) \\ 0 & , & -q_A^B(2) & , & q_A^B(1) & , & q_A^B(0) \end{pmatrix} \cdot \begin{pmatrix} 0 \\ \underline{\omega}_{A,B}^B \end{pmatrix}$$

Equation 22.10-26

22.10.6 Quaternion Propagation by Euler Increments

DQ_EULER takes the quaternion representing the orientation of frame (B) with respect to frame (A), and returns its value after time interval (Δt) using current and previous Euler angle increments.

$$\textbf{DQ\_EULER} \left(Q_A^B \, , \, {}_C\Delta E_A^B \, , \, {}_L\Delta E_A^B \right)$$

Equation 22.10-27

Dropping nomenclature for convenience, extending the results presented in §22.10.5, and expanding in a Taylor series about the current quaternion approximating to the 3rd order,

$$Q_{k+1} \coloneqq \Delta Q_k \otimes Q_k \coloneqq Q_k + \Delta t \cdot \dot{Q}_k + 2^{-1} \cdot \Delta t^2 \cdot \ddot{Q}_k + 6^{-1} \cdot \Delta t^3 \cdot \dddot{Q}_k$$

Equation 22.10-28

Expressing the time derivatives in terms of the angular rate and acceleration of frame (B) with respect to frame (A) - courtesy J.D. Stanley,

$$\dot{Q}_k \coloneqq {}^q\underline{\omega}_{A,B}^B \otimes Q_k \qquad \text{where} \quad {}^q\underline{\omega}_{A,B}^B \coloneqq \begin{pmatrix} 0 \\ -2^{-1} \cdot \underline{\omega}_{A,B}^B \end{pmatrix}$$

Equation 22.10-29

Differentiating and dropping the full notation,

$$\ddot{Q} \coloneqq {}^q\dot{\underline{\omega}} \otimes Q + {}^q\underline{\omega} \otimes \dot{Q} \coloneqq {}^q\dot{\underline{\omega}} \otimes Q + {}^q\underline{\omega} \otimes {}^q\underline{\omega} \otimes \dot{Q}$$

Equation 22.10-30

Since,

$${}^q\underline{\omega} \otimes {}^q\underline{\omega} \otimes Q \equiv -\left({}^q\underline{\omega} \bullet {}^q\underline{\omega} \right) \cdot Q$$

Equation 22.10-31

Quaternion acceleration is thus,

$$\ddot{Q} \;:=\; {}^{q}\underline{\dot{\omega}} \otimes Q + \left({}^{q}\underline{\omega} \bullet {}^{q}\underline{\omega} \right) \cdot \dot{Q}$$

Equation 22.10-32

Similarly for jerk,

$$\dddot{Q} \;:=\; {}^{q}\underline{\ddot{\omega}} \otimes Q + {}^{q}\underline{\dot{\omega}} \otimes \dot{Q} - 2 \cdot \left({}^{q}\underline{\omega} \bullet {}^{q}\underline{\dot{\omega}} \right) \cdot Q - \left({}^{q}\underline{\omega} \bullet {}^{q}\underline{\dot{\omega}} \right) \cdot \dot{Q}$$

Equation 22.10-33

Ignoring angular jerk, i.e. assuming piecewise constant angular acceleration,

$$\dddot{Q} \;:=\; \left({}^{q}\underline{\dot{\omega}} \times {}^{q}\underline{\omega} \right) \otimes Q - 3 \cdot \left({}^{q}\underline{\omega} \bullet {}^{q}\underline{\dot{\omega}} \right) \cdot Q - \left(\left({}^{q}\underline{\omega} \bullet {}^{q}\underline{\omega} \right) \cdot {}^{q}\underline{\omega} \right) \otimes \dot{Q}$$

Equation 22.10-34

Substituting for the time derivatives into Equation 22.10-28, using backward differences for the angular acceleration,

$$\Delta q_0 \left(t_{k+1} \right) \;:=\; 1 - 8^{-1} \cdot \Delta t \cdot \left(2 \cdot \underline{\omega}_k - \underline{\omega}_{k-1} \right) \bullet \underline{\omega}_k$$

Equation 22.10-35

$$\Delta \underline{q} \left(t_{k+1} \right) \;:=$$

$$- 4^{-1} \cdot \Delta t \cdot \left(3 \cdot \underline{\omega}_k - \underline{\omega}_{k-1} \right) + 48^{-1} \cdot \Delta t^2 \cdot \left(2 \cdot \underline{\omega}_k \times \underline{\omega}_{k-1} + \left(\underline{\omega}_k \bullet \underline{\omega}_k \right) \cdot \underline{\omega}_k \right)$$

Equation 22.10-36

Replacing the body rates with incremental Euler triplets, assuming that (Δt) is small, and the triplet (E_k) contains sensor angular increments over the period t_k to t_{k+1},

$$2 \cdot \Delta t \cdot \underline{\omega}^{B}_{A,B} \left(t_k \right) \;:=\; {}_{C}\Delta E^{B}_{A} + {}_{L}\Delta E^{B}_{A}$$

Equation 22.10-37

$$2 \cdot \Delta t \cdot \underline{\omega}^{B}_{A,B} \left(t_{k-1} \right) \;:=\; 3 \cdot {}_{L}\Delta E^{B}_{A} - {}_{C}\Delta E^{B}_{A}$$

Equation 22.10-38

22.10.7 Quaternion Error Evolution With Time

The true quaternion is the product of its estimate and an error quaternion,

$$Q^{B}_{A} \;:=\; \hat{Q}^{B}_{A} \otimes \Delta Q^{B}_{A}$$

Equation 22.10-39

Isolating the error quaternion and differentiating gives its dynamics,

$$\Delta\dot{Q}_A^B \;\coloneqq\; {}^*\hat{\dot{Q}}_A^B \otimes Q_A^B \;+\; {}^*\hat{Q}_A^B \otimes \dot{Q}_A^B$$

Equation 22.10-40

Substituting for the derivative of the estimated reference quaternion,

$$2 \cdot \Delta\dot{Q}_A^B \;\coloneqq\; -{}^q\hat{\underline{\omega}}_{A,B}^B \otimes {}^*\hat{Q}_A^B \otimes Q_A^B \;-\; {}^*\hat{Q}_A^B \otimes Q_A^B \otimes {}^q\hat{\underline{\omega}}_{A,B}^B$$

Equation 22.10-41

Substituting for the reference quaternion, and re-arranging,

$$2 \cdot \Delta\dot{Q}_A^B \;\coloneqq\; \Delta Q_A^B \otimes {}^q\underline{\omega}_{A,B}^B \;-\; {}^q\hat{\underline{\omega}}_{A,B}^B \otimes \Delta Q_A^B$$

Equation 22.10-42

Expanding and extracting the scalar quaternion component,

$$2 \cdot \Delta\dot{q}_A^B(0) \;\coloneqq\; -\Delta\underline{\omega}_{A,B}^B \otimes \Delta Q_A^B$$

Equation 22.10-43

Since by definition,

$$\Delta\underline{\omega}_{A,B}^B \;\coloneqq\; \underline{\omega}_{A,B}^B - \hat{\underline{\omega}}_{A,B}^B$$

Equation 22.10-44

Similarly, for the quaternion vector components,

$$2 \cdot \Delta\dot{\underline{q}}_A^B \;\coloneqq\; \Delta q_A^B(0) \cdot \underline{\omega}_{A,B}^B + \Delta\underline{q}_A^B \times \underline{\omega}_{A,B}^B - \Delta q_A^B(0) \cdot \hat{\underline{\omega}}_{A,B}^B + \Delta\underline{q}_A^B \times \hat{\underline{\omega}}_{A,B}^B$$

Equation 22.10-45

$$2 \cdot \Delta\dot{\underline{q}}_A^B \;\coloneqq\; \Delta q_A^B(0) \cdot \left(\underline{\omega}_{A,B}^B - \hat{\underline{\omega}}_{A,B}^B \right) + \Delta\underline{q}_A^B \times \left(\underline{\omega}_{A,B}^B + \hat{\underline{\omega}}_{A,B}^B \right)$$

Equation 22.10-46

$$2 \cdot \Delta\dot{\underline{q}}_A^B \;\coloneqq\; \Delta q_A^B(0) \cdot \Delta\underline{\omega}_{A,B}^B + \Delta\underline{q}_A^B \times \left(2 \cdot \hat{\underline{\omega}}_{A,B}^B + \Delta\underline{\omega}_{A,B}^B \right)$$

Equation 22.10-47

Normalising and ignoring 2nd order error terms,

$$\left(\Delta\dot{q}_A^B(0) \;,\; \Delta\dot{\underline{q}}_A^B \right) \;\coloneqq\; \left(1 - \left\| \Delta\underline{q}_A^B \right\|^2 \;,\; -\hat{\underline{\omega}}_{A,B}^B \times \Delta\underline{q}_A^B \right)$$

Equation 22.10-48

DQE_DT takes the quaternion error, and the estimated angular rate of frame (B) with respect to frame (A), and returns the time rate of change of the quaternion error.

$$\mathbf{DQE\_DT}\left(\Delta Q_A^B , \hat{\omega}_{A,B}^B , \Delta \dot{Q}_A^B \right)$$

Equation 22.10-49

22.10.8 Quaternion Transformation Matrix

Q_TO_DC takes a quaternion representing the orientation of frame (B) with respect to frame (A), and provides the transform between the two frames.

$$\mathbf{Q\_TO\_DC}\left(Q_A^B , T_A^B \right) \equiv \varphi_Q^{DC}\left(Q_A^B \right)$$

Equation 22.10-50

Expressing the direction cosines in terms of quaternion components,

$$T_A^B := \left(2 \cdot \left(q_A^B(0) \right)^2 - 1 \right) \cdot I_3 + 2 \cdot \left(\underline{q}_A^B \cdot \left(\underline{q}_A^B \right)^T - q_A^B(0) \cdot \left[\underline{q}_A^B \times \right] \right)$$

Equation 22.10-51

The skew symmetric quaternion operator is defined such that it is equivalent to the vector cross product,

$$\left[\underline{q} \times \right] := \begin{bmatrix} 0 & , & -q_3 & , & q_2 \\ q_3 & , & 0 & , & -q_1 \\ -q_2 & , & q_1 & , & 0 \end{bmatrix}$$

Equation 22.10-52

$$T_A^B := \begin{bmatrix} q_0^2 + q_1^2 - q_2^2 - q_3^2 & 2 \cdot \left(q_1 \cdot q_2 + q_0 \cdot q_3 \right) & 2 \cdot \left(q_1 \cdot q_3 - q_0 \cdot q_2 \right) \\ 2 \cdot \left(q_1 \cdot q_2 - q_0 \cdot q_3 \right) & q_0^2 - q_1^2 + q_2^2 - q_3^2 & 2 \cdot \left(q_2 \cdot q_3 + q_0 \cdot q_1 \right) \\ 2 \cdot \left(q_1 \cdot q_3 + q_0 \cdot q_2 \right) & 2 \cdot \left(q_2 \cdot q_3 - q_0 \cdot q_1 \right) & q_0^2 + q_1^2 - q_2^2 + q_3^2 \end{bmatrix}$$

Equation 22.10-53

The main diagonal of the direction cosine matrix is sometimes expressed in a form that takes into account the normalisation condition,

$$T_A^B := \begin{bmatrix} 1-2\cdot\left(q_2^2+q_3^2\right) & 2\cdot\left(q_1\cdot q_2+q_0\cdot q_3\right) & 2\cdot\left(q_1\cdot q_3-q_0\cdot q_2\right) \\ 2\cdot\left(q_1\cdot q_2-q_0\cdot q_3\right) & 1-2\cdot\left(q_1^2+q_3^2\right) & 2\cdot\left(q_2\cdot q_3+q_0\cdot q_1\right) \\ 2\cdot\left(q_1\cdot q_3+q_0\cdot q_2\right) & 2\cdot\left(q_2\cdot q_3-q_0\cdot q_1\right) & 1-2\cdot\left(q_1^2+q_2^2\right) \end{bmatrix}$$

Equation 22.10-54

Expressed the direction cosines in terms of the Glossary definitions,

$$T_A^B :=$$

$$\begin{bmatrix} \varphi_1+\varphi_3\cdot\left(n_b^{XA}\right)^2 & \varphi_3\cdot n_b^{XA}\cdot n_b^{YA}+\varphi_2\cdot n_b^{ZA} & \varphi_3\cdot n_b^{XA}\cdot n_b^{YA}-\varphi_2\cdot n_b^{YA} \\ \varphi_3\cdot n_b^{XA}\cdot n_b^{YA}-\varphi_2\cdot n_b^{ZA} & \varphi_1+\varphi_3\cdot\left(n_b^{YA}\right)^2 & \varphi_3\cdot n_b^{YA}\cdot n_b^{ZA}+\varphi_2\cdot n_b^{XA} \\ \varphi_3\cdot n_b^{XA}\cdot n_b^{ZA}+\varphi_2\cdot n_b^{YA} & \varphi_3\cdot n_b^{YA}\cdot n_b^{ZA}-\varphi_2\cdot n_B^{XA} & \varphi_1+\varphi_3\cdot\left(n_b^{ZA}\right)^2 \end{bmatrix}$$

Equation 22.10-55

$$\left(\varphi_1\ ,\ \varphi_2\ ,\ \varphi_3\right) := \left(\cos\alpha_A^B\ ,\ \sin\alpha_A^B\ ,\ \left(1-\cos\alpha_A^B\right)\right)$$

Equation 22.10-56

22.10.9 Quaternion Vector Transform

Q_V_TRANS takes a quaternion representing the transform from frame (A) to frame (B), and a vector expressed with respect to (A), returning a vector expressed in (B).

$$\mathbf{Q\_V\_TRANS}\left(Q_A^B\ ,\underline{V}^A\ ,\underline{V}^B\right)$$

Equation 22.10-57

$$\begin{pmatrix} 0 \\ \cdots \\ \underline{V}^B \end{pmatrix} := \left(Q_A^B\right)^* \otimes \begin{pmatrix} 0 \\ \cdots \\ \underline{V}^A \end{pmatrix} \otimes Q_A^B \equiv T_A^B\cdot\underline{V}^A$$

Equation 22.10-58

$$\underline{V}^B := \underline{V}^A - 2\cdot q_A^B(0)\cdot\left[\underline{q}_A^B\times\underline{V}^A\right] + 2\cdot\underline{q}_A^B\times\left[\underline{q}_A^B\times\underline{V}^A\right]$$

Equation 22.10-59

22.10.10 Quaternion from Direction Cosines

DC_TO_Q takes a transform from frame (A) to frame (B) and returns the normalised quaternion equivalent.

$$\mathbf{DC\_TO\_Q}\left(T_A^B , Q_A^B \right) \equiv \varphi_{DC}^{Q}\left(T_A^B \right)$$

Equation 22.10-60

A numerically stable implementation that avoids q(0) → 0 suggested by Dr. B.J. Hartley is as follows,

$$\varphi := \left(1 + \mathrm{tr}\left(T_A^B \right) \; , \; \begin{pmatrix} 1 + 2 \cdot T_A^B(1) - \mathrm{tr}\left(T_A^B \right) \\ 1 + 2 \cdot T_A^B(5) - \mathrm{tr}\left(T_A^B \right) \\ 1 + 2 \cdot T_A^B(9) - \mathrm{tr}\left(T_A^B \right) \end{pmatrix}^T \right)$$

Equation 22.10-61

$$\varphi(0) \geq \max(\varphi) \Rightarrow Q_A^B :=$$

$$\left(\frac{\sqrt{\varphi(0)}}{2} \; , \; \frac{T_A^B(8) - T_A^B(6)}{4 \cdot q_A^B(0)} \; , \; \frac{T_A^B(3) - T_A^B(7)}{4 \cdot q_A^B(0)} \; , \; \frac{T_A^B(4) - T_A^B(2)}{4 \cdot q_A^B(0)} \right)$$

Equation 22.10-62

$$\varphi(1) \geq \max(\varphi) \Rightarrow Q_A^B :=$$

$$\left(\frac{T_A^B(8) - T_A^B(6)}{4 \cdot q_A^B(1)} \; , \; \frac{\sqrt{\varphi(1)}}{2} \; , \; \frac{T_A^B(2) + T_A^B(4)}{4 \cdot q_A^B(1)} \; , \; \frac{T_A^B(7) + T_A^B(3)}{4 \cdot q_A^B(1)} \right)$$

Equation 22.10-63

$$\varphi(2) \geq \max(\varphi) \Rightarrow Q_A^B :=$$

$$\left(\frac{T_A^B(2) + T_A^B(4)}{4 \cdot q_A^B(2)} \; , \; \frac{T_A^B(3) - T_A^B(7)}{4 \cdot q_A^B(2)} \; , \; \frac{\sqrt{\varphi(2)}}{2} \; , \; \frac{T_A^B(6) + T_A^B(8)}{4 \cdot q_A^B(2)} \right)$$

Equation 22.10-64

$$\varphi(3) \geq \max(\varphi) \Rightarrow Q_A^B :=$$

$$\left(\frac{T_A^B(7) + T_A^B(3)}{4 \cdot q_A^B(3)} , \frac{T_A^B(6) + T_A^B(8)}{4 \cdot q_A^B(3)} , \frac{T_A^B(4) - T_A^B(2)}{4 \cdot q_A^B(3)} , \frac{\sqrt{\varphi(3)}}{2} \right)$$

Equation 22.10-65

22.10.11 Direction Cosine Jacobians

Q_DC_JACOB takes a quaternion defining the transform from frame (A) to frame (B), and returns the Jacobian matrix with respect to the quaternion component identified by (n).

$$\textbf{Q\_DC\_JACOB}\left(Q_A^B , \partial T_A^B / \partial Q_A^B(n), n \right)$$

Equation 22.10-66

$$n = 0 \Rightarrow \frac{\partial T_A^B}{\partial q_A^B(0)} := 2 \cdot \begin{bmatrix} q_A^B(0) & , & q_A^B(3) & , & -q_A^B(2) \\ -q_A^B(3) & , & q_A^B(0) & , & q_A^B(1) \\ q_A^B(2) & , & -q_A^B(1) & , & q_A^B(0) \end{bmatrix}$$

Equation 22.10-67

$$n = 1 \Rightarrow \frac{\partial T_A^B}{\partial q_A^B(1)} := 2 \cdot \begin{bmatrix} q_A^B(1) & , & q_A^B(2) & , & q_A^B(3) \\ q_A^B(2) & , & -q_A^B(1) & , & q_A^B(0) \\ q_A^B(3) & , & -q_A^B(0) & , & -q_A^B(1) \end{bmatrix}$$

Equation 22.10-68

$$n = 2 \Rightarrow \frac{\partial T_A^B}{\partial q_A^B(2)} := 2 \cdot \begin{bmatrix} -q_A^B(2) & , & q_A^B(1) & , & -q_A^B(0) \\ q_A^B(1) & , & q_A^B(2) & , & q_A^B(3) \\ q_A^B(0) & , & q_A^B(3) & , & -q_A^B(2) \end{bmatrix}$$

Equation 22.10-69

$$n = 3 \Rightarrow \frac{\partial T_A^B}{\partial q_A^B(3)} := 2 \cdot \begin{bmatrix} -q_A^B(3) & q_A^B(0) & q_A^B(1) \\ -q_A^B(0) & -q_A^B(3) & q_A^B(2) \\ q_A^B(1) & q_A^B(2) & q_A^B(3) \end{bmatrix}$$

Equation 22.10-70

22.11 Trigonometric Functions

Comparisons between 64 bit computations and function approximations were performed on a DEC ALPHA 4000-610 using the AXP V6.2 Operating system. The constants used in the approximations,

$$\left(\pi \quad , \quad \pi / 2 \quad , \quad 3 \cdot \pi / 2 \quad , \quad 2 \cdot \pi \right) :=$$

$$\left(3.14159 \quad , \quad 1.57080 \quad , \quad 4.71240 \quad , \quad 6.28318 \right)$$

Equation 22.11-1

22.11.1 Sine Approximation

SIN_F takes angle (X_I) in the range [-2π , 2π], and returns its sine in the range [-1 , 1].

$$y := \mathbf{SIN\_F}\left(X_I \right) := \frac{X \cdot \left(1 - X^2 \right) \cdot \left(2.8444 - X^2 \right)}{0.9048 + 0.273344 \cdot X^2}$$

Equation 22.11-2

$$X_I \in \left] \pi , 2 \cdot \pi \right] \Rightarrow X := \left(X_I / \pi \right) - 2$$

Equation 22.11-3

$$X_I \in \left[-\pi , \pi \right] \Rightarrow X := \left(X_I / \pi \right)$$

Equation 22.11-4

$$X_I \in \left[-2 \cdot \pi , -\pi \right[\Rightarrow X := \left(X_I / \pi \right) + 2$$

Equation 22.11-5

The error in this function is in the range [-250 , 250] ppm. A more accurate approximation is provided by *SIN_G,*

$$y := \mathbf{SIN\_G}\left(X_I \right)$$

Equation 22.11-6

$$y := \frac{X \cdot \left(1 - X^2 \right) \cdot \left(3.03209 - X^2 \right) \cdot \left(1.28452 + X^2 \right)}{\left(0.7412 + 0.36569 \cdot X^2 \right) \cdot \left(1.67279 + X^2 \right)}$$

Equation 22.11-7

The error in this function is [-50 , 50] ppm as shown in Figure 22-10.

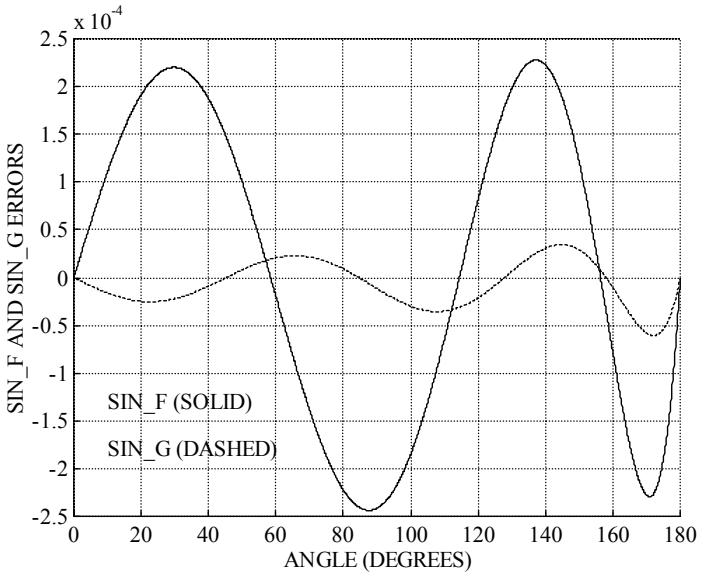

Figure 22-10 : Sine Function Errors

22.11.2 Cosine Approximation

COS_F takes an angle (X_I) in the range [-2π , 2π] and returns its cosine value in the range [-1 , 1].

$$y := \mathbf{COS\_F}\left(X_I\right) := \mathbf{SIN\_F}\left(X_I + 2^{-1}\cdot\pi\right)$$

Equation 22.11-8

COS_G provides a more accurate approximation that in turn invokes *SIN_G*.

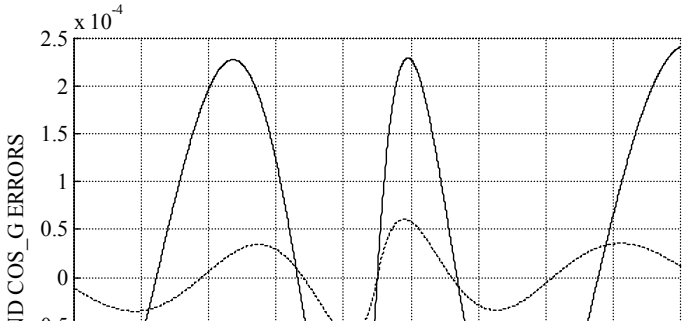

Figure 22-11 : Cosine Function Errors

Both approximations result in errors similar to the sine function with different phasing as shown in

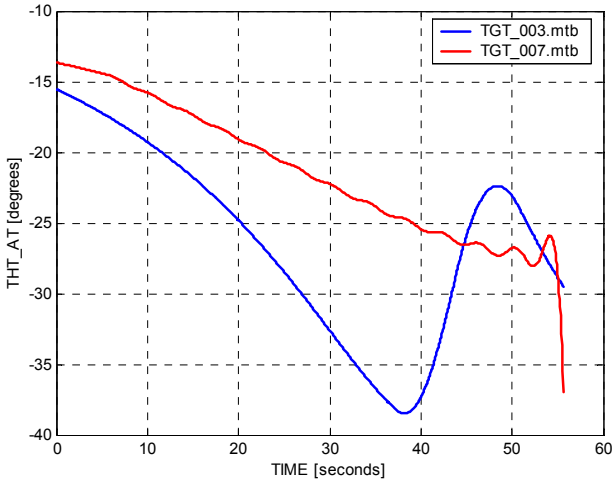

Figure 2-7.

22.11.3 Tangent Approximation

TAN_F takes angle (X_I) in the range [-2π , 2π], and returns its tangent.

$$y := \mathbf{TAN\_F}\left(X_I \right) := \frac{10.50496 \cdot X \cdot \left(1 - X^2 \right)}{\xi_1 \cdot \left(3.34485 - X^2 \right)}$$

Equation 22.11-9

$$\left(1 - 4 \cdot X^2 \right) \geq 10^{-8} \Rightarrow \xi_1 := 1 - 4 \cdot X^2$$

Equation 22.11-10

$$\left(1 - 4 \cdot X^2 \right) < 10^{-8} \Rightarrow \xi_1 := 10^{-8} \cdot \operatorname{sign}\left(1 - 4 \cdot X^2 \right)$$

Equation 22.11-11

$$X_I \in \left\{ \left[\pi , \frac{3 \cdot \pi}{2} \right] \cup \left[-\pi , -\frac{\pi}{2} \right] \right\} \Rightarrow X\left(X_I \right) \rightarrow \left[0 , \pi / 2 \right]$$

Equation 22.11-12

$$X_I \in \left\{ \left[-\frac{3 \cdot \pi}{2} , -\pi \right] \cup \left[\frac{\pi}{2} , \pi \right] \right\} \Rightarrow X\left(X_I \right) \rightarrow \left[-\pi / 2 , 0 \right]$$

Equation 22.11-13

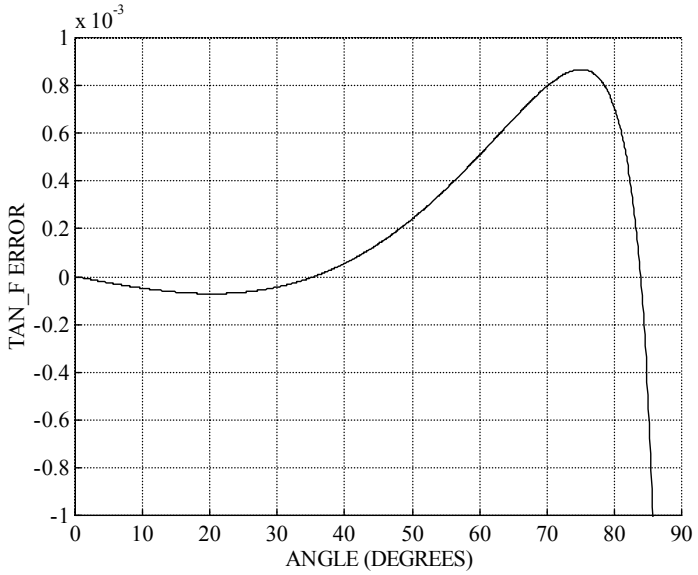

Figure 22-12 : Tangent Function Error

$$X_I \in [-2\cdot\pi, -3\cdot\pi/2] \Rightarrow X(X_I) \rightarrow [0, \pi/2]$$

Equation 22.11-14

$$X_I \in [3\cdot\pi/2, 2\cdot\pi] \Rightarrow X(X_I) \rightarrow [-\pi/2, 0]$$

Equation 22.11-15

The error in this function is [-0.02 , 0.02] for inputs [0° , 85.8°] as shown in Figure 22-12.

22.11.4 Arc-sine Approximation

ASIN_F takes the sine of (X_I) in the range [-1 , 1] and returns (X_I) in the range [-π , π].

$$y := \mathbf{ASIN\_F}(X_I) := \frac{X_I \cdot \left(4.13564 - 2.49527 \cdot \sqrt{1 - X_I^2}\right)}{1.63755 + X_I^2}$$

Equation 22.11-16

If the input is outside the specified input range it is truncated to sign (1 , X_I). The error in this function is [-0.15° , 0.15°] as shown in Figure 22-13.

22.11.5 Arc-cosine Approximation

ACOS_F takes the cosine of (X_I) in the range]-1 , 1[and returns (X_I) in the range]-π , π[.

$$y := \mathbf{ACOS\_F}(X_I) := (\pi/2) - \mathbf{ASIN\_F}(X_I)$$

Equation 22.11-17

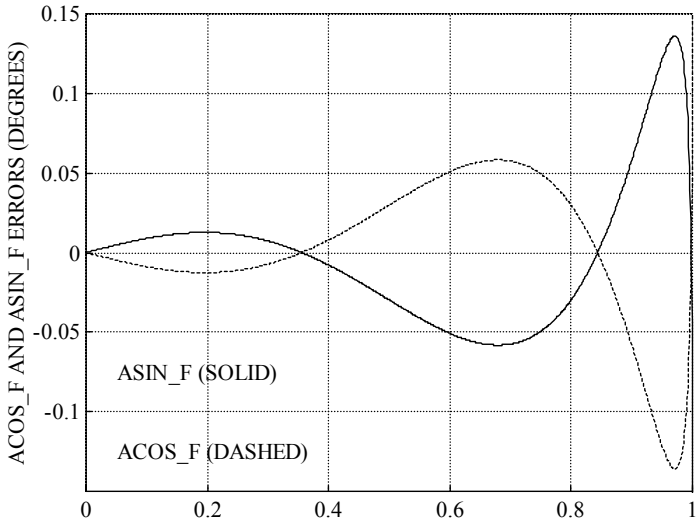

Figure 22-13 : Arc-Sine and Cosine Function Errors

The error in this function is the same as that for arc-sine but in anti-phase as shown in Figure 22-13.

22.11.6 Arc-tangent Approximation (Single Argument)

ATAN_F takes the tangent of (X_I), and returns (X_I) in the range]-π/2 , π/2[.

$$y \;:=\; \mathbf{ATAN\_F}\left(X_I\right) \;:=\; \frac{1.5708 \cdot X_I}{0.6287 + \sqrt{0.8822 + X_I^2}}$$

Equation 22.11-18

The error in this function is [-0.04°, 0.04°] over the range [0 , 15] as shown in Figure 22-14.

22.11.7 Arc-tangent Approximation (Two Arguments)

ATAN2_F takes in (Y_I) and (X_I) and returns an angle in the range]-π , π[.

$$y \;:=\; \mathbf{ATAN2\_F}\left(Y_I , X_I\right)$$

Equation 22.11-19

$$\left(\left|X_I\right| < 10^{-15}\right) \wedge \left(\left|Y_I\right| < 10^{-15}\right) \;\Rightarrow\; y \;:=\; \tan^{-1}\left(Y_I / X_I\right) \;:=\; 0$$

Equation 22.11-20

$$X_I < 0 \;\Rightarrow\; y \;:=\; 2 \cdot \mathrm{sign}\left(1 , \xi_1\right) - \xi_1$$

Equation 22.11-21

$$X_I \geq 0 \quad \Rightarrow \quad y := \pi \cdot \xi_1 / 2$$

Equation 22.11-22

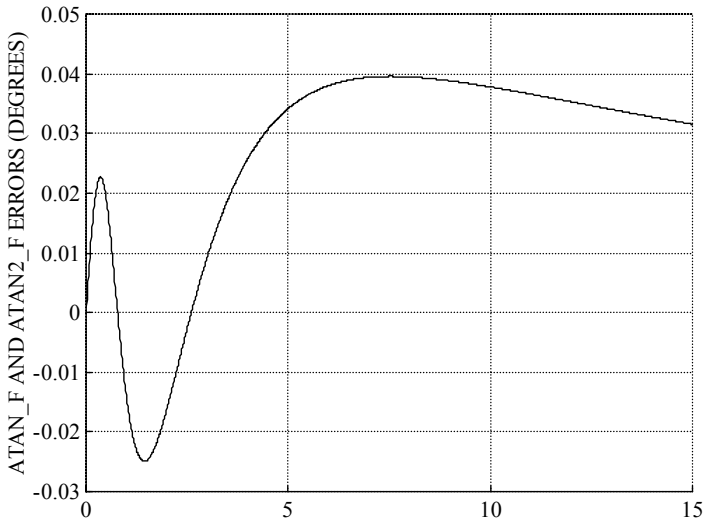

Figure 22-14 : Arc-tangent Function Error

$$|X_I| < 10^{-8} \quad \Rightarrow \quad \xi_1 := \frac{Y_I \cdot 10^8}{0.6287 + \sqrt{0.8822 + Y_I^2 \cdot 10^{16}}}$$

Equation 22.11-23

$$|X_I| \geq 10^{-8} \quad \Rightarrow \quad \xi_1 := \frac{Y_I}{|X_I| \cdot \left(0.6287 + \sqrt{0.8822 + \left(Y_I^2 / |X_I|^2 \right)} \right)}$$

Equation 22.11-24

The errors in the two arc-tangent functions over [0 , 15] are identical as shown in Figure 22-14.

22.12 Vector Utilities

Vector computations can be undertaken using matrix utilities with a redundant dimension. However, computational throughput and application dependent requirements often favour the use of a pure vector utilities. In particular, the vector utilities here are designed so that a subset of the input array can be processed as is required for dynamic trajectory optimisation.

22.12.1 Angle Between Vectors

V_ANGLE takes 3-vectors (A) and (B), and returns (C) the angle between them, and their magnitude (D) and (E) respectively.

$$\mathbf{V\_ANGLE}\ (\underline{A}, \underline{B}, C, D, E)$$

Equation 22.12-1

$$C := \cos^{-1}\left(\sum_{i:=1}^{3} (a_i \cdot b_i) \Big/ (D \cdot E) \right)$$

Equation 22.12-2

$$(D, E) := \left(\sqrt{\sum_{i:=1}^{3} (a_i)^2}, \sqrt{\sum_{i:=1}^{3} (b_i)^2} \right)$$

Equation 22.12-3

22.12.2 Constant x Vector Product

CXV_PRODUCT takes constant (A), and vector (B) of dimension (n), and returns vector (C) of the same dimension whose elements [1 ≤ k (1) m ≤ n] are scaled.

$$\mathbf{CXV\_PRODUCT}\ (A, \underline{B}, \underline{C}, k, m, n)$$

Equation 22.12-4

$$i \in [k(1)m] \Rightarrow c_i := a \cdot b_i$$

Equation 22.12-5

$$i \notin [k(1)m] \Rightarrow c_i := c_i$$

Equation 22.12-6

22.12.3 Vector Addition

V_ADD takes vectors (A) and (B) of dimension (n), and returns vector (C) whose elements [1 ≤ k (1) m ≤ n] are modified as follows.

$$\mathbf{V\_ADD}\left(\underline{A}, \underline{B}, \underline{C}, k, m, n\right)$$

Equation 22.12-7

$$i \in \left[k(1)m\right] \Rightarrow c_i := a_i + b_i$$

Equation 22.12-8

$$i \in \left\{\left[1(1)k\right[\cup \left]m(1)n\right]\right\} \Rightarrow c_i := c_i$$

Equation 22.12-9

22.12.4 Vector Cross Product

V_X_PRODUCT takes 3-vectors (A) and (B), and returns their vector cross product (C).

$$\mathbf{V\_X\_PRODUCT}\left(\underline{A}, \underline{B}, \underline{C}\right)$$

Equation 22.12-10

$$\underline{C} := \left(a_2 \cdot b_3 - a_3 \cdot b_2 \quad , \quad a_3 \cdot b_1 - a_1 \cdot b_3 \quad , \quad a_1 \cdot b_2 - a_2 \cdot b_1\right)^T$$

Equation 22.12-11

22.12.5 Scalar Product

V_DOT takes vectors (A) and (B) of dimension (n), and returns their scalar product (y) over the range [1 ≤ k (1) m ≤ n].

$$y := \mathbf{V\_DOT}\left(\underline{A}, \underline{B}, k, m, n\right) := \sum_{i:=k}^{m}\left(a_i \cdot b_i\right)$$

Equation 22.12-12

22.12.6 Vector Image

V_IMAGE takes vector (A) of dimension (n) and returns vector (B) whose elements [1 ≤ k (1) m ≤ n] are identical to those of vector (A).

$$\mathbf{V\_IMAGE}\left(\underline{A}, \underline{B}, k, m, n\right)$$

Equation 22.12-13

$$i \in \left[k(1)m\right] \Rightarrow b_i := a_i$$

Equation 22.12-14

$$i \notin \left[k(1)m\right] \Rightarrow b_i := b_i$$

Equation 22.12-15

22.12.7 Vector Magnitudes

V_MAG takes a 3-vector (A) returning its length (B), and its projected length on to the X-Y, Y-Z, and X-Z axes, (C), (D) and (E) respectively.

$$\mathbf{V\_MAG}\ (\underline{A}, B, C, D, E)$$

Equation 22.12-16

$$B := \sqrt{\sum_{i:=1}^{3} \left(a_i^2\right)}$$

Equation 22.12-17

$$(C, D, E) := \left(\sqrt{a_1^2 + a_2^2},\ \sqrt{a_2^2 + a_3^2},\ \sqrt{a_1^2 + a_3^2}\right)$$

Equation 22.12-18

22.12.8 Vector Spherical Magnitude

V_S_MAG takes a 3-vector (A), and returns its scalar length.

$$y := \mathbf{V\_S\_MAG}\ (\underline{A}) := \sqrt{\sum_{i:=1}^{3} \left(a_i^2\right)}$$

Equation 22.12-19

22.12.9 Vector X-Y Magnitude

V_H_MAG takes a 3-vector (A) with respect to a frame, and returns the scalar length of its projection onto the X-Y axes of that frame.

$$y := \mathbf{V\_H\_MAG}\ (\underline{A}) := \sqrt{a_1^2 + a_2^2}$$

Equation 22.12-20

22.12.10 Vector Y-Z Magnitude

V_R_MAG takes a 3-vector (A) with respect to a frame, and returns the scalar length of its projection onto the Y-Z axes of that frame.

$$y := \mathbf{V\_R\_MAG}\ (\underline{A}) := \sqrt{a_2^2 + a_3^2}$$

Equation 22.12-21

22.12.11 Vector X-Z Magnitude

V_V_MAG takes a 3-vector (A) with respect to a frame, and returns the scalar length of its projection onto the X-Z axes of that frame.

$$y \;:=\; \mathbf{V\_V\_MAG}\left(\underline{A}\right) \;:=\; \sqrt{a_1^2 + a_3^2}$$

Equation 22.12-22

22.12.12 Vector Negation

V_NEGATE takes vector (A) of dimension (n), and returns vector (B) the sign of whose elements [1 ≤ k (1) m ≤ n] have been reversed.

$$\mathbf{V\_NEGATE}\left(\underline{A}, \underline{B}, k, m, n\right)$$

Equation 22.12-23

$$i \in \left[k(1)m\right] \;\Rightarrow\; b_i \;:=\; -a_i$$

Equation 22.12-24

$$i \notin \left[k(1)m\right] \;\Rightarrow\; b_i \;:=\; b_i$$

Equation 22.12-25

22.12.13 Vector Subtraction

V_SUBTRACT takes vectors (A) and (B) of dimension (n) and returns real vector (C) whose elements [1 ≤ k (1) m ≤ n] are modified as follows.

$$\mathbf{V\_SUBTRACT}\left(\underline{A}, \underline{B}, \underline{C}, k, m, n\right)$$

Equation 22.12-26

$$i \in \left[k(1)m\right] \;\Rightarrow\; c_i \;:=\; a_i - b_i$$

Equation 22.12-27

$$i \notin \left[k(1)m\right] \;\Rightarrow\; c_i \;:=\; c_i$$

Equation 22.12-28

22.12.14 Vector Triple Product

V_3_PRODUCT takes vectors (A), (B) and (C) of dimension (n), and returns their scalar triple product over the range [1 ≤ k (1) m ≤ n].

$$y \;:=\; \mathbf{V\_3\_PRODUCT}\left(\underline{A}, \underline{B}, \underline{C}, k, m, n\right) \;:=\; \sum_{i:=k}^{m}\left(a_i \cdot b_i \cdot c_i\right)$$

Equation 22.12-29

22.12.15 Vector Zero

V_ZERO takes vector (A) of dimension (n), and returns the same vector with elements [1 ≤ k (1) m ≤ n] set to zero.

$$\mathbf{V\_ZERO}\left(\underline{A}, k, m, n\right)$$

Equation 22.12-30

$$i \in \left[k(1)m\right] \;\Rightarrow\; a_i \;:=\; 0$$

Equation 22.12-31

$$i \notin \left[k(1)m\right] \;\Rightarrow\; a_i \;:=\; a_i$$

Equation 22.12-32

22.12.16 Vector Summation

V_SUM takes vector (A) of dimension (n), and returns the sum of its elements [1 ≤ k (1) m ≤ n].

$$y \;:=\; \mathbf{V\_SUM}\left(\underline{A}, k, m, n\right) \;:=\; \sum_{i:=k}^{m}\left(a_i\right)$$

Equation 22.12-33

22.12.17 Vector Extraction from a Matrix

V_M_EXTRACT takes matrix [A(m,n)] and returns the row and column vectors (B) and (C) of dimension (n) and (m) identified by the indices (i) and (j) respectively where (i ∈ [1 (1) m]) and (j ∈ [1 (1) n]).

$$\mathbf{V\_M\_EXTRACT}\left(\left[A\right], \underline{B}, \underline{C}, i, j, m, n\right)$$

Equation 22.12-34

Row extraction,

$$\forall\, k \in \left[1(1)n\right] \;\Rightarrow\; b_k \;:=\; a_{i,k}$$

Equation 22.12-35

Column extraction,

$$\forall\, k \in [1(1)m] \;\Rightarrow\; c_k := a_{k,j}$$

Equation 22.12-36

22.12.18 Vector Insertion

V_INSERT takes vector (A) of dimension (i), and vector (B) of dimension (j), and returns (A) with the (B) inserted starting at the element (n) where $(n + j - 1 \le i)$.

$$\mathbf{V\_INSERT}\ (\underline{A}, \underline{B}, i, j, n)$$

Equation 22.12-37

$$i \in [1(1)j] \;\Rightarrow\; a(i + n - 1) := b(i)$$

Equation 22.12-38

22.12.19 Vector Extraction

V_EXTRACT takes vector (A) of dimension (i), and returns vector (B) of dimension (j) extracted from (A) starting at the element (n) where $(n + j - 1 \le i)$.

$$\mathbf{V\_EXTRACT}\ (\underline{A}, \underline{B}, i, j, n)$$

Equation 22.12-39

$$i \in [1(1)j] \;\Rightarrow\; b(i) := a(i + n - 1)$$

Equation 22.12-40

22.13 Covariance Extraction

22.13.1 Covariance Extraction and Statistics Controller

These utilities take an observer state and associated covariance, returning the state and guidance parameter uncertainties together with their statistics. The system state ($\underline{X}$) comprises target and missile reference vectors. The observer state vector has the same elements as the reference state vector.

To determine the rms error in the estimated value of a parameter (y) from the state covariances [C], express (y) as a function of the state vector,

$$y := \phi(\underline{X})$$

Equation 22.13-1

The error in the estimated value of (y) for small state errors is defined as a function of the error in the state vector, to the first order,

$$\delta y := \hat{y} - y := \left(\frac{\partial \phi(\underline{\hat{X}})}{\partial \underline{\hat{X}}} \right)^T \cdot \underline{\delta X} \qquad \text{where } \underline{\delta X} := \underline{\hat{X}} - \underline{X}$$

Equation 22.13-2

The expected error in (y) is then,

$$E(\delta y)^2 := \left(\frac{\partial \phi(\underline{\hat{X}})}{\partial \underline{\hat{X}}} \right)^T \cdot E\left(\underline{\delta X} \cdot \underline{\delta X}^T \right) \cdot \left(\frac{\partial \phi(\underline{\hat{X}})}{\partial \underline{\hat{X}}} \right)$$

Equation 22.13-3

Expressing this equation in elemental form,

$$E(\delta y)^2 := \sum_{i,j} \left(\frac{\partial \phi}{\partial \hat{X}_i} \cdot C_{i,j} \cdot \frac{\partial \phi}{\partial \hat{X}_j} \right)$$

Equation 22.13-4

Taking into account covariance matrix symmetry and scarcity in the Jacobians, the separate the auto-covariance and cross-covariance terms are,

$$(j \neq k) \vee (k > j) \Rightarrow E(\delta y)^2 :=$$

$$\sum_i \left(\left(\frac{\partial \phi}{\partial \hat{X}_i} \right)^2 \cdot C(i,i) \right) + 2 \cdot \sum_j \sum_k \left(\frac{\partial \phi}{\partial \hat{X}_j} \cdot C(j,k) \cdot \frac{\partial \phi}{\partial \hat{X}_k} \right)$$

Equation 22.13-5

This equation is implemented in *COV_SUM*. The uncertainty in commonly used tracking and guidance parameters is expressed in terms of the PVA state vectors, and associated covariances. Figure 22-15 shows two frames (B) and (C) located at point (a) rotating such that $\underline{X}^B$ passes through point (b), and $\underline{X}^C$ passes through the point (c). They both rotate independently with respect to the static frame (A) also located at point (a) the origin of all three frames.

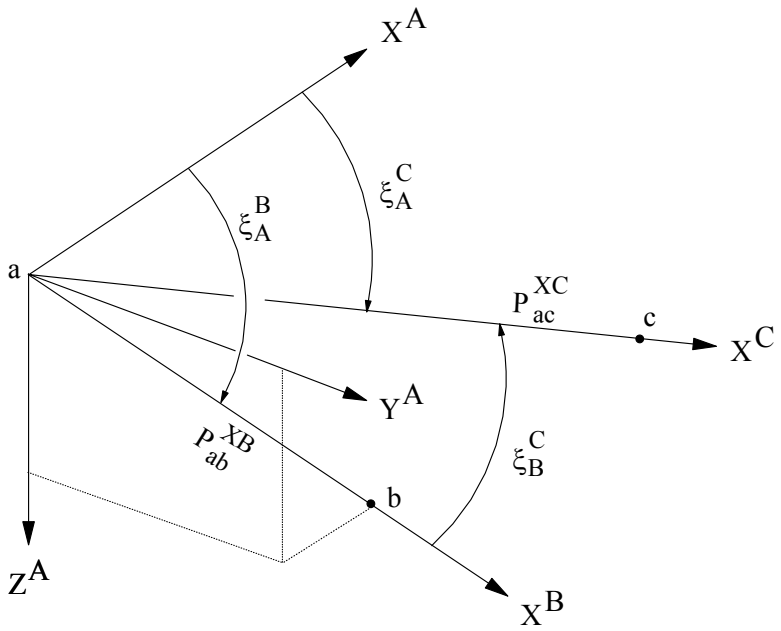

Figure 22-15 : Parameter Uncertainty – Frame Definitions

The following terms are used when defining generic uncertainty expressions in Cartesian PVA co-ordinates,

$$\left(\varphi_1 \quad , \quad \varphi_2 \right) \coloneqq \left(P_b^{XA} \cdot \dot{P}_b^{XA} + P_b^{YA} \cdot \dot{P}_b^{YA} \quad , \quad P_b^{XA} \cdot \dot{P}_b^{YA} - P_b^{YA} \cdot \dot{P}_b^{XA} \right)$$

Equation 22.13-6

$$\left(\dot{\varphi}_1 \quad , \quad \dot{\varphi}_2 \right) \coloneqq$$

$$\left(P_b^{XA} \cdot \ddot{P}_b^{XA} + P_b^{YA} \cdot \ddot{P}_b^{YA} + \left(\dot{P}_b^{hA} \right)^2 \quad , \quad P_b^{XA} \cdot \ddot{P}_b^{YA} - P_b^{YA} \cdot \ddot{P}_b^{XA} \right)$$

Equation 22.13-7

COV_CONTROL controls the computation of state vector errors, errors in parameters that are a function of the state vector, and (1σ,2σ,3σ) error statistics in respect of:

1 Target position $E\left(\underline{\delta P}_t^A \right)$

2 Target velocity $E\left(\underline{\delta \dot{P}}_t^A \right)$

3	Target acceleration	$E\left(\delta\underline{\ddot{P}}_t^A \right)$
4	Missile position	$E\left(\delta\underline{P}_m^A \right)$
5	Missile velocity	$E\left(\delta\underline{\dot{P}}_m^A \right)$
6	Missile acceleration	$E\left(\delta\underline{\ddot{P}}_m^A \right)$
7	Missile orientation with respect to the Alignment frame	$E\left(\delta E_A^B \right)$
8	Missile angular rate with respect to the Alignment frame	$E\left(\delta\underline{\omega}_{A,B}^B \right)$
9	Missile angular acceleration wrt the Alignment frame	$E\left(\delta\underline{\dot{\omega}}_{A,B}^B \right)$

Bits 1 to 9 of *ST_CV_EX* must be set to extract the above state uncertainties from the state observer. The following bits of *TP_CV_EX* must be set to obtain the uncertainty in the target parameters listed:

1	Target range with respect to the Alignment frame	$E\left(\delta P_{o,t} \right)$
2	Target range rate with respect to the Alignment frame	$E\left(\delta\dot{P}_t^{XT} \right)$
3	Target YP Euler angles with respect to the Alignment frame	$E\left(\delta E_A^T \right)$
4	Target LOS YP Euler rates wrt the Alignment frame	$E\left(\delta\dot{E}_A^T \right)$
6	Target velocity YP Euler angles wrt the Alignment frame	$E\left(\delta E_A^{TV} \right)$
7	Target velocity vector YP Euler rate wrt the Alignment frame	$E\left(\delta\dot{E}_A^{TV} \right)$
8	Target LOS angle with respect to the Alignment frame	$E\left(\delta\xi_A^T \right)$

The following bits of *MP_CV_EX* must be set to obtain the uncertainty in the missile parameters listed:

1	Missile range with respect to the Alignment frame	$E\left(\delta P_{o,m} \right)$
2	Missile range rate with respect to the Alignment frame	$E\left(\delta\dot{P}_m^{XM} \right)$
3	Missile YP Euler angles with respect to the Alignment frame	$E\left(\delta E_A^M \right)$
4	Missile YP Euler rates with respect to the Alignment frame	$E\left(\delta\dot{E}_A^M \right)$
6	Missile velocity YP Euler angles wrt the Alignment frame	$E\left(\delta E_A^{MV} \right)$
7	Missile velocity vector YP Euler rates	$E\left(\delta\dot{E}_A^{MV} \right)$
8	Missile LOS angle with respect to the Alignment frame	$E\left(\delta\xi_A^M \right)$

The following bits of *MT_CV_EX* must be set to obtain the uncertainty in the relative missile/target parameters listed:

1	Missile to target range	$E\left(\delta P_{m,t}\right)$
2	Missile to target range rate	$E\left(\delta \dot{P}_t^{XS}\right)$
3	Missile to target relative YP Euler angles	$E\left(\delta E_B^S\right)$
4	Missile to target relative YP Euler rates	$E\left(\delta \dot{E}_B^S\right)$
5	Target to Missile differential angle	$E\left(\delta \xi_T^M\right)$
6	Missile Body to Seeker angle	$E\left(\delta \xi_B^S\right)$

COV_STATS computes the (1σ,2σ,3σ) covariance statistics for each active parameter.

$$\text{COV\_STATS}\left({}_{REF}\underline{X}, {}_{SO}\underline{X}, [\,C\,], \text{STATS}, \text{ID}, \text{IR}\right)$$

Equation 22.13-8

The difference between the reference vector (${}_{REF}\underline{X}$) and the state observer estimate (${}_{SO}\underline{X}$) is determined. These errors are provided together with the percentage of them that fall within (1σ,2σ,3σ) of the expected error derived from the observer covariance matrix [C], returned in 3-vector *STATS*. If the reset flag *IR* changes from 0 to 1 the statistics associated with parameter *ID* are re-initialised, starting again when the flag returns to 0.

22.13.2 Quaternion to Euler Angle Variance Transformation

Missile orientation with respect to the earth is defined using quaternions. For interpretation purposes, quaternion covariances are converted into Euler angle uncertainties requiring the Euler Jacobians in *CV_QTE_COV*.

$$\frac{\partial \Phi_A^B}{\partial Q_A^B} := \frac{2 \cdot T_A^B(9)}{\left(T_A^B(8)\right)^2 + \left(T_A^B(9)\right)^2} \cdot \left(\begin{pmatrix} q_1 \\ q_0 \\ q_3 \\ q_2 \end{pmatrix} + \frac{2}{T_A^B(9)} \cdot \begin{pmatrix} 0 \\ q_1 \\ q_2 \\ 0 \end{pmatrix} \right)$$

Equation 22.13-9

$$\sqrt{1-\left[T_A^B(7)\right]^2} \cdot \partial \Theta_A^B / \partial Q_A^B := 2 \cdot \left(q_2 \;,\; -q_3 \;,\; q_0 \;,\; -q_1\right)^T$$

Equation 22.13-10

$$\frac{\partial \Psi_A^B}{\partial Q_A^B} := \frac{2 \cdot T_A^B(1)}{\left(T_A^B(1)\right)^2 + \left(T_A^B(4)\right)^2} \cdot \left(\begin{pmatrix} q_3 \\ q_2 \\ q_1 \\ q_0 \end{pmatrix} + \frac{2}{T_A^B(1)} \cdot \begin{pmatrix} 0 \\ 0 \\ q_2 \\ q_3 \end{pmatrix} \right)$$

Equation 22.13-11

22.13.3 Range Uncertainty

CV_PX_BAB returns the range uncertainty of point (b),

$$E\left(\delta P_{a,b}\right)^2 := \left(\frac{\partial P_{a,b}}{\partial \underline{P}_b^A}\right)^T \cdot E\left(\underline{\delta P}_b^A \cdot \left(\underline{\delta P}_b^A\right)^T\right) \cdot \left(\frac{\partial P_{a,b}}{\partial \underline{P}_b^A}\right)$$

Equation 22.13-12

$$P_{a,b} \cdot \partial P_{a,b} \,/\, \partial \underline{P}_b^A := \underline{P}_b^A$$

Equation 22.13-13

The target and missile range uncertainties,

$$E\left(\delta P_{o,t}\right) := \textbf{CV\_PX\_BAB}\left({}_{SO}\underline{X}_{TL}, {}_{SO}C_{TLL}, 9\right)$$

Equation 22.13-14

$$E\left(\delta P_{o,m}\right) := \textbf{CV\_PX\_BAB}\left({}_{SO}\underline{X}_{ML}, {}_{SO}C_{MLL}, 9\right)$$

Equation 22.13-15

22.13.4 Range Rate Uncertainty

CV_VX_BAB returns the range rate uncertainty of point (b),

$$E\left(\delta \dot{P}_b^{XB}\right)^2 := \left(\frac{\partial \dot{P}_b^{XB}}{\partial \underline{X}_{PV}}\right)^T \cdot E\left(\underline{\delta X}_{PV} \cdot \left(\underline{\delta X}_{PV}\right)^T\right) \cdot \left(\frac{\partial \dot{P}_b^{XB}}{\partial \underline{X}_{PV}}\right)$$

Equation 22.13-16

$$P_{a,b} \cdot \frac{\partial \dot{P}_b^{XB}}{\partial \underline{X}_{PV}} := \left(\left(\dot{\underline{P}}_b^A \cdot \left(1 - \left(\frac{\underline{P}_b^A}{P_{a,b}}\right)^2\right)\right)^T , \left(\frac{\underline{P}_b^A}{P_{a,b}}\right)^T \right)^T$$

Equation 22.13-17

The target and missile range rate uncertainty with respect to the Alignment frame,

$$E\left(\delta\dot{P}_t^{XT}\right) := \textbf{CV\_VX\_BAB}\left({}_{SO}\underline{X}_{TL}, {}_{SO}C_{TLL}, 9\right)$$

Equation 22.13-18

$$E\left(\delta\dot{P}_m^{XM}\right) := \textbf{CV\_VX\_BAB}\left({}_{SO}\underline{X}_{ML}, {}_{SO}C_{MLL}, 9\right)$$

Equation 22.13-19

22.13.5 Yaw Angle Uncertainty

CV_PSI_AB returns the yaw angle uncertainty of frame (B).

$$E\left(\delta\Psi_A^B\right)^2 := \left(\frac{\partial\Psi_A^B}{\partial\underline{P}_b^A}\right)^T \cdot E\left(\underline{\delta P}_b^A \cdot \left(\underline{\delta P}_b^A\right)^T\right) \cdot \left(\frac{\partial\Psi_A^B}{\partial\underline{P}_b^A}\right) \cdot c^2\,\Theta_A^B$$

Equation 22.13-20

$$P_b^{hA} \cdot P_{a,b} \cdot \cos\Theta_A^B \cdot \partial\Psi_A^B \,/\, \partial\underline{P}_b^A := \left(-P_b^{YA}, \; P_b^{XA}, \; 0\right)^T$$

Equation 22.13-21

The target and missile azimuth angle uncertainties,

$$E\left(\delta\Psi_A^T\right) := \textbf{CV\_PSI\_AB}\left({}_{SO}\underline{X}_{TL}, {}_{SO}C_{TLL}, 9\right)$$

Equation 22.13-22

$$E\left(\delta\Psi_A^M\right) := \textbf{CV\_PSI\_AB}\left({}_{SO}\underline{X}_{ML}, {}_{SO}C_{MLL}, 9\right)$$

Equation 22.13-23

22.13.6 Pitch Angle Uncertainty

CV_THT_AB returns the pitch angle uncertainty of frame (B).

$$E\left(\delta\Theta_A^B\right)^2 := \left(\frac{\partial\Theta_A^B}{\partial\underline{P}_b^A}\right)^T \cdot E\left(\underline{\delta P}_b^A \cdot \left(\underline{\delta P}_b^A\right)^T\right) \cdot \left(\frac{\partial\Theta_A^B}{\partial\underline{P}_b^A}\right)$$

Equation 22.13-24

$$P_{a,b}^2 \cdot \partial\Theta_A^B \,/\, \partial\underline{P}_b^A = \left(P_b^{XA} \cdot P_b^{ZA} \,/\, P_b^{hA}, \; P_b^{YA} \cdot P_b^{ZA} \,/\, P_b^{hA}, \; -P_b^{hA}\right)^T$$

Equation 22.13-25

The target and missile elevation uncertainties,

$$E\left(\delta\Theta_A^T\right) := \textbf{CV\_THT\_AB}\left({}_{SO}\underline{X}_{TL}, {}_{SO}C_{TLL}, 9\right)$$

Equation 22.13-26

$$E\left(\delta\Theta_A^M\right) := \textbf{CV\_THT\_AB}\left({}_{SO}\underline{X}_{ML}, {}_{SO}C_{MLL}, 9\right)$$

Equation 22.13-27

22.13.7 Velocity Yaw Angle Uncertainty

CV_PSI_AV returns the velocity yaw angle uncertainty at point (b).

$$E\left(\delta\Psi_A^V\right)^2 := \left(\frac{\partial\Psi_A^V}{\partial\underline{\dot{P}}_b^A}\right)^T \cdot E\left(\underline{\delta\dot{P}}_b^A \cdot \left(\underline{\delta\dot{P}}_b^A\right)^T\right) \cdot \left(\frac{\partial\Psi_A^V}{\partial\underline{\dot{P}}_b^A}\right) \cdot c^2\,\Theta_A^V$$

Equation 22.13-28

The Jacobian is given by Equation 22.13-21 replacing the position vector with the relative velocity vector. The target and missile velocity azimuth angle uncertainties,

$$E\left(\delta\Psi_A^{TV}\right) := \textbf{CV\_PSI\_AB}\left({}_{SO}\underline{X}_{TL}, {}_{SO}C_{TLL}, 9\right)$$

Equation 22.13-29

$$E\left(\delta\Psi_A^{MV}\right) := \textbf{CV\_PSI\_AB}\left({}_{SO}\underline{X}_{ML}, {}_{SO}C_{MLL}, 9\right)$$

Equation 22.13-30

22.13.8 Velocity Pitch Angle Uncertainty

CV_THT_AV returns the velocity pitch angle uncertainty at point (b).

$$E\left(\delta\Theta_A^V\right)^2 := \left(\frac{\partial\Theta_A^V}{\partial\underline{\dot{P}}_b^A}\right)^T \cdot E\left(\underline{\delta\dot{P}}_b^A \cdot \left(\underline{\delta\dot{P}}_b^A\right)^T\right) \cdot \left(\frac{\partial\Theta_A^V}{\partial\underline{\dot{P}}_b^A}\right)$$

Equation 22.13-31

The Jacobian is given by Equation 22.13-25 replacing the position vector with the relative velocity vector. The target and missile velocity pitch uncertainties,

$$E\left(\delta\Theta_A^{TV}\right) := \textbf{CV\_THT\_AV}\left({}_{SO}\underline{X}_{TL}, {}_{SO}C_{TLL}, 9\right)$$

Equation 22.13-32

$$E\left(\delta\Theta_A^{MV}\right) := \textbf{CV\_THT\_AV}\left({}_{SO}\underline{X}_{ML}, {}_{SO}C_{MLL}, 9\right)$$

Equation 22.13-33

22.13.9 Yaw Rate Uncertainty

CV_DPSI_AB returns the angular yaw rate uncertainty of frame (B).

$$E\left(\delta\dot{\Psi}_A^B\right)^2 := \left(\frac{\partial\dot{\Psi}_A^B}{\partial\underline{X}_{PV}}\right)^T \cdot E\left(\underline{\delta X}_{PV}\cdot\left(\underline{\delta X}_{PV}\right)^T\right)\cdot\left(\frac{\partial\dot{\Psi}_A^B}{\partial\underline{X}_{PV}}\right)\cdot c^2\,\Theta_A^B$$

Equation 22.13-34

$$\dot{P}_b^{hA}\cdot\dot{P}_{a,b}\cdot\partial\dot{\Psi}_A^B\,/\,\partial\underline{X}_{PV} :=$$

$$\begin{pmatrix}\left(\dot{P}_b^{YA}-2\cdot P_b^{XA}\cdot\dot{\Psi}_A^B \quad,\quad -\dot{P}_b^{XA}-2\cdot P_b^{YA}\cdot\dot{\Psi}_A^B \quad,\quad 0\right)^T\\ \cdots\\ \left(-P_b^{YA}\quad,\quad P_b^{XA}\quad,\quad 0\right)^T\end{pmatrix}$$

Equation 22.13-35

The target and missile sight-line azimuth angular rates,

$$E\left(\delta\dot{\Psi}_A^T\right) := \textbf{CV\_DPSI\_AB}\left({}_{SO}\underline{X}_{TL},\,{}_{SO}C_{TLL},9\right)$$

Equation 22.13-36

$$E\left(\delta\dot{\Psi}_A^M\right) := \textbf{CV\_DPSI\_AB}\left({}_{SO}\underline{X}_{ML},\,C_{MLL},9\right)$$

Equation 22.13-37

22.13.10 Pitch Rate Uncertainty

CV_DTHT_AB returns the pitch rate uncertainty of frame (B).

$$E\left(\delta\dot{\Theta}_A^B\right)^2 := \left(\frac{\partial\dot{\Theta}_A^B}{\partial\underline{X}_{PV}}\right)^T \cdot E\left(\underline{\delta X}_{PV}\cdot\left(\underline{\delta X}_{PV}\right)^T\right)\cdot\left(\frac{\partial\dot{\Theta}_A^B}{\partial\underline{X}_{PV}}\right)$$

Equation 22.13-38

$$P_b^{hA}\cdot P_{a,b}^2\cdot\partial\dot{\Theta}_A^B\,/\,\partial\underline{X}_{PV} :=$$

$$\begin{pmatrix}\left(\xi_1\quad,\quad\xi_2\quad,\quad\varphi_1\right)^T-2\cdot\dot{\Theta}_A^B\cdot P_b^{hA}\cdot\underline{P}_b^A\\ \cdots\\ \left(-P_b^{XA}\cdot P_b^{ZA}\quad,\quad P_b^{YA}\cdot P_b^{ZA}\quad,\quad-\left(P_b^{hA}\right)^2\right)^T\end{pmatrix}$$

Equation 22.13-39

$$\xi_1 := \dot{P}_b^{XA} \cdot P_b^{ZA} - P_b^{XA} \cdot \dot{P}_b^{ZA} - \varphi_1 \cdot P_b^{XA} \cdot P_b^{ZA} \cdot \left(P_b^{hA} \right)^{-2}$$

Equation 22.13-40

$$\xi_2 := \dot{P}_b^{YA} \cdot P_b^{ZA} - P_b^{YA} \cdot \dot{P}_b^{ZA} - \varphi_1 \cdot P_b^{YA} \cdot P_b^{ZA} \cdot \left(P_b^{hA} \right)^{-2}$$

Equation 22.13-41

The target and missile pitch rate uncertainties.

$$E\left(\delta\dot{\Theta}_A^T \right) := \textbf{CV\_DTHT\_AB} \left({}_{SO}\underline{X}_{TL} , {}_{SO}C_{TLL} , 9 \right)$$

Equation 22.13-42

$$E\left(\delta\dot{\Theta}_A^M \right) := \textbf{CV\_DTHT\_AB} \left({}_{SO}\underline{X}_{ML} , {}_{SO}C_{MLL} , 9 \right)$$

Equation 22.13-43

22.13.11 Differential Angle Uncertainty

The elevation and azimuth errors are combined to determine the expected pointing error whose generic form is,

$$E\left(\delta\xi_A^B \right)^2 := \left(\frac{\partial \xi_A^B}{\partial \underline{P}_b^A} \right)^T \cdot E\left(\underline{\delta P}_b^A \cdot \left(\underline{\delta P}_b^A \right)^T \right) \cdot \left(\frac{\partial \xi_A^B}{\partial \underline{P}_b^A} \right)$$

Equation 22.13-44

When using the individual Euler angles the cross-correlation terms must be taken into account whose expected value is determined from,

$$E\left(\delta\Theta_A^B , \delta\Psi_A^B \right) :=$$

$$\left(\left(\frac{\partial \Theta_A^B}{\partial \underline{P}_b^A} \right)^T \cdot E\left(\underline{\delta P}_b^A \cdot \left(\underline{\delta P}_b^A \right)^T \right) \cdot \left(\frac{\partial \Psi_A^B}{\partial \underline{P}_b^A} \right) \right) \cdot \cos\Theta_A^B$$

Equation 22.13-45

The estimated pointing error is then determined from the quadratic form,

$$A \equiv \begin{bmatrix} \sigma_\Theta^2 & \vdots & \sigma_{\Theta\Psi} \\ \cdots & \vdots & \cdots \\ \sigma_{\Psi\Theta} & \vdots & \sigma_\Psi^2 \end{bmatrix} := \begin{bmatrix} E\left(\delta\Theta_A^B \right)^2 & \vdots & E\left(\delta\Theta_A^B , \delta\Psi_A^B \right) \\ \cdots & \vdots & \cdots \\ E\left(\delta\Psi_A^B , \delta\Theta_A^B \right) & \vdots & E\left(\delta\Psi_A^B \right)^2 \end{bmatrix}$$

Equation 22.13-46

The estimated angular error is bounded by,

$$\max E\left(\delta\xi_A^B\right)^2 \;:=\; 2\cdot\max\left(\sigma_\Theta^2 \;,\; \sigma_\Psi^2\right)$$

Equation 22.13-47

To account for the cross-correlation term [A] is diagonalised, eigenvalues (λ_1 , λ_2) being the major and minor axes of the resulting uncertainty ellipse.

$$\left\| A - \lambda\cdot I_3 \right\| \;:=\; 0$$

Equation 22.13-48

$$\left(\sigma_\Theta^2-\lambda\right)\cdot\left(\sigma_\Psi^2-\lambda\right) - \sigma_{\Theta\Psi}^2 \;:=\; 0$$

Equation 22.13-49

$$\lambda^2-\lambda\cdot\left(\sigma_\Theta^2+\sigma_\Psi^2\right)+\left(\sigma_\Theta^2\cdot\sigma_\Theta^2-\sigma_{\Theta\Psi}^2\right) \;:=\; 0$$

Equation 22.13-50

$$2\cdot\left(\lambda_1 \;,\; \lambda_2\right) \;:=$$

$$\left(\sigma_\Theta^2+\sigma_\Psi^2\right)\pm\sqrt{\left(\sigma_\Theta^2+\sigma_\Psi^2\right)^2-4\cdot\left(\sigma_\Theta^2\cdot\sigma_\Psi^2-\sigma_{\Theta\Psi}^2\right)}$$

Equation 22.13-51

The estimated pointing error is the spectral radius of this quadratic form,

$$E\left(\delta\xi_A^B\right)^2 \;:=\; \rho\left(A\right) \;:=\; \max\left(\left|\lambda_1\right|,\left|\lambda_2\right|\right)$$

Equation 22.13-52

Since by definition the square root has only positive arguments,

$$2\cdot E\left(\delta\xi_A^B\right)^2 \;:=\; \sigma_\Theta^2+\sigma_\Psi^2+\sqrt{\left(\sigma_\Theta^2-\sigma_\Psi^2\right)^2-4\cdot\sigma_{\Theta\Psi}^2}$$

Equation 22.13-53

When the eigenvalues are different the spectral radius is a pessimistic estimate of the pointing error and the CEP defined in §22.13.17 should be used,

$$E\left(\delta\xi_A^B\right)^2 \;:=\; -2\cdot\sqrt{\lambda_1\cdot\lambda_2}\cdot\log_e\left(1-\mathrm{pr}\left(\delta\xi_C^{MD}\in\left[0\,,E\left(\delta\xi_C^{MD}\right)\right]\right)\right)$$

Equation 22.13-54

From Figure 22-16, if the true error is less than the expected pointing error 997 times in 1000 samples then pr(…) := 0.997 and,

$$E\left(\delta\xi_A^B\right)^2 \;:=\; 3.41^2 \cdot \sqrt{\lambda_1 \cdot \lambda_2} \;:=\; 3.41^2 \cdot \sqrt{\sigma_\Theta^2 \cdot \sigma_\Psi^2 - \sigma_{\Theta\Psi}^2}$$

Equation 22.13-55

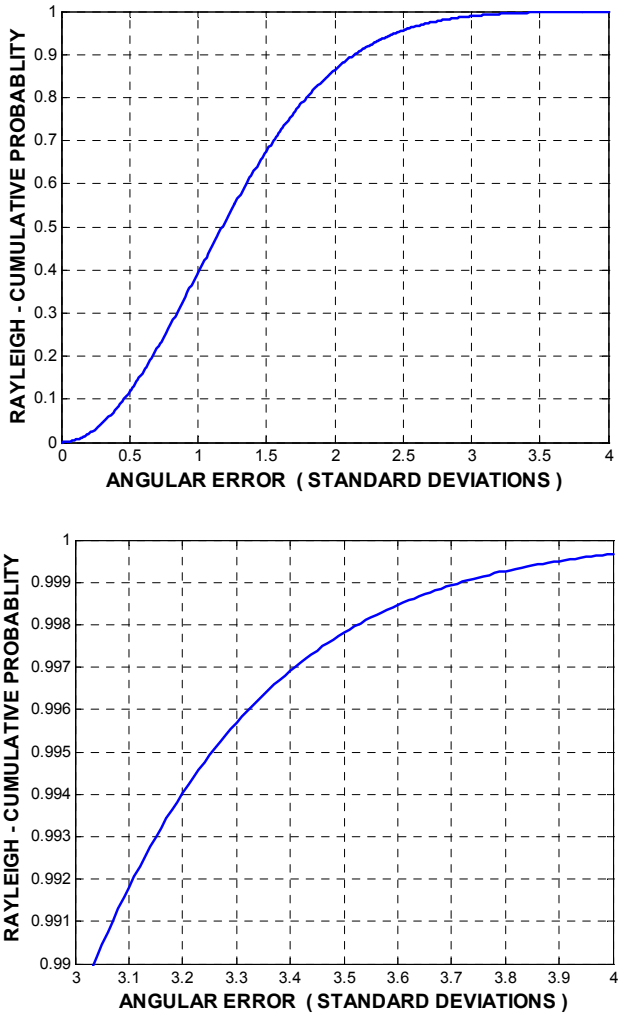

Figure 22-16

Rayleigh Cumulative Probability vs Standard Deviation

When determining the differential angular error for small angles,

$$E\left(\delta\xi_B^C\right)^2 \;\cong\; E\left(\delta\xi_A^B\right)^2 + E\left(\delta\xi_A^C\right)^2$$

Equation 22.13-56

22.13.12 Polar to Cartesian Covariance Conversion

COV_P_TO_C takes the range from point (a) to point (b), and the YP Euler angles defining the orientation of frame (B) with respect to frame (A), and their uncertainties, returning a [3x3] covariance matrix with respect to (A).

$$\mathbf{COV\_P\_TO\_C}\left(P_{a,b}, \Theta_A^B, \Psi_A^B, \sigma_R, \sigma_\Theta, \sigma_\Psi, [\sigma_C] \right)$$

Equation 22.13-57

$$\sigma_C(1) := \left(\sigma_R^2 \cdot c^2\Psi_A^B + P_{a,b}^2 \cdot \sigma_\Psi^2 \cdot s^2\Psi_A^B \right) \cdot c^2\Theta_A^B + P_{a,b}^2 \cdot \sigma_\Theta^2 \cdot c^2\Psi_A^B \cdot s^2\Theta_A^B$$

Equation 22.13-58

$$\sigma_C(4) := \left(\left(\sigma_R^2 - P_{a,b}^2 \cdot \sigma_\Psi^2 \right) \cdot c^2\Theta_A^B + P_{a,b}^2 \cdot \sigma_\Theta^2 \cdot s^2\Theta_A^B \right) \cdot c\Psi_A^B \cdot s\Psi_A^B$$

Equation 22.13-59

$$\sigma_C(7) := \left(P_{a,b}^2 \cdot \sigma_\Theta^2 - \sigma_R^2 \right) \cdot \cos\Theta_A^B \cdot \sin\Theta_A^B \cdot \cos\Psi_A^B$$

Equation 22.13-60

$$\sigma_C(5) := \left(\sigma_R^2 \cdot s^2\Psi_A^B + P_{a,b}^2 \cdot \sigma_\Psi^2 \cdot c^2\Psi_A^B \right) \cdot c^2\Theta_A^B + P_{a,b}^2 \cdot \sigma_\Theta^2 \cdot s^2\Theta_A^B \cdot s^2\Psi_A^B$$

Equation 22.13-61

$$\sigma_C(8) := \left(P_{a,b}^2 \cdot \sigma_\Theta^2 - \sigma_R^2 \right) \cdot \cos\Theta_A^B \cdot \sin\Theta_A^B \cdot \sin\Psi_A^B$$

Equation 22.13-62

$$\sigma_C(9) := \sigma_R^2 \cdot \sin^2\Theta_A^B + P_{a,b}^2 \cdot \sigma_\Theta^2 \cdot \cos^2\Theta_A^B$$

Equation 22.13-63

22.13.13 Covariance Matrix Main Diagonal Extraction

M_EXTDIAG takes a covariance matrix [C] of dimension (n) and returns the state uncertainties from its main diagonal in vector (U).

$$\mathbf{M\_EXTDIAG}\left([C], \underline{U}, n \right)$$

Equation 22.13-64

$$i \in [1(1)n] : \left\{ \begin{array}{c} C(i,i) > 10^{-8} \Rightarrow U(i) := \sqrt{C(i,i)} \\ \\ C(i,i) \le 10^{-8} \Rightarrow U(i) := 0 \end{array} \right\}$$

Equation 22.13-65

22.13.14 Covariance Matrix Eigenvalue Metric

EIGEN_METRIC uses *EIGEN* to obtain eigenvalues and eigenvectors of a covariance matric [C], returning the following state metric.

$$y := \textbf{EIGEN\_METRIC}\left([C], n, k \right)$$

Equation 22.13-66

$$(i, j) \in [1(1)n] \Rightarrow \varphi := \frac{C(i, j)}{\sqrt{C(i, i) \cdot C(j, j)}}$$

Equation 22.13-67

$$C_N := n \cdot \varphi / \operatorname{trace}(\varphi)$$

Equation 22.13-68

$$N_C < 30 \Rightarrow y := \lambda_{max}(C_N) / \lambda_{min}(C_N)$$

Equation 22.13-69

$$N_C \geq 30 \Rightarrow y := 0$$

Equation 22.13-70

(λ_{MAX} , λ_{MIN}) are the maximum and minimum eigenvalues. (N_C) is the number of iterations taken by the *EIGEN* to complete the annihilation of the off-diagonal terms in the covariance matrix. Care should be exercised if the number of iterations required for annihilation (k := 30).

22.13.15 Covariance Tracking Metric

STATE_METRIC takes covariance matrix [C] of rank (n), the estimated and actual state vectors, returning the Chi-squared tracking accuracy metric.

$$y := \textbf{STATE\_METRIC}\left(\underline{\hat{X}}, \underline{X}, [C], n, k \right)$$

Equation 22.13-71

$$k = 0 \Rightarrow y := \prod_{i:=1}^{n} \left(\frac{\left| \hat{X}(i) - X(i) \right|}{\sqrt{C(i, i)}} \right)$$

Equation 22.13-72

$$k = 1 \Rightarrow y := \sqrt{\left(\underline{\hat{X}} - \underline{X} \right)^T \cdot [C]^{-1} \cdot \left(\underline{\hat{X}} - \underline{X} \right)}$$

Equation 22.13-73

22.13.16 Mahalanobis Distance Metric

FF_D_METRIC takes the measurement residual (n)-vector ($\underline{Z}$), and the expected measurement uncertainty matrix [A], terms defined in §4.4, and returns the Mahalanobis distance metric, Pao[P.8],

$$y := \mathbf{FF\_D\_METRIC}\left(\underline{\Delta Z}, [A], n\right)$$

Equation 22.13-74

$$y := \sqrt{\underline{\Delta Z}^{T} \cdot [A]^{-1} \cdot \underline{\Delta Z}}$$

Equation 22.13-75

22.13.17 Circular Error Probable (CEP) Metric

Although elliptical distributions defined by orthogonal state uncertainties (σ_x,σ_y) are often encountered, the selection of a single performance metric is not so easily identified. The Circular Error Probable (CEP) metric is often used in such cases which is defined as the value from a radial distribution containing 50% of the errors. Consider two random variables (x,y) from a Normal distribution with a zero mean and a standard deviation of (σ). The pdf associated with such random variables is,

$$f(x,y) := \left(\frac{1}{2\cdot\pi\cdot\sigma^2}\right)\cdot \exp\left(-\frac{x^2+y^2}{2\cdot\sigma^2}\right)$$

Equation 22-76

Integrating gives the cumulative pdf,

$$p(x,y) := \left(\frac{1}{2\cdot\pi\cdot\sigma^2}\right)\cdot \int_0^X \int_0^Y \exp\left(-\frac{x^2+y^2}{2\cdot\sigma^2}\right)\cdot dx\cdot dy$$

Equation 22-77

In polar co-ordinates,

$$p(r) := \left(\frac{1}{2\cdot\pi\cdot\sigma^2}\right)\cdot \int_0^R \int_0^{2\cdot\pi} r\cdot\exp\left(-\frac{r^2}{2\cdot\sigma^2}\right)\cdot dr\cdot d\vartheta$$

Equation 22-78

$$p(r) := \frac{1}{\sigma^2}\cdot\int_0^R r\cdot\exp\left(-\frac{r^2}{2\cdot\sigma^2}\right)dr := 1-\exp\left(-\frac{R^2}{2\cdot\sigma^2}\right)$$

Equation 22-79

The radial distance (R) given the probability that a random variable (r) lies in the range [0,R] is thus,

$$R := \sqrt{-2\cdot\sigma^2\cdot\log_e\left(1-p\left(r\in[0,R]\right)\right)}$$

Equation 22-80

The CEP is defined by,

$$\text{CEP} \equiv p(0.5) := 1.177 \cdot \sigma$$

Equation 22-81

Module *CEP_METRIC* takes 2 orthogonal uncertainties and the probability that a random variable (r) lies in the range [0,R] and returns the CEP value,

$$y := \textbf{CEP\_METRIC}\left(\sigma, p, \text{CEP}\right)$$

Equation 22-82